

VRIJE UNIVERSITEIT BRUSSEL

DOCTORAL THESIS

**Investigation of the precursor phase of
gamma-ray bursts through gamma-ray and
high-energy neutrino observations**

Author:
Paul COPPIN

Promoter:
Prof. Dr. Nick VAN EIJDHOVEN

Co-promoter:
Prof. Dr. Krijn DE VRIES

*A thesis submitted in fulfillment of the requirements
for the degree of Doctor of Philosophy*

in the

Sciences & Bioengineering Sciences
Department of Physics and Astronomy
Inter-University Institute for High Energies

April, 2022

DOCTORAL EXAMINATION COMMISSION:

Chair: Prof. Dr. Jorgen D'Hondt
Inter-University Institute for High Energies – Vrije Universiteit Brussel

Secretary: Prof. Dr. Sophie De Buyl
Applied Physics Research Group – Vrije Universiteit Brussel

Promotor: Prof. Dr. Nick van Eijndhoven
Inter-University Institute for High Energies – Vrije Universiteit Brussel

Co-promotor: Prof. Dr. Krijn De Vries
Inter-University Institute for High Energies – Vrije Universiteit Brussel

Prof. Dr. Frank De Proft
Department of Chemistry – Vrije Universiteit Brussel

Prof. Dr. Markus Ahlers
Niels Bohr Institute – University of Copenhagen

Prof. Dr. Simona Toscano
Inter-University Institute for High Energies – Université Libre de Bruxelles

Prof. Dr. Gwenhaël de Wasseige
Institut de Recherche en Mathématique et Physique – Université Catholique de Louvain

Prof. Dr. Kumiko Kotera
*Institut d'Astrophysique de Paris – Université Pierre-et-Marie-Curie
and Department of Physics and Astronomy– Vrije Universiteit Brussel*

© 2022 PAUL COPPIN

All rights reserved. No parts of this book may be reproduced or transmitted in any form or by any means, electronic, mechanical, photocopying, recording, or otherwise, without prior written permission of the author.

Credit cover art: DESY, Science Communication Lab

Acknowledgements

At the time of writing, the final chapter has just been penned down. In other words, an ideal moment to take a step back, look at the whole output of just over four years of work, and reflect on how I managed to get here. Thinking about this a little, there are many memories that come to mind. One key aspect they all have in common. The journey that led me here was not a solitary one. Whenever paths were diverging, the road was not very visible, or I was just going about everyday tasks, there were colleagues, family, and friends to stand by my side. It is a certainty that the work presented here could not have been achieved without them. I therefore am extremely grateful to all of you! It feels as if any attempt to acknowledge how this work was shaped by your contributions will certainly do you injustice. Therefore, please consider this section to be at most a feeble representation of my true gratitude towards you.

To start, I will consider the advice written in the acknowledgment file of the L^AT_EX template used to format this thesis, which stated: “Don’t forget to include your project advisor!”. My first encounter with Nick already dates back quite a while, to when I was only a bachelor student. When attending the bachelor thesis presentations of my fellow students, I noticed that the two topics which most spiked my interest had both been performed in Nick’s IceCube group. One year later, this led me to ask Nick if I could perform my master thesis under his guidance. A decision which turned out so well that two years later, I was extremely pleased to also start my PhD with Nick as my advisor. Scroll forward a couple years and here we are. Aside from getting a little bit older, those years have allowed me to learn and pick up a lot of things from you. Science often relies on someone asking the right question and it seems to me that you somehow have an almost intuitive instinct for doing this. Whether it considered gamma-ray bursts, a project of the bachelor/master students, or something else entirely, you were always available to discuss any matter and open to our views of the situation. You also created a very warm research atmosphere. This made it truly a pleasure to be part of your research group.

Secondly, I very much want to thank Krijn for being an excellent co-supervisor. During our cycles between Hoeilaart and work, we touched upon many important topics. Who would win the next battle between Wout van Aert and Mathieu van der Poel, what the Tour de France would be like this year, and much more. Surprisingly, we sometimes also had time for physics. In fact, while cycling through the Sonian Forest is probably when we had many of our most interesting conversations. On finishing my PhD and moving on to a new opportunity somewhere else, this is one of the things that I will most definitely miss. Nevertheless, what you and Nick taught me will allow travel with me :)

As already previously hinted at, I have not only been blessed with my supervisors, but also with an amazing set of colleagues at the IIHE. Key to every new arrival at the institute was a warm welcome by Marleen. Albeit it for a well-earned retirement, that does not mean that I was any less sad to see you leave halfway through my PhD. Moving on to my fellow PhD students and postdocs, they also were particularly brilliant. Sure, we probably had discussions about physics at some point, but what I’ll remember were the friendships that were made. Going for a stroll through the Brussels Christmas market with a cup of glühwein, taking a paddle boat and some kayaks onto one of the lakes of Madison, ordering in pizza at the IIHE after work before going to see the new Star Wars movie, being caught by ~10 of you after doing a superman dive through ropes (long story), staying until 4 in the morning at Nadège’s wedding, and also simply having an afternoon coffee break in the IIHE kitchen with a piece of cake and a cup of tea. We truly did have a wonderful time together! Special thanks also go out to Pablo. Sharing an office with me cannot always have been

easy, with me kicking you at least every other day when I stretched my long legs, the smell of drying MTB cloths after a rainy cycle into work, and me overheating at any temperature above 20 degrees. Yet, we somehow always had a bloody good time together. I'll miss you buddy, all of you!

During my PhD, I not only gained many friends in the IIHE, but also internationally through conferences, summer schools, and the IceCube Collaboration. Many names again come to mind, but inside IceCube, I particularly want to thank Liz and Kunal. We all started our PhD roughly at the same time, all working on GRB searches within IceCube. While one could naturally expect this to induce a certain tension, wanting to perform 'competing analyses' as people sometimes called it, that was never an issue and never how we viewed it. Aside from each performing tasks that benefited the other two, we also were wonderfully well able to work together on things like combined conference proceedings. Even now, we are laying the finishing touches to a single paper that presents the results of our analyses. Thank you for this experience. It was truly a great pleasure to work together with the two of you. Inside IceCube, I also want to thank all the people that contributed to shaping my analysis. A lot of credit goes to Mike Richman. Not only for developing the *csky* analysis software used in this thesis, but also for the many interesting conversations on the best ways to implement new features, and for helping me debug my attempted implementation of those features on many instances. A thousand thanks also to everyone who provided helpful comments. In particular, I want to express my gratitude to all internal and external reviewers of the analysis, conference proceedings, and papers. Thanks you for so strenuously going through this esoteric matter, for taking the time to go over and verify minor details, and for often doing this recursively over many iterations.

A wise person once told me that, a key point about doing a PhD is having a strong support network. After all, writing a stellar thesis is not of much use if one loses their sanity in the process. This became especially relevant due to the COVID pandemic, which struck roughly halfway through my PhD. Virtual meetings and working from home everyday very suddenly replaced the merry in-person contacts described above. I'm really glad that through virtual coffee breaks, walks in the forest, and many other arrangements, we managed to stay close regardless. In particular, I would like to thank Rose. You have been an amazing friend throughout this whole period. Afternoon tea, cycles and home office have given me plentiful great memories to reminisce on during an otherwise often dreary year. Suffice it to say that, in this short period, you have gained yourself my friendship for life! Finally, I want to end this acknowledgement by thanking the people who have always been there for me, my parents and sister in particular. Thank you for supporting me in my pursuit of scientific knowledge. I realize that my expounds on 'what I was doing' were often quite hard to follow. Therefore, I am all the more grateful that you kept taking an interest and inquiring about my work. This document here is the final result of all that hard work. I fear that it might not be that enlightening to non-physicists, but as you know, you can always just ask me in person what all this stuff about GRBs actually means ;)

Summary

In the 1960s, during the cold war, the United States launched several satellites to verify that no nuclear bomb tests were secretly being performed in outer space. These satellites featured detectors designed to pick up the short flashes of highly-energetic light, called gamma-rays, produced in such explosions. After a couple of years of operation, as more sensitive and advanced satellites were being deployed, the detectors did sporadically begin to pick up gamma-ray signals. However, it soon became clear that the triggers were not caused by nuclear bomb tests, but by some unknown astrophysical phenomena. These events were accordingly named gamma-ray bursts (GRBs).

Much has since been learned about the nature of GRBs. They are now known to be extragalactic events, occurring at cosmological distances. Their huge brightness implies that GRBs are among the most powerful events in our Universe. In a timespan of only a few seconds, they can emit as much energy as the Sun will release in 10 billion years. Two processes have been shown to produce GRBs. Very-massive stars can induce a burst when all nuclear fuel is burned and the stellar core gravitationally collapses. This process generally leads to a burst lasting longer than 2 s. Alternatively, a GRB may also occur when a very compact object called a neutron star collides with either another neutron star or a black hole. These collision-induced bursts generally produce a gamma-ray signal shorter than 2 s.

Both types of progenitors induce an explosion in which material is ejected with extremely high energies. Ejecta are not emitted isotropically, but along a pair of conical shaped jets. Conventional models suggest that shock wave and collision processes in these jets lead to the production of high-energy particles. This includes the gamma rays that observationally characterise a GRB, but likely also high-energy cosmic rays (CRs) and neutrinos. A high-energy cosmic ray and neutrino flux is indeed observed at Earth. However, correlation analyses that aim to link these particles, of which neutrinos are far more ideal messengers than cosmic rays, to GRB observations have so far been unfruitful.

Previous correlation studies have mainly focused on the ‘prompt’ phase of GRBs, corresponding to the main gamma-ray emission period. A highly interesting feature is that a subset of bursts also exhibit precursor emission, i.e. a dim gamma-ray flash $\mathcal{O}(10 - 100)$ s prior to the main outburst. Several physical mechanisms have been proposed to explain these early gamma-ray signals, but currently there is still no consensus as to their origin. What many candidate models do have in common is that the high density during the early precursor phase can lead to high opacities. While the flux of gamma rays would therefore be reduced, high opacities can conversely lead to a significant increase in the neutrino flux. This argument motivates coincidences studies between GRB precursors and high-energy neutrinos. Observing such a precursor neutrino signal would be an important milestone in GRB research. Not only would it confirm current theories, it would also prove that GRBs are sources of both high-energy cosmic rays and neutrinos.

The goal of the research presented in this thesis is to obtain a better understanding of GRB physics through a study of the precursor phase. To this end, two types of analyses have been performed, combining aspects of gamma-ray and neutrino astronomy. First, a study of the gamma-ray light curves of GRBs was performed to identify and characterise precursor emission episodes. For this analysis, we made use of data recorded by the Gamma-ray Burst Monitor (GBM) onboard the Fermi satellite. New algorithms were developed to automate the identification of background data and the selection of likely signal time intervals. Analysing over 2,000 GRBs, the analysis found that $\sim 10\%$ of long GRBs and $\sim 1\%$ of short

GRBs show signs of precursor emission. When examining the temporal characteristics of these precursors, a novel bimodal feature was uncovered. This bimodality suggests that at least two physical mechanisms can induce the precursors of long GRBs. Another notable result is that the fraction of GRBs for which a precursor is observed significantly increases when only considering bright bursts, indicating an observational bias. Particularly GRBs detected by an imaging air Cherenkov telescope showed high precursor fractions. To encourage follow-up analyses, the properties of the identified precursors were published [1] and released in an online catalogue (https://icecube.wisc.edu/~grbweb_public/Precursors.html).

In the second part of our research, data from the IceCube neutrino observatory was used to search for neutrino signals from GRB precursors. Two unbinned likelihood analyses have been performed. One search aimed to determine if a neutrino excess is observed coincident with the identified gamma-ray precursor flashes. A second, more generic analysis was also performed to determine if a neutrino excess is observed from GRBs prior to the prompt emission. This second study was applied to bursts regardless of whether or not a gamma-ray precursor was observed, thus allowing a larger GRB sample. Both analyses produced a null result, indicating that no neutrino excess is observed from GRB precursors. An improved calculation was then developed to convert the analysis upper limits to constraints on the diffuse precursor neutrino flux. Compared to previous flux upper limits, our results represent an improvement by a factor ~ 10 . This allowed for the first time to fully rule out certain model predictions. Alternative models nonetheless remain viable, but will require future gamma-ray and neutrino observatories to be either confirmed or excluded.

Samenvatting

Onderzoek naar de voorloperfase van gammaflitsen door middel van gammastraal- en hoogenergetische neutrino observaties

In de jaren zestig, op het hoogtepunt van de koude oorlog, lanceerden de Verenigde Staten verschillende satellieten om te verifiëren of er geheimelijk geen kernbomproeven werden uitgevoerd in de ruimte. Deze satellieten waren uitgerust met detectoren die de korte flitsen van hoogenergetisch licht, gammastralen genaamd, konden opvangen die bij dergelijke explosies vrijkomen. Na enkele jaren, naarmate steeds gevoeliger en geavanceerdere satellieten werden ingezet, begonnen de detectoren sporadisch gammaflitsen op te pikken. Het werd echter al snel duidelijk dat deze niet gerelateerd waren aan kernbomproeven, maar veroorzaakt werden door een onbekend astrofysisch fenomeen. Deze gebeurtenissen kregen de naam gammaflitsen.

Sinds hun ontdekking is veel bekend geworden over de aard van gammaflitsen. Het is nu geweten dat gammaflitsen extra-galactische gebeurtenissen zijn, die zich op kosmologische afstanden voordoen. Hun enorme helderheid impliceert dat gammaflitsen tot de krachtigste gebeurtenissen in ons heelal behoren. In een tijdsbestek van slechts enkele seconden kunnen zij evenveel energie uitstralen als de zon in 10 miljard jaar. Er is aangetoond dat twee processen gammaflitsen kunnen produceren. Zeer massieve sterren kunnen een uitbarsting veroorzaken wanneer alle nucleaire brandstof is opgebrand en de stellaire kern gravitationeel ineenstort. Dit proces leidt meestal tot een uitbarsting die langer duurt dan 2 s. Een andere mogelijkheid is dat een gammaflits ontstaat wanneer een zeer compact object, een neutronenster genaamd, in botsing komt met een andere neutronenster of een zwart gat. Deze door botsingen veroorzaakte uitbarstingen produceren doorgaans een gammaflits die korter is dan 2 s.

Beide soorten systemen veroorzaken een explosie waarbij materiaal met extreem hoge energie naar buiten wordt geslingerd. De ejecta worden niet isotroop uitgestoten, maar langs een paar kegelvormige bundels. Conventionele modellen suggereren dat schokgolven en botsingsprocessen in deze bundels leiden tot de productie van hoogenergetische deeltjes. Dit omvat de waargenomen gammastralen die kenmerkend zijn voor een gammaflits, maar naar alle waarschijnlijkheid ook hoogenergetische kosmische stralen en neutrino's. Op aarde wordt inderdaad een flux van hoogenergetische kosmische straling en neutrino's waargenomen. Correlatieanalyses met als doel deze deeltjes te linken aan gammaflitsen, waarbij neutrino's veel betere kosmische boodschappers zijn dan kosmische stralen, hebben echter tot dusver nog geen verbanden kunnen leggen.

Eerdere correlatiestudies hebben zich voornamelijk gefocust op de hoofdfase van gammaflitsen, die overeenkomt met de periode waarin de meeste gammastraling wordt waargenomen. Een interessant kenmerk is dat een deel van de uitbarstingen ook voorloper-emissie vertoont, d.w.z. een zwakke gammaflits 10-100 s voorafgaand aan de hoofduitbarsting. Er zijn verschillende fysische mechanismen voorgesteld om deze vroege gammastralen te verklaren, maar er bestaat nog geen consensus over hun oorsprong. Wat veel kandidaatmodellen gemeen hebben, is dat de hoge dichtheid tijdens de vroege voorloperfase kan leiden tot een hoge opaciteit voor fotonen. Terwijl de flux van gammastralen daardoor zou verminderen, kunnen hoge dichtheden omgekeerd leiden tot een aanzienlijke toename van de neutrino-flux. Dit argument motiveert coincidentiestudies tussen de voorloperfase van gammaflitsen en hoogenergetische neutrino's. De waarneming van zo'n neutrino-signaal zou een belangrijke mijlpaal zijn in het onderzoek naar gammaflitsen. Niet alleen zou het

de huidige theorieën bevestigen, het zou ook bewijzen dat gammaflitsen bronnen zijn van zowel hoogenergetische kosmische straling als neutrino's.

Het doel van het onderzoek in deze dissertatie is om de fysica van gammaflitsen te onderzoeken tijdens de voorloperfase. Daartoe zijn twee soorten analyses uitgevoerd waarin aspecten van gamma- en neutrino-astronomie zijn gecombineerd. Ten eerste werd een studie van de gammastralen uitgevoerd om de episoden van voorloper-emissie te identificeren en te karakteriseren. Voor deze analyse werd gebruik gemaakt van gegevens die zijn opgenomen door de Gamma-ray Burst Monitor (GBM) aan boord van de Fermi-satelliet. Er werden nieuwe algoritmen ontwikkeld om de identificatie van achtergrondstraling en de selectie van waarschijnlijke signaal tijdsintervallen te automatiseren. Uit de analyse van meer dan 2000 gammaflitsen bleek dat $\sim 10\%$ van de lange gammaflitsen en $\sim 1\%$ van de korte gammaflitsen sporen van voorloper-emissie vertonen. Bij het onderzoek naar de temporele kenmerken van de voorloperfase werd een nieuw bimodaal kenmerk ontdekt. Deze bimodaliteit suggereert dat ten minste twee fysische mechanismen de voorloperfase van lange gammaflitsen kunnen induceren. Een ander opmerkelijk resultaat is dat de fractie van gammaflitsen waarvoor voorloper-emissie wordt waargenomen significant toeneemt wanneer alleen heldere uitbarstingen worden beschouwd, wat wijst op een waarnemingsbias. Met name gammaflitsen die gedetecteerd zijn met een beeldvormende Cherenkov-telescoop vertonen een hoge kans op verlopers-emissie. Om vervolg analyses mogelijk te maken werden de eigenschappen van de geïdentificeerde events gepubliceerd [1] en vrijgegeven in een online catalogus (https://icecube.wisc.edu/~grbweb_public/Precursors.html).

In het tweede deel van ons onderzoek werden gegevens van het IceCube neutrino observatorium gebruikt om te zoeken naar neutrino signalen van de voorlopersfase van gammaflitsen. Twee analyses werden uitgevoerd. De eerste analyse was erop gericht te bepalen of neutrino's werden waargenomen samenvallend met de geïdentificeerde gammaflitsen van de voorlopers-emissie. Een tweede, meer generieke analyse werd ook uitgevoerd om te bepalen of neutrino's werden waargenomen in een periode die de gammaflitsen voorafgaat. Deze tweede studie werd toegepast op uitbarstingen ongeacht of voorlopers-emissie werd waargenomen zodat een grotere gammaflits-steekproef gebruikt kon worden. Beide analyses leverden een nulresultaat op, wat aangeeft dat geen neutrino's werden waargenomen van gammaflitsen. Een nieuwe methode werd vervolgens ontwikkeld om de bovengrenzen van de analyse om te zetten in limieten op de diffuse voorlopers neutrino flux. Vergeleken met eerdere fluxbovengrenzen zijn onze resultaten een verbetering met een factor ~ 10 . Dit maakte het voor het eerst mogelijk om bepaalde modelvoorspellingen volledig uit te sluiten. Andere modellen blijven niettemin levensvatbaar, en zullen door toekomstige gamma- en neutrino-observatoria kunnen worden bevestigd of uitgesloten.

Contents

Acknowledgements	iii
Summary	v
Samenvatting	vii
Contents	ix
Preface	1
1 Gamma-ray bursts	5
1.1 Half a century of observations	6
1.1.1 The discovery of GRBs	6
1.1.2 Gamma-ray satellites in the 21st century	9
1.1.3 Gravitational waves	12
1.1.4 Ultra-high-energy gamma rays	15
1.1.5 Cosmic rays and neutrinos	16
1.2 GRBweb	18
1.2.1 Information resources	18
1.2.2 Data processing	20
1.2.3 Web interface	21
1.2.4 Earlier versions	23
1.3 Observational properties	23
1.3.1 Duration	23
1.3.2 Temporal and spectral evolution	24
1.3.3 Afterglow	25
1.3.4 Polarization	27
1.3.5 Supernovae	28
1.3.6 Host galaxies	29
1.4 GRB physics	30
1.4.1 Compactness paradox	30
1.4.2 Relativistic signals	31
1.4.3 Jet opening angle	33
1.4.4 Particle shock acceleration	34
1.4.5 Synchrotron radiation	36
1.4.6 Hadronic processes	38
1.5 Emission models	40
1.5.1 Central engines	40
1.5.2 Photospheric emission	43
1.5.3 Fireball model	43
1.5.4 Poynting flux	44
1.5.5 ICMART	46

1.5.6	Alternative models	46
1.5.7	Model limits from neutrino observations	47
1.6	Progenitors	49
1.6.1	Long bursts	49
1.6.2	Short bursts	51
1.6.3	GRB-like sources	52
2	Gamma-ray burst precursors	53
2.1	Observational overview	54
2.1.1	Definition of a precursor	54
2.1.2	Analyses techniques	55
2.1.3	Experimental properties	55
2.2	Emission models	57
2.2.1	Photospheric emission	57
2.2.2	Shock breakout	57
2.2.3	Multi-stage collapsar	59
2.2.4	NS magnetic interactions in binaries	59
2.2.5	NS crust cracking	60
2.2.6	Central engine reactivation	60
2.3	Precursor neutrino emission	61
2.3.1	Subphotospheric internal collisions	61
2.3.2	Supranova model	63
3	Identification of precursors in Fermi-GBM data	65
3.1	The Fermi Gamma-ray Space Telescope	66
3.1.1	Orbit	67
3.1.2	The Gamma-Ray Burst Monitor	68
3.1.3	The Large Area Telescope	70
3.2	Gamma-ray sources	71
3.2.1	Terrestrial sources	71
3.2.2	Solar system	72
3.2.3	Milky way	73
3.2.4	Extragalactic sources	74
3.3	Precursor selection	74
3.3.1	Data format & characteristics	74
3.3.2	Characterizing the background rate	77
3.3.3	Bayesian block light curves	78
3.3.4	Precursor selection criteria	79
3.3.5	Additional checks	81
3.4	Results	83
3.4.1	Precursors of short and long GRBs	83
3.4.2	Quiescent time	85
3.4.3	Temporal correlations	88
3.4.4	Imaging air Cherenkov telescope GRBs	89
4	The IceCube neutrino observatory	91
4.1	Neutrino astronomy with IceCube	91
4.2	Neutrino propagation	96
4.3	Detection principle	99
4.3.1	Neutrino cross sections	99
4.3.2	Cherenkov radiation	102

4.3.3	Interaction signatures	103
4.3.4	Non-optical signals	105
4.4	Detector instrumentation	105
4.4.1	Detector configuration	105
4.4.2	Digital optical modules	108
4.5	Data acquisition software and triggering	109
4.5.1	Triggering	109
4.5.2	Pulse series construction	110
4.6	Event reconstruction	111
4.6.1	Processing and filtering	111
4.6.2	Directional reconstruction	112
4.6.3	Estimated angular uncertainty	115
4.6.4	Energy reconstruction	117
4.7	Simulation	118
4.7.1	Neutrino interactions	119
4.7.2	Detector response	119
4.8	Event selections	120
4.8.1	The OnlineL2 filter	120
4.8.2	The GFU filter	121
4.8.3	Final event sample	123
5	IceCube GRB precursor analysis	127
5.1	GRB neutrino studies in IceCube	127
5.1.1	Past analyses	127
5.1.2	Current analyses	129
5.2	Unbinned likelihood analysis	129
5.2.1	Likelihood-ratio test	129
5.2.2	Likelihood for a single, well-localised GRB	131
5.2.3	Sky scans for GBM localised bursts	135
5.2.4	Stacking likelihood	136
5.3	Analyses	137
5.3.1	GBM coincidence study	137
5.3.2	Generic stacking search	145
5.3.3	Combined result	149
5.4	Systematic uncertainties	149
5.5	Results	150
5.5.1	GBM coincidence study	150
5.5.2	Generic stacking search	151
5.6	Flux upper limits	151
5.6.1	Time-integrated upper limits	152
5.6.2	Differential upper limits	153
5.6.3	Diffuse GRB flux	154
5.6.4	Comparison to model predictions	156
6	Conclusions & Outlook	159
A	Bayesian block algorithm	163
B	Modified background characterisations	167
C	GRB precursor catalogue	169

D	Supplemental results on the IceCube neutrino search	185
D.1	GBM coincidence study	185
D.1.1	GRB selection	185
D.1.2	Trial corrections	188
D.2	Generic stacking search	191
D.2.1	GRB sample	191
D.2.2	Fit bias tests	210
D.2.3	Sensitivity & discovery potential	212
D.2.4	Unblinding tests	214
	Bibliography	215

List of Abbreviations

ACS	Anti-Coincidence Shield
ANIS	All Neutrino Interaction Simulation
ATWD	Analogue Transient Waveform Digitiser
AXP	Anomalous X-ray Pulsar
BB	Bayesian Block
BDT	Boosted Decision Tree
BH	Black Hole
BZ	Blandford-Znajek
CC	Charged Current
CMB	Cosmic Microwave Background
CR	Cosmic Ray
CTA	Cherenkov Telescope Array
DAQ	Data Acquisition
DEC	Declination
DM	Dark Matter
DOM	Digital Optical Module
DPU	Data Processing Unit
fADC	fast Analogue to Digital Converter
FOV	Field-Of-View
FRT	Fixed-Rate Trigger
GBM	Gamma-ray Burst Monitor
GFU	Gamma-Ray Follow up
GRAND	Giant Radio Array for Neutrino Detection
GRB	Gamma-Ray Burst
GVD	Gigaton Volume Detector
GW	Gravitational Wave
GZK	Greisen-Zatsepin-Kuzmin
HLC	Hard Local Coincidence
HR	Hardness Ratio
IACT	Imaging Air Cherenkov Telescope
ICL	IceCube Laboratory
ICMART	Internal-Collision-induced Magnetic Reconnection and Turbulence
KM3NeT	Cubic Kilometre Neutrino Telescope
LAT	Large Area Telescope
LL	Low Luminosity
MC	Monte Carlo
MMC	Muon Monte Carlo
NC	Neutral Current
NDAF	Neutrino-Dominated Accretion Flow
NS	Neutron Star
PD	Polarisation Degree
PnF	Processing and Filtering

PMT	Photo-Multiplier Tube
PROPOSAL	Propagator with optimal precision and optimized speed for all leptons
PWB	Pulsar Wind Bubble
RA	Right Ascension
RET-CR	Radio Echo Telescope - Cosmic Rays
RNO-G	Radio Neutrino Observatory - Greenland
SAA	South Atlantic Anomaly
SFR	Star Formation Rate
SGR	Soft-Gamma Repeater
SMT	Simple Multiplicity Trigger
SN	SuperNova
SPE	Single Photo-Electron
TDE	Tidal Disruption Event
TS	Test Statistic
UHECR	Ultra High Energy Cosmic Ray
WR	Wolf Rayet
ZTF	Zwicky Transient Facility

Preface

Throughout thousands of years, astronomical observations have greatly improved our understanding of the Universe. Their practical applications also played an important role in the rise and development of civilisations. By tracking the positions of stars, planets, and the phases of the Moon, advanced calendars were developed, providing a sense of scale to the passing of time. Stellar charts were drafted and used as navigational charts, enabling large distance travel between continents. In the current age, the field of astronomy has progressed from naked-eye observations of the night sky to performing measurements with > 10 m optical telescopes, space-based gamma-ray telescopes, cubic-km scale neutrino detectors, and 4 km long gravitational wave observatories. These improvements in detector technology allow gaining scientific knowledge far beyond mere timekeeping or navigational purposes. However, we are still far from discovering all of the Universe's mysteries.

The astrophysical phenomenon studied in this thesis is that of gamma-ray bursts (GRBs). GRBs are some of the most extreme events in our Universe. An old physics joke states that, when asked by a farmer to figure out why his cows are not giving any milk, a visiting physicist does some calculations, and then tells him that he found the solution! Except, it only works for spherical cows in a vacuum. . . The clue to this story is that simplifications are often required to enable solving physics problems. GRBs are very much the opposite of spherical cows in a vacuum. In some instances, they involve a ~ 10 km radius sphere that has a density 10^{14} times higher than that of regular matter, is in a superconducting state, while rapidly rotating and carrying a $\sim 10^8$ tesla magnetic field, crashing into another such sphere at almost the speed of light. While GRBs are therefore extremely challenging to model, these processes make them highly interesting phenomena, allowing models to be tested under conditions that are utterly irreproducible in lab based experiments.

The work presented in this thesis aims to improve our current understanding of GRBs through experimental gamma-ray and neutrino observations. A short outline is included below, giving an overview of the following 6 chapters. Additionally, this outline serves to provide the reader with a clear overview of the author's specific contributions.

Chapter 1 - Gamma-ray bursts:

To kick things off, a general but detailed description will be given on GRBs. The nature of GRBs will first be described from a historical perspective. Focusing on experimental observations, the reader will be guided from the discovery of GRBs, to the state-of-the-art in the field. A within this work developed GRB catalogue, called 'GRBweb', will then be introduced, aimed at enabling follow-up searches of observed GRBs. The chapter will then go into more details on the physics of GRBs. Observational properties of bursts will first be described, followed by a description of the physics needed to explain these observations, emission models in which such physical mechanisms can take place, and finally the types of progenitors that can produce such emission. During this description, emphasis will be placed on particle acceleration and the production of neutrinos, as this will be of relevance at a later stage.

Contribution & achievements: Implementing an all new Python, SQL, and HTML5 based version

of the online GRBweb catalogue to construct an up-to-date database of GRBs that can be used for follow-up analyses (see 1.2).

Chapter 2 - Gamma-ray burst precursors:

A curious feature of GRBs is that a minority ($\sim 9\%$) of all bursts are detected to be preceded by a dim gamma-ray flash. These events typically occur several seconds to minutes before the main outburst. Currently, the physical origin of these precursors is still ill-understood. An overview on GRB precursors will be presented in this second chapter, as they will form the main object of our study. Similar to Chapter 1, a historically based introduction will first be given on GRB precursors, followed by a discussion of their observational aspects and probable emission mechanisms, with particular focus again going to models that predict a significant neutrino flux.

Chapter 3 - Identification of precursors in Fermi-GBM data:

Having discussed past studies on GRB precursors, this chapter will present a new precursor search performed as part of this thesis. As the analysis makes use of the Fermi-GBM data, a description will first be given on the Fermi satellite and its subdetectors. Subsequently, an overview will be presented on the main gamma-ray sources that can trigger Fermi. The actual analysis will then be described, detailing how GRB precursors are identified in the data. Results from this analysis serve two main purposes. First, the large precursor sample allows discerning new observational features. A detailed discussion is therefore presented on the properties of the observed GRB precursors. Second, constructing an up-to-date precursor catalogue enables multi-messenger follow-up studies. Such an analysis is described in Chapter 5.

Contribution & achievements: To enable the GRB precursor search, I developed a novel approach to automate the characterisation of background rates observed by Fermi-GBM. Additionally, a Bayesian binning algorithm was used to identify physical signals. Applying the analysis to more than 2,000 bursts, 217 GRBs with precursor emission were identified, of which 139 were previously unknown. Thanks to the large statistics of our sample, new temporal features of the precursors were uncovered. The results also showed an interesting correlations between the precursor rate and the different classes of GRBs: long, short and ultra-high-energy GRBs in particular (see 3.3 and 3.4).

Chapter 4 - The IceCube neutrino observatory:

Having constructed an up-to-date sample of GRB precursors, the next stage of our research is to search for neutrinos from these events. However, before proceeding to that analysis, an overview on neutrino astronomy and the IceCube neutrino observatory is presented in this chapter. Starting with a review of the state-of-the-art in neutrino astronomy, a short summary will be given on the propagation and interaction of neutrinos. Observational signatures from neutrino interactions will then be described, in addition to the methods that can be used to reconstruct those interactions, and the algorithms used to identify neutrino events. At the end of the chapter, an overview is presented on the general properties of the selected sample of candidate neutrino events.

Contribution & achievements: I developed a simulation module to sample neutrino interactions in ice. Given a certain signal flux, the module will provide the direction, energy, time and position, accounting for the different interaction channels and effects such as Earth absorption. A study of the distribution of muon kinematic angles was also performed and presented internally to the IceCube Collaboration.

Chapter 5 - IceCube GRB precursor analysis:

In this second to last chapter, two searches for neutrinos from GRB precursors are presented. The assumptions that go into the analyses and analysis method are presented, alongside an overview of past and current IceCube GRB searches to situate our work. The performance of both analyses is then characterised, followed by a discussion of the results. Finally, the analysis results are interpreted in terms of GRB precursor models.

Contribution & achievements: Both IceCube searches presented in this chapter were fully developed and carried out by the author. This includes the first neutrino coincidence search with gamma-ray precursors. While setting up the analyses, I demonstrated that localisation uncertainties used in previous IceCube GRB analyses had been too restrictive. This led to several modifications to the analysis software, performed by the author, to enable stacking analyses and efficient sky scans. New trial-correction methods were also developed, leading to improved sensitivities. Finally, the computation to convert a time-integrated upper limit to a diffuse flux was revised, leading to more accurate diffuse flux upper limits.

Chapter 6 - Conclusion & Outlook:

To conclude the story, a summary is given on the obtained results and their effect on the state-of-the-art in GRB research. This is followed by a short discussion of what can be expected in the coming years, emphasising new studies enabled by future GRB observatories.

Related literature with involvement of the author

Published results.

- A poster on the GRBweb catalogue (see 1.2) was presented in December 2020 at the ‘Cosmic Rays and Neutrinos in the Multi-Messenger Era’ conference [2].
- The analysis of Fermi-GBM data (see 3.3 and 3.4) has been published in Physical Review D [1] and was presented in a talk at the 2021 ICRC conference [3].
- Initial sensitivities of the IceCube analyses were presented in a poster at the 2019 ICRC conference [4]. The final analysis results were shown in a combined presentation of the four most recent GRB analyses by IceCube at the 2021 ICRC conference [5]. An IceCube paper on these four studies is at the time of writing in preparation.
- The simulation module developed to weight neutrino interactions has been used in one publication [6], one poster at the 2019 ICRC conference [7], and a poster at the 2020 ‘Neutrino’ conference [8].

Bachelor and master theses from students co-supervised during the PhD.

- Quinten Goens (2018 - 2019, MSc student)
Investigation of the precursor phase of gamma-ray bursts
iihe.ac.be/sites/default/files/thesis-quinten-goens-icecube-master-2019pdf/thesis-quinten-goens-icecube-master-2019.pdf
- Zeb Van Ranst (2019 - 2020, MSc student)
Multi-messenger study of gamma-ray bursts
iihe.ac.be/sites/default/files/thesis-zeb-van-ranst-icecube-master-2020pdf/thesis-zeb-van-ranst-icecube-master-2020.pdf

- Ruben Camphyn (2020 - 2021, BSc student)
Investigation of correlations between the IceCube realtime alerts and GRB archival observations
drive.google.com/file/d/14wsaBR_XAnD2cJCr5MUzT6ZqmlLsvw0N/view?usp=sharing
- Parel Springael (2020 - 2021, BSc student)
Investigation and interpretation of gamma-ray burst precursors
drive.google.com/file/d/19MaiJZtqMf94UU7lYr0tkXCOlz5W11xZ/view?usp=sharing
- Jannes Loonen (2021 - 2022, BSc student)
Investigation of the temporal features in gamma-ray burst light curves
—in progress at the time of writing—

Chapter 1

Gamma-ray bursts

When Gamma-Ray Bursts (GRBs) were discovered, it was soon realised that they presented an entirely new class of previously unknown astrophysical transients. To investigate the nature of these bursts, dedicated gamma-ray satellites were launched that continuously monitored the sky for their occurrence. The increase in data that resulted from these missions revealed that two categories of GRBs exist. Long bursts occur when the core of a massive star collapses to a compact object. Short burst, in contrast, are caused by the merger of two compact objects, at least one of which is a neutron star. While this division, based on whether or not the duration exceeds 2 s, is not clear cut, it illustrates that both classes of progenitors produce very similar observable phenomena. As a result, their physics can for a large part be described using the same set of physical models. Having been discovered just over 50 years ago, new advancements in the field of GRB physics research are still being made on a regular basis. Recent years, for instance, saw the detection of the first gravitational wave signal in coincidence with GRB 170817¹ [9, 10] and the first observation of TeV gamma-rays from GRB 190114C [11].

In this chapter, we start by delving into the rich history of GRB discoveries, highlighting important experimental milestones and their relation to GRB models. We then continue by giving an overview of the current state-of-the-art in GRB research, discussing among others the gravitational wave and Imaging Air Cherenkov Telescope (IACT) detection of GRBs. The second part of this chapter presents the GRBweb project. A central database that we constructed to combine the information of all major GRB detectors into a single publicly accessible catalogue. We then proceed to give a short overview of the observational properties of GRBs and the physics that can be derived from them. Special focus is placed on the potential of GRBs as particle accelerators, describing how they could contribute to the observed astrophysical cosmic-ray and neutrino fluxes. Finally, we conclude by discussing the progenitor sources that match the experimental and theoretical constraints. This can be viewed as a prelude to the next chapter, where we will specifically look at GRB precursor signals and how they can arise in the proposed progenitor models.

¹GRBs are named after the UTC date on which they occurred. For instance, GRB 120513 will have occurred on the 12th of May, 2013. If several GRBs were observed on a single day, the letter ‘A’, ‘B’, ‘C’, etc. are appended to distinguish between the different bursts.

1.1 Half a century of observations

1.1.1 The discovery of GRBs

Vela satellites. As is not uncommon in science, the discovery of GRBs was made accidentally by a detector designed for an entirely different purpose. On August 5th, 1963, the Soviet-Union, United Kingdom, and United States signed the nuclear test ban treaty, prohibiting tests of nuclear weapons under water, in the atmosphere, or in outer space [12]. A range of satellites were subsequently launched by the US Air Force to check that the treaty was not being violated by the other signees. These Vela satellites [13] were launched in pairs, orbiting on opposing sides of Earth to eliminate blind spots. To detect a nuclear blast, they were equipped with X-ray, gamma-ray and neutron detectors. Apart from confirming the signature of a nuclear blast, the gamma-ray detectors also served another purpose. If an explosion took place on the far side of the Moon, the X-ray flash would remain hidden, but gamma rays would be visible from the plume of radioactive materials. Solitary gamma-ray signals were indeed observed. However, their signature did not match that of a nuclear explosion. Triangulating the direction using the different satellites revealed that the Sun, Earth and Moon could be ruled out as the source for these events. Furthermore, a spectral analysis by the IMP-6 mission showed that the emission was not simply the extension of an X-ray source, but that the peak of the spectra occurred in gamma rays [14].

These findings were first published in 1973 [14–16], reporting the observation of 16 ‘cosmic gamma-ray bursts’ between July 1969 and July 1972. An archival search later revealed that a gamma-ray flash of similar characteristics was observed on the 2nd of July, 1967 [17]. This is the first known GRB that has been recorded. Figure 1.1 shows the light curve of GRB 670702 as observed by the Vela IVa satellite.

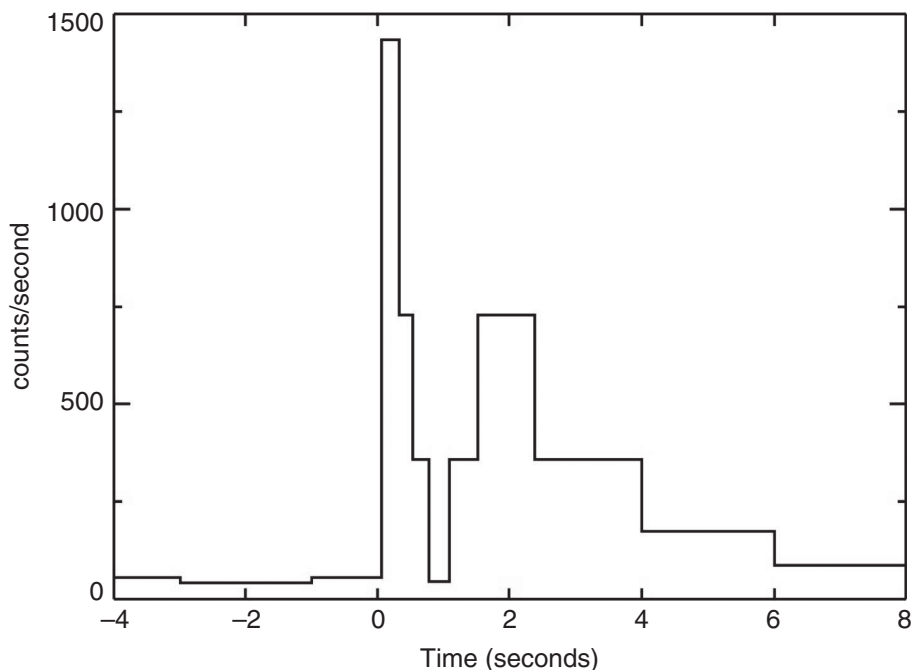


FIGURE 1.1: Light curve of the first recorded gamma-ray burst, GRB 670702, as observed by the Vela IVa satellite. From [18].

Apart from the apparent brightness and rudimental information of the temporal profile, very little was known about these bursts. This lack of restrictions allowed a wide range of astrophysical phenomena to be proposed as possible source candidates. A review paper [19] from 1994 lists a total of 118 different theoretical phenomena proposed as the sources of the gamma-ray flashes. These ranged from the accretion on compact objects, such as white dwarfs (WDs), neutron stars (NSs), and black holes (BHs), to the evaporation of primordial black holes, white holes and superflares from nearby stars. It would take until the first identification of a low frequency counterpart in 1997 before the extragalactic distance of GRBs and thus their absolute energy scale could be established [20, 21]. However, several observational features already hinted at their origins.

Isotropy. GRBs are observed to occur isotropically across the sky. The isotropic distribution was conclusively proven by the Burst And Transient Source Experiment (BATSE) on the Compton Gamma Ray Observatory (CGRO) [22, 23]. BATSE was the first experiment to observe GRBs at large rates, detecting on average one GRB per day. Before the launch of CGRO in 1991, data from previous space missions, including Ginga, Konus-Venera, UHURU, and Vela, had already indicated that the directions were isotropically distributed [15, 24–29]. Few bursts were detected, however, which combined with the coarse directional reconstruction could not yet exclude a significant galactic disk component. Following the BATSE results, the lack of correlation with the galactic plane strongly disfavoured models related to stellar objects in our Milky Way.

Fluence. Another indication that GRBs have an extragalactic origin resulted from observing their fluence distribution. Consider a GRB with an isotropically equivalent energy output E_{iso} , located at a distance r . In a Euclidean space, the fluence S observed from this burst is

$$S(r) = \frac{E_{iso}}{4\pi r^2}. \quad (1.1)$$

Assuming a detector with a fluence threshold S_t , the burst will be observable as long as it lies within a maximal distance $r_m \propto S_t^{-1/2}$. At the same time, the number of sources within a distance r_m will increase linearly with the observed volume V , thus $N(r < r_m) \propto r_m^3$. Combining this with the fluence relation from Equation (1.1), we find that

$$N(S > S_t) \propto S_t^{-3/2}. \quad (1.2)$$

While this correlation is largely recovered in experimental data, a shallower slope is observed at low fluences. This is illustrated in Figure 1.2 for the BATSE data [30]. The flattening at the lowest fluences is naturally expected when the detector threshold is reached. A change in slope is, nonetheless, already observed well above this threshold. This is mainly caused by the failing assumption of a Euclidean space, i.e. because the Universe is expanding. Such effects only become important for extragalactic sources, giving another hint at the cosmological origin of GRBs. A secondary factor is that the rate at which GRBs occur is redshift dependent [31], thus also affecting the shape of the slope.

Duration. As a result of the increased statistics that resulted from BATSE, it became apparent that GRBs can be grouped into two classes based on their duration [32]. The general accepted convention to determine the duration of a burst is that of the T90-procedure. Subtracting the expected background rate from the light curve, the points are determined at which 5% and 95% of the total photon count are observed. The T90 is then defined as the time difference between those two points. Near the start and end of the bursts, the observed rate will be close to the expected background rate. Using a 5% buffer reduces the chance that background fluctuations will artificially make a burst seem longer or shorter. Similarly, the T50 is defined as the central time interval in which 50% of the photons are observed. Figure

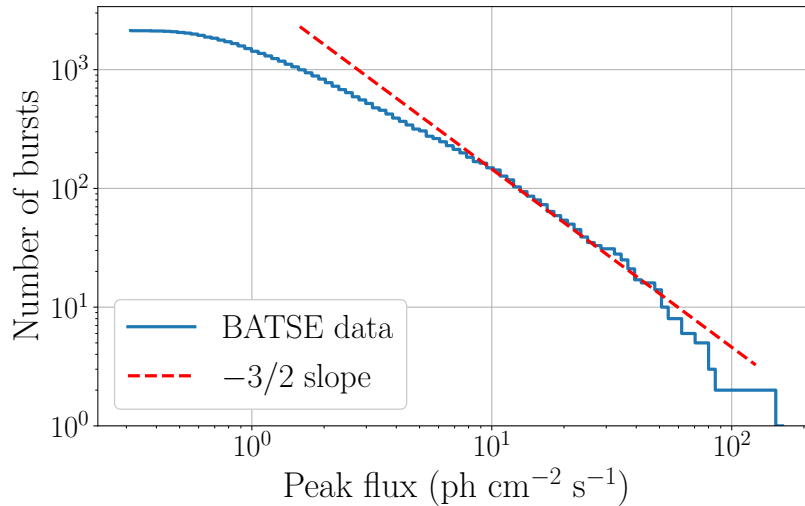


FIGURE 1.2: Relation between the peak flux on the 64 ms timescale of GRBs observed by BATSE [30]. The expected $-3/2$ slope is shown for the Euclidean expectation. A deviation is observed due to redshift effects at low fluxes, indicative of the cosmological nature of GRBs.

1.3 displays the T90-distribution for the BATSE data [30]. A clear bimodality is observed, suggesting that at least two source populations contribute to the observed GRBs.

This result was further strengthened by the observation that short and long bursts have different energy characteristics. Ideally, the energy dependence would be determined by fitting the background subtracted counts in different energy bands. However, low-count statistics prevent systematically applying this method to all burst. Therefore, an alternative approach often employed is to take the ratio between the number of photons above and below a fixed energy threshold. For BATSE bursts, this threshold was typically placed at 100 keV [32]. Defining this quantity as the hardness ratio (HR), bursts with a relative excess or lack of high-energy photons are said to be hard or soft, respectively. Comparing long ($T_{90} > 2$ s) to short ($T_{90} < 2$ s) bursts, long bursts are found to be softer on average [32].

Afterglow. A major breakthrough came in 1997, when the first optical counterpart of a GRB was discovered. Up until that time, the localization of GRBs had been too poor to establish a connection with optical sources. Early missions, such as BATSE and the Vela-satellites, had a localization uncertainty of several to tens of degrees [16, 30]. To allow more accurate localization, the Italian BeppoSAX satellite was launched in 1996 [33]. Apart from housing gamma-ray detectors, BeppoSAX also featured an X-ray telescope with a pointing resolution of one arcminute. BeppoSAX would slew to the direction of detected GRBs, to bring them into view of the X-ray telescope. Given that there are far fewer X-ray than optical sources in the sky, the coarse localization of the GRB gamma rays proved sufficient to identify a unique transient counterpart.

GRB 970228 was the first burst for which BeppoSAX identified an X-ray counterpart [20]. Follow-up optical observations identified a faint galaxy at the location of the X-ray signal, though the redshift of the galaxy could at that time not be determined. A second burst with an X-ray counterpart was discovered on May the 8th, 1997 [21]. This time, a counterpart was discovered by both optical and radio follow-up studies [21, 34]. Based on the shift of absorption lines in the optical spectrum, the redshift of the burst was determined to be $z = 0.835$ [21]. These two observations firmly established the, not only extragalactic, but cosmological origin of GRBs.

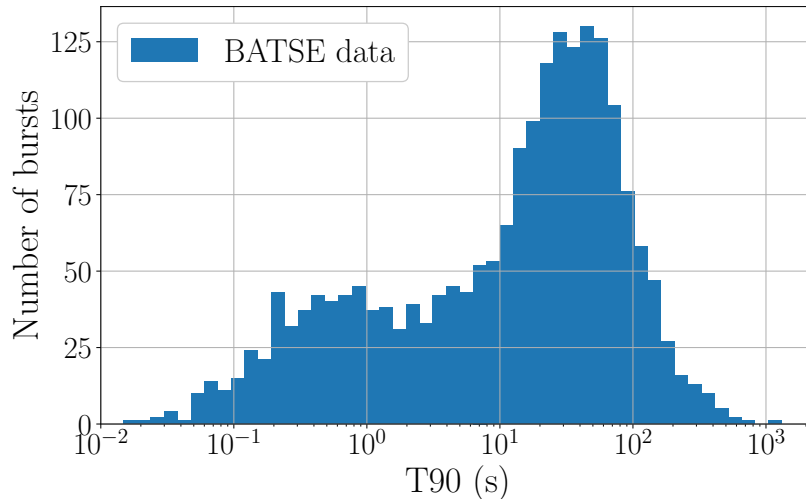


FIGURE 1.3: Distribution of the duration of GRBs detected by BATSE [30]. A clear bimodality is observed. Short and long GRBs are defined as bursts whose T90 is less than or exceeds 2 s, respectively.

Supernovae. One year later, the first tentative supernova (SN) connection was discovered between GRB 980425 and SN1998bw [35]. This provided evidence that long GRBs are related to massive stars that undergo core collapse at the end of their life. Given the small redshift $z = 0.00866$ derived for the supernova [36], corresponding to a distance of 40 Mpc, GRB 980425 remains one of the closest GRBs known to date if the correlation is physical. The GRB-SN connection was confirmed when the HETE-2 satellite localized GRB 030329 in coincidence with SN2003dh [37, 38]. Systematic studies [39–41] on the location of well localized long GRBs later showed that their occurrence is positively correlated with the star formation rate of galaxies and the region of the galaxy in which they occur. As such, this correlation provided a verification, independent of the connection to SN, that massive stars are the progenitors of long GRBs.

1.1.2 Gamma-ray satellites in the 21st century

After a 9 year mission and having detected over 2700 GRBs [30], BATSE was de-orbited in June 2000. A similar fate was bestowed on the other satellites discussed in Subsection 1.1.1, none of which remain active today. We therefore focus here on satellites that are currently taking data and thus contributed to the GRB sample used in this thesis. Apart from these active experiments, we also look at upcoming mission that are planned to be launched over the next decade.

Swift. Launched on the 20th of November 2004, Swift [42] can be regarded as the successor to BeppoSAX and HETE-2. Like its predecessors, Swift features X-ray detectors in addition to gamma-ray detectors to enable the detection of afterglow emission. Unlike its predecessors, the afterglow detection capability is extended to lower wavelengths by the addition of optical and UV telescopes. Another manner in which Swift offers improved performance is the speed with which it can slew to the direction of the burst. Swift can rotate 50° in less than 75 s [43], allowing early observations of the afterglow and explaining its name. A few noteworthy discoveries enabled by Swift are that

- through fast follow-up observations, it was discovered that the prompt gamma-ray emission is followed by X-ray flares in nearly half of all GRBs [44];

- the improved sensitivity to the X-ray afterglow allowed the observation of the first afterglow from a short GRB [45]; and
- GRB 090429B was determined to have a redshift of $z = 9.4$, making it the farthest known GRB and one of the most distant known astrophysical objects overall [46].

While originally intended to have a mission duration of two years, Swift is currently still operational. Having thus served for over 17 years already, detecting on average 90 GRBs per year, Swift has become one of the leading experiments in the history of GRB research.

Fermi. Almost four years after the Swift mission, NASA launched a second spacecraft dedicated to GRB observations on June 11th, 2008. This Fermi Gamma-ray Space Telescope, or Fermi in short, came at an estimated mission cost of 690 million dollar. While being three times as expensive as Swift, Fermi does not have the capability to observe or localise GRB afterglows. Instead, it focuses on the observation of the prompt phase. Fermi is the first gamma-ray telescope to have a combined energy range that spans more than seven orders of magnitude, from 8 keV to 300 GeV. This allowed the first detection of GRB photons with energies in excess of 100 GeV [47, 48]. High-energy ($\gtrsim 300$ MeV) emission is observed in $\sim 10\%$ of long GRBs and $\sim 4\%$ of short GRBs [48].

Having detected over 3000 GRBs since its launch, roughly one per day, Fermi has observed more GRBs than any other detector [49]. All GRB data, including the raw photon counts observed by the individual detectors, is made publicly available via the HEASARC archive [50]. For a more detailed description of the Fermi detector and data format, we refer the reader to Chapter 3, where Fermi data will be used for identification of GRB precursors.

Other active/recent missions. Particular emphasis was placed on the Swift and Fermi experiments as they observe the bulk of all detected GRBs. However, several other satellites with X-ray and/or gamma-ray detection instruments exist(ed) that contribute(d) to GRB observations. These include:

- *Konus-Wind (1994-present)*. The Konus detector on the NASA Wind satellite is the oldest GRB detector in operation. Located at the Lagrange L1 point, there is little to no Earth obscuration, giving Konus a near 4π sr field of view. However, Konus can only provide timing information, as the detector has no localization capability [51].
- *RHESSI (2002-2018)*. Designed to study the hard X-rays and gamma rays of solar flares, the RHESSI satellite from NASA is naturally also suited for the detection of GRBs. During its lifetime, it detected an average of 80 bursts per year [52].
- *Integral (2002-present)*. Integral is an ESA satellite that detects on average 0.3 GRBs per day. It features a gamma-ray spectrometer with a small angular aperture. This spectrometer is covered by an anti-coincidence shield (ACS) to reduce the contamination from gamma rays hitting the detector from the sides. Interestingly, though the ACS was not designed for this purpose, it is the main GRB detector on Integral [53].
- *SuzakuWAM (2005-2015)*. Suzaku was a Japanese satellite designed for X-ray astronomy. Similar to Integral, the X-ray telescope was covered by an ACS. Given the large thickness of the ACS, Suzaku had a larger effective area to MeV gamma rays than any other detector, including BATSE and Fermi, leading to the detection of 1155 GRBs over the course of its mission timespan [54].
- *SuperAGILE (2007-present)*. Developed and funded by the Italian space agency, AGILE is one of the most recent satellites launched to monitor the gamma-ray sky. On average, it detects around 40 GRBs per year through its hard X-ray monitor (SuperAGILE) and gamma-ray calorimeter (MCAL) [55, 56].

- *MAXI (2009-present)*. Unlike the previous instruments, MAXI is not a dedicated satellite, but is instead located on the international space station. It also does not have any gamma-ray detectors, but can observe hard X-rays up to 30 keV. As a result, follow-up or coincident detection by other instruments are required for a firm identification of GRBs. Nonetheless, for those events MAXI can contribute timing and spectral information. Up to ten GRBs are detected by MAXI each year [57].
- *AstroSAT (2015-present)*. While not technically a gamma-ray satellite, the capability of India's AstroSAT satellite to observe hard X-rays up to 300 keV allows it to detect ~ 50 GRB per year. A noteworthy feature that distinguishes it from other experiments is its capability to measure the polarisation of the prompt emission [58].

IPN network. When a GRB is observed by more than one of the spacecrafts described above, the difference in arrival time can be used to triangulate the position of the signal. Often this results in a better localisation than that of gamma-ray telescopes, which have a typical localisation uncertainty of several degrees [30, 49]. An illustration of this method is shown in Fig. 1.4. Consider two satellites, α and β , that are separated by a distance D . Both satellites observe the same GRB, but the signal reaches satellite β with a time delay Δt . Using the approximation that the distance to the GRB is infinitely larger than D , it follows that

$$\theta = \arccos\left(\frac{c \cdot \Delta t}{D}\right), \quad (1.3)$$

where θ is the angle the GRB makes with the axis of the two satellites. In three dimensions, the triangulated position thus corresponds to an annulus on the sky. Given that the positions of the satellites are extremely well known, the width of the annulus is essentially determined by the uncertainty on Δt . The degeneracy on the position can be resolved by performing multiple triangulations and determining the intersections of the different annuli. Alternatively, if the GRB was only observed by two satellites, the localisation provided by the individual satellites can also be used to reduce the uncertainty on the GRB location.

As the uncertainty on Δt is essentially independent of the uncertainty in D , extremely accurate localisations can be obtained if the satellites are sufficiently far apart. An interplanetary network (IPN) [59] is thus most suited for this purpose. Satellites currently contributing to the IPN network are:

- BepiColombo, a satellite in an orbit around the Sun that will make several close flybys of Mercury and Venus [60];
- Mars Odyssey, currently orbiting around Mars [61];
- Konus-Wind, located in the Lagrange 1 point of the Earth-Sun system; and
- INTEGRAL, Swift, Fermi, and AGILE, all in orbit around Earth.

Planned experiments. Apart from the experiments already described, a number of next-generation gamma- and X-ray observatories are expected to be launched over the next decade. Most notably, these include the Space Variable Objects Monitor (SVOM, [62]), the All-sky Medium Energy Gamma-ray Observatory (AMEGO, [63]), BurstCube [64], and e-ASTROGAM [65]. For a full review of upcoming high-energy spaced based observatories, we refer the reader to [66].

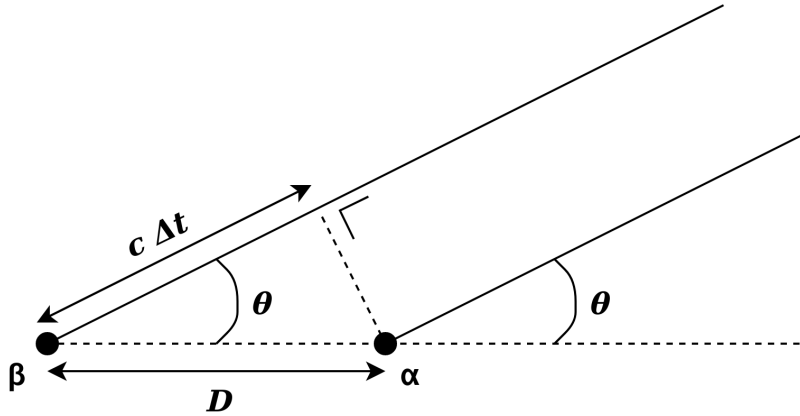


FIGURE 1.4: Illustration of the procedure used to triangulate the position of a GRB. The satellite are indicated by the black dots, α and β . Solid black lines denote the incoming gamma-ray signals. Based on the distance between the satellites, D , and the observed time delay, Δt , the angle θ can be derived.

1.1.3 Gravitational waves

GRB 170817. For fifty years, GRBs were only observed by means of electromagnetic radiation. This changed when on the 17th of August, 2017, the laser interferometer gravitational-wave observatory (LIGO) and Virgo detected a gravitational wave (GW) signal in coincidence with a short GRB observed by Fermi and Integral [9, 10]. The probability for this to be a chance coincidence corresponds to $5.0 \cdot 10^{-8}$ (5.5σ) [10]. Apart from being the first GRB progenitor detected by means of GWs, GRB 170817 was also the first electromagnetic counterpart observed to any GW signal. The electromagnetic follow-up campaign that ensued led to the identification of an optical transient in the galaxy NGC 4993 by the One-Meter, Two-Hemisphere (1M2H) experiment [67]. Given this precise localisation, other observatories were able to confirm and detect the transient in radio, infrared, optical, ultra-violet, and X-rays. While neutrino and cosmic-ray observatories also followed up the event, they did not observe any coincident events [68].

Based on the gravitational wave signal, the source of the emission was determined to be a binary NS merger. The remnant object has an estimated mass of $M_r = 2.82_{-0.09}^{+0.48} M_\odot$ and is thus most likely a black hole. Gravitational wave data allowed constraining the distance to 40_{-14}^{+8} Mpc [67]. This is in excellent agreement with the derived distance of (42.9 ± 3.2) Mpc for NGC 4993 [68]. It also makes GRB 170817, together with GRB 980425 which was also estimated to lie at ~ 40 Mpc [36], one of the two closest GRBs observed to date. Apart from its closeness, GRB 170817 was also peculiar in terms of its gamma-ray signal. The gamma-ray excess was observed starting (1.74 ± 0.05) s after the GW merger and had a T90 duration of (2.0 ± 0.5) s [10, 69]. Given its proximity, the signal was unexpectedly weak, making GRB 170817 the dimmest burst ever observed. This does not necessarily imply that GRB 170817 is different with respect to other short GRBs. Instead, the prevailing theory is that the jet of relativistic particles produced by the merger was not pointing directly at us, but was observed off-axis [10, 70, 71].

In the days and weeks that followed GRB 170817, an electromagnetic transient AT 2017gfo was observed at its location due to the kilonova explosion that followed the GRB [68]. Note that this is distinct from the GRB afterglow emission, which was not observed due to the burst being off-axis. Likely, this is what allowed the kilonova to be observed, as the kilonova is emitted isotropically and is therefore generally much fainter than the afterglow. During

the merger, not all the material of the neutron stars goes into the newly formed black hole. Around $10^{-3}M_{\odot}$ to $10^{-1}M_{\odot}$ of material is expelled, made up of neutrons and (light) elements up to iron from the neutron star crusts. The high density and abundant free neutrons then lead to rapid neutron capture (r-process), i.e. the neutrons are absorbed before they can undergo β decay. Heavier elements are thus synthesised, many of which are unstable, leading to radioactive decay. The photons released by these decays are what powers the kilonova. Because of the large opacity, high-energy photons are unable to escape directly, but get absorbed and converted to thermal energy. As a result, kilonovae are brightest at infrared and optical wavelengths [18]. The first kilonova unambiguously identified was that which followed the short burst GRB 130603B [72, 73]. Kilonovae signatures have, however, also been tentatively identified in earlier GRBs, including GRB 050709 [74] and GRB 060614 [75].

GWs and short GRBs. The detection of GWs in coincidence with GRB 170817 provided a strong confirmation of the leading model for short GRBs. Unlike long bursts, their progenitor is not a single massive star, but a binary system consisting of two compact objects. As they spiral around each other, the system will lose energy and angular momentum due to the emission of gravitational waves. Therefore, the distance between the two compact objects gradually decreases. When they inevitably collide, the system coalesces into a newly formed more massive compact object, most likely a black hole. It is this violent merger of a NS-NS or NS-BH system that produces a short GRB [76].

Paczynski in 1986 was the first to suggest a binary neutron star collision as the progenitor of short GRBs. He noted that when the binary radio pulsar PSR 1913+16 will coalesce in $\sim 10^8$ yr, it likely will be accompanied by an energy release of up to 10^{53} erg [77]. PSR 1913+16, also regularly referred to as the Hulse-Taylor binary, is the first discovered binary pulsar [78]. By monitoring the change in orbital period over the course of several years, it was demonstrated that the decrease in period follows the expected orbital decay predicted by general relativity [79]. This indirect detection of gravitational waves earned Hulse and Taylor the 1993 Nobel Prize for Physics [80].

Orbital dynamics. Emission of gravitational waves arises when the quadrupole² or higher order mass moments vary as a function of time. To illustrate the effect this has on the orbital dynamics of a binary neutron star system, a system is considered in which two compact objects of mass m_1 and m_2 are orbiting each other. For simplicity, the eccentricity of the system is assumed to be zero. This assumption is further motivated by the observation that the emission of GWs will reduce the eccentricity of the system and thus circularise the orbit [81]. Using a first-order post-Newtonian expansion, it can be shown [82] that the total power radiated via gravitational wave emission equals

$$P_r = -\frac{dE}{dt} = \frac{32}{5} \frac{G^4}{c^5} \frac{M^3 \mu^2}{a^5}, \quad (1.4)$$

where $M = m_1 + m_2$ is the total mass, $\mu = m_1 m_2 / (m_1 + m_2)$ is the reduced mass, a is the separation between the two objects, c is the speed of light and G is Newton's constant. As the energy loss is inversely proportional to a^5 , the emitted power greatly increases right before the merger. To first order, the evolution of the system can be derived by artificially imposing the energy loss of Eq. (1.4) in a Newtonian framework. In the classical limit, the

²Conservation of mass implies that the monopole moment is constant. Because of conservation of momentum, the centre of mass and thus also the dipole moment have a second order time derivative of zero. Hence, the quadrupole term is the first term that contributes to GW emission.

sum of the potential and kinetic energy in the centre of mass reference frame is equal to

$$E = -\frac{1}{2} \frac{GM\mu}{a}, \quad (1.5)$$

where contributions to the kinetic energy other than the orbital energy are neglected. Taking the derivative with respect to time in Eq. (1.5) and equating this to the expression from Eq. (1.4), we obtain

$$\frac{da}{dt} = -\frac{64}{5} \frac{G^3}{c^5} \frac{\mu M^2}{a^3}. \quad (1.6)$$

Solving this differential equation gives

$$a^4 = \frac{256}{5} \frac{G^3 \mu M^2}{c^5} (\tau - t), \quad (1.7)$$

where τ is the merger time, i.e. $a(t = \tau) = 0$, implying $t < \tau$. In reality, the coalesces will occur slightly earlier, when a approaches the combined radii of the two neutron stars. The GW frequency observed from the system will be equal to twice the orbital frequency $f_{GW} = 2 \cdot f_{orbit} = \Omega_{orbit}/\pi$, as the quadrupole moment is symmetric under rotations of π . Using Kepler's third law

$$\Omega_{orbit}^2 = \frac{GM}{a^3}, \quad (1.8)$$

and the result from Eq. (1.7), it follows that

$$f_{GW} = \frac{1}{\pi} \left(\frac{5}{256} \right)^{3/8} \left(\frac{GM_c}{c^3} \right)^{-5/8} (\tau - t)^{-3/8}, \quad (1.9)$$

where M_c is the chirp mass, defined as

$$M_c \equiv \frac{(m_1 m_2)^{3/5}}{(m_1 + m_2)^{1/5}} = \mu^{3/5} M^{2/5}. \quad (1.10)$$

For a more detailed discussion on the evolution of orbital dynamics, including non-zero eccentricities and the effect of higher order terms that become important near coalescence, we refer the reader to [18, 81–83]. Regarding the observation of gravitational waves, we also remark that the total emitted power, given by Eq. (1.4), is not released isotropically. An observer whose line of sight is parallel to the rotation axis of the binary system will observe a flux that is about an order of magnitude stronger than an observer who faces the system edge on [84]. The rotational axis of the system also corresponds to the direction along which the jet of the GRB will be launched. Hence, the detection of GWs is slightly favored for observable GRBs, i.e. bursts whose jets are pointing at us.

GW150914. GRB 170817 was the first electromagnetic counterpart to GW emission that was reliably identified. However, the Fermi satellite also observed a signal coincident with GW150914, the first GW event reported. GW150914 was caused by the merger of two black holes with initial masses $36_{-4}^{+5} M_\odot$ and $29_{-4}^{+4} M_\odot$ [85]. It was followed by a gamma-ray signal that arrived 0.4 s after the merger, from a direction consistent with the localisation by LIGO [86]. The energy spectrum of the gamma rays matched that of other short GRBs. Given the reported significance of 2.9σ and the fact that it was not observed by other gamma-ray satellites, the coincidence could nonetheless be a statistical fluctuation [86, 87]. Binary BH mergers are generally not expected to be accompanied by electromagnetic counterparts [18] and no coincident signals have thus far been reported for other binary BH mergers.

GW190425. A second likely binary NS merger was observed during LIGO's third observation run [88]. No coincident electromagnetic or neutrino events were found for this event. The merger presents an interesting case, as its total mass of $3.4_{-0.1}^{+0.3}M_{\odot}$ exceeds that of all known Galactic BNS systems. This may indicate that the system did not follow a standard evolution, but was formed due to e.g. dynamical capture [88].

GW190521. An possible electromagnetic counterpart was reported for the highest mass binary BH merger, GW190521, that LIGO and Virgo have yet observed [89]. The event is thought to be a dynamic merger between a $66_{-18}^{+17}M_{\odot}$ and $85_{-14}^{+21}M_{\odot}$ black hole in the vicinity of the galactic nucleus AGN J124942.3+344929 at $z = 0.438$. GWs from binaries with unequal masses carry linear momentum [90]. As a result, the merger product received a kick velocity that changed its orbit. The optical counterpart emission, first identified 43 days after the merger by the Zwicky Transient Facility (ZTF), is potentially due to the passage of the newly formed black hole through the accretion disk that surrounds the AGN. If correct, a repetition of the flare was predicted to be observed ~ 1.6 yr later, but no such observation has so far been reported.

1.1.4 Ultra-high-energy gamma rays

GRB 190114C. Less than two years following the detection of gravitational waves from a GRB, another major advancement was made in the field of GRB research. On the 19th of January, 2019, the Major Atmospheric Gamma Imaging Cherenkov Telescopes (MAGIC) in La Palma observed 0.2 TeV to 1 TeV gamma rays from long burst GRB 190114C with a significance in excess of 50σ [11, 91]. This marked the first observation of a GRB using a ground based gamma-ray telescope. Unlike space-based observatories, MAGIC [92] cannot directly detect gamma rays. Instead, it uses two optical reflectors, each with a diameter of 17 m, to collect the Cherenkov light emitted by gamma-ray induced particle cascades in the atmosphere. Telescopes operating in this manner are called Imaging Air/Atmospheric Cherenkov Telescopes (IACTs). MAGIC is sensitive to photon energies between 25 GeV and several tens of TeV. As such, it extends the monitored energy region into the high TeV range, while still providing overlap with space-based detectors, such as Fermi-LAT which is sensitive up to 300 GeV [93].

Attenuation. At energies $E > 0.71$ TeV, the significance of the excess photon counts observed from GRB 190114C exceeds the background expectation by 5σ . These were the most energetic gamma rays ever observed from a GRB. Given that GRB 190114C has a redshift of 0.42, the flux at these energies will have been strongly attenuated due to propagation effects. Ultra-high-energy (UHE) photons are liable to undergo pair production $\gamma\gamma \rightarrow e^+e^-$ if their energies, E_1 and E_2 , satisfy the threshold criterion

$$E_1 E_2 \geq \frac{2(m_e c^2)^2}{1 - \cos(\theta)}, \quad (1.11)$$

where θ is the angle between the propagation direction of the two photons, m_e is the electron mass and c is the speed of light. Assuming a head-on collision, a TeV gamma ray can interact with a photon of wavelength $\lambda = 5 \mu\text{m}$. Hence, for gamma rays in the 100 GeV to 10 TeV range, the infrared and optical component of the extragalactic background light (EBL) form the main background for pair production [94, 95]. Figure 1.5 shows the optical depth, $\tau_{\gamma\gamma}$, as a function of photon energy, E_{γ} , for sources at different redshifts. Given that the flux, f , exponentially decreases with optical depth, i.e. $f \propto e^{-\tau}$, UHE gamma rays can only be observed from nearby GRBs.

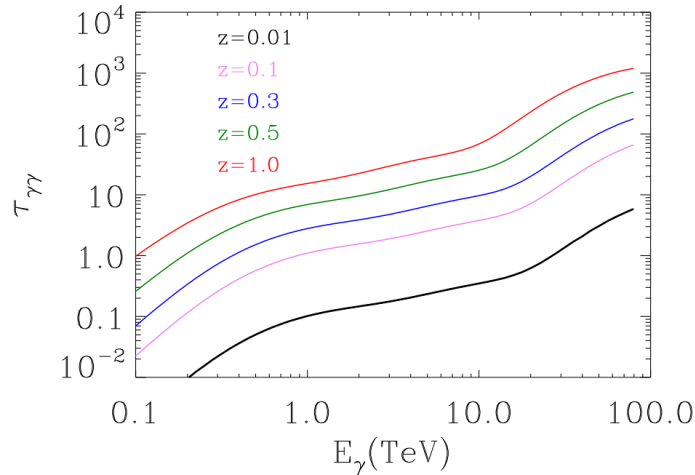


FIGURE 1.5: Optical depth of ultra-high-energy gamma rays due to pair production $\gamma\gamma \rightarrow e^+e^-$ interactions with photons from the extragalactic background light (EBL). From [94].

GRBs & IACTs. Following the announcement that UHE gamma ray were detected from the long burst GRB 190114C, the MAGIC Collaboration reported that a similar, but less significant excess was observed for the short burst GRB 160821B [96]. At energies $E > 0.5$ TeV, the observed photon counts exceeded the background expectation by 3σ . While thus insufficient to claim a discovery, GRB 160821B is likely the first GRB observed by an IACT. At a later stage, MAGIC also announced the detection of UHE gamma rays from GRB201015A and GRB 201216C [97, 98]. Other IACTs that follow up on GRBs include the High Energy Stereoscopic System (H.E.S.S.) [99] and the Very Energetic Radiation Imaging Telescope Array System (VERITAS) [100]. In 2019, H.E.S.S. reported the observation of two long bursts, GRB 180720B [101, 102] and GRB 190829A [103]. Veritas has not announced the observation of a GRB so far.

Milagrito event. An alternative method that can be used to detect UHE gamma rays is to observe the air shower they induce using an array of water Cherenkov tanks. So far, only one GRB has been reportedly observed using such a detector. This detection of GRB 970417A was made by the Milagrito experiment [104, 105]. Correcting for the number of GRBs that were followed up, an excess of 3σ significance was observed. This tentative discovery raised expectations for the follow-up Milagro experiment, but no similar coincidences have since been observed [106]. Currently, the water Cherenkov experiment most sensitive to GRBs is the High Altitude Water Cherenkov Experiment (HAWC) [107].

1.1.5 Cosmic rays and neutrinos

Apart from photons and gravitational waves, the two other detection channels in the field of multi-messenger astronomy are cosmic rays (CRs) and neutrinos. No CR or neutrino signal has been experimentally linked to GRBs so far. However, there is ample theoretical motivation that GRBs do produce these two messengers. It is thus worthwhile to also consider CR and neutrino observations in the context of GRBs. A detailed overview of neutrino searches from GRBs is presented in Chapter 4. Hence, we focus here on CR observations and the relation between the two messengers.

CR energy spectrum. Figure 1.6 shows the energy spectrum of CRs above 10 TeV as observed by air shower experiments. Overall, the spectrum can be well described using a broken power-law. Cosmic rays are charged particles and will thus gyrate in magnetic

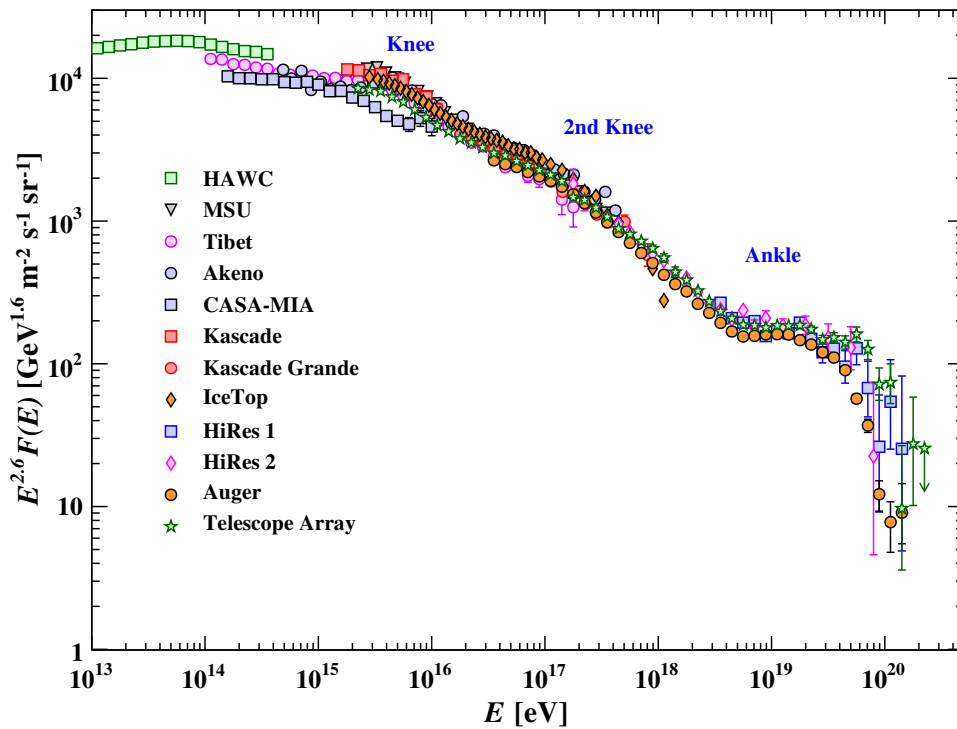


FIGURE 1.6: Energy spectrum of cosmic rays as measured by air shower experiments. To highlight the features in the spectrum, the y -axis display the particle flux multiplied by $E^{2.6}$. From [110].

fields. Equating the centrifugal to the Lorentz force, it follows that

$$r_L = \frac{p_{\perp}}{ZeB}, \quad (1.12)$$

where r_L is the Larmor radius, p_{\perp} the momentum of the CR orthogonal to the magnetic field, Z the CR charge number, e the elementary charge, and B the magnetic field strength. For highly relativistic particles ($\gamma \gg 1$), energy is proportional to the momentum $E \approx pc$. Taking the mean magnetic field strength of our Milky Way and the scale height of its disk to be $3 \mu\text{G}$ and 300 pc , respectively, it follows that protons with energies in excess of $\sim 10^{18} \text{ eV}$ are no longer confined to our galaxy. The ankle feature at $5 \cdot 10^{18} \text{ eV}$ is thus likely due to the transition from galactic to extragalactic CRs³. Earlier breaks in the spectrum are thought to occur when CRs reach the maximal energy E_m they can be accelerated to by galactic sources. E_m is proportional to the charge number, Z , resulting in two distinct kinks, one at $\sim 4 \cdot 10^{15} \text{ eV}$ for protons and one at 10^{17} eV for iron. These are the knee and the second knee transitions indicated in Fig. 1.6. An affirmation that the transition is due to the limited E_m of galactic sources is that the observed mass composition increases between the knee and the second knee [109]. It is also consistent with models for supernova remnants, which predict $E_m \sim 10^{15} \text{ eV}$ for protons [18].

At energies $E > 10^{20} \text{ eV}$, a strong cut-off of the CR flux is observed. A potential cause for this decrease is the Greisen-Zatsepin-Kuzmin (GZK) effect [111, 112], in which protons above $5 \cdot 10^{19} \text{ eV}$ interact with cosmic microwave (CMB) photons via the Δ -resonance, $p\gamma \rightarrow \Delta^+$. The interaction length for this process is $\sim 50 \text{ Mpc}$, imposing a horizon from

³It is likely that the transition from galactic to extragalactic sources occurs slightly below the ankle, though the exact transition energy is currently still undetermined [108].

which the highest energies protons can be observed. For CRs different from protons, photodisintegration with CMB photons and extragalactic background light imposes a similar limit [111], with an energy threshold that increases linearly with the atomic number, A . Given the limited statistics and knowledge of the mass composition of CRs at $E > 10^{20}$ eV, it is currently still unclear whether the observed cut-off is due to the GZK-effect or due to the maximal energy to which extragalactic sources can accelerate CRs. To resolve this question, radio neutrino telescopes are currently under construction that will be sensitive to the predicted neutrino signal from the decay products of GZK interactions [113, 114].

UHECRs & GRBs. The early 1990s saw the first detection of particles with energies larger than 10^{20} eV [115, 116]. This sparked three papers that appeared almost simultaneously in 1995, each suggesting that GRBs could be the origin of the ultra-high-energy cosmic rays (UHECRs). The paper by Waxman remarked that gamma rays observed from GRBs and UHECRs have the same energy density of $\sim 10^{44}$ erg Mpc $^{-3}$ yr $^{-1}$ in the local Universe [117]. Milgrom and Usov pointed out a potential correlation between the arrival direction and time of the UHECRs and the most energetic BATSE GRBs [118]. Finally, Vietri motivated that shock acceleration in GRBs could produce cosmic rays with energies up to 10^{20} eV [119].

For a GRB to accelerate CRs to the highest energies, the particles should be confined to the source region until they attain that energy. Hence, the Larmor radius, r_L , defined in Eq. (1.12) imposes a lower limit on the size of the accelerator, r_a . This limit $r_a > r_L$ is known as the Hillas criterion [120] and depends on the strength of the magnetic field of the accelerator since $r_L \propto B^{-1}$. GRBs along with active galaxies and galaxy clusters are some of the only sources satisfying this requirement and thus of being potentially capable of being the sources of the observed UHECRs [121, 122].

Neutrinos. Waxman and Bahcall were the first to note that if GRBs are sources of UHECRs, they are likely to be accompanied by a significant neutrino flux [123]. Due to the high photon density in GRBs, part of the accelerated hadronic particles will interact with photons before escaping the source. Assuming that UHECRs are protons with an E^{-2} spectrum that lose a fraction ϵ of their energy to pion production, the expected muon neutrino density is

$$E_v^2 \frac{dN_v}{dE_v} \approx \frac{1}{8} \cdot \epsilon \cdot t_H \cdot E_{CR}^2 \frac{dN_{CR}}{dE_{CR} dt}, \quad (1.13)$$

where $t_H = 1.4 \cdot 10^{10}$ yr is the Hubble time and $E_{CR}^2 dN_{CR}/(dE_{CR} dt) \approx 10^{44}$ erg Mpc $^{-3}$ yr $^{-1}$ the generation rate of CRs [124]. The factor $1/8$ accounts for the fact that half of the produced pions are neutral pions, which decay to gamma rays instead of neutrinos, and for the fact that the neutrinos carry roughly $3/4$ of the pion energy, $1/3$ of which goes to the muon channel after oscillations. Equation (1.13) provides an upper limit on the allowed neutrino density from production in UHECR sources. More detailed models for neutrino production in GRBs are discussed in Subsection 1.4.6.

1.2 GRBweb

1.2.1 Information resources

GCN. In the previous section we have discussed some of the main experiments that contribute to GRB observations. While the wide range of detectors are able to provide complementary information on bursts, the sheer number of potential observatories can make it challenging to identify and analyse all available data sources. To alleviate this problem,

the gamma-ray coordinates network (GCN) was set up by NASA⁴ [126]. GCN is a service via which observatories can publicly report their observations to the GRB community. Two GCN communication channels exist. Notices are reports that are sent out automatically after the satellite detection of a GRB. They contain basic information such as the estimated GRB location and are designed to enable rapid follow-up observations by other observatories. The second channel are the GCN circulars. Circulars are email messages that report on follow-up observations and that present the final results of gamma-ray satellites after the initial notice. They thus contain more information than the notices, often including more accurate localisations by ground based telescopes or redshift information. However, these unformatted text based messages generally do not have a consistent predefined structure, making it challenging to automatically extract the relevant information.

To nonetheless tap into this resource, we have constructed a Python project [127] to automate the read-out of GCN-circulars. As a first step, our program starts by retrieving new circulars that have not yet been processed from the online archive⁵. Circulars not related to GRB activity are removed by requiring that a GRB name appears in the circular subject or text. Our program then proceeds by identifying which experiment sent out the circular, as this will affect the parsing of the circular text. Fourteen major contributors were identified, for which the parsing was tailored to the typical format of the circular text. For all other circulars, a generic parsing scheme is used. Parsing mostly proceeds by using regular expressions to identify particular key words or phrases. Information extracted from circulars includes: the detection method, right ascension, declination, trigger time, redshift, and T90. Basic consistency checks are performed and a warning is raised if a parameter falls outside the expected range. The information is then stored in a database on a MySQL server [128].

GRB catalogues. Information from GCN circulars is supplemented with online catalogues from dedicated GRB experiments. In particular, the catalogues of Fermi-GBM [49], Fermi-LAT [48], Swift (BAT, XRT & UVOT) [129], IPN [59], BATSE [30], and BeppoSAX [130] are stored as separate tables in the MySQL database. Given that the latter two experiments are no longer active, their data is only added once. For the other experiments, new entries are identified and added to the relevant tables. Nearly all GRBs observed by these experiments will also have been reported via GCN-circulars and thus already be contained in the database. However, using these dedicated catalogues has two main advantages. First, archival data of GRB satellites is sometimes reprocessed, resulting in slightly updated values for parameters such as the location or duration of bursts. Second, parsing prose-style written messages can make it challenging to extract all relevant parameters. The dedicated catalogues in contrast are designed to be machine readable, making it possible to extract more parameters and strongly reducing the risk of incorrect entries.

Angular uncertainties. A last resource that is gathered relates to the uncertainty on the localisation of the bursts. Generally, a two-dimensional Gaussian distribution

$$\mathcal{P}_\theta(\theta, \sigma) = \frac{1}{2\pi\sigma^2} \cdot \exp\left(-\frac{\theta^2}{2\sigma^2}\right), \quad (1.14)$$

is used for this purpose, where θ is the angle with respect to the best fit sky location. This allows characterising the uncertainty using a single number, being the variance σ of the distribution. Note, however, that θ lies in the domain $[0, \pi]$, whereas the actual probability distribution assumes a range $\theta \in [0, \infty)$. For variances on the order of several degrees

⁴GCN is a more general successor of the BATSE coordinates distribution network (BACODINE), which provided a similar service but solely focused on the BATSE detector [125].

⁵https://gcn.gsfc.nasa.gov/gcn3_archive.html

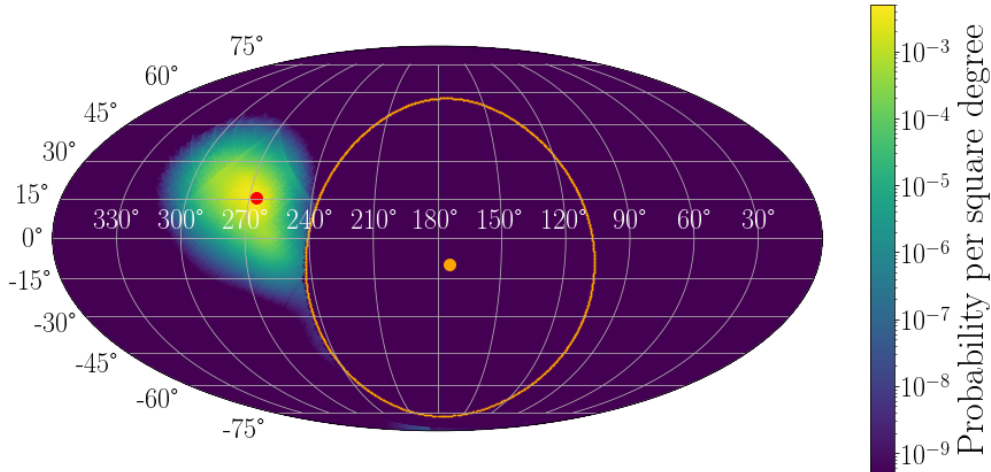


FIGURE 1.7: Localisation of GRB 090811A by the Fermi-GBM in equatorial coordinates. As the satellite follows a geocentric orbit, part of its field-of-view is obstructed by Earth. The orange dot and line show the centre and contours of Earth, respectively. The red dot indicates the best fit GRB position.

or less, Eq. (1.14) provides an excellent approximation. For larger variances, a generalisation of a two-dimensional Gaussian defined on the surface of the sphere, such as the Kent distribution

$$\mathcal{P}_\theta(\theta, \kappa) = \frac{\kappa}{4\pi \sinh(\kappa)} \cdot \exp(\kappa \cos(\theta)) , \quad (1.15)$$

should be used, where $\kappa \sim \sigma^{-2}$ in the Gaussian approximation.

Studies of the localisation uncertainty of Fermi-GBM bursts have shown that such a parameterisation ill describes the actual error contours [131–133]. As a result, Fermi-GBM instead releases sky maps that describe the numerical probability distribution as a function of right ascension and declination [134]. An example of such a sky map for GRB 090811A is shown in Fig. 1.7. When updating the GRBweb catalogue, the files describing these sky maps are automatically located and downloaded from the HEASARC FTP-server⁶.

1.2.2 Data processing

GBM uncertainties. As a first step, the GBM sky maps are processed to determine the size of the 39.3% containment region⁷. To allow an easy comparison to the uncertainty estimate of other satellites, this area A is converted into an effective opening θ angle following

$$\cos(\theta) = 1 - \frac{A}{2\pi} . \quad (1.16)$$

These values, once calculated, are then pushed to the GBM table of the MySQL server.

Merging data. Using the data from the resources listed above, a single summary table is constructed that lists the available information per GRB. In practice, this is achieved by grouping the entries in the different tables based on their GCN name. This unique identifier has the format *GRB-year-month-day-X*, where the last letter is added to differentiate between GRBs that occur on the same day. For two of the tables, in particular the Fermi-GBM and Fermi-LAT table, bursts do not come with a GCN name. Hence, the times and locations of

⁶<https://heasarc.gsfc.nasa.gov/FTP/fermi/data/gbm/bursts/>

⁷For a two-dimensional Gaussian distribution, the probability contained within 1σ is $e^{-1/2} \approx 0.393$.

those bursts are matched against those of GRBs that are already in the summary table. If no match is found, the burst is given a new GCN-style name before adding it to the table.

A few consistency checks are automatically performed after merging GRBs to tag and remove aberrant values. To determine which values are finally saved to the summary table, an ordering scheme is used based on the source of the information. For instance, the T90 duration is preferably taken from Fermi-GBM, then Swift-BAT, AstroSAT, etc. The right ascension and declination are taken from the source which reported the smallest localisation uncertainty and the GRB trigger time t_{tr} is set to the earliest time at which gamma-ray activity was observed. Apart from selecting variables, a new quantity called the T100 is also added to the summary table, taken to be time difference between the last and earliest reported gamma-ray activity. A burst's T100 is thus generally slightly larger than its T90. While the T90 provides a statistically more robust measure of GRB durations, the full duration of gamma-ray activity or T100 is generally what is used in follow-up multi-messenger analyses.

Statistics. GRBweb is updated once a week and contains data from bursts as early as April 1991, the time at which the BATSE detector was turned on. Previous versions of the summary table are archived during updates, such that changes in the catalogue can be retraced. At the start of 2021, GRBweb's summary table contained over 7.000 GRBs. For more than 500 of those GRBs, redshift information is included in the table. Apart from containing numerical variables, the summary table also includes a reference to the source from which the information was extracted. This allows to easily retrace the instrument linked to each variable.

Gravitational lensing. As an intermezzo, we discuss the possibility that GRBweb might contain multiple entries on the same GRB due to the effect of gravitational lensing. If a lensing event were to split a gamma-ray signal along two paths, the difference in arrival direction would be indistinguishable given the resolution of current gamma-ray telescopes. However, the difference in propagation length could lead to a significant time delay between the two signals. As such, the same GRB might be observed multiple times. For lensing events due to dark matter galaxy halos, the time delay between the different signals is estimated to be on the order of several months [135]. A study performed to search for similarities in the temporal and spectral properties of BATSE GRBs that originate from the same sky location found no conclusive evidence for gravitational lensing events [136]. A similar study based on Fermi-GBM data identified a single burst, GRB 210812A, whose light curve is consistent with being gravitational lensed by a million solar mass black hole [137]. This observation is consistent with recent estimates that indicate that one such events is expected to be observed every ~ 15 years with current GRB detectors [136].

1.2.3 Web interface

The GRBweb catalogue is made accessible by coupling the MySQL server to a web interface written in HTML5 [138]. This website is hosted on the servers of the IceCube Collaboration and can be accessed by visiting https://icecube.wisc.edu/~grbweb_public/. To facilitate the web design, an HTML5 'Elements' template was used⁸ instead of constructing the website from the ground up. The web page is separated into five sections: home, data, description, precursors, and contact.

⁸This template and other free to use predesigned web pages can be obtained from <https://www.html5webtemplates.co.uk>.

Home. This is the start page of the website. A short description is given on the GRBweb project. Links are included to the relevant pages of the website. In addition, the homepage can be used to check the time and date when the catalogue was last updated.

Data. Actual GRB data can be accessed in a number of different ways via the ‘data’ Tab. A first option is to view an online version of the summary table directly in the web browser. On this page, users are thus presented with a scrollable table that lists the main properties all the GRBs in the catalogue. GRB names in this table are given as a hyperlink that refers to a web page listing all known information of that bursts. A unique web page for each individual burst is thus generated. These web pages list the original data from the input catalogues, including all relevant GCN-circulars, and indicate from which resource the variables in the summary table were extracted.

Alternatively, the summary table can be viewed and downloaded as a plain text-file. Archived versions of the summary table, going back to December 2018, are also available in text-file format on the website. To access all available data, users can download an SQLite-file that contains a compressed version of the GRBweb SQL-data. A web page titled ‘Loading the data’ shows an example of how the SQLite-file can be retrieved and loaded into Python. This example script, illustrated by means of a Jupyter notebook [139], can be downloaded as a python script from the website.

Description. Two pages were added to the website that contain meta-data on the construction and content of GRBweb. The first page lists all the resources that are used when composing the catalogue. In particular, references are given for the individual GRB catalogues that are used as input. The second page provides a description of all the variables in GRBweb. When adding data to the catalogue, values are always first converted if required, to have a uniform format across all tables. For instance, the localisation uncertainty of some catalogues is given as the 90% opening angle and is thus first converted to the equivalent 1σ (39.3%) opening angle. Particular care should also be taken when using fluence values, as they depend on the considered energy band and thus detector. Fermi-GBM, Swift-BAT, BeppoSAX, and BATSE all use different energy ranges to calculate fluences. Fluence values should thus not be ‘mixed’ between different detectors.

Precursors. A dedicated web page presenting the results from our Fermi-GBM precursor analysis, described in Chapter 3, was added at a later stage. This page presents a short summary of the analysis, along with a table of the resulting precursors emission times. For each precursor, the table contains a hyperlink to an online interactive version of the light curve. A text-file version of the table is linked for download at the top of the page, to provide easy access to the data.

Contact. Since GRBweb is publicly available as an online tool for the GRB community, we welcome and encourage input from external users. Since the start of the project, five IceCube analyses⁹ have used a source selection based on the GRBweb data and three VUB students have performed their bachelor or master thesis with data from GRBweb. In addition, several people from outside the IceCube Collaboration or VUB have contacted us regarding the use of GRBweb data and provided us with helpful suggestions. Search statistics indicate that on average, GRBweb receives 3 clicks from Google search results per day.

⁹Including the analysis presented in this thesis.

1.2.4 Earlier versions

We conclude this section by noting that the current version of GRBweb was inspired by a similar, but now long obsolete IceCube project with the same name [140]. This archival version of the project was written entirely in php [128] and solely used information extracted from GCN-circulars. A lack of proper code maintenance caused the project to fall into disarray. This led to the unanimous decision within IceCube that it would be better to start the project completely anew in a modern coding language, than to try and patch the old software. Nonetheless, several features of the current project are based on and were inspired by the database structure and parsing expressions used in the old php-version of the code. We hence acknowledge and are grateful for the inspiration indirectly provided by the authors of the previous php-based version of GRBweb.

1.3 Observational properties

The GRBweb project presented in the previous section mainly focuses on providing the time and location of bursts for multi-messenger follow-up analyses. We here highlight some of the other observational characteristics of GRBs, presenting a short overview of ‘what is known’ about GRBs from an experimental point of view.

1.3.1 Duration

A short discussion on the duration of GRBs was already presented in Subsection 1.1.1. We here elaborate further on the properties of the T90 parameter. As mentioned previously, a burst’s T90 is taken to be the length of the central time window during which 90% of the photon fluence is observed. The strength of this T90 parameter, shown in Fig. 1.3, is that it can be easily calculated for each burst. In addition, it provides a strong indication of whether a burst is due to a NS merger or the collapse of a super-massive star. It should, however, be noted that the T90 parameter has to be interpreted with care when relating it to the intrinsic duration of GRBs. One important effect is that time durations are affected by cosmological redshift effects and thus appear a factor $(1 + z)$ longer than the intrinsic duration. GRBs located at far distances will also be prone to the tip-of-the-iceberg effect. A systematic study that downscaled the flux of bright GRBs to larger distances showed that the observed T90 varies on average by $\sim 7\%$ and $\sim 50\%$ for GRBs with a signal-to-noise-ratio of 15 and 5.5, respectively [141].

Detector effects. Apart from the GRB’s distance, the detector observing the burst also has a large effect on the estimated T90 value. For instance, the fraction of long to short bursts¹⁰ observed is 11:1 for Swift-BAT, 6:1 for Fermi-GBM and 9:1 for BATSE. This difference is mostly due to the varying energy ranges of the detectors. Short bursts are on average spectrally harder than long bursts, making them less likely to trigger a detector that is more sensitive to low-energy gamma rays. A second effect is that a significant fraction of short bursts are observed to have long and spectrally soft tails, which are harder to pick up in detectors that are less sensitive to low-energy gamma rays. It has been shown that, by splitting Fermi-GBM observations in different energy bands, corresponding to those of other GRB detectors, the T90 distributions of those detectors can be reproduced [142].

Other components. In addition to the energy dependence of the bimodality, it has also been argued that two components are simply insufficient to describe the T90-distribution of

¹⁰Using a threshold of 2 s and the data from GRBweb.

GRBs [143]. A third intermediate ‘bump’ at a T90 of about 5 s has been observed¹¹ in both the BATSE [143] and Swift-BAT [144] data, leading authors to suggest a third subclass of GRBs. While this feature is present in two independent data sets, reducing the probability that it is a statistical fluctuation, the third component has a significance of at most 2.4σ . Apart from their duration, these intermediary burst are further indistinguishable from regular long GRBs [18]. Another subclass are those of ultra-long GRBs, whose T90 can be in excess of 10^3 s [145, 146]. While a clear bimodality is thus observed between long and short bursts, describing the T90-distribution using a simple double Gaussian function appears to be an oversimplification due to various secondary features, most notable in the duration of long GRBs.

1.3.2 Temporal and spectral evolution

Band spectrum. Apart from duration, a second property by which GRBs can be characterised is the energy spectrum of the gamma-ray flash. The number of incoming photons per unit energy¹² can generally be well described the Band function [147],

$$\frac{dN}{dE} = \begin{cases} A \left[\frac{E}{100 \text{ keV}} \right]^\alpha \exp\left(-\frac{E}{E_0}\right) & E < (\alpha - \beta)E_0, \\ A \left[\frac{(\alpha - \beta)E_0}{100 \text{ keV}} \right]^{\alpha - \beta} \exp(\beta - \alpha) \left(\frac{E}{100 \text{ keV}} \right)^\beta & E \geq (\alpha - \beta)E_0, \end{cases} \quad (1.17)$$

where E_0 is the break energy, A is a normalisation constant, and α and β are the low- and high-energy spectral indices, respectively. Typical values for the spectral indices are $\alpha = -1_{-1}^{+1}$ and $\beta = -2_{-2}^{+1}$ [148]. The Band spectrum smoothly transitions from a broken power law with exponential cut-off to a regular power law with index β . It peaks in the spectral energy distribution $E^2 \frac{dN}{dE}$ at

$$E_p = (2 + \alpha)E_0. \quad (1.18)$$

Observed values for E_p range from a few keV to several MeV [18]. Fitting a Band function to the GRB observations requires binning the observed photons as a function of energy. For bursts with low overall count statistics, few signal events will remain per bin, making it challenging to obtain a reliable spectral fit. A further complication is that the energy response function of GRB detectors is generally a function of the direction of the burst in detector coordinates. The GRB position and energy spectrum are therefore often fitted simultaneously.

Temporal and spectral correlations. If a burst is sufficiently bright, the observed photons can be binned in both time and energy, allowing to trace the spectral evolution as a function of time. GRB light curves are often characterised by several pulses. This is illustrated in Fig. 1.8, which shows the light curves of nine BATSE GRBs. Trigger 1425 (centre left), for instance, shows five consecutive pulses, each increasing in brightness. Considering a single pulse from a long GRB in the keV to 10 MeV energy range, the arrival time of low-energy photons is generally observed to be delayed with respect to that of high-energy photons. In contrast, the highest energy gamma rays ($E > 100$ GeV) lag behind the lower keV to MeV emission of a pulse. This high-energy component thus likely originates from a different physical mechanism [149]. In contrast, no significant spectral lags are typically observed for short GRBs [18].

On top of the pulse structure, most GRB light curves exhibit rapid fluctuations on sub-second timescales. This characteristic can be clearly observed in for example the light curves

¹¹In addition to the standard double Gaussian components, which peak at ~ 0.25 s and ~ 25 s for short and long bursts, respectively.

¹²Note that the incoming photon count per unit energy dN/dE is distinct from the observed photon count per unit energy, as the former accounts for the instrument response function of the detector.

of BATSE trigger 1606 and trigger 143, shown in Fig. 1.8. Spike-like features have been shown to become less significant at low energies [18]. For long GRBs, the typical value of the minimal variability timescale is of the order of 100 ms and has been observed to be as low as ~ 30 ms. For short GRB, typical values of the minimal variability timescale correspond to 10 ms and go down to ~ 3 ms [150].

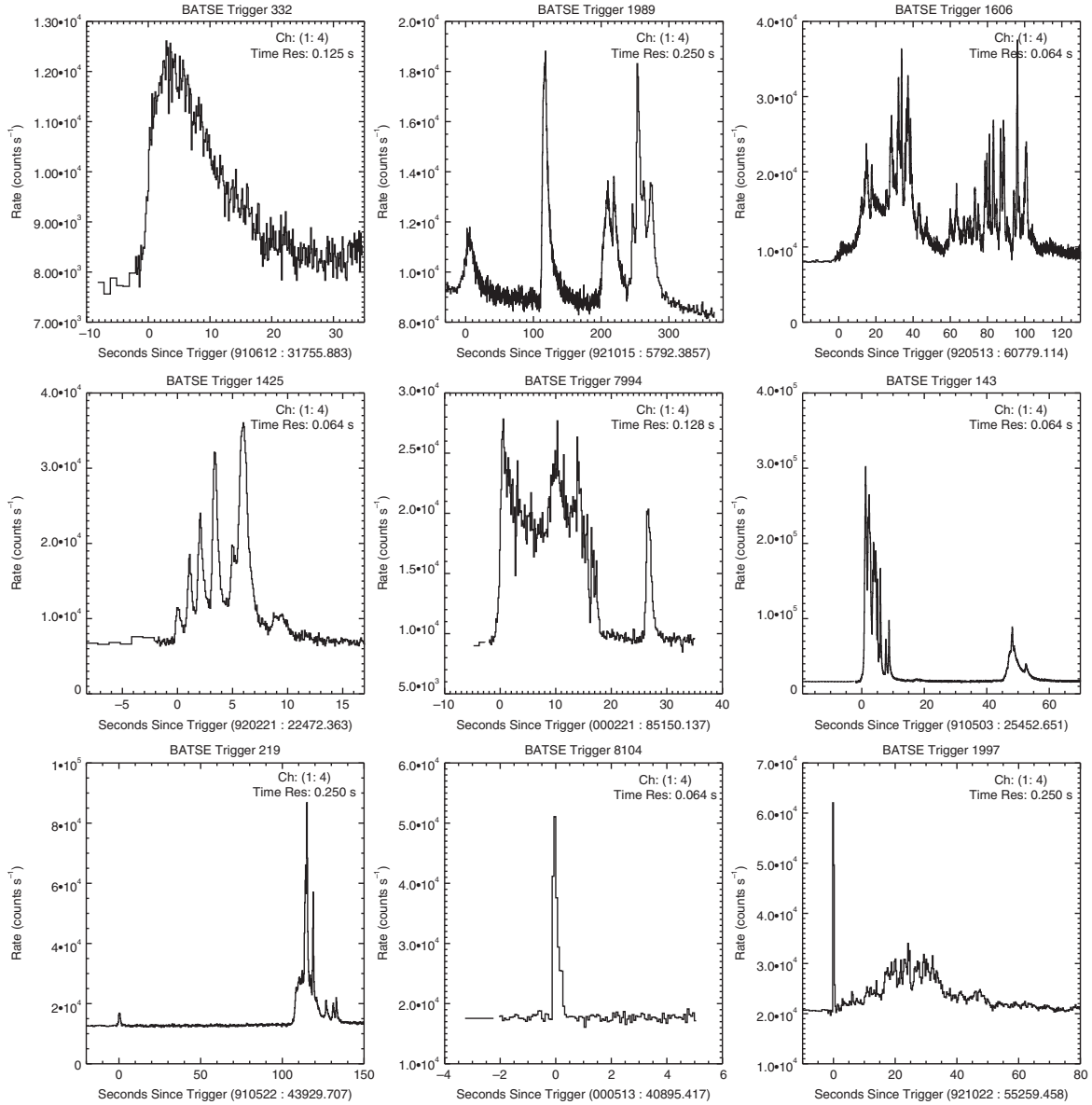


FIGURE 1.8: Sample of nine GRB light curves observed by the BATSE detector. A wide range of temporal evolutions can be observed. Trigger 1606 (top right) displays a clear example of the fast time variability ($\delta t \leq 1$ s) superimposed over a slowly ($\delta t \sim 30$ s) varying component. Trigger 219 (bottom left) is an example of a GRB preceded by a precursor. From [18].

1.3.3 Afterglow

Following the prompt gamma-ray emission, GRBs tend to remain visible at longer wavelengths for months afterwards. Optical transients are, however, much more common than X-ray or gamma-ray transients. Whether or not a low frequency counterpart can be linked to a GRB thus mainly depends on how well the GRB was localised. For $\sim 50\%$ of well-localised

GRBs, optical emission from the GRB afterglow can be observed. This number increases to 80% if the optical follow-up observations started within one hour of the GRB trigger [151]. It has been shown that at least the majority of the remaining 20% are optically dark due to the effect of absorption [151–153]. Absorption can occur in part due to the matter surrounding the burst, but also due to propagation through the intergalactic medium¹³. Hence, it is generally posited that every GRB is followed by a physical, if not observed, afterglow phase [18].

X-ray. The X-ray afterglow immediately follows the prompt emission. Its light curve can be described using a broken power law with five components, as illustrated in Fig. 1.9. Component I, the steep decay phase, can be regarded as the tail of the prompt emission. If one considers a shell of matter which abruptly stops emitting radiation, an observer would gradually see the flux, F , decrease, as signals emitted from higher latitudes will reach the observer at a later stage. The predicted temporal decay¹⁴, $F \propto t^{-2-\beta}$, due to this curvature effect matches the observed steep decay phase well [18]. A shallow decay phase, component II, is then reached. Most likely, this plateau-like feature is due to the decreased, but continual activity of the central engine [18]. When this activity concludes, the observed flux goes into the steep decay phase, component III and IV, and drops sharply.

In contrast to the above mentioned components, whose flux continually decreases, there is a fifth component, which starts off with a sharp increase of the X-ray flux. These X-ray flares are observed in $\sim 50\%$ of Swift bursts, with the average number of flares per GRB being ~ 2.5 [18, 154]. They typically occur several hundred seconds after the start of the bursts, but have been observed with delays of up to one day [154]. 10% of all GRBs are observed to have X-rays flare more than 10^4 s after the GRB trigger [155]. An analysis of the temporal evolution of individual flares strongly indicates that these flares are due to a reactivation of the central engine [156, 157].

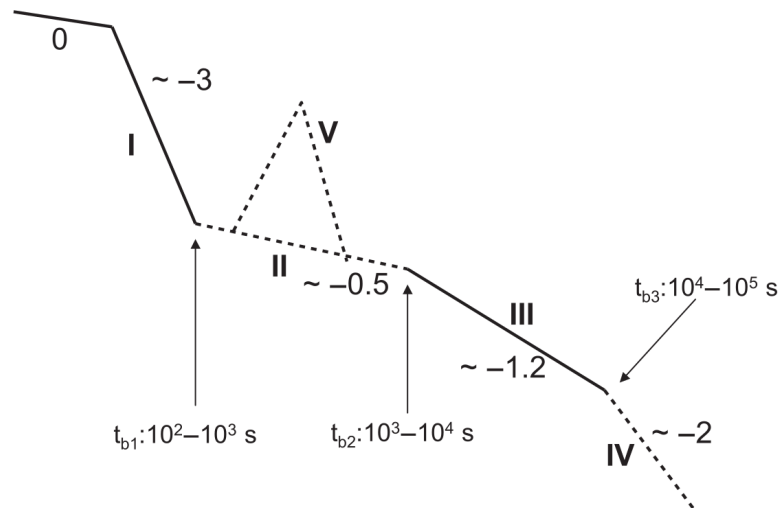


FIGURE 1.9: Time evolution of the X-ray afterglow. The spectrum is well described by a piecewise broken power law, with the addition of X-ray flares (V) for some GRBs. From [18].

High energy. Apart from X-ray emission, a high-energy gamma-ray component ($E > 100$ MeV) has also been observed for some GRBs in the $\sim 10^3$ s time window that follows

¹³Conform with the observation that GRBs with a high redshift ($z > 5$) are more likely to be optically dark [152].

¹⁴Assuming a power law spectrum with spectral index $-\beta$.

the prompt emission [48]. These gamma rays are thought to originate from the external forward shock collision¹⁵. The onset of the high-energy forward shock afterglow emission can start before the end of the prompt phase, causing the observed gamma-ray signal to be a superposition of both components [18].

Optical. In addition to producing the high-energy afterglow, the external forward shock also leads to optical synchrotron emission from shock accelerated electrons. Optical GRB counterparts have been observed starting less than 100 s and up to days and weeks after the GRB trigger. Their light curve follows a power law decay $f(t) \propto t^{-\alpha}$, where $\alpha \sim 1$ [18]. Re-brightening features are sometimes present, most notable of which are the optical flares. At least part of the optical flares are observed to be temporally correlated with late-time X-ray flares [158]. Minor re-brightening features are thought to be related due to local density structures in the circumburst medium [18]. A final re-brightening, visible as a red bump, is sometimes observed around one week after the GRB. This feature is, however, a signature of an accompanying supernova and thus not related to the GRB afterglow. The optical afterglow itself follows a nearly featureless spectrum [18].

Radio. As the external shock continues to sweep up material from the circumburst medium, it gradually slows down. Hence, the Lorentz factor decreases and the emitted electron synchrotron radiation shifts to longer wavelengths. GRBs can remain visible in radio for several weeks after the burst. While there is some debate as to whether there is a subclass of radio-quiet and radio-loud GRBs, complex detector threshold and calibration effects make it unclear whether this is a physical effect or simply an observational bias [159]. One interesting aspect of the radio afterglow is that it can be used to constrain the size, d , of the emission region. This was first demonstrated for GRB 970508 [34] and confirmed that after a period Δt of four weeks, the size of the emission region was in line with the expectation for a relativistically expanding source, i.e. $d \sim c\Delta t$.

1.3.4 Polarization

On top of the arrival time, direction, and energy of electromagnetic radiation, its polarisation offers a fourth observable characteristic. Particularly in regards to the emission mechanism, polarisation measurements can offer an important instrument to distinguish between different models. In the case of synchrotron radiation, the polarisation degree (PD) depends on the coherence of the magnetic field. Emission from a random, unstructured magnetic field will result in no polarisation. If the GRB jet is, in contrast, permeated by a magnetic field that has a coherent large scale structure, the emitted radiation will have a strong linear polarisation [18].

Afterglow. Polarisation measurements have so far been carried out mostly at optical wavelengths. During the early afterglow, i.e. within minutes after the prompt emission, PDs as high as 28% have been measured [160]. This strongly supports the idea that the emission stems from fast cooling electrons that emit synchrotron radiation in an ordered magnetic field. At later times, optical emission is still observed to be polarized, but to a lesser degree ($\sim 1.6\%$ on average [161]). Apart from synchrotron emission, other emission mechanisms such as inverse Compton scattering could potentially also lead to non-zero PDs [162, 163]. For a detailed overview and discussion, we refer the reader to [164].

It was recently (2019) confirmed that the emitted radiation is still polarised at later stages, when the afterglow has shifted to the millimeter radio band. Radio observations of GRB

¹⁵When the material ejected during the prompt phase collides with the circumburst medium, two shocks develop. One forward shock, travelling into the unshocked circumburst material, and one reverse shock, propagating backwards into the blastwave.

171205A found a small, but non-zero PD of $(0.27 \pm 0.04) \%$ [161]. While thus lower than typical optical PDs, radio emission can become (partially) depolarised before leaving the source due to Faraday depolarisation. This is the effect in which the polarisation angle of the emission rotates when travelling through a magnetised plasma. Integrating over the components of an extended source that have undergone various degrees of Faraday rotation thus decreases the observed PD [165].

Prompt. Polarisation is generally considered to be of key importance to determine the emission mechanism of the GRB prompt radiation. While a synchrotron origin is firmly established for the afterglow [18], several contending prompt models remain viable. These models, as will be discussed in Section 1.5, predict various PDs, often varying as a function of time. Measuring the time dependent polarisation of prompt emission would thus offer a method to distinguish between those models. Optical measurements of GRB prompt emission are, however, scarce, given the required time to re-point optical telescopes after they receive a trigger from GRB satellites. Bursts for which prompt optical measurements exist show high PDs on the order van 10% to 80%, albeit with large uncertainties [166, 167].

Dedicated instruments have also been launched to study the polarisation of the prompt gamma-ray component. Selecting a sample of five GRBs with sufficient statistics to reliably extract polarisation information, the POLAR experiment found a best fit average PD of 10%. The probability that the average PD of prompt gamma-ray emission is smaller than 5% could be excluded at 0.1% [168]. For one of the bursts, GRB 170114A, measurements showed a fast variation in both the polarisation degree and polarisation angle during the course of a single gamma-ray pulse [168, 169]. This illustrates the importance of measuring the polarisation properties in a time resolved manner, as a time integrated measurement would have resulted in a PD consistent with zero.

1.3.5 Supernovae

Supernovae (SNe) offer an independent channel to extract information about GRB progenitors and their environments. Since the first association between SN 1998bw and GRB 980425 [35], several tens of other coincident SNe have been identified (see e.g. [36] for a full review). All GRB-SNe with a reliable spectral classification belong to the broad-line type Ic subclass. Type Ic implies that there are no hydrogen, no helium and no silicon absorption lines in the spectrum. These SNe are thus related to the collapse of massive stars that have lost their outer hydrogen and helium shells¹⁶. Broad-line refers to the observed width of spectral lines. As ejected material will be travelling in different directions, the Doppler shift from material travelling to and away from an observer will broaden the spectral lines. Wider than average spectral lines thus indicate the material is moving fast and related to more energetic SN explosions. GRB-SN have wider spectral lines than regular broad-line type Ic SNe, suggesting not all broad-line type Ic SNe harbor a jet [41].

It should also be noted that SNe have only been observed in coincidence with long GRBs [36]. This provides an independent confirmation that long bursts are related to the gravitational collapse of massive stars. While this gravitational collapse is generally expected to produce a black hole, observations of X-ray GRBs¹⁷ indicate that the newly formed compact object can in some cases also correspond to a neutron star [170, 171]. The gravitational collapse that follows compact binary mergers is not expected to produce a SN explosion, in line with the absence of observed short GRB-SN coincidences.

¹⁶This can be either due to strong stellar winds or due to accretion in a binary system.

¹⁷Bursts whose prompt emission is only observed as an X-ray flash.

GRB-SNe typically achieve their peak brightness one to two weeks after the burst [18]. Observing the SN can be challenging if the GRB has a bright optical afterglow. For this reason, GRB-SNe tend to be identified more frequently in GRBs that have a lower than average intrinsic luminosity [18]. A second requirement is that the GRB should be sufficiently close for the SN to be observable. In conventional models, each long GRB for which both criteria are satisfied is expected to be followed by an observable SN explosion. A number of long GRBs have, however, been observed, for which no SN could be identified despite the proximity and accurate location of the GRB. One particularly striking example is GRB 060614, a burst with a T90 of ~ 100 s, located at a redshift of 0.125 [172]. Based on Hubble observations [173], the lack of associated optical emission implied that if the GRB was followed by a SN, the SN would have to be at least 30 times dimmer than any other previously observed SN. Further analysis revealed that GRB 060614 is most likely a short GRB whose duration is mostly driven by a prolonged period of soft emission following an initial 5 s long pulse [173]. Other SN-less long GRB likewise tend to be related to 'fake' short GRBs or caused by optical extinction [18, 171]. Nonetheless, some theoretical models do predict the collapse of a massive star to produce a GRB, but not a SN [174, 175].

1.3.6 Host galaxies

Long GRBs. Given the different progenitors, short and long GRBs are expected to occur in different physical environments. Long bursts result from the core collapse of a massive star. As massive stars have relatively short lifetimes of typically only a few ten million years, long GRBs essentially appear in the region where their progenitor was formed. Studies indeed find a strong positive correlation between the location of long GRBs and the star formation rate (SFR) [39, 176]. Hosts of long GRBs are generally faint, blue, irregular galaxies that have a low mass, low metallicity and a high SFR [177]. Moreover, the long GRB rate tracks the light within the galaxy, i.e. they occur most frequently in the brightest region of the galaxy, where the specific SFR is the highest [40]. The same holds for SN explosions, but to a less significant extent. This suggests that only the most massive stars can lead to a GRB [40]. Likewise, while low metallicity is a marker for regions with a high SFR rate, the hosts of GRBs are found to be more metal poor than hosts of regular type Ic SNe [41]. Low metallicity is thus likely an additional requirement for GRB formation.

Short GRBs. Short GRBs are found to occur in both early (20%) and late type¹⁸ galaxies [18, 178]. These galaxies tend to have a moderate to low SFR and moderate to high metallicity. The short GRB rate also does not track the brightest regions of the galaxy, but instead can have large offsets with respect to the galaxy centre. Numerous short GRBs have in fact been identified without a discernable host galaxy [179]. All these features are consistent with the binary merger model of short GRBs. Supernova explosions occur in an asymmetrical manner, giving the exploding star a kick of ~ 450 km s⁻¹ [180]. A binary neutron star system will have survived two SN explosion¹⁹ and will thus twice have received a kick. If neither kick broke up the binary system, it will eventually coalesce due to the loss of energy and angular momentum by the emission of gravitational waves. While the time delay between the second SN and the GRB is ill constrained, typical estimates correspond to a few Gyr²⁰ [183–185]. Depending on this merger delay time and the kick velocity, the binary can have left the system before the GRB occurs, resulting in a hostless burst.

¹⁸Early type galaxies are elliptical and lenticular galaxies. Late type galaxies are spiral and irregular galaxies.

¹⁹Unless the binary system was formed by dynamical capture.

²⁰Short merger times can result if the second kick bring the two objects closer together. Due to this effect, roughly 1 in 300 short GRB are expected to be preceded by a SN explosion less than $2(z + 1)$ years before the GRB [181, 182].

Redshift. Host galaxies also serve an important purpose for determining the distance to GRBs. Either the distance to the galaxy, if not already known, can be determined independently from the GRB by e.g. measuring the shift in its emission line spectra. Alternatively, the imprint of the galaxy on the afterglow can be used. GRB afterglows have an intrinsic spectrum that is essentially featureless [18]. Surrounding material from the host galaxy can, however, cause absorption lines in the observed spectrum, from which the redshift can be determined [176]. If a SN is observed following the GRB, the SN spectra can also be used to determine the distance.

1.4 GRB physics

Before transitioning to full fledged theoretical models of gamma-ray bursts, a number of relevant physical mechanisms will be discussed in this section. Particularly relativistic timing effects, of importance to essentially all GRB prompt and precursors models, will be presented. In addition, the mechanisms via which high-energy photons, charged particles and neutrinos are produced will also be shortly outlined.

1.4.1 Compactness paradox

Problem. Gamma-ray burst have been observed to show fast variability in their light curves on typical timescales of $\delta t \sim 10$ ms [150]. Causality thus implies that the size of the source can be at most $D \sim c\delta t$, corresponding to about $3 \cdot 10^6$ m. Given this maximal allowed source size, D , the optical depth for photons to undergo pair production $\gamma\gamma \rightarrow e^+e^-$ can crudely be approximated as

$$\tau_{\gamma\gamma} \sim \sigma_T n_\gamma D, \quad (1.19)$$

where σ_T is the Thomson cross section and n_γ the photon density [18]. Assuming a typical GRB with a isotropic equivalent energy E_{iso} of 10^{51} erg and an average photon energy \bar{E}_γ of 1 MeV [18], the particle density of photons for a source of size $D = 3 \cdot 10^6$ m corresponds to

$$n_\gamma \sim \frac{E_{iso}}{\bar{E}_\gamma} D^{-3} \sim 2 \cdot 10^{37} \text{ m}^{-3}. \quad (1.20)$$

If $\sim 20\%$ of those photons have sufficient energy to undergo pair production, then the optical depth equals $\tau_{\gamma\gamma} \sim 10^{15}$. Hence, the source is expected to be severely optically thick, implying that any observed radiation should follow a thermal spectrum.

Relativistic motion. Contrary to the prediction of thermal emission, GRB spectra are observed to follow the Band function, given in Eq. (1.17). This discrepancy can be resolved by assuming that the source is not stationary, but moving towards the observer with a relativistic velocity v . Consider two light signals that are emitted by the source, separated by a time difference Δt_e in the reference frame of the observer. At the time when the second signal is emitted, the source will be lagging behind the first signal by a distance $c\Delta t_e - v\Delta t_e$. An observer will thus detect a time difference²¹ between the two signals of

$$\Delta t_{obs} = \Delta t_e \frac{c - v}{c}. \quad (1.21)$$

Assuming a highly relativistic source, $\Gamma \gg 1$, the correction factor can be rewritten as

$$\frac{c - v}{c} = \frac{c - v}{c} \frac{c + v}{c + v} \approx \frac{1 - v^2/c^2}{2} = \frac{1}{2\Gamma^2}, \quad (1.22)$$

²¹In this calculation, redshift effects on the observed time delays are neglected.

Hence, the true emission region size, D , is larger by a factor $\sim 2\Gamma^2$ than that of the assumed stationary source. A second effect comes from the shift in the photon energies. In the reference frame of the source, photons have an energy that is a factor Γ lower than in the observer frame. This relaxes the pair production threshold from Eq. (1.11) to

$$h\nu_1 \cdot h\nu_2 \geq \Gamma^2 (m_e c^2)^2, \quad (1.23)$$

where ν_1 and ν_2 are the photon frequencies in the observer frame. Fixing the observed energy of the first photon to a constant value implies that the energy threshold ϵ_{th} for the second photon increases by a factor Γ^2 . Considering the high-energy component of the Band spectrum, Eq. (1.17), the photon energy density follows

$$\frac{dn_\gamma}{dE} \propto E^\beta, \quad (1.24)$$

where $\beta \sim -2.2$. Integrating this expression to find the total number of photons $N_\gamma(E > \epsilon_{th})$ above the energy threshold ϵ_{th} , it follows that $N_\gamma(E > \epsilon_{th}) \propto \epsilon_{th}^{\beta+1} \propto \Gamma^{2\beta+2}$. The number of photons with sufficient energy to undergo pair production is thus lowered by a factor $\Gamma^{-2.4}$. Together with the correction on the source size, $D \propto \Gamma^{-2}$, it follows that the true optical depth

$$\tau_{\gamma\gamma} \propto n_\gamma \cdot D \propto N_\gamma(E > \epsilon_{th}) \cdot D^{-2}, \quad (1.25)$$

decreases by a factor $\Gamma^{2\beta-2} \sim \Gamma^{-6.4}$. Returning to the example from Eq. (1.20) that led to an optical depth of $\sim 10^{15}$, a Lorentz factor $\Gamma \sim 220$ is required to reach an optical depth of unity and thus resolve the compactness paradox.

Constraining Γ . Whilst originally stated as a problem [186], the compactness argument can, with our current understanding of GRBs, be used to impose a lower limit on the Lorentz factor of bursts. More stringent limits can be placed the higher the energy of the observed photons. Alternatively, a direct measurement of Γ can be obtained if a high-energy cut-off, due to the source becoming optically thick for photons with energies above the pair production threshold, is observed in the spectrum [18, 149].

1.4.2 Relativistic signals

Doppler factor. For a source moving straight to the observer, the observed time between two signals was shown to be related to the emission time difference by Eq. (1.21). This expression can be generalized to the case where the source is moving at an angle θ with respect to the axis connecting the source and the observer. Given that the velocity component of the source along that axis corresponds to $v \cdot \cos(\theta)$, it follows that

$$\Delta t_{obs} = \Delta t_e \left(1 - \frac{v}{c} \cos \theta\right). \quad (1.26)$$

Both Δt_{obs} and Δt_e are measured in the reference frame in which the observer is at rest. For an observer moving along with the source, the emission time $\Delta t'_e$ will be shortened by a factor Γ due to relativistic time dilation. The Doppler factor, defined by $\Delta t'_e = \vartheta \Delta t_{obs}$, thus corresponds to [18]:

$$\vartheta = \frac{1}{\Gamma(1 - \frac{v}{c} \cos \theta)}. \quad (1.27)$$

In the case where $\theta = 0$ and assuming $\Gamma \gg 1$, the Doppler factor simplifies to $\vartheta \approx 2\Gamma$.

Relative Lorentz factors. As will be discussed in Section 1.5, GRB emission models generally rely on the assumption that the central engine ejects multiple shells of matter. These

shells will propagate at different relativistic speeds. As a result, a faster shell, travelling with speed v_2 , can catch up with slower shell, with speed v_1 , that was emitted at an earlier time. The dynamics of the ensuing collision will depend on the relative Lorentz factor between the two shells. Defining v_{12} as the speed of the second shell in the reference frame of the first shell (or vice versa), it follows from special relativity that [18]:

$$v_{12} = \frac{v_2 - v_1}{c^2 - v_1 v_2} c. \quad (1.28)$$

Using the approximation from Eq. (1.22), which assumes both shells are highly relativistic, i.e. $\Gamma_2 > \Gamma_1 \gg 1$, the relative Lorentz factor between the two shells Γ_{12} can be written as

$$\Gamma_{12} \approx \frac{\Gamma_1^2 + \Gamma_2^2}{2\Gamma_1\Gamma_2}. \quad (1.29)$$

After the collision, a single merged shell with Lorentz factor Γ_m will result [187]. Denoting the mass of the initial shells as m_1 and m_2 , it follows²² from conservation of 4-momentum that

$$\Gamma_m \approx \sqrt{\Gamma_1\Gamma_2 \frac{m_1\Gamma_1 + m_2\Gamma_2}{m_1\Gamma_2 + m_2\Gamma_1}}. \quad (1.30)$$

If both shells have a comparable mass, i.e. $m_1 \approx m_2$, Eq. (1.30) simplifies to $\Gamma_m \approx \sqrt{\Gamma_1\Gamma_2}$. The efficiency with which collisions dissipate kinetic energy thus corresponds to

$$\eta \equiv 1 - \frac{(m_1 + m_2)\Gamma_m}{m_1\Gamma_1 + m_2\Gamma_2} \approx 1 - \frac{(m_1 + m_2)\sqrt{\Gamma_1\Gamma_2}}{\sqrt{(m_1^2 + m_2^2)\Gamma_1\Gamma_2 + m_1m_2(\Gamma_1^2 + \Gamma_2^2)}}, \quad (1.31)$$

typically ranging between 1% and 10% for realistic GRB shell parameters [18].

Catch-up problem. Apart from the resulting Lorentz factor Γ_m , the radius R_c at which the two shells collide can also be determined. The time difference between the emission of the second shell and the collision of the two shells, Δt_c , will satisfy the relation

$$v_2\Delta t_c = v_1 \cdot (\Delta t_e + \Delta t_c). \quad (1.32)$$

Solving for Δt_c and noting that $R_c = v_2 \cdot \Delta t_c$, the collision radius is shown to correspond to²³

$$R_c = \frac{\Delta t_e}{v_1^{-1} - v_2^{-1}} \approx \frac{2c\Delta t_e}{\Gamma_1^{-2} - \Gamma_2^{-2}}, \quad (1.33)$$

Beaming angles. Electromagnetic radiation and particles that are generated by moving shells will generally be emitted isotropically in the reference frame in which the shell is at rest. For an observer on Earth, the emission will be boosted along the direction the shell is moving in and thus will appear to be anisotropic. To illustrate this process, consider a shell moving towards the Earth with velocity $\vec{v} = v \cdot \vec{1}_x$, corresponding to a Lorentz factor Γ . In the reference frame of the shell, a particle is emitted with a speed u'_{\parallel} parallel and u'_{\perp} perpendicular to the x -axis. In the reference frame of the Earth, denoted without primes,

²²Using again the approximation from Eq. (1.22).

²³The rightmost part of Eq. (1.33) is obtained by assuming that $\Gamma_2 > \Gamma_1 \gg 1$, which allows the inverse velocity to be approximated using a first order Taylor expansion $v^{-1} \approx \frac{1 + \frac{1}{2}\Gamma^{-2}}{c}$.

these velocities become

$$u_{\perp} = \frac{u'_{\perp}}{\Gamma \left(1 + \frac{u'_{\parallel} v}{c^2} \right)} \quad \text{and} \quad u_{\parallel} = \frac{u'_{\parallel} + v}{1 + \frac{u'_{\parallel} v}{c^2}}. \quad (1.34)$$

Defining θ_b to be the angle of \vec{v} with respect to the x -axis in the observer frame, it follows that

$$\tan \theta_b = \frac{v_{\perp}}{v_{\parallel}} = \frac{u'_{\perp}}{\Gamma (u'_{\parallel} + v)}. \quad (1.35)$$

A photon moving perpendicular with respect to the x -axis in the frame of the shell will thus appear to be moving under an angle $\tan \theta_b = \Gamma^{-1} c/v$ to an observer on Earth. For a highly relativistic shell, $v \sim c$, emission is therefore said to be beamed by an effective angle

$$\theta_b \sim \tan \theta_b \sim \Gamma^{-1}. \quad (1.36)$$

1.4.3 Jet opening angle

Theoretical models. In addition to relativistic beaming, the ejecta themselves are not emitted isotropically²⁴, but along a conical jet with opening angle θ_j . Typical values for θ_j range from 1° to 10° [188]. Current observations do not constrain the structure of the jet. For this reason, a simple uniform model

$$\frac{dE}{d\Omega} = \begin{cases} \epsilon_0 & \theta \leq \theta_j, \\ 0 & \theta > \theta_j, \end{cases} \quad (1.37)$$

is usually assumed, where ϵ_0 is a constant²⁵. Alternative models include replacing the hard cut-off at θ_j by a power-law decay or assuming $dE/d\Omega$ follows a two-dimensional Gaussian distribution, Eq. (1.14), with θ_j^2 corresponding to the variance [189].

Energetics. For a uniform model in which the jet is expelled in two opposite directions, the true total energy of the burst corresponds to

$$E_t = 4\pi(1 - \cos \theta_j) \cdot \frac{E_{iso}}{4\pi} \sim \frac{1}{2} \theta_j^2 E_{iso}, \quad (1.38)$$

where $4\pi(1 - \cos \theta_j)$ is the solid angle covered by the jet and E_{iso} is the isotropic equivalent energy defined in Eq. (1.1). Given the limited number of bursts for which θ_j can be determined [188–191], the energy of GRBs is generally quoted in terms of E_{iso} . By itself, E_{iso} already provides an indication that GRB emission cannot be emitted isotropically, as some of the most energetic GRBs, e.g. GRB 990123, can have E_{iso} values in excess $M_{\odot} c^2$ [190].

Achromatic steepening. The most common way to determine the jet opening angle is by observing the achromatic break of the afterglow spectrum. During the initial stage of the afterglow, the beaming angle will be negligible compared to the physical opening angle of the jet, i.e. $\theta_b \ll \theta_j$. This implies that all emitted electromagnetic radiation is effectively confined to the region $\theta < \theta_j$. As the ejecta sweep up increasingly more of the surrounding material, the Lorentz factor decreases, increasing the value of the beaming angle. When the

²⁴The reference frame considered here is that in which the progenitor is at rest. This also corresponds to the reference frame of an observer at Earth if both redshift effects and the proper motion of the progenitor and Earth with respect to the cosmic microwave background are neglected.

²⁵The same dependence is taken to hold for the Lorentz factor, i.e. $\Gamma(\theta \leq \theta_j) = \Gamma_0$ and $\Gamma(\theta > \theta_j) = 1$.

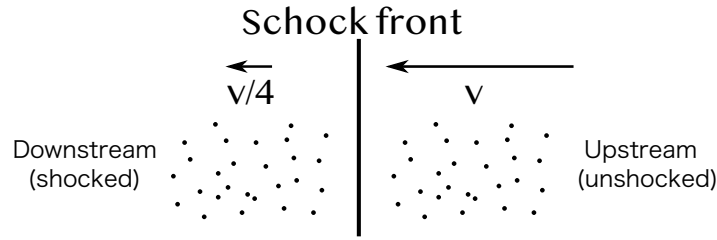


FIGURE 1.10: Illustration of the mean velocities in first order Fermi shock acceleration. Material through which the shock has passed is said to be downstream of the shock front.

beaming angle becomes comparable to the geometrical angle of the jet, a break will occur in the photon flux. Characteristic of this prediction is that the break occurs simultaneously at all wavelengths and is hence achromatic. Given the time at which the break is observed, t_{br} , the jet opening angle can be estimated as $\theta_j \sim \Gamma^{-1}(t = t_{br})$ [18].

Orphan afterglows. As θ_j gradually increases, an observer outside of the geometrical jet opening angle ($\theta_{obs} > \theta_j$) can come to fall in the emission cone of the GRB. Such an observer would thus not observe any prompt emission, but only the optical to radio GRB afterglow at an already developed stage [192, 193]. Searches for orphan afterglows have been performed, leading to a few candidates sources [194, 195]. However, the identification remains tentative as other transient phenomena could not be fully ruled out.

1.4.4 Particle shock acceleration

Non-relativistic shocks. Relativistic shells propagating through a medium will be characterised by a shock front. It was first realized by Enrico Fermi that particles near the vicinity of the shock front could, by crossing the shock multiple times, gain energy and thus be accelerated. This first order Fermi acceleration process²⁶ is believed to be the primary mechanism via which particles are accelerated in GRBs and other high-energy astrophysical sources [196, 197].

To illustrate the process of first order Fermi acceleration, consider a highly simplified scenario in which N_0 particles are injected near edge of a non-relativistic shock front. Each particle is assumed to have an initial energy E_0 . If the particle crosses the shock back and forth, its energy increases from E to $\beta E = (1 + \alpha)E$, where $\alpha > 0$. However, after each double crossing, there is a probability P that the particle streams away and will not cross the shock anymore. Hence, the number of particles that will cross the shock back and forth k times corresponds to $N = N_0 P^k$, implying that there are N particles with an energy greater than or equal to $E = E_0 \beta^k$. Solving both N and E for k and equating the two expression gives

$$\frac{N}{N_0} = \left(\frac{E}{E_0} \right)^{\ln P / \ln \beta} . \quad (1.39)$$

By taking the derivative of N with respect to energy, the power law dependence, as observed in the spectra of cosmic rays and astrophysical neutrinos, is retrieved

$$\frac{dN}{dE} \propto E^{-1 + \ln P / \ln \beta} . \quad (1.40)$$

²⁶A less efficient second order process was initially suggested by Fermi, based on the deflection of charged particles on 'magnetic mirrors'. For a description of this mechanism, see e.g. [18].

Taking the velocity of the shock wave \vec{v} to be such that the Mach number $\mathcal{M} = v/v_s \gg 1$, where v_s is the sound speed, it can be derived that shocked material in the downstream region, defined in Fig. 1.10, moves away from the shock at a speed $v/4$ [198]. As the upstream region is observed to approach the shock with speed v , the up- and downstream move with a speed $\frac{3}{4}v$ with respect to one another. A relativistic particle with momentum \vec{p} and energy $\epsilon \sim pc$ in the upstream region that traverses the shock will have an energy

$$\epsilon' = \Gamma \left(\epsilon + \frac{3}{4} \vec{v} \cdot \vec{p} \right) \approx \epsilon + \frac{3v}{4c} \cos \theta \cdot \epsilon, \quad (1.41)$$

in the downstream region, where θ is the angle between \vec{v} and \vec{p} and $\Gamma \sim 1$ is the Lorentz factor of the shock. Vice versa, the particle will gain the same energy travelling from the downstream to upstream region. Hence, the fractional energy gain of one cycle corresponds to

$$\frac{\Delta \epsilon}{\epsilon} \approx \frac{3v}{2c} \cos \theta. \quad (1.42)$$

Particles that cross the shock have a distribution that is uniform²⁷ in $\cos^2(\theta)$. The average value of $\cos \theta$ thus correspond to

$$\langle \cos \theta \rangle = - \int_0^{\pi/2} \cos(\theta) d \cos^2(\theta) = \frac{2}{3}, \quad (1.43)$$

implying that $\beta \approx 1 + v/c$.

As the bulk motion of particles in the upstream region is directed towards the shock, essentially all upstream particles will eventually pass through the shock again. In the downstream region, particles can either cross the shock again or be carried off indefinitely downstream. Downstream particles move at a bulk speed of $\frac{v}{4}$ away from the shock front. The rate per unit time and area at which particles are carried away to infinity thus corresponds to $\frac{v}{4}n$, where n is the downstream particle density. Particles near the shock will disappear across the boundary at a rate $\frac{c}{4}n$. The factor $1/4$ comes from considering that only of half the particles move towards the shock and that their crossing rate is proportional to $\cos \theta$. Averaging over $\cos \theta$, here following a uniform distribution assuming random motion, results in an additional factor $\frac{1}{2}$. The fraction of particles lost downstream is therefore

$$\frac{\frac{v}{4}n \cos \theta}{\frac{v}{4}n \cos \theta + \frac{c}{4}n \cos \theta} \approx \frac{v}{c}, \quad (1.44)$$

implying $P \approx 1 - v/c$. Combining the expression for β and P

$$\begin{cases} \ln \beta \approx \ln \left(1 + \frac{v}{c} \right) \approx \frac{v}{c}, \\ \ln P \approx \ln \left(1 - \frac{v}{c} \right) \approx -\frac{v}{c}, \end{cases} \quad (1.45)$$

and substituting the result in Eq. (1.40), it follows that $dN/dE \propto E^{-2}$. For non-relativistic shocks, first order Fermi acceleration thus predicts a spectral index of $\gamma = 2$.

Relativistic shocks. For relativistic shocks, the principle of first order Fermi acceleration remains valid. However, several of the approximations used in the above derivation required that $v \ll c$ and thus have to be revisited and treated in a more rigorous manner.

²⁷Once a particle crosses the shock, its direction is assumed to become randomised in the reference frame in which the up- or downstream region (whichever it has entered) is at rest. This implies that the spherical coordinate θ will be uniform in $\cos \theta$. However, the rate at which particles cross the shock is also proportional to $\cos \theta$, leading to the $\cos^2(\theta)$ dependence.

Another failing assumption is that particles instantly acquire a random motion in the new reference frame once they cross the shock boundary. In reality, this process will require a certain time and be dependent on additional parameters, such as the magnetic field configuration [197]. Finally, it has been noted that the shock boundary itself will be altered if significant particle acceleration takes place, such that feedback effects need to be accounted for [18, 199]. Using both semi-analytical methods and numerical simulations that include the relevant microphysics processes, it has been shown that for (ultra-)relativistic shocks, a slightly softer spectral index $\gamma \approx 2.2 - 2.4$ is obtained than predicted by the ideal case of non-relativistic first order Fermi acceleration [199–201].

1.4.5 Synchrotron radiation

Particles accelerated in shocks will be prone to lose their energy again through a variety of physical mechanisms. The dissipated energy is then usually released in the form of electromagnetic radiation. Synchrotron radiation plays an important role in this regard. Afterglow emission of GRBs has been shown to be strongly consistent with having a synchrotron origin. While the mechanism behind prompt and precursor emission is still unclear, it is not unlikely that both are primarily caused by synchrotron emission as well.

Single particle. Synchrotron emission arises when a particle moving through a magnetic field is deflected by the Lorentz force. Assuming a single particle with mass m , charge q , speed v , and Lorentz factor γ propagating at an angle θ with respect to a uniform magnetic field \vec{B} , the power P_ν radiated by the particle per unit frequency ν is given by [18]:

$$P_\nu(\nu, \gamma) = \frac{dE}{dt d\nu} = \frac{\sqrt{3}q^3 B \sin \theta}{mc^2} \frac{\nu}{v_c} \int_{\nu/\nu_c}^{\infty} K_{5/3}(\zeta) d\zeta, \quad (1.46)$$

where K is the modified Bessel function of the second kind and ν_c is the characteristic emission frequency, defined by

$$\nu_c \equiv \frac{3}{4\pi} \gamma^2 \frac{qB \sin \theta}{mc}. \quad (1.47)$$

Figure 1.11 shows the shape of the emitted power spectrum. Starting at low frequencies, the power initially increases as $P_\nu \propto \nu^{1/3}$. A maximum is reached at $\nu \sim 0.29\nu_c$, after which the spectrum essentially²⁸ falls off exponentially $P_\nu \propto e^{-\nu} \sqrt{\nu}$. Integrating over all frequencies, it can be shown [18] that the total power P radiated by the particle is equal to

$$P = \frac{dE}{dt} = \frac{2}{3c^5} \left[\frac{q}{m} \gamma v \sin \theta \right]^2. \quad (1.48)$$

Marking the $P \propto m^{-2}$ dependence, it follows that the synchrotron power output of relativistic protons will be suppressed by a factor $\sim 3.3 \cdot 10^{-6}$ compared to electrons with the same Lorentz factor. Hence, the synchrotron radiation observed from GRBs can, to a good approximation, be attributed solely to the emission from accelerated electrons.

Multiple particles. When a population of particles is considered, the synchrotron spectrum will simply be the linear combination of the spectra of the individual particles. For a population of electrons that follow a power-law distribution $dN/dE \propto \gamma^p$ inside the range $\gamma \in [\gamma_{min}, \gamma_{max}]$, with no electrons outside this range, the resulting bulk photon spectrum

²⁸At large frequencies, the increase due to the $\sqrt{\nu}$ dependence will be negligible compared to the $e^{-\nu}$ decay.

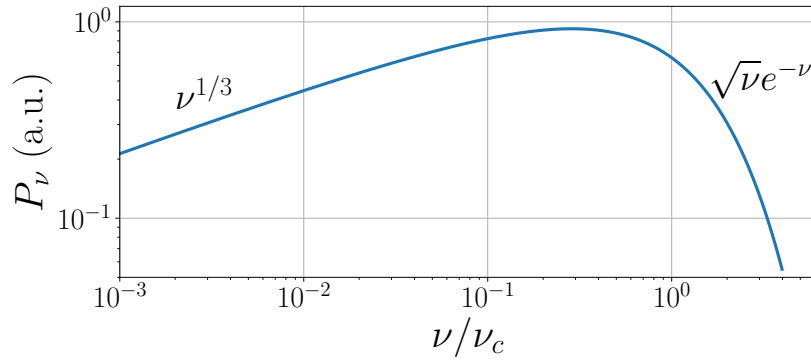


FIGURE 1.11: Power per unit frequency radiated by a single electron as it emits synchrotron radiation when moving through a uniform magnetic field.

per unit frequency $P_{\nu,b}$ corresponds to

$$P_{\nu,b}(\nu) \propto \int_{\gamma_{min}}^{\gamma_{max}} P_{\nu}(\gamma) \gamma^p d\gamma. \quad (1.49)$$

Solving²⁹ this expression, the resulting spectrum is found, to good approximation, to correspond to a broken power law consisting of three components

$$P_{\nu,b}(\nu) \propto \begin{cases} \nu^{1/3} & \nu < \nu_{min}, \\ \nu^{(p+1)/2} & \nu_{min} \leq \nu \leq \nu_{max}, \\ \nu^{1/2} e^{-\nu/\nu_{max}} & \nu > \nu_{max}, \end{cases} \quad (1.50)$$

with ν_{min} and ν_{max} equal to $\frac{3}{4\pi} \frac{qB \sin \theta}{mc} \gamma_{min}^2$ and $\frac{3}{4\pi} \frac{qB \sin \theta}{mc} \gamma_{max}^2$, respectively. For an observer on Earth, the spectrum given in Eq. (1.50) will be boosted by the bulk Lorentz factor Γ of the ejecta. This will leave the shape of the spectrum and thus the spectral indices unchanged, but will shift the frequencies at which the break occurs, ν_{min} and ν_{max} , by a factor Γ .

Additional effects. Having illustrated how a distribution of electrons leads to a broken power law photon spectrum, it should be noted that a range of secondary effects have to be accounted for to compute more realistic photon spectra. One obvious shortcoming in deriving Eq. (1.50) is that the magnetic field of astrophysical sources will not be uniform, but can vary as a function of both space and time. Another effect is that the energy distribution of the electrons will change as they experience cooling due to their radiative losses. At the same time, electrons can also be continuously accelerated near shock fronts. Apart from synchrotron emission, other mechanisms such as bremsstrahlung, (inverse) Compton scattering, synchrotron self-absorption, and pair production annihilation will also play a role [202]. The effect of these additional processes has been computed both analytically [18] and numerically [203], leading to modified spectra that are generally well-described by a broken power-law distribution.

Predictions. An important prediction of the synchrotron model is that the radiation will be strongly polarised if the magnetic field is spatially coherent over large scales. Assuming a uniform magnetic field and a power law distribution $dN/d\gamma \propto \gamma^p$ of electrons, where $p < 0$, the degree of polarisation Π is given by [18]:

$$\Pi = \frac{1-p}{7/3-p}. \quad (1.51)$$

²⁹See e.g. [18] for a detailed derivation.

For a typical spectral index in the range $p \in [-2, -2.5]$, this results in a polarisation degree of $\sim 70\%$. Such high degrees of polarisation have indeed been observed in some GRBs [167] (see Section 1.3.4 for more details). Lower polarisation degrees are expected if synchrotron photons undergo significant inverse Compton scattering [162, 163].

Another prediction by the synchrotron model is that, if the emission is coming from an optically thin region that contains isotropically distributed shocked electrons, the spectral index of the low-energy component of dN_γ/dE cannot be larger than $-2/3$ [204]. This constraint already appeared³⁰ in Eq. (1.50) and is commonly referred to as the ‘synchrotron line of death’. An analysis of the brightest BATSE bursts has shown that this lower threshold is violated in $\sim 20\%$ of all GRBs [167, 205]. While the discrepancy can be partially mediated by including the effects of secondary photon interactions [205], it indicates that synchrotron emission is not the main mechanism behind the prompt component of at least a subset of all bursts.

1.4.6 Hadronic processes

Interaction types. Hadronic interactions offer an alternative channel via which GRBs can produce high-energy particles. If a hadron interacts with a photon, the interaction can result in the production of a meson. Hence, these are referred to as photomeson or $p\gamma$ interactions. In the $p\gamma$ production channel, the Δ -resonance has the highest cross section of the photo-proton resonances [202]. The Δ -resonance produces a short-lived³¹ Δ^+ particle, which in more than 99% of all cases will decay into pions [110]. This process can be written down schematically as

$$p\gamma \rightarrow \Delta^+ \rightarrow \begin{cases} n + \pi^+ , \\ p + \pi^0 . \end{cases} \quad (1.52)$$

The branching ratio for a Δ^+ particle to decay to $n\pi^+$ and $p\pi^0$ is 1:2 [18]. Including processes beside the Δ -resonance, roughly equal amounts of π^0 and π^+ particles will be produced [18]. These pions will in turn decay into photons or leptons

$$\begin{cases} \pi^0 \rightarrow \gamma\gamma , \\ \pi^+ \rightarrow \mu^+ \nu_\mu \rightarrow e^+ \nu_e \nu_\mu \bar{\nu}_\mu . \end{cases} \quad (1.53)$$

During these decays, the charged pions will carry $\sim 20\%$ of the original proton energy E_p and distribute that energy equally among the four leptons. Hence, neutrinos generated in this manner will have an energy $E_\nu \sim 0.05E_p$. Photons that result from the neutral pion decay can contribute to the observed prompt gamma-ray flux [202]. At sufficiently large energies, the linear dependence between the neutrino and proton energy $E_\nu \propto E_p$ will no longer hold. Given the non-negligible decay time of pions and muons, $2 \cdot 10^{-8}$ s and $2 \cdot 10^{-6}$ s [110], respectively, these particles can undergo synchrotron losses before decaying if their energy is sufficiently high. As a result, the neutrinos will have less than 5% of the proton energy.

Photomeson interactions are generally considered to be the main hadronic channel in GRBs due to the assured abundance of high-energy gamma rays. Hadrons can nevertheless also simply interact amongst themselves. The most prominent examples of which would be pp and pn interactions. These processes will primarily lead to the production of pions and kaons, both of which decay into neutrinos and charged leptons. While the cross section for pp interactions is two orders of magnitude larger than that for $p\gamma$, pp interactions will only be dominant in the densest environments [202]. Particularly, high-energy emission from the

³⁰Noting the spectral index of the power and number density differ by -1 , i.e. $P(E) \propto E \frac{dN_\gamma}{dE}$.

³¹ Δ^+ particles have a lifetime of $6 \cdot 10^{-24}$ s [110].

pp -channel would effectively require a jet that is ploughing its way through the envelope of a massive star progenitor [18].

Waxman-Bahcall spectrum. Assuming that the neutrino flux from GRBs is purely due to photomeson production at the Δ -resonance, the neutrino flux is expected to follow a three component broken power law, as will now be shown. A $p\gamma$ interaction can produce a Δ^+ baryon if the following kinematic criterion is satisfied³²

$$E_\gamma \geq \frac{m_{\Delta^+}^2 - m_p^2}{2E_p(1 - \cos\theta)} c^4, \quad (1.54)$$

where θ is the angle between the propagation direction of the colliding particles. Based on first order Fermi acceleration, the protons can be assumed to follow a power-law energy density with spectral index $\gamma \sim 2$. Taking the gamma rays to be those observed in the prompt emission, their energy density can be approximated using a simplified version of the Band spectrum, Eq. (1.17),

$$\frac{dN_\gamma}{dE} \propto \begin{cases} E^{-\alpha} & E < E_0, \\ E^{-\beta} & E \geq E_0, \end{cases} \quad (1.55)$$

where $\alpha \sim 1$ and $\beta \sim 2$. Any gamma-ray above the energy threshold set by Eq. (1.54) will be able to interact with a proton of energy E_p . To first order, the number of photons above a threshold $E_{\gamma,min} \propto E_p^{-1}$ is proportional to either $E_p^{\alpha-1}$ or $E_p^{\beta-1}$. Multiplying the proton density with the number of available gamma rays and using $E_\nu \propto E_p$ then results in the Waxman-Bahcall prediction [123] for the neutrino flux

$$\frac{dN_\nu}{dE} \propto \begin{cases} E^{-\gamma+\beta-1} \sim E^{-1} & E < \epsilon_1, \\ E^{-\gamma+\alpha-1} \sim E^{-2} & \epsilon_1 \leq E \leq \epsilon_2, \\ E^{-\gamma+\alpha-3} \sim E^{-4} & E > \epsilon_2, \end{cases} \quad (1.56)$$

shown in Fig. 1.12. The first transition at $E_\nu = \epsilon_1$ is caused by the spectral break in the simplified Band function, Eq. (1.55), and is expected to occur at $E_\nu \sim 0.7$ PeV. A second break at a higher energy threshold $E_\nu = \epsilon_2$, expected³³ at $E_\nu \sim 300$ PeV, has been added to account for the synchrotron energy losses that pions and muons experience before decaying to neutrinos [18, 207].

The spectrum in Fig. 1.12 well describes the three main features of the spectrum, namely first a hardening due to the fact that higher energy protons can interact with lower energy photons, then a plateau between ϵ_1 and ϵ_2 , and finally a softening due to pion and muon cooling. These general trends are found to be reproduced in more complex numerical calculations that, besides the Δ -resonance, also account for other interaction channels. Nonetheless, including additional physics has been shown to alter both the shape and normalisation of the spectrum in a non-negligible way, in some scenarios decreasing the predicted neutrino flux by an order of magnitude [202, 208–211].

CR-neutrino correlation. Neutrinos will be free to escape the GRB environment after being created. Correcting for redshift effects, the observed neutrino energy spectrum will thus correspond to that at the source. Hadronic particles produced alongside the neutrinos,

³²Eq. (1.54) is valid in the co-moving frame of the ejecta. In the observer frame both E_γ and E_p are scaled by an additional factor $\Gamma/(z+1)$, where Γ is the bulk Lorentz factor and z the redshift.

³³ ϵ_1 and ϵ_2 are typically defined in the reference frame of the observer and thus among other things depend on the Lorentz and redshift of the burst [206].

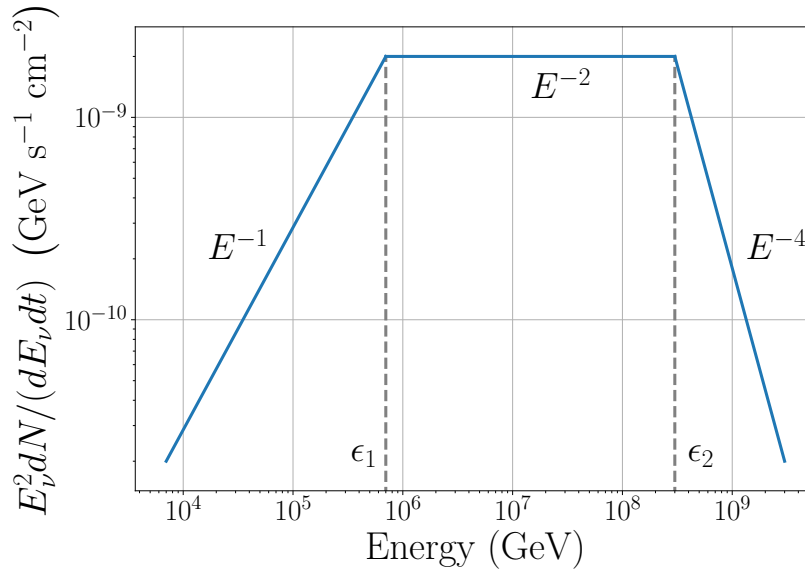


FIGURE 1.12: Shape of the Waxman-Bahcall flux, illustrating the two breaks in the energy spectrum. Both the location of the transition energies, ϵ_1 and ϵ_2 , and the normalisation of the flux depend on the particular emission model.

see Eq. (1.52), will in contrast be prone to undergo photo-hadronic interactions. Protons can additionally be magnetically confined. Predictions on the relation between CRs and neutrinos therefore depend on the escape mechanism of the CRs. For instance, whether only neutrons or both protons and neutrons are able to escape. While neutrino emission provides a clear proof of hadronic acceleration, the inverse does not hold. If protons are able to efficiently escape, e.g. due to shells colliding at large radii where the opacity is lower and the magnetic field weaker, significant CR production could take place with very little accompanying neutrino emission [212]. CR limits based on neutrino observations should thus always be regarded in context of the assumed interaction and CR escape model.

1.5 Emission models

In the previous section, a short review was given on the physical mechanisms which lead to the production of gamma rays, neutrinos, and cosmic rays. These derivations generally assumed a generic model in which particles are accelerated by a ‘central engine’ up to some bulk Lorentz factor Γ . If multiple of these relativistic shells are launched, interactions can occur between the different shells and with the environment through which the shells are propagating. The characteristics with which the ejecta are launched will to a large extent determine the properties of the observed signal. We therefore here discuss how a relativistic jet can be launched and what the relation is between the jet characteristics and the properties of the emitted signal.

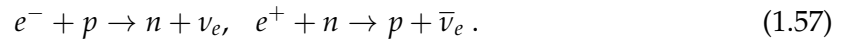
1.5.1 Central engines

Requirements. For an object to qualify as the central engine of a GRB, it has to be able to satisfy, among other things, the following observational constraints [18]:

- The object should be able to cause a burst of gamma rays with an equivalent isotropic radiated power $L_{iso} \gtrsim 10^{46} \text{ erg s}^{-1}$. Integrating over time, the total equivalent isotropic energy of the event should be $E_{iso} \gtrsim 10^{49} \text{ erg}$.

- Outflow ejected by the engine should typically be able to reach a bulk Lorentz factor Γ in excess of 100.
- Gamma rays produced by (the most) energetic bursts should be able to attain energies in excess of 1 TeV.
- The gamma radiation from the prompt outflow should be able to produce fast variability on top of one or multiple smoothly varying pulses. Given the large differences in the characteristics of GRB light curves, the outflow from the central engine must be generated in an erratic manner such that it differs from burst-to-burst.
- At a later stage, several thousands of seconds after emitting the prompt emission, the central engine should be able to get reactivated and power X-ray flares and, in some cases, lead to the steady X-ray plateau emission (see Subsection 1.3.3).

Black holes. The vanilla model to achieve highly energetic and at the same time erratic emission from an astrophysical transient is to assume the accretion of matter onto a black hole. Based on conservation of angular momentum, matter surrounding the black hole is expected to form a disk shape. This disk will feed the black hole, during which process, the infalling matter will gain a lot of kinetic energy due to the loss of gravitational potential energy. An extremely hot and dense environment is thus formed, allowing electron-positron capture processes to occur efficiently,



Neutrinos have a much smaller cross section than charged leptons and baryons [213]. Hence, they are the only particles that can escape the dense environment, carrying off energy as they do. Escaped neutrino pairs that annihilate above the disk will produce a plasma of photons and electron-positron pairs. Additionally, the neutrinos can interact with baryons, stripping them from the disk. Numerical models [214, 215] suggest that a broad ($\theta \sim 30^\circ$) hot fireball is thus launched³⁴, potentially acting as the source of the GRB jet.

An alternative to such a neutrino-dominated accretion flow (NDAF) is that the extracted energy can instead also be rotational in origin. The hot dense matter orbiting the black hole will carry an accompanying magnetic field. If the magnetic field lines thread the black hole while still being connected to the accreting particles, the field lines can get twisted, resulting in a magnetic torque. This Blandford-Znajek (BZ) mechanism [216] serves as a real-life example of the Penrose process [217] and allows spin energy to be extracted from the black hole. A Poynting flux dominated jet will be launched along the direction of the magnetic field lines, with a very limited³⁵ baryon content.

Which of these two mechanisms dominates, NDAF or BZ, will depend on a wide range of parameters, primarily among which are the strength of the magnetic field, the spin of the black hole, and the accretion rate \dot{M} . A strong magnetic field and spin favours a BZ-jet, whereas a large accretion rate³⁶ is in favour of a NDAF [18]. These two mechanisms should, however, not be considered in an either/or manner. Studies have shown that magnetic torque can significantly alter and enhance the emission from a NDAF, suggesting an aggregate of the two effects needs to be considered [218, 219]. One thing both mechanisms do have in common is that the rapid variability observed in GRB light curves is naturally

³⁴At a later stage, pressure from the surrounding material can collimate the jet opening angle to a few degrees.

³⁵Due to their small gyration radius, protons cannot penetrate the jet. Neutrons can be entrained either by inelastic collisions or by turning into a proton after capturing a positron or undergoing beta decay.

³⁶In the BZ-mechanism, the energy output of the jet is roughly linearly proportional to \dot{M} , while the NDAF power drops rapidly in the low \dot{M} regime [18].

expected from viscous instabilities that cause the infalling matter to be accreted in an erratic manner [220, 221].

Millisecond Magnetars. Neutron stars, being the astrophysical objects closest to a black hole in terms of density³⁷, are an alternative candidate as the GRB central engine. One key difference is that unlike black holes, neutron stars carry their own magnetic fields. Due to the superconducting properties, the magnetic field is effectively ‘frozen in’ after the neutron star is formed. While the manner in which the initial field is generated is still unclear [222], observations indicate that typical neutron stars have magnetic field strengths of the order $10^4 - 10^{11}$ T [223]. Magnetars form the subset of neutron stars that have the strongest magnetic fields, $B \gtrsim 10^8$ T. As explained below, the strong magnetic field can induce flashes of gamma rays and X-rays, making magnetars the accepted source of soft-gamma repeaters (SGRs) and anomalous X-ray pulsars (AXPs) [224, 225].

Magnetars will rapidly lose their rotational energy by emitting magnetic dipole radiation. The corresponding energy loss rate is

$$\dot{E} = -\frac{B^2 R^6 \omega^4}{6c^3}, \quad (1.58)$$

where R is the neutron star radius, B the surface strength of the magnetic field at the poles and ω the angular frequency [18]. Millisecond magnetars, being the neutron stars with the largest spins and magnetic fields, will thus dissipate their rotational energy much faster than regular neutron stars, which have typical orbital periods of ~ 1 s. Energy loss proceeding in this manner is a continuous process. It therefore lacks the erratic temporal fluctuations observed in GRB light curves. Stochasticity is nonetheless expected initially as neutron stars can undergo differential rotation in the first ~ 100 ms after their birth [226]. This can cause the eruption of magnetic bubbles along with a strong neutrino driven wind [18]. Differential rotation will also protect against further gravitational collapse [227], suggesting that some neutron stars are extremely short-lived.

An alternative is that, as described in the case of black holes, accretion on the neutron star can lead to a jet driven by neutrino anti-neutrino annihilation. Compared to the BH scenario, higher $\nu\bar{\nu}$ luminosities can be reached due the existence of a physical surface boundary between the accretion disk and the compact object, allowing the disk to cool more efficiently [228]. As accretion increases the mass and as the rotational speed decreases, the neutron star can be pushed over the mass limit causing it to further collapse. Numerous GRBs show a 10.000 s long X-ray plateaus right after the prompt emission, followed by a steep decline [18]. In the magnetar paradigm, this is naturally explained by the continuous magnetic dipole radiation abruptly ending when the neutron star collapses to a black hole.

Quark stars. A more exotic hypothesis is that GRBs are powered by a quark star central engine. At sufficiently high densities, it has been suggested that a quark-gluon-plasma of the three lightest quark flavours (up, down, and strange) will be more stable than a collection of individual baryons [229, 230]. Per baryon, the conversion from neutrons to strange quark matter would allow ~ 10 MeV of gravitational binding energy to be released [231]. For an entire neutron star, this corresponds to a total energy release on the order $10^{52} - 10^{53}$ erg [232]. Apart from being able to satisfy the energy constraints, other features such as the erratic temporal behaviour and late time X-ray flares can, under the right assumptions, also be reproduced [18].

³⁷A typical $1.4M_{\odot}$ neutron star is expected to have a radius of ~ 10 km.

Currently, the state of nuclear matter at these high densities is still badly constrained. Observations of the kilonova that followed GRB 170817 have confirmed that the two objects which merged are indeed neutron stars and not quark stars [233]. It can be expected that future observations will allow to further constrain the neutron star equation-of-state and either put limits on or potentially confirm the existence of quark stars.

1.5.2 Photospheric emission

Any plasma ejected by the central engine will initially be severely optically thick to radiation, i.e. $\tau \gg 1$ with τ is the photon optical depth. As the ejecta expand out, a radius R_{ph} will eventually be reached at which the following condition holds true

$$\int_{R_{ph}}^{\infty} d\tau = \int_{R_{ph}}^{\infty} n_e \sigma_T ds = 1. \quad (1.59)$$

In this expression n_e is the electron density, σ_T the Thompson scattering cross section and ds the distance travelled by the photon with respect to the surrounding ejecta. R_{ph} is defined as the photosphere radius at which the transition occurs from an optically thick to an transparent medium. A thermal emission component corresponding to the radiation escaping at the photosphere would thus naively be expected. This is in contrast to observed GRB spectra, which are generally well described by the Band function, Eq. (1.17). A shift to a quasi- or non-thermal spectrum can occur if the photons undergo significant boosting due to inverse Compton interactions with shock-accelerated electrons. Other observational characteristics of GRB prompt emission, such as e.g. the degree of polarisation, can given the right conditions³⁸, also be reproduced [234].

Relative to other emission models, an upside to the photospheric contribution is that this component is essentially guaranteed. While some models (e.g. [77, 235]) have in the past proposed photospheric emission as the source of the GRB prompt photons, the current consensus is that it is likely only a subdominant contribution. In particular, observations by Fermi and Swift have shown that a small fraction ($\sim 10\%$) of GRBs show evidence for a thermal component at low (X-ray) energies on top of the non-thermal spectrum [18, 236, 237]. Some GRBs, e.g. GRB 090902B, even have a spectrum in which the quasi-thermal component is dominant. Generally, no thermal component can, however, be resolved, likely in part due to the weakness of photospheric signal.

1.5.3 Fireball model

Given the erratic nature of GRB light curves, central engines must expulse their ejecta with a high degree of variability. Accretion on a black hole, for instance, is expected to be an intermittent process that results in the launch of several shells of ejecta with varying masses and Lorentz factors. Each shell will initially consist of a hot fireball in which electrons and positrons are in equilibrium with photons, along with a small amount of baryons. At the base of the jet, the ejecta will have a cross section radius³⁹ on the order $R_0 \sim 10^5$ m [18]. It can be derived (see e.g. [238]) that the shell will initially undergo an accelerated expansion according to $\Gamma \propto r$, where r is the distance from the base of the jet. Once the density has decreased sufficiently to transition from a radiation-dominated phase to a matter-dominated

³⁸For instance, a non-zero polarisation degree can be achieved in the case of photospheric radiation if the emission is observed (slightly) off-axis and if there is a strong gradient in the luminosity and Lorentz factor along the transverse direction of the jet axis [234].

³⁹Taking the innermost accretion radius of a black hole or the radius of the light cone of a millisecond magnetar results in the same order of magnitude estimate for R_0 [18].

phase, a coasting state is reached in which $\Gamma \sim \Gamma_0$ is constant. This transition is expected to occur at a radius $R_{cst} \sim \Gamma_0 \cdot \max(R_0, \Delta) \sim 10^7 - 10^8$ m, where Δ is the width of the shell. As the shell continues to propagate outward, it will keep sweeping up matter from the circumburst medium. Once the amount of swept off matter becomes comparable to the mass of the shell, the coasting-phase will transition to a deceleration-phase in which $\Gamma \propto m^{-1}$, with m the total mass of the shell and swept up material. For typical parameters of the interstellar medium, the deceleration radius will occur at $R_d \sim 10^{14} - 10^{15}$ m [18].

Internal collisions. In the fireball model, successive shells with different Lorentz factors can potentially catch up with one another. When this happens, an internal collision is said to take place, leading to a single merged shell. During the merger, the interface between the two shells will lead to particle shock acceleration as described before. Accelerated electrons will quickly lose their energy again by emitting synchrotron radiation. This mechanism is one of the leading candidates for the emission of the prompt gamma-ray signal from GRBs.

The radius R_c at which internal shocks occur is determined by the catch-up problem (section 1.4.2). A lower limit for R_c can be obtained by noting that Eq. (1.33) implies that

$$R_c \gtrsim 2c\Delta t_e \Gamma^2, \quad (1.60)$$

where Δt_e is the time delay between the emission of the two shells and Γ is the Lorentz factor of the slowest shell. For typical fast timescale fluctuations of the order $\Delta t_e \sim 10^{-2}$ s and a Lorentz factor $\Gamma \sim 100$, the collision radius corresponds to $R_c \sim 10^{10}$ m. Internal collisions are thus expected to occur during the coasting phase in which the shells have attained their maximal Lorentz factor.

External shock. The point at which the ejecta reach the deceleration radius marks the onset of the afterglow emission. Particles near the shock front that separates the ejecta from the circumburst medium will continuously be accelerated, leading to the shallow decay phase of the afterglow. Based on the time at which this shallow decay phase sets in, constraints can be placed on the coasting Lorentz factor of the ejecta⁴⁰ [239, 240].

Initially, it was also suggested that the prompt emission could also originate from the external shock, provided that the circumburst medium would be ‘clumpy’ enough to explain the observed variability [241]. This was disproved by Swift observations showing a steep decay phase following the prompt emission [240, 242]. In addition, Swift observations demonstrated that the decay of both prompt gamma rays and late time X-ray flares is in accordance with the curvature effect [157], thus confirming the internal origin of the latter.

1.5.4 Poynting flux

An alternative to the ‘fireball’ outflow, in which most of the energy is carried by the bulk kinetic motion of the shells, is that the energy is primarily carried by the magnetic field of the ejecta. To distinguish these two scenarios, the ratio between the matter and magnetic energy density, defined as the magnetisation factor:

$$\sigma_M \equiv \frac{B^2}{\mu_0 \Gamma \rho c^2}, \quad (1.61)$$

is considered. In this expression, B is the magnetic field strength, Γ the bulk Lorentz factor, ρ the mass density and μ_0 the vacuum permeability⁴¹. Ejecta for which $\sigma_M \gg 1$ are said to

⁴⁰Assuming a circumstellar medium with a known and constant density.

⁴¹Note that in most textbooks, Eq. (1.61) will be written with a factor 4π in the denominator instead of μ_0 , due to the use of CGS units. Here, the expression is given in SI units.

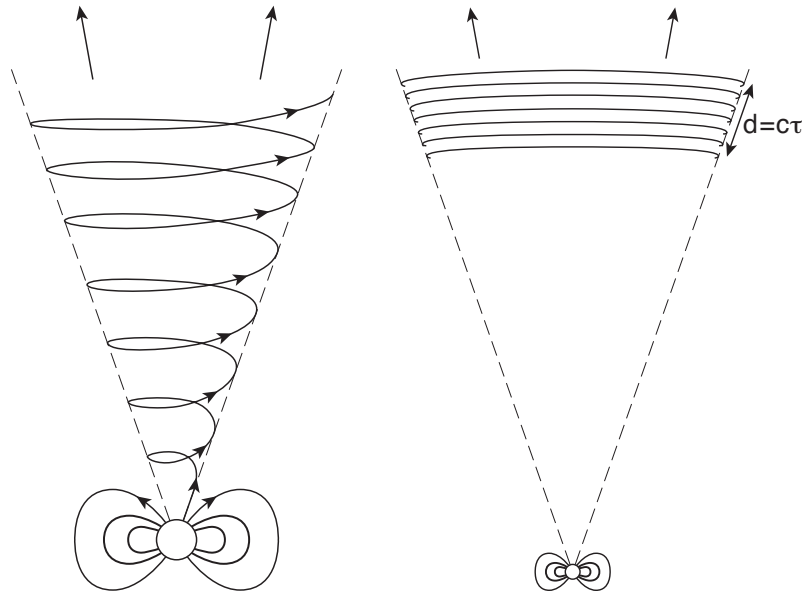


FIGURE 1.13: Left: Illustration of how the poloidal component of the magnetic field can be wrapped into a helical structure due to the rotation of the central engine. Right: Structure of the magnetic field long ($t \gg \tau$) after the central engine, with lifetime τ , has turned off. From [243].

be Poynting-flux dominated.

To illustrate how a magnetised outflow is launched, Fig. 1.13 shows the field lines for a central engine with a large-scale toroidally structured magnetic field that is aligned with the axis of rotation. A helical structure will result, which decouples from the central engine when it shuts down. This essentially turns the outflow into a ‘flying pancake’ of tightly wrapped magnetic field lines. More complicated configurations can be obtained by considering instances in which the axis of the B -field and rotation are not aligned.

While being magnetically dominated, the outflow will still carry an electron-positron plasma that is trapped by the magnetic field lines. Baryons will, by definition, be largely absent in the ejecta. A mini-fireball is thus launched, expanding due to the pressure of the plasma and the non-zero magnetic pressure gradient [18]. Similar to the fireball model, photospheric emission will appear when the plasma becomes optically thin. However, consistent with observations, this component is expected to be much weaker than the subsequent emission from accelerated electrons, contrary to the vanilla fireball model [244]. Another difference is that the main emission would result from electrons that get accelerated in magnetohydrodynamic (MHD) plasma instabilities [244, 245]. These instabilities are expected to occur at a radius of $10^{13} - 10^{14}$ m, thus much further from the central engine than in the fireball model.

The extent to which the magnetic field plays a role in the outflow is strongly coupled to the central engine that launches the ejecta. If the Blandford-Znajek mechanism is dominant, a magnetisation parameter $\sigma_M \gg 1$ is expected, leading to a Poynting flux dominated jet. If the neutrino-dominated accretion flow mechanism launches the jet, the magnetisation parameter will be $\sigma_M \ll 1$, leading to a fireball outflow.

1.5.5 ICMART

ICMART is an acronym for internal-collision-induced magnetic reconnection and turbulence. It builds on the standard assumption that GRB prompt emission is caused by internal shock collisions, but posits that the outflow is launched with a moderately large magnetisation parameter $\sigma_M \sim 10^2$.

Magnetised shells ejected by the central engine will initially have field lines that are globally ordered, e.g. in a helically wrapped ‘pancake’ as shown in Fig. 1.13. Upon a collision with another shell, ram pressure will lead to a slight distortion of the field lines. While field lines are expected to remain largely globally ordered after a single collision, the additive effect of multiple collisions will lead to a continual decrease of the coherence length of the magnetic field. Once the coherence has dropped sufficiently, a point might be reached in which a single reconnection⁴² of magnetic field lines, increasing the turbulence even further, causes a cascade of magnetic reconnection events. During this process, the snapping together of field lines would lead to the acceleration of electrons, quickly converting the tension in the magnetic field lines into kinetic energy until $\sigma_M \lesssim 1$. Observationally, the fast variability ($\Delta t \sim 10^{-2}$ s) of light curves can then be attributed to the turbulent nature of the process. Variability on larger timescale ($\Delta t \sim 1$ s), corresponding to individual pulses, is suggested as being due to several distinct ICMART events [247].

Apart from naturally explaining the two timescales, the ICMART model is also able to reproduce several other challenging GRB characteristics, such as high degrees of polarisation, weak photospheres, and the energy spectra of the prompt gamma rays [247]. Similarly to a Poynting-dominated outflow, ICMART events, requiring several internal collisions to occur before triggering a cascade, are expected to occur at relatively larger radii, $R \sim 10^{12} - 10^{14}$ m [247]. Numerical MHD simulations have confirmed that shell collisions can indeed trigger the predicted reconnection cascade [248, 249].

1.5.6 Alternative models

Finally, we also mention two additional models that have been suggested as emission mechanisms for prompt radiation, though are generally less discussed.

Cannonball. The first model uses the same starting ingredients as the fireball model, namely, a compact object surrounded by an accretion disk. It differs by assuming that the accretion is not a semi-continuous process, but proceeds in very short and sudden emission episodes. Each accretion period will result in the launch of dense ‘cannonballs’ of ejecta via a NDAF. Gamma radiation is then predicted to occur due to the propagation of these cannonballs through the circumburst medium. Fast variability would thus have to be caused by the clumpy nature of the medium through which the cannonballs propagate [250, 251]. A downside to the model is that the cannonballs are assumed to be almost invariant during their propagation, meaning they are treated as rigid bodies which do not expand due to their own pressure and that shock formation is not considered [18]. A similar mechanism called the ‘shotgun model’, describing a scenario in which dense ejecta with extreme Lorentz factors ($\Gamma \sim 10^3$) interact with the circumburst medium via shock formation has also been suggested [252].

Fireshell. The second model is based on the assumption that GRBs are produced by the sudden formation of a black hole that is rapidly spinning and carries a non-zero electric

⁴²Magnetic reconnection as an emission mechanism to explain the prompt radiation of GRB was first suggested by C. Thompson in 1994 [246].

charge. Immediately following its creation, the black hole would rapidly discharge an estimated energy of the order $E \sim 10^{54}$ erg by vacuum polarisation [253]. This discharge would result in an electron-positron plasma or ‘fireshell’, leading to the ‘proper GRB’ when the plasma becomes optically thin. The ‘proper GRB’ would thus be emitted isotropically and is expected to have a thermal spectrum. In terms of observational features, a similar signature to the photospheric emission would result. As a downside, only a single pulse from a GRB can come from this mechanism. Later pulses would have to be due to the interaction of the now optically thin fireshell with the circumburst medium [254, 255]. It is thus unlikely that the fireshell mechanism actually causes the main gamma-ray emission, but it could, in some cases, potentially contribute to an early thermal pulse.

1.5.7 Model limits from neutrino observations

The models described above can be compared to GRB data using a range of observational features. Aspects of the prompt gamma-ray signal previously discussed include the degree of polarisation, the photon energy spectrum, and the strength of a potential photospheric component. While these already offer a fair degree of distinction, fully rejecting a model remains difficult, as model predictions that deviate from the observed data can often still be fine-tuned to match the observations regardless [256]. Also, the data show a large variety of different features, which makes it hard to judge whether a certain model could describe a subclass of GRBs or not. To resolve this issue, channels complementary to the electromagnetic radiation can be used. In particular, GRB neutrino observations, or rather the lack thereof⁴³, can offer a powerful alternative to differentiate between GRB emission models.

Requirements. For GRBs to be sources of neutrinos⁴⁴, two criteria need to be satisfied.

1. The central engine should produce a jet with a non-negligible baryonic content. This requirement is generally quantified in terms of the baryon loading factor, $f_b \equiv E_b/E_\gamma$, defined as the total energy dissipated into baryons over that going into the electromagnetic component [122]. To avoid $f_b \ll 1$, baryons should be entrained by the jet, effectively requiring a central engine that launches a NDAF. Additionally, the baryons should at a later stage be accelerated to higher energies. This can proceed in either internal or external shocks.
2. A second criterion is that baryons should be accelerated in regions where the particle density is sufficiently large, so that they can undergo either pp or $p\gamma$ interactions. Particularly in the case of particles accelerated by internal shocks, larger collision radii correspond to lower shell densities, thus leading to less neutrinos [258].

Limits. Under these assumptions, neutrino emission spectra for GRBs have been computed numerically for the various models [257, 258]. Comparing those model predictions to observations by IceCube has already led to constraints on both the internal shock and the dissipative photosphere⁴⁵ model, as illustrated in Fig. 1.14. In particular, the single-zone fireball model [208], in which the neutrino flux is derived for a single baseline collision and then scaled linearly by the number of collisions, can already be excluded at 99% confidence [257]. The more realistic multi-zone models, which allow collisions to occur at various radii, including below the photosphere, predict significantly lower neutrino fluxes and are so far unconstrained [259]. Likewise, predictions for the ICMART model remain consistent with

⁴³No significant neutrino signal has yet been found in coincidence with GRBs [257].

⁴⁴Neutrinos here refer to the $E_\nu \gtrsim$ TeV secondaries of baryons accelerated by the GRB, not the ~ 10 MeV primary neutrinos generated during a NDAF.

⁴⁵The dissipative photosphere model assumes that internal collisions take place when the ejecta is still optically thick, i.e. that collisions occur below the photosphere.

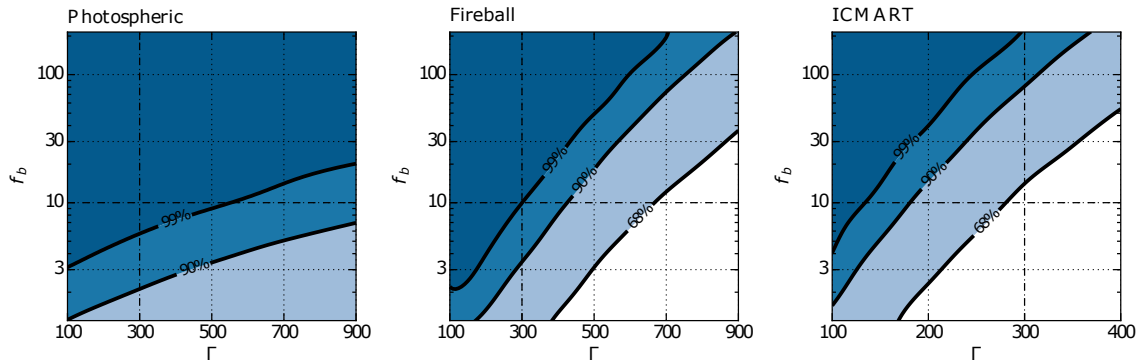


FIGURE 1.14: Prompt exclusion limits by IceCube for the single-zone collision models in terms of the baryonic loading f_b and bulk Lorentz factor Γ of the ejecta. From left to right, the exclusion regions are shown for the dissipative photosphere, the fireball and the ICMART model. From [257].

the non-detection of neutrinos, largely due to the larger radii at which the collisions are expected to occur.

In the multi-zone fireball model, the distribution of radii at which collisions occur will be determined by the time difference and velocity with which the various shells are expelled. A simulation study by Bustamante et al. [259] showed that disciplined engines, which are defined as engines that emit shells at regular intervals with similar velocities, produce relatively low neutrino fluxes. These GRBs would be identifiable by light curves that have one or several broad pulses overlaid with fast variability. In contrast, GRBs characterised by a light curve that lacks clearly identifiable pulse structures are linked to central engines that show a more erratic nature. Due to the wider range of collision radii, at least several collisions are expected to occur at regions with high photon densities, leading to a higher neutrino flux. Given that the intrinsic distribution of properties with which shells are launched is still highly uncertain, neutrino predictions remain challenging within the more complicated but more realistic multi-zone collision models.

Emission angle. Within the uniform jet model, Eq. (1.37), the opening angles of the prompt neutrino and gamma-ray emission are expected to be identical. This in fact applies to any jetted model in which particles are emitted within a beaming angle $\theta_b \sim \Gamma^{-1}$ that is much smaller than the opening angle of the jet. Only the cannonball model deviates from this prediction, as it assumes the ejecta to be invariant, thus keeping a fixed volume instead of a fixed angular size. Numerical simulations have shown that under this assumption, the neutrino beam is expected to have an opening angle that is an order of magnitude smaller than that of the gamma rays [250]. Hence, only $\sim 1\%$ of all electromagnetically observable GRBs would be accompanied by a neutrino signal in the cannonball model.

Energy range. On the low end of the neutrino energy spectrum, the flux will be dominated by the primary $\nu\bar{\nu}$ pairs that are generated by the NDAF. These primary neutrinos have a power distribution that is expected to peak around 10-20 MeV. Assuming a total energy output of 10^{52} erg, it was estimated that only 0.1-0.25 GRBs per century would lead to a signal of 3 or more neutrinos per burst in next-generation neutrino experiments such as Hyper-Kamiokande [260]. Hence, it is unlikely that these low-energy neutrinos will be detectable in the foreseeable future.

Low-energy neutrinos could also result from neutron-proton interactions. If a significant fraction of protons and neutrons are present at the base of the jet, then protons and neutrons will initially be coupled by elastic nuclear scattering [261]. As the ejecta flows outward

and becomes less dense, decoupling will at one point occur. This will result in a velocity gradient, as neutrons will no longer be dragged along with the accelerated protons. Inelastic proton-neutron collisions will thus occur, resulting in the production of pions. The decay of these pions is expected to produce neutrinos in the 1 to 100 GeV energy range [262].

Moving to higher energies, neutrinos in the TeV to PeV regime are expected to result from the internal collisions of GRB ejecta. For a detailed discussion on the energy distribution of these neutrinos, we refer the reader to Subsection 1.4.6.

At the upper end of the energy range, it is estimated that protons could be accelerated to energies of up to $10^{20} - 10^{21}$ eV at the external shock [263]. With ambient photons ranging from optical to X-ray, neutrinos from GRB afterglows are estimated to have energies ranging from 10^{16} to 10^{19} eV. Assuming an $\Phi_\nu \propto E^{-2}$ spectrum based on first order Fermi-acceleration, the particle flux drops off linearly as a function of $\log(E)$. In addition, the large radius at which the extended shock occurs implies relatively low-photon densities, leading to a decreased opacity for $p\gamma$ interactions [258], even further lowering the flux. At increasingly large energies, it therefore becomes observationally very challenging to detect afterglow neutrinos with current observatories such as IceCube.

1.6 Progenitors

1.6.1 Long bursts

Collapsars. As stated previously, the established model for long GRBs is that they are caused by a massive star that undergoes gravitational core collapse at the end of its life. Evidence for this collapsar model mainly comes from the coincident detection of supernovae following GRBs [35, 36] and the observation that long GRBs tend to be located in the most active star formation regions [39, 40, 176, 177]. Another indication is that the average duration of long GRBs matches the free-fall timescale⁴⁶ of massive stars. As a first order approximation, the progenitor star can be assumed to be a spherical non-rotating object with a mean density $\bar{\rho}$. Considering an infinitesimal mass element at an initial radius r_0 during the collapse, its gravitational potential energy will be converted into kinetic energy according to

$$\frac{1}{2} \left(\frac{dr}{dt} \right)^2 = \frac{GM(r_0)}{r} - \frac{GM(r_0)}{r_0}, \quad (1.62)$$

where $M(r_0)$ denotes the mass below the radius r_0 before the start of the collapse. Eq. (1.62) can be solved analytically for the free-fall time

$$\tau = \int_0^{r_0} dr \left[2GM(r_0) (r^{-1} - r_0^{-1}) \right]^{-1/2} = \sqrt{\frac{3\pi}{32G\bar{\rho}}}. \quad (1.63)$$

Hence, under these assumptions, the free-falling time only depends on the mean density $\bar{\rho}$ of the object. For a typical core stellar density of 100 g cm^{-3} [18], the predicted GRB duration is of the order ~ 210 s, in line with the collapsar model.

Wolf-Rayet stars. Not every star whose core collapses to a compact object is expected to produce a GRB. A first indication for the required progenitor properties stems from coincident supernova observations. All GRB-SN belong to the type Ic subclass, meaning that hydrogen and helium absorption lines are absent in the spectrum. This implies that the

⁴⁶The free-fall time is defined as the hypothetical time it would take for the entire star to gravitationally collapse into a single point.

progenitor star has shed its outermost layers⁴⁷. Both the hydrogen and helium shells can be blown away by the progenitor if there are strong stellar winds. This makes Wolf-Rayet (WR) stars the prime progenitor candidate in the collapsar model. WR stars are evolved stars that had an initial mass in excess of $20M_{\odot}$, but have lost their outer shells due to a continual strong stellar wind [18].

While this can explain the lack of hydrogen and helium features, a second constraint is that the specific angular momentum $\Sigma_i(\vec{r}_i \times \vec{p})_i / \Sigma_j m_j$ of the progenitor must be at least $3 \cdot 10^{16} \text{ cm}^2 \text{ s}^{-1}$ [264]. Below this threshold, matter would be able to fall into the newly formed black hole unimpeded without forming an accretion disk. This constraint is in apparent contradiction to the previous criterion, as strong stellar winds will carry off angular momentum. It has therefore been suggested that if the progenitor is extremely rapidly rotating at birth, strong mixing will prevent the formation of a separate hydrogen and helium shell, allowing essentially all hydrogen to be burned during the main sequence stage. As such the hydrogen shell is never formed and thus also does not need to be stripped. An alternative solution to this problem is that excessive mass loss and transfer of angular momentum can take place in close binary systems⁴⁸.

There is no intrinsic reason why non-WR stars, i.e. stars who have not shed their outer layers, would be unable to launch a jet following core collapse. However, if the remnant stellar envelope is too dense, the jet will stall below the stellar surface. No GRB emission would thus be observed. If the jet manages to break free just before the central engine shuts off, an intrinsically ‘long GRB’ caused by a collapsar could be associated with a very short T90 duration. An example of such a burst is GRB 200826A. While this burst had an intrinsic duration⁴⁹ of only 0.65 s, its afterglow and coincident supernova signature showed that this GRB was caused by a collapsar [266]. A study of similar short duration ‘long GRBs’ found that the T90 distribution of these events is in line with a gradual cut-off due to a transition to choked jets [267]. It is thus likely that the majority of jets launched by collapsars are smothered by the remnant stellar envelope, never leading to an observable GRB signal [268]. Smothering a jet would cause a significant fraction of the total jet energy to be transferred into neutrinos [11, 268–270]. Hence, choked GRBs could potentially explain the diffuse astrophysical neutrino flux observed by IceCube if they occur in sufficient quantities.

Ultra-long GRBs. A few subclasses of long GRBs might require alternative progenitor models to explain their observational features. Ultra-long GRBs, generally defined as having a $T90 > 10^3 \text{ s}$, have been shown to be statistically different from regular long GRBs [145]. Under the collapsar model, continuously feeding the central engine for over 15 minutes becomes challenging if the progenitor is assumed to be a WR star. Massive stars which have not yet blown away their entire hydrogen or helium shell, such as blue supergiants, have therefore been suggested as the progenitor for these ultra-long bursts [18]. More peculiar types of progenitors, such as mergers between a neutron star and a helium star, may be needed to explain ultra-long GRBs such as e.g. the ‘Christmas burst’ GRB 101225A, whose spectral and temporal features are difficult to explain in the collapsar model [271].

Low-luminosity GRBs. Another noteworthy subcategory is that of low-luminosity (LL) long GRBs. While there is clear turning point at which they become distinct from ‘regular’ high-luminosity (HL) bursts, LL GRBs are generally defined as bursts whose isotropic equivalent luminosity is below $10^{49} \text{ erg s}^{-1}$. Apart from having a lower brightness, LL GRBs

⁴⁷Before core collapse, massive stars will have an onion-like structure of shells. Starting from the edge of the star, the first shell will be made up of hydrogen, followed by increasingly heavier fusion products such as helium, etc. up to the most massive elements, which are at the core of the star.

⁴⁸It is estimated that the majority of massive stars are formed in a binary system [265].

⁴⁹Correcting for the redshift, $z = 0.7481$, of the burst [266].

tend to have very smooth light curves that exhibit little to no short time variability. Their emission is also less strongly collimated than that of HL GRBs. Due to detection bias, LL GRBs are only observed at low redshifts. However, their intrinsic density rate is significantly higher than that of HL GRBs [18].

To explain these features, it has been suggested that LL GRBs originate from the least massive stars that can produce a GRB. Core collapse would therefore lead to a neutron star central engine, producing a low-luminosity jet that is only mildly relativistic. Alternatively, the progenitors of LL GRBs might launch a regular jet that is choked due to the presence of a more extended stellar envelope. If the jet stalls shortly before it emerges from the envelope, shock breakout emission from the failed jet could also explain the signature of LL GRBs [18].

SN induced GRBs. It has been suggested that neutron stars in a binary system could produce a GRB if the second star undergoes a supernova explosion. In particular, events of this type could explain bursts such as GRB 110709B, in which two gamma-ray signals were observed separated by a time gap of 11 minutes [272]. In this scenario, the first flash would be caused when the SN ejecta reach the neutron star. Once the neutron star has accreted sufficient matter, it collapses to a black hole, causing the second gamma-ray flash⁵⁰. While thus significantly different from the standard collapsar model, numerical simulations have confirmed that such events could produce the observed gamma-ray signals [274, 275].

1.6.2 Short bursts

In the case of short GRBs, the accepted model is that they originate from the merger of a binary NS-NS or NS-BH system [18, 276]. The key observations in support of binary NS mergers are:

- the gravitational wave signal in coincidence with GRB 170817 [9, 10],
- well-localised, nearby short GRBs for which optical upper limits can exclude the presence of a coincident SN [178, 277],
- signatures of a kilonova observed in the aftermath of short GRBs [72–75, 165],
- positions that do not trace the most active star formation regions, with some short GRBs even having no identifiable host galaxy [18, 141].

Following Eq. (1.63) and taking the typical density of a NS ($\sim 10^{14}$ g cm⁻³ [18]) also indicates that the timescale of the gravitational collapse, $2 \cdot 10^{-4}$ s, is much smaller than that in the collapsar model, resulting in shorter burst durations.

NS-NS. Binary NS progenitors can merge into either a black hole or a single, more heavy NS. In the latter case, the newly formed NS is potential unstable, causing it to collapse to a BH at a later stage. This can happen after the phase of differential rotation, which lasts ~ 0.1 s [226], or during the spindown of a rigid supra-massive⁵¹ NS. Alternatively, the NS could also be stable if the masses of the initial neutron stars were sufficiently low [18, 178].

NS-BH. A collision between a NS and a BH will always result in a single, more massive BH. If the mass ratio of the NS to the BH is less than ~ 0.24 , no emission is expected as the NS will simply be swallowed by the BH [278]. For larger mass ratios, the NS will be tidally disrupted outside the event horizon of the BH, providing matter for the formation of an accretion disk [278, 279]. No coincident signals were observed from the two NS-BH mergers, GW 200105 and GW 200115, that have so far been observed [280].

⁵⁰A second GRB for which this progenitor scenario has been suggested is GRB 090618 [273].

⁵¹A NS is said to be supra-massive if it is rotationally supported against gravitational collapse.

Alternative scenarios. In the models described above, the progenitor is generally assumed to have started life as a binary system of two massive stars. However, the dynamic capture of two compact objects in a globular cluster could also lead to NS-NS or NS-BH binaries. Finally, mergers between a white dwarf and a BH have also been suggested as potential short GRB progenitors [17], though it is unclear if this scenario could produce a sufficiently massive accretion disk to power a GRB [281].

1.6.3 GRB-like sources

Soft gamma-ray repeaters. Not every astrophysical transient that produces an outburst of gamma radiation classifies as a GRB. An additional criterion is that the event must be cataclysmic, implying that the progenitor system gets destroyed during the explosion. This is not the case for soft gamma-ray repeaters (SGRs). As the name suggests, SGRs can be observed as flashes of gamma radiation⁵² repeating at irregular intervals from a single source. These short flashes, lasting typically less than a second, have been shown to originate from magnetars that undergo magnetic energy dissipation. As they are much less bright than GRBs, bursts from SGRs can generally only be observed from magnetars inside our Milky Way [18].

On the order of once a century, magnetars can undergo a giant flare with isotropic equivalent energies of up to 10^{47} erg s^{-1} [225]. These flares can be observed from other galaxies inside our local Universe. If no afterglow emission can be identified, distinguishing such a signal from regular short GRBs is very challenging. A correlation study that compared the positions of well-localised short GRBs to that of galaxies in the local Universe identified 4 out of 250 bursts (2%) that are most likely related to magnetar activity⁵³ [285]. For long GRBs, no such correlation is expected and indeed, also not observed [286].

X-ray outbursts. Some transients are cataclysmic outbursts, but only produce photons up to X-ray energies. These events are tagged as X-ray outbursts (XRO) and can be caused by the non-relativistic shock breakout from SNe. An example of such a burst is XRO 080109, which was observed in coincidence with a type Ib SN. To explain the X-ray signal, no collimation or jet-like structure is required, as the emission is consistent with originating from the shock breakout of the SN itself [287].

Tidal disruption events. When a star is orbiting the supermassive BH at the centre of a galaxy, the star may become tidally disrupted if it at one point during the orbit approaches the BH too closely. While being ripped apart, a fraction of the stellar material can be fed into the accretion disk of the BH, producing strong gamma-ray flares at a later stage. As a result, the first tidal disruption event (TDE), Sw J1644+57, was initially wrongly identified as a gamma-ray burst. Since the event triggered the Swift-BAT detector on and off for up to three days and had a non-standard afterglow light curve, it was soon realized that it was not a GRB [288].

⁵²Less energetic magnetars will result in flashes of X-ray pulses, explaining the anomalous X-ray pulsars (AXP).

⁵³Earlier result found a much higher correlation coefficient, suggesting that 10% to 25% of short bursts originate from a redshift $z < 0.025$ [282]. However, this result was recently shown to be an overestimation due to poorly localised GRBs erroneously being associated to nearby galaxies [283, 284].

Chapter 2

Gamma-ray burst precursors

In the previous chapter, gamma-ray bursts (GRBs) were defined as flashes of gamma radiation caused by astrophysical sources which undergo a cataclysmic event. The main outburst of gamma rays is called the prompt phase. During the seconds or sometimes minutes prior to the prompt emission, a weaker X-ray and gamma-ray signal is sometimes observed. Such events are termed precursors. They indicate that the emission of high-energy particles, likely originating from a different physical mechanism, can already take place prior to the prompt phase.

One of the first mentions of such a precursor component is that of the thermal peak which preceded GRB 900126 [289]. Figure 2.1 shows the light curve of this bursts in several energy bands. While occurring very close the prompt phase, the precursor is spectrally significantly different¹. This led Murakami et al. to suggest that it likely corresponds to a physically distinct emission component [289].

The first systematic search to identify precursors in the light curves of GRBs appeared a few years later, in 1995 [290]. Analysing an effective sample of 748 GRBs observed by BATSE, Koshut et al. found that $\sim 3\%$ of all bursts were preceded by a precursor. As this was the first large scale study of GRB precursor emission, a very restrictive definition was used to demonstrate that these events were not simply an early lead-out of the prompt component. In particular, the quiescent time, defined as the time in between the precursor and prompt emission during which the rate drops back to the background level, was required to be at least as long as the duration of the prompt phase. A second, more standard requirement was that precursors should have a lower peak intensity than the prompt component. Contrary to the result for GRB 900126, this study revealed that the precursor and prompt emission component generally have similar spectral characteristics [290]. Hence, while thermal precursors certainly have been observed, the majority of GRB precursors follow a non-thermal spectrum.

Following these two publications [289, 290], a range of questions were raised regarding the observational properties and physical origin of GRB precursors. Several precursor studies have since then been performed [4, 242, 291–305], greatly increasing what is known about these events. However, to this date, no clear consensus exists on their physical origin. This chapter proceeds by first presenting an overview of the experimental characteristics of GRB precursors, followed by a discussion of the various models that could explain these observations.

¹The precursor of GRB 900126 had an almost thermal spectrum, peaking at X-rays energies. In contrast, the prompt emission peaked in gamma rays and had a non-thermal spectrum.

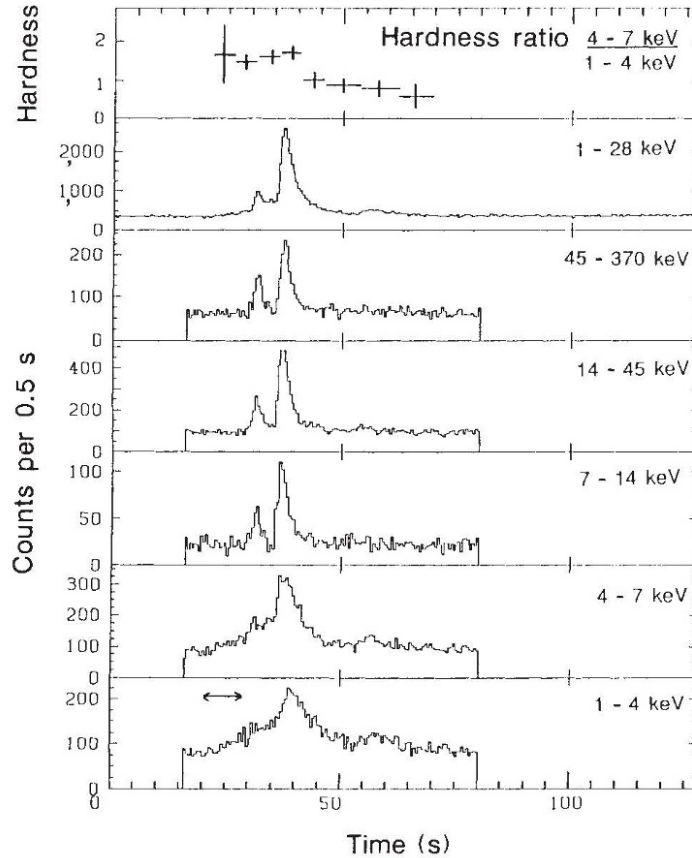


FIGURE 2.1: Light curve of GRB 900126 as observed by the Ginga satellite. The top panel depicts the hardness ratio, while those below show the detected photon rate in different energy bands. From [289].

2.1 Observational overview

Rather than reviewing each GRB precursor search on a publication-by-publication basis, analysis characteristics and results are in this section grouped per category. Therefore, instead of repeating all references in every subsection, it is noted here that the main references for the information presented below are [4, 242, 289–305].

2.1.1 Definition of a precursor

As keenly put by Lazzati et al. in [306]: “*Observationally, associating a precursor with a transient event is challenging, if at all possible.*” This statement is reflected in the wide variety of precursor definitions that have been employed in previous analyses. Nonetheless, each definition is broadly speaking based on the same two conditions.

1. Precursors must be ‘weaker’ than the main emission episode. A condition is therefore imposed on the peak flux and/or the time-integrated photon count. Precursors can either not exceed the value of the prompt emission, or if a more restrictive definition is used, have to be smaller than a fraction $X \in [0, 1]$ of the prompt value.
2. There should be a period of time in between the precursor and prompt phase during which the flux decreases. Generally, the flux is required to drop to a rate that is

consistent with the detector background². More stringent definitions have also been employed, in which either an absolute lower limit, or one that is relative with respect to the prompt duration, has been imposed on the length of the background time interval.

The exact criteria that are used to define a precursor can naturally have an effect on their observational characteristics. For instance, the fraction of GRBs that are preceded by a precursor has been estimated to correspond to $\sim 3\%$ by some studies [290] and $\sim 20\%$ by others [293]. These two results are not inconsistent with each other, as they correspond to two extreme cases in which a very stringent and a very loose precursor definition was used.

2.1.2 Analyses techniques

Another factor to be considered is the manner in which the data is analysed. The majority of analyses proceed by considering the raw photon counts observed by the detector³ and searching for an excess on a set of predefined timescales. Precursors whose duration most closely resembles one of the examined timescales will be most easily identifiable. Examining more timescales can thus boost the analysis sensitivity, but comes at the cost of increasing the number of expected false positives.

To avoid this issue, an approach can be taken in which the analysis algorithm automatically identifies the relevant timescales. In practice, this corresponds to applying a variable binning that is determined by the data. Several precursor searches (e.g. [242, 292]) have used the Bayesian block (BB) algorithm for this purpose. The BB method was specifically developed to enable the identification of signals in the light curves of GRBs and works by optimising both the number of bins and the location of the bin-edges [307]. A detailed description of this method is given in Subsection 3.3.3 and Appendix A.

An altogether different approach is to first convert the raw photon counts to a new parameter space, before proceeding to search for a signal excess. One such method that has been shown to be competitive with, and in some cases outperform the classic binned approach, is the wavelet algorithm. For an overview of this method in the context of GRB precursor searches, we refer the reader to [291, 298]. Other approaches include the use of algorithms used in gravitational wave searches to look for excesses in the time-frequency domain [295].

While each method has its advantages, each analysis technique also inadvertently induces a small bias toward the types of precursors it is most suited to detect. A final consideration is that differences in the examined data can also lead to divergent results. While the majority of searches target a time window that starts up to 150 – 1000 s before the prompt phase, some analyses (e.g. [308]) only looked up to 50 s before the start of the prompt emission. Along with the varying precursor definitions, these changes indicate why the resulting properties of GRB precursors can vary significantly from one analysis to the next.

2.1.3 Experimental properties

GRB fraction. Precursors have been observed in the light curves of both long and short GRBs. However, due to the two classes having different progenitors, the physical mechanism behind the precursor flash likely differs as well. Experimentally, this effect already

²Note that this does not imply that there is no gamma-ray emission, as the strongest statement that can be made is that there is no emission above the sensitivity threshold of the detector.

³Alternatively, the data might also already be pre-binned, which naturally strongly reduces to sensitivity of the analysis to precursors that have a duration that is comparable to or smaller than the bin size.

shows up in the fraction of bursts for which a precursor flash is observed. While the typical value for long bursts⁴ is of the order $\sim 15\%$, precursor emission is only observed for a few percent of all short GRBs⁵.

By definition, precursors are required to be weaker than the prompt emission. If a burst is located too far away, only the prompt component might lead to a detectable signal, causing the intrinsic rate of GRBs with precursors to be underestimated. To alleviate this issue, some analyses [293, 297, 299, 301] have restricted their GRB sample to bursts that exceed a given brightness threshold. Consistent with this interpretation, these are the analyses which report the highest precursor fractions.

Quiescent time. The dichotomy between short and long GRBs also shows up in the duration of the quiescent time. This variable is defined as the length of the time interval that separates two emission episodes during which the rate is consistent with the background expectation. Precursors to short GRBs are generally observed to precede the prompt emission by less than 3 seconds [291, 305]. In contrast, quiescent times of long GRBs typically correspond to a few tens of seconds up to ~ 250 s [293, 309].

As will be shown in Section 2.2, precursors occurring less than ~ 100 s before the start of the prompt phase are predicted by a multitude of models. Most challenging to explain are the longest observed quiescent times. Two particular bursts, for which quiescent times in excess of 600 s were observed⁶, are GRB 091024 [296] and GRB 110709B [242, 272, 273]. In Subsection 1.6.1, this latter burst was therefore already suggested to have a different physical progenitor from regular long GRBs. In GRB 091024, the large time delay between the precursor and prompt phase allowed the observation of an early afterglow signal before the prompt emission had even started. While restricted to a single GRB, this observation implies that the precursor of GRB 091024 must have launched its own outflow, thus having a physical origin that is very similar to the successive prompt phase.

Spectral properties. Because fewer photons are observed from GRB precursor emission, obtaining a reliable spectral fit is generally harder than for the prompt phase. To cope with low statistics, the first systematic precursor study [290] instead examined the hardness ratio (HR) for a sample of 995 BATSE bursts. They found that precursors tend to be spectrally softer than the prompt phase, though with limited statistical significance. A later study [293], which examined 133 of the brightest long BATSE GRBs, confirmed this result by demonstrating that all 25 precursors observed in that study were spectrally softer than the prompt emission. Based on this result, the hypothesis that precursors have the same softness as prompt emission could be rejected at 5σ confidence.

Contrary to these findings, more recent analyses of BATSE and Swift GRBs found the spectral properties of precursors to be indistinguishable from those of the prompt phase [242, 294, 297]. Rather than simply looking at the HR, these studies performed power-law fits to precursors with sufficient statistics. The spectral indices of precursor emission were generally found to be fully consistent with those of the prompt phase. This would thus suggest that the precursor and prompt component are caused by the same emission mechanism.

What all studies do agree on is that spectra of GRB precursors are primarily non-thermal. A few GRBs with precursor spectra that are extremely well described by a blackbody component have been observed⁷. However, they are estimated to only contribute between 5%

⁴Analyses of long GRBs found values of 9% [242], $> 10\%$ [295], 14% [294] and 20% [293].

⁵Analyses of short GRBs found fractions of 0.4% [308], 2% [242], 3% [300], 6% [291] and 7% [305].

⁶Both GRBs had a redshift of the order $z \sim 1$, eliminating the possibility that the long time delays are simply induced by an extreme case of redshift time dilation [272, 296].

⁷A clear-cut example of a burst with a thermal precursor is e.g. GRB 106025B [166]

to 10% of all observed precursors [293, 297].

Temporal correlations. Contradictory findings have also been reported on the relation between the duration of subsequent emission episodes and that of the intermediate quiescent time⁸. Three possible combinations can be constructed based on the three phases.

- *Precursor - quiescent:* No significant correlation has been observed between the duration of a precursor and that of the subsequent quiescent episode [290, 293, 299].
- *Precursor - prompt:* While one study reported a lack of correlations between the precursor and prompt duration [301], three other analyses found a mild correlation of up to 3σ significance [290, 293, 301].
- *Quiescent - prompt:* A stronger disagreement in the literature exists on whether the quiescent time and the subsequent prompt phase are correlated. Two analyses found no evidence for such a correlation [293, 301], while two other analyses rejected the null hypothesis of there being no correlation at 4σ [299] and $> 5\sigma$ [297]. If physical, such a correlation is of particular interest as it points towards the reservoir accretion model [299]. Regardless of the exact emission mechanism, this model states that during the quiescent time, energy is built up in the system during a meta-stable state. Once a critical threshold is reached, the system again becomes unstable, triggering the release of the built-up energy. Hence, such a system would naturally explain why a long quiescent time would lead to a longer lasting prompt phase.

2.2 Emission models

2.2.1 Photospheric emission

One of the earliest and most established models for precursor gamma-ray flashes is that they can in some cases correspond to the photospheric emission component [236, 254]. A short overview on photospheric emission in the context of the GRB prompt phase was already presented in Subsection 1.5.2. Hence, it is here only reiterated that this emission arises when the ejecta transition from the optically thick to the optically thin phase, releasing the thermal radiation isotropically. Photospheric precursors will occur in both long and short GRBs, but are in most cases likely too dim to be observed.

Models which predict photospheric precursor components indicate that they should have a (quasi-) thermal spectrum. The time delay between the precursor and prompt phase is estimated to be on the order of a few milliseconds to a few seconds⁹ [310, 311]. Both these characteristics indicate that photospheric emission can be ruled out as the source for the majority of GRB precursors. In fact, the scarcity of such short time-delay thermal precursors suggests that the dissipation of energy into bulk kinetic motion only takes place at a late stage. Jet models with high-magnetisation parameters, such as the Poynting flux and ICMART model, are thus favoured in this regard.

2.2.2 Shock breakout

An alternative precursor scenario is possible in the case of long GRBs. When the central engine launches a jet, the ejecta will first have to traverse through the remnant stellar envelope

⁸Due to the limited data, none of the studies presented below correct for redshift effects, which can induce artificial correlations between the observed time durations.

⁹Longer time delays can be achieved in models in which the prompt emission originates from internal shocks that occur at larger collision radii [292].

of the progenitor. This propagation process is illustrated in Fig. 2.2. Material at the head of the jet will collide with the cold stellar envelope, significantly increasing the local pressure of the latter. As a result, high-pressure material from the stellar envelope will overflow to the sides, creating vortices that feed a cocoon. During the propagation of the jet through the envelope, matter will continually be fed to the cocoon. This will increase the pressure of the cocoon material, leading to a bow shock in the stellar envelope as illustrated in Fig. 2.2. In addition, the high-pressure cocoon material will collimate the jet, reducing its opening angle until an equilibrium is reached.

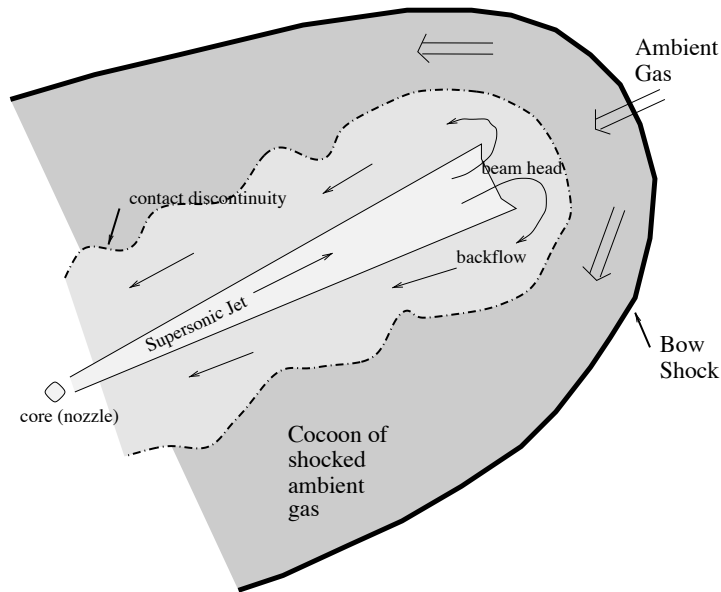


FIGURE 2.2: Illustration of the propagation of a GRB jet through a cold dense stellar envelope. Due to the pressure at the jet of the head, a cocoon will be formed that envelopes and collimates the jet. From [312].

When the bow shock reaches the edge of the stellar envelope, the breakout of the hot cocoon material is expected to lead to a dim thermal X-ray signal¹⁰. Such shock breakout emission will be emitted largely isotropically and is expected to precede the prompt emission by 1 s to 10 s [292]. Larger time delays of up to 100 s can be achieved if the observer is slightly outside the geometrical opening angle of the jet. Such an observer would be unable to see any early radiation produced by the jet, but might still detect an emission component at a later stage, when the relativistic beaming angle $\theta_b \sim \Gamma^{-1}$ has widened sufficiently [306, 314].

The shock breakout model thus presents an improvement over the photospheric model, as the quiescent times correspond to those of the observed precursors. However, a thermal spectrum is still expected, in contrast to observations. It has been suggested that interactions with the jet could, at a later stage, boost the breakout emission to gamma rays with a non-thermal spectrum. Such a signal would be observed as a second precursor, visible only ~ 1 s before the prompt phase [292]. Finally, it should be noted that, while originally only

¹⁰Thermal emission from the jet cocoon will become observable in the UV and optical wavelengths at a later stage. Such emission was first observed for GRB 171205A, conforming that jets of long GRBs create a cocoon [313].

developed for long GRBs, short bursts could also be accompanied by shock breakout emission. Particularly, if the merger leads to a strong baryonic wind, a similar scenario could occur in which the jet has to ‘escape’ from a dense circumburst medium [315].

2.2.3 Multi-stage collapsar

Following the core collapse of a massive star or the merger of two compact binaries, a short-lived neutron star (NS) might be formed which eventually decays into a black hole (BH). Hence, it has been suggested that precursors relate to the initial formation of a NS central engine, while the more energetic prompt phase is caused by the collapse into a BH.

Fallback collapsar. In the case of long GRBs, the gravitational collapse to a NS will be accompanied by a SN explosion that ejects the outer layers of the star. Material located closer to the central object can, while being initially dragged out by the explosion, remain gravitationally bound to the NS. Such material will eventually fall back, either forming an accretion disk around or falling directly unto the NS. If a sufficient amount of matter is accreted, the NS will further collapse to a BH, typically after a timescale of ~ 100 s [316].

At the time of its birth, the NS can launch a jet via various mechanisms. For instance, a weak jet could be powered by the eruption of magnetic bubbles or the early accretion of matter onto the NS (see Subsection 1.5.1). Such a weak jet could either stall below the stellar envelope, leading to shock breakout emission, or lead to a successful jet that escapes from the star. Particularly the last scenario is of interest, as this would lead to non-thermal precursors with quiescent times consistent with those of the observed events [316].

Supranova. A two-stage collapsar can also result from a newborn NS that is initially supported against further gravitational collapse by rigid body rotation. In such a supranova system, the NS will lose angular momentum by emitting magnetic dipole radiation [317]. Predicted time delays between the formation of the NS and BH can match the observed quiescent times of GRB precursors, but strongly depend on the NS equation-of-state and are therefore badly constrained [18]. Otherwise, this model is largely analogous to that of the fallback collapsar discussed previously.

In principle, the supranova model is applicable to both long and short GRBs. In the case of long bursts, the final GRB would be powered by an accretion disk that is formed from the infalling stellar matter outside of the collapsed core. For short bursts, a similar accretion disk could potentially be formed by the break-up of the NS during the collapse into a BH. However, it is currently unclear whether a NS to BH collapse can leave any remnant matter or whether the NS would rather disappear completely into the BH [318].

Spinar. The concept of a supranova can be generalized in the spinar paradigm. Spinars are defined as rapidly rotating magnetized objects that are supported against gravitational collapse by the centrifugal force. Apart from supranovae, another example of a spinar would be the magnetized accretion disks around the BH of a collapsar [319, 320]. A population synthesis study suggests that $\sim 10\%$ of long GRBs are expected to have a precursor within 100 s of the prompt phase due to spinar formation [321]. Exact predictions on the quiescent time and spectra nonetheless remain challenging due to the generality of the model.

2.2.4 NS magnetic interactions in binaries

Having primarily focused on precursor mechanisms of long GRBs, two models will now be presented that relate to the merger of a NS with another compact object. The first mechanism considered here relates to the configuration of the magnetic field. Consider a binary system of two NSs, in which one of the NSs carries a strong magnetic field. The other NS

can in this scenario be considered as a superconducting sphere moving through an external magnetic field. Since the magnetic field lines within the second NS cannot change, a varying magnetospheric current will be induced on the NS surface, shielding its internal structure [322].

This effect can lead to precursor signals via at least two emission mechanisms. Firstly, free charges on the surface and near the vicinity of the NS will be accelerated to relativistic energies due to the strong electric fields. While propagating through the magnetic field, these charges will radiate off curvature photons that subsequently annihilate into an electron-positron plasma. Such an electromagnetic fireball is expected to lead to a quasi-isotropic thermal X-ray precursor signal a few seconds prior to the coalescence of the two neutron stars. Additionally, the Poynting flux itself might also produce a detectable precursor signal¹¹ [322, 323].

A complementary magnetic effect that has been considered is that, if a binary NS merger leads to a magnetar that subsequently collapses to a BH, the magnetic field lines around the compact object will suddenly be decoupled. Such an event would produce a signal akin to that of giant magnetar flares. Hence, if the prompt emission occurs at a later stage, e.g. powered by accretion onto the newly formed black hole, such a flare-like signal would be detected as a short gamma-ray precursor flash [324].

2.2.5 NS crust cracking

Apart from precursors related to the NS magnetic field, the other canonical precursor candidate for short GRBs is NS crust cracking. When a NS is undergoing the final stage of the inspiral process, the tidal forces exerted by the other compact object, either a BH or a NS, can lead to a restructuring of the NS crust [276]. This sudden dissipation of built-up tidal stress is estimated to release a total energy of the order 10^{46} - 10^{47} erg [325]. If the NS has a strong magnetic field ($B \gtrsim 10^9$ T), most of the energy will be carried out in the form of Alfvén waves [326], leading to a non-thermal precursor. Alternatively, if the NS has a weaker magnetic field, an electromagnetic plasma will be emitted, leading to a thermal precursor [327]. Tidal forces will also cause a general heating of the NS crusts, but this overall effect has been shown to be too insignificant to lead to an observable signal [328].

Considering just the tidal force required to fracture a NS crust, a very short quiescent time of the order ~ 0.1 s is expected. More detailed calculations show that longer timescales, up to 20 s prior to the merger, can be achieved if resonance effects are considered. In particular, as the orbital frequency continually increases during the inspiral process, resonances can amplify the effect of the tidal force, causing the NS to crack at an earlier stage [327].

Two predictions by the NS crust cracking model are that they should only be observable for relatively nearby GRBs, i.e. within ~ 100 Mpc [328], and that the precursor signal should occur prior to the coalescence of the two compact objects. With the advent of GW detectors, this latter observation could become testable in the foreseeable future. Crust cracking would also leave a minor imprint on the GW signal itself. However, even for next-generation GW observatories, this effect is likely too feeble to be detectable [329].

2.2.6 Central engine reactivation

All previously discussed models have assumed that there is an intrinsic difference between the emission of the precursor and prompt radiation. As a final option, the possibility is discussed that they are caused by the same physical mechanism. An argument in support of

¹¹A similar analysis can be made for NS-BH binary systems [76, 322].

this viewpoint is that most precursors have spectral and temporal features consistent with those of the prompt radiation [242]. The quiescent time between the two phases would in this scenario be caused by the turning on and off of the central engine. Precursors would then be an early analogous variant of the late time X-ray flares.

For a magnetar central engine, the launch of a jet can temporarily be halted due to non-continuous accretion onto the NS. Unlike black holes, neutron stars carry their own co-rotating magnetosphere. Matter from the accretion disk will only be able to fall onto the NS if the gravitational force and disk pressure are sufficiently large to overcome the centrifugal force exerted by the magnetosphere. During periods in which no accretion takes place, the magnetar is said to be in a propeller phase. Different emission episodes observed in the light curves of GRBs in this model thus correspond to different periods of time during which accretion onto the magnetar was possible [330]. Note that this is an example of a reservoir model (see 2.1.3), implying that longer quiescent time intervals are predicted to be followed by more energetic emission episodes.

Even if the central engine keeps ejecting shells of matter without large intermittent time intervals, it is possible to achieve long quiescent times by tuning the shell structure. Consider a central engine which emits two heavy, slow shells, each of which is followed by a number of less massive but considerably faster shells. In this scenario, internal collisions would effectively only occur when the fast shells catch up with their respective preceding slow shell. This would lead to two distinctive emission episodes, one for each slow shell [331]. While this quickly becomes a fine-tuning problem, essentially any distribution of quiescent times can thus be recovered by varying the properties of the ejected shells.

2.3 Precursor neutrino emission

Precursors have up till this point been presented in terms of their electromagnetic signature, with particular focus on experimentally observable characteristics such as their quiescent time and spectrum. Similar to the mechanisms discussed for the prompt phase, any precursor model in which gamma-ray emission occurs due to shock acceleration can lead to an accompanying neutrino flux if there is sufficient baryonic loading. In fact, if the emission region is still opaque to gamma rays during the precursor phase, only neutrinos would be observable. Below, we present the two mechanisms considered to be the main candidates for GRB precursor neutrinos.

2.3.1 Subphotospheric internal collisions

The standard model for long GRBs is that they are induced by the core collapse of a massive star. As it is only the stellar core which collapses to a NS or BH, the compact object will initially still be surrounded by remnant layers, i.e. the stellar envelope. A jet launched by the central engine will first need to punch through this envelope before gamma rays can be observed¹². Depending on the properties of the massive star progenitor, a time delay of the order 10-100 s is expected between the jet launching and it breaking through the envelope [333, 334]. During this period, the jet will not yet have attained its final Lorentz factor. Internal collisions occurring below the beam head (see Fig. 2.2) are expected to accelerate protons up to PeV energies, leading to ~ 5 -100 TeV neutrinos [269, 335]. Insignificant baryonic loading is not an issue in this scenario, as hadronic particles are amply provided by the envelope. The abundance of so much target material can even lead to non-negligible

¹²To choke a GRB jet, a surrounding remnant from the progenitor is required as the regular circumstellar medium has been shown to be insufficiently dense to achieve this [332].

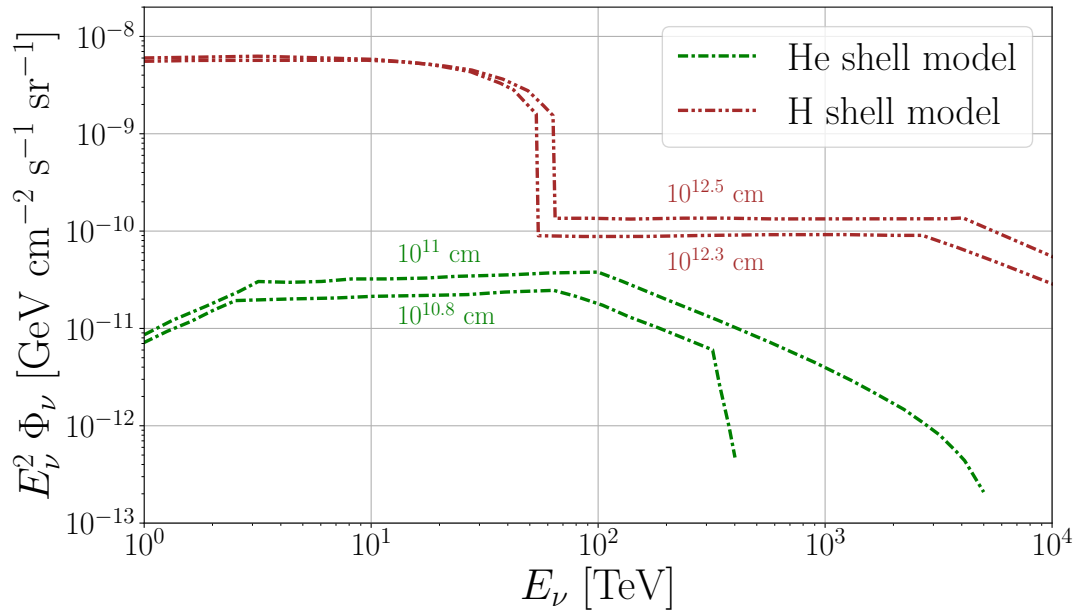


FIGURE 2.3: Four model predictions [333] are shown for the diffuse precursor muon neutrino flux from long GRBs, assuming progenitors that have either an outer hydrogen (brown lines) or helium (green lines) envelope. The distance measure next to the model predictions indicates the collision radius, i.e. the radius at which particle acceleration is assumed to take place.

neutrino absorption. Hence, most observable neutrinos are expected from internal shocks that occur sufficiently close to the edge of the envelope [333].

Simulations in which a jet propagates through the stellar envelope have been carried out by Razzaque et al to determine the energy spectra of the produced neutrinos [333]. In their model, progenitors are assumed to have either an outer hydrogen (H) or helium (He) shell. Two sets of collision radii are probed for each model. The corresponding diffuse neutrino flux predictions are shown in Fig. 2.3, assuming a canonical 10^3 long GRBs per year that are beamed towards us.

In the H star model, the main neutrino flux below ~ 60 TeV comes from proton-proton collisions with cold material from the stellar envelope. At higher energies, a transition occurs to neutrino production by proton-photon collisions at the head of the jet. Initially, the flux will only be suppressed by inverse Compton processes, but at higher energies ($E \gtrsim 30$ PeV) synchrotron losses further reduce the flux. In the He star model, neutrino production by proton-proton and proton-photon processes is heavily suppressed by inverse Compton losses. The difference in flux for the two collision radii primarily stems from neutrino absorption. If the collisions occur deeper below the surface of the envelope, then neutrinos will have to traverse a larger optical depth before they can emerge from the star. For the H and He star model, an optical depth of unity is typically reached for neutrino energies that exceed $\sim 2.5 \cdot 10^8$ TeV and $\sim 2.5 \cdot 10^2$ TeV, respectively [333].

While the exact energy spectrum and time delay depend on the characteristics of the progenitor, an early GRB neutrino signal is essentially expected for every long GRB. These neutrinos can in some cases also be related to gamma-ray precursor emission. If the central engine initially launches a weak jet followed by a period in which it returns to a quiescent state, three scenarios can result. Very weak jets will stall far below the envelope surface. As such, their energy will be dissipated within the envelope and no significant shock breakout

emission will occur. In contrast, more energetic jets stalling just below the envelope will lead to shock breakout emission. Finally, the third option is that the jet manages to break out, leading to gamma rays from internal shocks that can be directly observed.

A more powerful jet, launched at a later stage, can go through the exact same process again. While the initial jet will have already created a low-density funnel, it is estimated that pressure from the envelope will effectively close the funnel after ~ 10 s of jet inactivity [316]. Hence, the second jet will have to plough its way through the envelope again. Counter-intuitively, low-power jets are expected to be more efficient particle accelerators and thus lead to higher neutrino fluxes [336]. A more energetic prompt gamma-ray flash can thus be accompanied by a weaker neutrino flux than a gamma-ray dim precursor.

2.3.2 Supranova model

In terms of gamma-ray and neutrino precursor emission, the supranova model is largely similar to the generic collapsar model. However, much longer time delays, potentially up to several days, can be achieved due to the two stage central engine [337, 338]. During the first collapse into a supra-massive NS, the accompanying supernova explosion will produce a shock wave that expulses the outer layers of the star. When at a later stage the GRB jet is launched, prompted by the collapse into a BH, the supernova remnant provides additional target material for shock accelerated protons to interact with. As such, the expected neutrino flux from the prompt phase is significantly enhanced [207, 338].

In between the two collapses, the rapidly spinning supra-massive neutron star will be emitting magnetic dipole radiation. This will result in the loss of angular momentum causing a spin-down of the NS [317]. An additional effect is that the neutron star can emit a pulsar-like wind, resulting in the formation of a pulsar wind bubble (PWB) around the central engine. By interacting with the surrounding material, protons accelerated in the PWB can produce neutrinos up to ~ 10 TeV energies [339]. These neutrinos would be emitted continuously until the central engine collapses to a BH. This second collapse would trigger the abrupt end to the replenishing of protons inside the PWB, leading to an exponential decay of the neutrino signal [339].

Chapter 3

Identification of precursors in Fermi-GBM data

Given the results from previous analyses, the gamma-ray signals observed from GRB precursors are currently still consistent with a variety of theoretical models. Most likely, a single model will also be insufficient to explain all GRB precursor observations. Several of the established models predict that a significant neutrino flux is produced alongside the precursor gamma rays. This motivates us to perform the IceCube analysis presented in this thesis, where we look for neutrinos arriving close in time to observed GRB precursors.

To enable an IceCube coincidence study, a GRB precursor catalogue is required that provides a large overlap with the IceCube data taking period. IceCube was completed in December 2010. Hence, precursor studies relating to e.g. the BATSE detector cannot be used. At the time of writing, precursor studies based on the Fermi and Swift data likewise do not provide full overlap with the IceCube dataset used in our analysis. This motivated us to construct such a catalogue ourselves. The Fermi satellite is currently the most prolific GRB observatory in orbit. As it was launched in 2008 and is still active today, Fermi provides full overlap with the IceCube data taking period. Another aspect of key importance is that the Fermi data is made publicly available via the HEASARC archive [50]. All these characteristics make the Fermi Gamma-ray Burst Monitor (GBM) the ideal candidate to construct our GRB precursor catalogue.

In this chapter, we present an analysis of the Fermi-GBM data to identify gamma-ray precursor emission in the light curves of GRBs. An overview will first be given on the Fermi detector, followed by a discussion of the main steady-state and transient sources that it detects. As these non-GRB sources form a background for our analysis, we introduce a novel procedure that we developed to construct background subtracted light curves. The Bayesian block algorithm [340] is then applied to identify periods of increased gamma-ray emission that precede the prompt phase. In this manner, we construct a GRB precursor catalogue that in Chapter 5 will be used as input for our IceCube coincidence analysis. Given this catalogue, we also study the temporal properties of the identified precursor events.

3.1 The Fermi Gamma-ray Space Telescope

The Fermi Gamma-ray Space Telescope¹, from now on referred to as ‘Fermi’, was launched on the 11th of June 2008 [341]. The telescope consists of two separate instruments, namely the Gamma-ray Burst Monitor (GBM) and the Large Area Telescope (LAT). Figure 3.1 shows a schematic illustration of the spacecraft, including a zoomed in view of the two detectors. A detailed description of these two instruments is given below, with focus going primarily to the GBM detector, as this is the instrument used for our GRB precursor analysis.

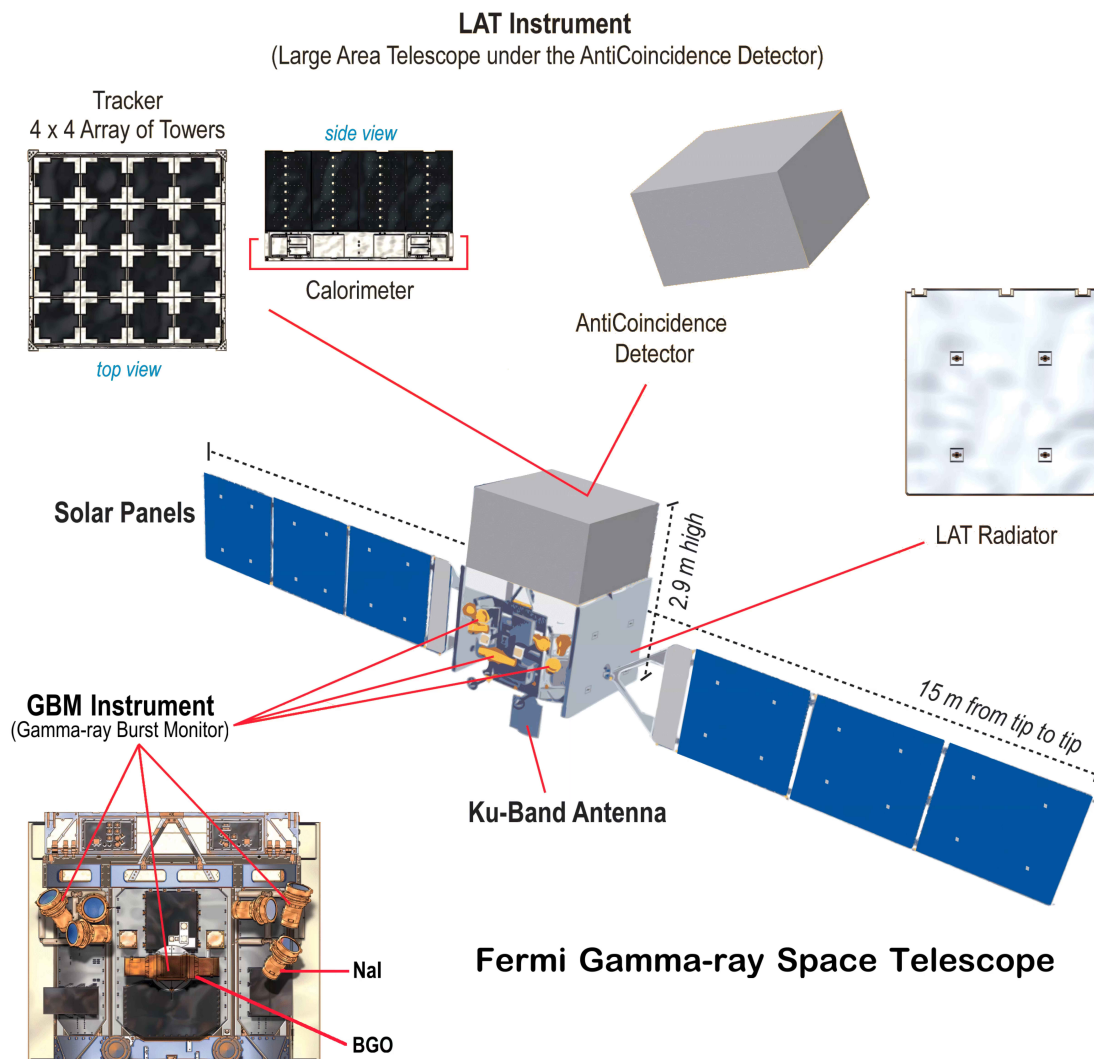


FIGURE 3.1: Visualisation of the Fermi Gamma-ray Space Telescope. A schematic view of the Large Area Telescope (LAT) and Gamma-ray Burst monitor (GBM) are shown at the top and bottom of the image, respectively. Credit: NASA/Fermi LAT Collaboration.

After a series of checks and initialization procedures, Fermi detected its first GRB on the 14th of July 2008 [49]. Since then, it has triggered on more than 3000 bursts [49]. Most GRBs are solely observed by the GBM instrument, which is sensitive in the energy range

¹Originally, the experiment was named the ‘Gamma-ray Large Area Space Telescope (GLAST)’. In August 2008, shortly after the launch of the spacecraft, it was renamed to the ‘Fermi Gamma-ray Telescope’ in honour of the famous physicist Enrico Fermi [93].

from 8 keV to 40 MeV and continually observes the full region of the sky not occulted by Earth² [341]. The LAT instrument is sensitive to higher energy gamma rays, from 20 MeV to 300 GeV [93], and has a field-of-view (FOV) of 2.4 sr at 1 GeV [93]. On average, the GBM and LAT each observe 240 and 18 GRBs per year, respectively [48, 49].

3.1.1 Orbit

Orbit height. Like other geocentric gamma-ray satellites, the Fermi spacecraft is located in a low-Earth orbit. Its launch placed it at an altitude of 565 km, thus corresponding to an orbital period of 96 minutes. At this height, the satellite is still located within the thermosphere layer of Earth's atmosphere. Hence, Fermi experiences a small yet non-negligible drag. Over the course of a 10 year period, this has caused the orbit height to decrease by 19 km [342]. Geocentric gamma-ray satellites are mainly placed in low-Earth orbits such that Earth's magnetic field shields them from low-energy cosmic rays [343]. As a downside, the satellite is subjected to an additional background. When cosmic rays reach the outer layers of Earth's atmosphere, they interact causing a cascade of secondary particles. Gamma rays produced in these interactions are the main background³ for Fermi at energies larger than 150 keV. At lower energies, most background photons observed by Fermi are due to the diffuse X-ray background [341].

South Atlantic Anomaly. Apart from interacting with Earth's atmosphere, charged particles can also interact with its magnetosphere. In particular, particles can get trapped by the magnetic field, forcing them to spiral around the field lines. These regions are called Van Allen⁴ belts. Earth has two such regions, referred to as the inner and outer belt. Most of the particles in these belts come from the solar wind. The region where the inner belt approaches the Earth most closely is located above the Atlantic ocean and is referred to as the South Atlantic Anomaly (SAA). During its orbit, Fermi passes through this area. No data is taken during the SAA passage, as both the LAT and GBM detector lower the voltage of their photo-multiplier tubes (PMTs) to deal with the increased background. The SAA passage causes an effective dead time of 15% [93]. Otherwise, both detectors are continually taking data.

Orientation. As the LAT detector can at any instant observe only $\sim 19\%$ of the full sky, Fermi mainly operates in a sky-survey mode. This implies that the spacecraft rocks its orientation angle between⁵ -50° and $+50^\circ$. A full rocking period, and therefore full sweep of the sky, is achieved every two orbits. Fermi-LAT is also regularly pointed at a specific right ascension (RA) and declination (DEC), to follow up on or perform more detailed observations of known astrophysical sources. If a particularly bright GRB is observed by GBM, the spacecraft will autonomously repoint itself to bring the burst into the FOV of LAT for a nominal period of 5 hours [341]. Repointing was initially done immediately following the GBM trigger. However, this proved detrimental to GBM observations, as the background rate strongly depends on the detector orientation and thus became very hard to characterise. A 30 s time delay has therefore been in effect since August 2011 [292].

On March 2018, a mechanical failure occurred that prevents the spacecraft from moving one of its two solar panels. A modified sky-survey mode has since been used, in which the

²At an orbit height of 565 km, 30% of the field-of-view is blocked by Earth.

³An additional subdominant contribution comes from cosmic rays that interact directly with the spacecraft [341].

⁴The Van Allen belts are named after the person who discovered them, James Van Allen [344].

⁵Up to September 2009, the rocking angle ranged from -35° to $+35^\circ$. This was changed to $-50^\circ \rightarrow +50^\circ$ to improve the efficiency of the thermal radiators at the bottom of the spacecraft, by decreasing the time that they are pointing towards Earth [292].

spacecraft orientation is changed less frequently. While thus no longer monitoring the full sky every ~ 3 hours, this modified plan ensures that LAT still obtains a full and uniform sky coverage. Due to the mechanical failure, the autonomous repointing to the direction of bright GRBs has since been disabled [342].

3.1.2 The Gamma-Ray Burst Monitor

Fermi's main instrument to detect GRBs is the Gamma-ray Burst Monitor (GBM). GBM consists of 14 independent subdetectors, all of which use an inorganic scintillator to image gamma rays. Out of those 14, 12 are identical sodium iodine (NaI) scintillators that are sensitive from 8 keV to 1 MeV. Each NaI subdetector is pointing in a different direction, allowing GBM to observe the full unocculted sky. The two remaining subdetectors use a bismuth germanate (BGO) crystal. They are sensitive from 200 keV to 40 MeV and are positioned on opposite sides of the spacecraft. For the triggering and localisation of GRBs, GBM solely relies on the NaI subdetectors. The BGO scintillators mainly serve to cover the energy gap with the LAT. By providing overlap with the energy range of both the NaI and LAT detector, they also allow for a cross calibration of the two instruments [341].

NaI subdetectors. Every NaI crystal is shaped cylindrically with a radius of 6.35 cm and a height of 1.27 cm. At the back end, this disk is attached to a PMT. The front end of the crystal is covered by a 0.2 mm thick beryllium sheet and a 0.7 mm thick silicon layer. This latter component is added for mechanical reasons and determines the lowest energy (8 keV) to which the NaI subdetectors are sensitive. An aluminium cover is placed at the remaining sides of the crystal, with a reflective white cover on the inside to increase the light yield. The PMT attached to the back end is a 10-stage R877-MOD PMT by Hamamatsu, which has the same 12.7 cm diameter as the crystal. Output voltages from the PMTs⁶ are sent to a charge sensitive amplifier and pulse shaper, before passing the signal on to the data processing unit⁷ (DPU) which determines whether the input leads to a GRB trigger.

Figure 3.2 shows the measured and simulated effective area of the NaI and BGO scintillators. As these are lab measurements, small variations are still expected for the in-orbit effective area due to gamma rays scattering off the spacecraft [341]. For the NaI subdetectors, a drop-off is observed at energies above ~ 200 keV. Below this threshold, most gamma rays will interact with the NaI crystal via the photo-electric effect, thus depositing all their energy into a single electron. By inelastic collisions, this electron can generate secondary free electrons in the crystal, leading to a collection of electron-hole pairs. Upon recombination, the decay of excited states leads to the isotropic emission of optical photons⁸ that can be observed by the PMTs. At energies exceeding ~ 200 keV, photons become more likely to interact via Coulomb scattering. While still ionising the medium, they thus do not produce the characteristic photo-peak signal⁹ which the PMTs are primed to detect. The transition from photo-electric absorption to Coulomb scattering is illustrated in Fig. 3.3, where the dashed line shows the cross section for gamma rays to interact with iodine.

BGO subdetectors. The two BGO subdetectors each use a cylindrical $\text{Bi}_4\text{Ge}_3\text{O}_{12}$ crystal with a diameter and height of 12.7 cm. A PMT¹⁰ is placed at both sides of the cylinder. Using double PMTs improves the light yield and provides redundancy if one of the two PMTs were

⁶External factors such as variations in the temperature and magnetic field are expected to affect the PMT gain and thus the output voltage by less than 2% on average.

⁷Fermi-GBM actually houses two identical DPU boards, to ensure redundancy if one of the boards fails.

⁸The NaI is doped with a 0.1% mole concentration of thallium to increase the fraction of scintillation photons that are emitted as optical light and that are thus detectable by the PMT.

⁹The photo-peak is the signal that results from a gamma ray depositing all its energy in a single interaction.

¹⁰The same R877-MOD PMT is used, but operating a different high-voltage than those of the NaI subdetectors.

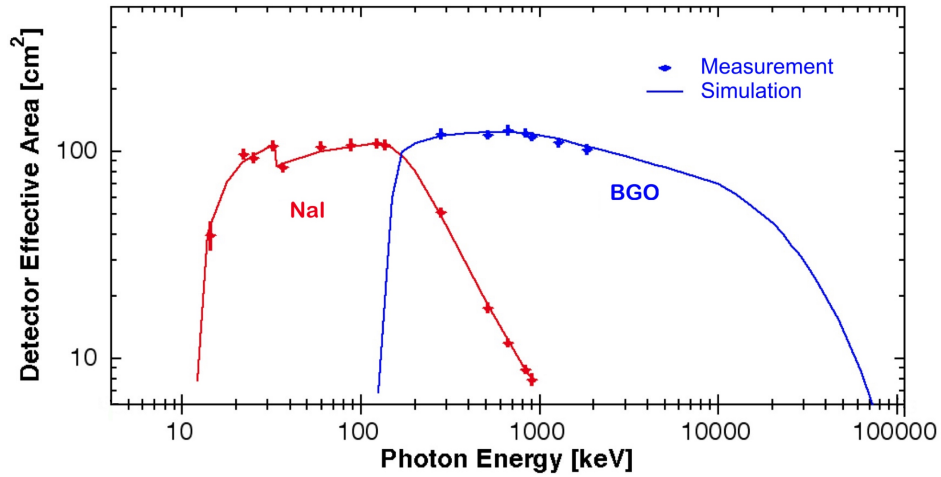


FIGURE 3.2: Effective area of the NaI and BGO scintillator, averaged over all detectors. Dots correspond to lab measurements that were taken before the detectors were mounted on the spacecraft. The ‘dip’ at 33.2 keV in the NaI curve corresponds to the K-band excitation level of iodine [345]. From [341].

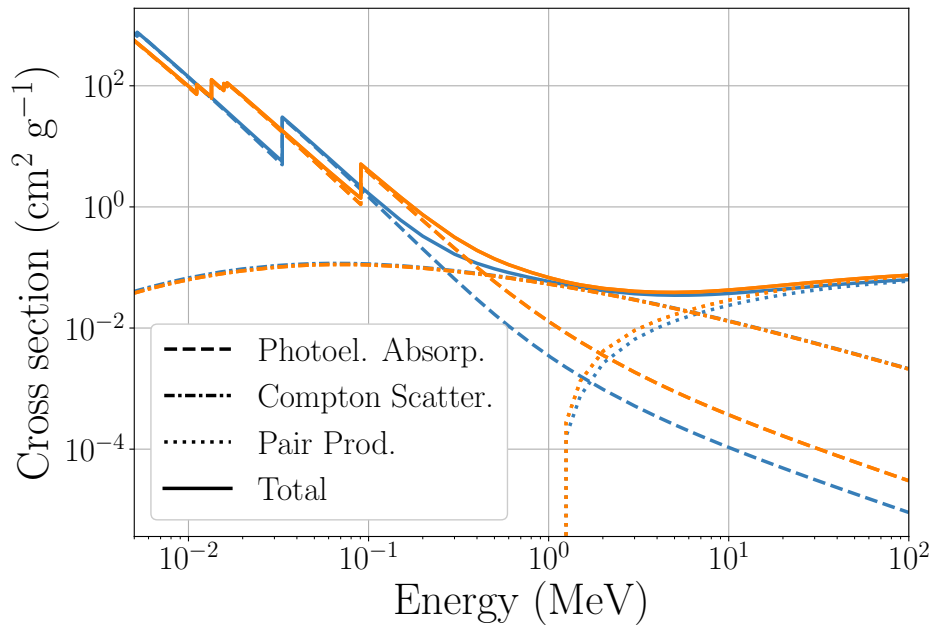


FIGURE 3.3: Cross section for gamma rays to interact with NaI (blue) and Bi₄Ge₃O₁₂ (orange). The four contributions correspond to coherent scattering, Compton scattering, photoelectric absorption, and pair conversion. Data obtained from XCOM [346].

to fail. While the scintillator edges on the sides of the PMTs are polished to mirror grade quality, the remaining cylindrical surface was roughened to aid to reflection of photons off the cylinder walls. In terms of read-out, the signal from the two PMTs is first combined before sending it through the same read-out system as that of the NaI subdetectors [341, 345].

Read-out. Each NaI and BGO subdetector has its individual read-out channel on the DPU. After passing through a charge sensitive amplifier and pulse shaper, a digital-analogue-converter samples the processed PMT signal at a frequency of 9.6 MHz into 4096 linear

voltage bins. The detection of a photon is triggered when the observed signal exceeds a programmable voltage threshold. When such an excess occurs, the DPU will wait until the voltage drops over 4 successive samples to identify the signal peak. At that stage, the voltage is then allowed 21 samples to return to its baseline state. Following an observed excess, a dead time of $2.6 \mu\text{s}$ has thus been implemented during which no new photons can trigger that particular subdetector [341].

Apart from the above described dead time, a second limiting factor is that the arrival time and energy of individual photons can no longer be stored if the rate summed over all 14 subdetectors exceeds $3.75 \cdot 10^5 \text{ Hz}$. Such high rates are very rare, but have been observed in a few GRBs. In such an event, part of the photon data will simply not be saved and will therefore be irretrievably lost. However, it should be noted that aside from the individual photon counts, data is also stored pre-binned in time and energy (see 3.3.1). This binned data is not affected by the aforementioned limitation on the total rate [341].

Triggering & localisation. To trigger and localise GRBs, Fermi-GBM uses the data from the 12 NaI subdetectors. No single trigger criterion is imposed that all bursts should satisfy. Instead, multiple trigger conditions are used, allowing the identification of signal excesses in several energy bands and over timescales ranging from 16 ms to 8 s. To reduce the possibility that triggers occur due to statistical fluctuations, every excess is required to occur in at least two subdetectors. Simulations indicate that the sensitivity¹¹ of Fermi-GBM corresponds to a flux of $0.74 \text{ photons cm}^{-2} \text{ s}^{-1}$ in the energy range from 50 keV to 300 keV [341].

At the time of the trigger, a burst direction will automatically be calculated by the spacecraft. This is done by comparing the background subtracted rate in each of the 12 subdetectors to precomputed values for 1634 burst directions. By quantifying the agreement using a χ^2 -estimator and picking the direction with the lowest χ^2 -value, an initial estimate of the burst direction is obtained with a resolution of $\sim 5^\circ$ [341]. At a later stage, once the burst data has been transferred to the ground, more advanced reconstruction algorithms are applied to determine the burst direction more accurately [131–133].

3.1.3 The Large Area Telescope

The second instrument on the Fermi spacecraft is the Large Area Telescope (LAT). Named for its considerable size, LAT has a dimension of $1.8 \text{ m} \times 1.8 \text{ m} \times 0.72 \text{ m}$. Such large dimensions are required¹² as LAT operates in the high-energy regime ($E \gtrsim 20 \text{ MeV}$), where gamma rays primarily undergo pair production (see Fig. 3.3). Hence, the composition of the telescope is inherently very different from GBM, making use of a separate tracker, calorimeter and anti-coincidence shield (ACS). While the first two components allow reconstructing the direction and energy of the gamma rays, respectively, the ACS is used to identify charged cosmic rays that are the detector's main background.

ACS. The ACS consists of 89 plastic scintillator plates that cover both the tracker and calorimeter. Only charged particles¹³ will cause a signal while travelling through the ACS, allowing LAT to veto incoming cosmic rays. On the outside, the ACS is wrapped in an anti-meteoroid shield. This wrapping reduces the risk that small meteoroids or space debris puncture the light tight wrapping surrounding the detector.

¹¹The sensitivity threshold is defined as the signal flux that will trigger the detector 50% of the time.

¹²Defining the FOV of LAT as the directions for which 50% of the particles that enter the top of the detector also reach its bottom, it follows from the detector aspect ratio of 0.4 that the FOV is roughly 2.4 sr.

¹³Signal gamma rays can in some cases trigger the ACS indirectly. When they produce an electromagnetic shower in the calorimeter, 100-1000 keV photons are produced in sufficient numbers that a fraction of those photons travelling back upwards can undergo Compton scattering in the ACS, thus triggering a veto. To reduce this effect, the ACS is segmented and only signals near the initial tracker hits are used to veto an event.

Tracker. As illustrated in Fig. 3.1, the tracker sits on top of the calorimeter and consists of 16 ‘towers’ arranged in a 4×4 grid. Each tower has 18 layers comprising two components. The first is a sheet of tungsten which, being a dense material ($\rho = 19.28 \text{ g cm}^{-3}$) with a high atomic number ($Z = 74$), acts as a target for the gamma rays to interact with. Electron-positron pairs produced by gamma rays interacting with the tungsten will then travel through the second layer, which consists of silicon strips. The strips, arranged in a hodoscopic configuration, allow detecting the electron-positron pairs and determining their positions in the plane of the strips.

In the top 12 strips, the tungsten sheets have a width of only 0.035 radiation lengths¹⁴ to minimize the effect of multiple scattering. A thicker sheet of 0.18 radiations lengths is used in the following 4 sheets, to increase the likelihood that photons which passed through the previous layers unimpeded will still interact. Finally, the bottom two sheets consist only of silicon sheets, as hits in 3 consecutive layers are required to trigger an event, making it pointless to induce further gamma-ray interactions [292].

Calorimeter. Directly below every tracking tower sits a stack of 96 cesium iodine scintillators¹⁵. These crystals have a dimension of $2.7 \text{ cm} \times 2.0 \text{ cm} \times 32.6 \text{ cm}$ and are stacked in 8 layers of 12 scintillators each. At both ends of each crystal are two photodiodes. One diode is sensitive to energy depositions in the energy range from 2 MeV to 1.6 GeV, while the second diode covers energies from 100 MeV to 70 GeV. Scintillators in adjacent layers are placed perpendicular to each other. As a result, the LAT calorimeter cannot only reconstruct the total energy of the shower, but also its full three dimensional profile. This also allows identifying and correcting for energy leakage at the detector edge. Combined, the 8 layers of scintillator crystals have a total depth of 8.6 radiation lengths [93].

3.2 Gamma-ray sources

With its large FOV, unprecedented effective area, and an energy range spanning more than 7 orders of magnitude, Fermi has majorly contributed to the field of gamma-ray astronomy. In the fourth Fermi Gamma-ray LAT (4FGL) catalogue, published in 2019, 5064 steady-state gamma-ray sources outside the solar system are identified [347]. Figure 3.4 shows the corresponding Fermi-LAT sky map, in which a number of these sources, both galactic and extragalactic, can be observed as hotspots.

Since our analysis focuses solely on GRBs, these steady-state sources and other non-GRB gamma-ray transients are considered to be a background. This is particularly so since some non-GRB transients can cause false GRB triggers. A short overview is therefore presented here on Fermi sources other than GRBs. Sources closest to the telescope will first be discussed, before moving on to galactic and extragalactic distance scales.

3.2.1 Terrestrial sources

Cosmic rays. As noted previously, the majority of gamma rays detected by Fermi-GBM are produced by cosmic rays that create a particle shower in Earth’s atmosphere [242]. These gamma rays present a continual diffuse background that gradually varies as the satellite moves along its orbit. While the observed background is thus constantly changing, the rate varies smoothly enough that this effect does not induce any false GRB triggers.

¹⁴The radiation length is defined as the distance over which high-energy electrons on average lose a fraction $1 - e^{-1} \approx 63\%$ of their energy due to radiation losses. It also corresponds to $7/9$ of the photon mean free path to undergo pair production [110].

¹⁵As the NaI detectors from GBM, these are doped with thallium to increase the visible light yield.

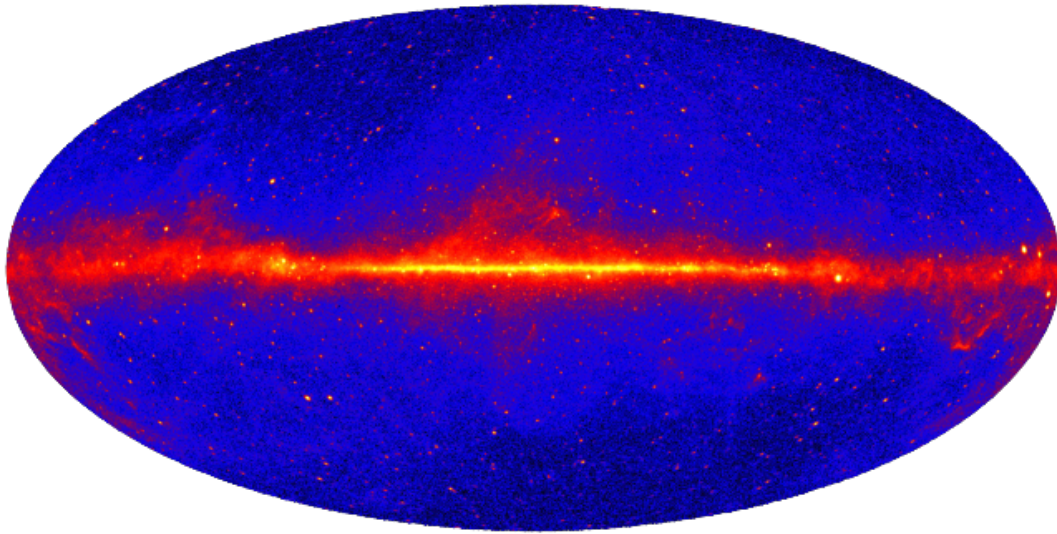


FIGURE 3.4: Image of the gamma-ray sky in galactic coordinates, created using 9 years of Fermi-LAT data. The central band corresponds to the Milky Way disk. While essentially all extended hotspots are galactic sources, such as pulsar wind nebulae and supernova remnants, extragalactic objects, such as active galaxies and blazars, are also visible as point-like hotspots [347].

Credit: NASA/Fermi LAT Collaboration.

Lightning. GBM triggers can be caused by terrestrial lightning strikes. During a strike, free electrons can be accelerated up to energies of 100 MeV by the electric field in the atmosphere. When such high-energy electrons pass close to an atomic nucleus, they will produce bremsstrahlung up to MeV energies [348]. The combined emission from a distribution of electrons will lead to a very short gamma-ray flash that has a duration of the order $30 \mu\text{s}$ to 3 ms [349]. On average, GBM observes 800 such events per year [349]. Based on their direction, i.e. coming from Earth, and their extremely short duration¹⁶, these can easily be distinguished from GRBs.

Terrestrial electron beams. A second terrestrial effect that can trigger GBM relates to the secondary electrons¹⁷ produced by a lightning strike. These electrons will spiral around Earth's magnetic field lines, effectively forming a beam. If such a beam by chance happens to strike a gamma-ray satellite, it will produce a signal largely comparable to that of the gamma rays from a lightning strike. However, electron beams can travel significant distances and thus be detected even when the satellite is not overhead an area in which lighting occurs. While electron beam events are much more rare than lighting flashes observed directly, a handful of such events have been detected by GBM [349, 350].

3.2.2 Solar system

Moon. Apart from Earth itself, the gamma-ray source in our solar system with the highest apparent brightness¹⁸ is the Moon. Essentially, the exact same mechanism takes place as

¹⁶In the seconds to minutes prior to a lightning strike, a very dim increase in gamma rays is already observed. This is believed to be a consequence of the additional acceleration that cosmic-ray air shower electrons and positrons experience due to the strong electric fields [348].

¹⁷These are electrons produced by the Compton scattering and pair production of gamma rays.

¹⁸For a low-orbit geocentric satellite such as Fermi.

discussed for Earth's atmosphere. Cosmic rays will interact with the lunar surface and produce a cascade of secondary particles, among which gamma rays. While most gamma rays will be absorbed, the fraction escaping the lunar surface is non-negligible [351]. Satellites orbiting around the Moon for instance have been able to perform gamma-ray spectroscopy of the lunar surface using this signal [352]. Since the cosmic-ray density is approximately constant, so too is the gamma-ray flux from the Moon. A slight modulation is observed over the course of years, in line with the change in cosmic-ray density due to the solar cycle [352].

Sun. Cosmic-ray interactions in the Sun similarly lead to a steady-state gamma-ray emission. The Sun and Moon have close to the same angular size, but unlike the Moon, the Sun is shielded by a magnetic field. Cosmic rays therefore have a smaller probability to interact per unit surface, leading to relatively fewer gamma rays [353].

In addition, solar gamma rays are also produced in transient events called solar flares. During periods of increased solar activity, the Sun will sporadically expulse blobs of charged plasma. This plasma will carry its own magnetic field, that at one point will need to decouple from the field lines connected to the Sun. A magnetic reconnection event will thus be triggered, leading to particle acceleration. Over a period of 10 years, GBM triggered on the gamma rays produced in 1176 solar flares [49]. Gamma-ray emission from these events generally lasts on the order of ~ 20 minutes [354]. Along with other characteristics, primarily among which the location of the flare, these events can be distinguished from long GRBs.

Other planets. Gamma rays produced by cosmic-ray interactions in the albedo of other planets have also been observed (see e.g. [355]), but are too dim to be discernable with current geocentric satellites such as Fermi. Hence, they do not pose a background for our analysis.

3.2.3 Milky way

Excluding contributions from our solar system and looking at the sky in galactic coordinates, the Milky Way becomes the dominant source of gamma rays. As illustrated in Fig. 3.4, emission primarily originates from the region of the galactic plane and the galactic centre. Gamma rays local to the Milky Way comprise two components¹⁹. Firstly, there is diffuse emission that mainly stems from cosmic rays, electrons, and positrons interacting with the interstellar gas and radiation fields [353]. Secondly, emission can also result from local sources that are sites of particle acceleration.

Steady-state sources. In the context of GRBs, almost all local sources can be considered to be in a 'steady-state' since the timescale over which their flux varies is orders of magnitude larger than the typical duration of long GRBs. The primary sources making up this category are: supernovae, pulsars, globular clusters, star forming regions, and X-ray binaries [347]. Like the diffuse component, gamma-ray emission from these objects can be considered to be invariant. For GRB searches, these objects will thus not lead to any false GRB triggers.

Transients. One class of galactic sources that can produce transient signals very similar to those of GRBs are soft gamma-ray repeaters (SGRs). These sources are thought to be millisecond magnetars local to our galaxy²⁰. Over a 10 year period, GBM triggered 258 times on SGR events [49]. However, these triggers are caused by only a handful of SGRs. The trigger rate itself strongly fluctuates depending on the activity of these sources. For instance, more

¹⁹Apart from the known contributors to the gamma-ray flux discussed in this section, more exotic alternatives such as dark matter annihilation are of course also possible.

²⁰For a more extended discussion on SGRs, see 1.6.3.

than 100 of the 258 triggers occurred in the first quarter of 2009. Other galactic sources that can trigger GBM are binary systems in which accretion takes place on a stellar mass black hole. Such systems have a trigger rate similar to SGRs and also produce irregular but repetitive signals, allowing them to be distinguished from GRBs [49].

3.2.4 Extragalactic sources

At the largest distance scale, i.e. considering extragalactic sources, detectable transients become extremely rare as essentially only GRBs²¹ are powerful enough to produce a gamma-ray flux above the GBM detection threshold. Likely the sole exception to this rule are giant magnetar flares. Unlike GRBs, they can only be observed in our local Universe. Current estimates suggest that $\sim 2\text{--}8\%$ of short GRBs are likely misidentified giant magnetar flares [284, 285].

In contrast to non-GRB transients, the majority of the 5064 steady-state sources identified in the 4FGL catalogue are of extragalactic origin. In particular, 3130 association are with active galaxies²² [347]. Other source classes include: starburst galaxies, radio galaxies, Seyfert galaxies, and less bright but close by galaxies such as the Large Magellanic Cloud. Similar to the observed galactic gamma rays, there is also a diffuse extragalactic component. However, due to the large distances, extragalactic diffuse emission is only in part intrinsically diffuse and instead, mostly due to the large number of extragalactic steady-state sources that are too distant to be distinguished on an individual basis [84].

3.3 Precursor selection

Of all the sources mentioned above, this chapter will from here on solely focus on the observations of GRBs by Fermi-GBM. A description will first be given on the GBM data format, followed by a detailed overview of how we analysed this data to identify GRB precursor activity. The analysis procedure consists of two main stages. After selecting the two or three relevant NaI subdetectors for each burst, an analysis is first performed on raw time data to characterize the background rate. Subsequently, the Bayesian Block (BB) method [307] is applied to identify the physical signal regions. The results from our study are then presented in the Section 3.4.

3.3.1 Data format & characteristics

Level 1 data. For every GRB that triggers the detector, the Fermi-GBM Collaboration releases data files that contain the photon counts observed by the 12 NaI and 2 BGO subdetectors. This data corresponds to *level 1*, having undergone two steps of processing. Raw telemetry data that is sent from the spacecraft to Earth first undergoes minimal processing at the NASA Goddard Space flight centre in Maryland, US. During this step, duplicate data packets are removed, basic quality checks are performed, and the data get ordered in time. No information is thus lost in the conversion from telemetry data into *level 0* data [341].

For further processing, the data is subsequently transferred to the GBM Instrument Operation Center in Alabama, US. As a first step, an automated pipeline is applied to calibrate the detector gain of each of the 14 subdetectors. This allows converting the output pulse-heights measured by the PMTs to an effective energy. The reformatted data thus produced

²¹Blazar flares occur on timescales of several months to only a few minutes, and can also be detected as extragalactic gamma-ray transients [356]. However, they are easily distinguishable from GRBs as they also produce steady-state emission.

²²Active galaxies are galaxies in which the central black hole produces a jet due to the accretion of matter.

contains the arrival time and energies of the incident photons. In addition, meta-data about the trigger conditions and orientation of the spacecraft is also included. These *level 1* files serve as the basis for GRB analyses performed by the GBM Collaboration [341]. To also enable analyses from non-collaboration members, all *level 1* files are made publicly available at <https://fermi.gsfc.nasa.gov/ssc/data>. The analysis presented here makes use of the public *level 1* data files of all GRBs detected by GBM between its launch and the start of the year 2020, corresponding to a total of 2705 bursts.

CTIME, CSPEC & TTE. Limitations in the amount of data that can be downlinked from the satellite imply that not all individual photon triggers can be stored. Data is therefore to a certain degree binned onboard the spacecraft before transmitting it to the ground. Three types of files are made available for every GRB trigger to optimally deal with downlink limitations. Around the time of the trigger, time-tagged event (TTE) data is made available. TTE files contain the arrival time of every individual photon with a resolution of $2.6 \mu\text{s}$. The photon energy is stored as an index that can range from 1 to 128, corresponding to 128 linearly spaced energy bins. After a software upgrade in August 2010, TTE data has become available starting 135 s before the trigger time up to 300 s after the trigger time. Before this date, TTE data is available from 30 s prior to the GRB trigger, but again up to 300 s after [341].

To extend the time range of available data, the remaining formats bin the photon counts in both time and energy. Two formats were chosen to ensure both good temporal and spectral resolution. CSPEC data, like TTE data, maintains 128 linear energy bins, but has very broad temporal bins with a nominal width of 4.096 s. CTIME data in contrast offers a smaller temporal bin size of only 256 ms, while reducing the energy resolution to 8 linear energy bins. Both CTIME and CSPEC data are made available in a 2000 s time window centred on the trigger time of the burst [341].

The analysis presented here aims at reliably identifying the times at which precursor emission is observed. Our analysis thus primarily focuses on the temporal, rather than the spectral properties of the precursor events. TTE data is therefore used whenever available. Regions outside the TTE time range are extended using CTIME data. To select the relevant subdetectors, the trigger conditions are examined. GRB triggers require that an excess is observed simultaneously in at least two of the twelve NaI subdetectors. As a start, subdetectors that were triggered by the burst are selected. If more than three subdetectors contributed to the trigger, the selection is further restricted to the three subdetectors pointing closest to the burst location, as they will have observed the strongest signal. Other subdetectors are then not included, as it is unlikely that a precursor signal that does not show in the selected subdetectors would show in a subdetector with a dimmer signal.

Poisson background rates. On timescales sufficiently small for the background rate not to undergo any significant fluctuations ($\lesssim 100$ s), the rate at which photons are observed is determined by Poisson statistics. The analysis procedure described below will therefore make use of the Poisson uncertainty to determine the significance of a given photon count. To motivate this methodology, we here demonstrate the Poisson nature of the background rates observed by the individual NaI detectors.

TTE data at least 30 s prior to any triggers by GBM is used to perform a total of 10^4 trials. Each trial starts by randomly selecting a GRB, a subdetector, and a reference time t_r in the background regime. The photon count in the time interval $[t_r - 25\lambda^{-1}, t_r + 25\lambda^{-1}]$ is then determined, where λ is the rate averaged over a 10 s period centred on t_r . Background rates are typically of the order $\sim 10^3$ Hz, leading to time windows of ~ 0.05 s. Figure 3.5 shows a normalised histogram of the observed counts next to the Poisson function with mean 50.

The close agreement between the two distributions confirms that on these small timescales, variations in the observed photon counts are indeed Poissonian.

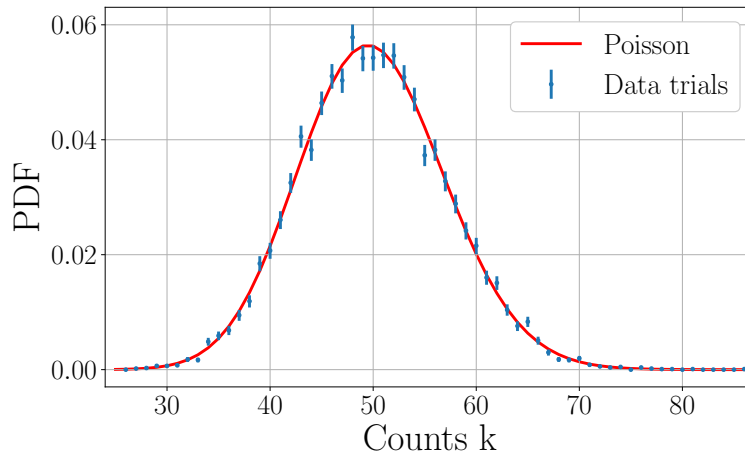


FIGURE 3.5: Number of counts observed by a single NaI detector in a background time window for which the mean number of expected events is 50. 10^4 trials are performed over numerous GRBs and subdetectors to demonstrate that the counts closely follow Poisson statistics.

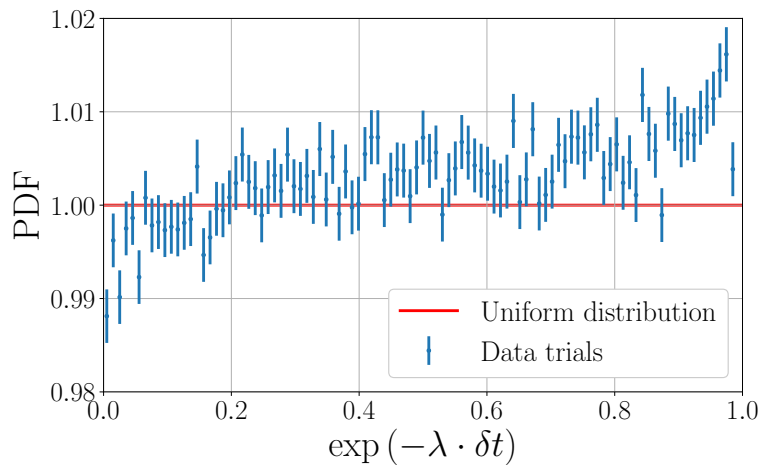


FIGURE 3.6: Distribution of the variable $w = \exp(-\lambda \cdot \Delta t)$, where Δt is the time delay between two photons and λ is the average rate. 10^7 trials are performed to show that w matches a uniform distribution.

To fully verify the Poisson nature of background counts, a second check is performed to show that the time delay Δt between two subsequently observed photons follows an exponential distribution. 1 s of data from the same 10^4 trial time windows is used to generate a set of $\sim 10^7$ values for Δt . Poisson statistics then predict that Δt will follow an exponential distribution. If this is the case, then the variable

$$w \equiv \exp(-\lambda \cdot \Delta t), \quad (3.1)$$

should be uniformly distributed. The probability distribution of all $\sim 10^7$ values for w is shown in Fig. 3.6. Good agreement is observed to the expected uniform distribution, with deviations generally being smaller than 1%. At the smallest time delays, i.e. as $w \rightarrow 1$, an increase initially occurs due to pulse pile-up in the detector. This is followed by a sudden

drop-off due to the effect of detector dead time. As a result, the rightmost bin, which has a PDF value of 0.7, is not visible in Fig. 3.6 [341].

3.3.2 Characterizing the background rate

Method outline. Figure 3.7 displays the GBM light curve for a single NaI detector of a typical GRB, namely bn150422703²³. While all GRB emission is contained within a ~ 50 s time window, significant changes to the rate still occur outside this range due to fluctuations in the background rate. These fluctuations are caused by a plethora of phenomena, primarily among which are the continually changing orientation and position of the spacecraft²⁴. Due to the complexity and interplay of these effects [357], no model has so far been constructed that can reliably predict what the background rate will be at a given time and date [358].

For this reason, GRB studies by the Fermi-GBM Collaboration employ an empirical approach in which background time intervals are identified by eye. Given such an interval before and after the period of GRB emission, the background rate in the intermediate signal region can be interpolated. First or higher order polynomials are generally used for this purpose. Our analysis will use a similar approach, with the distinction that we developed a new method to automatically identify the periods of background emission used to perform the interpolation. In doing so, we ensure that our results are fully reproducible and that the selection of background intervals is based on physically motivated parameters. This characterisation of the background rate will then, at a later stage of the analysis, allow the construction of a background subtracted light curve.

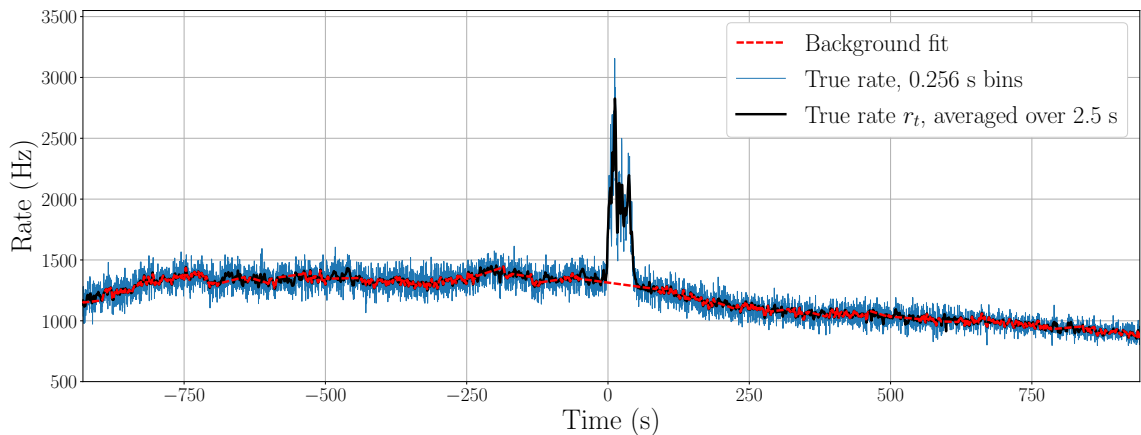


FIGURE 3.7: Observed rate (full lines) and estimated background rate (dashed line) of bn150422703 and the GBM subdetector labeled nb.

Procedure. During periods in which no signal emission is present, the observed rate is prone to two effects. On short timescales (~ 10 s), variations in the rate are well described by Poisson fluctuations, as shown in 3.3.1. On times scales of ~ 100 s, significant long term increases and decreases in the rate can be observed in Fig. 3.7. Nonetheless, these long-term effects are a smooth variation superimposed on the Poisson fluctuations, distinguishing them from the sudden increase in the rate that characterises signal emission.

²³Fermi bursts are given a trigger name based on the date and UTC time of the trigger. For instance, bn150422703 occurred on the 22th of April, 2015, roughly $86400 \cdot 0.703$ seconds after midnight.

²⁴Other effects include the current state of Solar activity, which affects the magnetic field lines of Earth and therefore the flux of charged particles that the spacecraft is exposed to.

Our algorithm to identify periods of background emission proceeds as follows. Starting at the earliest time t_i for which data is available, a linear fit is performed to data in the time interval²⁵ $[t_i, t_i + 20 \text{ s}]$. This fit function is then evaluated at the time $t_i + 30 \text{ s}$ to obtain a prediction r_p for the rate at that time. This prediction is compared to the true rate r_t at that time, averaged over 2.5 s. If the observed rate does not exceed the predicted rate by 3σ significance, i.e.

$$r_t < r_p + 3 \cdot \sqrt{\frac{r_p}{2.5 \text{ s}}}, \quad (3.2)$$

then the time $t_i + 30 \text{ s}$ is tagged as a background time. The procedure is then repeated for $t_i + 1 \text{ s}$ instead of t_i , until the end of the available data is reached or until Eq. (3.2) no longer holds. When the start time t_s of a period that contains excess emission is identified, we immediately advance 25 s with the aim of overshooting the potential signal region. To verify that the rate has returned to a stable level, the RMS of $r_p - r_t$ is determined over a 10 s period centred on $t_s + 25 \text{ s}$. If the RMS exceeds the Poisson expectation by 1.5σ , then the time is advanced by 1 s and the RMS of a 10 s period centred on $t_s + 26 \text{ s}$ is considered. When, after repeating this process, a time $t_s + \alpha$ is found at which the RMS criterion is satisfied, then $t_s + \alpha$ is labelled as a background time and the above described procedure of verifying Eq. (3.2) is repeated. When the full light curve has been covered, a set of background times is thus obtained. At times within this set, the background rate is set equal to the true rate, averaged over 2.5 s. At intermediate times, the background rate is taken to be the linear interpolation of the two surrounding background times.

The procedure described above was developed to generalise the identification of background intervals in an empirical, but consistent manner, rather than performing the selection by eye. Various configurations of the numerical input parameters were explored. The values implemented in the finalised version of the code correspond to those for which the selection of background intervals best agreed with the selection that would have been made by eye, when considering a representative subset of bursts. A visualisation of the background characterisation procedure is shown in Fig. 3.7 for a single NaI subdetector of the burst bn150422703. It should be noted that this method focuses on providing a reliable selection of background times. Hence, most times not tagged as such are likely not real signals, but rather background fluctuations removed out of precaution to ensure that our background characterisation is not contaminated by any signal events.

3.3.3 Bayesian block light curves

Having characterised the background rate, the next step in the analysis procedure is to apply a suitable binning to the light curves. Numerous rules of thumb exist to determine the optimal bin width for a given set of data. However, we have opted to apply a more advanced procedure in which a Bayesian algorithm is applied to find the optimal piecewise constant representation of the data. This method was developed by J. Scargle to analyse the gamma-ray data of the BATSE telescope and is referred to as the Bayesian Block (BB) procedure [340]. A light curve with variable binning is thus produced, in which the transition of one bin to the next signifies that a statistically significant decrease or increase in the rate has occurred. Further details on the BB algorithm are provided in Appendix A.

For every GRB in our analysis, a BB light curve is constructed for each of the 2 or 3 relevant NaI subdetectors. In addition, a single BB light curve is constructed using the summed

²⁵By applying our background characterization method to a wide range of light curves, we found that a duration of 20 s is sufficiently large to have a stable/converging fit and yet still sufficiently small to be unaffected by long term fluctuations.

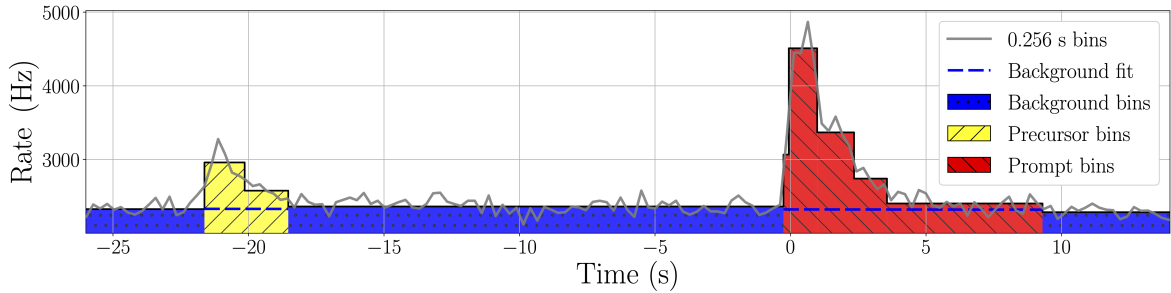


FIGURE 3.8: Bayesian block light curve of bn120308588, using the summed data of the three NaI subdetectors triggered by the burst.

photon counts of those subdetectors. While the combined light curves will be the main resource used to identify precursors, having corresponding BB light curves of the individual subdetectors will allow us to verify that the signal was present in more than one subdetector. An example of a BB block light curve for one the GRBs in our analysis is shown in Fig. 3.8.

3.3.4 Precursor selection criteria

Using the BB light curves, the piecewise continuous background characterisation from 3.3.2 is integrated over each bin. By subtracting that integrated background count from the observed photon count and dividing by the bin duration, an estimate is obtained of the signal rate. Regions of GRB emission are then identified as periods in which the background subtracted rate is significantly larger than zero, as outlined in more detail below.

Time intervals. The time range that can be searched for precursor emission is naturally limited by the availability of the Fermi-GBM data and the requirement that a characterisation of the background rate is needed. Given the procedure outlined in 3.3.2, the earliest time at which a stable background estimate can be obtained is 30 s after the first available data point. More than 90% of the GRBs in our sample have a background characterisation that starts between 1000 s and 800 s before the GRB trigger time. The end of the time interval considered in this analysis is the end of the prompt phase. To be conservative, an endpoint 50 s past the T90 interval is used. If the burst is extremely long ($T_{90} > 250$ s), 20% of the T90 duration is used instead of 50 s.

A complication arises for a small subset of bursts, which have gaps in their light curves due to missing data. In those cases, only the continuous data taking period that encompasses the GRB trigger time is used. Including also the data from earlier, distinct data taking periods would increase the available time range for less than 1% of all GRBs. Hence, the gain would be negligible. At the same time, it would severely complicate the interpretation of our results. We have therefore opted to restrict the analysis to uninterrupted data taking periods. Additionally, 21 out of the 2705 GRBs had either no TTE data available at the time of the bursts, or an average background rate so high that a BB light curve could not be constructed within a reasonable time frame. The analysis was therefore restricted to the 2684 GRBs for which good data is available.

Required excess rate. To determine if an observed excess is a signal, the statistical uncertainty in the count rate, \sqrt{N} , as well as a systematic uncertainty from the background characterization (3.3.2) have to be accounted for. The statistical uncertainty is implicitly taken into account by the BB mechanism, as a block/bin is effectively a period of time during which the rate is consistent with Poisson fluctuations around a fixed mean. Therefore, only the systematic uncertainty due to the background characterization has to be considered.

To verify that this method indeed leads to a competitive selection, three different threshold conditions were implemented. These include:

- (A) a fixed excess rate threshold,
- (B) a $\frac{\text{signal}}{\sqrt{\text{background}}}$ approach, quantifying the statistical significance of the excess,
- (C) a combination of the upper 2 approaches, quadratically adding the statistical uncertainty on the observed count to a fixed systematic uncertainty that results from the background estimation.

For every variable, a range of threshold values were tested to find those that offer the optimal performance. To quantify the loss of signal events, the fraction of GRBs for which a signal was detected within a 10 s period centred on the trigger time, t_{tr} , was computed. We thus aim for our analysis to be able to pick up every event that triggered the GBM detector. As a tracer of the false positive rate, the number of GRBs for which our analysis found a signal more than 500 s prior to t_{tr} was used²⁶. Figure 3.9 shows these two variables as a function of the threshold rate for method (A). Above 30 Hz a plateau is reached, after which the number of false positives stagnates. Since higher threshold rates would only serve to reduce the sensitivity, the threshold rate was therefore fixed to 30 Hz.

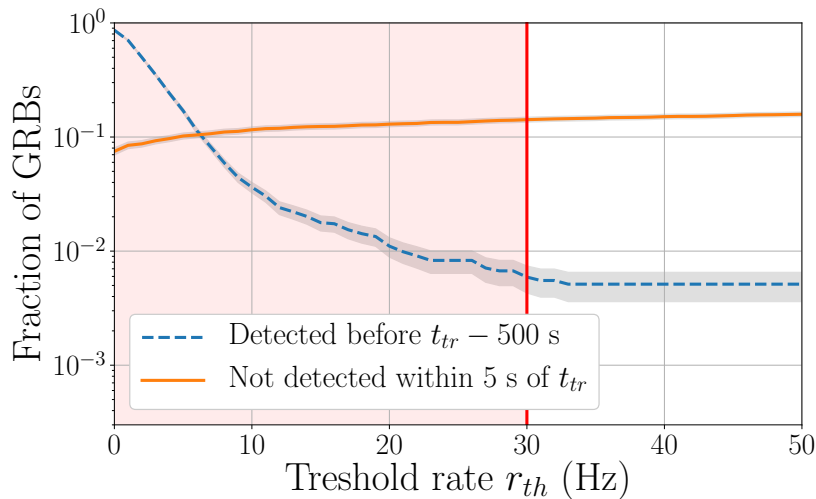


FIGURE 3.9: Illustration of how the threshold rate parameter, r_{th} , is optimised. The full orange curve shows the probability that a real physical signal is not picked up by our method. The dashed blue line, in contrast, is a tracer for the possibility that a non-physical excess is falsely identified as signal.

The same procedure can be repeated for method (B) and (C). In their context, the threshold variable takes on a different physical meaning. To offer a fair comparison, the tracer of the false positive rate (dashed blue line in Fig. 3.9) is therefore plotted in Fig. 3.10 as a function of the failure rate to identify a physical signal (full orange line in Fig. 3.9). Comparing the three variables, option (B) clearly offers the worst performance, while option (A) and (C) provide the same results up to statistical fluctuations. Since option (A) is a less complicated variant of option (C), the former was used in this analysis.

²⁶A previous Fermi-GBM study by Charisi et al. [295] showed that only a single burst out of a sample of 956 GRBs showed signs of precursor emission more than 500 s before t_{tr} .

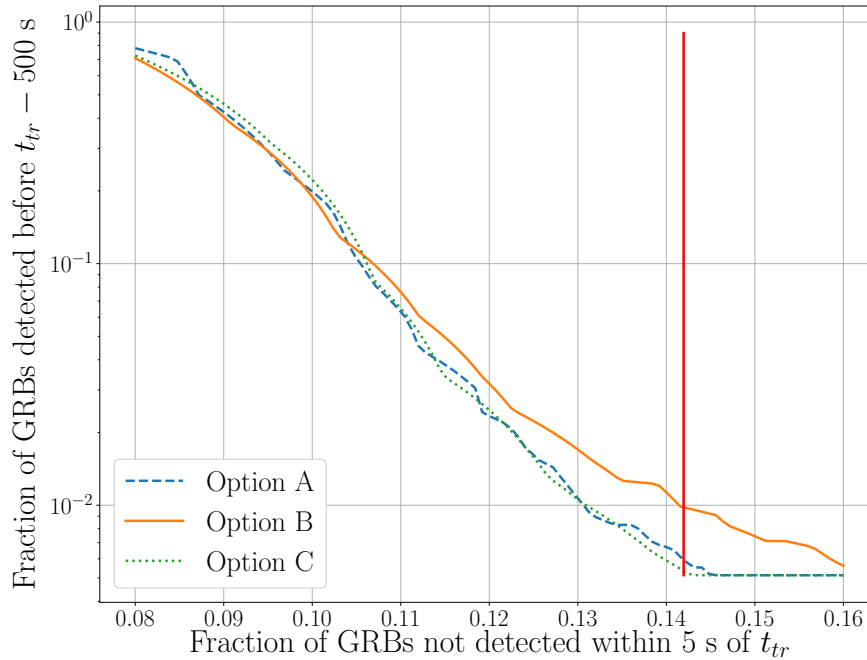


FIGURE 3.10: Tracer for the number of falsely identified signal events as a function of the probability that a true signal is missed by the analysis. Considering the same x -value, larger y -values indicate a worse performance. The red line indicates the x -value that method (A) has for the threshold rate of 30 Hz used in the analysis.

Emission episodes. Bins in the combined BB light curves that exceed the required excess rate are tagged as potential signal. To validate a potential signal bin, at least two of the contributing subdetectors are required to have one or more overlapping bins in their BB light curves that also satisfy the threshold condition. Once validated, subsequent signal bins in the combined light curve are grouped into an ‘emission episode’.

Emission episodes thus represent continual periods of GRB activity. By definition, they are separated from one another by quiescent intervals in which the rate has dropped back to the background level. It is conceivable that a downward fluctuation would cause two emission episodes to be artificially separated by a very short low-statistics quiescent time. An additional criterion is therefore imposed that the relative Poisson uncertainty on the average rate of a quiescent interval should be less than 5%. In practice, this implies that quiescent times smaller than ~ 0.2 s will be rejected. Such short quiescent times are expected in e.g. the NS crust cracking model (Subsection 2.2.5). Our analysis will thus not be able to constrain models that predict precursors on timescales of the order $\lesssim 0.2$ s.

Precursor definition. If a GRB only has a single emission episode, then that is automatically the prompt phase of the burst. If there are multiple emission episodes, then the one which has the largest background subtracted photon count is defined to be the main outburst or prompt phase. Precursors are then defined as any emission episode that precedes the prompt phase.

3.3.5 Additional checks

Expected false positives. Before proceeding to the actual results, the fraction of fake precursors, caused by statistical fluctuations, is first estimated. As previously stated, it is extremely

rare that a GRB would emit gamma rays more than 500 s before the GBM trigger time²⁷. The rate at which such emission episodes occur is therefore determined to obtain a conservative estimate of the probability that our method identifies a signal in a region that essentially contains only background. Normalising by the size of the scanned time window, the false alarm rate is estimated to be $1.7 \cdot 10^{-5}$ Hz. A total of 36.1 ± 8.8 false positives are thus expected, as $2.1 \cdot 10^6$ s of data is available prior to the prompt phase²⁸.

Relative count ratios. When a precursor signal is identified, an additional check is performed to verify that this early emission episode is not caused by some unrelated transient event that occurred in a different location of the sky. The relative count ratio is therefore introduced, defined as

$$r_\alpha = \frac{N_\alpha}{\sum_\beta N_\beta}, \quad (3.3)$$

where N_α is the background subtracted photon count observed by the NaI detector with index α and the summation runs over the two or three selected NaI detectors. The value of r_α can be computed separately for each emission episode. If both the precursor and prompt emission originate from the same direction, then for any NaI detector α , the value of r_α should be consistent. Figure 3.11 displays the cumulative distribution of

$$\left| \frac{r_{\alpha,precursor} - r_{\alpha,prompt}}{r_{\alpha,prompt}} \right|, \quad (3.4)$$

for all of the selected subdetectors and precursors identified by our analysis. Values close to zero indicate a good agreement of the localisations of the two emission episodes. Eight precursors are observed to substantially deviate from the expected value. By verifying the background characterisations of those bursts, we found that there were three GRBs for which an improved background rate resolved the high values of r_α . This is further motivated in Appendix B. For the remaining five bursts: bn090428441, bn110227229, bn130504314, bn150506398, and bn160908136, we cannot confirm that the localisation of the precursor and prompt emission are consistent with one another based on this method. These five bursts are included in our precursor catalogue, though they are highlighted in the results section and catalogue as potentially being unphysical events.

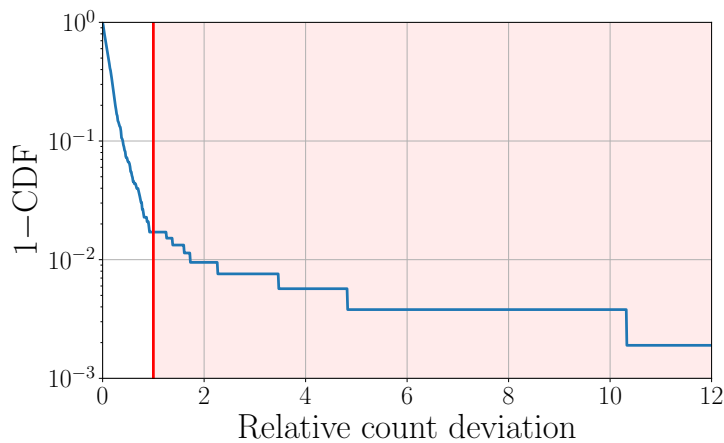


FIGURE 3.11: Distribution of the relative count deviation, defined in Eq. (3.4) for every subdetector of all GRBs with precursors. Eight bursts are found to have deviating values.

²⁷One example of an exception to this rule is GRB 091024 [296].

²⁸Summed over all 2364 GRBs that show a signal in our analysis.

3.4 Results

The results presented in this section have been published in Physical Review D [1]. Hence, the structure and content of this text will largely follow those of the article.

Of the 2684 GRBs that triggered Fermi-GBM, there are 320 bursts that do not show a signal following our selection criteria. We therefore restrict the analysis to the remaining 2364 GRBs for which a prompt signal can reliably be identified. Out of those 2364 bursts, there are 217 GRBs (9%) for which one or more precursor emission episodes were observed²⁹. In total, 244 precursor emission episodes are observed, with a single GRB having at most 3 precursors. The number of bursts with 1, 2, and 3 precursors corresponds to 192, 23, and 2, respectively. Appendix C presents a complete catalogue of the identified precursors, listing their start time, duration, time separation with respect to the prompt phase, and redshift. A digital format of this table that includes an interactive light curve for every precursor GRB has been made available on GRBweb at https://icecube.wisc.edu/~grbweb_public/Precursors.html.

Ordering the GRBs by the time at which they occurred, a basic consistency check is to verify that the number of precursors increases linearly with the size of the analysed GRB sample. Figure 3.12 shows that this is indeed the case. It thus follows that the software upgraded from August 2010 that made TTE data available at earlier times (see 3.3.1) does not affect our analysis sensitivity in a notable way.

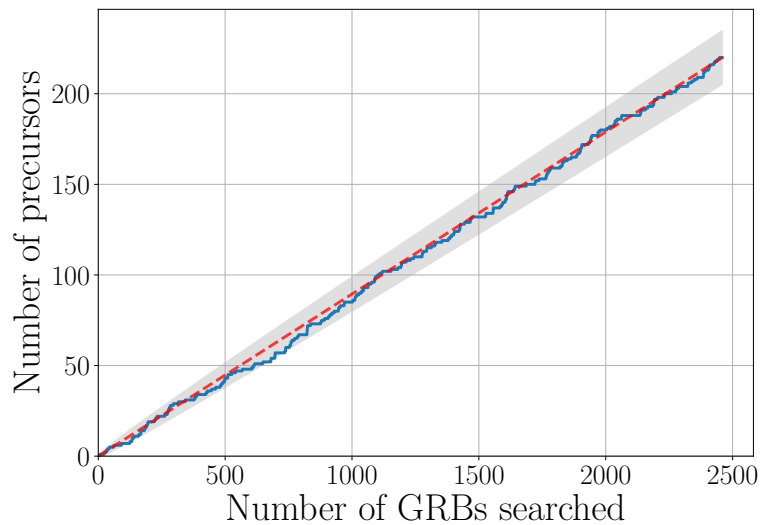


FIGURE 3.12: Searching only the earliest N GRBs observed by Fermi-GBM, the full blue line displays the number of precursors contained in that sample. As expected, the observed dependence is consistent with a linear increase (dashed red line) within the Poisson statistical uncertainty (grey band).

3.4.1 Precursors of short and long GRBs

Short GRBs. A notable difference is observed between short and long GRBs. While short GRBs constitute 14% of the analysed GRB sample, only 4 of the 333 ($\sim 1\%$) short GRBs are observed to have a precursor. These four bursts are: bn090510016, bn100827455, bn130919173, and bn141102536. No single short GRB in our sample has more than one precursor.

²⁹Comparing to published GRB precursor catalogues in the literature [290–295, 300], 139 out of the 217 GRBs with precursor emission were previously unidentified.

As will be shown in Fig. 3.14, GRB precursors are typically followed by a quiescent time that lasts a few tens of seconds. In contrast, the quiescent times of the four short GRBs ranges from 0.40 s to 1.18 s. We also note that the precursor duration of short GRBs is in each instance shorter than that of the prompt phase. Additional statistics would be required to draw more ironclad conclusions. However, based on the current selection, we observe that the time delay between the onset of the precursor and the prompt emission is smaller than the 1.74 s time gap between the gravitational waves and the gamma rays observed from GRB 170817 [10]. Such short times scales are also consistent with binary NS models that predict precursors due to NS crust cracking and/or magnetic interactions.

Long & bright GRBs. Another subcategory that has received special attention in the literature is that of bright and long GRBs. By definition, precursors are required to have a lower fluence than the prompt phase. If a burst's prompt emission is close to the sensitivity threshold of the detector, it can thus be argued that any precursor emission will be indistinguishable from the background. Including dim bursts in the analysis would therefore cause the true fraction of GRBs with precursors to be underestimated. On the other hand, if the prompt emission of a very dim burst has multiple peaks, the first peak(s) could falsely be identified as a precursor. To eliminate such effects, a number of analyses [293, 297, 299, 301] have restricted their GRB sample to long³⁰ and 'sufficiently bright' GRBs. These analyses report the highest numbers of GRBs with precursors, up to 20% [293], indicating that the intrinsic fraction of GRBs with precursors is likely underestimated when all GRBs are included.

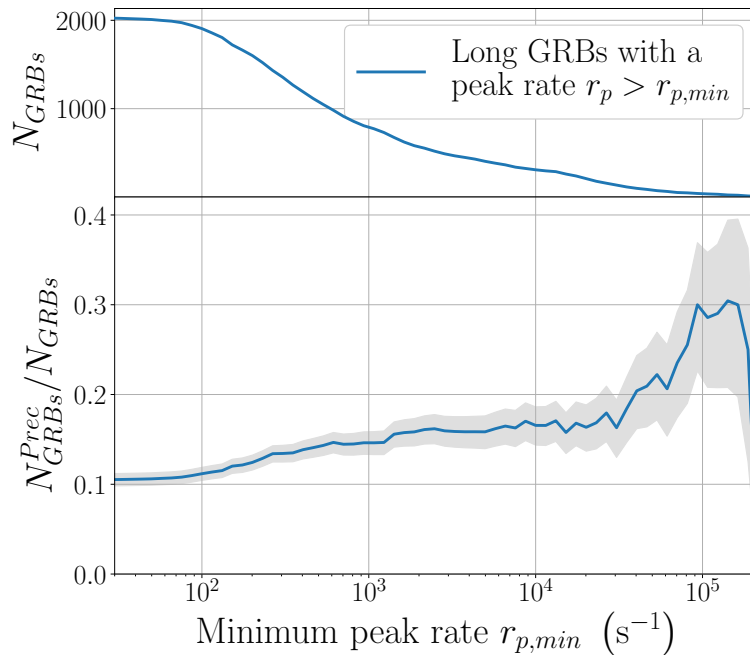


FIGURE 3.13: Top: Number of long GRBs whose peak rate exceeds the threshold value displayed on the x -axis. Bottom: fraction of those GRBs for which precursors are observed. When selecting increasingly bright bursts, we observe an increase in the fraction of GRBs with precursors. The shaded grey band shows the 1σ statistical uncertainty.

³⁰Short GRBs are generally also excluded due to their much lower precursor rate.

In our analysis sample, we studied the effect that including dim bursts has by imposing a lower threshold on the peak photon rate³¹. The top panel of Fig. 3.13 shows the number of bursts that have a peak photon rate larger than the value displayed on the x -axis. In the bottom panel, the fraction of those GRBs for which a precursor is observed is displayed. A clear increase initially occurs, which levels off around 16% once $r_{p,min} > 2 \cdot 10^3$ Hz. At peak rates in excess of $3 \cdot 10^4$ Hz, a second rise is observed. However, due to the rapidly decreasing number of increasingly bright bursts, this second rise is statistically insignificant. We thus find that the intrinsic fraction of long GRBs that has a precursor is likely closer to 16% than the initial estimate of 10% based on all long GRBs in our sample.

3.4.2 Quiescent time

Bimodal feature. A quantity of particular relevance to distinguish different emission models is the duration of the quiescent time between subsequent emission episodes. Figure 3.14 shows the distribution of all quiescent times identified in our analysis. These values are not corrected for redshift as redshift data is only available for $\sim 10\%$ of GRBs³². A bimodal feature³³ can be observed, with a cross-over between the two contributions around $\Delta t_Q \sim 1.4$ s. This suggests that there are two physical mechanisms contributing to the observed precursors. Performing a two-component Gaussian likelihood fit to the data, the peaks of the distribution are found to occur at (0.552 ± 0.059) s and (24.2 ± 1.2) s, with the first bump having a relative weight of $(11.1 \pm 2.6)\%$.

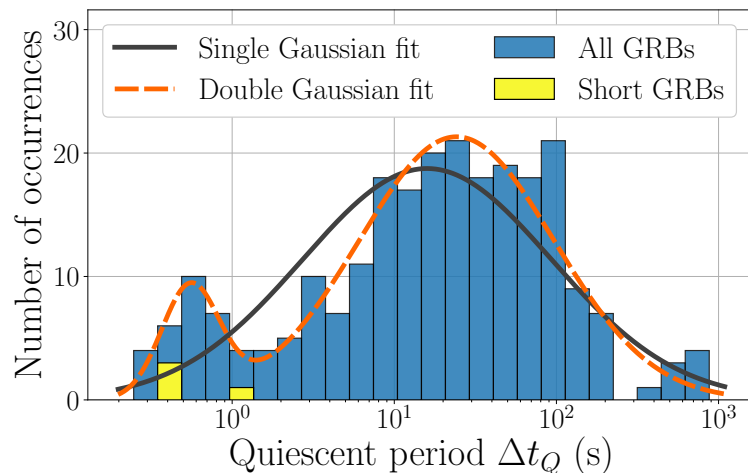


FIGURE 3.14: Distribution of the quiescent time between two subsequent emission episodes. The data is found to be well described by the sum of two Gaussian functions. The 4 short GRBs are indicated in yellow.

To test the goodness-of-fit, the likelihood value is determined to obtain the observed bin counts given the best fit parameters. A set of 10^6 Monte-Carlo (MC) trials were then performed, in which each trial consists of using Poisson statistics to randomly drawing 244 quiescent times from the fitted PDF. By calculating the binned-likelihood value of those trials, a test statistic (TS) distribution was constructed. Comparing the likelihood value of the actual data to the TS distribution results in a p -value of 0.36. It can thus be concluded

³¹The peak photon rate is defined as the maximal background subtracted rate in the combined BB light curve, normalised by the number of detectors that contributed.

³²The effect of redshift on the identified time intervals is discussed later on in this section.

³³An apparent third component shows up in the last three bins of Fig. 3.14. However, this contribution is most likely not physical, as the expected number of false positives is proportional to the width of the bin, thus linearly increasing from left to right on the logarithmic x -scale.

that the two-component distribution provides a good model for the data. As a reference, a single component Gaussian fit was also performed. Repeating the same procedure of MC trials, a p -value of only $8 \cdot 10^{-5}$ is obtained. The single component Gaussian model is thus shown to be incompatible with the data and can be rejected with a significance of 3.9σ .

Part of the leftmost component in Fig. 3.14 comes from the contribution of short GRBs. However, these can only account for $\sim 15\%$ of the observed excess. The remaining fraction thus corresponds to very short delay precursors to long GRBs. As a first step to ensuring that this is a physical component, it was verified that none of the five potential false precursors with deviating count ratios contribute to the first component. Secondly, these apparent short delay precursors could possibly correspond to dim bursts whose flux drops below the observable limit in between different peaks of the prompt phase. In this case, bursts with quiescent times below ~ 1.4 s are expected to be less bright than bursts with longer quiescent periods. Figure 3.15 illustrates that GRBs with short quiescent times are indeed less bright on average. It is therefore worthwhile to probe the effect of dim bursts on the bimodal feature by repeating the analysis using only bright, long bursts. Based on Fig. 3.13, a minimal peak rate of $3 \cdot 10^3$ Hz was imposed to ensure that only sufficiently bright GRBs are selected. Figure 3.16 shows the quiescent time distribution of these bright long bursts. A bimodal feature is still observed. The two Gaussians now peak at (0.54 ± 0.14) s and (31.6 ± 5.3) s, with the first bump having a weight of $(8.3 \pm 3.3)\%$. These results are thus consistent with the previously obtained best-fit parameters. Based on the goodness-of-fit, we find that the double component Gaussian distribution ($p = 0.57$) again performs better than the single-component Gaussian ($p = 0.076$) model. As expected, the disagreement between the data and single Gaussian fit is now less significant due to the smaller number of quiescent times leading to reduced statistics.

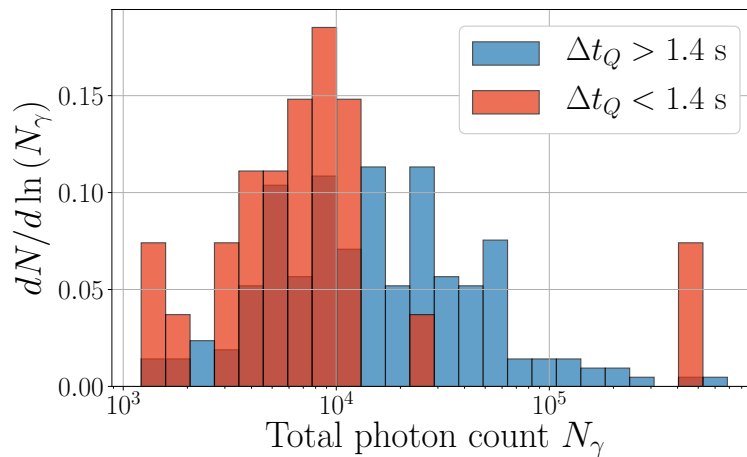


FIGURE 3.15: Distribution of the total photon counts for GRBs with short and long delay precursor. Both distributions are normalised such that their y -values sum to unity. Bursts for which the quiescent times is less than 1.4 s are observed to be less bright on average.

Physical origin. The bimodal feature in Fig. 3.14 might indicate that two physical mechanisms contribute to the observed precursors. Precursors that are followed by a quiescent time of tens to a few hundreds of seconds are predicted by models³⁴ in which a jet

³⁴The distribution in Fig. 3.14 shows the quiescent time as observed on Earth. No correction for redshift effects is applied, as redshift information is only available for $\sim 10\%$ of all GRBs. Models, in contrast, provide the quiescent time duration at the source. To offer a fair comparison, all observed quiescent times should thus be downscaled by an average factor ~ 2 when comparing to model predictions.

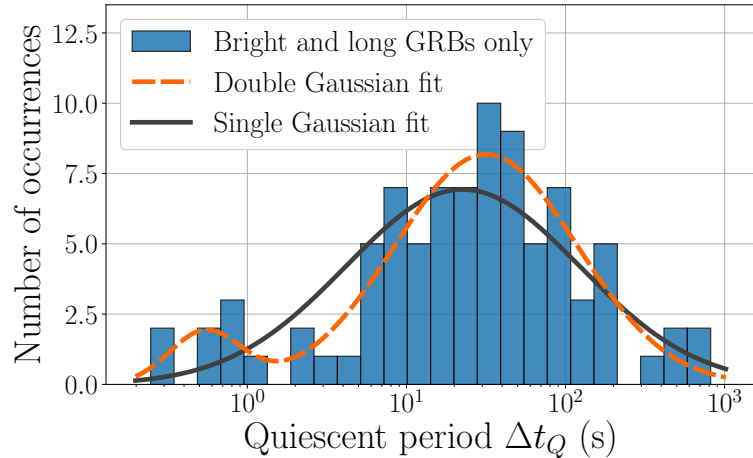


FIGURE 3.16: Distribution of the quiescent time when only including bright, long GRBs. While statistics are significantly reduced, a double component Gaussian fit is still preferred over a single Gaussian distribution.

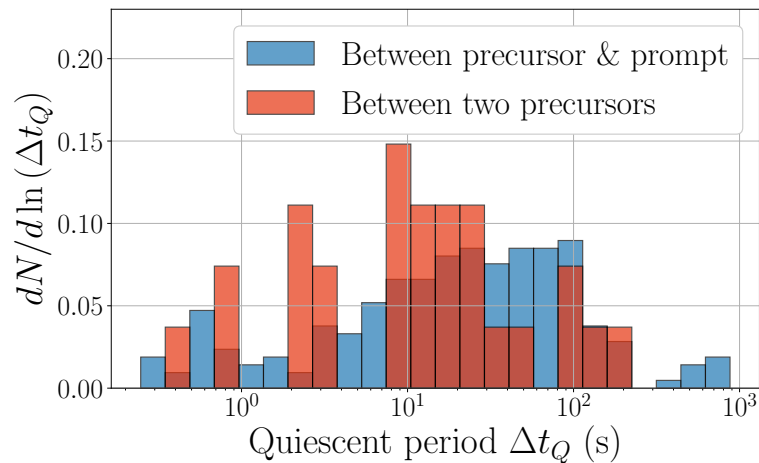


FIGURE 3.17: Distribution of the quiescent time Δt_Q between two precursors (red) and between a precursor and the prompt emission (blue). The normalization is taken such that the y-values sum to unity.

is launched multiple times. Short delay precursors of long GRBs, in contrast, are consistent with being due to photospheric or shock-breakout emission. Based on this reasoning, we predict that the short delay precursors should have an almost thermal energy spectrum. On the other hand, a non-thermal energy spectrum consistent with that of the prompt emission is expected for long delay precursors. An interesting follow-up analysis would thus be to perform spectral fits to the precursors identified by our analysis to verify this claim.

Precursor - prompt distinction. In previous studies, precursor emission episodes were generally found to exhibit the same spectral properties as the prompt emission [242, 290, 291, 294, 297]. In the case of long GRBs, this result points towards models in which the precursor and prompt emission are caused by different accretion episodes of the central engine [18, 296, 297]. In such models, there is thus no intrinsic physical difference between the precursor and prompt signal. Following this argument, the quiescent time between two subsequent precursor emission episodes is expected to follow the same distribution as that between the

precursor and prompt emission³⁵. Figure 3.17 shows a normalised histogram of the two distributions. A two-sample Kolmogorov-Smirnov test is applied to test the hypothesis that the two samples were sampled from the same underlying distribution. While the resulting p -value of 0.030 is not significant, it does indicate that there could potentially be a difference between the two samples.

3.4.3 Temporal correlations

Reservoir models. As previously mentioned in 2.1.3, a tension exists in the literature on whether there is a correlation between the duration of the quiescent time, Δt_Q , and that of the subsequent emission episode, Δt_{sub} . Two studies [297, 337] found a strong positive linear correlation, while two other studies [293, 359] reported the lack of any correlation. If precursors are caused by a reservoir model, in which energy is continually built up during the quiescent stage, a positive linear correlation would indeed be expected.

None of the above mentioned studies correct the durations for the redshift of the burst. In the study by Burlon et al. [297], however, it is remarked that redshift effects could artificially induce a positive correlation by simultaneously increasing both Δt_Q and Δt_{sub} by the same factor $z + 1$. As a result of the large precursor catalogue that we have constructed, our sample contains 22 bursts with a known redshift. As two of those bursts have two precursors, this results in a set of 24 quiescent times, shown in the left panel of Fig. 3.18. While significantly smaller than the full precursor sample, the selection of GRBs with a known distance thus provides us with sufficient statistics to determine the correlation coefficient of the redshift corrected sample. A Pearson correlation factor of 11% is obtained. To quantify the significance of this result, a TS distribution of correlation coefficients is constructed by taking random combinations of Δt_Q and Δt_{sub} . Comparing this distribution to the value of the unscrambled data, we obtain a p -value of 0.25. No significant linear correlation is thus observed between the duration of the quiescent time and that of the subsequent emission episode.

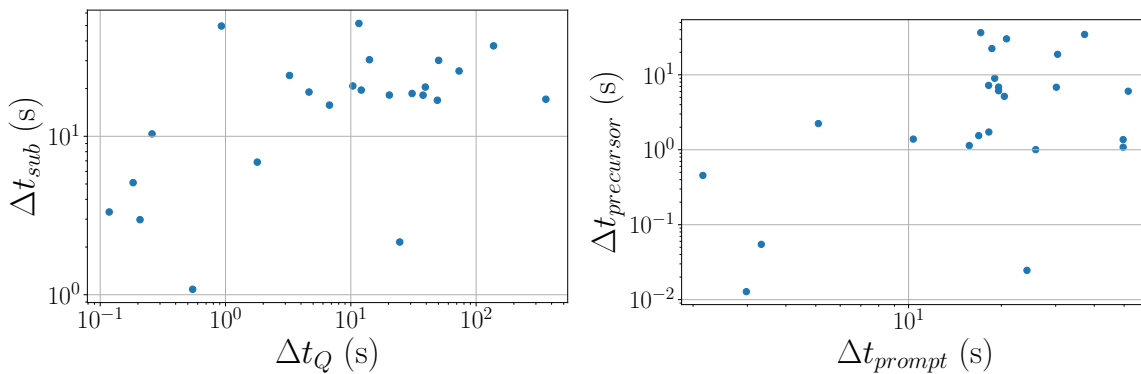


FIGURE 3.18: Left: Correlation between the duration of the quiescent time (x -axis) and that of the subsequent emission episode (y -axis). Right: Correlation between the duration of the prompt phase (x -axis) and that of the precursor (y -axis).

A second check is performed to test for the existence of non-linear but monotonic correlations. For this purpose, the Spearman's rank test is used. The rank correlation coefficient between the redshift corrected values of Δt_Q and Δt_{sub} corresponds to $\rho = 0.43$, resulting in a p -value of 0.034. We thus find a slight tension with the null hypothesis that the two samples are uncorrelated.

³⁵Considering only the 'last' precursor that occurs right before the prompt phase.

Signal durations. The analysis described above was repeated on the same sample of bursts, but using the redshift corrected values of precursor and prompt durations. For this sample, shown in the right panel of Fig. 3.18, a linear correlation coefficient of 15% is obtained, giving a p -value of 0.24. Applying the non-linear monotonic correlation test results in a Spearman rank coefficient $\rho = 0.29$, corresponding to a p -value of 0.17. No significant correlation is thus observed between the duration of the precursor and that of the prompt phase.

3.4.4 Imaging air Cherenkov telescope GRBs

Of the 2364 GRBs studied in our analysis, there are four bursts that have been detected by an Imaging Air Cherenkov Telescope (IACT). Remarkably, three out of those four GRBs show signs of precursor emission. These bursts, whose light curves are shown in Fig. 3.19, are: GRB 180720B, GRB 190114C, and GRB 190829A. A short description is given below on each of these GRBs. The IACT burst not preceded by a precursor, GRB 160821B, was only detected at a significance of 3σ by the MAGIC telescope. If the UHE gamma-ray signal of GRB 160821B corresponds to a physical excess, it is thus by far the least significant detection out of these four bursts.

GRB 180720B. As evident from the light curve in Fig. 3.19, GRB 180720B is an extremely bright burst. At the time of its detection, it ranked as the 7th brightest GRB observed by Fermi-GBM. All three of the IACT precursor bursts correspond to long GRBs. GRB 180720B was observed by Fermi-GBM to have a T90 duration of 48.9 s. Its redshift corresponds to 0.65 [101]. A single precursor is observed that has a duration of 10.0 s. Considering only the statistical Poisson uncertainty of the observed excess, the precursor has a significance of 12.9σ .

GRB 190114C. Like GRB 180720B, GRB 190114C is an extremely bright burst, coming in as the 4th brightest GRB recorded by Fermi-GBM. Its T90 duration and redshift correspond to 116 s and 0.42, respectively [91]. Our analysis identified two faint precursors. These precursors occurred 5.6 s and 2.9 s before the start of the prompt emission and lasted 1.9 s and 1.5 s, respectively. The background subtracted photon count of the first and second precursor bin have a significance of 6.5σ and 7.9σ , respectively. Given the closeness of this emission to the prompt phase, these precursors could potentially correspond to the photospheric component of the burst.

GRB 190829A. In terms of signal strength, GRB 190829A differs from the two previously discussed bursts by having a fairly average apparent brightness. At a redshift of only 0.079, it is nonetheless located extremely close to Earth. Given that the precursor itself has a fairly non-negligible photon fluence, it marks the start of the T90 interval, leading to a T90 duration of 59 s [102]. In terms of a statistical significance over the background, the count excess corresponds to $> 30\sigma$. The precursor emission lasts for 5.5 s and is first observed 48.0 s before the start of the prompt phase.

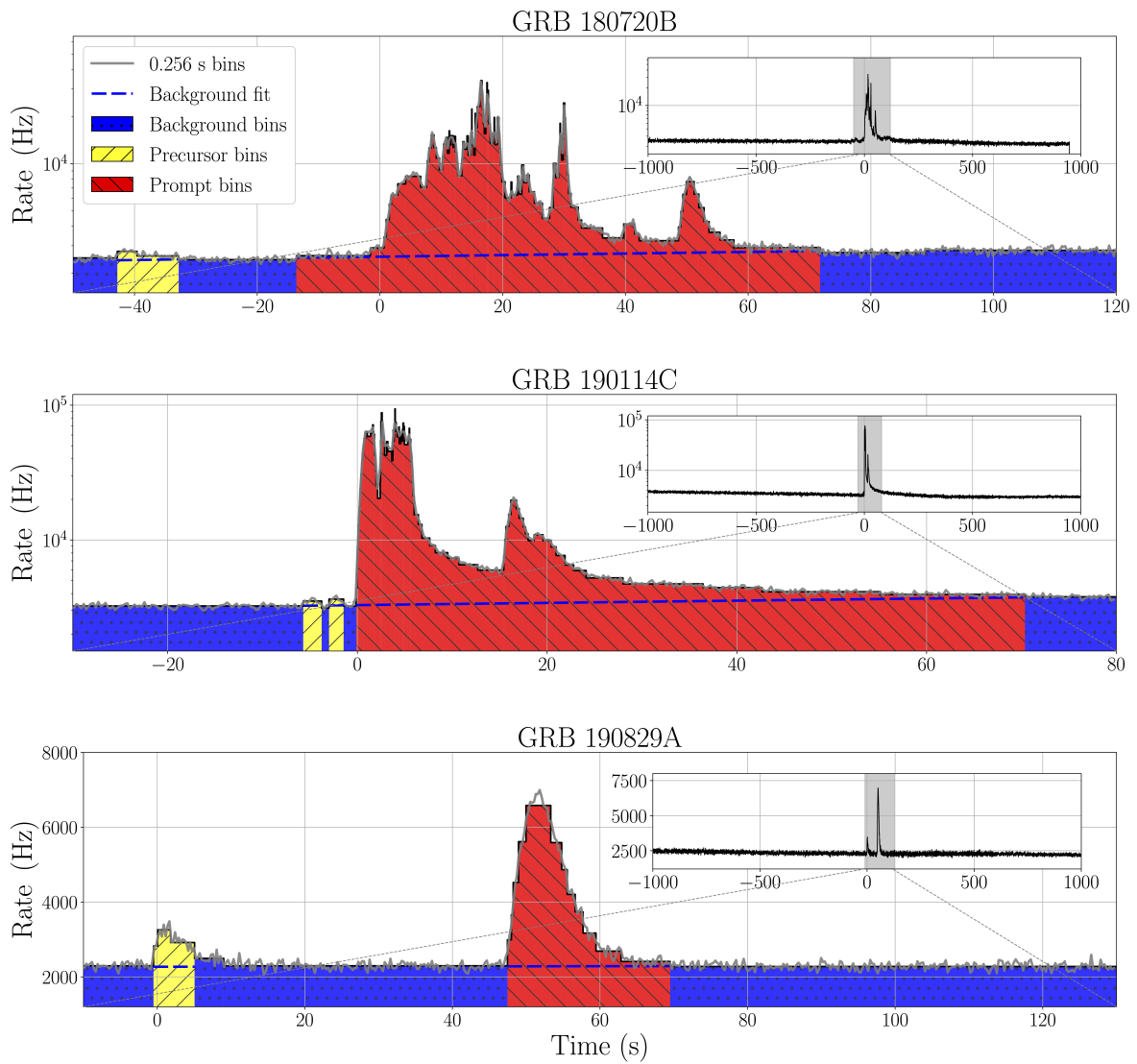


FIGURE 3.19: Light curves of the three bursts detected by an IACT for which our analysis identified precursor emission. The inset images on the top right display the full light curve, with the grey shaded band corresponding to the range of the x -axis.

Chapter 4

The IceCube neutrino observatory

Having constructed a catalogue of GRB precursors, the focus in this thesis now shifts from gamma-ray to neutrino astronomy. A short introduction will first be given on IceCube's pioneering role in the advent of neutrino astronomy, primarily highlighting studies related to GRB searches. The remainder of the chapter will then consist of two main parts. First, the journey of neutrinos will be described as they leave the source, undergo propagation effects, interact near the detector and produce an observable signal. In the second part, the opposite perspective will be taken. After providing a detailed description of the IceCube detector, it will be discussed how the observable event signatures can be used to reconstruct the original characteristics of the neutrinos and how signal neutrinos can be distinguished from background events. These components then provide the necessary ingredients to perform the neutrino-GRB coincidence study that is presented in the next chapter.

4.1 Neutrino astronomy with IceCube

The concept of performing astronomy using neutrinos has been around for several decades [360]. However, its practical realisation only came about in 2013, when the IceCube Collaboration presented the first evidence for the existence of a high-energy, cosmic neutrino flux [361]. Two of the reigning factors in proving the cosmic, extragalactic origin of these neutrinos are their hard energy spectrum and isotropic arrival direction.

Isotropy. Figure 4.1 shows a sky map in equatorial coordinates of the muon (anti-)neutrinos detected by IceCube. Slight clusterings of events can be observed in the figure. Without prior knowledge on the location of potential neutrino sources, these clusterings are consistent with being purely coincidental¹ [362, 363]. No excess is likewise seen along the direction of the galactic plane, denoted by the black line. This marks a strong difference with the gamma-ray sky (see Fig. 3.4), in which the Milky Way disk shows up as the brightest component.

Spectrum. As the arrival direction of cosmic neutrinos follows a uniform distribution on the sky, their flux can be parametrized solely as a function of energy. IceCube analyses [364–366] have found that a simple unbroken power law

$$\phi_{\nu+\bar{\nu}} = \frac{dN_{\nu+\bar{\nu}}}{dE dA dt d\Omega} = \Phi_0 \left(\frac{E}{100 \text{ TeV}} \right)^{-\gamma} \cdot 10^{-18} \text{ GeV}^{-1} \text{ cm}^{-2} \text{ s}^{-1} \text{ sr}^{-1}, \quad (4.1)$$

normalised per unit energy, surface, time, and steradian, generally provides the best fit. In this expression, the only free fit parameters are the normalisation constant, Φ_0 , and the

¹As will be discussed later on, $> 3\sigma$ excesses are observed when linking IceCube observations to known sources.

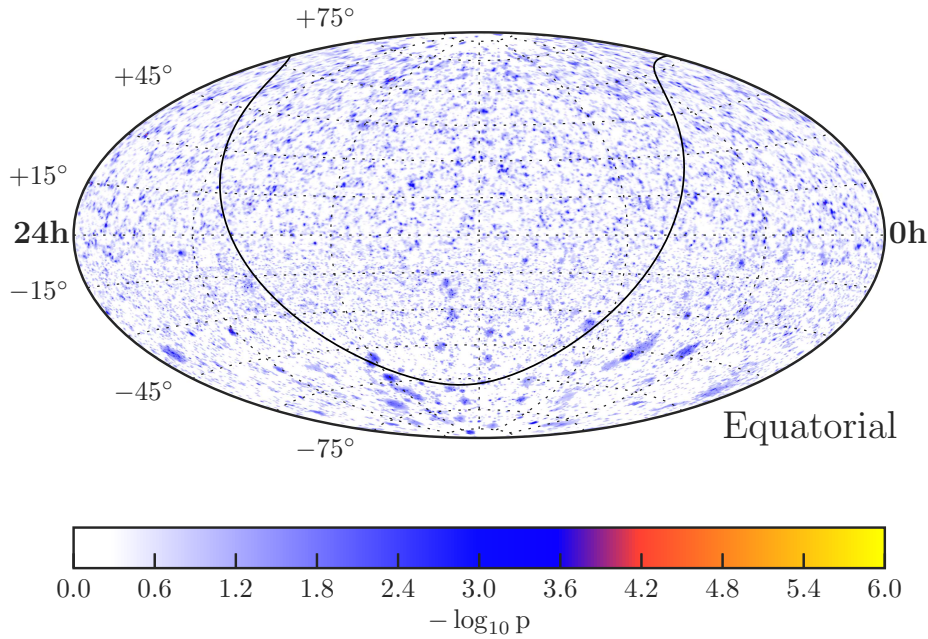


FIGURE 4.1: Sky map showing the significance of the astrophysical neutrino excess in terms of the p -value. The observed hotspots are consistent with a sampling drawn from a uniform distribution. From [363].

TABLE 4.1: The normalisation, Φ_0 , and spectral index, γ , are given for three IceCube analyses [364–366] that characterise the diffuse neutrino flux. For each search, the effective energy range and flavour of the neutrinos to which the analysis is sensitive are also shown.

Analysis	Φ_0	γ	Energy range	Flavours
HESE [364]	$2.12^{+0.49}_{-0.54}$	$2.87^{+0.21}_{-0.19}$	[16 TeV, 2.6PeV]	e, μ, τ
Cascade [365]	$1.57^{+0.23}_{-0.22}$	$2.48^{+0.08}_{-0.08}$	[40 TeV, 3.5PeV]	e, τ
Muon [366]	$1.44^{+0.25}_{-0.24}$	$2.28^{+0.08}_{-0.09}$	[12 TeV, 2.1PeV]	μ

spectral index, γ , of the flux. All normalisation constants of the neutrino flux in this thesis are given per flavour, but summed over both neutrinos and anti-neutrinos². The best-fit parameters to Eq. (4.1) are listed for three different IceCube analyses in Tab. 4.1 and are graphically shown in Fig. 4.2. As evident from Fig. 4.2, the parameter space allowed by the three analyses only narrowly overlaps within 2σ significance. If physical, such tension could indicate that the neutrino flux is not identical between all flavours. Alternatively, it might be that a single power law is too simple to describe the data, leading to differences in the best-fit spectral index depending on the energy range of the examined neutrino sample.

Identified sources. At the current stage, the origin of cosmic neutrinos is still largely unclear. Numerous IceCube analyses have been performed to look for potential correlations with known astrophysical sources. In general, potential sources can be categorised depending on whether they produce steady-state and/or transient emission. Sources such as blazars³ can be expected to alternate between steady and flaring states based on their

²Assuming an 1:1:1 flavour ratio at Earth, the total flux from all flavours thus has a normalisation $3 \cdot \Phi_0$.

³Blazars are active galaxies for which the jet of the supermassive black hole is pointed towards Earth.

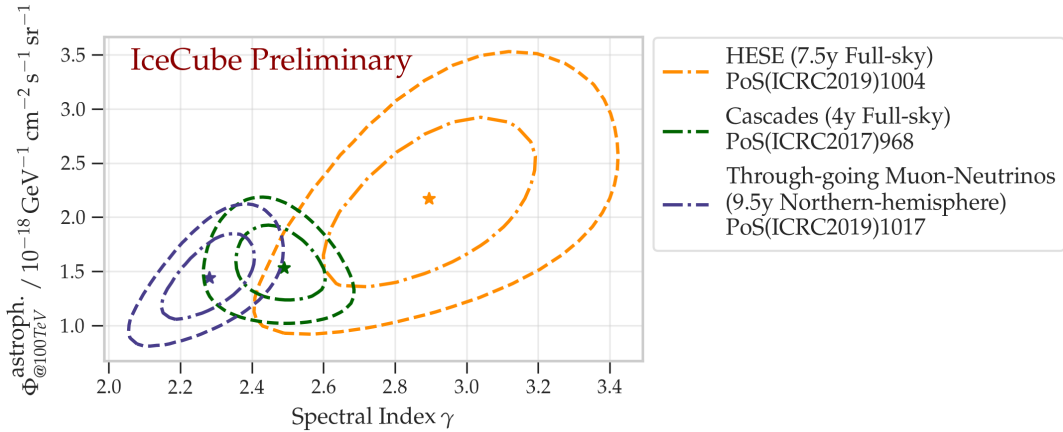


FIGURE 4.2: Spectral index (x) and normalisation (y) of the astrophysical neutrino flux, defined by Eq. (4.1). The results from three different IceCube analyses [364–366] are shown. Inner and outer rings correspond to the 68% and 95% confidence levels, respectively. From [366].

activity in gamma-rays. Flaring emission corresponds to periods in which the flux significantly increases, while at the same time showing fast temporal variability.

Because of their energetic nature, blazars have long been considered as potential sources of astrophysical neutrinos. Searches for coincidences between blazars revealed the observation of a high-energy (~ 290 TeV) neutrino in coincidence with a gamma-ray flare from the blazar TXS 0506+056 in September 2017. Based on the arrival time and direction of the neutrino, a chance coincidence of the two events could be ruled out at a significance of 3σ [367]. What made the event particularly interesting was that IceCube had already observed a neutrino flare from the direction of TXS 0506+056 in 2015. This flare, corresponding to an excess of (13 ± 5) events over a period of 158 days, had a significance of 3.5σ by itself⁴ [369].

So far, TXS 0506+056 remains the only cosmic neutrino source that has been identified at a significance in excess of 3σ . Other, more tentative correlations have been established in recent years. A study looking for steady-state emission from astrophysical point sources found a neutrino excess of 2.9σ from the direction of the starburst galaxy NGC 1068 [362]. Based on the spectral features of its gamma-ray flux, this galaxy had previously already been identified as a likely source of extragalactic cosmic rays [370]. Another potential correlation was observed between a Tidal Disruption Event (TDE), AT2019dsg, and a high-energy (~ 200 TeV) neutrino, detected by the Zwicky Transient Facility (ZTF) and IceCube, respectively. The significance for both events to be observed in temporal and spatial coincidence corresponds to 2.8σ [371]. Finally, a recent analysis which is currently under investigation by the IceCube Collaboration points to radio-bright blazars as potential sources [372]. Improved analyses using more data should in the near future be able to establish whether and to which extent blazars, starburst galaxies, and TDEs contribute to the cosmic neutrino flux.

Generic constraints on transients. As aptly voiced by Haim Harari [373]: “*Neutrino physics is largely an art of learning a great deal by observing nothing.*” While a few correlations have so far been identified, the vast majority of studies aiming to link cosmic neutrinos to astrophysical sources have produced a null result. A particular case in point are GRB searches. No analysis has been able to identify a significant neutrino excess from GRBs so far⁵. Most analyses therefore have resulted in upper limits on the potential contribution

⁴At the time of the neutrino flare, TXS 0506+056 was not flaring in gamma rays [368].

⁵A detailed account of previous searches for neutrinos from GRBs is given in Section 5.1

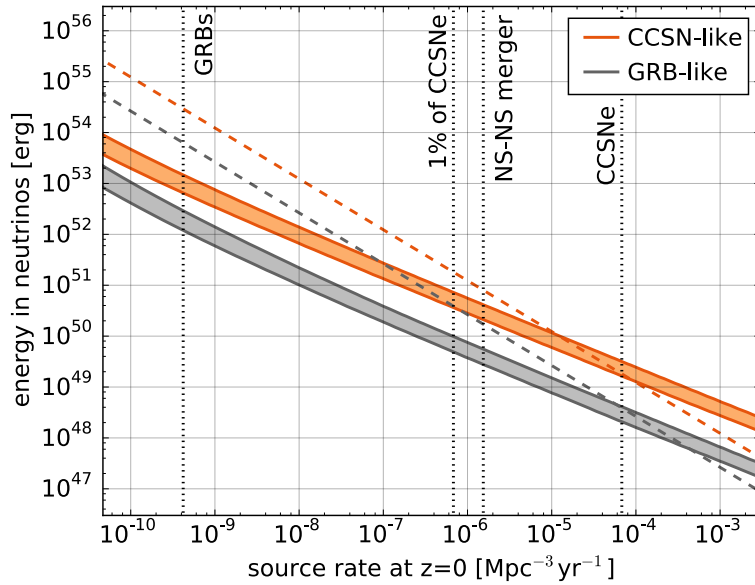


FIGURE 4.3: Constraints on the allowed energy and density of minute-scale transients like core-collapse SNe and GRBs. Dashed diagonal lines indicate the configuration that produces 100% of the cosmic (muon) neutrino flux. The parameter space above the coloured band has been excluded by multiplet constraints. The upper and lower line correspond to a signal spectrum of $E^{-2.13}$ and $E^{-2.5}$, respectively. From [376].

from GRBs to the cosmic neutrino flux.

Focusing on minute-scale transients like GRBs, a generic constraint can be placed on the median energy and density of sources based on multiplicity analyses. These limits are shown in Fig. 4.3. The parameter space above the full lines can be excluded at 90% confidence, as such sources would overpredict the number of multiplets, i.e. neutrino events that occur in close spatial and temporal coincidence⁶, observed by IceCube. One of the source classes considered by the analysis are transients that follow the redshift evolution and luminosity distribution of long GRBs. For such sources, the contribution to the cosmic neutrino flux can be constrained to 5% and 30% for an $E^{-2.5}$ and $E^{-2.13}$ signal spectrum, respectively [376].

Science output. Having primarily presented results from analyses that aim to link the cosmic neutrino flux to known astrophysical sources, it is worth noting that the science output of IceCube extends far beyond this topic. In terms of beyond the standard model physics, IceCube searches for neutrinos from the centre of the Earth [377], Sun [378], and Milky Way [379] have produced world leading constraints on the self-annihilation cross section of dark matter. Other, more exotic beyond the standard model analyses are also being performed, such as e.g. searches for magnetic monopoles [380]. Standard model particle physics analyses include studying the flavour ratio of atmospheric neutrinos to provide constraints on the neutrino oscillation parameters [381]. In addition to atmospheric neutrinos, the atmospheric muons can also be treated as a signal, effectively turning IceCube into a cosmic-ray observatory. As a result of its unique location at the geographical South

⁶For the analysis corresponding to Fig. 4.3, multiplets are taken to be IceCube events that occur within 100 s of one another, with a spatial separation smaller than 3.5° . Removing the temporal constraint, the same argument can be used to constrain the source density and luminosity of steady-state sources [374, 375].

Pole⁷, studying the muon component has allowed a precise determination of the spectra, composition, and anisotropy of cosmic rays in the Southern Hemisphere around the knee [382, 383]. Finally, a yet entirely different scientific domain in which IceCube has been able to contribute is the field of glaciology. A precise knowledge of the propagation of light in ice is required to correctly reconstruct observed events. A side-effect to continually improving the ice model is that IceCube has been able to provide unprecedented measurements of the inclination angle of the South Pole ice sheet. In addition, it was recently discovered that the attenuation of light in ice is anisotropic, providing new information on the crystal structure of ice itself [384].

The collaboration. The above mentioned results represent but a subjective selection of the science output by IceCube. A full description of the experiment will be given in Section 4.4. However, equally important are the people behind the experiment. In its current configuration, the IceCube Collaboration consists of over 300 people spread over 53 institutes in 13 countries. A full, up-to-date list of all collaborators can be accessed via <https://icecube.wisc.edu/collaboration/institutions>.

Other experiments. At the time of writing, IceCube has been the only experiment sufficiently sensitive to unambiguously identify the high-energy astrophysical neutrino flux⁸. As will be explained in Section 4.8, a common technique to filter background events is to look for up-going particles. Similar experiments in opposite hemispheres can thus provide complementary measurements. Two large scale neutrino telescopes that have been active in the Northern Hemisphere, ANTARES [386] and Baikal [387]. While these are significantly smaller than IceCube, combined analyses using data from e.g. IceCube and ANTARES (see e.g. [379]) have been performed to obtain optimal sensitivities. New, gigaton scale detectors are currently under construction in both the Mediterranean and in lake Baikal. These detectors, KM3NeT [388] and GVD⁹ [389], will serve as a next-generation version of the ANTARES and Baikal detector, respectively. Following 16 years of continuous operation, ANTARES was decommissioned in February 2022.

The most stringent limits on neutrinos from GRBs, other than those by IceCube, have been placed by ANTARES [390–395]. Other notable constraints include those by the Super-Kamiokande experiment in Japan [396]. Limits on GRB neutrinos by IceCube and ANTARES effectively go down to energies of ~ 10 GeV. Because of its much more densely instrumented detection volume, Super-Kamiokande was able to extend these limits down to energies of only a few MeV [396]. At the other end of the scale, IceCube limits on GRB neutrinos typically extend up to energies of a few PeV [257, 397]. Air shower and radio experiments have been able to constrain the cosmic neutrino flux at higher energies [398–402], though these effectively correspond to the $\gtrsim 10^{17}$ eV regime. To enable neutrino searches down to energies of 10^{16} eV, a radio neutrino observatory in Greenland (RNO-G) is currently under construction [113]. Once completed, RNO-G will offer an unprecedented sensitivity to both astrophysical and cosmogenic¹⁰ neutrinos with a sensitivity peaking in the EeV regime.

⁷Observatories at different declinations can monitor complimentary regions of the sky. IceCube is the only large-scale CR observatory in Antarctica.

⁸The ANTARES telescope can exclude the null cosmic flux assumption at a significance of 1.6σ [385].

⁹KM3NeT and GVD are an acronym for Cubic Kilometre Neutrino Telescope and Gigaton Volume Detector.

¹⁰Cosmogenic neutrinos are neutrinos that are produced by the interaction of ultra-high-energy cosmic rays with the cosmic microwave background and the extragalactic background light [403].

4.2 Neutrino propagation

Before proceeding to the actual detection of astrophysical neutrinos, it is worthwhile to first consider the effect that propagation has on their characteristics. While travelling from their sources to a detector on Earth, the neutrino flavour, flux, energy, and time delay with respect to simultaneously emitted gamma rays will be altered. It is therefore motivated below why our analysis can focus on muon neutrinos that arrive in temporal coincidence with the gamma-ray photons observed from GRBs.

Time delay. Oscillation experiments have shown that neutrinos have very small, yet non-zero masses. Currently, the most stringent upper limits come from cosmology. Data taken by the Planck mission has shown that the summed mass of the three mass eigenstates of neutrinos $\sum_{i=1}^3 m_i$ is smaller than 0.12 eV [404]. Model independent constraints unrelated to cosmology have been placed by precisely measuring the energy distribution of electrons in beta decay processes. Using this method, the KATRIN experiment placed an upper limit of 1.1 eV on the mass of the anti-electron neutrino¹¹ [405].

Neutrinos observed by IceCube can have energies between 10 MeV and several PeV. These neutrinos are thus highly relativistic, travelling close to the speed of light. Since GRBs are located at cosmological distances, any small differences in speed might nonetheless result in measurable time delays at Earth. Assuming a neutrino with mass m , energy E , and speed v that is emitted simultaneously with a photon, the time delay, Δt , measured by an observer on Earth corresponds to

$$\Delta t = (\Delta t)_\gamma \cdot \left[\frac{c}{v} - 1 \right], \quad (4.2)$$

where $(\Delta t)_\gamma$ is the propagation time of the photon. Setting $(\Delta t)_\gamma$ equal to the age of the Universe, $13.8 \cdot 10^9$ yr, to obtain a conservative estimate¹² and assuming a neutrino with a mass of $m_\nu = 1$ eV and energy $E_\nu = 100$ GeV, the time delay becomes

$$\Delta t \sim 2.2 \cdot 10^{-5} \left(\frac{m_\nu}{1 \text{ eV}} \right)^2 \left(\frac{100 \text{ GeV}}{E_\nu} \right)^2 \text{ s}. \quad (4.3)$$

From a practical standpoint and assuming standard-model physics, GRB neutrinos can thus be assumed to arrive without time delay from the observed photons. If neutrinos are not emitted simultaneously, but with a time difference $(\Delta t)_e$ in the source frame, then the time difference at Earth will correspond to $(1+z) \cdot (\Delta t)_e$ due to the expansion of the Universe.

Oscillations. Due to their mass, neutrino flavours can change during propagation. A free neutrino in vacuum will assume a mass eigenstate, $\nu_i \in \{\nu_1, \nu_2, \nu_3\}$, while during weak interactions, the neutrino assumes a flavour eigenstate, $\nu_i \in \{\nu_e, \nu_\mu, \nu_\tau\}$. Mass and flavour eigenstates are related to each other by

$$\begin{pmatrix} \nu_e \\ \nu_\mu \\ \nu_\tau \end{pmatrix} = U \cdot \begin{pmatrix} \nu_1 \\ \nu_2 \\ \nu_3 \end{pmatrix}, \quad (4.4)$$

where U is the PMNS matrix¹³, a 3×3 unitary matrix parametrized by three angles and three phases¹⁴ [406]. After travelling a distance L , the probability that a neutrino of initial

¹¹The anti-electron neutrino mass is taken to be the weighted linear combination of that of its mass eigenstates.

¹²For a GRB at redshift $z = 1$, $(\Delta t)_\gamma$ is roughly equal to half the age of the Universe.

¹³The PMNS matrix is named after four physicists: B. Pontecorvo, Z. Maki, M. Nakagawa and S. Sakata.

¹⁴Only one phase is required if neutrinos are not Majorana particles [406].

flavour α interacts under a flavour state β is

$$P(\nu_\alpha \rightarrow \nu_\beta, L) \approx \sum_{j,k} U_{\alpha k}^* U_{\beta k} U_{\alpha j} U_{\beta j}^* \exp\left(-i \frac{m_k^2 - m_j^2}{2E_\nu} L\right), \quad (4.5)$$

where the double summation runs over the three mass eigenstates. For cosmic neutrinos, the propagation distance is sufficiently large that oscillations effectively average out. The only term from Eq. (4.5) which remains is

$$P(\nu_\alpha \rightarrow \nu_\beta, L) \approx \delta_{\alpha\beta} - 2 \sum_{k>j} \Re \left[U_{\alpha k}^* U_{\beta k} U_{\alpha j} U_{\beta j}^* \right], \quad (4.6)$$

where $\delta_{\alpha\beta}$ is the Kronecker delta symbol and \Re denotes taking the real part of the expression.

Figure 4.4 shows the final fraction of muon neutrinos for all possible initial flavour ratios, obtained by substituting the mixing angles and phases of the ν fit project¹⁵ [407] in Eq. (4.6). For a beam that initially purely consists of electron, muon and tau neutrinos, the muonic content at Earth corresponds to¹⁶ 20.4%, 41.9%, and 37.8%, respectively. Regardless of the initial flavour ratio, a significant muon neutrino flux is thus expected. Since muon neutrinos offer the best directional reconstruction, as outlined in 4.3.3, this motivates why our analyses can be restricted to only a single neutrino flavour.

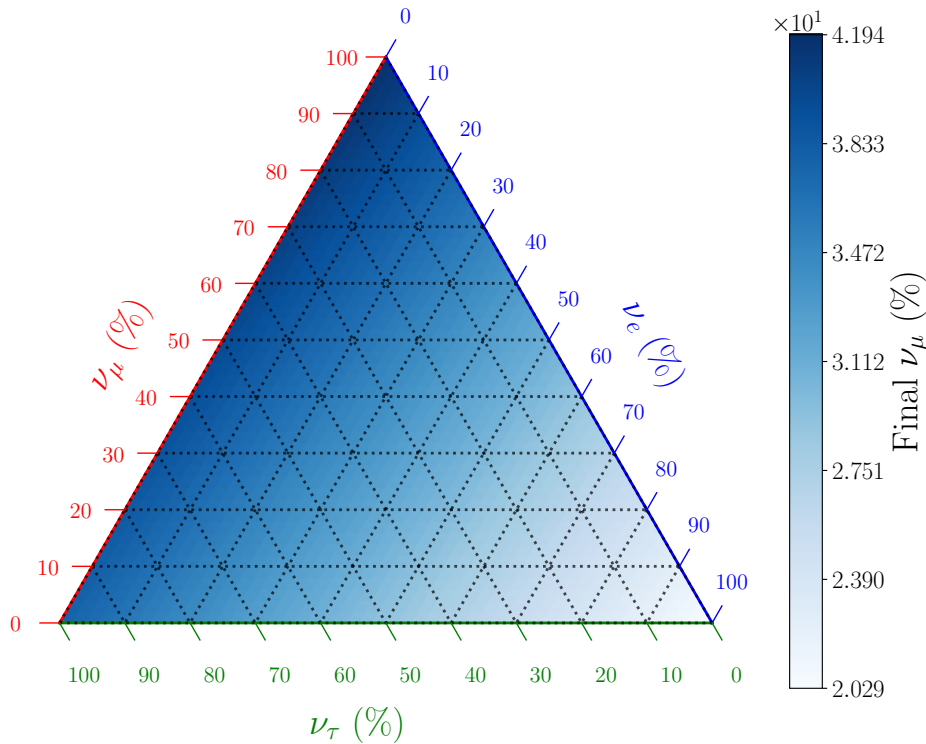


FIGURE 4.4: Ternary image in which the colour gradient shows the fraction of muon neutrinos after oscillations. The flavour ratio of the initial sample of neutrinos corresponds to the position in the triangle.

¹⁵www.nu-fit.org

¹⁶Uncertainties on mixing parameters are sufficiently small that they do not induce significant changes on the oscillation probabilities [408]. Calculating the oscillation probability for anti-neutrinos requires replacing the PMNS matrix U by its complex conjugate U^* . From Eq. (4.6) it follows that Fig. 4.4 thus looks identical for anti-neutrinos.

Redshift. A third consideration is that, analogous to photons, the energy of neutrinos decreases during their propagation due to the expansion of the Universe. A neutrino emitted at redshift z with energy E will arrive at Earth with an energy $E/(z+1)$. If the energy distribution of the neutrinos at the source follows a power-law distribution, as predicted by Fermi acceleration and assumed in this analysis, the resulting spectrum at Earth remains a power law with the same spectral index.

Earth absorption. When arriving at Earth, neutrinos that originate from the Northern Hemisphere will still have to propagate through the globe before they reach the IceCube detector. Particularly at high energies¹⁷, there is a non-negligible chance that the neutrinos will be absorbed by Earth. For instance, a 30 TeV neutrino coming from the North Pole has a $\sim 50\%$ probability of reaching the detector. The full distribution¹⁸ of the absorption probability as a function of the arrival direction and energy of the neutrino is shown in Fig. 4.5. As can be observed, Earth effectively becomes fully opaque to neutrinos with energies in excess of a few PeV.

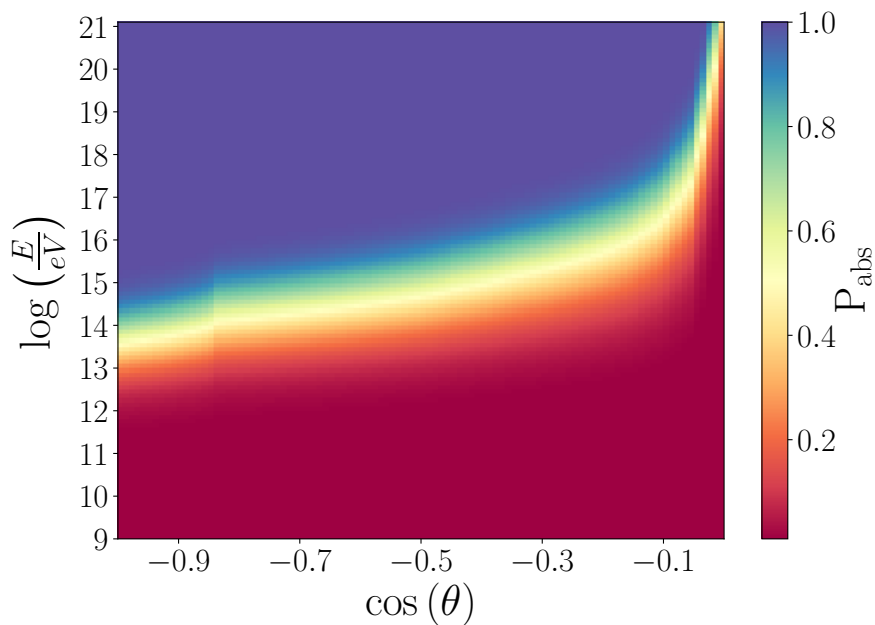


FIGURE 4.5: Probability that a neutrino is absorbed by Earth before it reaches the IceCube detector. The x - and y -axis indicate the zenith angle from which the neutrino is coming and its energy, respectively.

¹⁷As will be shown in the following section, 4.3.1, the interaction cross section increases with neutrino energy.

¹⁸For details on the calculation and assumptions that go into Fig. 4.5, we refer the reader to [409].

4.3 Detection principle

4.3.1 Neutrino cross sections

Interaction types. Neutrinos can interact with matter via two of the four fundamental forces, gravity and the weak interaction. Gravitational effects can be of importance near compact objects such as black holes, but do not offer practical prospects for neutrino detections. This leaves only the second force, the weak interaction, as a viable detection channel.

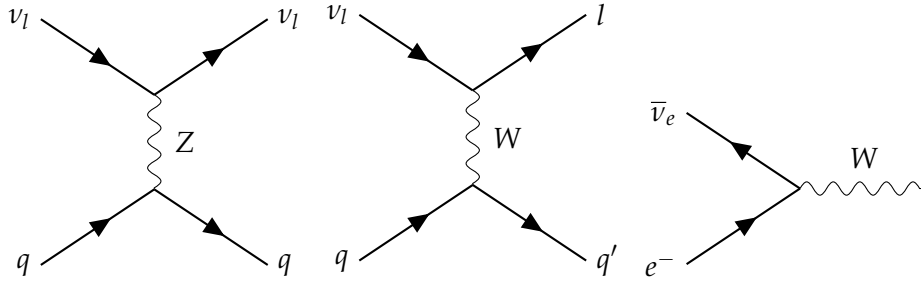


FIGURE 4.6: Leading order interactions between neutrinos and matter. Neutral-current (NC) and charged-current (CC) interactions are displayed on the left and in the middle, respectively. Glashow events are shown on the right.

Figure 4.6 shows the three dominant types of weak interactions that cosmic neutrinos can undergo. The first kind, indicated by the left diagram, are neutral-current (NC) interactions. In this process, a neutrino effectively scatters off a quark via the exchange of a Z-boson. A fraction y of the neutrino energy, defined as the inelasticity¹⁹, will be carried over to the quark. Figure 4.7 shows the mean value of the inelasticity as a function of neutrino energy. The actual value of y is determined by the differential cross section [411]:

$$\frac{d\sigma}{dy}(E, y) = a(E) + b(E) \cdot (1 - y)^2, \quad (4.7)$$

where a and b are energy dependent constants²⁰. Due to the chiral coupling constants, the inelasticity for anti-neutrinos slightly differs from that of neutrinos [411]. A second possibility is that the neutrino undergoes a charged-current (CC) interaction. In this process, shown in the middle panel of Fig. 4.6, the neutrino transitions into a lepton of the same flavour by the emission of a W-boson. Similar to NC interactions, the fraction of energy carried away by the lepton corresponds to $1 - y$, with the distribution of y again determined by Eq. (4.7) and Fig. 4.7. Figure 4.8 shows the evolution of the cross section as a function of energy using the data from [411–413]. On average, the cross section for CC interactions is a factor ~ 2 larger than that of NC interactions.

NC and CC interactions can occur for both neutrinos and anti-neutrinos of any flavour. The third interaction type, shown in the right panel of Fig. 4.6, is in contrast only open to anti-electron neutrinos. It corresponds to the resonant production of a W-boson at an energy of [414]:

$$E_{\bar{\nu}_e} = \frac{m_W^2}{2m_e} \approx 6.3 \text{ PeV}. \quad (4.8)$$

¹⁹The formal definition of inelasticity is $y \equiv \frac{p_2 \cdot q}{p_1 \cdot p_2}$, where p_1 , p_2 , and q are the four momentum of the neutrino, quark and Z-boson, respectively [410].

²⁰In Eq. (4.7), the value of $a(E)$ and $b(E)$ are fully determined by the constraint that $\int dy d\sigma/dy = 1$ for any given energy, and by the requirement that $\langle y(E) \rangle$ must satisfy the value shown in Fig. 4.7.

At the resonance peak, an anti-electron neutrino is ~ 200 times more likely to interact via the Glashow resonance than via CC or NC interactions. IceCube has so far identified a single event at the Glashow resonance [415].

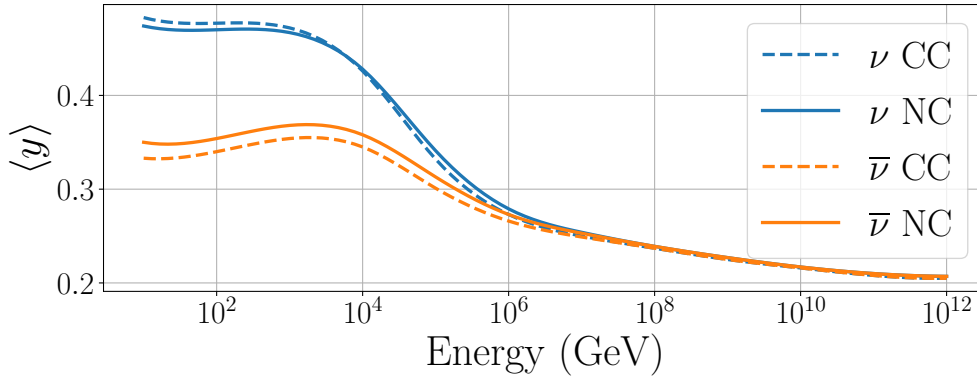


FIGURE 4.7: Mean value of the inelasticity parameter, i.e. the fraction of energy that the (anti-)neutrino transfers to the particle it interacts with in CC and NC interactions, as parametrised by [411].

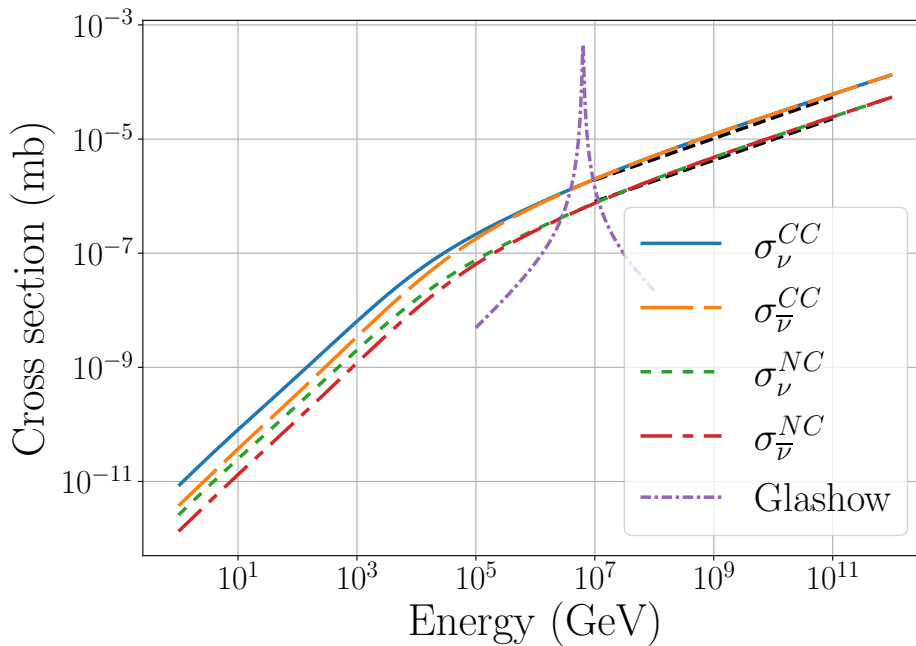


FIGURE 4.8: Cross section for neutrinos to interact with matter. The charged- and neutral-current cross section correspond to the interaction of a neutrino, independent of its flavour, with a nucleon and are derived from the CTEQ5 parametrisation [213]. Glashow interactions are events in which an anti-electron neutrino collides with an electron to form a W-boson [414].

Kinematic angles. Detailed knowledge of the neutrino cross section is required to allow an accurate reconstruction of the energy and flux of observed events. The cross section also comes into play when considering reconstructed directions. As mentioned previously, the analysis in this thesis focuses on a sample of muons induced by cosmic neutrinos. The relevant channel is thus that of muon (anti-)neutrinos undergoing a CC interaction. As a neutrino telescope only observes the muon, reconstructed directions by IceCube correspond to an estimate of the direction of the muon. However, the direction of the muon differs from that of the neutrino by the kinematic angle of the CC event. At a neutrino energy of 1 TeV,

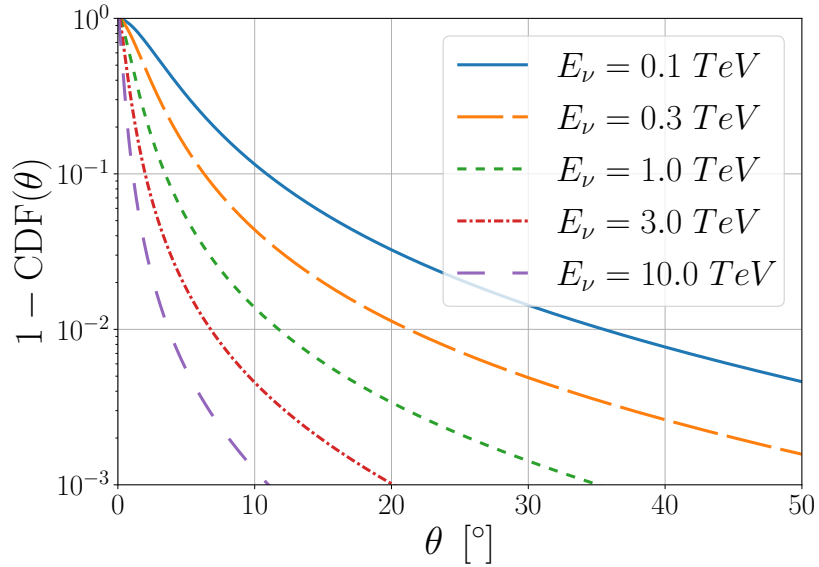


FIGURE 4.9: Cumulative distribution of the kinematic angle in the case of a CC interaction from a muon neutrino, as derived from Eq. (4.11) and the ‘NNPDF31_lo_as_0118’ parton distribution function.

the median kinematic angle, θ_m , corresponds to $\sim 1^\circ$. At higher energies, it decreases with the square root of the neutrino energy [109]:

$$\theta_m \sim 1^\circ \cdot \sqrt{\frac{\text{TeV}}{E_\nu}}. \quad (4.9)$$

Aside from the median angle, it is also worthwhile to consider the full distribution of the kinematic angle. An interaction between a muon (anti-)neutrino and a nucleon of mass m_N will result in a kinematic angle that corresponds to

$$\cos(\theta) = \frac{E_\mu - x \cdot y \cdot m_N - \frac{m_\mu^2}{2E_\nu}}{E_{\mu,kin}}, \quad (4.10)$$

where E_μ and $E_{\mu,kin}$ are the total and kinetic energy of the muon, respectively, x is the Björken- x ²¹, and y the inelasticity [410]. To determine the likelihood of obtaining a kinematic angle θ for a given neutrino energy E_ν , a set of parton distribution functions are required that determine the distribution of x and y . Figure 4.9 shows the cumulative distribution of θ , weighted by the double differential cross section

$$\frac{d\sigma_\nu}{dx dy} = G_F^2 \frac{m_N}{\pi} E_\nu \left(\frac{m_W^2}{m_W^2 - q^2} \right)^2 (\sum q + (1-y)^2 \cdot \sum \bar{q}), \quad (4.11)$$

where G_F is Fermi’s constant and the summation runs over the parton distribution function of quarks and anti-quark²² [410]. In this computation, the ‘NNPDF31_lo_as_0118’ parametrisation of the parton distribution functions, obtained from <https://lhapdf.hepforge.org>, was used. Figure 4.9 illustrates that despite the relatively low median angle, as given

²¹The Björken- x variable is defined as $x \equiv \frac{-q^2}{2 \cdot p_2 \cdot q}$, where p_2 and q are the four momentum of the quark and W-boson, respectively [410].

²²Equation (4.11) applies to neutrinos. For anti-neutrinos, the summations between quarks and anti-quarks should be interchanged.

in Eq. (4.9), kinematic angles of several tens of degrees are possible for neutrinos energies up to ~ 10 TeV due to the long tail of the distribution. This effect is naturally accounted for in IceCube analyses as kinematic angles are included in the simulations used to represent signal events.

4.3.2 Cherenkov radiation

What all types of above described neutrino interactions have in common is that they produce highly-relativistic particles. In a dielectric medium, such as the volume of ice in which the IceCube telescope is embedded, these particles will emit Cherenkov light [416, 417] if they are electrically charged and moving faster than the local speed of light, i.e.

$$v > \frac{c}{n}, \quad (4.12)$$

where n is the refractive index of the medium and v the speed of the particle. For IceCube, the index of refraction is roughly $n = 1.32$, varying by $\sim 2\%$ as a function of the density of the ice and the wavelength ($300 \text{ nm} \lesssim \lambda \lesssim 600 \text{ nm}$) of the light. A muon in ice will produce Cherenkov radiation as long as $E_{\mu,kin} \gtrsim 56 \text{ MeV}$. Photons generated via the Cherenkov mechanism are emitted perpendicular to the shock front, along a cone whose central axis corresponds to the propagation direction of the charged particle, as indicated in Fig. 4.10.

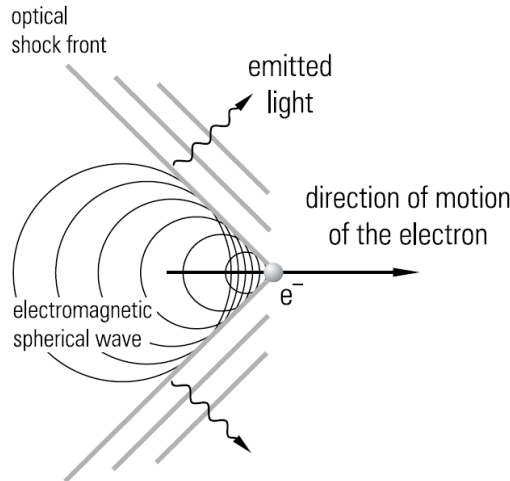


FIGURE 4.10: Illustration of the Cherenkov emission mechanism. From [418].

The angle ϑ at which the photons are emitted corresponds to

$$\cos(\vartheta) = \frac{c}{v \cdot n}. \quad (4.13)$$

For a highly relativistic ($v \sim c$) particle in ice, $\vartheta \sim 41^\circ$. Knowing in which direction the photons are travelling, it remains to specify the rate at which they are produced. Per unit distance and wavelength, this rate is given by the Frank-Tamm formula

$$\frac{d^2N}{d\lambda dx} = \frac{2\pi\alpha}{\lambda^2} \sin^2(\vartheta), \quad (4.14)$$

where N is the number of emitted photons, x the distance covered by the charged particle, λ the wavelength of the photons and $\alpha \sim 1/137$ the fine-structure constant [419]. Integrating

Eq. (4.14) over the wavelength range to which IceCube is sensitive²³, i.e. from 300 nm to 600 nm, it follows that a single particle will produce $\sim 3.3 \cdot 10^4$ photons per meter distance by the Cherenkov mechanism.

4.3.3 Interaction signatures

Cascades & tracks. IceCube is built to identify neutrinos by detecting the optical Cherenkov light that results from their interactions. Light patterns observed by IceCube can roughly be classified in two topologies, cascades and tracks. Cascades correspond to events in which a shower of charged particles is produced in a small (~ 10 m) volume [420]. Given that the typical distance that light can travel in ice is roughly an order of magnitude larger than the area in which it is produced, the light distribution from a cascade corresponds to an almost spherical blob. A visualisation of such an event from data is shown in the right panel of Fig. 4.11.

Tracks are events in which the charged particle can cover a distance significantly larger than the typical propagation length of light in ice. Muons are effectively the only particle that fit this bill. A cylindrical light distribution is thus produced that is centred on the propagation direction of the muon. Such events, illustrated in the left panel of Fig. 4.11, provide a much better directionality than the cascade topology. In contrast, cascades have the advantage that all light emitted by the event can be contained within the detector. Since the amount of photons in a cascade scales linearly with the deposited energy, cascades allow for an accurate estimation of the event energy.

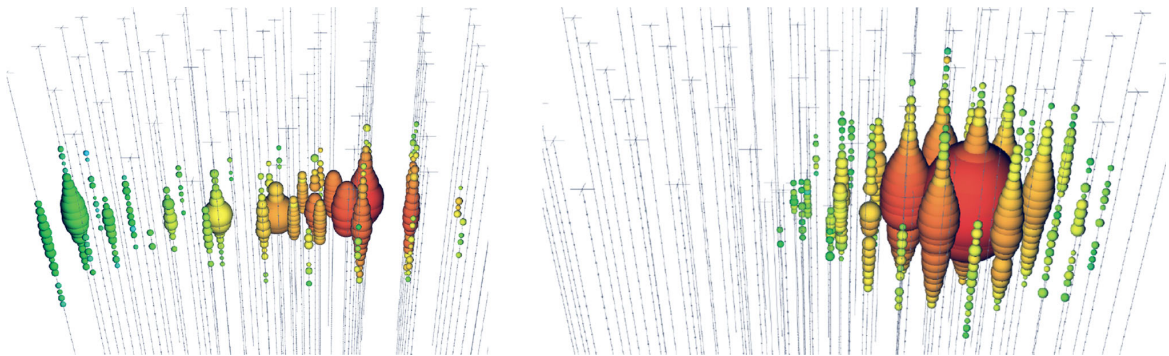


FIGURE 4.11: Event topologies of neutrino interactions in IceCube. Left: A high-energy muon moving through ice will produce a track-like trail of Cherenkov light. Right: Interactions that produce an electromagnetic or hadronic cascade lead to an almost spherical blob of Cherenkov light. Red and green spheres indicate light observed at early and late times, respectively, with the size of the sphere indicating the amount of light at that location. Both images have a scale of ~ 1 km. From [421].

Interaction topologies. Essentially all types of high-energy neutrinos induce a cascade when they interact with matter²⁴. In the case of NC events, the cascade is initially purely hadronic in nature, caused by the scattering of a neutrino on one of the quarks inside a proton or neutron. CC and Glashow interactions can have more involved event signatures. For Glashow events, the topology purely depends on the decay channel. 67% of the time, a

²³While the integral of Eq. (4.14) over all wavelengths can seem divergent at first sight, this is not the case due to the wavelength dependence of n . When the wavelength decreases below a critical value λ_t , n will become smaller than one, making the emission of Cherenkov photons at wavelengths shorter than λ_t impossible.

²⁴The only exception are Glashow events in which the W -boson decays to a muon, or to a tau that decays to a muon.

W-boson will decay hadronically into a quark/anti-quark pair [110]. Such events thus have the same intrinsic signature as NC interactions, though they appear at the characteristic energy of the Glashow resonance. The remaining 33% of the time, W-bosons will decay leptonically. Those decays are split evenly between the three flavours, resulting in three possible scenarios.

- *Electrons* will quickly lose all their energy by emitting bremsstrahlung, inducing an electromagnetic shower. Such particle cascades have a similar size as those of hadronic showers, typically of the order of 10 m, but produce a $\sim 15\%$ higher light yield²⁵ [420].
- *Muons* can travel several kilometres through ice before losing all their energy, producing a track-like signal of Cherenkov light.
- *Tau* particles will on average travel 50 m per unit PeV energy before they decay. 65% of decays will produce a hadronic shower, while the remaining 35% is roughly equally split between the decay into an electron or muon alongside two neutrinos [110].

The third possible interaction channel is that of CC interactions. These can essentially be viewed as a combination of a NC interaction, i.e. a hadronic cascade, with the above described production of an electron, muon, or tau, depending on the neutrino flavour. Of all possible interaction channels, muons produced in CC interactions offer the best signature for point source studies. In terms of detectable light yield, the cylindrical topology allows for a significantly better directional reconstruction than that of cascades. A second advantage is that muon neutrinos do not need to interact inside IceCube to produce a detectable signal. Because of their large propagation length (see below), muons can reach IceCube even if they are produced several kilometers away, significantly enhancing the detector's effective volume. For these two reasons, our analysis focuses on the selection of a sample of neutrino induced muon events. Given that cascades are thus not used in our analysis, the remainder of this section is devoted to describing the propagation and light emission of muons in ice.

Propagation distance. For a muon travelling through ice, the Bethe-Bloch formula can be approximated as

$$\frac{dE}{dx} = a + bE \quad , \quad (4.15)$$

where $a = -0.24 \text{ GeV m}^{-1}$ is due to ionization and $b = -3.3 \cdot 10^{-4} \text{ m}^{-1}$ is due to bremsstrahlung, pair production and nuclear interactions [110]. At energies above $\sim 1 \text{ TeV}$, the second term in Eq. (4.15) becomes dominant. This energy likewise marks the transition point from which the total light emission from stochastic processes starts to exceed the Cherenkov light produced by a bare muon²⁶. Below 1 TeV, the muon can be considered to be minimum ionizing.

Equation (4.15) can be solved using the method of variation of constants to find the total distance, x_t , that a neutrino of initial energy E_0 can travel

$$x_t = -\frac{1}{b} \ln \left(1 + \frac{b}{a} E_0 \right) \quad . \quad (4.16)$$

²⁵While electromagnetic and hadronic cascades have very similar signatures, they can in some cases be distinguished from one another via the presence of early muons. These muons, produced by pion decay in hadronic cascades, can outrun the Cherenkov wavefront of the main shower, leaving a detectable imprint [415].

²⁶Bare denotes that only radiation from the muon itself is considered. When the muon travels through ice, it will create low-energy ($< 500 \text{ MeV}$) secondary charged particles along its track, such as knocked off electrons, which can also produce Cherenkov radiation. The additional light from these secondary particles can be approximated as a continuous process and will create $\sim 10\%$ additional photons compared to the bare muon track [422].

To cover a distance larger than 1 km, roughly the scale of the IceCube detector, muons must have an initial energy larger than ~ 300 GeV.

4.3.4 Non-optical signals

Aside from Cherenkov light, high-energy neutrinos could potentially also be detected via other channels. Three alternative methods that have been explored in the literature and have been followed up in various experiments are here shortly discussed.

Skimming tau neutrinos. A detection channel restricted to tau neutrinos exists at energies exceeding $\sim 10^{17}$ eV. When such a neutrino skims a dense medium, e.g. by entering a mountain or hitting Earth at zenith angles close to 90° , the probability exists that a CC interaction produces a tau particles that is able to exit that medium again. The tau particle will subsequently decay in the atmosphere, leading to an air shower that is either up-going or coming from a mountain. Sensitivity to this channel primarily comes from large-scale cosmic-ray observatories, such as Telescope Array [399] and the Pierre Auger observatory [398]; balloon based radio experiments such as Anita [400]; and ground based radio observatories, such as the planned Giant Radio Array for Neutrino Detection (GRAND) [423].

Radio in dense media. Radio offers a promising alternative to observe neutrinos in the energy range from 10^{15} eV up to the highest energies. When a neutrino induced cascade develops in a dense dielectric medium, such as water or ice, a charge anisotropy will arise. This macroscopic charge distribution will radiate off coherent bremsstrahlung and coherent Cherenkov radiation when moving faster than the speed of light in the medium [424]. New telescopes, such as the RNO-G observatory [113], are currently being constructed to measure this Askaryan radio signal [113]. A downside to this technique is that cascades only emit radio waves along the Cherenkov cone, limiting the aperture of such a detector. An alternative detection principle has therefore been developed, in which neutrinos are detected by scattering a radio wave on the cascade and measuring the reflected signal. The Radio Echo Telescope for Cosmic Rays (RET-CR) is currently being developed to test this concept on cascades initiated by cosmic-ray interactions, as a pathfinder for future neutrino experiments [114, 425–427].

Acoustic. When a high-energy neutrino induces a cascade, the production of numerous energetic particles will locally heat the medium. If the acoustic and thermal properties of the material are suitable, this heating can lead to a pressure pulse that can be detected as a sound wave [428]. Acoustic detectors have been included in all major cosmic neutrino telescopes, including IceCube, ANTARES, KM3NeT and Baikal. However, these hydrophones primarily served to determine background levels and provide positional calibration data [429–432]. No neutrinos have so far been measured using acoustic signals, mainly due to the high-energy threshold ($E_\nu \gtrsim 1$ EeV) from which acoustic detections become viable.

4.4 Detector instrumentation

4.4.1 Detector configuration

In-ice array. In 1960, M. A. Markov suggested that by instrumenting a large natural body of water with optical sensors, it could be turned into a neutrino telescope [360]. Naturally, the idea applies to any dielectric medium that is transparent to optical light. IceCube [433] is currently the only operational realisation of this concept that uses ice as an interaction medium. As illustrated in Fig. 4.12, the primary component of the detector consists of 5160

Digital Optical Modules (DOMs, see 4.4.2), that are distributed equally over 86 vertical cables or ‘strings’. At the surface, strings are arranged along a hexagonal pattern with an inter-string distance of 125 m. DOMs are located at the lower part of the strings, between a depth²⁷ of 1450 m to 2450 m. The majority of strings carry 60 DOMs with a vertical spacing corresponding to 17 m. IceCube has an effective instrumented volume of 1 km³.

Between the 7 central strings of the hexagonal pattern are 8 DeepCore strings that reduce the horizontal string spacing to 72 m on average. On DeepCore strings, 50 DOMs are deployed between depths of 2100 m to 2450 m (7 m vertical spacing) and 10 DOMs are deployed above 2000 m with a 10 m vertical spacing. These upper DOMs act as a veto, enabling the rejection of down-going muons. As a result of the significantly reduced DOM spacing, DeepCore has a lower energy threshold of only a few hundred MeV, more than ten times smaller than that of the general IceCube array. This enhanced sensitivity to low-energy neutrinos is of particular relevance to oscillation and beyond the standard model studies.

Drilling. Deployment of the IceCube detector effectively started on January 22th, 2005, when the first hole was ‘drilled’ into the ice sheet. A heated drill bit was first used to melt the upper ~ 50 m layer of firn (compacted snow). Upon reaching the ice sheet, a 5 MW hot water drill was then deployed to create a 60 cm diameter²⁸ hole down to a depth of 2500 m. After a string had been lowered in the melted hole, the water freezes again, locking the DOMs in the ice sheet. Due to the extreme climate, drilling could only take place during the Austral summers. Construction of the IceCube detector finished on December 18th, 2010. Prior to its completion and in between its construction, IceCube was taking data in partial detector configurations. Due to the reduced number of strings and less well developed filter algorithms, partial configurations of the IceCube detector had a significantly lower effective area [375]. As a result, only data recorded by the fully-finished detector will be used in this thesis.

IceTop. Located at the top of the detector are 162 water Cherenkov tanks, allowing cosmic-ray air showers to be detected before they enter the ice layer. Tanks are grouped per two in 81 stations whose layout roughly follows that of the in-ice strings. Each tank encloses a cylindrical volume of ice, with a height and diameter of 0.9 m and 1.86 m, respectively. Enclosed in the clear ice are two DOMs, operating at different gains. To increase the light yield, tanks are internally lined with a reflective coating. IceTop is sensitive to cosmic-ray air showers in the PeV to EeV regime [433], corresponding to the knee of the cosmic-ray spectrum (see Fig. 1.6). No data from IceTop is used in this work.

ICL. All data collected by the in-ice and IceTop DOMs is sent via copper cables to the IceCube laboratory (ICL), which is located at the centre of the detector array. The ICL houses the necessary servers to perform triggering and apply an initial reconstruction and filtering of the data (for details, see 4.5). Subsequently, this data is sent to computing centres in the Northern Hemisphere for further processing. Because of the large amount of heat produced by the servers, the ICL is one of the few buildings at the South Pole that requires active cooling²⁹.

²⁷Results from the AMANDA experiment showed that air bubbles are present in the ice layer at depths down to 1400 m. These bubbles reduce to photon scattering length by more than an order of magnitude, to less than 2 m [434]. For this reason, all IceCube DOMs are deployed below 1400 m.

²⁸Holes are made significantly wider than the DOMs to ensure that sufficient time will be available to deploy the string after drilling and to limit the danger that a DOM gets stuck during deployment due to irregularities in the hole diameter.

²⁹The total power consumption of IceCube is ~ 53 kW, with DOMs on average consuming 5.7 W each [433].

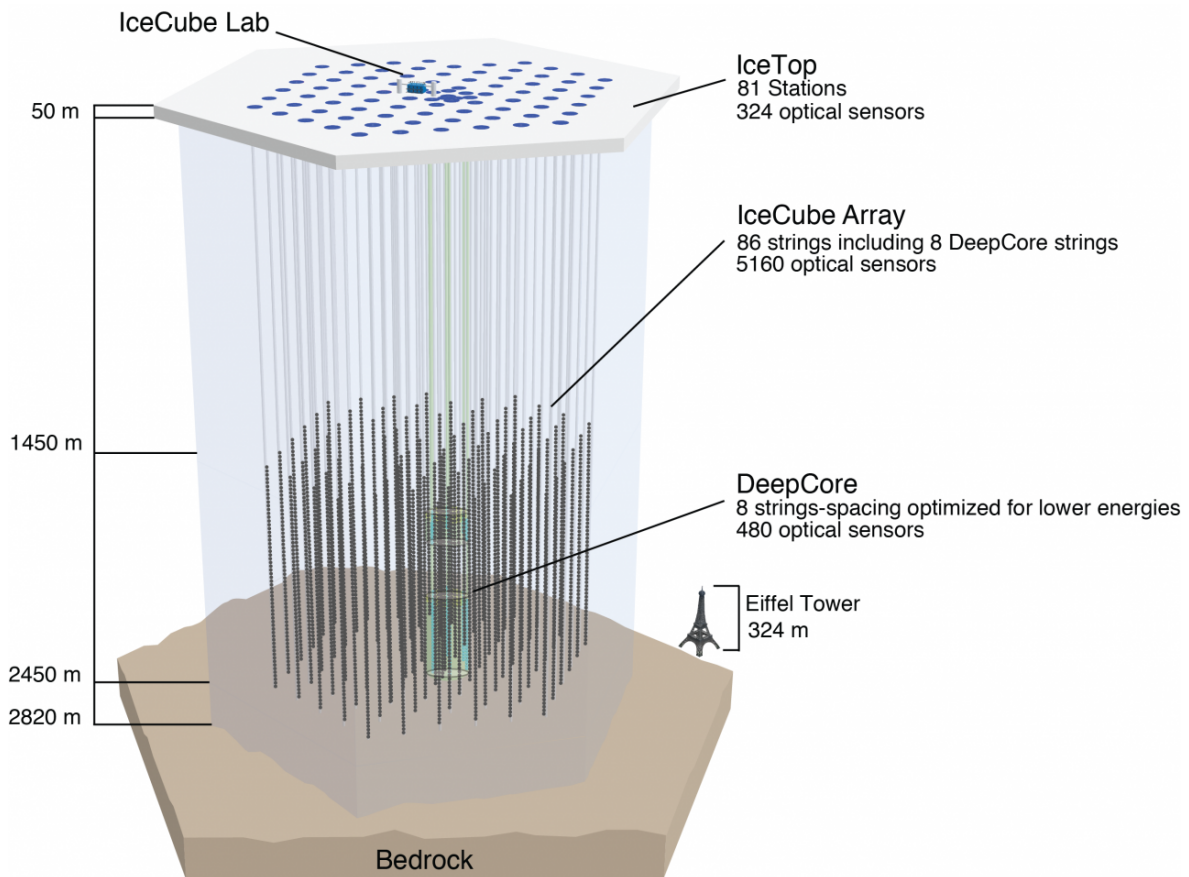


FIGURE 4.12: Visualisation of the IceCube experiment. To provide a scale of reference, the Eiffel tower is shown next to the detector. The dimensions of IceCube largely determine the energy range to which it is sensitive. Below ~ 100 GeV, DOMs are spaced too far apart to be effective at detecting the light produced by low-energy neutrino interactions. At very-high energies, above ~ 10 PeV, the neutrino flux becomes too low to induce sufficient numbers of interactions. From [433].

Upgrade & extension plans. Having described the geometry of the IceCube detector, it is worthwhile to note that an extension to the existing array is planned in the near future. Seven new strings will be added at the centre of the DeepCore array, using a vertical spacing between DOMs of only 3 m. This IceCube upgrade will significantly lower the energy threshold, allowing detailed oscillation studies and a determination of the neutrino mass hierarchy. Strings in the IceCube upgrade will carry several newly developed DOMs. In this manner, the IceCube upgrade will act as a test bed for the future IceCube-Gen2 detector [435]. IceCube-Gen2 will have an instrumented volume about eight times the size of IceCube and will thus enable characterising the neutrino flux up to energies of several tens of PeV. In addition, it will feature an even larger radio extension of about 500 km^2 to extend the energy threshold even further. Deployment of the IceCube upgrade is planned to take place during the 2022-2023 and 2023-2024 austral summers, if allowed for by COVID restrictions. Construction of IceCube-Gen2 will take place following the completion of the IceCube upgrade [433, 435].

4.4.2 Digital optical modules

Figure 4.13 shows an illustration of a digital optical module (DOM) of the IceCube detector. DOMs consist of 1.3 cm thick glass spheres that enclose a photo-multiplier tube (PMT) alongside the read-out electronics to digitize the PMT's signal, and LED flasher lights used for calibration purposes. The glass shell protects the DOM against extreme pressures, capable of withstanding 690 bar during freeze-in and 250 bar long-term [433].

PMTs. The photo-multiplier tubes used by IceCube are 10 stage R7081-02 PMTs constructed by Hamamatsu. PMTs in the in-ice array are operated at a gain of 10^7 and are sensitive to photons in the wavelength range from 300 nm to 600 nm. At a wavelength of 420 nm, PMTs reach their peak quantum efficiency³⁰ of 25% for photons travelling upwards, parallel to the PMT axis. DOMs that are part of the DeepCore array use an upgraded version of the same PMT, whose peak quantum efficiency goes up to 34% [433]. To shield the PMTs from the influence of Earth's magnetic field, they are enveloped by a mu-metal grid that lowers the internal magnetic field by a factor ~ 2.8 . As a result, the PMTs have a 5% to 10% higher light collection efficiency, resulting in an improved sensitivity and resolution [433].

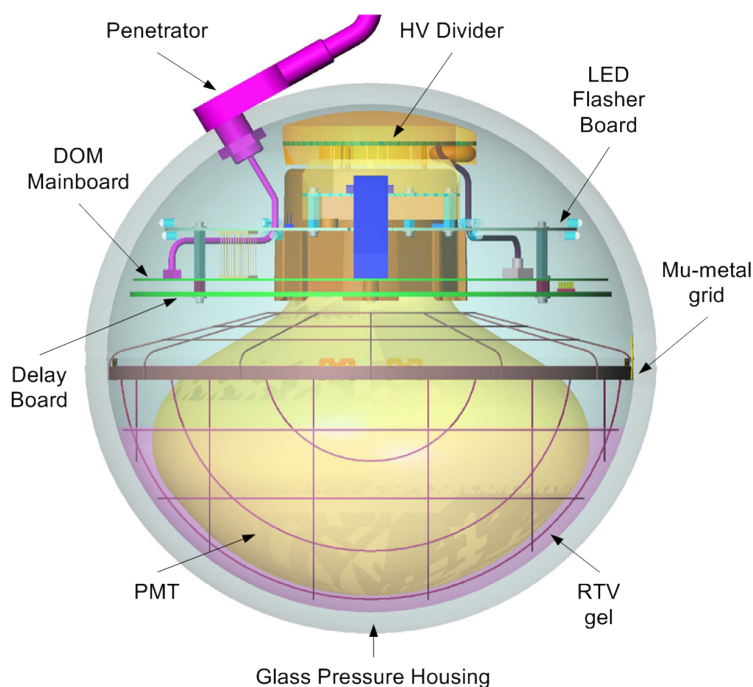


FIGURE 4.13: Graphic representation of the IceCube DOM. From [436].

Read-out. DOMs have two sets of systems in place to read out the signal from PMTs. A fast analogue-to-digital converter (fADC) continually samples the PMT waveform at a rate of 40 MHz. If a voltage is observed that exceeds 25% times that of single photo-electron, the DOM is said to be triggered. At this point, the fADC will store 256 samples, covering a $6.4 \mu\text{s}$ period. At the same time, one of the two analogue transient waveform digitizers (ATWDs) will be activated. This ATWD will save 128 samples at a rate of 300 MHz ³¹, corresponding to 427 ns. Like the fADC, the ATWDs digitize the signal using a 10-bit resolution. As the PMT signal is routed through a delay-board before it reaches the ATWD, the effective start

³⁰The quantum efficiency is defined as the probability that a photon incident on the PMT is converted into a photo-electron, thus producing an observable signal.

³¹Aside from offering a better timing precision, ATWDs also have a larger dynamic range than the fADC as they use 3 channels operating at different amplifier gains [433].

time of the ATWD data taking period is 75 ns prior to the trigger. After an activation, it will take 29 μs for the ATWD to digitize the signal before it can be triggered again. During this period, the second ATWD stands by in case a new trigger were to occur. Triggers observed when both ATWDs are processing data will generally be lost. During normal operations, the fractional dead time in which the fADC and both ATWDs are not taking data corresponds to $6.6 \cdot 10^{-5}$ for in-ice DOMs [433].

The majority of DOM triggers that occur in IceCube are due to dark noise³². To maximize the read-out availability of the data acquisition (DAQ) system³³ at the ICL, a system of local coincidence is used. A trigger is said to be a hard-local coincidence (HLC) hit if one of the (next-to) nearest neighbouring DOMs on the same string was also triggered within a 1 μs time window. Waveform data is only sent to the ICL for HLC hits. If no coincident hits were observed in the (next-to) neighbouring DOMs, only a limited data packet of twelve bytes is transmitted, containing a timestamp and coarse information about the fADC waveform around its peak voltage [436].

Timing. To ensure the precision time keeping of observed signals, each DOM contains a 20 MHz oscillator that runs with a certified relative uncertainty of less than 10^{-11} . Oscillators are synchronised once per second with the master clock at the ICL, ensuring that the DOMs are synchronised with respect to one another within 2 ns. The central master clock at the ICL is synchronised once per day by GPS satellite. During this period, it generally drifts by $\lesssim 10$ ns [436].

Reliability. DOMs have proven to be extremely reliable. At the time of writing, only 92 of the 5484 DOMs have either died completely or no longer have a functioning high voltage. 55 DOMs failed during or directly after deployment, prior to the commissioning of the detector. These failures are likely related to damaged housings and cables during freeze-in. Most of the remaining 37 DOMs failed during non-standard events, such as calibration runs, system upgrades, or power outages. Aside from failed DOMs, there are ~ 180 DOMs that have developed issues that affect their data-taking, but are still usable. For instance, some DOMs exhibit unstable rates or only have a single functioning ATWD chip leading to increased dead times [433].

4.5 Data acquisition software and triggering

4.5.1 Triggering

In the previous section, a description was given of how individual DOMs autonomously³⁴ trigger on the PMT output if a significant excess is observed. Trigger information and digitized waveforms of the 5484 DOMs is sent to 97 ‘DOMHub’ DAQ computers at the ICL, where the information is buffered. Once every second, the central DAQ triggering computer requests the timestamps of all newly recorded HLC hits. If the amalgamation of these hits satisfies one of the triggering conditions listed below, the data buffered in the DOMHubs is constructed into ‘events’ and saved to disk [438].

IceCube triggers generally require that several HLC hits are observed within a fixed time window, sometimes with an additional constraint on their relative spatial separation.

³²Dark noise hits are mostly due to radioactive decay and scintillation in the glass sphere and occur at an average rate of ~ 300 Hz per PMT [437].

³³Transmitting a digitised waveform to the ICL takes 75 ns [436].

³⁴Aside from the HLC input of the (next-to) neighbouring DOMs.

- *SMT*: One of the most used and simplest criteria is the simple multiplicity trigger (SMT). The SMT trigger requires that a total of N HLC hits are observed in a fixed time window. For regular in-ice DOMs, the criterion is that 8 HLC hits are required in a $5 \mu\text{s}$ period (SMT8). DeepCore and IceTop DOMs have their own distinct SMT trigger conditions [438].
- *String and volume*: Only 5 HLC hits are required if they occurred in 7 adjacent DOMs on the same string during a $1.5 \mu\text{s}$ window. Alternatively, if 4 HLC hits are observed that can be enveloped by a cylindrical volume with a height of 75 m, radius of 175 m and within $1 \mu\text{s}$, the detector will also trigger [438].
- *FRT*: 10 ms of data is read out every 5 minutes induced by the fixed-rate trigger (FRT). The FRT is used to provide samples of untriggered background data.

Combined, all trigger criteria, including those not listed here, lead to a read-out by the IceCube DAQ system at an average rate of 2.7 kHz. This results in a total DAQ data rate of ~ 1 TB per day [433]. Events analysed in this thesis make use of data that satisfies the SMT8 trigger, which triggers the detector at a rate of 2.1 kHz [438]. As outlined later on, more advanced filtering techniques are then applied that reduce the SMT8 data to the event sample used in the likelihood analysis in Chapter 5.

Event builder. The start time of the SMT8 trigger is set to the time at which the first of the 8 or more HLC hits was observed. Following the trigger start, a sliding $5 \mu\text{s}$ interval is moved forward in time until it no longer contains 8 HLC hits. The end of that time window then marks the end of the trigger interval. Having established the end of the trigger condition, all data buffered in the DOMHubs is requested by the DAQ system to build an ‘event’. To ensure a conservative data collection, events start $4 \mu\text{s}$ before to the start of the trigger interval and end $6 \mu\text{s}$ after it has finished. Events include data from the full detector, containing all non-HLC hits in addition to waveform data for HLC hits.

HitSpool. Raw data from the DOMs is continually being ring-buffered by the DOMHubs. Full raw waveforms and non-HLC hits remain available for up to 8 hours [438]. This ‘hit-spooling’ ensures that IceCube data can be manually stored if an interesting astrophysical transient is observed, such as a nearby supernova explosion.

Up-time. IceCube is able to achieve an uptime, defined as the fraction of time during which the detector is taking data, in excess of 99%. However, sometimes the detector will be taking data in partial configurations due to e.g. a failure in one of the string read-out systems. Over the past years, a clean uptime of $\sim 97\%$ has consistently been achieved, corresponding to the fraction of time for which analysis-ready is available. Minimizing the time during which the detector is not taking data was one of the design goals of IceCube, to ensure that the detector is operating when rare astrophysical transients occur [433].

4.5.2 Pulse series construction

Waveform reconstruction. Given a single recorded event, the first step in the reconstruction process is to deconvolve the waveforms captured by the fADC and ATWDs into a set of incident photons. To start, the baseline or pedestal voltage at the fADC and ATWDs is determined based on measurements taken once every 0.83 s in the absence of any signals [433]. This baseline is then corrected for by subtracting it from the observed voltage. Baseline corrections are performed by the ‘WaveCalibrator’ algorithm [439], which also corrects for other artificial features introduced by the read-out electronics. As the response of the read-out electronics has a known transfer function, the calibration inversion is a well-behaved process provided that the waveform did not exceed the dynamic range of the digitizer.

Calibrated waveforms are then deconvolved using the ‘WaveDeform’ algorithm [439]. WaveDeform starts by fitting the template of a single photo-electron to the observed waveform. In an iterative process, the next steps will then perform fits using the sum of two, three, etc. templates, until a point is reached at which adding additional pulses no longer sufficiently reduces the square error of the fit. As four channels are typically available, one from the fADC and three gain channels from the ATWD, the waveform is optimised to fit all four channels simultaneously. To avoid negative pulse amplitudes, a non-negative least-squares algorithm (in particular, the Lawson-Hanson method [440]) is used. Finally, a correction is applied to the reconstructed times of the pulses to account for the time it took for the pulse to propagate through the PMT and the delay board [433].

Pulse cleaning. Not all reconstructed photo-electrons are related to charged particles moving through the ice. DOMs observe an average dark noise rate of ~ 300 Hz [437]. These hits are primarily induced by radioactive decay processes and scintillation in the DOM’s glass sphere. Another type of background hits occurs following events in which a large number of photo-electrons were produced. Remnant gas in the PMT will be ionised by the stream of accelerated electrons in between the dynodes. The positively charged ions thus produced will be accelerated towards the photo-cathode and can liberate an electron upon impact. Signals related to these electrons are called afterpulses. They are a common feature in PMTs. In IceCube, afterpulses produce signals on timescales of 300 ns to 11 μ s after the start of the event [437].

To remove isolated hits that are likely unrelated to the physical event, a pulse cleaning algorithm called ‘seededRT’ is applied. As a starting point, the collection of all HLC is used. Any non-HLC hit is then added to the collection if it occurred within 150 m and 1 μ s of one of the already accepted hits. This procedure is then repeated two more times.

In this analysis, only muon induced events will be used. Given that muons can traverse the detector in ~ 3 μ s, a time cut can be imposed. By moving a 6 μ s sliding time window over the event, the interval is identified that contains the largest number of cleaned hits. All hits outside this time window are then removed. The input to the reconstruction algorithms described below corresponds to the cleaned hits within the selected 6 μ s time windows [441].

4.6 Event reconstruction

4.6.1 Processing and filtering

PnF. At the South Pole, all cleaned hits get processed in real-time by the processing and filtering (PnF) system. PnF checks the output and trigger rates of DOMs to verify that the detector is running in a stable manner. In addition, a number of data quality checks are performed. The main job of the PnF system, aside from monitoring the detector, is to filter events in real-time to reduce the data stream to a limit that is within the available satellite bandwidth (~ 100 GB/day [433]) and to enable online analyses.

Online filters. Filter algorithms that run at the South Pole are updated once per year. Generally, there are about 25 filter algorithms that run online, selecting $\sim 15\%$ of the triggered events [433]. For analyses of astrophysical point sources, the most used filter algorithm is the ‘muon filter’, which aims at identifying track-like events produced by muons passing through the detector. The algorithm proceeds by first performing a Linefit³⁵ to estimate the propagation direction of the particle, followed by a single photo-electron (SPE) fit³⁵ that uses the Linefit direction as its seed. Denoting the best-fit zenith angle of the SPE

³⁵A detailed description of the directional reconstruction algorithms is given in 4.6.2.

method as θ and its log likelihood value as \mathcal{L} , the filter criteria can be written as:

$$\frac{\mathcal{L}}{N_d - 3} \leq 8.7 \quad \text{for } -1 < \cos(\theta) \leq 0.2, \quad (4.17)$$

$$\log_{10}(Q_{tot}) > 3.9 \cdot \cos(\theta) + 0.65 \quad \text{for } 0.2 < \cos(\theta) \leq 0.5, \quad (4.18)$$

$$\log_{10}(Q_{tot}) > 0.6 \cdot \cos(\theta) + 0.65 \quad \text{for } 0.5 < \cos(\theta) \leq 1, \quad (4.19)$$

where N_d is the number of hit DOMs and Q_{tot} the total photo-electron charge of the event [441]. As the degrees of freedom in the SPE-fit corresponds to 5, its reduced log-likelihood is $\mathcal{L}/(N_d - 5)$. However, the ability of the reduced log-likelihood to identify well-reconstructed events varies with the event energy. Eq. (4.17) therefore uses a modified reduced log-likelihood that includes a factor $N_d - 3$ in the denominator, as this has been shown to offer a more consistent performance over the considered energy range [441, 442].

For up-going particles, the criterion in Eq. (4.17) aims at ensuring that only well-reconstructed events are included. For down-going events, the vast majority of detected particles will be atmospheric muons. Since the atmospheric background flux has a much steeper decline, $dN/dE \propto E^{-3.7}$, than the expected astrophysical flux, $dN/dE \propto E^{-2}$, a charge cut is imposed to select only the most energetic events. Using these criteria, the muon filter reduces the SMT8 trigger rate of 2.1 kHz down to 40 Hz [441]. The only online filter on which our analysis relies is the muon filter. Other online selections are e.g., the ‘high-charge filter’, which selects the events in which the total photo-electron count exceeds 10^3 , and the ‘shower filter’, which aims at identifying cascade type events [433].

4.6.2 Directional reconstruction

Following the initial selection made by the muon filter, reconstruction algorithms are applied to characterize the properties of the selected events. To start, algorithms that reconstruct the muon direction will be discussed. Three different methods will be presented, each increasing in complexity and computational cost. Inexpensive methods will first be applied to obtain a crude estimate of the muon’s direction, which recursively will be used as a seed for the next algorithm. All methods assume that the muon propagates through the full detector. For particularly interesting events, the most advanced algorithms (e.g. Millipede [439]) are applied, which can also fit for tracks that start inside the detector. However, as these methods are too computationally expensive, they cannot be applied to events on a systematic basis and will therefore not be discussed here.

Linefit. One of the most straightforward methods to fit the muon direction is to apply a χ^2 -fit that minimizes

$$\chi^2 = \sum_{i=1}^{N_d} \|\vec{r}_0 + t_i \cdot \vec{v} - \vec{x}_i\|^2. \quad (4.20)$$

In this expression, the summation runs over all hits, with \vec{x}_i and t_i denoting the position and the time of the hits, respectively. The fit for quantities are the velocity of the muon, \vec{v} , and an anchor point along the muon track, \vec{r}_0 . Linefit thus minimises the sum of the square distances between hits and the location of the muon. This fit implicitly assumes a model in which the muon is accompanied by a plane wave of light, travelling perpendicular to the muon propagation direction. While this is not the correct physical model, it has the

advantage that Eq. (4.20) has an analytic solution for the muon velocity³⁶

$$\vec{v} = \frac{\langle t_i \vec{x}_i \rangle - \langle t_i \rangle \langle \vec{x}_i \rangle}{\langle t_i^2 \rangle - \langle t_i \rangle^2}, \quad (4.21)$$

where the angle brackets denote averaging over all hits. To improve its accuracy, the Linefit algorithm used in IceCube differs from the standard χ^2 -method described here by applying additional hit cleaning and by replacing the square in Eq. (4.20) by a Huber loss function [443]. While these modifications lower the speed of the algorithm by a factor ~ 6 , it remains fast enough to be run in real-time at the South Pole and has been shown to significantly improve the performance [444].

SPE. The single photo-electron (SPE) fit is the next step in the IceCube chain of directional reconstruction algorithms. It performs a likelihood fit to the first hit observed by every DOM, disregarding any hits that occurred at a later time. Such an approach is justified by the reasoning that photons can be scattered and absorbed by impurities within the ice. In particular, scattering can lead photons to go on a random walk, arriving at DOMs significantly later than if they had travelled a straight path. By only considering the first hit observed by every DOM, the likelihood is thus minimized that these hits are related to scattered photons.

A significant improvement with respect to Linefit is that the SPE algorithm will correctly account for the expected time delay of the observed hits. Assuming that a hit is produced by an unscattered photon, the expected time of the hit is given by

$$t_{e,i} = t_0 + \frac{\vec{v} \cdot (\vec{x}_i - \vec{r}_0) + d \cdot \tan(\theta_c)}{c}, \quad (4.22)$$

with all variables defined in Fig. 4.14. Residual hit times, $t_{r,i}$, are defined as the time difference between the time at which a hit was observed, t_i , and the time at which the Cherenkov wavefront would have arrived at the DOM, $t_{e,i}$, i.e. $t_{r,i} \equiv t_i - t_{e,i}$. The SPE algorithm has 5 free parameters, corresponding to an anchor point along the muon track, \vec{r}_0 , at an arbitrary time t_0 and the direction that the muon is travelling in, given in the spherical coordinates θ and ϕ . As the algorithm is essentially only applied to highly-relativistic muons, the speed of the muon is assumed to be c . Calibration measurements by the Baikal experiment showed that good agreement could be obtained by defining the likelihood as

$$\mathcal{L} = \prod_{i=1}^{N_d} p(t_{r,i} | \vec{r}_0, \theta, \phi), \quad (4.23)$$

where p is a modified form of the gamma distribution called the Pandel function [445]:

$$p(t) = \frac{\rho^\xi t^{\xi-1}}{\Gamma(\xi)} e^{-\rho \cdot t}. \quad (4.24)$$

In Eq. (4.24), the variables ρ and ξ are phenomenological constants of the medium that are determined by Monte-Carlo simulations [446]. A disadvantage to the Pandel function is that it returns a probability of zero for pulses that have a negative time residual. Such negative values can arise due to noise hits that survived the pulse cleaning and due to the fact that observed photon times are measured with a finite temporal accuracy. To cope with these effects, the SPE likelihood used in IceCube is a convolution between the Pandel function and a Gaussian distribution [446].

³⁶The best fit value for \vec{r}_0 , corresponding to the mean of \vec{x}_i , is irrelevant to point source analyses.

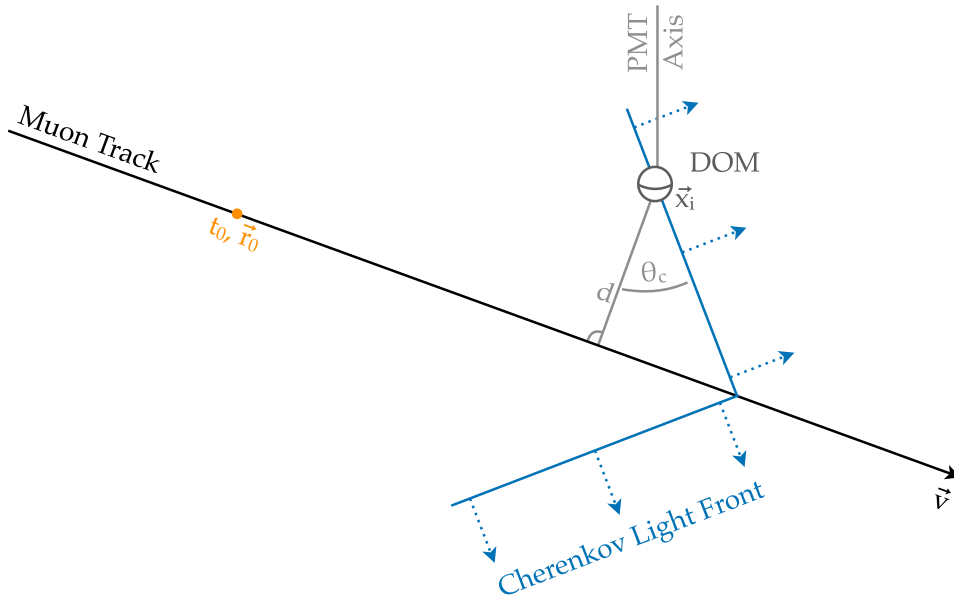


FIGURE 4.14: Geometrical quantities used to determine the arrival time and direction of unscattered photons. Adapted from [441].

Ideally, the SPE likelihood would be minimized by performing a brute force scan of the available parameter space. Due to computational constraints, such an approach is not viable. The output from Linefit is therefore used as an initial seed, producing a new best-fit parameter. To ensure that the minimizer did not get stuck in a local minimum, several new minimisations are then performed in which the seed for the muon direction is slightly scattering around the input parameters. This procedure is repeated two times.

MPE. The SPE likelihood is intrinsically a biased estimator as it only uses the earliest hit from each DOM. A modified likelihood is therefore considered in which an additional factor is added to account for the probability that the remaining $N_i - 1$ out of N_i hits in a single DOM would have a residual time that is larger than that of the first hit [447]:

$$\mathcal{L} = \prod_{i=1}^{N_d} N_i \cdot p(t_{r,i} | \vec{r}_0, \theta, \phi) \cdot \left[\int_{t_{r,i}}^{\infty} p(t_{r,i} | \vec{r}_0, \theta, \phi) \right]^{N_i-1}. \quad (4.25)$$

For muons with energies in excess of 1 TeV, it becomes very likely that multiple hits will occur in single DOM. Particularly the directional reconstruction of high-energy muons thus benefits from the use of the MPE over the SPE algorithm.

SplineMPE. As a final step in the directional reconstruction chain, the MPE likelihood from Eq. (4.25) is again applied to the hits. However, instead of using the Pandel function to evaluate p , the probability is evaluated numerically. Sets of simulated events are used to create look-up tables as a function of the distance between the muon and the DOM, the propagation angle of the muon with respect to the PMT axis, and the depth within the ice-sheet. A spline characterisation of the table is then used to enable a quick evaluation of the likelihood function and to reduce the memory footprint.

Using a Monte Carlo based likelihood has several advantages over the analytical Pandel function. While the Pandel function assumes a homogeneous medium, the use of SplineMPE makes it possible to account for the depth dependent scattering and absorption coefficients of light in ice, as shown in Fig. 4.15. Another advantage is that simulations can account for

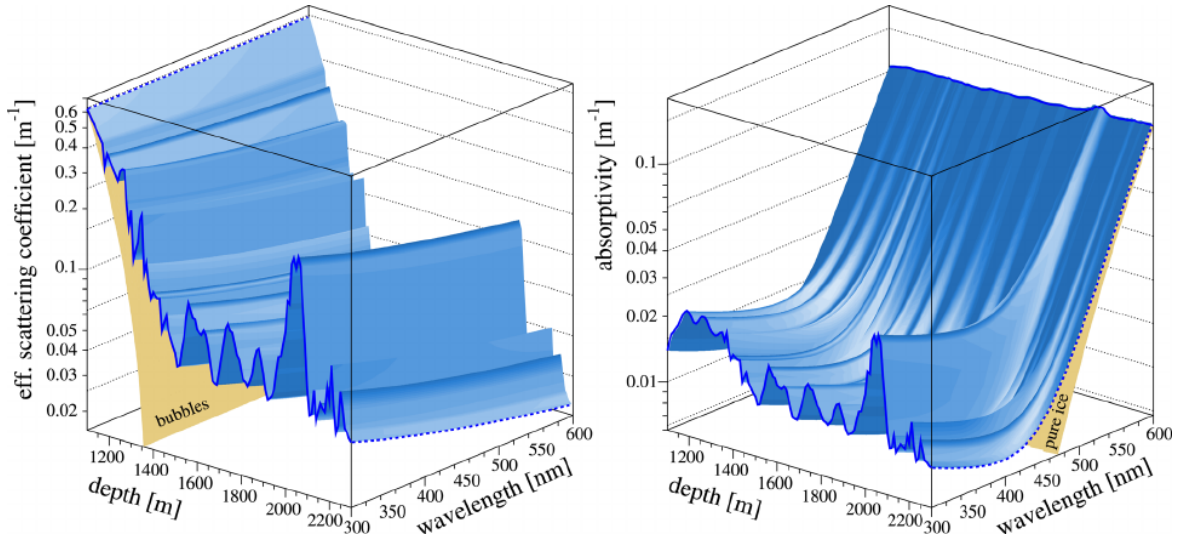


FIGURE 4.15: Effective scattering (left) and absorption (right) coefficient of light in ice as a function of depth and wavelength. From [448].

detector effects, such as late noise pulses and the resolution with which DOMs can timestamp a hit. Finally, it is also worthwhile to consider that the light emission of muons with energies above ~ 1 TeV is dominated by stochastic processes (see 4.3.3). Using Monte Carlo simulation makes it possible to account for this effect, in contrast to the Pandel function, which assumes that equal amounts of light were emitted along the entire track.

A comparison of the four directional reconstruction methods is shown in Fig. 4.16. As can be observed, the median angular error, defined as the opening angle between the true and reconstruction propagation direction of the muon, decreases with each more advanced reconstruction algorithm. The analysis presented in this thesis makes use of directions that were reconstructed with the SplineMPE method.

4.6.3 Estimated angular uncertainty

In the next chapter, the location of GRBs will be compared to those of the reconstructed muons, as they reflect the arrival direction of the parent neutrinos. To determine if a correlation exists between the two samples, an estimate of the uncertainty on the reconstructed muon direction is required. Event uncertainties largely vary as function of the number of hits, the zenith angle, the depth in the detector and the length of the muon track. As a result, uncertainties are estimated on an event-by-event basis.

Cramér-Rao. For the SPE and MPE method, the Cramér-Rao bound [452, 453]:

$$\text{Cov}(x_i, x_j) \geq \frac{1}{I(\vec{x})_{ij}}, \quad (4.26)$$

is used to obtain a conservative estimate of the uncertainty of the fit parameters, \vec{x} . In the above expression, $I(\vec{x})_{ij}$ is the Fisher information matrix,

$$I(\vec{x})_{ij} = \left\langle \frac{\partial^2}{\partial x_i \partial x_j} \ln(\mathcal{L}(\vec{t}_r | \vec{x})) \Big|_{\vec{x}=\vec{x}_{fit}} \right\rangle, \quad (4.27)$$

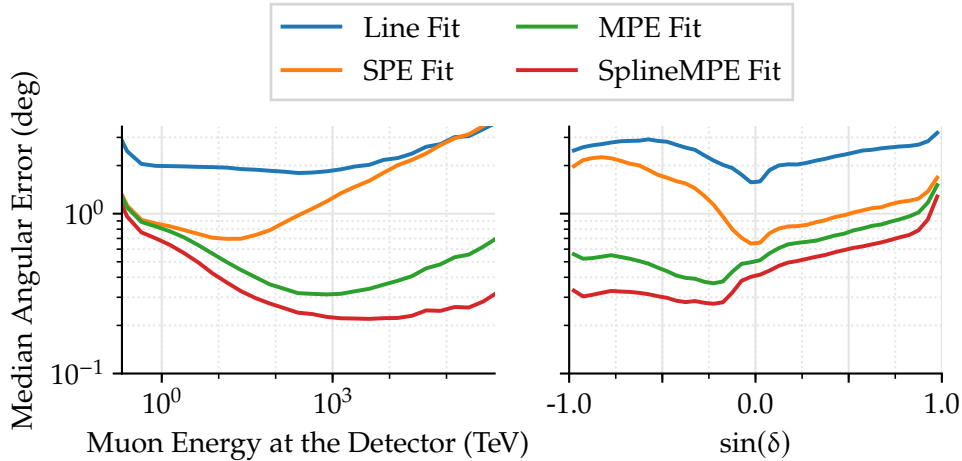


FIGURE 4.16: Median angular uncertainty of the four directional reconstruction algorithms on the final event sample. The left figure shows the uncertainty as a function of muon energy, averaged over all declinations. The right figure shows the uncertainty as a function of declination, averaged over all energies. Studies of the Sun and Moon shadow have validated that IceCube can achieve an angular pointing accuracy of 0.2° [449–451]. From [441].

where t_r is the residual time and the angular brackets denote averaging over all possible values of \vec{t}_r weighted by $\mathcal{L}(\vec{t}_r|\vec{x})$. Analytical expressions exist for the θ and ϕ diagonal components of the SPE and MPE Fisher information matrix [454]. These enable a fast evaluation of the directional uncertainty, on the order of $\sim 1 \mu\text{s}$ per event. Given the uncertainty on the reconstructed values of θ and ϕ , a circularised angular error, σ , is then constructed by quadratically averaging the uncertainties

$$\sigma^2 = \frac{1}{2} \cdot \left(\sigma_\theta^2 + \sin^2(\theta) \cdot \sigma_\phi^2 \right). \quad (4.28)$$

Cramér-Rao based uncertainties are used as one of the inputs of event selection algorithms.

Paraboloid. A similar approach is used to estimate the uncertainties of the SplineMPE fit parameters. However, due to the numerical nature of the algorithm, the likelihood landscape has to be evaluated numerically. Measurement errors of residual times approximately follow a Gaussian distribution [447]. As a result, the likelihood function in the θ and ϕ plane can be well-described by a two-dimensional Gaussian function or paraboloid around the global minimum. Uncertainties can then be extracted by finding the points at which the likelihood drops by a factor $e^{-1/2}$,

$$\ln(\mathcal{L}(\vec{x} + \vec{\sigma}_i)) = \ln(\mathcal{L}(\vec{x})) - \frac{1}{2}. \quad (4.29)$$

An error ellipse can thus be constructed in the θ and ϕ plane. The circularised uncertainty is then obtained by taking the quadratic mean of the semi-major and semi-minor axis of the ellipse³⁷. Numerical studies have shown that the Paraboloid estimator produces more accurate event uncertainties than the Cramér-Rao method. A downside is that the Paraboloid algorithm requires a parametrisation of the likelihood landscape, making the method much more computationally expensive. This prevents it from being applied in online analyses or

³⁷Taking the quadratic average of the semi-minor and semi-major axis was shown to offer the best sensitivity in previous analyses [455].

online filters. Paraboloid generated angular uncertainties are computed for all events only after the final stage of the event selection.

Pull correction. Reconstruction algorithms like paraboloid produce an estimate for the muon direction. Due to the kinematic angle (see 4.3.1), uncertainties are underestimated if they are used to model the angular separation between the reconstructed muon and the original neutrino. Additionally, unmodelled systematics can worsen this effect. A pull-correction is therefore implemented, defined as an energy dependent³⁸ factor that all event uncertainties are multiplied with to ensure that the true angular separation is less than 1σ for 39.3% of Monte-Carlo simulated events. Given that the pointing of the IceCube telescope has been validated down to 0.2° by studies of the Moon shadow [449, 450], an angular error floor is applied after applying the pull corrections, implying that the minimal angular uncertainty of any event used in our analysis is 0.2° .

4.6.4 Energy reconstruction

Aside from the reconstructed muon direction and uncertainty, the likelihood analysis in the following chapter will also make use of the muon energy. Astrophysical events are expected to follow a harder spectrum than atmospheric background events. High-energy muons will therefore receive a larger weight in the likelihood. Ideally, the neutrino rather than the muon energy would be included in the likelihood. As described in 4.3.1, muons produced by neutrinos will only carry a certain fraction of the neutrino energy. A second effect is that muons will already have undergone energy losses, as our analysis uses a sample of through-going-events, in which the neutrino interactions thus took place outside of the detector. For these two reasons, reconstructed muon energies should only be considered as lower limits to the neutrino energies.

At energies of the order $\lesssim 300$ GeV, muons can no longer propagate through the full IceCube detector. A calorimetric approach can thus be used to estimate the energy of the entering muon. Up to energies of ~ 1 TeV, muons will experience an approximately constant energy loss, as shown in Eq. (4.15). Above 1 TeV, the energy loss and light production becomes dominated by large stochastic energy losses. While this linear dependence makes it possible to estimate the energy of through-going muons, the stochastic nature implies that reconstructed energies will inescapably be prone to relatively large uncertainties.

MuE. Using the approximate linear dependence between the muon energy, E , and the emitted light intensity, a simple model can be constructed for the amount of hits, λ , that a DOM is expected to observe:

$$\lambda = E \cdot \Lambda + \rho. \quad (4.30)$$

In this expression, ρ is a constant that accounts for the background from noise hits. The variable Λ depends on the observing DOM and the characteristics of the muon track, i.e. its direction and anchor point. Monte Carlo simulation have been used to construct templates³⁹ of the expected light yield of all 5160 in-ice DOM for the 5 dimensional parameter space. Using the result from the SplineMPE reconstruction, a spline function is then used to interpolate λ for every DOM given the best-fit track parameters [420].

³⁸In practice, the MuEX energy proxy (see 4.6.4) is used to determine the pull-correction factor.

³⁹These template functions account for the depth dependent scattering and absorption of light in ice.

For a particular DOM, indicated by the subscript i , the number of observed hits is expected to follow a Poisson distribution around the mean predicted by the template. A likelihood function can thus be constructed that considers the product of these Poisson probabilities for every DOM

$$\mathcal{L} = \prod_{i=1}^{N_d} \frac{\lambda_i^{k_i}}{k_i!} e^{-\lambda_i}, \quad (4.31)$$

where the summation runs over all DOMs and k_i is number of hits observed in the i 'th DOM [420]. The only free parameter in the likelihood corresponds to the muon energy E , allowing for an efficient minimisation.

MuEX. A slight alteration has been made to this likelihood function that reduces the uncertainty of the estimator. This modification corresponds to smearing the Poisson probability with a kernel function

$$\mathcal{L} = \prod_{i=1}^{N_d} \int_0^\infty G(\lambda_i, \lambda) \cdot \frac{\lambda^{k_i}}{k_i!} e^{-\lambda} d\lambda. \quad (4.32)$$

An empirical study using simulated events [420] showed that the kernel

$$G(\lambda_i, \lambda) \equiv \frac{\alpha}{\lambda} \cdot \left[e^{-\beta \cdot \ln(\lambda/\lambda_i)} + \left(\frac{\ln(\lambda/\lambda_i)}{\sigma} \right)^2 \right], \quad (4.33)$$

significantly increased the reliability of the reconstruction algorithm. In Eq. (4.33), α is normalisation coefficient, while β and σ are empirically determined constants. The reasoning behind the inclusion of a kernel function is that stochastic energy losses can cause a few DOMs to have significantly more hits than predicted by the template function. These stochastic energy losses, which can be regarded as small shower-like events along the muon track, can thus lead to large over-fluctuations in the number of observed hits. Such excesses are ill-described by the Poisson likelihood. By convolving the probability with a kernel function, the likelihood is given longer tails, allowing for such over-fluctuations. Compared to the MuE algorithm, MuEX has been shown to produce a $\sim 30\%$ better energy resolution [456].

4.7 Simulation

The characterisation of event reconstruction algorithms relies on simulated events, as this allows comparing reconstructed quantities to the known Monte Carlo truth. Simulations are additionally used to characterise the performance of the event selection and likelihood analysis. Two main steps make up the simulation chain. First, neutrinos⁴⁰ are sampled in such a way that they will undergo an interaction in the vicinity of the IceCube detector. In interactions that lead to a muon particle, the muon is propagated through the ice, simulating its energy loss and accompanying production of Cherenkov photons. In the next step, the light collection and triggering by IceCube DOMs is simulated, after which the Monte Carlo events go through the same processing chain as that which is applied to real data.

⁴⁰In this section, 'neutrino' will refer to both neutrinos and anti-neutrinos.

4.7.1 Neutrino interactions

Neutrinos. Neutrino events and interactions are generated using a modified version of the ANIS⁴¹ program [457]. At the start of the simulation chain, neutrinos are sampled on Earth's surface. They are then propagated in a direction that passes through or in the vicinity of the IceCube detector. During their propagation, neutrinos can undergo interactions in which they are either absorbed or lose energy. Energy loss primarily occurs due to NC interactions, or CC interactions of a tau neutrino in which the resulting tau particle decays leptonically. Absorption, in contrast, is mainly caused by CC interactions of electron and muon neutrinos. Propagation through matter will also alter the neutrino eigenstates, affecting the oscillation parameters and thus the flavour composition of the sample.

The absorption, energy loss and flavour oscillations are effectively independent of the chemical composition of Earth. Instead, they vary mainly as a function of its matter density. ANIS assumes the parametrisation by the Preliminary Reference Earth Model (PREM) [458], in which Earth's density is determined as a function of the distance from its core. A second requirement is that a model is needed for the neutrino-nucleon cross section. Here, ANIS assumes the CTEQ5 parametrisation [213], previously shown in Fig. 4.8.

Muons. Neutrinos are forced to undergo an interaction near or inside the IceCube detector volume⁴². Muon particles produced in these interactions are then propagated through the bedrock and ice sheet using the PROPOSAL⁴³ software package [460]. PROPOSAL simulates the muon energy loss and corresponding light yield. Stochastic energy losses due to bremsstrahlung, pair production and nuclear interactions are randomly sampled along the muon track and added to the continual energy loss due to ionization.

Photons. For low-energy muons, the total number of emitted photons is sufficiently small that each individual photon can be tracked. GPUs are used to efficiently model the scattering of photons as they propagate through the ice sheet [461]. Photon tracks end either when the photon gets absorbed by the ice or when it hits a DOM. At the final stage of the simulation, the properties of all photon tracks that reached a DOM are stored to disk, serving as the input for the detector simulation.

For high-energy muons, a slightly different approach is taken. When tracking individual photons becomes too computationally intensive, the light deposition pattern along the muon track is used to directly sample the photon count at each of the DOMs. Tabulated expectation values are used that were pre-generated for a set of light emission patterns in the detector. While this approach is much more efficient, large computational efforts are initially required to compose the tabulated expectation values⁴⁴.

4.7.2 Detector response

Given a set of files containing the characteristics of photons that managed to reach a DOM, it remains to simulate the detector response. The conversion process from incident photons to the output signal of individual DOMs is realised via the DOMLauncher program [462]. As a first step, DOMLauncher starts by modelling the response of the PMT. Depending on the location, angle and wavelength of the incident photon, DOMLauncher determines the probability that the photon will liberate an electron in the photo-cathode of the PMT. If an electron is liberated, the PMT's response is modelled and converted into an output charge.

⁴¹ANIS is an acronym for 'All Neutrino Interaction Simulation'.

⁴²The weighting method used to produce realistic event rates naturally accounts for these 'forced interactions'.

⁴³PROPOSAL is an acronym for 'Propagator with optimal precision and optimized speed for all leptons' and is effectively a more efficient implementation of the 'Muon Monte Carlo' (MMC) framework [459].

⁴⁴These simulations need to be repeated each time a new ice model is introduced.

Ensuingly, DOMLauncher models the effects of the DOM mainboard, fADC and ATWDs to construct a waveform given the PMT's input signal.

The output from the DOMLauncher program produces simulated events that have an identical format to that of actual IceCube data. From this stage, the exact same filtering, event reconstruction and event selection algorithms are applied, ensuring that the real data and simulated events go through the same processing chain.

4.8 Event selections

The vast majority of events that trigger the IceCube detector are not caused by astrophysical neutrinos, but by particles produced in cosmic-ray air showers. In the Northern Hemisphere, atmospheric neutrinos are the only type of particle that will be able to propagate through Earth and reach the detector. In the Southern Hemisphere, atmospheric muons can also reach the detector, outnumbering atmospheric neutrino induced interactions by a factor $\sim 10^6$ at trigger level. Stringent event selection techniques are thus required to enable potential astrophysical events to be identified over this atmospheric background.

As described in 4.6.1, the muon filter is applied to all IceCube events that satisfied the SMT8 trigger. This step reduces the rate of events from 2.1 kHz to 40 Hz. Since the muon filter is the first stage during which the event rate is reduced, data is said to go from level 0 to level 1. Level 1 data is then further reduced by applying two more filter algorithms. These are the OnlineL2 filter [463] and the gamma-ray follow up (GFU) filter [441, 464], both of which are described in detail below. Our analysis thus makes use of level 3 data, corresponding to the events selected by the GFU filter.

4.8.1 The OnlineL2 filter

The OnlineL2 filter operates by placing a collection of direct cuts on reconstruction variables⁴⁵. While it intrinsically operates very similar to the muon filter, two primary differences enable the OnlineL2 filter to further improve the removal of background events. To start, the initial rate reduction, going from level 0 to level 1 data, allows applying an MPE fit to all events. A more reliable estimate of the zenith angle can thus be used, compared to the SPE-fit result used by the muon filter.

Direct hits. A second difference is that the OnlineL2 filter considers an additional variable⁴⁶ when placing cuts. This extra parameter is based on 'direct hits', which are defined as hits for which the time residual⁴⁷ lies in the interval $[-15 \text{ ns}, 75 \text{ ns}]$. Direct hits are thus hits with small time residuals, corresponding to DOM triggers caused by (relatively) unscattered photons. By considering the orthogonal projection of direct hits on the muon track, a reasonable estimate can be obtained of the track length inside the IceCube detector. Short lengths indicate that the muon only passed through the edge or corners of the detector. Such events will generally result in an unreliable directional reconstruction, fooling filter algorithms in accepting down-going muons as up-going events. By placing a lower bound on the minimal effective track length, such background events can be identified and removed [463].

Performance. Overall, the OnlineL2 filter further reduces the background by a factor ~ 6 , decreasing the rate from 40 Hz at level 1 to 6 Hz. Assuming an E^{-2} spectrum, level 2 data retains $>99\%$ of up-going and $>80\%$ of down-going signal events [441].

⁴⁵For a detailed overview of the cuts and parameters of the OnlineL2 filter, we refer the reader to [463].

⁴⁶Aside from the modified reduced log-likelihood, total charge, and reconstructed zenith angle.

⁴⁷The residual time is defined as the time difference between the observed hit and the expected arrival time of the Cherenkov wavefront. See Eq. (4.22) for a formal definition.

4.8.2 The GFU filter

The GFU filter was developed by T. Kintscher [441] with the aim of creating a sample of candidate neutrino events optimised for short scale transient searches. Given its excellent performance, described in detail at the end of this section, the GFU selection has been used in several IceCube analyses (e.g. [465, 466]). An overview will here be presented on the filter algorithm. For a full, detailed description, we refer the reader to [441].

Backgrounds. As input data, the GFU filter takes the events that were selected by the OnlineL2 filter. Level 2 data mainly consists of events caused by atmospheric muons, outnumbering neutrino induced events by a factor $\sim 10^3$. In the Southern Hemisphere, the reasoning behind the filter algorithm is that the atmospheric background can be removed by selecting the highest-energy muons. Atmospheric muons and atmospheric neutrinos both follow an energy spectrum, $dN/dE \propto E^{-3.7}$, that declines much faster than that of the expected astrophysical signal, $dN/dE \propto E^{-2}$. Above a certain energy threshold, the astrophysical signal will thus dominate the atmospheric background. The main background in the Southern Hemisphere comes from sets of atmospheric muons that were produced in the same air shower and are travelling almost parallel to each other. If the intermediate distance between the muons is much smaller than the IceCube string spacing, then a bundle of several low-energy muons will produce a signal that is very similar to that of a single high-energy muon. However, light emission from such muon bundles will not be dominated by large stochastic energy losses. In addition, the muons will not be travelling perfectly collinear, smearing the distribution of residual times and worsening the likelihood of directional reconstruction algorithms. These features are used to identify and remove muon bundle events.

In the Northern Hemisphere, there are two main types of background events. The first class corresponds to events which have been misidentified as up-going muons. In reality, these are mostly edge or corner clipping down-going muons. Neutrino induced cascade events are in some cases also misreconstructed as up-going muons. Tagging these events mainly relies on applying more robust reconstruction algorithms, such as SplineMPE, and requiring that these offer a good fit to the data. In addition, event topology features can be used to remove events that only pass through the edge of the detector, or events that do not exhibit track-like features. The second class of background events consists of up-going muons produced by atmospheric neutrinos. Aside from their energy spectrum, these are indistinguishable from astrophysical neutrinos and thus largely kept in the event sample.

Boosted decision trees. To remove background events, the GFU algorithm first applies a set of pre-cuts and then makes use of boosted decision tree (BDT) classifiers [441]. A BDT is a collection of ‘trees’ that aim to classify events into background or signal bins. Each tree consists of several layers (5 for the GFU algorithm). The first or top layer of a tree consists of a single node that performs a binary classification of events by determining if a variable is above or below a certain threshold. Based on this classification, the node feeds the events into two new nodes in the second layers. This process is repeated recursively, implying that the N ’th layer has 2^{N-1} nodes. At the final level, nodes are called the leaves of the tree.

Given a particular variable, the cut used by a node is optimised to separate events into signal and background. Denoting the two children of a node by the subscripts $_1$ and $_2$, the cut is chosen which optimises the separation gain

$$\Delta S = w \cdot S(p) - w_1 \cdot S(p_1) - w_2 \cdot S(p_2) . \quad (4.34)$$

In this expression, p is defined as the purity of the node, corresponding to the relative weight of the signal events, $p = w_s / (w_s + w_b)$, and the function S is the Gini separation criterion $S(p) = p \cdot (1 - p)$. At every node, three variables are randomly selected from a list of pre-identified quantities that were found to offer good separating power. The candidate which offers the best separation power at that particular node is then used. Once a tree has been completed, a new tree is started which takes as input the same events with slightly modified weights. In particular, the weight of wrongly classified events is increased by a factor 0.1 in a processes called boosting. Given the classification by the ensemble of trees, a BDT score is computed that reflects the possibility that an event is signal or background. Events are filtered by the algorithm if they exceed the GFU BDT score threshold.

Separate BDTs are constructed for events from the Northern and Southern Hemisphere due to the different backgrounds. As IceCube DOMs are located at an average depth of 1950 m, significant shielding still occurs for particles coming from zenith angles slightly smaller than 90° . For this reason, the optimal cut to separate up- from down-going events in different BDT selections was found to correspond to a zenith angle of 82° . For up-going events, a BDT with 300 trees is used, while the BDT of down-going events uses 400 trees. The events used to train the BDTs are based on Monte Carlo simulations⁴⁸. Signal events are weighted to the astrophysical neutrino flux, while background events are modelled to reflect the observed atmospheric background as accurately as possible.

Overtraining. Figure 4.17 and 4.18 shows the performance of the down- and up-going BDT, respectively. To ensure that the event selections were not overtrained, they were trained on one sampled and then applied to another. The p -value shows the results of a Kolmogorov-Smirnov test, which checks if the two cumulative distributions of the two independent samples are consistent with one another. Since these indicate a good agreement, it follows that the filter algorithm is not overtrained.

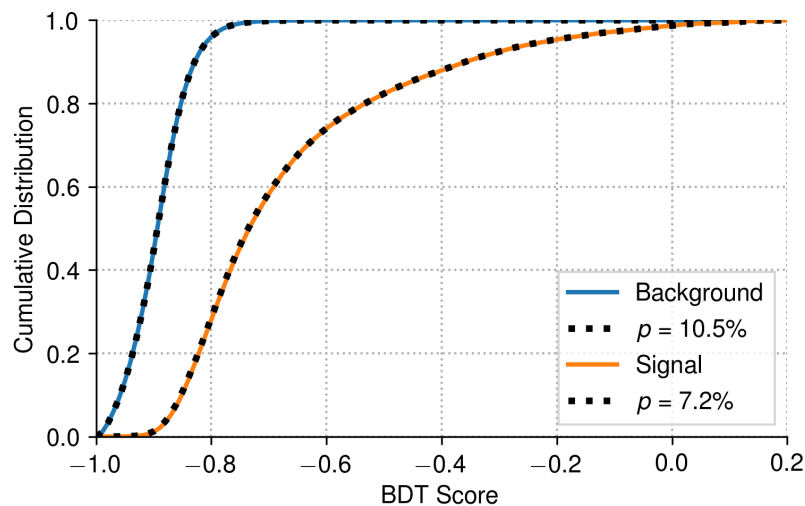


FIGURE 4.17: Cumulative distribution of the number of events that pass the down-going BDT. Solid and dashes lines show the training and test sample, respectively. The p -value corresponds to the result of a Kolmogorov-Smirnov test applied on the two samples. The final BDT cut is at -0.7 . From [441].

⁴⁸Using real data was shown to offer decreased performance due to signal contamination [441].

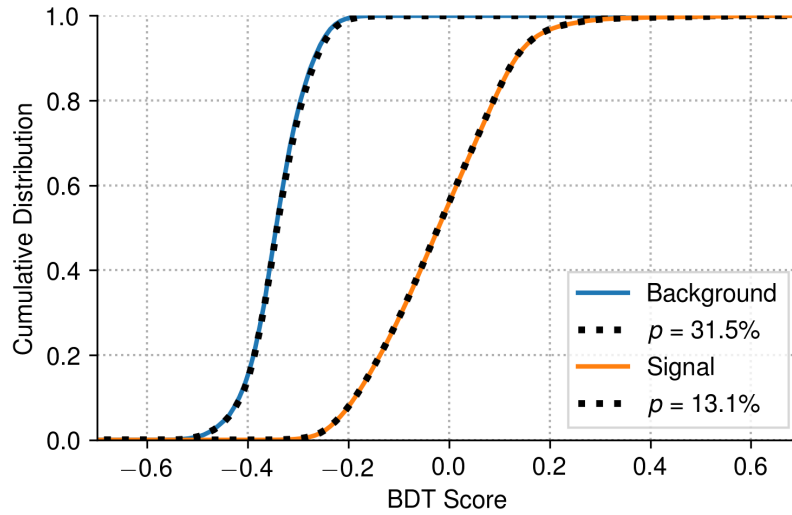


FIGURE 4.18: Same as Fig. 4.17 but for up-going events. The final BDT cut is at -0.12 . From [441].

4.8.3 Final event sample

The data used in our precursor analyses corresponds to events which were observed by IceCube between the 13th of May 2011 and the 14th of October 2018. In this period, IceCube was taking data in a stable configuration 96.5% of the time, corresponding to an effective uptime of 2,615.97 days. A total of 1,502,612 events were selected by the GFU filter. The GFU event rate for the Northern Hemisphere is 3.5 mHz, effectively corresponding to the irreducible background from atmospheric neutrinos. In the Southern Hemisphere the rate is 3.1 mHz, as the BDT cut was in part chosen to provide roughly the same number of events in both hemispheres.

Efficiency. Figure 4.19 shows the selection efficiency of the up- and down-going BDT as a function of the neutrino energy. In the Northern sky, an efficiency $> 90\%$ is consistently achieved for neutrino energies in excess of a few TeV. The analysis is significantly less sensitive in the Southern sky, where a $\geq 50\%$ efficiency is only achieved above ~ 300 TeV.

Effective area. Another manner in which the performance of the event selection can be evaluated, is by considering the effective area, defined as

$$\mathcal{A}_{eff} = \frac{\text{Observed event rate}}{\text{Incoming flux}}, \quad (4.35)$$

where the incoming flux is taken to be the true astrophysical neutrino flux as it arrives at Earth⁴⁹. Figure 4.20 shows the effective area as a function of energy, averaged over a selection of zenith bands. For events coming from the Northern Hemisphere (purple line), the effect of Earth absorption clearly becomes visible at energies above ~ 100 TeV. In contrast, events from the Southern Hemisphere (blue line) are largely removed at energies below ~ 100 TeV due to the stringent event selection required to deal with the large atmospheric muon background. The region around the horizon offers the best effective area, as the detector is shielded by a layer of ice sufficiently thick to stop all charged particles from atmospheric air showers, but not so thick that it will cause the neutrino flux to be attenuated.

⁴⁹This differs from the flux at the detector, which is affected by Earth absorption effects.

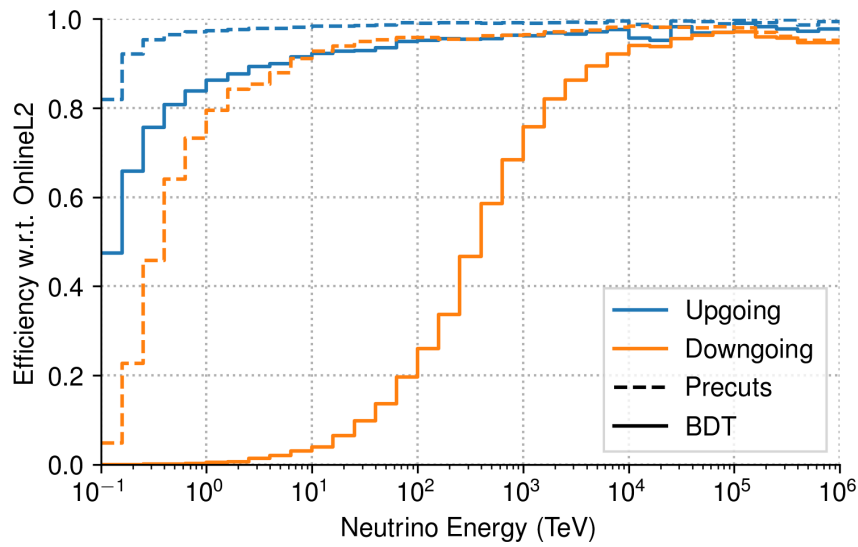


FIGURE 4.19: Efficiency of the up- and down-going event selection to filter signal neutrinos as a function of the neutrino energy. From [441].

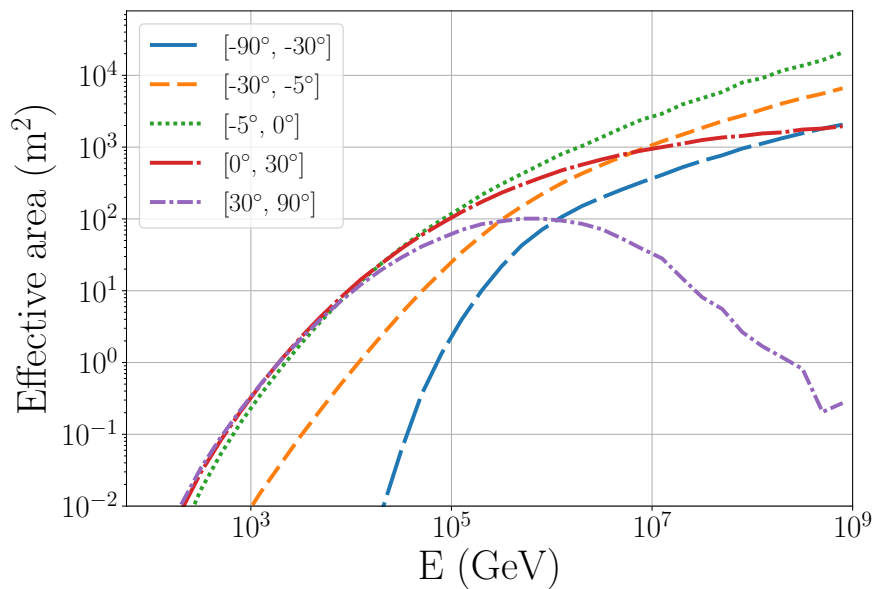


FIGURE 4.20: Effective area of the GFU event selection, averaged over a set of declination ranges. Due to the effective shielding from charged particles, but a negligible absorption of neutrinos, IceCube is most sensitive to events around the horizon.

Energy range. Given a particular model for the astrophysical flux, the effective area can be used to determine the number of signal events that will be in the GFU sample as a function of energy. Figure 4.21 shows the cumulative distribution of signal events for an E^{-2} spectrum. Defining the effective energy range of the sample as the central band that contains 90% of the signal events, a range from 1.25 TeV to 4.14 PeV is obtained. Repeating this computation for spectral indices between 1.5 to 4, the resulting 90% energy bands are shown in Fig. 4.22. Harder and softer spectra naturally shift the central range of signal events selected by the GFU filter to higher and lower energies, respectively.

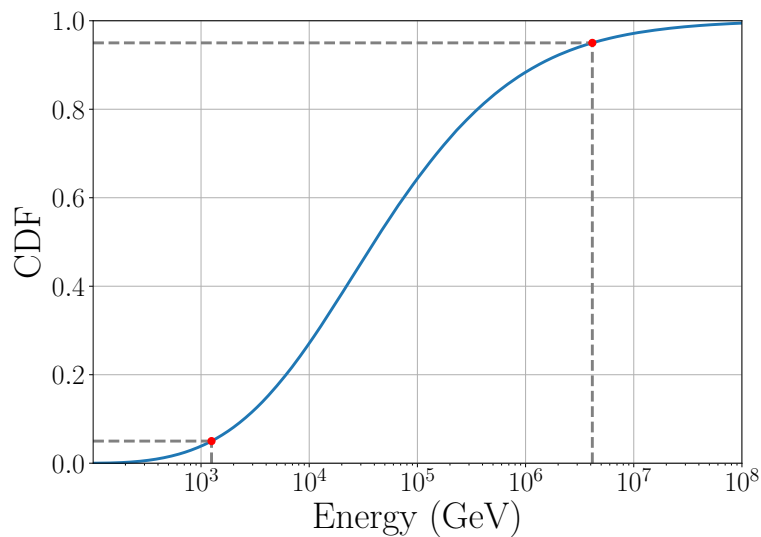


FIGURE 4.21: Fraction of signal events in the GFU sample that have an energy smaller than the value displayed on the x -axis, assuming an E^{-2} spectrum. The central 90% interval ranges from 1.25 TeV to 4.14 PeV.

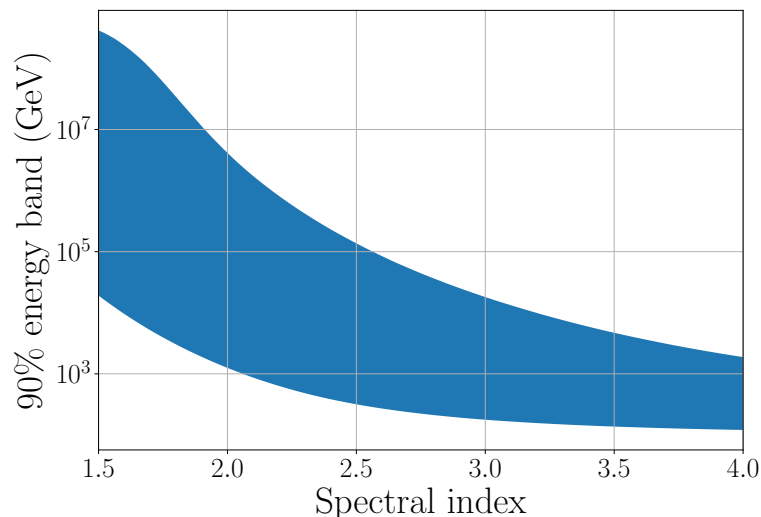


FIGURE 4.22: Range of the central energy band that contains 90% of all signal events in the GFU selection, assuming a power law flux for which the value of the spectral index is shown on the x -axis.

Chapter 5

IceCube GRB precursor analysis

In this chapter, all previously presented information is brought together. Chapter 1 gave an introductory overview on GRBs, which was followed by a more detailed discussion of gamma-ray precursors in Chapter 2. Of key importance is that past analyses [242, 290, 293, 294, 297, 300, 303, 304] have shown that precursors generally have a non-thermal spectrum, indicating that they do not simply correspond to photospheric emission. If precursors are instead related to a jet ploughing its way through remnant layers of the progenitor, then precursor gamma-ray signals could be accompanied by a significant neutrino flux. Alternatively, if the initial jet is too weak, it might be fully choked by the stellar envelope. In this scenario, there would still be precursor neutrino emission, ~ 100 s before the start of the prompt phase, but it would not be accompanied by a gamma-ray counterpart.

To enable a search for neutrinos from GRB precursors, we performed an analysis of the Fermi-GBM data, described in Chapter 3, to produce a catalogue of gamma-ray precursors. Ensuingly, we presented an overview of the IceCube detector in Chapter 4, describing how the neutrino flux from astrophysical sources can be identified and reconstructed. Given all these elements, we are now ready to describe the final likelihood analysis that will determine whether a neutrino signal is effectively observed from GRB precursors. Two searches will be described. One analysis will look for neutrinos that arrive in coincidence with observed gamma-ray precursors, while the other will look for neutrino emission before the start of the prompt phase. Our final analysis result is then related to the model predictions from Chapter 2 and compared to the astrophysical diffuse neutrino flux seen by IceCube.

5.1 GRB neutrino studies in IceCube

Before proceeding to our actual analysis, a short overview will first be given on past and current IceCube GRB analyses. This will provide the necessary context for the choices that shaped our analysis. In addition, it will enable highlighting how the analyses have progressed over the years, with each new search, this work included, adding novel aspects to the analysis method.

5.1.1 Past analyses

IC22 (2010). GRB analyses were one of the first searches that were performed once IceCube data started to become available. After the third deployment season, 22 strings had been installed in the ice-sheet. This configuration of the IceCube detector is called IC22. In the following years, the number of strings increased to 40, 59, 79 and 86. Data taken in the IC22 configuration led to the first IceCube GRB paper [467]. Two searches were performed on a set of 41 GRBs from the Northern Hemisphere. The first search targeted the prompt phase, looking for neutrinos that arrived coincident with the observed gamma-rays. The

second search targeted extended emission, using a 4 h time window that starts 1 h before the prompt phase. No coincidences were observed, leading to the first upper limits by IceCube on the GRB neutrino flux.

IC40 (2011). While the IC22 analysis had been unable to constrain mainstream model predictions, this already changed after the following season. Using data from the IC40 configuration, 117 GRBs from the Northern Hemisphere were examined [468–470]. Rather than instantly switching from a ‘prompt’ time window to a 4 h interval, the concept of ‘extending time windows’ was introduced. Starting from the prompt interval, the time range of all GRBs was extended by 1 s on either side until a period of ± 1 day was covered. At first sight, this seemingly introduces a huge trial-correction factor. However, when accounting for the strong correlation between the p -value of different time windows due to large overlaps, the method becomes feasible. With this analysis, IceCube was able to put a 90% upper limit on the GRB prompt neutrino flux that corresponds to 82% of the predicted Waxman-Bahcall flux [468].

IC40 + IC59 (2012). One year later, the same two analyses were re-applied. In addition to the 117 Northern GRBs from the IC40 analysis, 190 GRBs from both the Northern and Southern Hemisphere were also included for the IC59 period [439, 471]. This search thus became the first IceCube GRB analysis to include events from the Southern sky, as improved event selection algorithms combined with the increased number of strings made it possible to sufficiently suppress the background. Upper limits for the prompt phase decreased to 27% of the Waxman-Bahcall prediction [471], for the first time firmly excluding the model.

IC40 + IC59 + IC79 + IC86 (2015). Following the ‘IC40 + IC59’ paper, published results started to specifically focus on prompt GRB emission [472]. Only the analysis looking for coincidences with the observed gamma-ray signal was thus performed, omitting the ‘extending time window’ search. Another change was that, to achieve the best sensitivity averaged over all GRBs, the sample was again restricted to events from the Northern Hemisphere only. 506 GRBs were studied, using data taken in 3 years of partial and 1 year of the full detector configuration. The novelty of this analysis is that upper limits on the prompt neutrino flux were directly interpreted in terms of the parameters of the physical models. In particular, the baryonic loading and bulk Lorentz factor of the fireball, photospheric, and ICMART models were constrained, as previously shown in Fig. 1.14.

IC79 + 2xIC86 (2016). As more data taken in the full detector configuration became available, the inclusion of IC40 and IC59 data no longer had a notable effect on the analysis sensitivity. Since data from these seasons was taken using different filter algorithms and required dedicated event selections, their inclusion would only serve to increase the systematic uncertainty on the analysis results. Hence, they were omitted from further searches [397, 473–475]. Using three years of data, an analysis was performed to identify neutrinos from the prompt phase of 807 GRBs from both hemispheres. Contrary to previous analyses, it was not restricted to muon-track events, but also included cascades, effectively making the analysis sensitive to all neutrino flavours [397, 475].

IC79 + 5xIC86 (2017). The most recent IceCube publication [257] studied a sample of 1,172 GRBs from both the Northern and Southern Hemisphere. Only track-like events were examined, restricting the analysis again to the muon neutrino flavour. Limits were placed on the fireball, photospheric, and ICMART models. The analysis showed that prompt emission from GRBs can contribute less than 1% to the diffuse neutrino flux observed by IceCube¹.

¹As will be detailed later on (see 5.6.3), the claim that GRBs can contribute $<1\%$ to the diffuse flux only applies assuming a set of very specific assumptions and has since the IC79 + 5xIC86 analysis again been relaxed.

Precursor limits. In terms of the neutrino flux from GRB precursors, the most stringent constraints come from an analysis [476] that searched for muon neutrinos from 468 long GRBs in the Northern Hemisphere. Using 4 years of IC86 data, the analysis was able to lower previous upper limits [467] by a factor of ~ 10 . This led to a slight constraint on precursor emission models [333]. As will be shown later on, the analysis presented here has a significantly improved sensitivity compared to the previous upper limit, thus allowing to either confirm or firmly rule out the model prediction.

5.1.2 Current analyses

This analysis. All previous IceCube GRB precursor analyses searched for a neutrino excess in a generic manner. Our analysis differs in this regards, as we for the first time make use of gamma-ray precursor observations to identify the periods of time that are of interest. This enables a more targeted neutrino search, leading to significantly improved sensitivities.

Related searches. Aside from the analysis described in this chapter, it is worth noting that two other IceCube GRB searches were performed during the same timespan [5]. The first analysis, by Liz Friedman, used a sample of 2,096 GRBs to search for neutrino emission in a set of 10 expanding time windows, ranging for 10 s to 15 days. The second analysis, by Kunal Deoskar, studied 733 well-localised GRBs and fitted the optimal spectral index and time window (± 14 days) for each burst. These two searches look for neutrinos from the precursor, prompt, and afterglow phase of GRBs in a way that is complementary to this work. A publication on the combined results of our analysis has been composed and is at the time of writing undergoing internal review in the IceCube Collaboration.

5.2 Unbinned likelihood analysis

5.2.1 Likelihood-ratio test

Likelihood-ratio. To test if GRB precursors are sources of neutrinos, our analysis will examine the IceCube data and apply a likelihood-ratio test to compare two hypotheses. The first or null hypothesis, \mathcal{H}_0 , is that none of the events observed by IceCube are related to GRB precursors. \mathcal{H}_0 will therefore be referred to as the ‘background-only hypothesis’. The alternative hypothesis, \mathcal{H}_1 , is that the data can contain a non-zero contribution from GRB precursors. Denoting the true number of signal events as $n_{s,t}$, \mathcal{H}_1 thus states that $n_{s,t} \geq 0$. The likelihood-ratio of the two hypotheses can be used to define a test statistic,

$$\text{TS} = 2 \cdot \ln \left(\frac{\mathcal{L}(\vec{x} | n_{s,t} \geq 0)}{\mathcal{L}(\vec{x} | n_{s,t} = 0)} \right). \quad (5.1)$$

If the data, \vec{x} , results in a TS value that is strictly positive, then this indicates that a scenario is favoured in which the contribution from signal events is non-zero.

Significance. Even if the event sample does not contain any signal events ($n_{s,t} = 0$), the data can result in a positive TS value due to an upward fluctuation of the background. A significance level, α , is therefore used to indicate the probability that the observed result is consistent with a background fluctuation. In more rigorous terms, the significance is defined as the probability under the null hypothesis that a TS value at least as extreme as the observed value, TS' , is obtained, i.e.

$$\alpha = \mathcal{P}(\text{TS} \geq \text{TS}' | n_{s,t} = 0). \quad (5.2)$$

Background trials. In practice, Eq. (5.2) is generally evaluated numerically. So-called ‘background trials’ are performed to construct the TS distribution when $n_{s,t} = 0$. Each trial uses real data, but scrambled in such a way that it is consistent with the background hypothesis. The procedure to generate background trials can be summarised in four steps.

1. The expected number of background events, $\langle n_b \rangle$, in a declination band centred around the GRB position is calculated by counting the total number of events in that band, dividing by the total uptime of the detector, and multiplying with the duration of the examined time window. Events contribute to the band if they have a declination that is consistent within a significance 5σ of the GRB’s declination.
2. Poisson statistics are used to randomly sample the number of background events that will be injected, n_b , given the expected mean $\langle n_b \rangle$.
3. n_b events are randomly selected from the declination band used in step 1.
4. The times of the n_b events are set to values that are randomly sampled from a uniform distribution covering the examined time window. As the direction of the event in detector coordinates (azimuth & zenith) remains the same, the declination stays constant, while the right ascension is changed to make it consistent with the randomly sampled time of the event.

For each background trial constructed in this manner, the TS from Eq. (5.1) is evaluated. A numerical TS distribution consistent with the null hypothesis is thus constructed. Significances can then be determined as the fraction of background trials that have a TS value that is larger than or equal to the observed TS value.

Sensitivity and discovery potential. If the neutrino flux from GRB precursors is such that the expected number of signal events is $n_{s,t}$, then the actual number of signal events in the data, $n_{s,d}$, will be a value sampled from a Poisson distribution with mean $n_{s,t}$. Repeating the experiment several times, the number of signal events in the data sample can thus vary with each iteration or trial. Different TS values will be obtained for every trial, leading to different significances. As a result, the analysis performance is graded based on the fraction of trials that exceeds a certain predefined TS threshold.

- The sensitivity of the analysis is defined as the threshold from which $n_{s,t}$ leads to a significance below 50% in 90% of all trials. This threshold thus provides a conservative estimate for the smallest number of signal events to which the analysis is sensitive.
- The discovery potential is defined as the value of $n_{s,t}$ that leads to a significance below $5.7 \cdot 10^{-7}$ ($> 5\sigma$ for a single-sided Gaussian) in 50% of all trials. It thus indicates the minimal signal that can reasonably be expected to lead to a 5σ discovery.

Figure 5.1 graphically illustrates the definition of the sensitivity and discovery potential. The black line shows the TS distribution when $n_{s,t} = 0$, while the full red and blue line show the distribution of the TS when $n_{s,t}$ corresponds to the sensitivity and discovery potential threshold, respectively.

Alternative statistical methods. Before further going into the analysis, we will first motivate why a likelihood-ratio test is used rather than some other statistical test. In the null hypothesis, n_s is fixed to a single value. \mathcal{H}_0 is therefore a ‘simple’ hypothesis. In contrast, n_s can be any real positive number in the alternative hypothesis. \mathcal{H}_1 is therefore a ‘composite’ hypothesis.

The Neyman-Pearson lemma [477] states that the likelihood ratio is the most powerful test to compare two simple hypotheses to each other. Since \mathcal{H}_1 is a composite hypothesis,

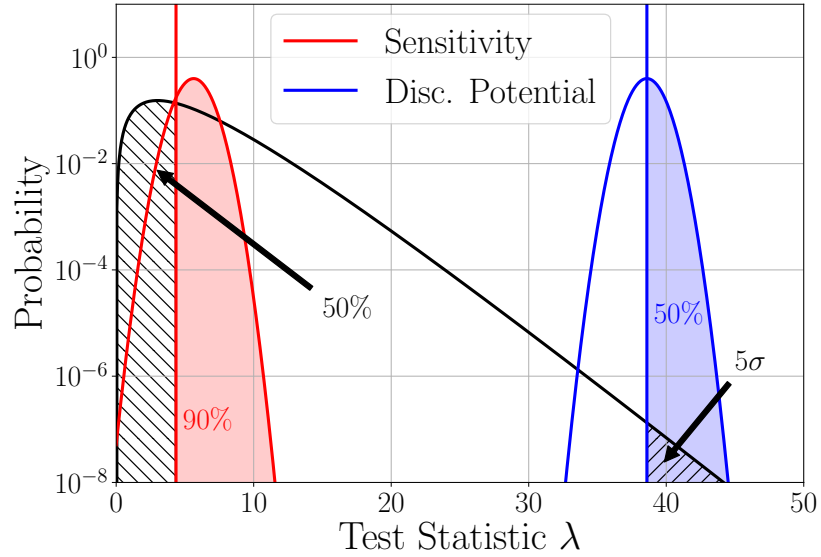


FIGURE 5.1: Cartoon illustrating the definition of sensitivity and discovery potential. The background TS distribution corresponds to the black line. In case sufficient signal is injected to satisfy the sensitivity or discovery potential criterion, the TS distribution changes to the red or blue line, respectively. Credit: René Reimann.

this theorem does not apply to our analysis. Nonetheless, IceCube studies that compared several statistical methods, including: the Li-Ma method [478], the likelihood-ratio test [479], the PLT-method [480], and the Ψ -method [481], found that for an analysis that is similar to the one presented in this thesis, the likelihood-ratio test offers the best overall performance [476, 482]. This motivates our choice of the likelihood-ratio test as the statistical tool used in our analysis.

5.2.2 Likelihood for a single, well-localised GRB

Having described how the significance and performance of a likelihood-ratio analysis can be quantified, it remains to specify the likelihood function itself. As a starting point, the likelihood of a single, well-localised² GRB will first be considered. This case will then be generalised to the likelihood of a badly-localised GRB, i.e. one whose localisation comes in the form of a HEALPix sky map [134]. Finally, the likelihood will also be extended such that it can be applied to a set of multiple well-localised GRBs, in what is called a stacking analysis.

Consider a set of N candidate neutrino events observed by the IceCube detector. For each event, the probability density can be specified that it is either a signal or a background event³. This probability density will be based on three characteristics of the events, namely their reconstructed direction, energy, and time.

Signal PDFs. The first component in the total signal PDF, S , is the spatial contribution, S_{sp} , that relates the direction of the neutrino to that of the GRB. While presenting the GRB-web project (see 1.2), it was shown that the probability density of burst localisations can be described using a two-dimensional Gaussian distribution, Eq. (1.14). In the likelihood, this

²A well-localised GRB is taken to be a burst whose localisation uncertainty is smaller than the majority of events uncertainties in the IceCube GFU sample. In this thesis, a cut at an uncertainty threshold of 1.5° is used.

³Signal events are defined as through-going muons that were induced by GRB neutrinos. Background events correspond to any type of event that is not a signal event.

Gaussian is used as the spatial PDF, with the slight modification that the variance now corresponds to the quadratic sum of the GRB and neutrino localisation uncertainty, and with θ taken to be the opening angle between the GRB position and the neutrino arrival direction.

The second probability density, S_t , is determined by the arrival time of the neutrino with respect to the GRB. For each burst, a box profile with width Δt around the time of the GRB will be used. The exact location and width of the time window will depend on the analysis and will hence be specified later on. If the neutrino arrives within this time range, it gets a weight $1/\Delta t$. Otherwise, its weight is zero.

The third and final component, S_E , is based on the reconstructed energy of the events. As previously illustrated in Fig. 4.20, the effective area of IceCube significantly varies as function of both declination, δ , and energy, E . For this reason, simulations of through-going signal neutrinos, assuming an E^{-2} energy spectrum, are used to construct a two-dimensional histogram of the number of expected events as a function of $\sin(\delta)$ and $\log_{10}(E)$. This distribution is then normalised along the $\log_{10}(E)$ axis and characterised using a spline to allow the PDF to be evaluated at arbitrary energies. The total signal PDF corresponds to $S = S_{sp} \cdot S_t \cdot S_E$.

Background PDF. A similar procedure is used to construct the background PDF, B , which can be written as $B = B_{sp} \cdot B_t \cdot B_E$. To construct the spatial component, B_{sp} , off-time data⁴ is binned as a function of declination. A normalised spline fit to the binned event counts is then used as the spatial PDF to observe a background event from that direction. In this computation, the right ascension of the GRB is not considered as IceCube is approximated to have a uniform detection efficiency in right ascension.

Given that all events which arrive outside of the GRB time window automatically get a weight of zero by the signal PDF, there is no point in considering these events in our analysis. Only background events inside the GRB time window are thus included. As a result, they likewise receive a weight $1/\Delta t$. If an event thus arrives on-time, it is considered to be equally likely that it is a signal or background event purely based on the timing of the event.

Finally, the background PDF for the energy, B_E , is constructed analogously to the signal energy PDF, S_E . However, instead of using simulated signal events, off-time data is used to compose the two-dimensional histograms. A normalised spline fit is then again employed to characterise the energy distribution of events as a function of zenith.

Likelihood. Based on the signal and background PDF, an expression can be obtained for the likelihood that the sample of N events contains n_s signal events, given that $\langle n_b \rangle$ background events were expected

$$\mathcal{L} = \frac{(n_s + \langle n_b \rangle)^N}{N!} e^{-(n_s + \langle n_b \rangle)} \cdot \prod_{i=1}^N \left[\frac{n_s}{n_s + \langle n_b \rangle} S(x_i) + \frac{\langle n_b \rangle}{n_s + \langle n_b \rangle} B(x_i) \right], \quad (5.3)$$

where x_i denotes the reconstructed properties of the i 'th event. In Eq. (5.3), the first term in the likelihood is the Poisson probability $\lambda^N e^{-\lambda} / N!$ that N events would be observed, given that a total of $\lambda = n_s + \langle n_b \rangle$ events are expected. The second term takes the product of the probability densities of all events. A priori, before considering the event properties, it can be stated that the probability that a randomly selected event is a signal event corresponds to $n_s / (n_s + \langle n_b \rangle)$. This factor is therefore multiplied with the signal PDF, S . Analogously,

⁴Off-time data is defined as all data outside of the considered GRB time windows.

the prior probability that an event corresponds to background is multiplied with the background PDF, B .

The likelihood in Eq. (5.3) has a single free parameter, namely the number of signal events, n_s . Under the background-only hypothesis, $n_s = 0$. This leads to the following expression for the background-only likelihood,

$$\mathcal{L}_0 = \frac{\langle n_b \rangle^N}{N!} e^{-\langle n_b \rangle} \cdot \prod_{i=1}^N B(x_i). \quad (5.4)$$

Taking the logarithm of the likelihood ratio, the following expression is obtained

$$\ln \left(\frac{\mathcal{L}}{\mathcal{L}_0} \right) = -n_s + \sum_{i=1}^N \ln \left(\frac{n_s S(x_i)}{\langle n_b \rangle B(x_i)} + 1 \right). \quad (5.5)$$

This log-likelihood ratio, corresponding to half of the TS value, is maximised to find the number of signal events that optimally describes the observed event sample.

Example TS distribution. The GRB time windows considered in this analysis are typically of the order 100 s. Given that the full-sky rate of the IceCube GFU sample is 6.6 mHz, the number of expected background events, $\langle n_b \rangle$, satisfies $\langle n_b \rangle \ll 1$. For instance, in case of a GRB with a conservative angular uncertainty of $\sigma = 1^\circ$ and a 100 s time duration, the expected number of background events that overlaps within 5σ corresponds to ~ 0.001 . Most background trials will therefore not have any events that contribute to the likelihood. As a result, the best-fit TS value automatically corresponds to zero. Figure 5.2 shows an example of a background TS distributions for a well-localised GRB in which this feature is clearly visible. The exact shape of the distribution will vary on a GRB-by-GRB basis, depending on the declination and the duration of the burst.

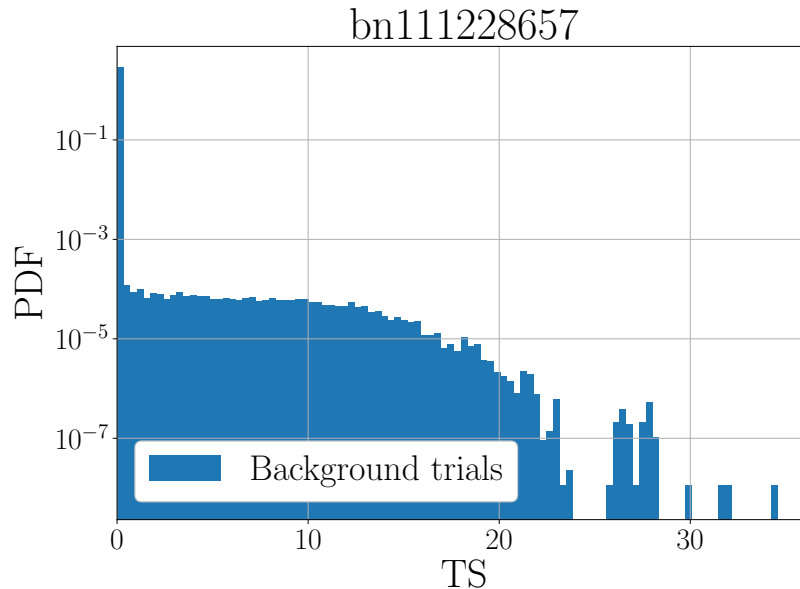


FIGURE 5.2: Background TS distribution of the burst bn111228657, which was localised to $\sigma \lesssim 10^{-4}$ degrees by Swift.

Sensitivity. Considering the low-background rate, the case of a well-localised, short timescale transient approaches the ideal scenario of a background free search. This implies that essentially any coincident event will automatically lead to a positive TS value. The

sensitivity threshold is therefore reduced to a simple counting experiment. For a median background TS value of zero, the sensitivity can be determined as the average number of events λ that will produce at least one event in 90% of all trials. An alternative way of phrasing this is that 10% of all trials should not contain any events, i.e.

$$0.1 = P(k = 0) = \frac{\lambda^0}{0!} e^{-\lambda} = e^{-\lambda}. \quad (5.6)$$

Solving for λ , it follows that the sensitivity corresponds to the flux that on average leads to $\ln(10) \sim 2.3$ events. The effective area of the IceCube GFU sample can be used to find the corresponding time-integrated flux as a function of declination. This quantity is shown in Fig. 5.3 and applies to any well-localised transient if the timescale is such that $\langle n_b \rangle \ll 1$.

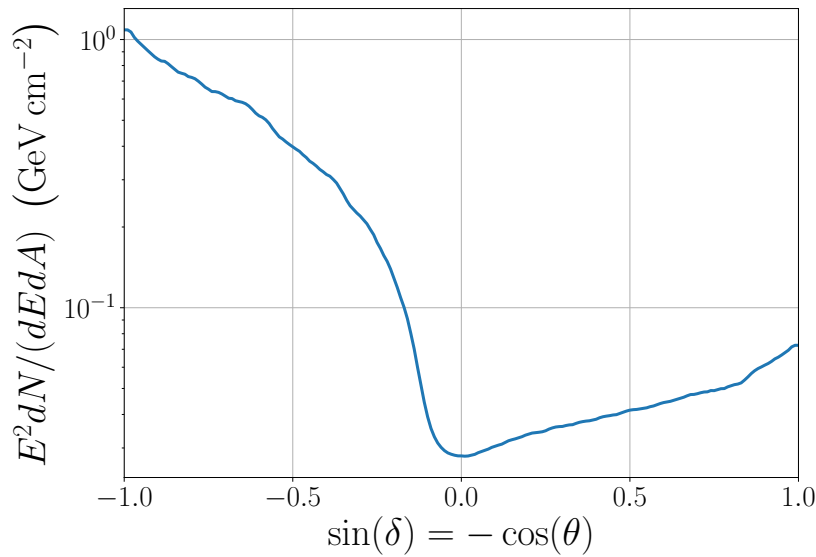


FIGURE 5.3: Sensitivity of IceCube to the time-integrated flux of a single GRB as a function of the GRB declination, δ , and zenith angle, θ .

An interesting feature is that the inclusion of background events can seemingly lead to an improvement of the sensitivity. From Eq. (5.6) it follows that the minimal number of events required to reach the sensitivity threshold is $\lambda = \ln(10) \sim 2.3$, where λ is the sum of both signal and background events. A non-zero background contribution will thus lower the number of signal events required to reach the sensitivity threshold. This holds true as long as the median of the background TS distribution corresponds to zero. To illustrate the effect, Fig. 5.4 shows the sensitivity threshold to observe an excess in a simple counting experiment. Initially, the sensitivity improves as the average number of background events increases. Once an average background count of $n_b = \ln(2) \sim 0.69$ is reached, the median number of background events jumps from 0 to 1, causing a sudden increase in the sensitivity. For a test statistic derived from Eq. (5.5) rather than a simple counting experiment, the sensitivity will follow a similar pattern, though without the discontinuous jumps introduced by the discrete nature of the counting TS. It should be noted that this effect is purely mathematical and is not representative of a physical improvement in analysis sensitivity.

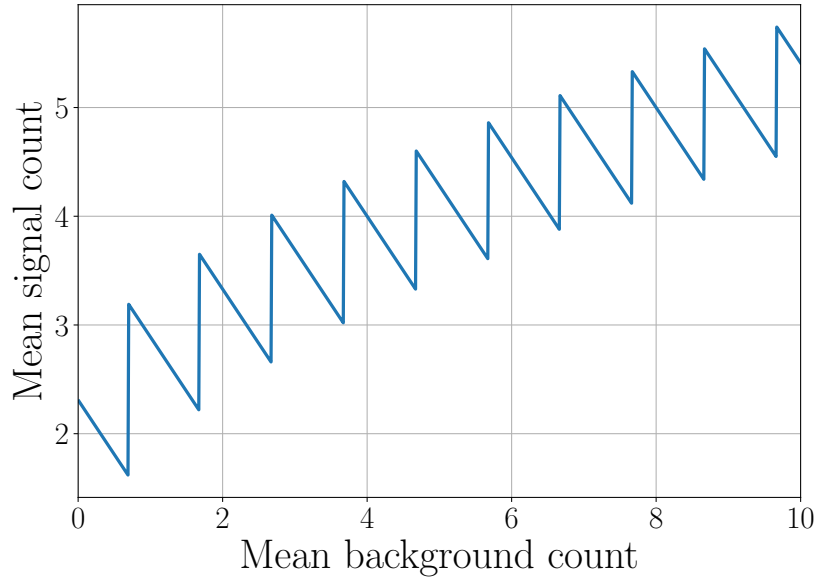


FIGURE 5.4: Number of signal events (y -axis) required to satisfy the sensitivity criterion in a simple counting experiment. The minimal allowed for signal count corresponds to $\ln(5) \sim 1.61$ at a background count of $\ln(2) \sim 0.69$.

5.2.3 Sky scans for GBM localised bursts

HEALPix. For GRBs that were localised by Fermi-GBM, an additional step is needed to compute the TS. Rather than localising a bursts to a single position, Fermi-GBM releases HEALPix maps [134] to characterise the localisation uncertainty. HEALPix maps divide the sky into pixels of equal size⁵. The maps released by Fermi-GBM contain the probability for each pixel that the true location of the GRB falls within that pixel. An example of such a sky map was previously shown in Fig. 1.7 when presenting the GRBweb project.

Sky scans. To find the most likely GRB-neutrino association, a sky scan is performed to find the pixel that will produce the most significant result. In particular, the TS from Eq. (5.5) is evaluated at every pixel individually under the assumption that the true position of the GRB corresponds to the pixel centre. The resulting log-likelihood ratios are then multiplied with the probability content of each pixel, $P_{\text{GBM},i}$, leading to the following test statistic:

$$\text{TS}_{\text{GBM}} = \max_i \{ \text{TS}_i + 2 \times [\ln(P_{\text{GBM},i}) - \ln(P_{\text{GBM},m})] \} . \quad (5.7)$$

In this expression, the constant $P_{\text{GBM},m} \equiv \max_i \{ P_{\text{GBM},i} \}$ is purely added for conventional reasons, as it does not influence the maximization of the TS.

Example TS distribution. Figure 5.5 shows the background TS distribution for a burst whose TS is described by Eq. (5.7). Overall, background TS distributions from HEALpix bursts are very similar to those of well-localised bursts. The exact characteristics of the distribution will depend on the duration and the sky map of the GRB. For each burst, a unique background TS distribution thus has to be constructed.

Sensitivity. As stated previously, the sensitivity curve shown in Fig. 5.3 applies to any transient whose timescale is sufficiently small that $\langle n_b \rangle \ll 1$. For a source described by a HEALPix map, the sensitivity will effectively be a mixture of the sensitivities from Fig. 5.3,

⁵The HEALPix maps released by Fermi-GBM contain 196,608 pixels, implying that each pixel has an angular size of ~ 0.2 square degrees.

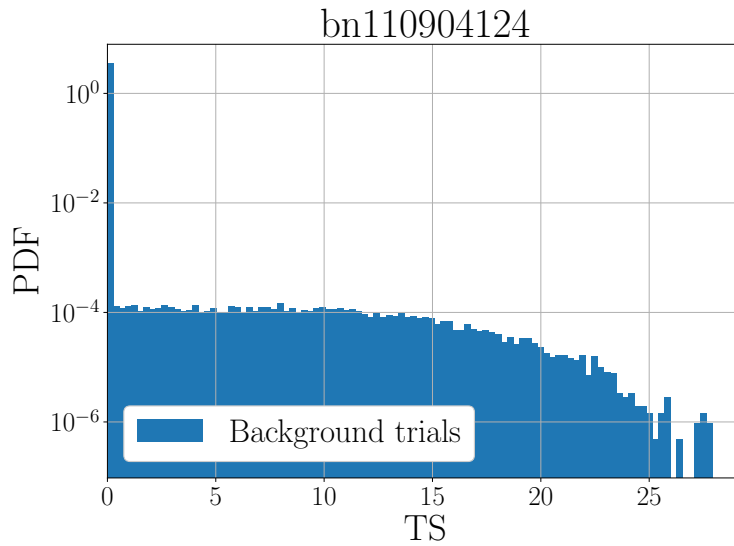


FIGURE 5.5: Background TS distribution of the burst bn110904124, whose localisation is described by a sky map in the HEALPix format.

determined by the probability contained in different declination bands of the HEALPix map. In rigorous terms, signal trials are performed by first randomly sampling the simulated true GRB position based on the probability content of the pixels. From this step onwards, the simulation chain is identical to that of a well-localised GRB. It follows from these simulations that despite their worse localisation, the sensitivity to GRBs for which a sky scan is performed is comparable to that of well-localised GRBs as long as the criterion $\langle n_b \rangle \ll 1$ remains true.

5.2.4 Stacking likelihood

Using a small modification, the likelihood for a single well-localised GRB (see 5.2.2) can be adjusted to the likelihood for N well-localised GRBs. In this new formalism, the expression for the likelihood remains identical and is thus given by Eq. (5.3). The difference to a single source stems from the interpretation of the variables in the likelihood. When considering multiple sources, n_s corresponds to the total number of signal events summed over all GRBs. Each GRB is assumed to have the same time-integrated neutrino flux at Earth⁶. The number of neutrinos per GRB will therefore be proportional to the GFU effective area at the declination of the burst, $\mathcal{A}_{eff}(\delta)$. A second modification to the likelihood is therefore that the signal PDF is replaced by the sum of the N signal PDFs, weighted by their relative contribution to the number of signal events

$$S = \frac{\sum_{i=1}^N \mathcal{A}_{eff}(\delta_i) \cdot S_i}{\sum_{i=1}^N \mathcal{A}_{eff}(\delta_i)}, \quad (5.8)$$

where δ_i and S_i are the declination and signal PDF of the i 'th burst, respectively.

The method described above is generally referred to as a 'stacked likelihood'. A major advantage compared to analysing each GRB on an individual basis is that stacking reduces the number of fit-parameters by a factor N . In addition, it allows accumulating the

⁶A more physical assumption would be to weight the flux of GRBs by the inverse square of their luminosity distance. However, as only $\sim 10\%$ of all bursts have a redshift measurement, GRBs are typically [442, 466, 476, 483] given equal weights.

signal and background events of all GRBs in a single likelihood, leading to more competitive results. A downside to stacking is that practical implementations do not allow for the inclusion of HEALPix maps in the likelihood. Hence, stacking can only be applied to well-localised GRBs. Performance figures for the stacking analysis performed in this thesis, including a background TS distribution and sensitivity calculation, will be given in section 5.3.2.

5.3 Analyses

Two analyses are performed to look for neutrino emission from GRB precursors. These analyses examine 972 bursts in total, using different assumptions about the neutrino emission time. An overview of the two analyses and their performance will be given in this section. For the actual analysis results, we refer the reader to Section 5.5.

Review. To avoid biasing the analyses, both searches were performed in a blind fashion. This implies that the actual IceCube data was only examined at the final stage of the analysis after a review by the IceCube Collaboration. Prior to unblinding, scrambled data and Monte Carlo simulations were used to test the analysis framework and characterise its performance. The IceCube review process to approve unblinding consisted of two stages. First, regular presentations were given in the corresponding IceCube working group. A working group reviewer was then appointed to scrutinize the analysis specifics. Following approval by the working group, a second reviewer from the collaboration was appointed. Having satisfied the questions from both reviewers, the analysis was presented to the full collaboration. This was followed by a two week comment period, after which unblinding approval was granted.

5.3.1 GBM coincidence study

The first analysis aims to identify neutrinos that arrived coincident with or close in time to observed gamma-ray precursor flashes. This search will be referred to as the ‘GBM coincidence study’. To enable the analysis, a GRB precursor catalogue was composed as described in Chapter 3. The gamma-ray precursors from that analysis of Fermi-GBM data will now serve as the input for the IceCube search presented here.

GRB sample. In total, the Fermi-GBM precursor analysis from Chapter 3 identified 217 GRBs that showed evidence for precursor emission. Two selection criteria are imposed on this sample to identify the bursts that can be included in our coincidence study.

- 3 out of the 217 GRBs do not have a Fermi-GBM HEALPix map⁷, nor were they localised by another satellite. For this reason, they are removed from the sample.
- Of the remaining 214 bursts, there are 138 GRBs that fall inside the time range of the IceCube GFU sample. Five of those bursts occurred while the detector was not taking data in a stable configuration. This leaves a total of 133 GRBs that will be analysed in this search. One burst’s (bn121113544) time window only partly overlaps with the period during which GFU data is available. This effect is accordingly accounted for in the analysis.

Table D.1 in Appendix D presents an overview of the 133 analysed GRBs.

⁷The RoboBA algorithm that Fermi uses to produce HEALPix maps will generally fail for $\lesssim 3\%$ of all GRBs. As a result, no sky map localisations are available for these bursts [484].

Time windows. The time windows examined for each GRB correspond to the precursor time ranges from Tab. D.1, extended by 2 s on either side to set a conservative time range. At a later stage, our analysis could be used to place limits on the flux from GRB precursors. A modification is therefore made to the time window of bursts whose precursor ended very close in time to the start of the prompt emission. If the quiescent time between the precursor and prompt phase is less than 2 s, the end of the time window used in this analysis is cut short such that it does not overlap with the prompt phase of the burst. Combined, the summed duration of all 133 time windows corresponds to a 3344.53 s period that will be searched for precursor emission.

TS distribution. Of the 133 GRBs in our sample, there are 33 bursts that were accurately ($\sigma \leq 1.5^\circ$) localised by a satellite other than Fermi-GBM. Those bursts are treated as ‘well-localised’ GRBs and are thus analysed using the TS from Eq. (5.5). For the remaining 100 bursts, a sky scan is performed based on the TS defined in Eq. (5.7). The background TS distribution for two of the 133 GRBs was previously shown in 5.2.2. Fig. 5.2 showed the TS distribution for a well-localised GRB, bn111228657, and Fig. 5.5 that of a HEALPix burst, bn110904124. Background TS distributions are similarly built for all other GRBs in our sample. Due to the small time windows, all 133 analyses are relatively background free. This implies that for any particular GRB, the majority of background trials will not have any coincident events. As a result, most trials will end up at a TS value of zero. Figure 5.6 shows the fraction of non-zero background trials for each GRB. Depending on the size of the time window and how well the GRB was localised, this fraction varies from $\sim 5 \cdot 10^{-5}$ to ~ 0.1 .

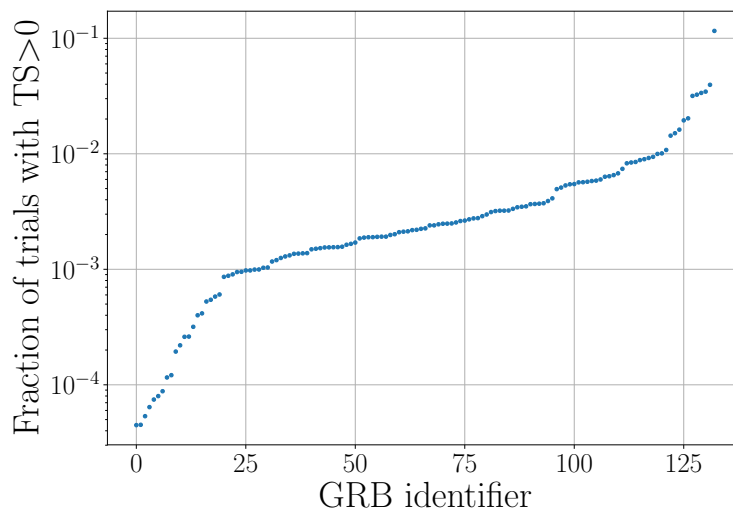


FIGURE 5.6: Each point along the x -axis represents one of the 133 GRBs analysed in this search. For every GRB (dot), the y -axis indicates the fraction of background trials for which the best-fit n_s and TS value is larger than zero.

When one background trial is performed, this results in 133 TS values, one for each GRB. A quantity which will be of interest at a later stage of the analysis is the fraction of trials for which there are exactly N TS values that are non-zero. The distribution of this number is shown in Fig. 5.7. Under the background-only hypothesis, the probability that all 133 GRBs will result in a TS value of zero is 47.8%.

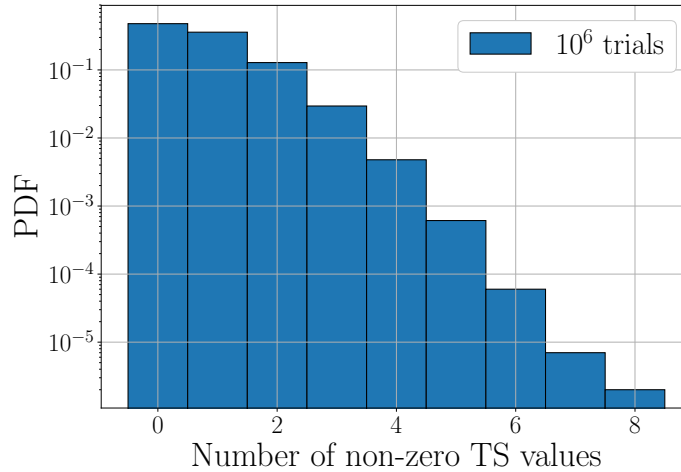


FIGURE 5.7: When performing a single background trial, a TS value is obtained for each of the 133 GRBs. This distribution shows the probability that exactly N of those 133 TS values will be different from zero.

Fit bias. To ensure that the analyses are able to accurately reconstruct the true number of signal events, trials are performed in which a fixed number of simulated signal events are injected. Figure 5.8 shows the fitted n_s value as a function of the true number of injected signal events. This distribution is shown for the well-localised and HEALPix GRBs whose TS distributions were previously shown in Fig. 5.2 and 5.5, respectively. The true number of signal events is generally well recovered. Due to the low background, most trials do not contain any signal events. Few upper fluctuations are thus observed as the fitted value of n_s cannot be larger than the total number of events in the sample. Similar figures of merit can be constructed for the remaining GRBs in the sample and show the same general characteristics.

Trial corrections. When examining the ensemble of all bursts, the output of the analysis corresponds to 133 p -values. A trial-correction factor is therefore needed to determine if the collection of those p -values constitutes a statistically significant result. Three methods are examined to combine the 133 p -values into a single trial-corrected p -value.

1. *'Binomial' method:* Consider a set of N p -values, one for each GRB, that are ordered from smallest to largest, i.e. $p_1 \leq p_2 \leq \dots \leq p_N$. Under the background-only hypothesis, those N p -values are expected to be uniformly distributed between zero and one. The probability that k or more p -values would be smaller than or equal to p_k is given by the binomial probability

$$\mathcal{P}(k) = \mathcal{P}(n \geq k | N, p_k) = \sum_{m=k}^N \frac{N!}{(N-m)!m!} p_k^m (1-p_k)^{N-m}. \quad (5.9)$$

In essence, this procedure thus combines the k out of N most significant p -values into a single significance. Rather than pre-specifying the value of k , all values from $k = 1$ to $k = N$ are scanned to find the one which offers the smallest probability $\mathcal{P}(k)$. An empirical correction factor is then applied to account for the fact that N values were scanned. The trial-corrected p -value is taken to be the fraction of background trials that result in a $\mathcal{P}(k)$ smaller than or equal to the observed value. Given that the probabilities $\mathcal{P}(k)$ are highly correlated, this correction factor is only minor.

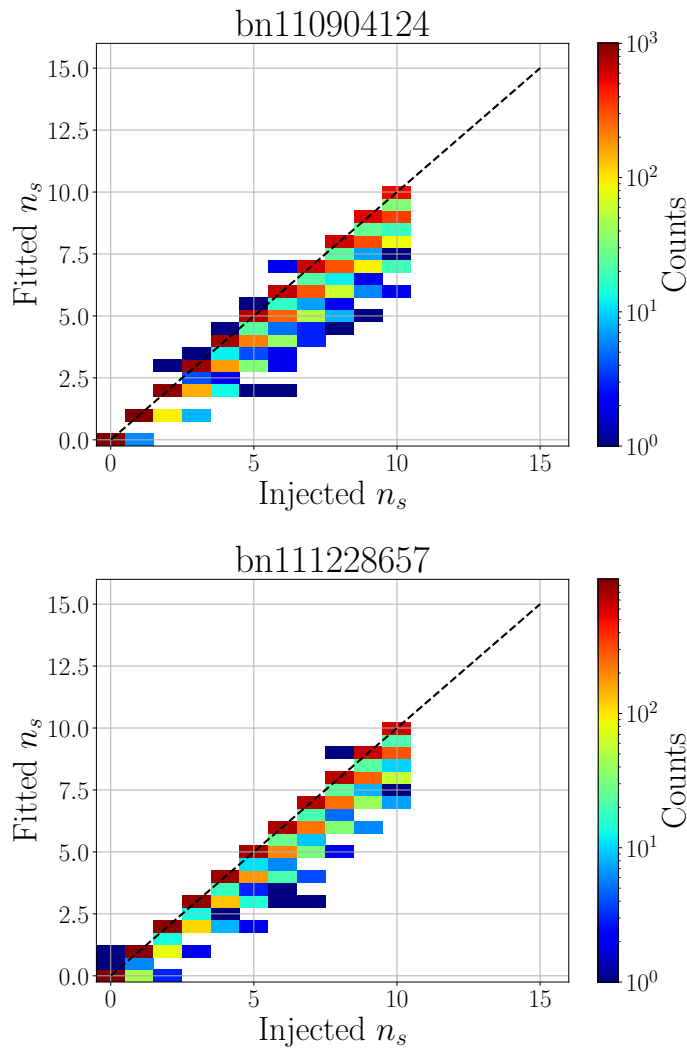


FIGURE 5.8: Distributions showing that the injected number of signal events can be well-recovered by the likelihood fit. The upper figure corresponds to a well-localised GRB, while the lower figure is a GRB whose localisation is described by a HEALPix map.

A small modification to this approach is needed to apply the binomial method to the GBM coincidence study. For every GRB, the p -value is derived by comparing its value to the background TS distribution. Assuming that the fraction of events that end up at a TS of zero corresponds to x , it follows that the p -value distribution under the background-only hypothesis is $d\mathcal{P}/dp = 1$ if $p < (1 - x)$, with the remainder probability located at $\mathcal{P}(p = 1) = x$. As the individual p -values are thus not uniformly distributed between zero and one, Eq. (5.9) cannot be applied. The value of $\mathcal{P}(k)$ is therefore determined numerically, using background trials to determine the probability that k p -values are smaller than p_k . Figure 5.9 illustrates how this empirical trial correction differs from the ideal case of Eq. (5.9).

2. *'Full product' method:* An alternative approach is to consider the product of all p -values, $\alpha \equiv \prod_{i=1}^N p_i$. In practice, the majority of p -values will be equal to one (see Fig. 5.7), meaning that typically only a few GRBs will contribute to the value of α . Background trials can again be used to construct the distribution of α under the background-only hypothesis. The trial-corrected p -value of the analysis then corresponds to the fraction

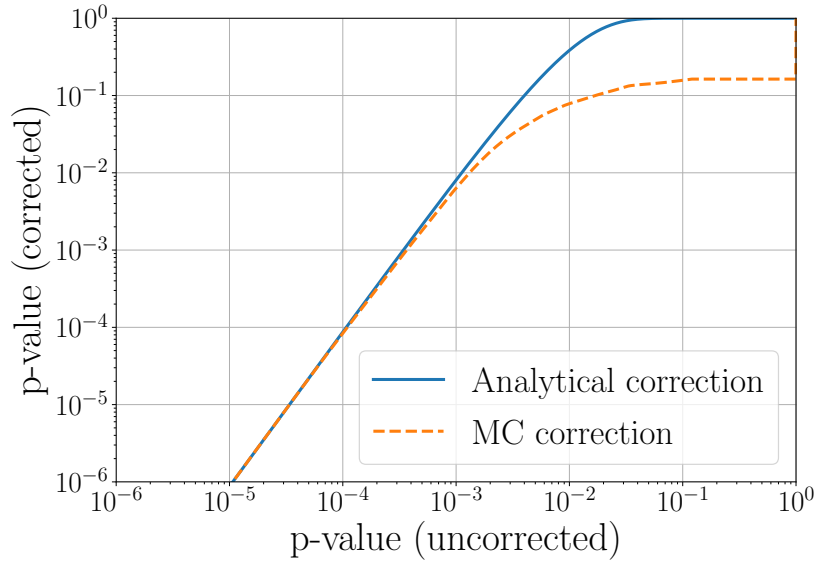


FIGURE 5.9: Correction of the binomial p -value for the case where $k = 2$, obtained via the analytical formalism, Eq. (5.9), and Monte Carlo simulations. The analytical expression requires that the contributing p -values are uniformly distributed between zero and one. Since this is not the case, a deviation is observed from the ideal, analytical curve.

of trials that have a value α smaller than or equal to the observed result.

3. *'Partial product' method:* As a third method, a combination of the two upper approaches is examined. Rather than taking the product of all p -values, the product is taken of the k most significant p -values, $\alpha(k) \equiv \prod_{i=1}^k p_i$. This parameter, $\alpha(k)$, is then treated analogous to p_k in the binomial method. That is, the probability, $\mathcal{P}(k)$, of observing a value that is at least as small as $\alpha(k)$ is determined for each k based on background trials. The most significant $\mathcal{P}(k)$ is then selected and an empirical correction is applied⁸ for having looked at N possible values of $\mathcal{P}(k)$.

Comparing the three methods, it was found that the partial product procedure offers the best overall performance. A comparison between the partial product and binomial method is shown in Fig. 5.10. In these plots, each dot represents a trial that includes one (upper image) or two (lower image) injected signal events. The x - and y -value represent the final trial-corrected p -value obtained using the partial product and binomial method, respectively. As most points lie above the diagonal, the partial product method is generally found to result in the most significant p -value. Figure 5.11 shows the same quantities, but comparing the partial product to the full product method. Overall, the partial product procedure is again found to offer the best performance⁹. Given these results, it was decided to use the partial product method to perform the trial correction in this analysis. Figure 5.12 shows the background distribution of the variable $\log_{10}(\min_k\{P(k)\})$ for the partial product method. The final TS distributions of the binomial and full product method are included in Fig. D.2 of Appendix D.

⁸In essence, the principle 'build a background TS distribution and use that to determine a p -value' is applied three consecutive times: first on the log-likelihood ratio of the individual GRBs, then on $\alpha(k)$, and finally on $\mathcal{P}(k)$.

⁹To further illustrate the difference between the three methods, we refer the reader to Fig. D.1 in Appendix D, where the distribution of p -value ratios is shown for the same signal trials.

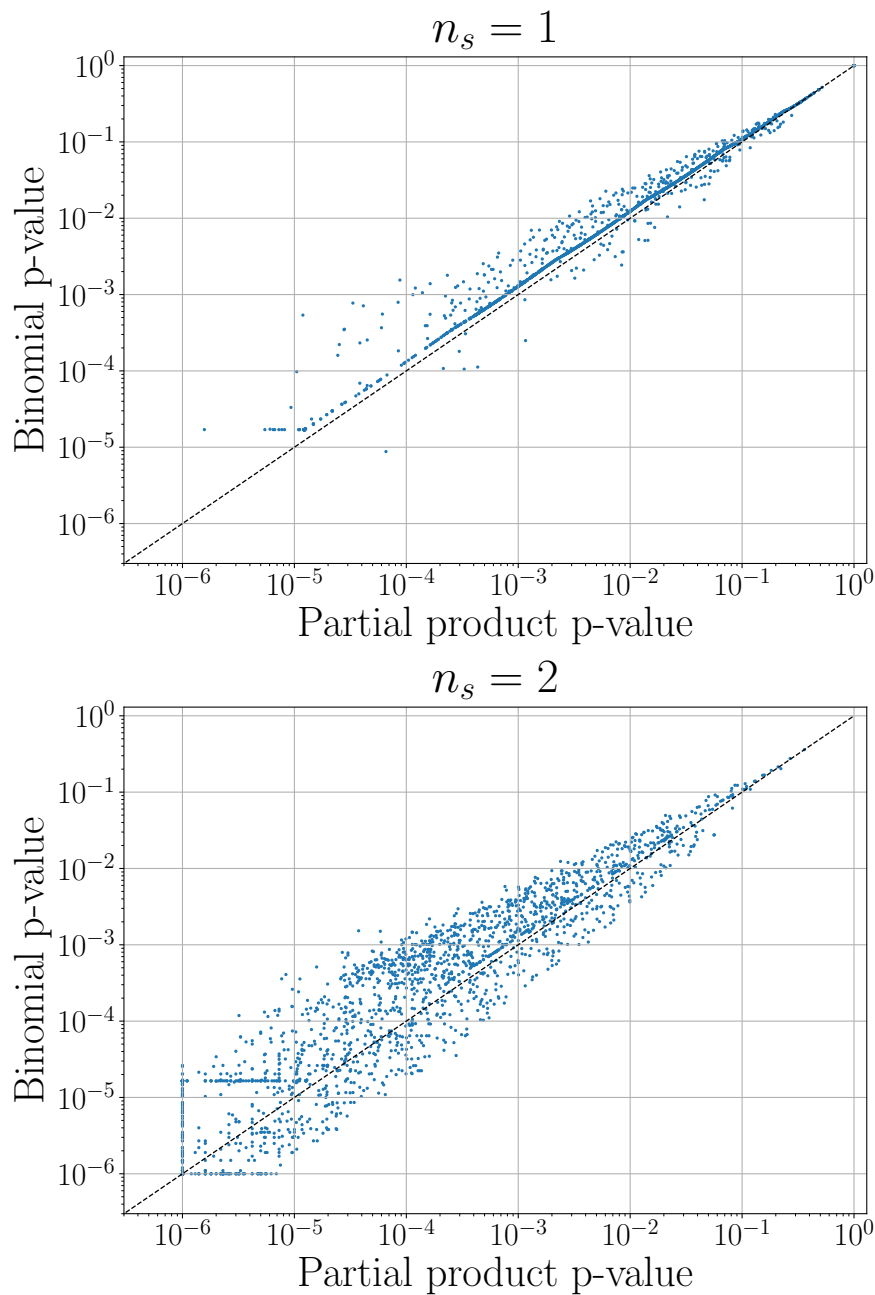


FIGURE 5.10: Each dot represents the final trial-corrected p -values of a single pseudo experiment. On the x -axis, the result is shown using the partial product method, while the y -value shows the result from the binomial method. Points which lie above the diagonal line correspond to trials for which the partial product method produces the most significant result. The upper and lower figure correspond to trials in which one and two signal event are injected, respectively.

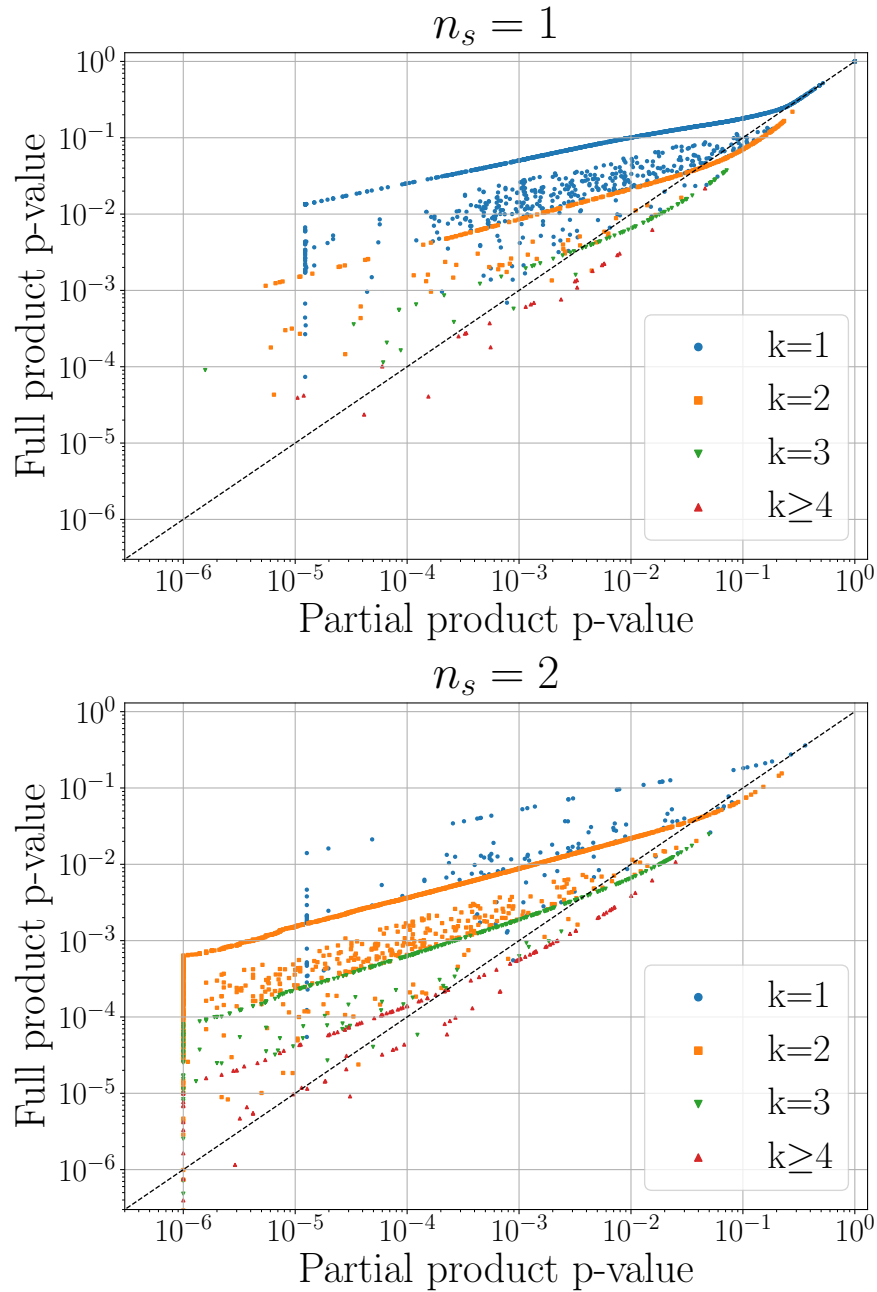


FIGURE 5.11: Same as Fig. 5.10, but comparing the performance of the partial product and full product method. Points are coloured and shaped based on the value of k used in the partial product method to highlight the origin of the features in the graph.

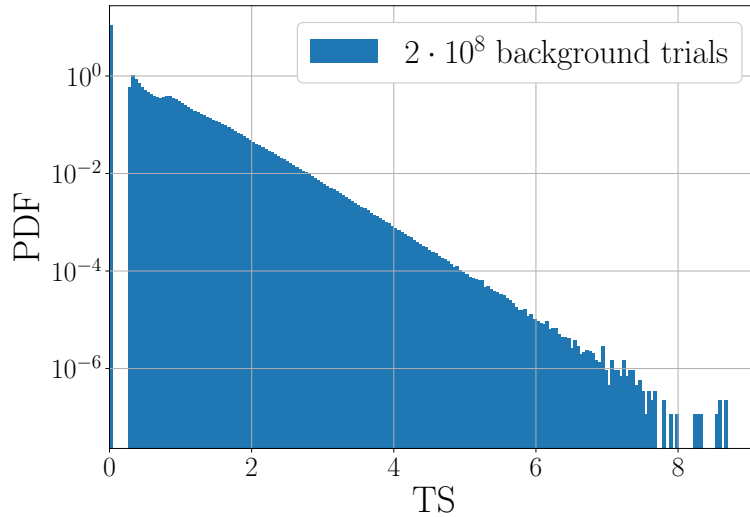


FIGURE 5.12: Test statistic distribution of background trials corrected using the partial product method. The first bin contains 47.8% of all trials. TS values larger than zero cannot be smaller than $-\log_{10}(p)$, where p is the probability that at least one of the 133 TS values is non-zero. As a result, the smallest non-zero TS value corresponds to $-\log_{10}(0.522) \sim 0.28$.

Sensitivity & discovery potential. Having specified the analysis procedure, it remains to characterise its performance. Figure 5.13 shows the fraction of trials for which the final trial-corrected TS values exceeds the median ($TS = 0.301$) of the background distribution. By fitting a sigmoid of the form

$$f(x) = \frac{c_1}{1 + e^{-c_2 \cdot (x - c_3)}} + c_4, \quad (5.10)$$

in which c_i are the free parameters, the point is identified at which the sensitivity criterion is satisfied. 90% of all trials exceed the median TS value when the average number of injected signal events corresponds to 1.679. From the discussion in 5.2.2 (see also Fig. 5.4), it follows that the analysis sensitivity is thus close to optimal.

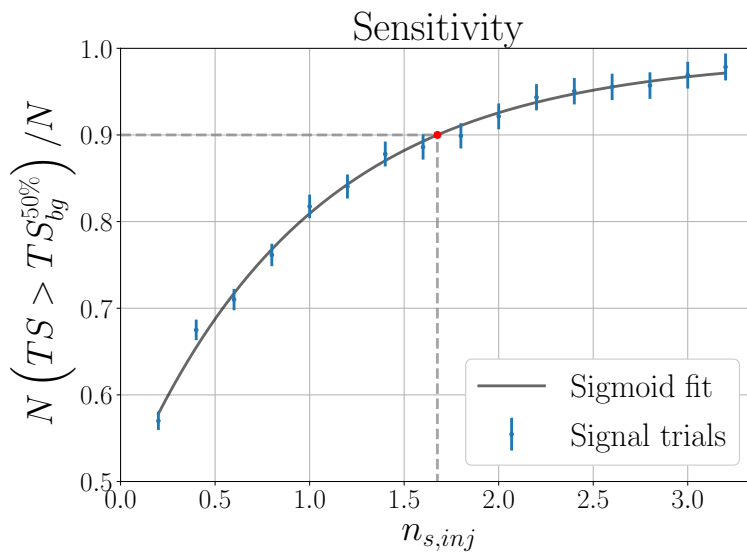


FIGURE 5.13: A sigmoid fit to signal trials is used to determine the sensitivity threshold ($n_{s, inj} = 1.679$) of the analysis.

Similarly, the discovery potential threshold of the analysis can be determined. Fitting the sigmoid function from Eq. (5.10) to signal trials, the average number of signal events from which 50% of all trials exceeds the 5σ threshold ($TS \geq 6.962$) is found to correspond to 3.678 as shown in Fig. 5.14.

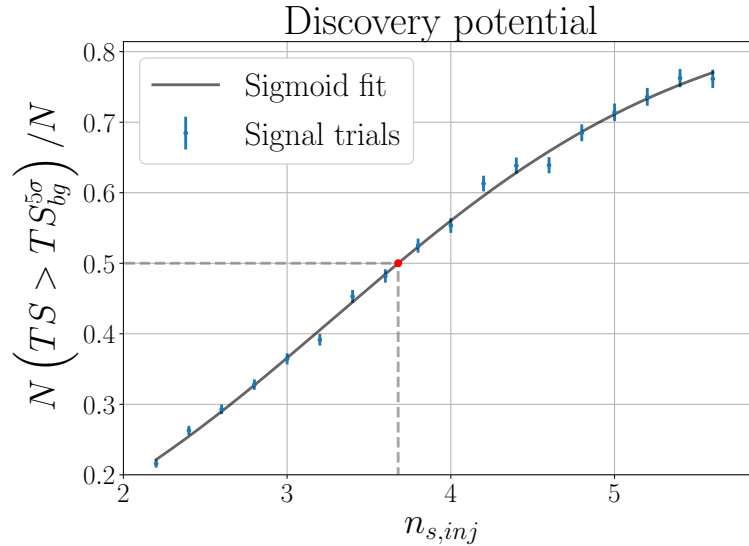


FIGURE 5.14: A sigmoid fit to signal trials is used to determine the discovery potential threshold ($n_{s,inj} = 3.678$) of the analysis.

5.3.2 Generic stacking search

In the GBM coincidence study, a search was made to identify neutrinos that arrive in time with observed gamma-ray precursors. This enabled a well-targeted search with very-low backgrounds. As a downside, only GRBs for which Fermi-GBM recorded a gamma-ray precursor could be analysed, limiting the GRB sample to 133 bursts. Precursors are by definition dimmer than the prompt emission. The non-observation of a precursor hence does not exclude its presence, as the burst might simply be too far away for the precursor to be resolvable over the background. A second analysis, called the ‘generic stacking search’, is therefore performed. This analysis looks for GRB precursor neutrinos, regardless of whether or not the GRB was preceded by precursor gamma-ray activity. As will be motivated below, a generic 250 s time window is examined for each burst. A second difference with the GBM coincidence study is that this analysis makes use of a stacking TS (see 5.2.4). As a consequence, the analysis is restricted to well-localised GRBs.

GRB sample. Starting from all GRBs in the GRBweb catalogue (see 1.2), every burst is selected that falls inside the time range of the IceCube GFU data and was localised to an uncertainty $\sigma < 1.5^\circ$. These criteria result in a selection of 872 GRBs. An overview of the properties of these bursts is given in Tab. D.2 of Appendix D. This selection includes the 33 well-localised GRBs from the GBM coincidence study.

Time windows. When analysing the properties of gamma-ray precursors in 3.4.2, an important result was that the time delay between the start of the precursor emission and the start of the prompt phase is less than 250 s for $> 95\%$ of all precursors. This motivates the use of a 250 s time range in this analysis to look for GRB precursor neutrinos. The 250 s time window is selected such that it ends at the start of the prompt phase, which is taken to be the start of the burst’s T100 interval in GRBweb. Aside from this experimental argument, the time window is also chosen based on theoretical motivations. Several models suggest that

precursor neutrinos from choked jets will precede the prompt phase by 10 – 100 s [269, 333]. A 250 s interval thus corresponds to a conservative choice. If no excess events are observed, our results will therefore be able to directly constrain these models.

TS distribution. Figure 5.15 shows the background TS distribution when applying the stacking formalism from 5.2.4 to the 872 bursts in our sample. The majority of background trials (98.9%) have a TS value of zero. Considering only strictly positive values, the TS distribution is observed to closely follow a χ^2 -function. This feature is expected from Wilks' theorem [485]. Assuming a TS which is defined as two times the log-likelihood ratio, where the null hypothesis is a special case of the alternative hypothesis, Wilks' theorem states that the background TS distribution will approach a χ^2 -function as the number of events that contributes to the likelihood goes to infinity¹⁰. The χ^2 -function is predicted to have a degree of freedom, f , equal to the dimensionality difference between the alternative and null hypothesis. Performing a χ^2 -fit to the background trials, as shown in Fig. 5.15, the fitted degree of freedom $f = 0.929$ is found to be in close agreement with the value $f = 1$ expected from Wilks' theorem.

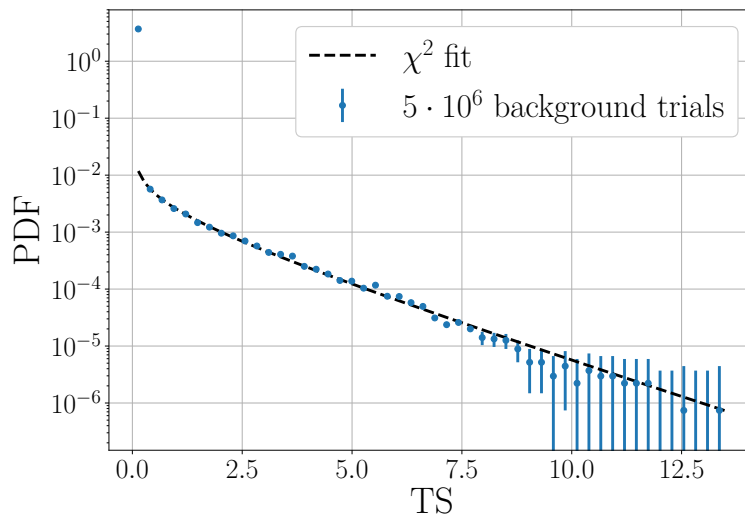


FIGURE 5.15: Background TS distribution in the generic stacking search. 98.9% of all events fall into the first bin.

Fit bias. Similar to the GBM coincidence study, a check is performed to verify that the injected number of signal events is correctly recovered by the TS. Figure 5.16 shows the distribution of the fitted number of signal events as a function of the injected number of signal events. A slight conservative bias is observed, causing the true number of signal events to be underestimated. Such biases have also been observed in similar IceCube analyses when stacking a large number ($N \gtrsim 100$) of sources [486].

To further study this effect, signal events were with injected with spectral indices corresponding to $\gamma_{inj} = 1.5; 2.5; 3.0$. For a harder spectral index (e.g. $\gamma_{inj} = 1.5$), the bias largely disappears. When softening the spectral index, signal events become less distinct from background events and the bias worsens. Figure D.3 in Appendix D shows the fit-bias for these additional three spectral indices, demonstrating the effect. Potential methods to remove the fit bias for $\gamma_{inj} = 2$ are currently still being investigated. Among others, these include replacing the spatial term in the likelihood, currently a two-dimensional Gaussian, by kernel-density estimators based on Monte Carlo simulations [486].

¹⁰In the GBM coincidence study, Wilks' theorem did not apply as the number of events contributing to the likelihood was generally at most a few.

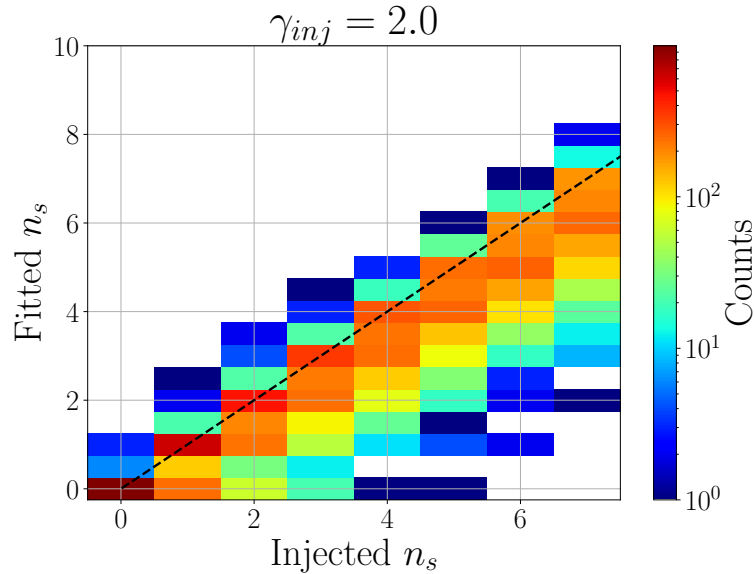


FIGURE 5.16: Distribution of the fitted number of signal events as a function of the true number of injected signal events. A slight conservative bias is observed, causing the number of signal events to be underestimated.

Sensitivity & discovery potential. The analysis performance is quantised by determining the sensitivity and discovery potential threshold. Contrary to the GBM coincidence study, the 5σ threshold of the background TS distribution is determined indirectly due to the large computational cost of running background trials. Based on Wilks' theorem, the 5σ significance threshold is therefore derived from a χ^2 -fit to the background TS distribution (see Fig. 5.15). Figure 5.17 and 5.18 illustrate how the required number of signal events is found from a sigmoid fit, Eq. (5.10), to signal trials. To reach the sensitivity and discovery potential threshold, an average of 3.048 and 3.124 signal events need to be injected, respectively. These thresholds were also determined for the spectral indices $\gamma_{inj} = 1.5; 2.5; 3.0$. The results of this study, as further detailed in D.2.3 of Appendix D, are shown in Tab. 5.1.

TABLE 5.1: Average number of signal events required to reach the sensitivity and discovery potential threshold. For softer spectral indices, signal events become less distinct from background events, increasing the threshold.

Spectral index (γ_{inj})	1.5	2.0	2.5	3.0
Sensitivity (n_s)	2.496	3.049	3.930	4.964
Discovery potential (n_s)	1.947	3.124	5.111	7.493

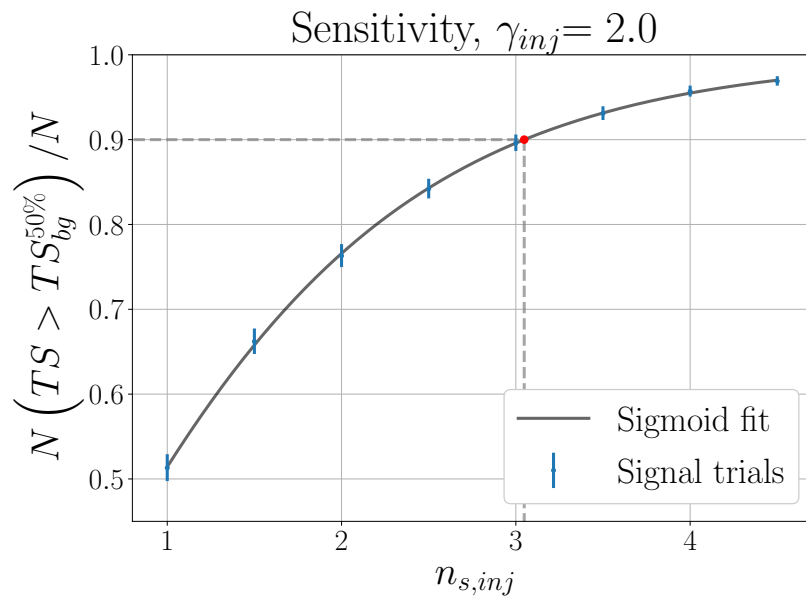


FIGURE 5.17: Based on a sigmoid fit to signal trials, the analysis sensitivity is found to correspond to $n_{s,inj} = 3.048$ for an E^{-2} spectrum.

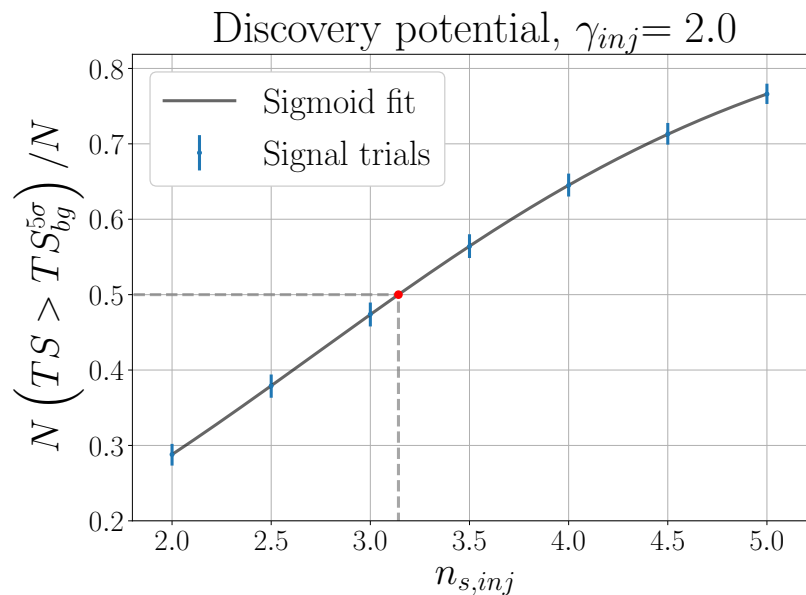


FIGURE 5.18: A sigmoid fit is applied to signal trials to determine the discovery potential threshold, $n_{s,inj} = 3.124$, for an E^{-2} spectrum.

5.3.3 Combined result

Both the GBM coincidence study and the generic stacking search result in a single p -value. Out of these two, the most significant p -value, p_m , will be selected. A trial-correction factor based on the binomial procedure will then be applied to correct this result. Considering the case where $N = 2$ and $k = 1$ in Eq. (5.9), it follows that

$$p_f = 2p_m - p_m^2, \quad (5.11)$$

where p_f is the final, corrected p -value of the two analyses.

5.4 Systematic uncertainties

In the previous section, simulated signal events were used to characterise the analysis performance. Model parameters and assumptions that go into these simulations unavoidably introduce a systematic uncertainty. The same holds true for event reconstruction algorithms. Several IceCube studies [442, 466, 487] have been performed to investigate the influence of systematic uncertainties on the final analysis result. An overview is given below on the main parameters that affect the analysis performance, as identified in a related GRB study that made use of the same event sample [466].

Ice parameters. To model the propagation of Cherenkov photons in IceCube, a parametrisation of the South pole ice is required. Photon propagation models rely on two main parameters. These are the effective scattering and absorption length as a function of the photon wavelength (see Fig. 4.15). Experimental studies using LED flashers indicate that the relative uncertainty on both the scattering and absorption length is $\lesssim 10\%$. Particularly, shorter absorption lengths can deteriorate analysis sensitivities, as less photons will be able to reach the DOMs. Varying the effective absorption and scattering length by $\pm 10\%$ in the simulation of signal events has shown that the flux to which the analysis is sensitive can vary by $\sim 5\%$.

DOM efficiency. A second parameter that introduces a systematic uncertainty is the efficiency with which DOMs can detect photons. Lower efficiencies will result in less photon counts per event. Given that the IceCube GFU selection relies on several charge cuts, this would imply that less events enter into the sample. Secondly, the reduced number of photons would also have an adverse effect on the performance of event reconstruction algorithms. Event energies would be underestimated, implying that signal events would receive a lower weight in the likelihood. Assuming a conservative relative uncertainty of 10% and propagating this effect into the final event uncertainty, it has been shown that the analysis sensitivity would worsen by $\sim 4\%$.

Cross section & matter density. Besides the ice model and DOM efficiency, a third important factor is the neutrino cross section. Figure 4.21 illustrated that the IceCube GFU sample is effectively sensitive to neutrinos with energies above 1 TeV. In this energy range, the neutrino cross section has not yet been verified in accelerator experiments, but only been inferred indirectly. Higher cross sections would lead to more neutrino interactions, increasing the event rate in the Southern Hemisphere. In the Northern Hemisphere, the effect would be twofold, as a higher cross section also implies a decreased probability that neutrinos will be able to propagate through Earth.

A related uncertainty stems from Earth's matter density. IceCube simulations rely on the PREM [458] to model the absorption probability of neutrinos as a function of declination. Additionally, the matter density in the vicinity of the detector is of particular importance.

The rate of up-going events scales linearly with the density of the bedrock that is located below the ice sheet. Lower bedrock densities would thus decrease the analysis sensitivity. Altogether, it has been estimated that the uncertainty on the neutrino cross section and matter density produces an uncertainty of $\sim 8\%$ in the event rate and thus the flux to which the analysis is sensitive.

Seasonal variations. Another effect that can influence the analysis performance is related to seasonal variations in the observed background rate. Temperature changes in the air lead to variations in atmospheric densities. These changes affect the rate at which muons and neutrinos are produced in atmospheric air showers. The effect is declination dependent and shows up as a long term fluctuation in the rate, with a period of one year. Deviations from the median rate generally go up to $\pm 5\%$ at a given declination and do not exceed $\pm 10\%$ overall. This effect has been shown to affect the sensitivity by less than 5%.

Azimuthal symmetry. Background rates not only vary as a function of time, but also depend on azimuth. This is a purely artificial effect that is due to the symmetrical arrangement of the IceCube strings. The intrinsic rate at which background muons and neutrinos pass through the detector is uniform in azimuth, but reconstruction algorithms show a tendency to return azimuthal angles along directions in which the strings align¹¹. Deviations are typically within 5% of the median rate and are overall no larger than 18%. The effect on the sensitivity corresponds to 7%.

Total error. The total systematic uncertainty is obtained by quadratically summing the individual contributions listed above. It follows that, assuming an E^{-2} signal spectrum, these effects introduce a $\sim 14\%$ uncertainty on the flux to which the analysis is sensitive. As will become clear in the next section, this uncertainty does not affect the interpretation of our analysis results.

5.5 Results

5.5.1 GBM coincidence study

Coincidences. Applying the analysis to the unscrambled data, 28 neutrino candidate events are identified that arrive during the precursor time windows. Under the background hypothesis, 22.2 events¹² would have been expected. The observed count is thus consistent at 1.5σ with the expected background count.

Considering also spatial constraints, none of the 28 neutrino candidate events are found to be consistent with the localisation of their respective GRB. A best-fit p -value of $p = 1$ is thus obtained for every bursts. Consequently, the trial-corrected p -value also corresponds to $p = 1$. This result is therefore fully consistent with the background hypothesis, in which 47.8% of all trials also do not show an excess for any of the GRBs.

Post-unblinding checks. Additional checks were performed for the burst bn141029134. This GRB had a single neutrino which arrived on time, 0.32 s before start of the gamma-ray precursor. bn141029134 is one of the 33 well-localised GRBs in the sample, having a localisation uncertainty of $\sigma = 1^\circ$. However, after the unblinding it was noted that this IPN localisation is likely too optimistic. IPN located the GRB to a narrow but extended band on the sky [488], which is shown in Fig. 5.19. The only other localisation was by Fermi-GBM, corresponding to the HEALPix map shown in the same figure. Combining the IPN and

¹¹For analyses with large time durations, on the order of half a day or more, this effect averages out.

¹²A total time interval of 3344.53 s was scanned in which the expected background rate is 6.6 mHz

GBM measurement, a new spatial prior can be obtained by setting the weight of all pixels that fall outside the IPN ring to zero, and renormalising the sky map.

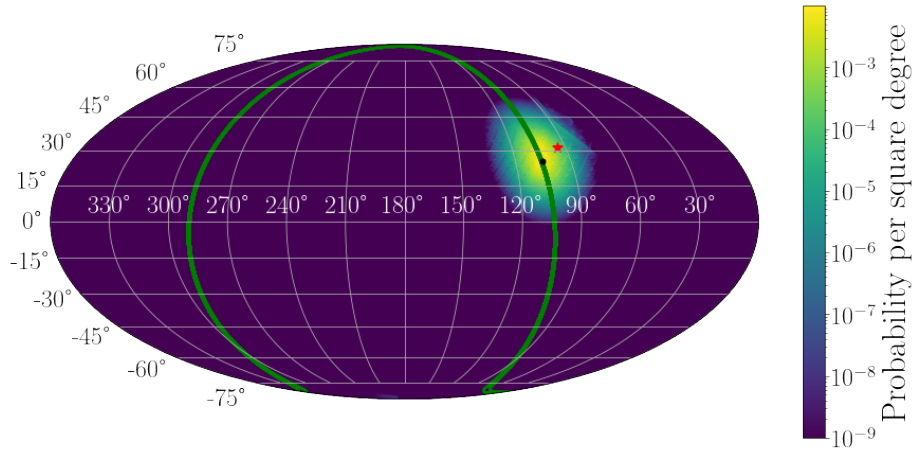


FIGURE 5.19: Localisation of the burst bn141029134. The colour scale shows the HEALPix prior by Fermi-GBM, while the green band is the 3σ containment interval by IPN. A single neutrino, denoted by a red star, was observed 11.3° away from the best-fit Fermi-GBM position (black dot).

Based on this newly defined spatial prior, the minimal angular separation between the GRB and neutrino is 9.8° . In terms of the angular uncertainty on the neutrino localisation ($\sigma_\nu = 1.6^\circ$), the minimal separation corresponds to 6.3σ . Repeating the analysis using the mixed GBM-IPN prior thus would have produced the same null result.

5.5.2 Generic stacking search

Coincidences. Starting again by considering those neutrino candidate events that arrive on time, 1439 coincidences are observed. This is highly consistent with the 1449 events expected under the background hypothesis. Selecting those events that spatially overlap within 5σ of their respective GRB, 5 out of the 1439 events remain. The spatial separation, estimated energy, and time delay of these 5 events are given in Tab. 5.2. Figure 5.20 shows the probability of observing N background events in temporal and 5σ spatial coincidence¹³. Similar distributions for a spatial significance of 1, 2, 3, and 4 standard deviations are shown in Fig. D.6 of Appendix D. From Fig. 5.20, it follows that the observed number of coincident events, $N = 5$, corresponds to the most likely outcome under the background hypothesis¹⁴. Applying the full likelihood framework, a best-fit TS value of zero is obtained. The final p -value of the analysis is therefore $p = 1$.

5.6 Flux upper limits

As no excess was observed, an upper limit is placed on the total time-integrated precursor neutrino flux of the analysed GRBs. A description of this limit is given below, detailing also how it can be converted to a diffuse GRB neutrino flux to allow a comparison to model predictions. Given that the generic stacking search used the largest GRB sample, it results in more constraining upper limits for GRB populations than the GBM coincidence study.

¹³Figure 5.20 was constructed by performing 10^3 trials on the unblinded data. In each trial, the GRB locations were randomised by setting them equal to positions randomly sampled on a unit sphere. Subsequently, the number of spatial and temporal coincidences was counted.

¹⁴98.9% of all background trials result in a TS value of zero.

TABLE 5.2: Properties of the neutrinos arriving in coincidence with GRBs in the generic stacking search. For each neutrino, the angular separation, angular uncertainty, a proxy for the event energy (MuEX) and the arrival time before the GRB is shown.

GCN name	$\Delta\theta$ ($^\circ$)	σ_θ ($^\circ$)	E (GeV)	Δt (s)
GRB 130131B	10.3	2.6	676	54.0
GRB 141220A	2.0	2.2	47	247.3
GRB 160314B	5.8	1.2	1023	158.4
GRB 160705B	5.2	1.5	794	91.5
GRB 160912A	6.1	2.3	525	106.4

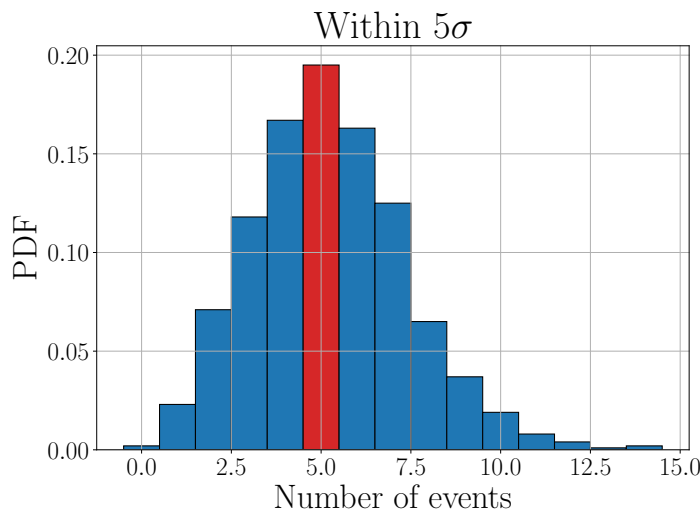


FIGURE 5.20: Probability that a background trial will result in N events (x -axis) that overlap with one of the 872 GRBs within a localisation error of 5σ . This probability density effectively corresponds to a Poisson distribution with mean $\mu = 5.3$. The red bin indicates the true, observed count.

Additionally, the fixed 250 s time window of the generic stacking search allows for a more direct comparison to model predictions. For these two reasons, the upper limits presented in this section are based on the generic stacking search.

5.6.1 Time-integrated upper limits

Upper limits are taken to be the flux that produces a TS value more significant than the unblinded result in 90% of all cases. For the analysis considered here, $TS_{\text{obs}} = 0$. The upper limit therefore corresponds to the sensitivity threshold of the analysis ($n_s = 3.049$, see Tab. 5.1). Flux upper limits are calculated assuming that each GRB has the same time-integrated flux, ϕ , at Earth and assuming an E^{-2} energy spectrum. To satisfy the sensitivity threshold, ϕ has to meet the following criterion

$$n_s = 3.049 = \sum_{i=1}^{872} \left[\int_0^{\infty} dE (\mathcal{A}_{eff}(\delta_i, E) \cdot \phi(E)) \right], \quad (5.12)$$

where the summation runs over all GRBs and $\mathcal{A}_{eff}(\delta_i)$ is the effective area at the declination of each burst. The total time-integrated flux of all GRBs is found to correspond to

$$\frac{dN}{dEdA} = \Phi = 872 \cdot \phi = 0.0902 \cdot E^{-2} \text{ GeV cm}^{-2}. \quad (5.13)$$

5.6.2 Differential upper limits

The limit given in Eq. (5.13) applies under the assumption that neutrinos produced by GRBs follow an $\phi \propto E^{-2}$ energy spectrum. A measure of the sensitivity can also be presented for arbitrary spectra. Rather than considering the total event count, n_s , the differential count per decade of energy is considered

$$\eta(E) \equiv \frac{dn_s}{d \log_{10}(E)}. \quad (5.14)$$

In Eq. (5.14), $\eta(E)$ is taken to be the number of neutrino events with an energy E required to obtain a strictly positive TS value in 90% of all cases. Figure 5.21 shows how $\eta(E)$ varies as a function of the neutrino energy.

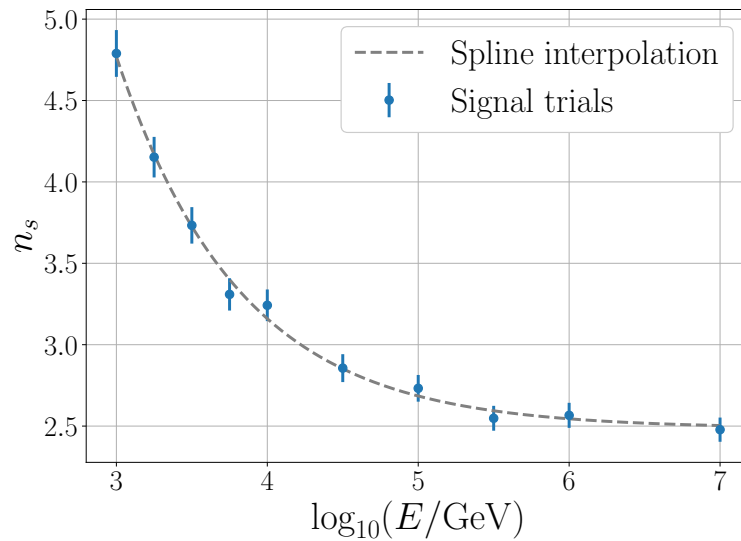


FIGURE 5.21: Signal events are injected over a narrow energy range $[E - \delta E, E + \delta E]$ to determine the number of events with energy E required to obtain a strictly positive TS value in 90% of all trials. A 4th order smoothing spline is used to obtain a continuous characterisation of the curve.

A conversion can be applied to determine the corresponding differential flux. As previously noted in Eq. (4.35), the time-integrated flux, effective area, and number of signal events are related to each other by

$$\frac{dn_s}{dE} = \mathcal{A}_{eff} \cdot \phi. \quad (5.15)$$

Combining this result with Eq. (5.14) and noting that

$$\frac{dn_s}{d \log_{10}(E)} = \ln(10) \cdot E \cdot \frac{dn_s}{dE}, \quad (5.16)$$

if follows that the differential time-integrated flux is given by

$$\phi = \frac{\eta}{\mathcal{A}_{eff} \cdot E \cdot \ln(10)}. \quad (5.17)$$

5.6.3 Diffuse GRB flux

The upper limits from 5.6.1 and 5.6.2 are limits on the combined flux of the 872 GRBs analysed in the generic stacking search. To compare to model predictions, the quantity of interest is the total neutrino flux from all GRBs in the Universe. A multiplicative factor is therefore required to scale up the flux limit on the analysed GRBs to a flux limit on all GRBs.

Historical conversion. Up to this analysis, all previous IceCube GRB studies have converted time-integrated flux limits to a diffuse flux through the following expression

$$\frac{dN}{dt d\Omega dEdA} = 667 \cdot \frac{1}{N_{GRB}} \cdot \frac{1}{\Delta t} \cdot \frac{1}{4\pi} \cdot \frac{dN}{dEdA}, \quad (5.18)$$

where the factor 4π averages the flux per unit steradian, Δt corresponds to 1 year, and N_{GRB} is the number of analysed GRBs. The value 667 is a proxy for the total number of GRBs per year that are beamed towards Earth. This estimate stems from the BATSE experiment, which was estimated to detect ~ 667 GRBs per year if the detector had a perfect field-of-view (FOV) and no dead time [30]. A downside to this approach is that it neglects the neutrino flux from GRBs that are too dim or too far away to be detectable. Using the number 667 could hence lead to upper limits which are too stringent. A new conversion method was therefore developed to allow for a more accurate diffuse flux calculation.

Novel conversion method. To determine the diffuse GRB flux, two effects need to be accounted for. The first is the sensitivity of the gamma-ray satellite. If the peak flux of a GRB is too low, it will be unable to trigger the satellite. Hence, these correspond to bursts that cannot be observed. The second effect relates to the efficiency of the detector. Due to a limited field-of-view, occultation, and dead time, gamma-ray telescopes will fail to observe some GRBs to which they are sensitive. Considering these two effects, the diffuse flux conversion becomes

$$\frac{dN}{dt d\Omega dEdA} = \epsilon_s \cdot \epsilon_e \cdot \frac{1}{\Delta t} \cdot \frac{1}{4\pi} \cdot \frac{dN}{dEdA}, \quad (5.19)$$

where ϵ_s and ϵ_e account for the detector sensitivity and efficiency, respectively, and $\Delta t \sim 7.16$ yr is the time range of the examined GRB-neutrino sample.

Calculating ϵ_s and ϵ_e requires that specific assumptions are made about the detector characteristics and GRB redshift evolution. This presents a challenge to the examined GRB sample, which contains both short and long bursts¹⁵ observed by a wide range of detectors. Limits will therefore be set on a subset of the analysed GRBs. Out of the 872 well-localised bursts, 657 GRBs were detected by the Swift-BAT detector. The selection is therefore first limited to those 657 Swift bursts. A second filter is then applied to only select the long Swift-BAT GRBs. This results in a final selection of 569 bursts.

Upper limits were previously (see 5.6.1 and 5.6.2) derived on the total time-integrated flux, Φ , of all 872 GRBs. It can conservatively be stated that the total flux of a subset of bursts cannot be larger than that of all bursts. The upper limit for all 872 GRBs will therefore be used directly as an upper limit on the flux of the 657 long Swift GRBs.

¹⁵Long and short burst do not follow the same redshift evolution as they originate from different progenitors.

Efficiency. As a first step, the efficiency will be characterised. The effective field-of-view¹⁶ of the Swift-BAT detector is $1.4/(4\pi) \sim 0.11$ [43]. In this FOV, Swift-BAT observes on average 82.67 long GRBs every year, of which $569/7.16 \sim 79$ have a localisation uncertainty smaller than 1.5° . It follows that the efficiency correction factor is given by

$$\epsilon_e = \frac{7.16 \text{ yr}}{569 \text{ GRBs}} \cdot (82.67 \text{ GRBs yr}^{-1}) \cdot \frac{4\pi}{1.4}. \quad (5.20)$$

$\epsilon_e \sim 9.3$ thus scales the time-integrated flux to that of all GRBs which could have been observed by Swift-BAT if the detector had no dead time and a 4π sr unobscured FOV.

Sensitivity. After correcting for the efficiency, a second correction factor is still required to account for the detector sensitivity. Canonical long GRBs are typically defined as bursts whose isotropic equivalent power output, L_{iso} , exceeds $10^{50} \text{ erg s}^{-1}$ [18]. Swift-BAT is estimated to have a trigger threshold of $f \geq 10^{-8} \text{ erg cm}^{-2} \text{ s}^{-1}$ [43]. The luminosity distance up to which Swift is able to observe all canonical long GRB is thus

$$d_L = \sqrt{\frac{L_{iso}}{4\pi \cdot f}} \sim 9.1 \text{ Gpc}. \quad (5.21)$$

This luminosity distance corresponds to a redshift $z \sim 1.29$. After applying the efficiency correction, the conservative assumption is made that the flux upper limit applies to all canonical long GRBs up to that redshift. It thus remains to determine how many GRBs outside a redshift $z = 1.29$ contribute to the neutrino flux at Earth.

Figure 5.22 shows a parametrisation by the Swift experiment [31] of the density of long GRBs as a function of redshift¹⁷. As can be observed, the vast majority of bursts occurs outside the redshift threshold $z = 1.29$. However, the flux contributed by a single GRB also drastically decreases the higher its redshift. These counteracting effects are accounted by the ξ factor [491], defined as

$$\xi_\gamma(z) \equiv \int_0^z dz' \frac{n(z') \cdot (1+z')^{-\gamma}}{\sqrt{\Omega_M(1+z')^3 + \Omega_\Lambda}}, \quad (5.22)$$

where $n(z')$ is the GRB density (see Fig. 5.22), γ the spectral index of the neutrino flux, and Ω_Λ and Ω_M are the value of the Universe's matter and dark energy density as measured by WMAP¹⁸, respectively.

The fraction of the total neutrino flux that originates from GRBs within a redshift z is given by

$$r(z) = \frac{\xi_\gamma(z)}{\xi_\gamma(\infty)}, \quad (5.23)$$

and is shown in Fig. 5.23. For a spectral index $\gamma = 2$, the sensitivity correction factor is $\epsilon_s = r^{-1}(z = 1.29) \sim 2.07$.

¹⁶The effective FOV includes a correction for the dead time of the detector.

¹⁷The redshift evolution of short GRBs is generally modelled by convolving the star-formation rate of massive stars with a time delay distribution to account for the duration of the inspiral process. Due to this time delay, the average redshift of short GRBs is smaller than that of long GRBs. Parametrising the redshift evolution of short GRB, however, remains challenging due to the limited number of short GRBs with known redshift [18, 489, 490].

¹⁸To be in line with the parametrisation used for the GRB density [31], the cosmological parameters are taken to be those by the WMAP mission [492]: $\Omega_m = 0.274$, $\Omega_\Lambda = 0.726$, and $H_0 = 70.5$, rather than the newer results obtained by the Planck mission [404].

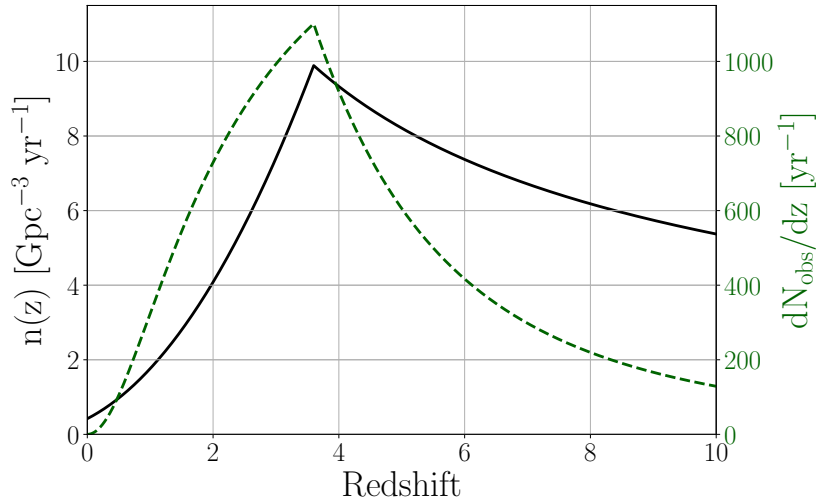


FIGURE 5.22: The black full line (left y -axis) shows a parametrisation based on Swift data [31] of the density of long, bright GRBs as a function of redshift. The actual number of GRBs, indicated by the dashed green line (right y -axis), scales linearly with the product of the density and the physical size of each redshift slice. At high redshifts, the size of the Universe rapidly decreases, causing the number of GRBs to drop more steeply than the GRB density.

5.6.4 Comparison to model predictions

Using the above described efficiency and sensitivity correction factors of the Swift-BAT detector, the integral and differential flux upper limits can be converted into a diffuse neutrino flux. These two flux upper limits are shown in Fig. 5.24. To provide a scale of reference, the diffuse astrophysical neutrino flux as measured by two IceCube analyses [364, 366] is also displayed in the figure.

Predicted neutrino flux. The upper limits from this analysis are compared to model predictions by Razzaque et al [333], which were previously discussed in Section 2.3. The model applies to long GRBs, and assumes that the core-collapse of the massive star progenitor produces a black hole that is enveloped by the remnant layers of the star. Flux predictions are shown in Fig. 5.24 for four possible configurations. Progenitors are simulated to either have an outer hydrogen (H) or helium (He) envelope. Two collision radii are then probed for each shell configuration.

Precursor neutrinos produced in this model are expected to arrive between 10 and 100 s before the light of the prompt phase, with a typical estimated time delay of ~ 30 s [333]. As such, the upper limits from the generic stacking search are ideally suited to constrain the predicted neutrino flux. Since all four model predictions have a unique energy spectrum, the spectra were implemented in the IceCube analysis software. This allowed determining the number of signal events required to obtain a strictly positive TS value in 90% of all cases. The upper limits thus obtained are displayed in Tab. 5.3.

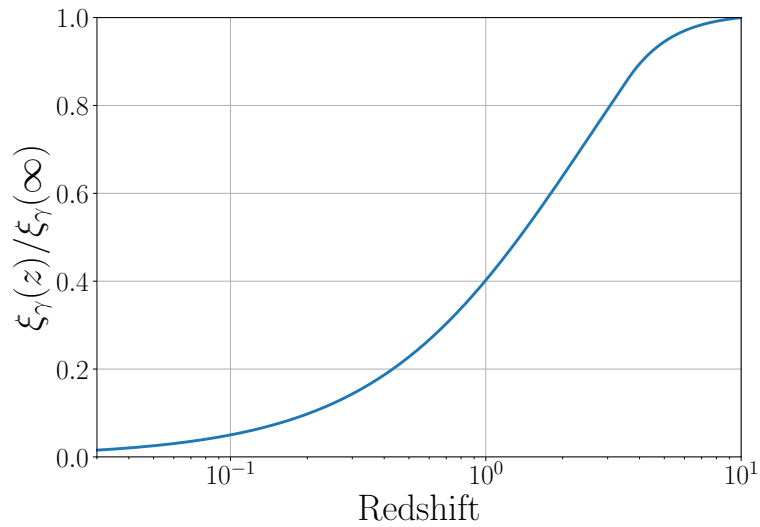


FIGURE 5.23: Relative ζ factor, defined in Eq. (5.22), as a function of redshift. The y -values indicates which fraction of the total neutrino flux comes from GRBs within a redshift given by the x -value.

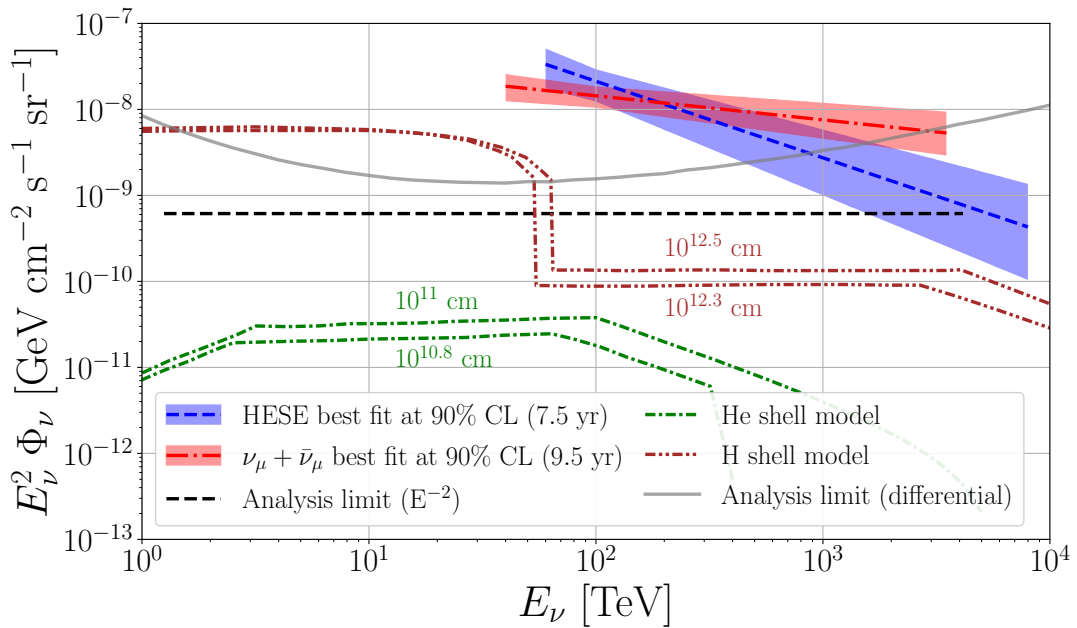


FIGURE 5.24: Flux upper limits from our analysis are compared to model predictions and the diffuse astrophysical neutrino flux. The integral upper limit (black dashed line) assumes an E^{-2} spectrum. Its energy range, from 1.25 TeV to 4.14 PeV, corresponds to the central interval that contributes 90% of all events (see Fig. 4.21). The differential upper limit, shown as a full grey line, is derived from the spline parametrisation in Fig. 5.21. Two measurements of the astrophysical diffuse neutrino flux by IceCube are shown. These correspond to the diffuse flux measured by the muon (red dash-dotted line [366]) and HESE (blue dashed line [364]) analysis. Finally, four model predictions [333] are shown for GRB progenitors that have either an outer hydrogen (brown lines) or helium (green lines) envelope. The distance measure next to the model predictions indicates the collision radius at which the particle acceleration is assumed to take place.

TABLE 5.3: Comparison between the number of signal events expected in the precursor stacking search based on model predictions [333] and the 90% upper limits placed by the analysis. The first column indicates the radius at which internal collisions take place in the model, and whether the progenitor is assumed to have an outer hydrogen (H) or helium (He) shell. For an H star progenitor, the allowed flux is below 10% of the predicted neutrino flux. In the case of an He outer layer, the analysis limit is a factor ~ 10 above the predicted flux.

Progenitor model	Model prediction (n_s)	Analysis upper limit (n_s)	ratio
H (12.5 cm)	36.0	3.37	0.094
H (12.3 cm)	35.8	3.37	0.094
He (11 cm)	0.296	2.90	9.8
He (11.8 cm)	0.182	3.08	16.9

Number of expected events. For each of the four predicted neutrino fluxes shown in Fig. 5.24, the number of expected signal events can be determined by multiplying the flux with the IceCube GFU effective area. The model predictions by Razzaque et al [333] assume that the diffuse flux is caused by 10^3 GRBs per year. A conversion factor

$$\alpha = \frac{872 \text{ analysed GRBs}}{(10^3 \text{ GRBs per year}) \cdot (7.16 \text{ years})} \quad (5.24)$$

is therefore multiplied with the total number of predicted neutrino events, to scale this value down to the number of events expected from the 872 analysed GRBs. These values are displayed in Tab. 5.3 under the column ‘Model prediction’.

Model constrains. The ratio between the upper limit and model prediction, shown in the last column of Tab. 5.3, indicates which fraction of the predicted neutrino flux is allowed by the analysis. Our results indicate that the predicted neutrino flux exceeds the 90% upper limit by a factor ~ 10 for H star progenitors. As such, this model can be fully excluded. In case of a He star progenitor, the 90% upper limit is a factor ~ 10 below the model prediction. Our analysis is thus not able to constrain this latter model.

Comparison to previous results. Two earlier IceCube studies placed limits on the H (12.5 cm) model. The earliest analysis [467] used IC22 data and resulted in an upper limit that was 10 times higher than the model prediction. In the second search [476], which used 4 years of IC86 data, the 90% upper limit constrained the allowed neutrino flux to 88% of the model prediction. This second search thus presented a factor 10 improvement with respect to the IC22 search. A slight tension was observed, but insufficiently so to exclude the model.

The generic stacking search presented in this thesis has improved the upper limit on the flux of GRB precursor neutrinos by roughly an order of magnitude. As such, it is now for the first time possible to fully exclude the model prediction that assumes a central engine surrounded by a remnant hydrogen shell. The scenario in which the progenitor has an outer helium shell remains plausible.

Chapter 6

Conclusions & Outlook

Gamma-ray bursts (GRBs) are among the most powerful astrophysical transients in the Universe. As was shown in Chapter 1, they are most commonly classified based on their duration. Long GRBs, generally lasting more than 2 s, are caused by the core-collapse of a massive star. Short bursts, whose duration is typically less than 2 s, are due to the collision of a neutron star (NS) with another compact object. In the half a decade since their discovery, a wealth of information has been gained about GRBs. At the same time, several key problems regarding their nature remain to this day unsolved¹. These include: finding out if the central engine is a black hole or a magnetar, determining the extent to which the outflow is magnetised, uncovering the processes via which energy is dissipated, and identifying the origin of GRB precursors. The research presented in this thesis relates to the last question. To obtain a better understanding of GRB precursors, two types of analyses were performed. One search studied precursors based on gamma-ray light curves of GRBs, while a second search was aimed at identifying coincident neutrino signals.

Gamma-ray precursor analysis. In the first study presented in this work (see Chapter 3), gamma-ray precursors were identified using data from the Gamma-Ray Burst (GBM) instrument on the Fermi telescope. Analysing the light curves of 2364 GRBs, 217 bursts were shown to be preceded by one or more episodes of precursor emission. Our results thus indicate that $\sim 9\%$ of all GRBs exhibit signs of precursor emission, consistent with previous studies. 139 of the 217 precursor bursts are newly identified. In this regard, our analysis presents a major gain for follow-up studies, providing an up-to-date precursor selection that includes all GBM detected bursts up to the start of the year 2020.

Examining short and long GRBs separately, our analysis showed a significant difference in the rate of observed precursor emission. When only including short GRBs, 4 of the 333 bursts ($\sim 1\%$) showed signs of precursor emission. All precursors to short GRBs occurred within 2 s of the prompt emission. Such short delays are consistent with model predictions of neutron star mergers, in which magnetic interactions or crust cracking can lead to energy dissipation on timescales $\mathcal{O}(0.1 - 1)$ s prior to the merger.

When only examining long GRBs, 213 out of 2031 bursts ($\sim 10\%$) had one or more precursor episodes. It was shown that the fraction of long GRBs with precursors increases when the sample is restricted to increasingly bright bursts. Therefore, the true fraction of long GRBs that has a precursor is likely higher than 10%. A novel feature uncovered by our analysis is that the observed quiescent time, defined as the period between the subsequent emission episodes, follows a bimodal distribution. The quiescent times were shown to be well-described by a two-component Gaussian function ($p = 0.36$) with peaks at (0.552 ± 0.059) s and (24.2 ± 1.2) s. In contrast, a single component Gaussian model could be rejected at a significance of 3.9σ . These two components indicate that at least two physical mechanisms

¹For an overview on open questions in GRB research, see e.g. [177] or [18].

are likely responsible for the observed precursors of long GRBs. Short time delay precursors in long GRBs are expected due to photospheric and/or shock-breakout emission. Longer quiescent times, on the other hand, point to models in which the central engine has multiple emission episodes, effectively turning off between the precursor and prompt emission. A prediction that follows from this interpretation is that a difference is expected in the energy spectrum of the two types of precursors. Short delay precursors are expected to have an energy spectrum closely resembling that of a black body, while long delay precursors are expected to follow a spectrum consistent with the prompt emission. An interesting follow-up study would thus be to perform a spectral analysis of the identified precursors. Other relevant follow-up searches would be to study the temporal features of precursor and prompt emission. Such a study, based on applying a Fourier transform to the data, is at the time of writing already ongoing.

As a final remark on the analysis, it is worth noting that this search was one of the first precursor analyses to include GRBs detected by an imaging air Cherenkov telescope (IACT) in its sample. Of the 4 IACT detected GRBs, 3 bursts were found to exhibit signs of precursor emission. As more GRB detections by IACT observatories become available by current and future experiments such as e.g. the Cherenkov Telescope Array (CTA) [493, 494], it will be interesting to explore whether this high relative precursor fraction (75%) holds up.

Neutrino coincidence study. Precursors present an excellent candidate for neutrino coincidence studies. GRBs in general have been and to this day remain long sought for sources of astrophysical neutrinos. Several neutrino coincidence studies have been performed [257, 390–399, 439, 467–474, 476], but no significant neutrino excess has so far been observed. Previous coincidence studies primarily searched for neutrinos that arrive during the prompt phase of GRBs. However, as suggested in the literature [269, 333], neutrino production could predominantly take place during the optically thick precursor phase.

Two analyses were performed to search for neutrinos from GRB precursors. The first analysis looked for direct coincidences between gamma-rays and neutrinos using the precursor catalogue constructed in the Fermi-GBM study. This allowed for a very-low background search. A total of 133 GRBs with precursor emission were analysed. Consistent with the background expectation, no coincident neutrino events were observed. A slightly more generic search was performed in the second analysis. Rather than only including bursts for which a gamma-ray precursor was observed, all well-localised GRBs were examined. This led to a selection of 872 bursts. Based on the results from the Fermi-GBM analysis and model predictions, a generic 250 s time window was scanned for each burst. Five low-energy events were observed, fully consistent with the background expectation.

Both neutrino searches produced best-fit values indicating that none of the observed events are related to GRB precursors. These null results were therefore used to place an upper limit on the allowed flux of GRB precursor neutrinos. This flux was then compared to model predictions for a massive star progenitor with an outer hydrogen (H) shell or helium (He) shell. IceCube studies had previously reported a slight tension with the H-shell model, which predicts the highest neutrino flux. Upper limits from those analyses constrained the neutrino flux to 88% of the H-shell model prediction. Our results improve this upper limit to less than 9.4% of the predicted flux. The H-shell model can now thus be fully ruled out for the first time. Flux predictions for an outer He-shell are roughly two orders of magnitude below those of the H-shell model. An order of magnitude improvement in statistics will thus be needed to constrain the He-shell model.

Future observatories. The IceCube analyses presented in this work use over 7 years of data taken with the full 86 string detector configuration. As probing the He-shell model

requires an order of magnitude more data, new neutrino observatories will realistically be needed to test this model. An upgrade to the IceCube detector is currently planned for deployment in the 2022-2023 and 2023-2024 austral summer. Seven new strings will be added at the centre of the detector to increase IceCube's sensitivity to low-energy neutrinos. A much larger extension will thereafter be constructed with IceCube-Gen2, which will increase the instrument volume and thus the observed event rate of high-energy neutrinos by a factor ~ 10 [433, 435]. Aside from IceCube, new neutrino observatories are also being deployed in the Northern Hemisphere with KM3NeT [388] and Baikal-GVD [389]. KM3NeT in particular will offer a significantly improved sensitivity to the $\mathcal{O}(1 - 10)$ TeV neutrinos expected from the GRB precursor phase.

New experimental observatories are also planned in the field of gamma-ray astronomy. For instance, the SVOM satellite [62], planned to be launched in early 2023, is expected to significantly improve the sensitivity to dim GRBs that peak at low energies. The SVOM project will also feature dedicated ground-based telescopes that can instantly follow up on observed GRBs. These features make SVOM particularly suited for the identification of (nearly) choked burst. As argued in 1.6.1, choked GRB are expected to produce significantly higher neutrino fluxes than regular GRBs. Given that current GRB analyses typically include on the order $\mathcal{O}(10^3)$ bursts, it is very well possible that the signal of a few choked bursts in this sample is too diluted to produce a significant excess. Performing new analyses restricted to only candidate choked GRBs thus offers an exciting prospect in this regard.

Concluding remarks. Since the very start of high-energy neutrino astronomy, GRBs have been one of the main candidates considered as a source of astrophysical neutrinos. Various analyses have been performed, so far only producing null results. These analyses have thus led to upper limits on the allowed neutrino fluxes, constraining model predictions. However, only the most optimistic models can so far be constrained. While prompt upper limits can rule out single-zone emission models, the more realistic multi-zone models effectively remain unconstrained. Similarly, only precursor models that assume a remnant hydrogen envelope can so far be excluded. With the advent of new gamma-ray and neutrino observatories, it will become possible to probe the more realistic and so far unconstrained neutrino emission models over the coming years. Exciting times thus lie ahead!

Appendix A

Bayesian block algorithm

Method outline. The idea behind the BB algorithm will here be shortly outlined. For a detailed description, we refer the reader to [307, 340]. Consider a sorted array $[t_1, t_2, \dots, t_N]$ that contains the times at which the detector observed a gamma-ray photon. In total 2^{N-1} options exist to arrange the photons into bins. For instance, all photons could be placed in a single bin, each photon in its own individual bin or any possibility in between those two. Suppose now that we wish to compare two of these binning options or models, M_1 and M_2 . To determine which of these is more likely, the Bayes factor:

$$\mathcal{O} = \frac{P(M_1|DI)}{P(M_2|DI)} = \frac{P(D|M_1I)}{P(D|M_2I)} \cdot \frac{P(M_1|I)}{P(M_2|I)}, \quad (\text{A.1})$$

is introduced¹, where D denotes the data and I is the background information². If $\mathcal{O} > 1$, then the binning of M_1 outperforms that of M_2 and vice versa. If both models are a priori assumed to be equally likely, the second ratio in the right-hand-side of Eq. (A.1) is equal to 1. It thus remains to find a mathematical expression for the likelihood terms $P(D|M_iI)$.

For simplicity, it is assumed that the first model, M_1 , groups all the photons into a single bin. To calculate the likelihood, $P(D|M_1I)$, the observation of photons by the detector is described by a Bernoulli process. This is justified by the statement that TTE data by a NaI subdetector can be considered as a continuous collection of $2.6 \mu\text{s}$ intervals in which either one single or no photon is observed. If there are K such intervals, the local likelihood equals

$$P(D|M_1pI) = p^N(1-p)^{K-N}, \quad (\text{A.2})$$

where p is the chance that an interval contains a photon. For a Poisson process, the average rate λ of events is related to the probability p via³

$$p \approx 1 - e^{-\lambda t}. \quad (\text{A.3})$$

Assuming a prior for p that is uniformly distributed between 0 and 1 and using the result from Eq. (A.2), the likelihood becomes

$$P(D|M_1I) = \int_0^1 P(D|M_1pI) dp = \frac{N!(K-N)!}{(K+1)!} \equiv \phi(N, K). \quad (\text{A.4})$$

¹Equation (A.1) follows directly from Bayes' theorem, which states that $P(M|DI) = \frac{P(D|MI)P(M|I)}{P(D|I)}$.

²The background information corresponds to the knowledge of the allowed binning options, along with all other assumptions that are relevant to the considered binning model.

³The average time delay between the two subsequently observed photons is generally much larger than $2.6 \mu\text{s}$.

In this simple model, M_1 , there is only one free parameter that is integrated out, namely the height of the bin. In a slightly more complex model M_2 that has two bins, there will be three free parameters⁴: the height of the first bin, the height of the second bin and the change-point separating the two bins. To streamline the procedure, only discrete change-points are considered that correspond to the arrival time of a photon. Denoting the change-point n_{cp} by the index of the photon at which it occurs, the integral over n_{cp} becomes a discrete sum. For a prior of n_{cp} that is uniform in time, the resulting likelihood is

$$P(D|M_2I) = \frac{1}{t_N - t_1} \sum_{n_{cp}}^{N-1} \Delta t_{n_{cp}} \cdot \phi(n_{cp}, m_{cp}) \cdot \phi(N - n_{cp}, K - m_{cp}), \quad (\text{A.5})$$

where $\Delta t_{n_{cp}}$ is the time delay between subsequent photons and m_{cp} the index of the change-point in terms of the $2.6 \mu\text{s}$ bins. In Eq. (A.5), the property was used that the events in the two bins are fully independent of each other, allowing their contribution to be written as the product of two ‘single-bin likelihoods’. Given the expression in Eq. (A.5) and (A.4), the Bayes factor from Eq. (A.1) will determine which of these configurations provides the best result. This formalism can naturally be extended to include more than two bins. Once the model and thus the optimal number of bins has been determined, the location of the change-points and bin heights are then set to those that optimise the local likelihood of that model.

Practical implementation. Implementing a brute-force method to find the optimal configuration is computationally unviable as the number of possible configurations increases as $\mathcal{O}(2^N)$. However, an algorithm has been devised to find the optimal configuration in $\mathcal{O}(N^2)$ trials. Suppose that for a partial array $[t_1, t_2, \dots, t_k]$ that contains only the first k photons times, the optimal binning has been found⁵ for all k up to a certain index L . In the next step, where $L + 1$ photons are used, the likelihood will need to be calculated only $L + 1$ times. In particular, the configuration of the last bin needs to be determined. For instance, if the last bin is set to contain η photons, then the optimal configuration of the preceding $L + 1 - \eta$ photons and their contribution to the likelihood⁶ will have already been determined in one of the previous steps. Hence, the only configuration that need to be considered are $\eta \in [1, 2, \dots, L + 1]$. Repeating this procedure for N photons thus results in a method that is $\mathcal{O}(N^2)$.

Optimisation parameter. In the above derivation, the prior $P(M|I)$ for the number of bins was taking to follow a uniform distribution. For a realistic light curve, typically containing on the order $N \gtrsim 10^6$ photons, it is reasonable to state that the expected number of bins N_b should satisfy $N_b \ll N$. GRB analyses therefore generally use a geometric prior,

$$P(M|I) = P(N_b) = \frac{1 - \gamma}{1 - \gamma^{N+1}} \gamma^{N_b}, \quad (\text{A.6})$$

where $\gamma \in [0, 1]$. To optimise the value of gamma, the false alarm probability p_α is considered that the algorithm falsely reports a change-point in the data even though there is no signal present. Based on Monte-Carlo simulation, Scargle et al. found a numerical relation between γ and p_α [307]:

$$\ln(\gamma) = \ln(73.53 p_\alpha N^{-0.478}) - 4. \quad (\text{A.7})$$

⁴While adding more and more parameters can significantly boost the likelihood locally, an effective penalty arises as a larger parameter space will be scanned by the likelihood.

⁵If $k = 1$, the solution is trivially a single bin containing a single photon.

⁶This property essentially comes down to the characteristic illustrated by Eq. (A.5), namely that the likelihood is the product of independent terms that represent the likelihood of the individual bins.

In our analysis, Eq. (A.7) with $p_\alpha = 0.05$ is used to determine the prior distribution for the number of bins. It is worth noting that the optimal number of bins found by the BB algorithm is very robust against changes in γ , as demonstrated using both BATSE [307] and Fermi-GBM [292] data.

Appendix B

Modified background characterisations

When studying the relative count ratio of GRB precursors, defined by Eq. (3.4) in 3.3.5, eight bursts were found to have strongly deviating values. By examining the light curves of the individual subdetectors in more detail, we found that there were three instances in which our background characterisation procedure had included data from a time interval that likely includes a physical signal. These three light curves are shown in Fig. B.1.

A common feature can be observed for those three bursts. A 'background' point is included in between the precursor and prompt phase that lies significantly higher than the background rate at the start of the precursor emission and that at the end of the prompt phase. After observing this feature, these points were therefore removed from the background characterisation. In other words, the background rate was now solely determined based on data prior to the precursor phase and data after the prompt phase. Re-applying the relative count ratio test with the improved background characterisation, all three bursts are observed to pass criterion from Eq. (3.4).

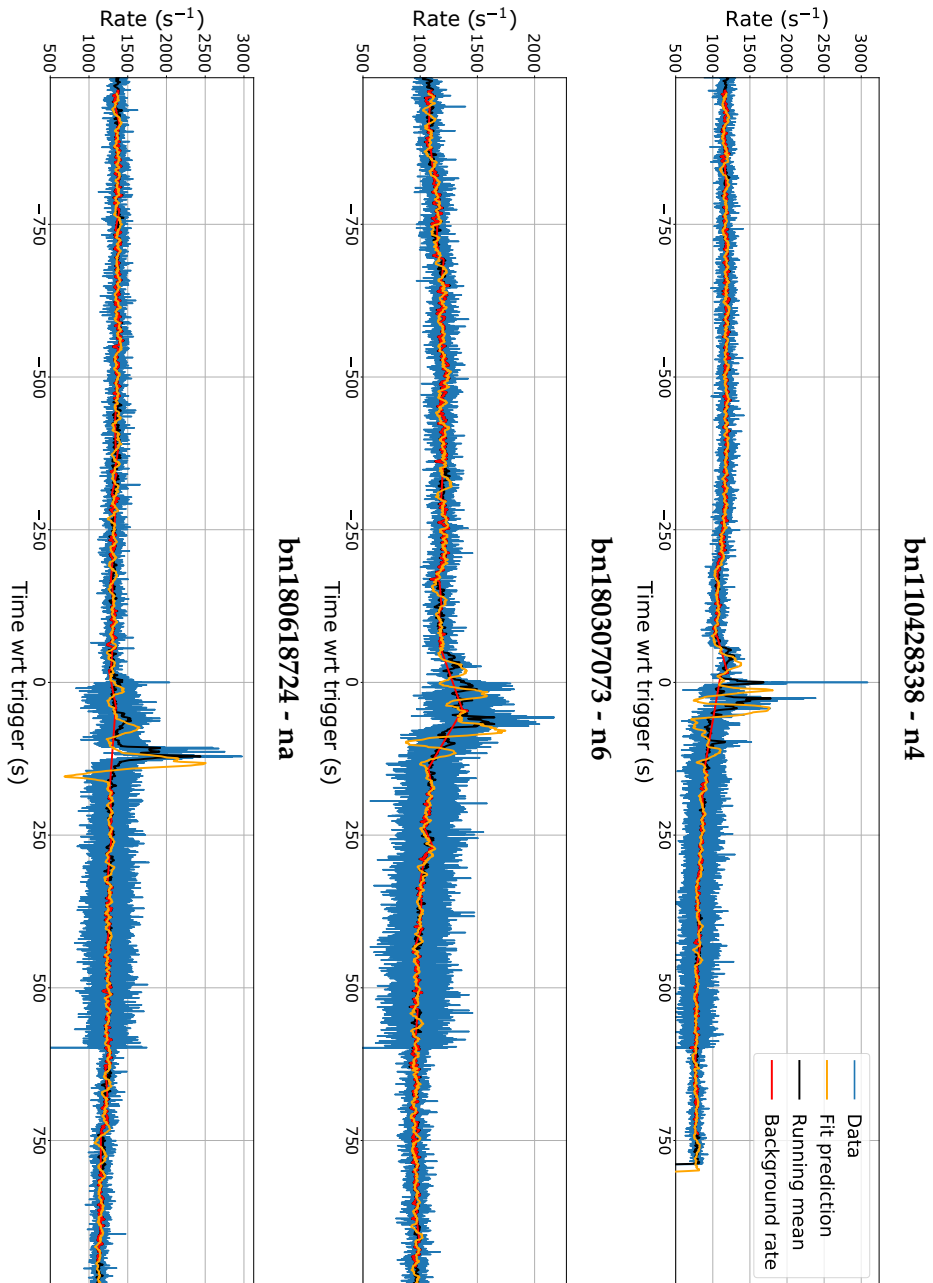


FIGURE B.1: Light curves of the three GRBs for which the excessive relative count ratio was caused by an inaccurate background characterisation.

Appendix C

GRB precursor catalogue

Precursor GRBs. As part of this thesis, we performed an analysis on the Fermi-GBM data that led to the identification of 244 precursor flashes in the light curves of 217 GRBs. A detailed description of the analysis method and results is given Chapter 3. To enable follow-up studies of the identified precursor events, an overview of the properties of the identified precursor emission episodes is presented in Tab. C.1.

TABLE C.1: Temporal properties of the identified precursors. For every GRB, the start time of the prompt emission t_{prompt} , the start time of the precursor emission with respect to t_{prompt} , the duration of the precursor emission, and the redshift are provided. The five potential false precursors with deviating count ratios are marked in *italic*. The four short GRBs are marked in **bold**. To access this table in a digital format and the light curves of these GRBs, please visit https://icecube.wisc.edu/~grbweb_public/Precursors.html.

GCN name	t_{prompt} (UTC)	$t_{precursor}$ (s)	Duration (s)	Redshift
bn080723557	13:22:55.412	-34.284	28.319	—
bn080807993	23:50:44.177	-11.612	1.032	—
bn080816503	12:04:39.495	-21.823	1.823	—
bn080818579	13:54:44.589	-20.361	5.596	—
bn080830368	08:50:22.699	-8.559	5.112	—
bn081003644	15:27:27.738	-11.363	4.320	—
bn081121858	20:35:31.671	-8.498	7.855	2.512
bn090101758	18:13:07.574	-86.950	6.082	—
bn090113778	18:40:38.870	-0.475	0.150	1.749
bn090117335	08:02:26.183	-24.653	1.296	—
bn090131090	02:09:43.196	-22.324	12.445	—
bn090309767	18:25:41.699	-36.134	6.122	—
bn090326633	15:10:16.566	-583.057	0.256	—
— —	— —	-580.753	5.376	—
bn090419997	23:55:38.751	-37.348	23.251	—
bn090425377	09:04:14.740	-44.805	2.705	—
<i>bn090428441</i>	10:34:37.862	-26.762	18.048	—
bn090502777	18:40:11.917	-37.539	3.065	—
bn090510016	00:23:00.368	-0.420	0.024	—
bn090602564	13:32:22.296	-1.242	0.683	—
bn090610723	17:22:58.385	-90.937	6.686	—
bn090618353	08:29:16.651	-50.628	28.946	0.540
bn090720710	17:02:57.665	-0.776	0.264	—

Continued on next page

Table C.1 continued: Properties of the identified precursors.

GCN name	t_{prompt} (UTC)	$t_{precursor}$ (s)	Duration (s)	Redshift
bn090810659	15:50:40.542	-94.594	43.262	—
bn090811696	16:41:54.351	-4.958	1.583	—
bn090814950	22:48:30.233	-43.778	18.577	—
bn090815946	22:44:41.956	-179.466	12.722	—
bn090820509	12:13:25.368	-8.951	4.124	—
bn090907017	00:24:10.767	-1.967	1.664	—
bn090929190	04:33:04.488	-0.571	0.122	—
bn091109895	21:28:49.421	-9.606	2.788	—
bn100116897	21:32:19.006	-83.382	6.319	—
bn100130729	17:30:19.867	-65.378	23.215	—
bn100204566	13:34:36.243	-16.948	15.677	—
bn100323542	13:01:32.005	-54.935	9.109	—
bn100326402	09:37:30.596	-55.808	32.512	—
bn100424876	21:03:54.875	-123.791	2.521	—
bn100517154	03:42:30.304	-22.365	1.362	—
bn100619015	00:22:24.001	-77.870	9.918	—
bn100625891	21:22:58.362	-15.645	4.029	—
bn100709602	14:28:25.731	-56.254	16.328	—
bn100718160	03:50:13.287	-25.036	6.090	—
— —	— —	-7.415	6.808	—
bn100730463	11:06:50.220	-41.808	12.805	—
— —	— —	-18.243	0.001	—
bn100827455	10:55:49.710	-0.442	0.079	—
bn100923844	20:15:31.462	-24.128	4.019	—
bn101030664	15:56:24.411	-69.697	31.744	—
bn101224578	13:53:30.861	-33.455	10.658	—
bn101227536	12:51:49.785	-3.895	3.646	—
bn110102788	18:55:41.740	-67.434	25.256	—
<i>bn110227229</i>	05:30:09.611	-111.145	21.120	—
bn110428338	08:07:18.821	-70.448	42.874	—
— —	— —	-18.748	13.398	—
bn110528624	14:59:12.297	-217.477	11.264	—
— —	— —	-35.653	13.654	—
— —	— —	-21.303	13.839	—
bn110725236	05:39:57.932	-16.720	7.619	—
bn110729142	03:30:47.288	-342.504	52.731	—
— —	— —	-185.188	51.556	—
bn110825102	02:26:58.702	-7.864	0.814	—
bn110903111	02:42:41.553	-187.466	22.062	—
bn110904124	02:58:55.085	-44.632	7.665	—
bn110909116	02:47:01.914	-4.433	1.670	—
bn110926107	02:34:30.183	-45.717	3.110	—
bn111010709	17:01:07.319	-34.749	31.018	—
bn111015427	10:15:22.011	-25.770	17.144	—
bn111228657	15:45:16.506	-46.111	10.496	0.714
— —	— —	-32.543	11.776	— —
bn111230683	16:23:06.415	-11.301	4.631	—

Continued on next page

Table C.1 continued: Properties of the identified precursors.

GCN name	t_{prompt} (UTC)	$t_{precursor}$ (s)	Duration (s)	Redshift
bn111230819	19:39:41.521	-9.814	1.304	—
— —	— —	-8.120	4.234	—
bn120118709	17:00:24.779	-6.498	5.475	2.943
bn120308588	14:06:05.511	-21.363	3.092	—
bn120319983	23:35:18.709	-17.629	5.551	—
bn120412920	22:05:51.344	-71.057	5.502	—
bn120504945	22:40:07.713	-1.369	0.799	—
bn120513531	12:44:14.932	-15.008	1.330	—
bn120530121	02:54:31.969	-50.475	7.974	—
bn120611108	02:35:54.181	-8.321	6.602	—
bn120710100	02:25:09.865	-113.086	4.857	—
bn120711115	02:45:52.633	-61.735	4.838	1.804
bn120716712	17:08:00.170	-176.365	5.383	2.486
bn120819048	01:09:20.076	-60.316	7.618	—
— —	— —	-30.405	1.638	—
bn121005340	08:10:54.001	-101.730	38.794	—
bn121029350	08:24:27.774	-11.090	8.798	—
bn121031949	22:50:21.029	-191.769	38.495	0.113
bn121113544	13:03:25.589	-45.362	31.652	—
bn121125356	08:32:50.026	-29.374	20.325	—
bn121217313	07:29:53.089	-714.103	65.792	0.800
bn130104721	17:18:12.706	-5.969	3.898	—
bn130106995	23:52:56.117	-33.325	17.558	—
bn130208684	16:24:43.858	-21.975	5.099	—
bn130209961	23:03:46.502	-5.102	4.597	—
bn130219775	18:36:47.745	-56.310	20.260	—
bn130310840	20:09:45.591	-4.755	1.194	—
bn130318456	10:57:50.305	-82.735	6.897	—
bn130320560	13:29:06.051	-159.315	42.085	—
bn130404840	20:10:25.030	-21.354	8.355	—
bn130418844	20:16:08.506	-87.313	16.452	—
<i>bn130504314</i>	07:32:36.037	-32.672	0.464	—
bn130623130	03:07:03.470	-26.744	1.821	—
bn130720582	13:59:14.940	-146.139	115.366	—
bn130813791	18:59:18.842	-5.810	1.680	—
bn130815660	15:51:22.993	-31.482	6.925	—
bn130818941	22:34:29.441	-70.463	8.706	—
bn130919173	04:09:40.924	-0.686	0.236	—
bn131014513	12:18:34.911	-20.917	2.089	—
bn131108024	00:34:43.981	-2.395	1.815	—
bn140104731	17:34:01.991	-120.439	66.204	—
— —	— —	-24.501	1.459	—
bn140108721	17:19:53.720	-71.900	11.570	0.600
bn140126815	19:33:40.215	-62.234	20.478	—
— —	— —	-24.368	14.110	—
bn140304849	20:25:37.760	-189.609	30.654	—
bn140329295	07:04:57.833	-19.534	0.630	—

Continued on next page

Table C.1 continued: Properties of the identified precursors.

GCN name	t_{prompt} (UTC)	$t_{precursor}$ (s)	Duration (s)	Redshift
bn140404030	00:43:22.825	-71.917	7.657	—
bn140512814	19:33:23.687	-98.421	11.788	0.725
bn140621827	19:50:14.988	-4.111	0.718	—
bn140628704	16:54:21.456	-66.005	4.910	—
bn140709051	01:13:51.906	-11.597	5.700	—
bn140714268	06:27:35.035	-109.468	27.544	—
bn140716436	10:29:26.513	-89.084	2.218	—
bn140818229	05:31:17.613	-69.604	10.233	—
bn140824606	14:34:24.964	-73.928	12.933	—
bn140825328	07:53:42.446	-59.289	11.821	—
— —	— —	-38.258	3.215	—
bn140917512	12:17:10.292	-4.434	3.940	—
bn141029134	03:14:24.675	-66.449	3.739	—
— —	— —	-41.574	6.940	—
bn141102536	12:51:40.471	-1.269	0.088	—
bn150126868	20:51:32.131	-55.037	13.019	—
bn150127398	09:32:49.909	-6.512	5.747	—
bn150226545	13:08:44.224	-202.152	1.028	—
— —	— —	-155.467	7.878	—
— —	— —	-41.188	16.158	—
bn150330828	19:53:59.254	-98.194	11.512	—
bn150416773	18:33:22.811	-824.534	42.496	—
bn150422703	16:52:31.997	-468.581	15.616	—
<i>bn150506398</i>	09:33:46.679	-116.285	27.791	—
bn150508945	22:40:36.620	-102.265	15.712	—
bn150512432	10:23:46.759	-86.467	43.029	—
— —	— —	-28.593	20.212	—
bn150522433	10:24:07.264	-19.511	7.822	—
bn150523396	09:30:14.993	-28.370	19.748	—
bn150627183	04:23:22.017	-458.665	3.072	—
bn150702998	23:56:45.108	-6.691	2.490	—
bn150703149	03:33:54.082	-13.280	0.008	—
bn150830128	03:04:38.646	-14.638	14.021	—
bn151027166	04:00:00.254	-96.360	40.571	0.810
bn151030999	23:59:47.634	-88.314	17.686	—
bn151211672	16:07:28.188	-151.405	26.022	—
bn160131174	04:12:52.609	-179.691	44.007	—
bn160201883	21:11:44.177	-1.590	0.968	—
bn160215773	18:36:08.605	-109.239	44.645	—
bn160219673	16:11:34.712	-110.393	12.546	—
bn160223072	01:45:54.364	-95.615	10.496	—
bn160225809	19:25:09.731	-48.115	23.215	—
bn160512199	04:45:57.662	-56.663	9.377	—
bn160519012	00:18:55.054	-83.260	3.345	—
— —	— —	-65.164	17.101	—
bn160523919	22:04:13.977	-38.410	5.424	—
bn160625945	22:43:14.090	-178.317	2.418	1.406

Continued on next page

Table C.1 continued: Properties of the identified precursors.

GCN name	t_{prompt} (UTC)	$t_{precursor}$ (s)	Duration (s)	Redshift
bn160724444	10:40:02.521	-7.324	1.790	—
bn160821857	20:36:22.642	-117.067	31.832	—
bn160825799	19:10:50.313	-1.449	0.599	—
<i>bn160908136</i>	03:16:48.679	-87.733	6.845	—
bn160912521	12:31:42.840	-57.422	36.635	—
— —	— —	-17.072	5.193	—
bn160919613	14:43:36.685	-24.729	0.498	—
— —	— —	-15.527	0.761	—
bn161105417	10:01:18.575	-30.217	12.749	—
bn161111197	04:44:50.633	-102.555	11.125	—
bn161117066	01:37:14.177	-103.474	77.027	1.549
bn161119633	15:11:02.131	-10.916	7.666	—
bn161129300	07:11:45.292	-5.373	0.040	0.645
bn170109137	03:21:41.186	-245.940	18.163	—
— —	— —	-217.040	6.377	—
bn170115662	15:54:01.580	-95.287	18.563	—
bn170209048	01:09:05.007	-28.188	8.228	—
bn170302719	17:15:41.992	-22.294	12.259	—
bn170323775	18:36:31.186	-12.963	12.697	—
bn170402961	23:03:40.777	-15.936	1.501	—
— —	— —	-12.442	0.230	—
bn170416583	14:00:34.758	-35.298	12.494	—
bn170514152	03:38:43.989	-5.895	0.678	—
bn170514180	04:19:54.177	-79.666	35.908	—
bn170830069	01:38:59.546	-19.395	5.987	—
bn170831179	04:18:03.061	-73.621	8.547	—
— —	— —	-43.400	6.309	—
bn170923188	04:31:15.015	-10.012	1.018	—
bn171004857	20:33:34.433	-2.263	1.378	—
bn171102107	02:34:03.231	-29.516	10.393	—
bn171112868	20:50:13.004	-198.952	8.192	—
— —	— —	-43.928	9.502	—
bn171120556	13:20:33.596	-31.460	4.221	—
bn171211844	20:17:18.932	-82.541	12.393	—
bn180124392	09:23:59.613	-4.987	0.611	—
bn180126095	02:16:29.991	-820.685	11.776	—
bn180307073	01:44:35.183	-39.275	23.342	—
bn180411519	12:28:28.650	-54.086	26.673	—
bn180416340	08:10:01.701	-36.541	10.291	—
bn180426549	13:10:59.907	-13.182	5.544	—
bn180618724	17:22:55.701	-61.611	26.238	—
bn180620354	08:29:22.735	-72.842	5.855	—
bn180710062	01:29:21.269	-49.933	13.542	—
bn180720598	14:21:26.039	-29.189	10.000	0.654
bn180728728	17:29:11.437	-15.219	10.040	0.117
bn180822423	10:08:32.522	-5.898	2.803	—
bn180822562	13:30:29.570	-128.070	7.513	—

Continued on next page

Table C.1 continued: Properties of the identified precursors.

GCN name	t_{prompt} (UTC)	$t_{precursor}$ (s)	Duration (s)	Redshift
— —	— —	-118.178	6.344	—
bn180906988	23:42:36.388	-2.471	1.039	—
bn180929453	10:52:35.121	-1.456	0.606	—
bn181007385	09:14:19.608	-23.373	3.996	—
bn181008877	21:04:29.161	-131.183	27.879	—
bn181119606	14:32:19.202	-2.566	1.798	—
bn181122381	09:09:04.964	-1.937	0.299	—
bn181203880	21:06:37.705	-6.482	0.870	—
bn181222279	06:42:52.975	-79.631	40.808	—
bn190114873	20:57:02.490	-5.573	1.942	0.420
— —	— —	-2.854	1.537	— —
bn190205938	22:31:11.876	-40.086	9.198	—
bn190228973	23:21:30.204	-15.148	7.989	—
bn190310398	09:33:20.756	-49.157	4.120	—
bn190315512	12:17:39.138	-366.193	6.912	—
bn190323879	21:05:17.600	-893.855	26.624	—
bn190324947	22:44:18.392	-17.146	2.474	1.171
bn190326314	07:32:13.823	-27.769	1.672	—
— —	— —	-18.099	2.115	—
bn190610750	18:00:04.042	-14.819	1.160	—
bn190611950	22:48:51.696	-62.594	20.082	—
bn190719624	15:00:01.045	-86.830	1.579	2.469
bn190806675	16:12:34.836	-1.664	1.188	—
bn190828542	12:59:58.210	-46.588	38.536	—
bn190829830	19:56:40.582	-47.965	5.565	0.079
bn190901890	21:21:37.555	-63.144	20.014	—
bn190930400	09:38:17.809	-162.830	40.308	—
bn191019970	23:18:48.942	-96.333	29.779	—
bn191026350	08:23:43.801	-5.943	4.110	—
bn191031025	00:39:28.692	-178.171	10.422	—
bn191101895	21:28:37.561	-44.664	1.903	—
bn191111364	08:44:52.025	-25.765	16.425	—
bn191225309	07:26:50.763	-94.689	2.024	—

Analysed GRBs. The precursor analysis performed on the Fermi-GBM data was applied on the light curves of 2684 GRBs. As detailed in Section 3.4, 2364 of those bursts showed signs of one or multiple emission episodes following our selection criteria. These 2364 GRBs served as the starting point of our precursor search, leading to the 244 identified events given in Tab. C.1. We here include a list of the names of all 2684 bursts to allow readers to identify those GRBs for which no precursor emission was found. In this list, the 320 bursts for which not a single emission episodes was found are marked in *italic*.

bn080714086, bn080714425, bn080714745, bn080715950, bn080717543, bn080719529,
 bn080723557, bn080723913, bn080723985, bn080724401, *bn080725435*, bn080725541,
 bn080727964, bn080730520, *bn080730786*, bn080802386, bn080803772, bn080804456,
 bn080804972, bn080805496, *bn080805584*, bn080806584, bn080806896, bn080807993,
 bn080808451, bn080808565, bn080808772, bn080809808, bn080810549, bn080812889,
 bn080815917, bn080816503, bn080816989, bn080817161, bn080817720, bn080818579,
 bn080818945, bn080821332, bn080823363, bn080824909, bn080825593, *bn080828189*,
bn080829790, bn080830368, *bn080831053*, *bn080831921*, bn080904886, bn080905499,
 bn080905570, bn080905705, bn080906212, bn080912360, bn080913735, *bn080916009*,
 bn080916406, bn080919790, bn080920268, bn080924766, bn080925775, bn080927480,
 bn080928628, bn081003644, bn081006604, bn081006872, bn081008832, bn081009140,
 bn081009690, bn081012045, bn081012549, bn081017474, bn081021398, *bn081022364*,
 bn081024245, bn081024851, bn081024891, bn081025349, bn081028538, *bn081101167*,
 bn081101491, bn081101532, bn081102365, bn081102739, *bn081105614*, bn081107321,
 bn081109293, bn081110601, bn081113230, *bn081115891*, bn081118876, *bn081119184*,
 bn081120618, bn081121858, bn081122520, bn081122614, bn081124060, bn081125496,
 bn081126899, bn081129161, bn081130212, bn081130629, bn081204004, bn081204517,
 bn081206275, bn081206604, bn081206987, bn081207680, bn081209981, bn081213173,
 bn081215784, bn081215880, bn081216531, bn081217983, bn081221681, bn081222204,
 bn081223419, bn081224887, bn081225257, bn081226044, bn081226156, bn081226509,
 bn081229187, bn081229675, *bn081230871*, bn081231140, bn090101758, bn090102122,
 bn090107681, bn090108020, bn090108322, bn090109332, bn090112332, bn090112729,
 bn090113778, bn090117335, bn090117632, bn090117640, bn090120627, bn090126227,
bn090126245, bn090129880, bn090131090, bn090202347, bn090206620, bn090207777,
bn090213236, bn090217206, bn090219074, bn090222179, bn090225009, bn090227310,
 bn090227772, bn090228204, bn090228976, bn090301315, bn090304216, bn090305052,
 bn090306245, *bn090307167*, bn090308734, bn090309767, bn090310189, bn090316311,
 bn090319622, bn090320045, bn090320418, bn090320801, bn090323002, bn090326633,
 bn090327404, bn090328401, bn090328713, bn090330279, bn090331681, bn090403314,
 bn090405663, *bn090409288*, bn090411838, bn090411991, *bn090412061*, bn090413122,
 bn090418816, bn090419997, *bn090422150*, bn090423330, bn090424592, bn090425377,
 bn090426066, bn090426690, *bn090427644*, bn090427688, bn090428441, bn090428552,
 bn090429530, bn090429753, bn090502777, bn090509215, bn090510016, bn090510325,
 bn090511684, bn090513916, bn090513941, bn090514006, bn090514726, bn090514734,
 bn090516137, bn090516353, bn090516853, bn090518080, bn090518244, bn090519462,
 bn090519881, bn090520832, bn090520850, bn090520876, bn090522344, bn090524346,
 bn090528173, bn090528516, bn090529310, bn090529564, bn090530760, bn090531775,
 bn090602564, *bn090606471*, *bn090608052*, bn090610648, bn090610723, bn090610883,
 bn090612619, bn090616157, bn090617208, bn090618353, bn090620400, *bn090620901*,
 bn090621185, bn090621417, bn090621447, bn090621922, bn090623107, bn090623913,
bn090625234, bn090625560, bn090626189, bn090626707, *bn090629543*, bn090630311,
 bn090701225, bn090703329, bn090704242, bn090704783, bn090706283, bn090708152,
 bn090709630, bn090711850, *bn090712160*, bn090713020, bn090717034, bn090717111,

bn090718720, bn090718762, bn090719063, bn090720276, bn090720710, bn090725838,
bn090726218, bn090730608, bn090802235, bn090802666, bn090804940, bn090805622,
bn090807832, bn090809978, bn090810659, bn090810781, bn090811696, bn090813174,
bn090814368, bn090814950, bn090815300, bn090815438, bn090815946, bn090817036,
bn090819607, bn090820027, bn090820509, bn090823133, bn090824918, bn090826068,
bn090828099, bn090829672, bn090829702, bn090831317, bn090902401, bn090902462,
bn090904058, bn090904581, bn090907017, bn090907808, bn090908314, bn090908341,
bn090909487, bn090909854, bn090910812, bn090912660, bn090915650, bn090917661,
bn090920035, bn090922539, bn090922605, bn090924625, bn090925389, bn090926181,
bn090926914, bn090927422, bn090928646, bn090929190, bn091002685, bn091003191,
bn091005679, bn091006360, bn091010113, bn091012783, *bn091013989*, bn091015129,
bn091017861, bn091017985, bn091018957, bn091019750, bn091020900, bn091020977,
bn091023021, bn091024372, bn091026485, *bn091026550*, bn091030613, bn091030828,
bn091031500, bn091101143, bn091102607, bn091103912, *bn091106762*, bn091107635,
bn091109895, bn091112737, bn091112928, *bn091115177*, bn091117080, bn091120191,
bn091122163, bn091123081, bn091123298, bn091126333, bn091126389, bn091127976,
bn091128285, bn091201089, bn091202072, bn091202219, bn091207333, bn091208410,
bn091209001, bn091215234, bn091219462, bn091220442, bn091221870, bn091223191,
bn091223511, *bn091224373*, bn091227294, *bn091230260*, bn091230712, bn091231206,
bn091231540, *bn100101028*, bn100101988, bn100107074, bn100111176, bn100112418,
bn100116897, bn100117879, *bn100118100*, bn100122616, bn100126460, bn100130729,
bn100130777, bn100131730, bn100201588, bn100204024, bn100204566, *bn100204858*,
bn100205490, bn100206563, bn100207665, bn100207721, *bn100208386*, bn100210101,
bn100211440, bn100212550, bn100212588, bn100216422, bn100218194, bn100219026,
bn100221368, bn100223110, bn100224112, bn100225115, *bn100225249*, bn100225580,
bn100225703, *bn100228544*, bn100228873, bn100301068, bn100301223, bn100302061,
bn100304004, bn100304534, *bn100306199*, bn100307928, bn100311518, bn100313288,
bn100313509, *bn100315361*, bn100318611, bn100322045, bn100323542, bn100324172,
bn100325246, bn100325275, bn100326294, bn100326402, bn100328141, bn100330309,
bn100330856, bn100401297, bn100406758, bn100410356, bn100410740, *bn100411516*,
bn100413732, bn100414097, bn100417166, *bn100417789*, bn100420008, bn100421917,
bn100423244, bn100424729, bn100424876, bn100427356, bn100429999, bn100502356,
bn100503554, *bn100504806*, bn100506653, bn100507577, *bn100510810*, bn100511035,
bn100513879, bn100515467, *bn100516369*, *bn100516396*, bn100517072, bn100517132,
bn100517154, bn100517243, bn100517639, bn100519204, bn100522157, bn100525744,
bn100527795, bn100528075, bn100530737, bn100604287, bn100605774, bn100608382,
bn100609783, bn100612545, bn100612726, bn100614498, bn100615083, *bn100616773*,
bn100619015, bn100620119, bn100621452, *bn100621529*, bn100625773, bn100625891,
bn100629801, bn100701490, bn100704149, *bn100706693*, bn100707032, bn100709602,
bn100713980, bn100714672, bn100714686, bn100715477, bn100717372, bn100717446,
bn100718160, bn100718796, *bn100719311*, bn100719825, bn100719989, bn100722096,
bn100722291, bn100724029, bn100725475, bn100727238, bn100728095, bn100728439,
bn100730463, *bn100802240*, bn100804104, *bn100805300*, bn100805845, bn100810049,
bn100811108, bn100811781, bn100814160, bn100814351, bn100816009, bn100816026,
bn100819498, bn100820373, bn100825287, bn100826957, bn100827455, bn100829374,
bn100829876, bn100831651, bn100902990, bn100905907, bn100906576, bn100907751,
bn100910818, bn100911816, *bn100915243*, bn100916779, bn100918863, bn100919884,
bn100922625, bn100923844, bn100924165, bn100926595, bn100926694, bn100929235,
bn100929315, bn100929916, *bn101002279*, bn101003244, bn101004426, bn101008697,
bn101010190, *bn101011707*, bn101013412, bn101014175, *bn101015558*, bn101016243,
bn101017619, bn101021009, bn101021063, bn101023951, bn101024486, *bn101025146*,

bn101025267, bn101026034, *bn101027230*, bn101030664, bn101031625, bn101101744,
bn101101899, *bn101102840*, bn101104810, bn101107011, bn101112924, bn101112984,
bn101113483, bn101116481, bn101117496, *bn101119685*, bn101123952, bn101126198,
bn101127093, *bn101127102*, bn101128322, bn101129652, bn101129726, bn101130074,
bn101201418, *bn101202154*, bn101204343, *bn101205309*, bn101206036, bn101207536,
bn101208203, bn101208498, bn101211485, bn101213451, bn101213849, bn101214748,
bn101216721, bn101219686, bn101220576, bn101223834, bn101224227, bn101224578,
bn101224614, bn101224998, bn101225377, bn101227195, bn101227406, bn101227536,
bn101231067, *bn110101202*, bn110101506, bn110102788, bn110105877, *bn110106893*,
bn110107886, bn110108977, bn110112934, *bn110117364*, bn110117626, bn110118857,
bn110119931, bn110120666, bn110123804, *bn110124784*, bn110125894, bn110128073,
bn110130230, *bn110131780*, bn110201399, bn110204179, *bn110205027*, *bn110205588*,
bn110206202, *bn110207470*, *bn110207959*, bn110209165, bn110212550, bn110213220,
bn110213876, *bn110217591*, bn110220761, bn110221244, bn110226989, bn110227009,
bn110227229, bn110227420, bn110228011, bn110228792, bn110301214, bn110302043,
bn110304071, bn110307972, bn110311812, *bn110316139*, bn110318552, bn110319628,
bn110319815, bn110321346, bn110322558, bn110328520, bn110331604, bn110401920,
bn110402009, bn110407998, bn110409179, bn110410133, bn110410772, bn110411629,
bn110412315, *bn110413938*, bn110415541, bn110420946, bn110421757, bn110422029,
bn110424758, bn110426629, bn110428338, bn110430375, bn110503145, bn110505203,
bn110509142, bn110509475, bn110511616, *bn110517453*, bn110517573, *bn110520302*,
bn110521478, bn110522256, bn110522296, bn110522633, bn110523344, bn110526715,
bn110528624, bn110529034, bn110529262, bn110529811, bn110531448, bn110601681,
bn110605183, *bn110605780*, bn110609185, bn110609425, bn110610640, bn110613631,
bn110616648, *bn110618366*, bn110622158, *bn110624906*, bn110625579, bn110625881,
bn110626448, bn110629174, bn110702187, bn110703557, bn110705151, bn110705364,
bn110706202, bn110706477, bn110706728, bn110706977, bn110709463, bn110709642,
bn110709862, bn110710954, bn110716018, bn110717180, bn110717319, bn110720177,
bn110721200, bn110722694, bn110722710, bn110725236, bn110726211, bn110728056,
bn110729142, *bn110730008*, bn110730660, bn110731465, bn110801335, bn110803783,
bn110806934, bn110809461, bn110812899, bn110813237, bn110817191, *bn110818860*,
bn110819665, bn110820476, bn110824009, bn110825102, bn110825265, bn110831282,
bn110901230, bn110903009, bn110903111, bn110904124, bn110904163, bn110904531,
bn110906302, bn110909116, *bn110911071*, *bn110916016*, bn110919634, bn110920338,
bn110920546, bn110921444, bn110921577, bn110921912, *bn110923481*, bn110923835,
bn110926107, bn110928180, bn110929187, bn110930564, *bn111001804*, bn111003465,
bn111005398, *bn111008992*, bn111009282, bn111010237, *bn111010660*, bn111010709,
bn111010899, bn111011094, bn111012456, bn111012811, bn111015427, bn111017657,
bn111018595, bn111018785, bn111022854, bn111024722, *bn111024896*, bn111025078,
bn111103441, bn111105457, bn111107035, bn111107076, *bn111109453*, bn111109873,
bn111112908, bn111113410, bn111114233, bn111117510, bn111117526, *bn111120556*,
bn111124308, bn111127810, bn111201599, bn111203054, *bn111203609*, *bn111207512*,
bn111208353, bn111216389, bn111220486, bn111221739, bn111222619, bn111226795,
bn111228453, bn111228657, bn111230683, bn111230819, *bn111231622*, bn120101354,
bn120102095, bn120102416, bn120105584, bn120107384, bn120109824, bn120111051,
bn120114433, bn120114681, *bn120117291*, bn120118709, bn120118898, bn120119170,
bn120119229, bn120119354, bn120120432, bn120121101, bn120121251, bn120122300,
bn120129312, bn120129580, bn120130699, bn120130906, bn120130938, bn120203812,
bn120204054, *bn120205285*, bn120206949, bn120210650, *bn120212353*, bn120212383,
bn120213606, bn120217808, bn120217904, bn120218276, bn120219563, bn120220210,
bn120222021, bn120222119, bn120223933, bn120224282, bn120224898, bn120226447,

bn120226871, bn120227391, bn120227725, bn120302080, bn120302722, bn120304061,
 bn120304248, bn120308588, bn120312671, bn120314412, bn120316008, bn120319983,
 bn120323162, bn120323507, bn120326056, *bn120327418*, bn120328268, bn120331055,
 bn120402669, bn120403857, bn120410585, bn120411925, bn120412055, bn120412920,
 bn120415076, bn120415891, bn120415958, bn120420249, bn120420858, bn120426090,
 bn120426585, bn120427054, *bn120427153*, bn120429003, bn120429484, bn120430980,
 bn120504468, bn120504945, bn120506128, bn120509619, bn120510900, bn120511638,
 bn120512112, bn120513531, bn120519721, bn120520949, bn120521380, bn120522361,
 bn120524134, bn120526303, bn120528442, bn120530121, bn120531393, bn120603439,
 bn120604220, bn120604343, bn120605453, bn120608489, bn120608777, bn120609580,
 bn120611108, bn120612680, bn120612687, bn120616630, bn120618128, bn120618919,
 bn120619884, bn120624309, bn120624933, bn120625119, *bn120629565*, *bn120701654*,
 bn120703417, bn120703498, bn120703726, bn120707800, bn120709883, bn120710100,
 bn120711115, bn120711446, bn120712571, bn120713226, bn120715066, bn120716577,
 bn120716712, bn120719146, *bn120727354*, bn120727681, bn120728434, bn120728934,
 bn120729456, bn120801920, *bn120805706*, bn120806007, bn120811014, bn120811649,
 bn120814201, *bn120814803*, *bn120817057*, bn120817168, bn120819048, bn120820585,
bn120822628, *bn120824594*, bn120827216, bn120830212, bn120830297, bn120830702,
 bn120831901, bn120905657, bn120907017, bn120908873, bn120908938, bn120909070,
 bn120911298, bn120913846, bn120913997, bn120914144, *bn120915000*, bn120915474,
bn120916085, bn120916173, bn120919052, bn120919309, bn120919816, bn120920003,
 bn120921877, bn120922939, bn120926335, bn120926426, *bn120926753*, bn121004211,
bn121005030, bn121005340, bn121008424, bn121011469, bn121012724, *bn121014638*,
 bn121019233, bn121023322, bn121027038, *bn121028280*, bn121029350, bn121031949,
 bn121102064, bn121104627, bn121109338, *bn121112806*, bn121113544, bn121116459,
 bn121117018, bn121118576, *bn121119579*, bn121122564, bn121122870, bn121122885,
 bn121123442, bn121124606, bn121125356, bn121125469, bn121127914, bn121128212,
 bn121202181, *bn121205507*, bn121210081, bn121211574, bn121211695, *bn121216419*,
 bn121217313, bn121220311, bn121221916, bn121223300, bn121225417, bn121229533,
 bn121231445, bn130104721, bn130106829, bn130106995, bn130109206, bn130112286,
 bn130112353, bn130114019, bn130115716, *bn130116415*, *bn130117087*, bn130118482,
 bn130121835, bn130123843, *bn130127299*, bn130127743, bn130131511, bn130204484,
 bn130206482, bn130206817, bn130208684, bn130209961, bn130213905, *bn130214137*,
 bn130214800, bn130215063, bn130215649, bn130216790, bn130216927, bn130217688,
 bn130218261, bn130219197, bn130219626, bn130219775, bn130220964, bn130224370,
 bn130228111, bn130228212, bn130304410, bn130304658, bn130305486, bn130305526,
 bn130306991, bn130307126, *bn130307238*, bn130310840, bn130314147, bn130318456,
 bn130320560, bn130324042, *bn130325005*, bn130325203, bn130327350, bn130331566,
bn130403866, bn130404428, bn130404840, *bn130404877*, bn130406288, bn130406334,
 bn130406354, bn130407800, bn130408653, bn130409960, bn130416690, bn130416770,
 bn130418844, bn130420313, bn130420343, bn130420422, bn130420539, bn130425327,
 bn130427324, bn130502327, bn130502743, *bn130503214*, bn130504314, bn130504978,
 bn130505955, bn130507545, bn130509078, bn130509839, bn130510877, bn130514560,
 bn130515056, bn130515430, bn130515755, bn130517781, bn130518551, bn130518580,
 bn130522510, bn130523095, bn130523198, bn130527627, bn130528503, bn130528695,
 bn130530719, bn130604033, bn130606316, bn130606497, bn130609129, bn130609902,
 bn130610133, bn130611538, bn130612141, bn130612456, bn130614997, bn130615398,
 bn130617564, bn130620498, bn130622615, bn130623130, bn130623396, bn130623488,
 bn130623699, bn130623790, bn130624093, bn130626452, bn130626596, bn130627372,
 bn130628531, bn130628860, bn130630272, bn130701060, bn130701761, bn130702004,
bn130702951, bn130704560, bn130705398, bn130706900, *bn130707505*, bn130708488,

bn130715906, *bn130716352*, bn130716442, *bn130717734*, bn130720116, bn130720582,
bn130722021, bn130722990, bn130723092, bn130725527, bn130727698, bn130730243,
bn130802730, bn130803419, bn130804023, bn130808253, bn130811186, bn130813791,
bn130815420, bn130815660, bn130816074, bn130818941, bn130819394, bn130821674,
bn130828306, bn130828808, bn130829672, *bn130830864*, bn130830921, bn130831058,
bn130903033, bn130905377, bn130906222, bn130906435, bn130907760, *bn130908677*,
bn130909817, bn130912358, bn130919173, *bn130919352*, bn130919985, bn130924255,
bn130924910, bn130925164, bn130925173, bn130925546, bn130928537, *bn130929375*,
bn131002288, bn131004904, *bn131006367*, bn131006840, bn131008858, bn131011741,
bn131014215, bn131014513, bn131018673, *bn131020113*, bn131021352, *bn131024900*,
bn131028076, bn131029973, bn131029990, *bn131030653*, bn131030791, bn131031482,
bn131102622, bn131105087, bn131108024, bn131108862, bn131110373, bn131113483,
bn131117766, bn131118958, bn131119781, bn131122490, bn131123543, bn131125689,
bn131126163, *bn131127480*, bn131127592, bn131127696, bn131128629, bn131202633,
bn131202906, bn131204937, bn131209547, bn131209963, bn131211510, bn131212814,
bn131214705, bn131215298, bn131216081, bn131217108, bn131217183, bn131217506,
bn131229277, bn131230529, bn131230808, bn131231198, bn140102887, bn140104731,
bn140105065, *bn140105748*, bn140106345, bn140108721, *bn140109771*, *bn140109877*,
bn140110263, *bn140110411*, *bn140110814*, bn140112060, bn140113183, bn140113624,
bn140115863, bn140115899, bn140118064, bn140122597, bn140124527, bn140126815,
bn140129499, bn140204547, bn140206275, bn140206304, bn140209313, bn140211091,
bn140213807, bn140216331, bn140217043, bn140218427, bn140219319, bn140219824,
bn140223495, bn140224382, bn140224788, *bn140227738*, bn140302342, bn140304557,
bn140304849, bn140306146, bn140308710, bn140311453, bn140311618, bn140311885,
bn140319964, bn140320092, bn140322424, bn140323433, bn140327065, bn140328560,
bn140329272, bn140329295, bn140330180, *bn140402007*, bn140404030, bn140404171,
bn140404900, bn140405033, bn140406120, bn140406144, bn140408553, bn140414693,
bn140416060, bn140422194, bn140423356, *bn140426515*, *bn140427702*, bn140428906,
bn140429975, bn140430716, *bn140501139*, bn140501497, bn140502354, bn140506880,
bn140508128, *bn140508179*, *bn140508629*, bn140511095, bn140511995, bn140512814,
bn140513724, bn140516700, bn140516765, bn140517813, *bn140518709*, bn140519043,
bn140521184, bn140521732, bn140523129, bn140526449, *bn140526571*, bn140528837,
bn140603476, bn140605377, bn140606133, bn140608153, bn140608713, bn140610487,
bn140610689, bn140612294, bn140616165, bn140619475, bn140619490, bn140620219,
bn140621827, bn140623224, bn140624423, bn140626843, bn140627401, bn140628626,
bn140628704, *bn140630505*, *bn140701567*, bn140701833, bn140703026, bn140705539,
bn140706815, bn140709051, bn140709637, bn140710537, bn140710901, *bn140711691*,
bn140712706, bn140712973, bn140713780, bn140714268, bn140715231, bn140716306,
bn140716436, bn140717827, bn140720158, bn140720280, bn140721336, bn140723067,
bn140723499, *bn140724533*, bn140725583, bn140727748, bn140729026, bn140801792,
bn140807500, bn140808038, *bn140809133*, bn140810782, bn140817229, bn140817293,
bn140818229, bn140818781, bn140819160, *bn140824548*, bn140824606, bn140825328,
bn140825980, bn140827763, bn140828288, *bn140829880*, *bn140831215*, bn140831374,
bn140901262, bn140901821, bn140905454, *bn140906175*, bn140906429, bn140907429,
bn140907672, *bn140911012*, bn140912664, bn140916234, bn140917512, bn140918379,
bn140919636, bn140928100, bn140928437, bn140929677, *bn140930134*, bn141003564,
bn141003788, bn141004150, bn141004973, bn141005217, bn141005535, bn141011282,
bn141011467, bn141012773, bn141013803, bn141016897, *bn141020439*, bn141022061,
bn141022087, bn141026742, bn141028455, bn141029134, bn141030746, bn141031257,
bn141031304, bn141031998, bn141102112, bn141102536, bn141102779, bn141105358,
bn141105406, bn141109447, bn141110232, *bn141111435*, *bn141112539*, bn141112828,

bn141113346, bn141114687, bn141118678, bn141121414, bn141122087, bn141122875,
bn141122956, bn141124277, bn141126233, bn141128962, bn141202470, bn141205018,
bn141205337, bn141205763, bn141206254, bn141207800, bn141208038, bn141208632,
bn141209131, bn141213300, bn141215560, bn141220252, bn141221338, bn141221897,
bn141222298, bn141222691, bn141223240, bn141225959, bn141226880, bn141229492,
bn141229911, bn141230142, bn141230834, bn141230871, bn150101270, bn150101641,
bn150105257, bn150106921, bn150110433, bn150110923, bn150118409, bn150118927,
bn150120123, bn150120685, bn150122960, bn150126868, bn150127398, bn150127589,
bn150127935, bn150128624, bn150128791, bn150131335, bn150131951, bn150201040,
bn150201574, bn150201590, bn150202999, bn150203173, bn150203545, bn150204272,
bn150206285, bn150206407, bn150208573, bn150208929, bn150210935, bn150211239,
bn150213001, bn150214293, bn150215026, bn150216415, bn150219522, bn150220598,
bn150222450, bn150222832, bn150226223, bn150226545, bn150226948, bn150227702,
bn150228845, bn150228981, bn150301045, bn150301818, bn150303516, bn150305724,
bn150306993, bn150309958, bn150312403, bn150313657, bn150314205, bn150316400,
bn150318521, bn150319271, bn150320462, bn150322066, bn150323395, bn150323712,
bn150324164, bn150324319, bn150325696, bn150326521, bn150326542, bn150329288,
bn150330828, bn150403913, bn150404733, bn150411026, bn150412507, bn150412931,
bn150415029, bn150416773, bn150418819, bn150422294, bn150422703, bn150423285,
bn150424403, bn150425617, bn150426594, bn150428305, bn150430015, bn150501017,
bn150502435, bn150506398, bn150506630, bn150506972, bn150507026, bn150508945,
bn150510139, bn150511362, bn150512432, bn150514774, bn150520893, bn150522433,
bn150522944, bn150523396, bn150523690, bn150527283, bn150527662, bn150528656,
bn150530488, bn150601904, bn150602840, bn150603105, bn150603823, bn150604284,
bn150604434, bn150605782, bn150607330, bn150609316, bn150612702, bn150613420,
bn150613995, bn150614073, bn150618674, bn150619287, bn150622393, bn150627183,
bn150628767, bn150629564, bn150630223, bn150630958, bn150702998, bn150703149,
bn150703259, bn150705009, bn150705588, bn150707124, bn150708339, bn150710646,
bn150711766, bn150712846, bn150715136, bn150716552, bn150717795, bn150718656,
bn150721242, bn150721431, bn150721732, bn150723608, bn150724398, bn150724782,
bn150726877, bn150727793, bn150728151, bn150729517, bn150802127, bn150802207,
bn150804806, bn150805445, bn150805746, bn150806348, bn150809516, bn150810485,
bn150811849, bn150815604, bn150817087, bn150817251, bn150819440, bn150820880,
bn150821406, bn150822178, bn150824079, bn150824125, bn150826557, bn150827785,
bn150828333, bn150828901, bn150830128, bn150831930, bn150901924, bn150902733,
bn150904479, bn150908408, bn150911315, bn150911588, bn150912443, bn150912600,
bn150913161, bn150917148, bn150919606, bn150922234, bn150922718, bn150922883,
bn150923297, bn150923429, bn150923864, bn150923995, bn150928359, bn151001348,
bn151001628, bn151003729, bn151006413, bn151009949, bn151011136, bn151014592,
bn151021791, bn151022577, bn151023104, bn151024179, bn151026169, bn151026523,
bn151027166, bn151030999, bn151107851, bn151111356, bn151114645, bn151117442,
bn151118554, bn151120349, bn151122709, bn151126293, bn151129333, bn151130160,
bn151202565, bn151205657, bn151210041, bn151211672, bn151212030, bn151212064,
bn151218857, bn151219567, bn151222340, bn151227072, bn151227218, bn151228129,
bn151229285, bn151229486, bn151231443, bn151231568, bn160101030, bn160101215,
bn160102500, bn160102936, bn160104475, bn160104918, bn160106948, bn160107931,
bn160111115, bn160113398, bn160118060, bn160119072, bn160123095, bn160125368,
bn160131116, bn160131174, bn160201883, bn160206430, bn160211119, bn160215773,
bn160216801, bn160218711, bn160219289, bn160219673, bn160220059, bn160220868,
bn160221993, bn160222070, bn160223072, bn160223416, bn160223670, bn160224911,
bn160225720, bn160225809, bn160226913, bn160227831, bn160228034, bn160301215,

bn160303201, bn160303971, bn160308709, bn160310016, bn160310291, bn160314473,
bn160314929, *bn160315739*, bn160316139, bn160316573, *bn160317385*, bn160318342,
bn160323293, bn160325291, bn160326062, bn160330827, bn160401065, bn160406023,
bn160406503, bn160406570, bn160407673, bn160408268, *bn160411062*, bn160416022,
bn160419637, bn160421137, bn160422499, bn160423066, bn160424492, *bn160428412*,
bn160503567, bn160508290, bn160509374, bn160512199, bn160512536, *bn160513553*,
bn160513962, bn160515819, bn160516237, bn160518039, bn160518985, bn160519012,
bn160519060, bn160519677, bn160521385, bn160521839, bn160522445, bn160523919,
bn160527080, *bn160528276*, bn160530667, *bn160603719*, bn160605847, *bn160609690*,
bn160609941, bn160612842, bn160621497, bn160623209, bn160624477, bn160625230,
bn160625240, bn160625945, *bn160628136*, bn160628579, bn160629930, bn160709370,
bn160709826, bn160710233, bn160711968, bn160714097, bn160716144, bn160717813,
bn160718975, bn160720275, bn160720767, bn160721806, bn160724444, bn160726065,
bn160727971, bn160728337, bn160731024, bn160802259, bn160804065, bn160804180,
bn160804775, bn160804968, bn160806584, bn160813297, *bn160814622*, bn160815299,
bn160815490, bn160816414, bn160816730, bn160818198, bn160818230, bn160819852,
bn160820496, bn160821857, bn160821937, bn160822672, bn160824598, bn160825799,
bn160826938, bn160827586, bn160827616, bn160827837, bn160829334, bn160831411,
bn160905471, bn160908136, bn160909061, bn160910722, bn160912350, bn160912521,
bn160912674, bn160917456, bn160917479, bn160917921, bn160919613, bn160919858,
bn160920249, bn160921087, bn160922856, *bn160924253*, bn160925221, bn160928825,
bn160929529, bn161001045, bn161004964, bn161005977, bn161007009, bn161009651,
bn161012214, *bn161012416*, bn161012637, bn161013948, bn161014522, bn161015400,
bn161015710, *bn161017745*, bn161020024, bn161020759, bn161020767, *bn161022114*,
bn161026373, bn161105417, bn161106499, bn161106786, bn161109263, *bn161110179*,
bn161111197, bn161112496, bn161115745, bn161117066, bn161119633, *bn161121186*,
bn161125931, bn161128216, bn161129300, bn161201342, bn161205561, bn161206064,
bn161207224, bn161207813, bn161210524, *bn161212652*, bn161213295, bn161214722,
bn161217128, bn161218356, bn161220605, bn161227498, bn161228032, *bn161228388*,
bn161228405, bn161228553, bn161229878, bn161230298, bn161230511, bn170101116,
bn170101374, *bn170106968*, bn170109137, *bn170110967*, bn170111760, bn170111815,
bn170112970, bn170113420, bn170114833, bn170114917, bn170115662, bn170115743,
bn170116238, bn170119228, bn170120471, bn170121067, bn170121133, bn170121614,
bn170124238, bn170124528, bn170124874, *bn170125022*, *bn170125102*, bn170126480,
bn170127067, bn170127634, bn170130302, bn170130510, *bn170130697*, bn170131969,
bn170203486, bn170205521, bn170206453, bn170207906, bn170208553, bn170208758,
bn170208940, bn170209048, bn170210116, bn170212034, bn170214649, bn170219002,
bn170219110, bn170222209, bn170228773, bn170228794, bn170301812, bn170302166,
bn170302719, bn170302876, bn170304003, bn170305256, bn170306130, bn170306588,
bn170307851, bn170308221, bn170310417, bn170310883, bn170313125, bn170315582,
bn170316710, bn170317666, bn170318644, bn170323058, bn170323775, bn170325331,
bn170326489, bn170329387, bn170402285, bn170402961, bn170403583, bn170403707,
bn170405777, bn170409112, bn170412917, bn170412988, bn170414551, bn170416583,
bn170419898, bn170419983, bn170422343, bn170423719, bn170423872, bn170424425,
bn170428136, bn170429799, bn170430204, bn170501467, *bn170504734*, bn170506169,
bn170510217, bn170511249, *bn170511477*, *bn170511648*, bn170514152, bn170514180,
bn170516808, bn170520202, bn170521882, bn170522657, bn170527480, bn170530581,
bn170604603, bn170606968, bn170607946, bn170607971, bn170610689, bn170611937,
bn170614255, bn170614486, bn170614505, bn170616047, *bn170616165*, bn170618475,
bn170621784, bn170625692, bn170626401, bn170627931, bn170629537, bn170705115,
bn170705200, bn170705244, bn170708046, bn170709334, bn170710340, bn170711019,

bn170711713, bn170711931, bn170714049, bn170715878, *bn170717952*, bn170718152,
bn170722525, bn170723076, *bn170723677*, *bn170723882*, bn170724543, bn170726249,
bn170726794, bn170727841, bn170728961, bn170730133, bn170731751, bn170801690,
bn170802638, *bn170803172*, bn170803415, bn170803729, bn170804911, bn170805901,
bn170808065, bn170808936, bn170810918, bn170813051, *bn170816258*, bn170816599,
bn170817529, bn170817908, bn170818137, bn170821265, bn170825307, bn170825500,
bn170825784, bn170826369, bn170826819, bn170827818, bn170829414, bn170829674,
bn170830069, bn170830135, bn170830328, bn170831179, bn170901007, bn170901255,
bn170901345, bn170903534, bn170906030, bn170906039, *bn170906485*, *bn170910368*,
bn170911267, bn170912273, bn170912985, bn170915161, bn170915520, *bn170916700*,
bn170918139, bn170921168, bn170923101, bn170923188, *bn170923566*, bn170926528,
bn170926782, bn170928607, bn170929513, bn170929699, bn171002969, bn171004672,
bn171004857, *bn171007498*, *bn171008080*, bn171009138, bn171010792, bn171010875,
bn171011162, *bn171011810*, bn171013350, *bn171017823*, bn171020813, bn171022085,
bn171022885, bn171023097, *bn171024977*, bn171025213, bn171025416, *bn171025913*,
bn171029020, bn171030729, bn171102107, bn171103655, bn171106498, *bn171108656*,
bn171112868, bn171117515, bn171119992, bn171120556, bn171124235, bn171126216,
bn171126235, bn171201068, bn171202113, bn171206122, bn171207055, bn171207809,
bn171208733, bn171209671, bn171210493, bn171211844, bn171212222, bn171212434,
bn171212948, *bn171213061*, *bn171215705*, bn171219279, *bn171222684*, bn171223818,
bn171227000, bn171230048, bn171230119, bn171230955, bn180102660, bn180103090,
bn180110608, bn180111815, bn180112842, bn180113011, bn180113116, bn180113418,
bn180116026, *bn180116678*, bn180119837, bn180122129, *bn180123820*, bn180124392,
bn180125891, bn180126095, bn180127049, bn180127879, bn180128215, bn180128252,
bn180128881, bn180130049, *bn180130744*, *bn180131528*, bn180201706, bn180201780,
bn180204109, bn180205184, bn180205323, bn180206203, *bn180208764*, bn180210517,
bn180210991, bn180211754, bn180218635, bn180219482, bn180222239, bn180225417,
bn180227211, bn180305393, bn180306479, bn180306973, bn180307073, bn180309322,
bn180311074, bn180313978, bn180314030, bn180330891, bn180401280, bn180401846,
bn180402406, *bn180402481*, bn180403565, bn180404091, bn180404848, bn180405169,
bn180409346, *bn180410336*, bn180411519, *bn180411546*, bn180412425, bn180413118,
bn180416340, bn180416924, bn180417689, bn180418281, bn180420031, bn180420107,
bn180423033, bn180423266, *bn180426005*, bn180426549, bn180427442, bn180428102,
bn180504136, bn180505540, bn180506077, bn180506902, bn180511364, bn180511437,
bn180511606, *bn180513815*, bn180515814, bn180516229, *bn180517309*, bn180521935,
bn180522607, bn180522678, bn180523782, bn180524416, bn180524920, bn180525151,
bn180528371, *bn180528465*, bn180602938, bn180605458, bn180606730, bn180610377,
bn180610568, *bn180610791*, bn180611145, bn180612785, bn180614327, bn180615462,
bn180617872, bn180618030, bn180618724, bn180620354, bn180620660, bn180622273,
bn180622578, bn180623849, bn180625941, bn180626392, bn180630335, bn180630467,
bn180701469, bn180703876, bn180703949, bn180706351, bn180709099, bn180710062,
bn180712358, bn180712651, bn180715087, bn180715741, bn180715755, bn180718082,
bn180718201, bn180718763, bn180720213, bn180720598, bn180720933, bn180721642,
bn180722120, bn180722418, bn180722993, bn180723133, bn180723757, bn180724807,
bn180724984, bn180727594, bn180728575, bn180728728, bn180728882, bn180730018,
bn180731891, bn180801276, bn180801492, *bn180803590*, bn180804554, bn180804765,
bn180804909, bn180804931, bn180805543, *bn180806665*, bn180806944, bn180807097,
bn180809485, bn180810278, bn180812349, *bn180814505*, bn180816088, bn180816930,
bn180818179, *bn180818520*, bn180821653, bn180822423, bn180822562, bn180823442,
bn180826055, bn180828790, bn180905400, bn180906597, bn180906759, bn180906988,
bn180910032, bn180910156, bn180910352, bn180912274, bn180913783, bn180914522,

bn180917477, bn180922461, bn180922734, bn180923931, *bn180925407*, bn180927993,
bn180929453, bn181002617, bn181007385, bn181007737, bn181008269, bn181008877,
bn181010247, bn181014479, *bn181016718*, bn181020424, bn181020792, bn181022846,
bn181026540, bn181027076, bn181028590, bn181029892, *bn181103046*, bn181111654,
bn181116484, bn181117663, bn181119606, bn181119649, bn181120265, *bn181121307*,
bn181121401, bn181122381, bn181125092, bn181125371, *bn181126162*, bn181126413,
bn181126729, *bn181127274*, bn181128129, bn181128751, bn181203880, bn181206970,
bn181208188, bn181212693, bn181215110, bn181216551, bn181217665, bn181221565,
bn181222279, bn181222841, *bn181224987*, bn181225489, bn181225786, bn181226600,
bn181227262, bn181227571, bn181228120, *bn181231144*, bn181231359, bn181231954,
bn190102258, bn190106866, *bn190107050*, *bn190109217*, bn190109497, bn190110726,
bn190114873, bn190117369, bn190118937, *bn190119249*, bn190122305, bn190123513,
bn190129515, bn190129539, bn190131109, bn190131964, bn190202069, bn190202234,
bn190202634, bn190204627, bn190205938, bn190212482, bn190215772, bn190217188,
bn190218330, *bn190220844*, bn190222312, bn190222537, bn190226515, bn190228973,
bn190303240, bn190304371, bn190304818, bn190306943, bn190307151, bn190308923,
bn190310398, bn190311600, bn190312446, bn190315512, bn190319353, bn190319375,
bn190320052, bn190321363, bn190323179, bn190323303, *bn190323548*, bn190323879,
bn190324348, bn190324947, bn190325999, bn190326314, bn190326975, bn190327111,
bn190330694, bn190331093, bn190401139, bn190404293, bn190406450, bn190406465,
bn190406745, bn190407575, bn190407672, bn190407788, *bn190409901*, bn190411407,
bn190411579, bn190415173, bn190419414, bn190420981, bn190422284, bn190422670,
bn190422957, *bn190425089*, bn190427190, bn190428783, bn190429743, bn190501794,
bn190502168, bn190504415, bn190504678, bn190505051, bn190507270, bn190507712,
bn190507970, *bn190508808*, bn190508987, bn190510120, bn190510430, bn190511302,
bn190512611, bn190515190, bn190517813, bn190519309, bn190525032, bn190530430,
bn190531312, bn190531568, bn190531840, bn190601325, bn190603795, bn190604446,
bn190605974, bn190606080, bn190607071, bn190608009, bn190609315, bn190610750,
bn190610834, bn190611950, bn190612165, bn190613172, bn190613449, bn190615636,
bn190619018, bn190619595, bn190620507, bn190707285, bn190707308, bn190708365,
bn190712018, bn190712095, bn190714573, *bn190716019*, bn190716917, bn190719113,
bn190719499, bn190719624, bn190720613, bn190720964, bn190723309, bn190724031,
bn190726642, bn190726843, bn190727668, bn190727846, bn190728271, bn190731943,
bn190804058, bn190804792, bn190805106, bn190805199, bn190806535, bn190806675,
bn190808498, bn190808752, bn190810675, bn190813520, bn190814837, bn190817953,
bn190821716, bn190822705, bn190824616, *bn190825171*, bn190827467, bn190828542,
bn190828614, bn190829830, bn190830023, bn190830264, *bn190831332*, bn190831693,
bn190901890, bn190903722, bn190904174, bn190905985, bn190906767, bn190910028,
bn190913155, bn190914345, bn190915240, bn190916590, bn190919764, bn190921699,
bn190923617, bn190930400, bn191001279, bn191008297, bn191009298, bn191011192,
bn191015327, bn191017391, bn191017957, bn191019469, bn191019970, bn191022285,
bn191022341, bn191023630, bn191026350, bn191027638, *bn191028174*, bn191028589,
bn191031025, bn191031635, bn191031780, bn191031891, bn191101895, bn191108003,
bn191110587, bn191111347, bn191111364, bn191111547, *bn191112369*, bn191113578,
bn191117006, bn191117637, bn191118925, *bn191119261*, bn191125206, bn191125634,
bn191129141, bn191130253, bn191130507, bn191202867, *bn191203290*, *bn191205741*,
bn191213254, bn191213784, bn191220589, bn191221802, bn191225309, bn191225735,
bn191227069, bn191227723.

Appendix D

Supplemental results on the IceCube neutrino search

D.1 GBM coincidence study

D.1.1 GRB selection

The GBM coincidence analysis was applied to the sample of GRBs shown in Tab. D.1. These 133 bursts present a subset of the 217 GRBs for which a gamma-ray precursor was observed in the Fermi-GBM study from Chapter 2 (see Tab. C.1). Specifically, they are the bursts for which both GFU data and a reliable burst localisation is available. Additional details on this GRB selection are given in 5.3.1.

TABLE D.1: List of the 133 GRBs examined in the GBM coincidence study. The position of the burst is given in right ascension and declination (J2000). Localisation uncertainties (σ) for which the value is ‘HP’ indicate those bursts for which a sky scan was performed. In this case, the ‘ra’ and ‘dec’ are only indicative of the GRB position, corresponding to the most significant pixel of the map. For every burst, the start time and duration of the interval that was searched for neutrino emission is also given.

GCN name	Fermi name	ra (°)	dec (°)	σ (°)	t_s (MJD)	Duration (s)
—	bn110528624	47.813	-1.492	HP	55709.6219076389	214.013
—	bn110725236	272.461	-23.318	HP	55767.2358705151	11.619
—	bn110729142	354.727	4.780	HP	55771.1423933394	212.872
GRB110825A	bn110825102	46.758	14.478	HP	55798.1019541501	4.814
—	bn110904124	348.398	41.014	HP	55808.1237089527	11.665
—	bn110909116	348.750	-26.277	HP	55813.1159199275	5.670
—	bn110926107	66.094	12.942	HP	55830.1067415075	7.110
—	bn111010709	70.664	39.451	HP	55844.7086871579	35.018
—	bn111015427	222.187	-60.434	HP	55849.4270166832	21.144
GRB111228A	bn111228657	150.067	18.298	0.001	55923.6558842014	29.344
—	bn111230683	155.742	34.954	HP	55925.6825591988	8.631
—	bn111230819	241.172	-22.347	HP	55925.8190938402	9.928
—	bn120308588	48.364	50.091	HP	55994.5872933828	7.092
—	bn120319983	72.839	-45.784	HP	56005.9826282475	9.551
—	bn120412920	40.430	7.783	HP	56029.9198875929	9.502
—	bn120530121	188.036	79.753	HP	56077.1205959964	11.974
—	bn120611108	326.538	-46.178	HP	56089.1081465393	10.149

Continued on next page

Table D.1 continued: Properties of the 133 GRBs that were searched for neutrino emission in the GBM coincidence analysis.

GCN name	Fermi name	ra (°)	dec (°)	σ (°)	t_s (MJD)	Duration (s)
—	bn120710100	119.180	-31.388	HP	56118.0994766214	8.857
GRB120711A	bn120711115	94.678	-70.999	0.001	56119.1144548343	8.838
GRB120716A	bn120716712	311.484	14.786	HP	56124.7118264583	9.383
—	bn120819048	181.758	34.954	HP	56158.0474277780	35.549
—	bn121005340	147.305	30.692	HP	56205.3397022176	42.794
GRB121029A	bn121029350	228.164	-25.944	HP	56229.3501699670	12.798
GRB121031A	bn121031949	170.770	-3.517	0.001	56231.9493895881	42.495
—	bn121113544	323.060	65.322	HP	56244.5434979945	35.652
GRB121125A	bn121125356	228.527	55.313	0.001	56256.3557714406	24.325
GRB121217A	bn121217313	153.710	-62.351	0.001	56278.3041317940	69.792
—	bn130104721	174.375	21.703	HP	56296.7208881628	7.762
—	bn130106995	25.800	62.320	HP	56298.9946850882	21.558
—	bn130208684	187.759	57.780	HP	56331.6835634566	9.099
—	bn130209961	33.047	-27.616	HP	56332.9608726898	7.051
GRB130219A	bn130219775	299.180	39.451	HP	56342.7748777208	24.260
GRB130310A	bn130310840	142.340	-17.230	0.450	56361.8400328308	5.194
—	bn130318456	202.500	8.084	HP	56369.4558515188	10.897
GRB130320B	bn130320560	203.062	-60.434	HP	56371.5600085217	46.085
—	bn130404840	149.414	-41.810	HP	56386.8402971820	12.355
—	bn130418844	220.781	-16.646	HP	56400.8435091854	20.452
GRB130504B	bn130504314	352.617	-5.379	HP	56416.3139046952	4.464
—	bn130623130	190.848	48.141	HP	56466.1295685913	5.821
—	bn130720582	338.906	-11.720	HP	56493.5810972322	119.366
—	bn130813791	184.760	51.256	HP	56517.7910999128	5.680
—	bn130815660	111.094	-1.492	HP	56519.6602952726	10.925
—	bn130818941	191.897	57.780	HP	56522.9397798491	12.706
—	bn130919173	297.773	-13.248	HP	56554.1733592517	2.641
—	bn131014513	16.875	22.993	HP	56579.5126388264	6.089
—	bn131108024	352.969	33.869	HP	56604.0240692886	4.337
GRB140104B	bn140104731	218.754	-9.028	0.001	56661.7305503785	101.397
GRB140108A	bn140108721	325.112	58.744	0.001	56665.7212942224	15.570
—	bn140126815	208.477	31.388	HP	56683.8143053464	55.976
—	bn140304849	339.609	-33.153	HP	56720.8489137930	34.654
GRB140329A	bn140329295	145.698	-32.229	0.200	56745.2948645814	4.630
—	bn140404030	46.406	78.284	HP	56751.0292697772	11.657
GRB140512A	bn140512814	289.370	-15.094	0.001	56789.8136952174	15.788
GRB140621A	bn140621827	73.279	14.650	0.717	56829.8264916383	4.718
GRB140709A	bn140709051	304.662	51.225	0.001	56847.0511378334	9.700
GRB140714A	bn140714268	219.023	23.318	HP	56852.2678653687	31.544
GRB140716A	bn140716436	108.171	-60.175	0.001	56854.4360582075	6.218
GRB140818A	bn140818229	199.512	6.800	1.000	56887.2292362143	14.233
GRB140824B	bn140824606	22.500	59.678	HP	56893.6063545827	16.933
—	bn140825328	354.023	24.624	HP	56894.3282541416	28.245
—	bn140917512	165.938	24.296	HP	56917.5118502219	6.384
GRB141029B	bn141029134	105.200	25.100	1.000	56959.1342155799	35.816
GRB141102A	bn141102536	208.614	-47.100	0.031	56963.5358472492	3.151

Continued on next page

Table D.1 continued: Properties of the 133 GRBs that were searched for neutrino emission in the GBM coincidence analysis.

GCN name	Fermi name	ra (°)	dec (°)	σ (°)	t_s (MJD)	Duration (s)
GRB150126A	bn150126868	350.500	-12.367	0.567	57048.8684617500	17.019
GRB150127A	bn150127398	288.984	-6.880	HP	57049.3977013566	8.436
—	bn150226545	55.547	30.345	HP	57079.5453712092	181.122
GRB150330A	bn150330828	331.875	51.256	HP	57111.8279983948	15.512
GRB150416A	bn150416773	59.559	52.030	HP	57128.7636143171	46.496
GRB150422A	bn150422703	215.156	-20.424	HP	57134.6977015856	19.616
—	bn150508945	70.842	-52.416	HP	57150.9436615288	19.712
GRB150512A	bn150512432	198.562	60.434	HP	57154.4321561599	82.087
—	bn150522433	289.688	-33.153	HP	57164.4331684364	11.822
GRB150523A	bn150523396	115.286	-45.420	0.001	57165.3956553683	23.748
GRB150627A	bn150627183	117.471	-51.489	0.001	57200.1775619560	7.072
GRB150702A	bn150702998	52.780	-57.000	0.360	57205.9976437199	6.490
—	bn150703149	142.031	-16.646	HP	57206.1483657749	4.008
—	bn150830128	206.625	-44.994	HP	57264.1280324999	16.577
GRB151027A	bn151027166	272.487	61.353	0.001	57322.1655311774	44.571
GRB151030A	bn151030999	300.586	25.283	HP	57325.9988115758	21.686
—	bn151211672	256.008	45.389	HP	57367.6700785185	30.022
—	bn160131174	107.930	17.583	HP	57418.1735060044	48.007
—	bn160201883	327.717	73.127	HP	57419.8831086533	3.528
—	bn160215773	350.859	-4.481	HP	57433.7738121086	48.645
—	bn160219673	235.547	36.054	HP	57437.6734064760	16.546
GRB160223A	bn160223072	147.598	9.370	0.001	57441.0724160746	14.496
GRB160225B	bn160225809	150.117	-40.228	HP	57443.8085603760	27.215
—	bn160512199	244.336	-31.388	HP	57520.1979050913	13.377
GRB160519A	bn160519012	71.122	31.246	0.017	57527.0121504033	39.197
—	bn160523919	265.078	-11.720	HP	57531.9191385129	9.424
GRB160625B	bn160625945	308.598	6.919	0.001	57564.9446038522	6.418
—	bn160724444	56.250	16.646	HP	57593.4443657169	5.790
GRB160821A	bn160821857	171.257	42.335	0.001	57621.8572173076	35.832
GRB160825A	bn160825799	329.766	8.687	HP	57625.7991535231	3.364
GRB160908A	bn160908136	243.633	13.862	HP	57639.1356359615	10.845
—	bn160912521	339.961	30.692	HP	57643.5213358583	49.543
—	bn160919613	98.289	-76.077	HP	57650.6133096816	13.964
—	bn161105417	233.060	-65.322	HP	57697.4172032234	16.749
—	bn161111197	207.070	32.090	HP	57703.1965981281	15.125
GRB161117A	bn161117066	322.052	-29.614	0.001	57709.0663044437	81.027
GRB161119A	bn161119633	45.756	-45.389	HP	57711.6325140707	11.666
GRB161129A	bn161129300	316.228	32.135	0.001	57721.2997444356	4.040
GRB170109A	bn170109137	116.367	-9.594	HP	57762.1371903578	39.276
—	bn170115662	79.805	-19.471	HP	57768.6613922854	22.563
GRB170209A	bn170209048	112.290	-50.091	HP	57793.0476252297	12.228
—	bn170302719	198.984	0.298	HP	57814.7189548409	16.259
—	bn170323775	348.047	-66.444	HP	57835.7751877805	14.936
—	bn170402961	308.517	-45.784	HP	57845.9606810278	7.725
—	bn170514152	119.634	74.972	HP	57887.1518066423	4.678
GRB170514A	bn170514180	121.641	-24.953	HP	57887.1795429524	39.908

Continued on next page

Table D.1 continued: Properties of the 133 GRBs that were searched for neutrino emission in the GBM coincidence analysis.

GCN name	Fermi name	ra (°)	dec (°)	σ (°)	t_s (MJD)	Duration (s)
GRB170830B	bn170830069	352.617	18.839	HP	57995.0684971148	9.987
GRB170831A	bn170831179	160.529	51.256	HP	57996.1783268644	40.530
—	bn170923188	223.125	81.220	HP	58019.1882292061	5.018
—	bn171004857	26.645	-61.944	HP	58030.8565991914	4.175
GRB171102A	bn171102107	187.729	54.033	0.817	58059.1066170800	14.393
GRB171112A	bn171112868	20.075	-59.633	1.000	58069.8658802344	168.526
GRB171120A	bn171120556	163.790	22.459	0.001	58077.5555571303	8.221
—	bn171211844	80.156	0.298	HP	58098.8443795385	16.393
—	bn180124392	329.766	-41.411	HP	58142.3915813229	4.611
GRB180126A	bn180126095	304.200	43.009	HP	58144.0852697569	15.776
—	bn180307073	127.266	23.643	HP	58184.0721517163	27.342
GRB180411A	bn180411519	356.854	66.778	0.001	58219.5191269005	30.673
GRB180416A	bn180416340	116.920	-48.141	HP	58224.3398513966	14.291
—	bn180426549	202.500	56.637	HP	58234.5491287731	9.544
GRB180618B	bn180618724	317.461	7.181	HP	58287.7235195724	30.238
—	bn180620354	146.953	11.720	HP	58289.3528691366	9.855
GRB180720B	bn180720598	0.529	-2.919	0.001	58319.5978570668	14.000
GRB180728A	bn180728728	253.565	-54.044	0.001	58327.7284053025	14.040
—	bn180822423	210.938	-16.024	HP	58352.4225072271	6.803
—	bn180822562	184.091	-61.567	HP	58352.5613368049	20.237
—	bn180906988	318.867	-5.379	HP	58367.9878694116	4.328
—	bn180929453	242.930	-11.415	HP	58390.4531442785	3.371
—	bn181007385	301.992	-14.478	HP	58398.3846555036	7.996
GRB181008B	bn181008877	94.570	-38.682	HP	58399.8765738204	31.879

D.1.2 Trial corrections

Comparison of methods. Three different approaches were considered in 5.3.1 to trial-correct the sample of 133 p -values. These three options are the binomial, partial product, and full product method. To investigate which of these offers the best performance, a common set of signal trials was evaluated using all three methods. A direct comparison of the resulting p -values was shown in Fig. 5.10 and 5.11. These figures illustrate that the partial product and binomial method both outperform the full product method. They also show that the partial product method outperforms the binomial method. Since the difference between these latter two approaches was less clearly visible, an additional visualisation, Fig. D.1, is included here that shows the ratio of the p -values obtained using both methods. Values that are smaller than unity correspond to signal trials for which the partial product method offers the best performance. Fig. D.1 thus illustrates that the partial product method outperforms the binomial method for the majority of signal trials.

TS distributions. While the binomial and full product method were not used to trial-correct the final analysis result, their TS distributions are included in Fig. D.2 for the sake of completeness. Similar to the partial product method, the TS value of both methods is defined as $-\log_{10}(x)$, where x is either the binomial p -value or the product of all 133 p -values.

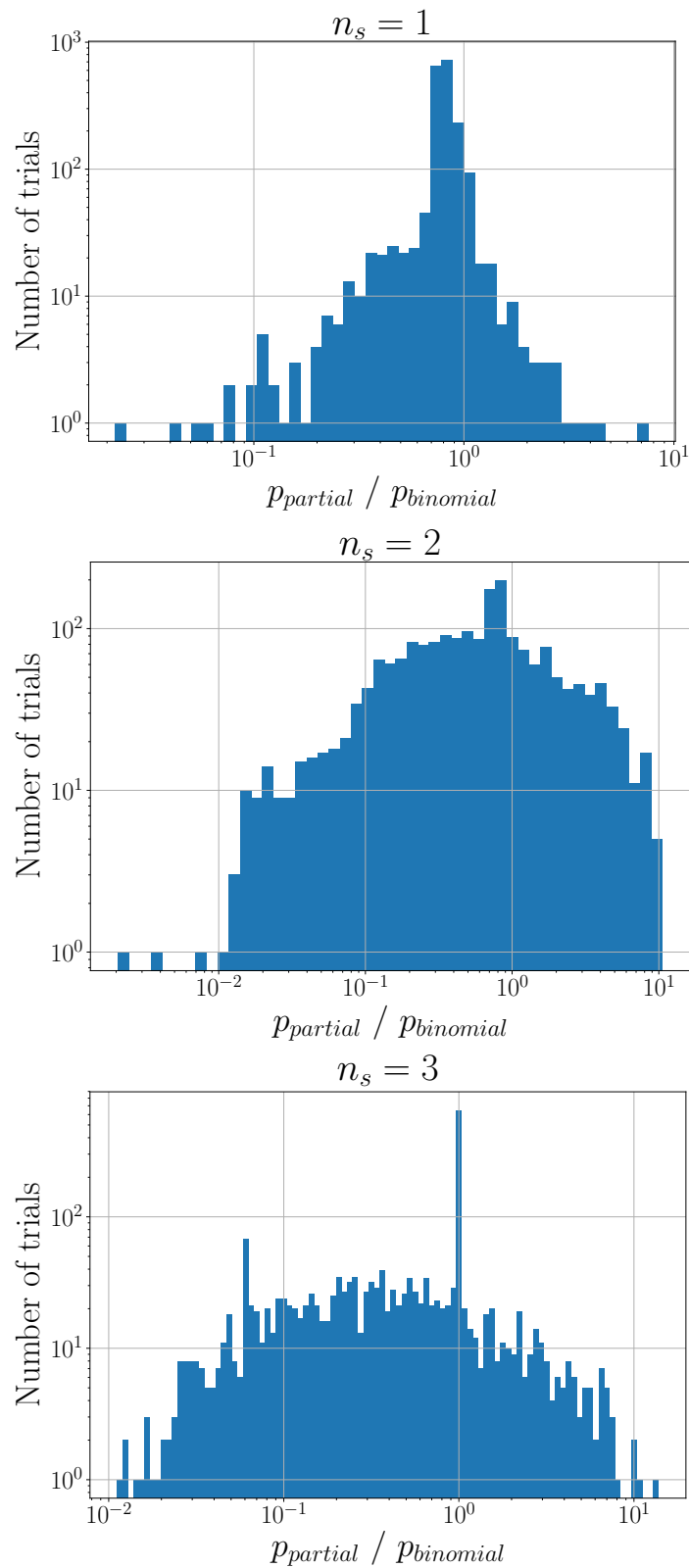


FIGURE D.1: Ratio of the final p -value obtained using the partial product and binomial method, when evaluating trials in which one (top), two (middle), or three (bottom) signal events are injected. All three distributions have their peak and median at a value that is smaller than or equal to unity. As a result, the partial product method is shown to offer the best overall performance.

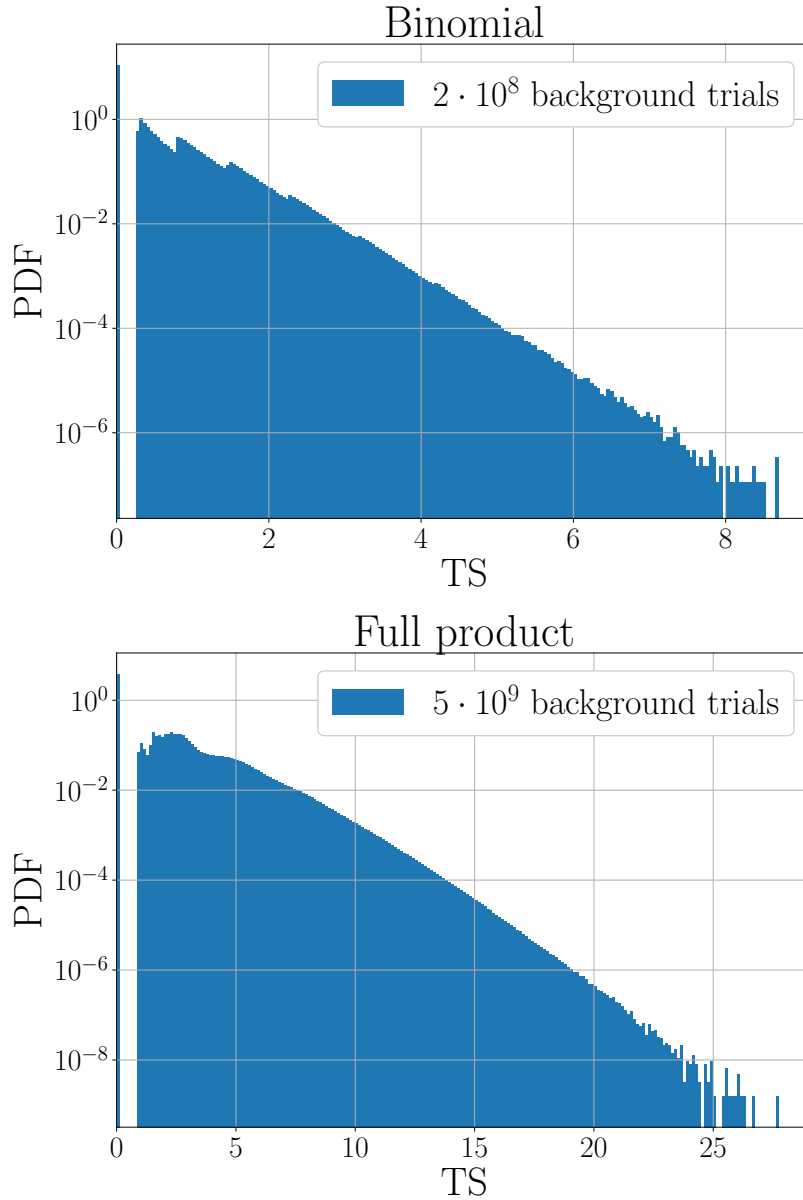


FIGURE D.2: Final TS distribution when applying the binomial (top) and full product (bottom) trial-correction method. The structure in the binomial TS distribution is due to the discrete nature of the method itself. For instance, in the case where $k = 1$, see Eq. (5.9), the highest possible value that $P(k)$ can attain is the fraction of trials that returns at least one p -value different from unity. This corresponds to $P(k) = 0.52$, which translates into a TS value of $-\log_{10}(0.52) = 0.28$. The second bump occurs at a TS-value of $-\log_{10}(0.16) = 0.80$, as 16% of all background trials have at least two p -values that are different from unity.

D.2 Generic stacking search

D.2.1 GRB sample

Table D.2 presents the properties of the 872 GRBs analysed in the generic stacking search. This selection was obtained by considering all bursts in the GRBweb catalogue that fall within the GFU time range and have an angular uncertainty $\sigma \leq 1.5^\circ$. Further details on the construction of this catalogue are provided in 5.3.2.

TABLE D.2: List of the 872 GRBs examined in the generic stacking search. The direction of the bursts is given in right ascension and declination (J2000) along with the localisation uncertainty (σ). A 250 s time interval is examined for every burst, the start time of which is given in the last column of the table.

GCN name	ra ($^\circ$)	dec ($^\circ$)	σ ($^\circ$)	t_s (MJD)
GRB110519A	261.638	-23.426	0.008	55700.0889583333
GRB110520A	134.341	56.427	0.001	55701.8504398148
GRB110521A	120.133	45.827	0.001	55702.6578865741
GRB110530A	282.068	61.929	0.001	55711.6436574074
GRB110604A	271.004	18.467	0.083	55716.6149961343
GRB110610A	308.178	74.825	0.001	55722.6370013542
GRB110625A	286.733	6.755	0.001	55737.8778731019
GRB110708A	340.083	53.950	0.050	55750.1938888889
GRB110709A	238.891	40.924	0.001	55751.6390856481
GRB110709B	164.655	-23.455	0.001	55751.8947800926
GRB110715A	237.684	-46.235	0.001	55757.5483796296
GRB110719A	24.581	34.586	0.001	55761.2534837963
GRB110721A	333.659	-38.593	0.001	55763.1969097222
GRB110726A	286.717	56.071	0.001	55768.0600694444
GRB110731A	280.504	-28.537	0.001	55773.4620254630
GRB110801A	89.437	80.956	0.001	55774.8232870370
GRB110802A	44.454	32.600	0.833	55775.6354883218
GRB110808A	57.268	-44.194	0.001	55781.2602314815
GRB110812A	358.408	72.200	0.050	55785.0110879630
GRB110815A	85.296	32.450	0.533	55788.4005320718
GRB110818A	317.337	-63.981	0.001	55791.8566462616
GRB110820A	343.192	70.299	0.001	55793.7321412037
GRB110827A	164.059	53.817	0.017	55799.9984027778
GRB110903A	197.037	59.000	0.050	55807.1079064236
GRB110915A	310.825	-0.723	0.001	55819.5531712963
GRB110915B	77.550	1.933	0.067	55819.7639930556
GRB110918A	32.575	-27.283	0.333	55822.8908895370
GRB110921A	294.098	36.329	0.001	55825.5741014120
GRB110928A	257.733	36.536	0.001	55832.0745486111
GRB111005A	223.315	-19.722	0.016	55839.3340740741
GRB111008A	60.451	-32.709	0.001	55842.9227777778
GRB111016A	153.834	27.462	0.001	55850.7728472222
GRB111016B	290.500	-4.583	1.067	55850.9427167014
GRB111018A	271.489	-3.907	0.001	55852.7237731482
GRB111020A	287.052	-38.012	0.001	55854.2705902778
GRB111022A	275.871	-23.666	0.008	55856.6686805556

Continued on next page

Table D.2 continued: Properties of the 872 GRBs that were searched for neutrino emission in the generic stacking analysis.

GCN name	ra (°)	dec (°)	σ (°)	t_s (MJD)
GRB111022B	108.965	49.684	0.001	55856.7145138889
GRB111024A	222.175	25.850	0.300	55858.3036689815
GRB111026A	244.256	-47.435	0.014	55860.2800810185
GRB111029A	44.784	57.111	0.001	55863.4031250000
GRB111103A	327.111	-10.532	0.009	55868.4382291667
GRB111103B	265.693	1.610	0.001	55868.4547571759
GRB111107A	129.478	-66.520	0.001	55872.0321058796
GRB111109A	118.204	-41.584	0.001	55874.1205555556
GRB111117A	12.704	23.017	0.050	55882.5066087963
GRB111121A	154.761	-46.671	0.001	55886.6820907407
GRB111123A	154.846	-20.645	0.001	55888.7563773148
GRB111126A	276.057	51.461	0.023	55891.7871759259
GRB111129A	307.434	-52.713	0.001	55894.6764351852
GRB111201A	190.478	32.987	0.001	55896.5962206944
GRB111204A	336.628	-31.375	0.001	55899.5647916667
GRB111205A	134.488	-31.967	0.650	55900.5462962963
GRB111207A	92.925	-39.500	0.050	55902.5922337963
GRB111208A	290.224	40.676	0.001	55903.3499617245
GRB111209A	14.344	-46.801	0.001	55904.2971990741
GRB111210A	191.477	-7.166	0.001	55905.6061689815
GRB111211A	153.092	11.183	0.050	55906.9259606482
GRB111212A	310.432	-68.612	0.001	55907.3881597222
GRB111215A	349.556	32.494	0.001	55910.5833101852
GRB111215B	222.404	16.433	0.517	55910.8499157407
GRB111225A	13.155	51.572	0.001	55920.1572569444
GRB111228A	150.067	18.298	0.001	55923.6531411343
GRB111229A	76.287	-84.711	0.001	55924.9400694444
GRB120102A	276.225	24.713	0.001	55928.0914930556
GRB120106A	66.108	64.038	0.001	55932.5918287037
GRB120107A	246.400	-69.930	0.500	55933.3805838542
GRB120114A	317.904	57.036	0.018	55940.6776359259
GRB120116A	16.241	33.931	0.001	55942.7515972222
GRB120118B	124.871	-7.185	0.001	55944.7056668518
GRB120119A	120.029	-9.082	0.001	55945.1668409722
GRB120121A	249.354	-23.961	0.001	55947.4014930556
GRB120202A	203.517	22.800	0.050	55959.9000810185
GRB120211A	87.754	-24.775	0.001	55968.4960416667
GRB120212A	43.100	-18.021	0.001	55969.3799936343
GRB120213A	301.012	65.411	0.001	55970.0160763889
GRB120215A	30.048	8.802	0.001	55972.0257523148
GRB120218A	319.764	-25.463	0.015	55975.0313888889
GRB120219A	129.791	51.032	0.001	55976.6013657407
GRB120224A	40.942	-17.761	0.001	55981.1915046296
GRB120229A	20.033	-35.796	0.015	55986.6048726852
GRB120302A	122.398	29.628	0.001	55988.0773611111
GRB120305A	47.537	28.492	0.001	55991.8148148148

Continued on next page

Table D.2 continued: Properties of the 872 GRBs that were searched for neutrino emission in the generic stacking analysis.

GCN name	ra (°)	dec (°)	σ (°)	t_s (MJD)
GRB120308A	219.084	79.687	0.001	55994.2565740741
GRB120311A	273.092	14.296	0.001	55997.2287962963
GRB120311B	258.562	-13.051	0.001	55997.6277777778
GRB120312A	251.788	23.858	0.001	55998.6682594792
GRB120316A	57.016	-56.288	0.584	56002.0047685185
GRB120320A	212.518	8.696	0.001	56006.4945023148
GRB120323A	340.408	29.717	0.750	56009.5042357639
GRB120324A	291.078	24.130	0.001	56010.2465365394
GRB120326A	273.905	69.260	0.001	56012.0529976852
GRB120327A	246.864	-29.415	0.001	56013.1188194444
GRB120328A	241.614	-39.336	0.001	56014.1264930556
GRB120328B	228.140	22.800	1.000	56014.2653935185
GRB120401A	58.083	-17.636	0.001	56018.2222800926
GRB120403A	42.458	40.489	0.018	56020.0425115741
GRB120403B	55.278	-89.009	0.001	56020.8539875579
GRB120404A	235.010	12.885	0.001	56021.5325462963
GRB120419A	187.371	-63.033	0.050	56036.5362847222
GRB120422A	136.910	14.019	0.001	56039.2971412037
GRB120510A	44.288	72.850	0.050	56057.3635879630
GRB120514A	283.001	-4.264	0.001	56061.0476736111
GRB120521A	148.725	-49.417	0.001	56068.2468981482
GRB120521B	197.010	-52.755	0.001	56068.3775231481
GRB120521C	214.286	42.145	0.001	56068.9707986111
GRB120522A	165.996	-62.100	0.317	56069.1298263889
GRB120612A	126.722	-17.575	0.001	56090.0841319444
GRB120622A	205.429	-1.717	0.333	56100.1372222222
GRB120624B	170.885	8.929	0.001	56102.9274063194
GRB120703A	339.357	-29.723	0.001	56111.7229976852
GRB120709A	318.173	-49.973	0.001	56117.8802083333
GRB120711A	94.678	-70.999	0.001	56119.1115509259
GRB120711B	331.691	60.023	0.001	56119.1297752315
GRB120712A	169.589	-20.034	0.001	56120.5682154398
GRB120714A	167.983	-30.627	0.001	56122.3212500000
GRB120714B	355.409	-46.184	0.001	56122.8851454861
GRB120722A	230.497	13.251	0.001	56130.5342129630
GRB120724A	245.181	3.508	0.001	56132.2742129630
GRB120728A	137.095	-54.437	0.001	56136.9312615741
GRB120729A	13.074	49.940	0.001	56137.4527967708
GRB120802A	44.843	13.768	0.001	56141.3310300926
GRB120803A	269.531	-6.733	0.019	56142.3042361111
GRB120803B	314.236	53.304	0.001	56142.4596759259
GRB120804A	233.948	-28.782	0.001	56143.0347685185
GRB120805A	216.538	5.825	0.001	56144.8916550926
GRB120807A	241.260	-47.480	0.001	56146.2954513889
GRB120811B	43.721	-30.233	1.400	56150.0113425926
GRB120811A	257.165	-22.711	0.001	56150.1049537037

Continued on next page

Table D.2 continued: Properties of the 872 GRBs that were searched for neutrino emission in the generic stacking analysis.

GCN name	ra (°)	dec (°)	σ (°)	t_s (MJD)
GRB120811C	199.683	62.301	0.001	56150.6462722685
GRB120815A	273.958	-52.131	0.001	56154.0901388889
GRB120816A	282.144	-6.938	0.001	56155.8016666667
GRB120817B	8.310	-26.428	0.022	56156.1654976852
GRB120817A	250.689	-38.354	0.001	56156.2816203704
GRB120819A	235.908	-7.309	0.001	56158.5458796296
GRB120821A	255.271	-40.517	0.033	56160.5552662037
GRB120830A	88.503	-28.702	0.001	56169.2936689815
GRB120907A	74.750	-9.315	0.001	56177.0140346181
GRB120908A	230.775	-25.500	1.000	56178.9352478704
GRB120909A	275.737	-59.449	0.001	56179.0674957176
GRB120911B	172.030	-37.510	0.300	56181.2646296296
GRB120911A	357.979	63.099	0.001	56181.2946702315
GRB120913A	146.400	26.959	0.009	56183.8431828704
GRB120913B	213.660	-14.508	0.008	56183.9939440856
GRB120916A	205.810	36.660	0.300	56186.1691450926
GRB120918A	181.042	-32.762	0.009	56188.4666666667
GRB120919A	214.767	-45.567	0.517	56189.3058865394
GRB120922A	234.748	-20.182	0.001	56192.9347894444
GRB120923A	303.795	6.221	0.001	56193.2166203704
GRB120927A	136.614	0.416	0.001	56197.9420833333
GRB121001A	276.032	-5.666	0.001	56201.7631018519
GRB121011A	260.213	41.110	0.001	56211.4661458333
GRB121014A	166.645	-29.105	0.016	56214.8387268518
GRB121017A	288.830	-1.605	0.001	56217.8050694444
GRB121024A	70.472	-12.291	0.001	56224.1194675926
GRB121025A	248.750	27.733	0.300	56225.3210648148
GRB121027A	63.598	-58.830	0.001	56227.3113310185
GRB121028A	271.899	-2.294	0.001	56228.2085763889
GRB121031A	170.770	-3.517	0.001	56231.9462717014
GRB121102A	270.901	-16.958	0.001	56233.0991898148
GRB121108A	83.194	54.474	0.001	56239.7385300926
GRB121117A	31.611	7.420	0.001	56248.3658101852
GRB121123A	307.318	-11.860	0.001	56254.4156365741
GRB121125A	228.527	55.313	0.001	56256.3529338310
GRB121127A	176.438	-52.417	0.483	56258.9109640046
GRB121128A	300.600	54.300	0.001	56259.2093402778
GRB121201A	13.467	-42.943	0.001	56262.5149537037
GRB121202A	256.797	23.948	0.001	56263.1777148611
GRB121209A	326.787	-8.235	0.001	56270.9132060185
GRB121211A	195.533	30.148	0.001	56272.5714180324
GRB121212A	177.793	78.037	0.001	56273.2861342593
GRB121217A	153.710	-62.351	0.001	56278.3002795718
GRB121225A	264.863	-66.067	0.283	56286.4071064815
GRB121226A	168.642	-30.406	0.001	56287.7955208333
GRB121229A	190.101	-50.594	0.001	56290.2056828704

Continued on next page

Table D.2 continued: Properties of the 872 GRBs that were searched for neutrino emission in the generic stacking analysis.

GCN name	ra (°)	dec (°)	σ (°)	t_s (MJD)
GRB130102B	310.904	-72.083	1.000	56294.1927314815
GRB130102A	311.423	49.818	0.001	56294.7546643519
GRB130122A	194.285	59.015	0.001	56314.9860995370
GRB130131A	171.127	48.076	0.001	56323.5779166667
GRB130131B	173.956	15.038	0.001	56323.7958101852
GRB130206A	140.377	-58.194	0.001	56329.8140959722
GRB130211A	147.536	-42.342	0.001	56334.1474768519
GRB130215A	43.486	13.387	0.012	56338.0605369444
GRB130216B	58.866	2.036	0.012	56339.7874588773
GRB130216A	67.901	14.670	0.008	56339.9244354977
GRB130228A	255.460	55.020	0.500	56351.1081271065
GRB130305A	116.748	52.033	0.001	56356.4826504630
GRB130306A	279.461	-11.681	0.001	56357.9881701968
GRB130310A	142.340	-17.230	0.450	56361.8371643519
GRB130313A	236.410	-0.369	0.001	56364.6694560185
GRB130315A	157.548	-51.794	0.001	56366.5287268519
GRB130325A	122.780	-18.900	0.250	56376.1998148148
GRB130327A	92.039	55.715	0.001	56378.0718055556
GRB130327B	217.875	-69.403	0.001	56378.3471527778
GRB130407A	248.096	10.517	0.250	56389.9811458333
GRB130408A	134.405	-32.361	0.001	56390.9079629630
GRB130418A	149.037	13.667	0.001	56400.7893865741
GRB130419A	355.278	9.900	0.020	56401.5599421296
GRB130420A	196.106	59.424	0.001	56402.3085532407
GRB130420B	183.128	54.391	0.001	56402.5362942130
GRB130427A	173.136	27.698	0.001	56409.3214814815
GRB130427B	314.899	-22.546	0.001	56409.5531365741
GRB130502B	66.650	71.083	0.183	56414.3243171296
GRB130502A	138.569	-0.123	0.001	56414.7405092593
GRB130504A	272.456	-16.313	0.001	56416.0843055556
GRB130504C	91.630	3.834	0.001	56416.9755439815
GRB130505A	137.061	17.485	0.001	56417.3460305324
GRB130508A	305.322	34.958	0.001	56420.7116087963
GRB130511A	196.646	18.710	0.001	56423.4768171296
GRB130513A	144.746	-5.233	0.050	56425.3151620370
GRB130514A	296.283	-7.976	0.001	56426.2982754630
GRB130514B	147.608	-18.967	0.050	56426.5571990741
GRB130515A	283.440	-54.279	0.001	56427.0535532407
GRB130518B	321.555	-20.148	0.014	56430.4489351852
GRB130518A	355.668	47.465	0.001	56430.5767013889
GRB130521B	281.642	22.717	0.917	56433.8891550926
GRB130521A	87.568	14.470	0.012	56433.9479861111
GRB130527A	309.276	-24.725	0.001	56439.5953506944
GRB130528A	139.505	87.301	0.001	56440.6924931713
GRB130529A	24.282	-64.147	0.001	56441.4661458333
GRB130603A	86.891	82.909	0.001	56446.2467824074

Continued on next page

Table D.2 continued: Properties of the 872 GRBs that were searched for neutrino emission in the generic stacking analysis.

GCN name	ra (°)	dec (°)	σ (°)	t_s (MJD)
GRB130603B	172.201	17.071	0.001	56446.6562962963
GRB130604A	250.187	68.226	0.001	56447.2849074074
GRB130605A	134.536	-33.461	0.001	56448.9843981481
GRB130606B	218.529	-22.102	0.001	56449.4940162037
GRB130606A	249.396	29.796	0.001	56449.8753356481
GRB130608A	24.611	41.503	0.001	56451.9654050926
GRB130609A	152.669	24.132	0.001	56452.1256712963
GRB130609B	53.771	-40.174	0.001	56452.8989075232
GRB130610A	224.420	28.207	0.001	56453.1305317361
GRB130612A	259.794	16.720	0.001	56455.1376250116
GRB130615A	274.829	-68.161	0.001	56458.4031828704
GRB130623A	20.853	-77.773	0.001	56466.4851238426
GRB130625A	343.278	82.174	0.001	56468.2892245370
GRB130626A	273.128	-9.525	0.014	56469.4492245370
GRB130627A	184.415	-37.087	0.001	56470.3684955324
GRB130627B	181.913	-55.701	0.001	56470.4976851852
GRB130701A	357.229	36.100	0.001	56474.1760666782
GRB130702A	217.312	15.774	0.001	56475.0008449074
GRB130708A	17.474	0.003	0.019	56481.4853437500
GRB130716A	179.577	63.053	0.001	56489.4393865741
GRB130719A	89.038	-11.591	0.015	56492.2386458333
GRB130722A	260.652	-2.973	0.001	56495.3438541667
GRB130725A	230.032	0.628	0.001	56498.4812615741
GRB130725B	214.241	-11.128	0.001	56498.7328472222
GRB130727A	330.798	-65.539	0.001	56500.6952490741
GRB130803A	220.253	-2.492	0.001	56507.4157456597
GRB130806A	35.928	67.532	0.001	56510.1162384259
GRB130807A	269.801	-27.616	0.001	56511.4316319444
GRB130812B	7.404	-79.183	1.100	56516.4521412037
GRB130812A	92.396	-13.288	0.001	56516.9296527778
GRB130816A	197.140	-58.945	0.001	56520.0710357755
GRB130816B	170.016	-57.557	0.001	56520.2010185185
GRB130821A	313.927	-11.966	0.001	56525.6710416667
GRB130822A	27.922	-3.208	0.001	56526.6598032407
GRB130828A	259.788	28.221	0.002	56532.3026620370
GRB130829A	182.426	46.520	0.010	56533.2356828704
GRB130831A	358.625	29.430	0.001	56535.5417361111
GRB130831B	192.420	-29.183	0.001	56535.5723263889
GRB130903A	82.138	-0.117	0.043	56538.0299768519
GRB130907A	215.892	45.608	0.001	56542.8993749653
GRB130912A	47.593	13.997	0.001	56547.3547106481
GRB130913A	341.960	1.294	0.026	56548.0167939815
GRB130919A	207.281	-10.353	0.012	56554.4605787037
GRB130925A	41.179	-26.153	0.001	56560.1612204398
GRB130929A	135.024	-47.561	0.001	56564.3974884259
GRB130930A	190.663	-35.500	0.050	56565.7953935185

Continued on next page

Table D.2 continued: Properties of the 872 GRBs that were searched for neutrino emission in the generic stacking analysis.

GCN name	ra (°)	dec (°)	σ (°)	t_s (MJD)
GRB131001A	8.304	25.557	0.012	56566.2314120370
GRB131002A	253.221	82.054	0.001	56567.2848485417
GRB131002B	75.122	-75.703	0.001	56567.4515972222
GRB131004A	296.113	-2.958	0.001	56569.9006134259
GRB131014A	100.303	-19.097	0.002	56579.2116898148
GRB131018A	98.471	-19.896	0.001	56583.5303009259
GRB131018B	304.410	23.110	0.130	56583.6697703356
GRB131024A	290.482	-64.603	0.001	56589.5153935185
GRB131024B	144.503	44.272	0.001	56589.8967192361
GRB131029A	200.785	48.298	0.260	56594.9698909491
GRB131030A	345.067	-5.368	0.001	56595.8695348495
GRB131031A	29.610	-1.579	0.001	56596.4787152778
GRB131103A	348.919	-44.640	0.001	56599.9189236111
GRB131105A	70.967	-62.995	0.001	56601.0837268519
GRB131108A	156.502	9.662	0.001	56604.8595248495
GRB131110A	69.268	-17.259	0.006	56606.4923726852
GRB131117A	332.331	-31.762	0.001	56613.0207638889
GRB131118A	349.863	-66.833	1.000	56614.9547106481
GRB131120A	278.937	-12.026	0.023	56616.6067824074
GRB131122A	152.554	57.733	0.027	56618.8894791667
GRB131127A	332.730	36.609	0.001	56623.4218171296
GRB131128A	355.308	31.306	0.001	56624.6265509259
GRB131202A	344.054	-21.662	0.001	56628.6305150347
GRB131205A	131.628	-60.156	0.001	56631.3850462963
GRB131209A	136.500	-33.200	0.900	56635.5442936111
GRB131215A	259.029	-7.583	1.000	56641.3778935185
GRB131218A	113.800	-64.717	0.047	56644.8759490741
GRB131224B	163.722	-14.177	0.023	56650.1395601852
GRB131224A	296.833	31.667	0.033	56650.7017013889
GRB131225A	95.038	5.317	1.000	56651.4101851852
GRB131226A	301.309	-64.943	0.008	56652.2385186690
GRB131227A	67.378	28.883	0.001	56653.1949189815
GRB131229A	85.232	-4.396	0.001	56655.2744675926
GRB131231A	10.590	-1.653	0.001	56657.1952092593
GRB140102A	211.919	1.333	0.001	56659.8843315394
GRB140103A	232.087	37.759	0.001	56660.0184375000
GRB140104B	218.754	-9.028	0.001	56661.7276984954
GRB140108A	325.112	58.744	0.001	56665.7184259259
GRB140110A	28.900	-36.260	0.500	56667.2600425926
GRB140114A	188.522	27.951	0.001	56671.4954861111
GRB140118A	330.999	-17.937	0.012	56675.0602625000
GRB140129A	37.891	-1.595	0.001	56686.1387615741
GRB140129B	326.757	26.206	0.001	56686.5326273148
GRB140206B	315.260	-8.510	0.230	56694.2722113542
GRB140206A	145.334	66.761	0.001	56694.3008101852
GRB140209A	81.329	32.498	0.001	56697.3102662037

Continued on next page

Table D.2 continued: Properties of the 872 GRBs that were searched for neutrino emission in the generic stacking analysis.

GCN name	ra (°)	dec (°)	σ (°)	t_s (MJD)
GRB140211A	124.223	20.243	0.001	56699.5131134259
GRB140213A	105.155	-73.137	0.001	56701.8037308796
GRB140215A	104.149	41.787	0.001	56703.1687500000
GRB140221A	107.446	-17.333	0.400	56709.2976851852
GRB140226A	221.492	15.000	0.002	56714.4158217593
GRB140301A	69.558	-34.257	0.001	56717.6393402778
GRB140302A	253.859	-12.878	0.001	56718.3394444444
GRB140304A	30.643	33.474	0.001	56720.5543530787
GRB140305A	344.497	15.448	0.013	56721.6223379630
GRB140306A	27.942	48.983	0.983	56722.1427278472
GRB140308A	357.562	-33.350	0.933	56724.1564225231
GRB140311A	209.305	0.642	0.001	56727.8757638889
GRB140311B	252.325	52.724	0.001	56727.8821643519
GRB140318A	184.089	20.209	0.001	56734.0034375000
GRB140320A	281.855	-11.194	0.001	56736.0892927894
GRB140320B	145.567	60.250	0.053	56736.3901620370
GRB140320C	134.383	71.200	0.053	56736.5508101852
GRB140323A	356.959	-79.905	0.001	56739.4296657407
GRB140329A	145.698	-32.229	0.200	56745.2919907407
GRB140331A	134.864	2.717	0.001	56747.2400231482
GRB140402A	207.592	5.971	0.022	56749.0041203704
GRB140408A	290.716	-12.595	0.001	56755.5498148148
GRB140412A	144.974	-65.822	0.001	56759.9282291667
GRB140413A	65.455	-51.183	0.001	56760.0038194444
GRB140414A	195.310	56.902	0.031	56761.2516087963
GRB140419A	126.990	46.240	0.001	56766.1685300926
GRB140423A	197.286	49.842	0.001	56770.3523377315
GRB140428A	194.369	28.385	0.001	56775.9421296296
GRB140430A	102.936	23.024	0.001	56777.8537731481
GRB140502A	319.188	48.970	0.001	56779.3514880903
GRB140506A	276.775	-55.636	0.001	56783.8773484838
GRB140509A	46.595	-62.639	0.001	56786.0958680556
GRB140509B	313.121	21.150	1.000	56786.6767129630
GRB140512A	289.370	-15.094	0.001	56789.8107928241
GRB140515A	186.064	15.105	0.001	56792.3808564815
GRB140515B	289.467	-11.000	1.000	56792.5393865741
GRB140516A	252.989	39.963	0.001	56793.8518981481
GRB140518A	227.252	42.418	0.001	56795.3844444444
GRB140521A	320.177	67.587	0.009	56798.7292592593
GRB140523A	133.300	24.950	0.400	56800.1262384259
GRB140528A	280.729	-58.750	0.950	56805.8341753472
GRB140529A	228.782	-41.053	0.001	56806.3916203704
GRB140604A	263.171	-40.400	1.267	56812.1986226852
GRB140606A	201.799	37.599	0.019	56814.4542013889
GRB140607A	86.373	18.904	0.015	56815.7148263889
GRB140610A	286.269	3.908	0.001	56818.6856080556

Continued on next page

Table D.2 continued: Properties of the 872 GRBs that were searched for neutrino emission in the generic stacking analysis.

GCN name	ra (°)	dec (°)	σ (°)	t_s (MJD)
GRB140611A	349.917	-40.104	0.001	56819.1575694444
GRB140614A	231.169	-79.129	0.001	56822.0422337963
GRB140614B	322.631	14.930	0.001	56822.2736226852
GRB140614C	147.423	71.945	0.023	56822.8352546296
GRB140619B	132.680	-9.660	0.060	56827.4725725000
GRB140619A	27.109	-39.259	0.001	56827.4822337963
GRB140621A	73.279	14.650	0.717	56829.8235821528
GRB140622A	317.173	-14.419	0.001	56830.3971527778
GRB140626A	77.378	-82.630	0.001	56834.0200347222
GRB140628A	40.666	-0.385	0.001	56836.5635069444
GRB140629A	248.977	41.877	0.001	56837.5925925926
GRB140703A	12.996	45.102	0.001	56841.0228841435
GRB140706A	49.293	-38.052	0.001	56844.8119217593
GRB140709A	304.662	51.225	0.001	56847.0479894560
GRB140709B	146.055	63.530	0.001	56847.6330037616
GRB140710A	41.068	35.499	0.001	56848.4253472222
GRB140710B	204.667	-58.550	0.050	56848.8981481481
GRB140713A	281.106	59.633	0.001	56851.7774884259
GRB140716A	108.171	-60.175	0.001	56854.4331824769
GRB140719A	171.601	-50.135	0.001	56857.2428842593
GRB140719B	39.731	-2.384	0.013	56857.8648805556
GRB140723A	210.630	-3.730	0.350	56861.0641245023
GRB140729A	193.950	15.350	0.333	56867.0227281134
GRB140730A	56.399	-66.545	0.001	56868.8192245370
GRB140810A	119.042	27.550	0.117	56879.7791676620
GRB140814A	182.512	49.350	0.333	56883.2974652778
GRB140815A	86.896	-8.667	0.042	56884.9103587963
GRB140817A	127.263	58.190	0.001	56886.2900344213
GRB140818A	199.513	6.800	1.000	56887.2263787037
GRB140818B	271.135	-1.386	0.001	56887.7777904514
GRB140824A	206.617	33.294	0.001	56893.3585416667
GRB140825A	88.713	-11.833	0.450	56894.2855902778
GRB140828A	142.029	14.569	0.010	56897.2847000347
GRB140901B	112.184	-29.209	0.016	56901.2591698495
GRB140903A	238.014	27.603	0.001	56903.6224537037
GRB140906C	314.962	1.933	1.000	56906.9909606481
GRB140907A	48.146	46.605	0.001	56907.6686493866
GRB140909A	193.612	63.517	0.001	56909.2865856482
GRB140916A	40.399	-39.686	0.001	56916.4441782407
GRB140919A	221.537	-32.176	0.001	56919.6326798148
GRB140927A	291.792	-65.394	0.001	56927.2159837963
GRB140928A	43.699	-55.929	0.001	56928.4344074306
GRB140930B	6.348	24.295	0.001	56930.8177314815
GRB141004A	76.734	12.820	0.001	56934.9699537037
GRB141005A	291.093	36.095	0.001	56935.2145370370
GRB141011A	257.938	-9.683	0.700	56941.2792553935

Continued on next page

Table D.2 continued: Properties of the 872 GRBs that were searched for neutrino emission in the generic stacking analysis.

GCN name	ra (°)	dec (°)	σ (°)	t_s (MJD)
GRB141015A	87.519	18.330	0.001	56945.3811226852
GRB141017A	93.630	-58.582	0.001	56947.7647916667
GRB141020A	224.996	55.313	0.001	56950.3225578704
GRB141022A	241.870	-72.125	0.001	56952.0580092593
GRB141026A	44.085	26.928	0.001	56956.1060300926
GRB141028A	322.602	-0.231	0.001	56958.4518145833
GRB141029B	105.200	25.100	1.000	56959.1313497338
GRB141031A	128.609	-59.168	0.001	56961.3014646875
GRB141031B	356.905	41.352	0.001	56961.6198495370
GRB141102A	208.614	-47.100	0.031	56963.5329474074
GRB141104A	279.488	-12.700	0.850	56964.9994157060
GRB141109A	144.531	-0.608	0.001	56970.2401041667
GRB141109B	222.303	73.131	0.001	56970.3218634259
GRB141121A	122.669	22.217	0.001	56982.1472569444
GRB141130A	222.822	47.319	0.001	56991.9630324074
GRB141205A	92.859	37.876	0.016	56996.3341087963
GRB141207A	159.855	3.711	0.001	56998.7966562500
GRB141212A	39.125	18.147	0.001	57003.5068402778
GRB141212B	250.876	31.750	0.001	57003.5553009259
GRB141215A	179.054	-52.750	1.100	57006.5569866319
GRB141220A	195.066	32.146	0.001	57011.2490924768
GRB141221A	198.287	8.205	0.001	57012.3353300000
GRB141222A	178.040	-57.350	0.100	57013.2949692361
GRB141225A	138.779	33.792	0.001	57016.9562152778
GRB141229A	72.428	-19.233	0.001	57020.4894656944
GRB150101A	312.603	36.733	0.001	57023.2671643519
GRB150101B	188.021	-10.934	0.001	57023.6380787037
GRB150103A	131.666	-48.886	0.001	57025.8320370370
GRB150110B	289.375	32.523	0.001	57032.9196759259
GRB150110C	68.575	-16.867	0.183	57032.9839236111
GRB150118B	240.240	-35.750	0.500	57040.4056365741
GRB150118C	160.075	-27.417	1.000	57040.9238733796
GRB150120A	10.319	33.995	0.001	57042.1205555556
GRB150120B	39.291	8.078	0.001	57042.3039930556
GRB150123A	111.558	-9.683	0.133	57045.6233796296
GRB150126A	350.500	-12.367	0.567	57048.8655761343
GRB150201A	11.833	-37.619	0.001	57054.5713154282
GRB150202A	39.227	-33.148	0.001	57055.9624074074
GRB150202B	86.600	59.100	0.050	57055.9965046296
GRB150203A	98.399	6.954	0.001	57056.1700981366
GRB150204A	160.237	-64.039	0.001	57057.2686721181
GRB150206A	10.074	-63.182	0.001	57059.6012962963
GRB150210A	112.180	13.310	0.300	57063.9321064815
GRB150211A	254.859	55.393	0.001	57064.4916520833
GRB150212A	285.482	47.364	0.001	57065.4535763889
GRB150213B	253.453	34.189	0.001	57066.9356481482

Continued on next page

Table D.2 continued: Properties of the 872 GRBs that were searched for neutrino emission in the generic stacking analysis.

GCN name	ra (°)	dec (°)	σ (°)	t_s (MJD)
GRB150219A	271.267	-41.600	0.055	57072.5187761458
GRB150222B	155.896	-41.167	0.400	57075.2222916667
GRB150222A	198.786	-12.152	0.001	57075.7031250000
GRB150301A	244.305	-48.713	0.001	57082.0418750000
GRB150301B	89.166	-57.970	0.001	57082.8152083333
GRB150302A	175.531	36.811	0.001	57083.2350231481
GRB150309A	277.102	86.429	0.001	57090.9553316898
GRB150311A	235.096	-15.817	0.283	57092.6764583333
GRB150314A	126.670	63.834	0.001	57095.2018518519
GRB150317A	138.985	55.466	0.001	57098.1795370370
GRB150318A	325.006	-61.457	0.001	57099.2921643518
GRB150323A	128.178	45.465	0.001	57104.1146296296
GRB150323B	260.453	38.318	0.001	57104.3919907407
GRB150323C	192.617	50.191	0.001	57104.7088576620
GRB150402A	173.658	40.992	0.019	57114.0233333333
GRB150403A	311.505	-62.711	0.001	57115.9097332176
GRB150407A	216.603	38.541	0.023	57119.0187500000
GRB150413A	190.396	71.839	0.015	57125.5769444444
GRB150418A	160.546	-4.933	1.000	57130.0333101852
GRB150423A	221.579	12.284	0.001	57135.2665972222
GRB150424A	152.306	-26.631	0.001	57136.3185995370
GRB150428A	188.538	6.954	0.001	57140.0600694444
GRB150428B	292.639	4.125	0.001	57140.1304745370
GRB150430A	326.480	-27.902	0.001	57142.0117077662
GRB150510A	16.160	4.790	0.360	57152.1358623264
GRB150513A	49.044	-22.868	0.008	57155.8517137500
GRB150514A	74.876	-60.968	0.001	57156.7714714120
GRB150518A	234.208	16.267	1.000	57160.9014351852
GRB150523A	115.286	-45.420	0.001	57165.3928018518
GRB150527A	288.960	4.202	0.001	57169.2796772222
GRB150530A	327.512	57.517	0.001	57172.4847752662
GRB150530B	7.496	44.290	0.023	57172.5586574074
GRB150607A	139.988	68.436	0.001	57180.3270717593
GRB150608A	13.650	-0.133	1.000	57181.4869883218
GRB150615A	107.565	-22.449	0.001	57188.1932523148
GRB150616A	314.717	-53.394	0.001	57189.9480208333
GRB150622A	251.738	-52.933	1.000	57195.4302430556
GRB150626A	111.337	-37.781	0.001	57199.0893402778
GRB150626B	187.633	66.772	0.001	57199.8463194444
GRB150627A	117.471	-51.489	0.001	57200.1800115741
GRB150702A	52.780	-57.000	0.360	57205.9947633102
GRB150710A	194.470	14.318	0.001	57213.0165703935
GRB150710B	83.219	-46.942	0.001	57213.3343046528
GRB150711A	221.627	-35.456	0.001	57214.7627575694
GRB150716A	278.488	-12.980	0.001	57219.2934375000
GRB150720A	119.581	-28.262	0.001	57223.5819328704

Continued on next page

Table D.2 continued: Properties of the 872 GRBs that were searched for neutrino emission in the generic stacking analysis.

GCN name	ra (°)	dec (°)	σ (°)	t_s (MJD)
GRB150722A	218.278	-35.196	0.001	57225.4123032407
GRB150724A	97.560	-19.165	0.001	57227.2377893518
GRB150724B	351.890	3.818	0.068	57227.7787813657
GRB150725A	220.421	-2.417	0.117	57228.3611621528
GRB150727A	203.969	-18.325	0.001	57230.7901019907
GRB150728A	292.229	33.916	0.001	57231.5326504630
GRB150801A	255.925	-9.433	1.000	57235.0519097222
GRB150801B	82.966	-5.389	0.001	57235.9428009259
GRB150811A	291.339	-15.425	0.001	57245.1680439815
GRB150817A	249.631	-12.053	0.001	57251.0840003704
GRB150818A	230.356	68.343	0.001	57252.4808101852
GRB150819A	42.333	9.807	0.001	57253.0319212963
GRB150819B	59.388	39.700	1.400	57253.4369097222
GRB150821A	341.913	-57.894	0.001	57255.4026620370
GRB150824A	161.250	-55.917	1.000	57258.0759273032
GRB150831A	221.024	-25.635	0.001	57265.4374944329
GRB150831B	271.040	-27.259	0.001	57265.9272626620
GRB150901A	183.609	25.076	0.021	57266.6405671296
GRB150902A	214.980	-69.354	0.001	57267.7301894676
GRB150906B	159.237	-25.600	0.500	57271.3598444444
GRB150907A	224.842	-47.600	0.067	57272.6643518519
GRB150907B	255.304	-63.785	0.001	57272.9738078704
GRB150910A	5.667	33.473	0.001	57275.3754398148
GRB150911A	67.434	5.735	0.001	57276.7751273148
GRB150912A	248.433	-20.983	0.050	57277.4398148148
GRB150915A	319.658	-34.914	0.001	57280.8848842593
GRB150919A	132.958	44.067	0.983	57284.8604745370
GRB150922A	294.379	-5.483	1.250	57287.2314699074
GRB150925A	227.534	-19.633	0.001	57290.1703472222
GRB151001A	233.729	10.967	0.001	57296.6249125000
GRB151001B	336.839	64.694	0.001	57296.7676620370
GRB151004A	213.632	-64.939	0.001	57299.7534027778
GRB151006A	147.426	70.503	0.001	57301.4102748380
GRB151021A	337.643	-33.197	0.001	57316.0588719329
GRB151022A	349.197	55.812	0.001	57317.5849768519
GRB151023A	270.985	-8.316	0.001	57318.5686805556
GRB151027A	272.487	61.353	0.001	57322.1626620370
GRB151027B	76.219	-6.450	0.001	57322.9420138889
GRB151029A	38.528	-35.386	0.001	57324.3232523148
GRB151031A	83.196	-39.122	0.001	57326.2405092593
GRB151107A	217.139	-59.680	0.021	57333.7190509259
GRB151111A	56.845	-44.161	0.001	57337.3535882870
GRB151112A	2.054	-61.663	0.001	57338.5698842593
GRB151114A	120.943	-61.028	0.001	57340.4134722222
GRB151118A	57.172	65.902	0.001	57344.1266203704
GRB151120A	157.242	-32.517	0.047	57346.3462962963

Continued on next page

Table D.2 continued: Properties of the 872 GRBs that were searched for neutrino emission in the generic stacking analysis.

GCN name	ra (°)	dec (°)	σ (°)	t_s (MJD)
GRB151122A	299.704	-19.899	0.023	57348.7059027778
GRB151127A	19.476	-82.771	0.001	57353.3782291667
GRB151205A	229.289	35.744	0.001	57361.6540509259
GRB151205B	41.190	-43.461	0.018	57361.9021296296
GRB151210A	65.117	-71.251	0.001	57366.1310879630
GRB151212A	68.108	-3.767	0.517	57368.5807523148
GRB151215A	93.584	35.516	0.001	57371.1231250000
GRB151216A	323.913	24.767	0.333	57372.7910300926
GRB151222A	354.942	34.100	0.967	57378.3375389815
GRB151227B	290.283	35.417	1.300	57383.2150171181
GRB151228A	214.017	-17.665	0.014	57384.1257175926
GRB151228B	344.424	8.082	0.001	57384.9465281134
GRB151229A	329.370	-20.732	0.001	57385.2821412037
GRB160101A	219.729	-13.817	0.150	57388.0275686458
GRB160101B	1.400	55.200	1.400	57388.2125115741
GRB160102A	80.837	-21.033	0.217	57389.1493750000
GRB160104A	76.796	11.324	0.001	57391.4722180093
GRB160107A	299.667	6.417	0.217	57394.9276157407
GRB160117A	20.367	-0.655	0.001	57404.4232523148
GRB160117B	132.195	-16.367	0.001	57404.5800578704
GRB160119A	211.922	20.461	0.001	57406.1263657407
GRB160121A	109.088	-23.592	0.001	57408.5739236111
GRB160123A	150.313	-33.775	0.001	57410.3709490741
GRB160127A	225.982	0.073	0.001	57414.3603819444
GRB160131A	78.168	-7.050	0.001	57418.3446875000
GRB160203A	161.951	-24.789	0.001	57421.0895833333
GRB160206A	132.696	-36.100	0.350	57424.1170486111
GRB160216A	311.684	-71.548	0.001	57434.7960663079
GRB160220A	236.953	-18.566	0.001	57438.0564236111
GRB160220B	259.865	-18.124	0.001	57438.4629976852
GRB160221A	232.079	-28.450	0.053	57439.9899537037
GRB160223A	147.598	9.370	0.001	57441.0695878125
GRB160223B	94.975	33.400	0.053	57441.4130555556
GRB160225A	164.230	53.670	0.001	57443.5949768519
GRB160227A	194.808	78.679	0.001	57445.8110879630
GRB160228A	107.316	26.932	0.001	57446.7294212963
GRB160303A	168.701	22.742	0.001	57450.4517592593
GRB160310A	98.822	-7.216	0.001	57457.0130494213
GRB160313A	183.797	57.283	0.001	57460.1063078704
GRB160314A	112.791	17.000	0.001	57461.4782523148
GRB160314B	167.560	45.670	0.650	57461.9261561806
GRB160321A	99.420	5.748	0.001	57468.6606134259
GRB160325A	15.651	-72.696	0.001	57472.2883160880
GRB160327A	146.702	54.013	0.001	57474.3832986111
GRB160401A	89.737	26.683	0.033	57479.8446759259
GRB160408A	122.625	71.128	0.001	57486.2649652778

Continued on next page

Table D.2 continued: Properties of the 872 GRBs that were searched for neutrino emission in the generic stacking analysis.

GCN name	ra (°)	dec (°)	σ (°)	t_s (MJD)
GRB160409A	289.705	-5.390	0.023	57487.2431018519
GRB160410A	150.685	3.479	0.001	57488.2122453704
GRB160411A	349.357	-40.242	0.001	57489.0588078704
GRB160412A	33.046	-67.627	0.001	57490.1803703704
GRB160417A	120.257	7.663	0.001	57495.1802199074
GRB160419A	16.418	-27.341	0.008	57497.6333901505
GRB160422A	42.095	-57.875	0.001	57500.4964098380
GRB160424A	319.485	-60.415	0.001	57502.4895351505
GRB160425A	280.327	-54.360	0.001	57503.9736226852
GRB160501A	286.384	-17.241	0.001	57509.0252430556
GRB160503A	0.540	-1.930	0.520	57511.5641139815
GRB160504A	170.072	56.002	0.001	57512.8100347222
GRB160506A	265.849	-46.134	0.001	57514.1424189815
GRB160509A	311.754	76.108	0.001	57517.3712525347
GRB160519A	71.122	31.246	0.017	57527.0092796065
GRB160521A	129.717	46.900	0.053	57529.1480324074
GRB160521B	147.667	79.031	0.001	57529.3817943287
GRB160525A	103.575	-0.199	0.026	57533.0623726852
GRB160525B	149.385	51.207	0.001	57533.3895486111
GRB160601A	234.935	64.541	0.001	57540.6103240741
GRB160607A	13.667	-4.948	0.001	57546.4651264236
GRB160611A	164.422	-70.392	0.001	57550.9002777778
GRB160612A	348.364	-25.375	0.023	57551.8393220023
GRB160620A	250.663	30.317	1.450	57559.2097569444
GRB160623A	315.297	42.221	0.001	57562.2051804861
GRB160624A	330.193	29.644	0.001	57563.4742013889
GRB160625B	308.598	6.919	0.001	57564.9417277778
GRB160625A	176.916	-65.145	0.001	57564.9419097222
GRB160629A	4.821	76.983	0.052	57568.9273148148
GRB160630A	198.259	-56.042	0.001	57569.1666550926
GRB160702A	230.887	8.717	1.200	57571.5126620370
GRB160703A	287.417	36.917	0.001	57572.5041087963
GRB160705B	168.109	46.700	0.001	57574.8735763889
GRB160709A	235.996	-28.188	0.019	57578.8228298611
GRB160712A	304.160	-26.958	0.001	57581.8259953704
GRB160714A	234.490	63.809	0.021	57583.0938078704
GRB160716A	190.438	-61.351	0.001	57585.0446759259
GRB160726A	98.809	-6.617	0.010	57595.0624457755
GRB160801A	212.763	13.489	0.001	57601.3918981481
GRB160802A	28.029	71.367	0.883	57602.2564771991
GRB160804A	221.630	9.999	0.001	57604.0615393519
GRB160814A	136.071	-20.967	1.000	57614.8810763889
GRB160815A	288.540	84.314	0.001	57615.4867904282
GRB160816A	322.411	37.133	0.001	57616.7269440972
GRB160819A	114.138	-22.350	1.100	57619.8496005671
GRB160821A	171.257	42.335	0.001	57621.8543981481

Continued on next page

Table D.2 continued: Properties of the 872 GRBs that were searched for neutrino emission in the generic stacking analysis.

GCN name	ra (°)	dec (°)	σ (°)	t_s (MJD)
GRB160821B	279.976	62.391	0.001	57621.9340625000
GRB160824A	80.088	40.028	0.001	57624.9710069444
GRB160826A	183.113	-67.664	0.001	57626.2558796296
GRB160827A	179.274	-29.178	0.019	57627.6545717593
GRB160829A	201.700	-56.770	0.120	57629.3315583333
GRB160905A	162.247	-50.801	0.001	57636.4685753472
GRB160910A	221.442	39.067	0.001	57641.7190856481
GRB160912A	301.499	57.566	0.001	57643.6691319444
GRB160917A	295.666	46.403	0.001	57648.4764930556
GRB160927A	256.243	17.332	0.001	57658.7504513889
GRB161001A	71.920	-57.261	0.001	57662.0424305556
GRB161004A	263.152	-0.951	0.001	57665.5377083333
GRB161004B	112.151	-39.898	0.001	57665.9609295949
GRB161007A	103.409	23.307	0.001	57668.8899652778
GRB161010A	275.238	-28.767	0.045	57671.5641435185
GRB161011A	245.729	8.311	0.001	57672.2435648148
GRB161014A	332.648	7.469	0.001	57675.5187799306
GRB161015A	269.150	30.183	0.210	57676.7076029977
GRB161017A	142.769	43.127	0.001	57678.7414213889
GRB161020A	161.033	-54.767	0.033	57681.0211721181
GRB161022A	129.002	54.348	0.001	57683.1106487153
GRB161023A	311.033	-47.667	0.043	57684.9406250000
GRB161104A	77.894	-51.460	0.001	57696.4015740741
GRB161105A	120.184	-44.775	0.001	57697.2006018519
GRB161108A	180.788	24.868	0.001	57700.1447106482
GRB161109A	157.860	61.800	0.260	57701.2601233796
GRB161113A	179.794	-5.309	0.001	57705.7265740741
GRB161117A	322.052	-29.614	0.001	57709.0634416319
GRB161117B	298.825	-67.703	0.001	57709.4066319444
GRB161123A	32.212	-39.650	1.000	57715.1262500000
GRB161129A	316.228	32.135	0.001	57721.2968634259
GRB161202A	356.903	19.646	0.001	57724.9636437731
GRB161214A	190.729	6.833	0.053	57736.1957986111
GRB161214B	3.851	7.352	0.001	57736.7194444444
GRB161217A	150.651	52.359	0.001	57739.0579166667
GRB161218A	245.250	-4.113	0.008	57740.1551153935
GRB161219A	188.438	10.467	0.053	57741.6759953704
GRB161219B	91.714	-26.792	0.001	57741.7806632870
GRB161220A	350.848	-47.498	0.001	57742.3537037037
GRB161224A	204.816	-18.029	0.001	57746.9232018519
GRB170101A	267.089	11.642	0.009	57754.0984699306
GRB170105A	138.304	61.100	0.050	57758.2569097222
GRB170111A	20.697	-32.565	0.001	57764.0203472222
GRB170112A	15.232	-17.233	0.019	57765.0818287037
GRB170113A	61.733	-71.943	0.001	57766.4166087963
GRB170115B	189.120	-46.850	0.260	57768.7396184028

Continued on next page

Table D.2 continued: Properties of the 872 GRBs that were searched for neutrino emission in the generic stacking analysis.

GCN name	ra (°)	dec (°)	σ (°)	t_s (MJD)
GRB170115A	332.138	13.728	0.001	57768.8652546296
GRB170126A	263.633	-64.760	0.001	57779.4767390394
GRB170127C	339.329	-63.933	0.400	57780.0635956019
GRB170127A	174.360	-45.836	0.001	57780.5951967593
GRB170127B	19.977	-30.358	0.001	57780.6314583333
GRB170131A	341.447	64.006	0.023	57784.9658194213
GRB170202A	152.515	5.012	0.001	57786.7665740741
GRB170203A	332.861	25.186	0.017	57786.9996643519
GRB170205A	262.170	-0.063	0.001	57789.5242939815
GRB170206A	212.792	14.483	0.850	57790.4498575926
GRB170206B	271.771	11.194	0.001	57790.9119791667
GRB170208A	166.565	-46.768	0.001	57792.7549305556
GRB170208B	127.144	-9.030	0.001	57792.9370207870
GRB170214A	256.341	-1.888	0.001	57798.6460175926
GRB170219A	54.842	50.067	1.417	57802.9992607060
GRB170222A	292.954	28.217	0.800	57806.2060940741
GRB170228A	239.550	-3.583	0.283	57812.7908531250
GRB170306A	263.069	-44.748	0.001	57818.2930787037
GRB170306B	154.620	51.590	0.610	57818.5855471065
GRB170307A	13.510	9.538	0.019	57819.8473495370
GRB170311A	280.589	-30.046	0.001	57823.3364814815
GRB170311B	354.917	31.183	1.417	57823.5699074074
GRB170317A	93.062	50.493	0.001	57829.4040393519
GRB170318A	305.667	28.406	0.001	57830.5053935185
GRB170318B	284.306	6.299	0.001	57830.6414464815
GRB170325A	127.483	20.526	0.016	57837.3283327546
GRB170329A	356.000	23.790	0.600	57841.3839478588
GRB170330A	283.331	-13.431	0.001	57842.9328813194
GRB170331A	323.792	-24.386	0.001	57843.0670833333
GRB170405A	219.828	-25.243	0.001	57848.7744546991
GRB170409A	347.530	-7.160	0.150	57852.1096005787
GRB170419A	79.855	-21.424	0.001	57862.5572916667
GRB170419B	60.494	-15.121	0.011	57862.8955555556
GRB170424A	343.700	-45.117	0.450	57867.4224623843
GRB170428A	330.078	26.916	0.001	57871.3815823958
GRB170510A	159.912	-39.333	0.333	57883.2140709491
GRB170511A	300.629	33.317	0.283	57884.2465499537
GRB170516A	41.568	-55.910	0.001	57889.5313657407
GRB170519A	163.427	25.374	0.001	57892.2124074074
GRB170522A	139.342	25.667	0.183	57895.6537532407
GRB170524B	90.869	-17.083	0.001	57897.4419962384
GRB170524A	319.486	48.607	0.001	57897.8229745370
GRB170526A	4.707	1.277	0.001	57899.5631712963
GRB170531A	121.252	-14.023	0.001	57904.8356712963
GRB170531B	286.884	-16.418	0.001	57904.9152662037
GRB170604A	342.656	-15.412	0.001	57908.7949074074

Continued on next page

Table D.2 continued: Properties of the 872 GRBs that were searched for neutrino emission in the generic stacking analysis.

GCN name	ra (°)	dec (°)	σ (°)	t_s (MJD)
GRB170607A	7.366	9.243	0.001	57911.9679333218
GRB170610A	92.567	-9.417	0.233	57914.8602777778
GRB170626A	165.394	56.477	0.001	57930.3980329630
GRB170629A	129.985	-46.571	0.001	57933.5342780903
GRB170705A	191.704	18.307	0.001	57939.1122337963
GRB170710A	231.820	-38.485	0.001	57944.0288657407
GRB170710C	352.254	51.300	0.042	57944.2090856482
GRB170710B	43.122	42.679	0.008	57944.3374566088
GRB170711A	45.800	47.849	0.001	57945.9279400810
GRB170714A	34.350	1.991	0.001	57948.5148379630
GRB170724A	150.057	-1.025	0.019	57958.0309490741
GRB170728A	58.888	12.182	0.001	57962.2842361111
GRB170728B	237.981	70.122	0.001	57962.9577362500
GRB170730A	245.300	-60.883	0.050	57964.0035879630
GRB170803A	174.934	-16.311	0.001	57968.7265847222
GRB170804A	6.393	-64.784	0.001	57969.4982291667
GRB170807A	143.434	-17.348	0.012	57972.9110995370
GRB170808A	157.562	-28.283	0.333	57973.1137384259
GRB170808B	145.658	2.183	0.333	57973.9329767014
GRB170810A	187.939	3.661	0.001	57975.9147444560
GRB170813A	201.058	-5.491	0.001	57978.0478968866
GRB170822A	94.386	55.004	0.001	57987.3803356482
GRB170823A	188.713	35.549	0.008	57988.9254398148
GRB170827A	276.151	-40.202	0.001	57992.2140972222
GRB170830A	267.242	-2.000	0.083	57995.1318287037
GRB170903A	254.526	34.979	0.001	57999.5312066319
GRB170906A	203.955	-47.101	0.001	58002.0270619213
GRB170906B	232.204	-28.256	0.001	58002.0357707755
GRB170906C	128.654	70.812	0.001	58002.3070254630
GRB170911A	72.096	30.917	0.383	58007.2639421528
GRB170912A	167.373	-54.326	0.001	58008.0625694444
GRB170912B	215.459	-61.997	0.001	58008.2705555556
GRB170921A	26.849	30.907	0.001	58017.6004398148
GRB171001A	22.077	-11.894	0.001	58027.7649305556
GRB171004A	139.169	52.693	0.001	58030.3273379630
GRB171007A	135.600	42.819	0.001	58033.4954629630
GRB171010A	66.740	-10.530	0.200	58036.7893518519
GRB171010B	34.134	-54.391	0.001	58036.8716888426
GRB171011A	236.766	-10.064	0.008	58037.7698726852
GRB171020A	39.248	15.204	0.001	58046.9604166667
GRB171022A	204.270	10.970	0.170	58048.8820199421
GRB171027A	61.691	-2.622	0.001	58053.3464814815
GRB171102A	187.729	54.033	0.817	58059.1037615741
GRB171102B	288.078	22.444	0.001	58059.6363310185
GRB171103A	249.510	-10.206	0.012	58060.9627219444
GRB171112A	20.075	-59.633	1.000	58069.8630508681

Continued on next page

Table D.2 continued: Properties of the 872 GRBs that were searched for neutrino emission in the generic stacking analysis.

GCN name	ra (°)	dec (°)	σ (°)	t_s (MJD)
GRB171115A	278.388	9.125	0.001	58072.7827546296
GRB171120A	163.790	22.459	0.001	58077.5526699421
GRB171123A	186.246	32.501	0.001	58080.5907060185
GRB171124A	335.476	35.332	0.001	58081.2317801042
GRB171205A	167.415	-12.588	0.001	58092.3031597222
GRB171209A	139.403	-30.520	0.001	58096.6125694444
GRB171210A	335.290	24.440	0.150	58097.4896412037
GRB171211A	98.134	-58.691	0.001	58098.3912268519
GRB171212B	39.442	-70.617	0.383	58099.4306422338
GRB171212A	293.918	20.592	0.001	58099.4952662037
GRB171216A	211.991	-50.485	0.001	58103.1269560185
GRB171216B	340.067	52.050	0.400	58103.5983449074
GRB171222A	148.278	35.627	0.001	58109.6811226852
GRB180102A	203.067	62.172	0.001	58120.6565858449
GRB180103A	159.601	-53.556	0.001	58121.0446759259
GRB180111A	149.780	48.267	0.001	58129.6930092593
GRB180113A	19.211	68.682	0.008	58131.1131481481
GRB180115A	12.039	-15.631	0.001	58133.1749189815
GRB180116A	215.654	18.967	0.133	58134.0226969329
GRB180204A	330.133	30.838	0.001	58153.1055891435
GRB180205A	126.820	11.542	0.001	58154.1814074190
GRB180210A	1.800	18.350	0.180	58159.5142129630
GRB180222A	256.543	-36.813	0.001	58171.5457407407
GRB180224A	202.684	38.079	0.001	58173.9284375000
GRB180305A	49.671	32.100	0.110	58182.3902505440
GRB180311A	3.388	-54.491	0.001	58188.7497569444
GRB180314A	99.265	-24.496	0.001	58191.0271978935
GRB180314B	297.887	23.624	0.001	58191.9301620370
GRB180316A	265.429	0.748	0.001	58193.2036458333
GRB180324A	76.527	56.714	0.001	58201.1895717593
GRB180325A	157.427	24.463	0.001	58202.0756018519
GRB180329A	329.314	-15.043	0.018	58206.0373842593
GRB180329B	82.904	-23.691	0.001	58206.5862615741
GRB180331A	66.025	13.399	0.001	58208.1741319444
GRB180331B	196.783	61.726	0.001	58208.6489467593
GRB180402A	251.934	-14.969	0.001	58210.4033449074
GRB180404A	83.549	-37.168	0.001	58212.0287615741
GRB180404B	53.393	-50.215	0.001	58212.0885190856
GRB180407A	35.236	33.513	0.014	58215.0768402778
GRB180409A	175.842	36.300	0.817	58217.3431559028
GRB180410A	95.957	12.811	0.001	58218.3325115741
GRB180411A	356.854	66.778	0.001	58219.5163306597
GRB180418A	170.122	24.933	0.001	58226.2777314815
GRB180425A	64.452	-32.952	0.001	58233.2792939815
GRB180504A	331.144	-14.659	0.001	58242.8208680556
GRB180510A	276.331	-31.908	0.001	58248.8058333333

Continued on next page

Table D.2 continued: Properties of the 872 GRBs that were searched for neutrino emission in the generic stacking analysis.

GCN name	ra (°)	dec (°)	σ (°)	t_s (MJD)
GRB180510B	77.969	-62.324	0.001	58248.8413425926
GRB180512A	201.938	21.404	0.001	58250.9150115741
GRB180514A	197.371	36.972	0.001	58252.5565162037
GRB180529A	97.946	-54.900	1.417	58267.3507407407
GRB180602A	142.332	32.067	0.001	58271.3407407407
GRB180613A	211.521	-43.072	0.001	58282.6473148148
GRB180614A	3.078	46.953	0.001	58283.8000347222
GRB180618A	169.941	73.837	0.001	58287.0270972338
GRB180620A	279.896	23.244	0.001	58289.3547222222
GRB180620B	357.521	-57.962	0.001	58289.6572400810
GRB180623A	214.529	-60.253	0.001	58292.6928935185
GRB180624A	318.097	-2.338	0.001	58293.5732638889
GRB180626A	243.576	14.757	0.001	58295.3450694444
GRB180630A	48.982	-87.478	0.001	58299.4636689815
GRB180703A	6.542	-67.083	0.300	58302.8732638889
GRB180703B	96.920	-29.880	0.400	58302.9462804745
GRB180704A	32.660	69.964	0.001	58303.2306973843
GRB180705A	212.613	-11.647	0.001	58304.6507407407
GRB180706A	181.643	66.037	0.001	58305.3475694444
GRB180709A	38.118	60.349	0.001	58308.4498842593
GRB180714A	242.908	33.267	0.052	58313.5396412037
GRB180715A	235.085	-0.899	0.016	58314.7520239468
GRB180718A	336.019	2.790	0.023	58317.0788721412
GRB180718B	44.680	-31.500	0.650	58317.7598842593
GRB180720B	0.529	-2.919	0.001	58319.5954745370
GRB180720C	265.636	-26.629	0.001	58319.9302627778
GRB180721A	347.711	4.856	0.001	58320.4601620370
GRB180722A	302.892	24.217	0.217	58321.2464814815
GRB180727A	346.666	-63.052	0.001	58326.5911805556
GRB180728A	253.565	-54.044	0.001	58327.7255787037
GRB180805A	167.566	-45.332	0.001	58335.3754513889
GRB180805B	25.782	-17.493	0.001	58335.5405787037
GRB180809A	297.792	-34.667	0.133	58339.4812484607
GRB180809B	299.700	-15.299	0.001	58339.8504398148
GRB180812A	245.835	74.665	0.001	58342.3460648148
GRB180818A	169.637	-48.345	0.001	58348.1304861111
GRB180818B	104.225	39.316	0.001	58348.5167956944
GRB180821A	7.790	-38.627	0.001	58351.6919444444
GRB180823A	210.356	14.893	0.001	58353.7919212963
GRB180824A	10.058	56.617	0.050	58354.4174652778
GRB180828A	268.718	-25.798	0.001	58358.7869974190
GRB180904A	274.250	46.630	0.001	58365.8919212963
GRB180905A	91.063	-4.570	0.001	58366.5788888889
GRB180914A	52.742	-5.267	0.400	58375.5191782407
GRB180914B	332.450	24.883	0.333	58375.7631018519
GRB180923A	38.304	6.300	1.000	58384.1696180556

Continued on next page

Table D.2 continued: Properties of the 872 GRBs that were searched for neutrino emission in the generic stacking analysis.

GCN name	ra (°)	dec (°)	σ (°)	t_s (MJD)
GRB180924A	49.199	-58.533	0.001	58385.6376388889
GRB180925A	315.203	-64.457	0.001	58386.6064926736
GRB180930A	76.863	-25.117	0.001	58391.5275347222
GRB181002A	64.747	15.213	0.001	58393.4739930556
GRB181003A	52.529	-33.965	0.001	58394.2131134259
GRB181010A	52.570	-23.038	0.001	58401.2442209144
GRB181011A	93.338	20.383	0.267	58402.1472453704
GRB181013A	207.652	40.108	0.001	58404.1078587963

D.2.2 Fit bias tests

When injecting a fixed number of signal events, $n_{s,inj}$, the distribution of the fitted number of signal events should ideally be closely centred on $n_{s,inj}$. Figure 5.16 in 5.3.2 showed that a slight tendency is observed to underestimate the true number of signal events when injecting an E^{-2} spectrum. The bias disappears when hardening the spectral index, as this makes signal events more distinct from background events. Vice versa, softer spectral indices result in a worse bias. These features are illustrated in Fig. D.3. A further discussion on this effect is given in 5.3.2.

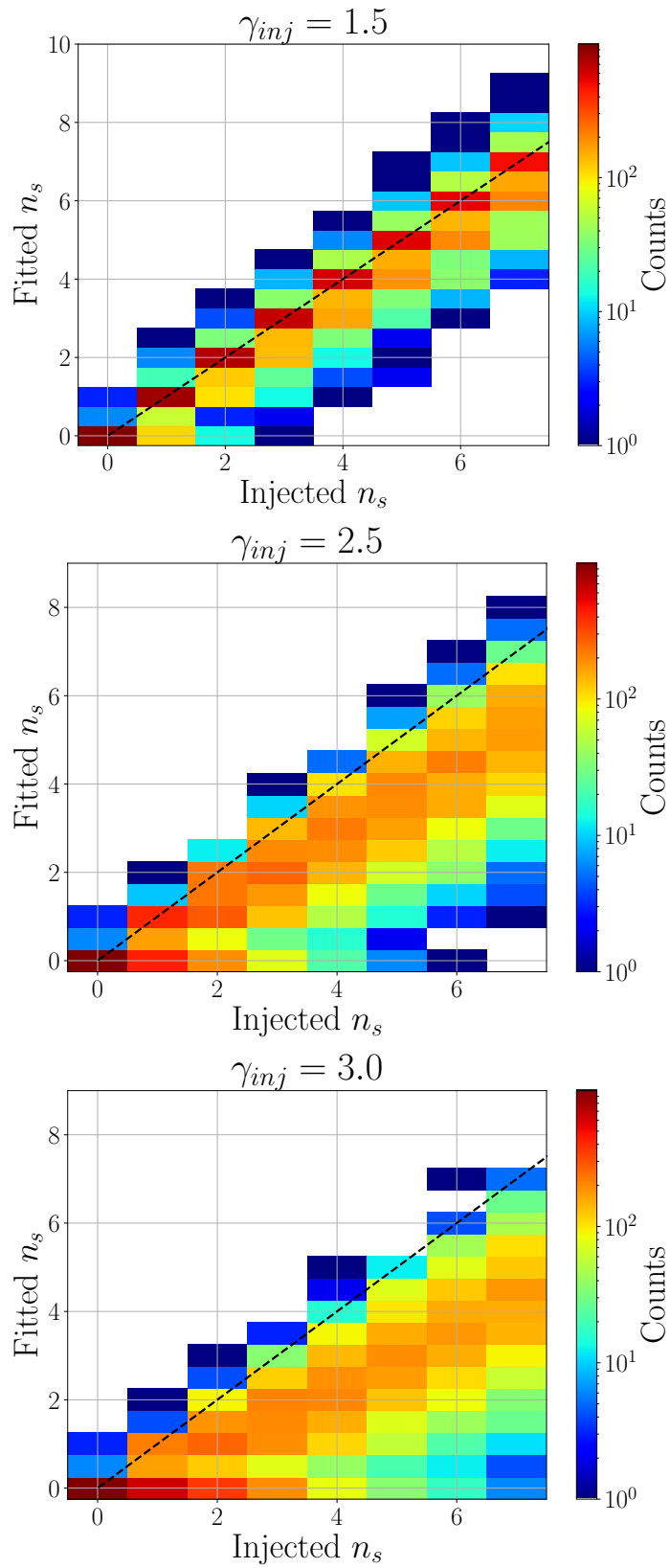


FIGURE D.3: Two-dimensional distribution of the injected and fitted number of signal events. A conservative fit bias is observed that becomes more prominent for softer spectra. The distribution for $\gamma_{inj} = 2$ is shown in Fig. 5.16.

D.2.3 Sensitivity & discovery potential

Figure D.4 and D.5 serve as an addendum to 5.3.2. These figures show the signal trials and sigmoid fits that are used to determine the sensitivity and discovery potential threshold for spectral indices other than $\gamma_{inj} = 2$. The numerical value of the sensitivity and discovery potential obtained through these fits are given in Tab. 5.1.

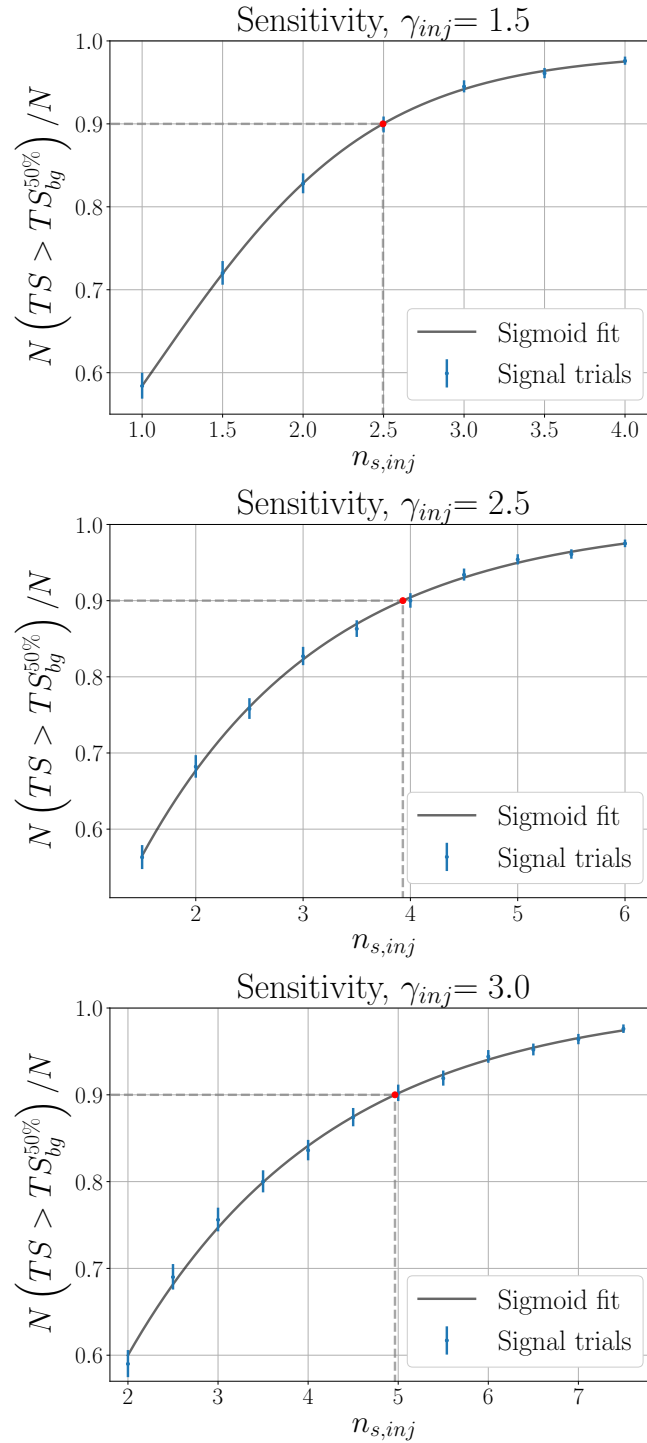


FIGURE D.4: A sigmoid fit to signal trials is used to determine the sensitivity threshold when injecting events with a spectral index, γ_{inj} , of 1.5, 2.5, and 3. The image for $\gamma_{inj} = 2$ was previously shown in Fig. 5.17.

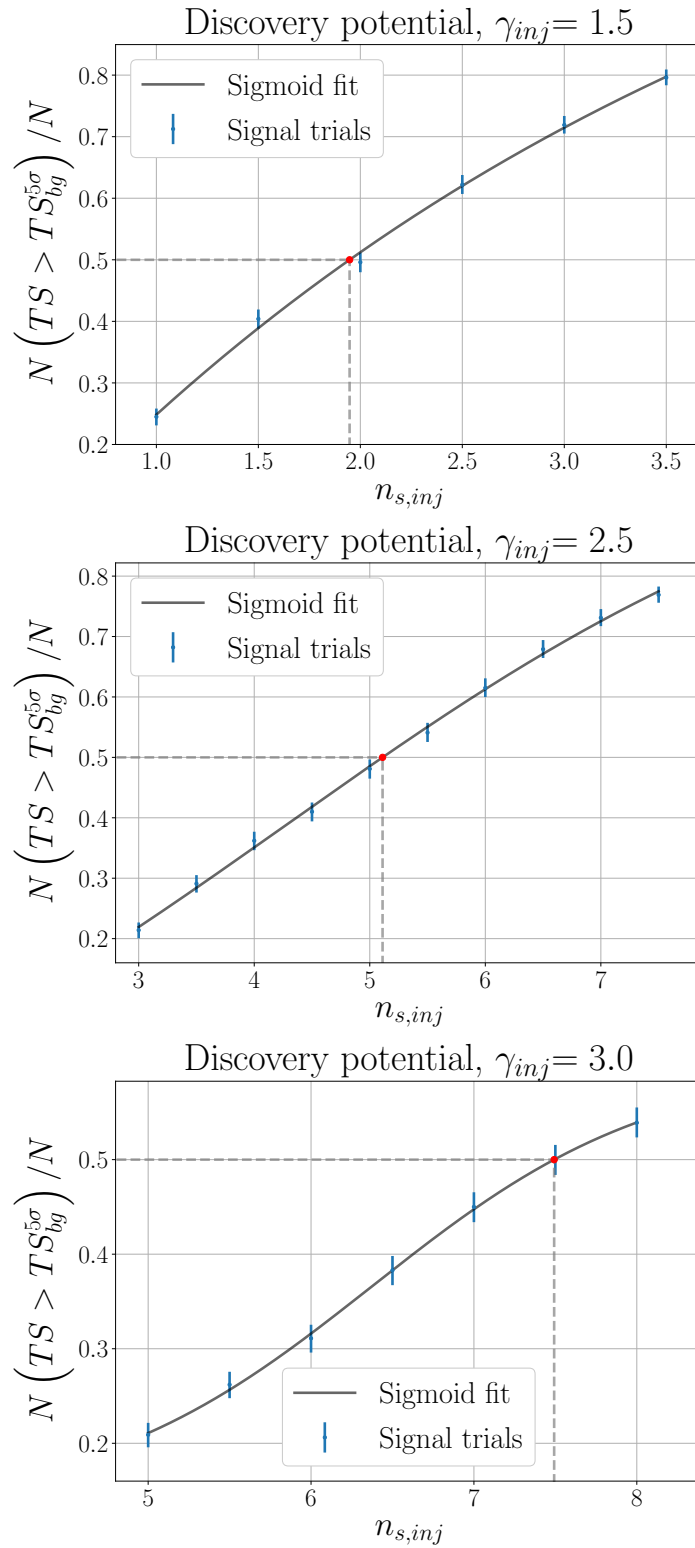


FIGURE D.5: Discovery potential threshold for trials in which the signal events follow a spectral index, γ_{inj} , of 1.5, 2.5 and 3. See Fig. 5.18 for the equivalent image in case of $\gamma_{inj} = 2$.

D.2.4 Unblinding tests

As an unblinding check, the distribution of the number of temporally coincident events that spatially overlap within 5σ was shown in Fig. 5.20 of 5.5.2. For completeness, the equivalent plots are included in Fig. D.6 for a spatial overlap within a significance of 1, 2, 3, and 4 standard deviations. Red bins again indicate the value of the unblinded result. Good agreement is observed between the analysis result and the expected distributions. In all cases, the unblinded result either falls in the most likely or the second most likely bin. This indicates that the results are to a high degree consistent with the expectation from background.

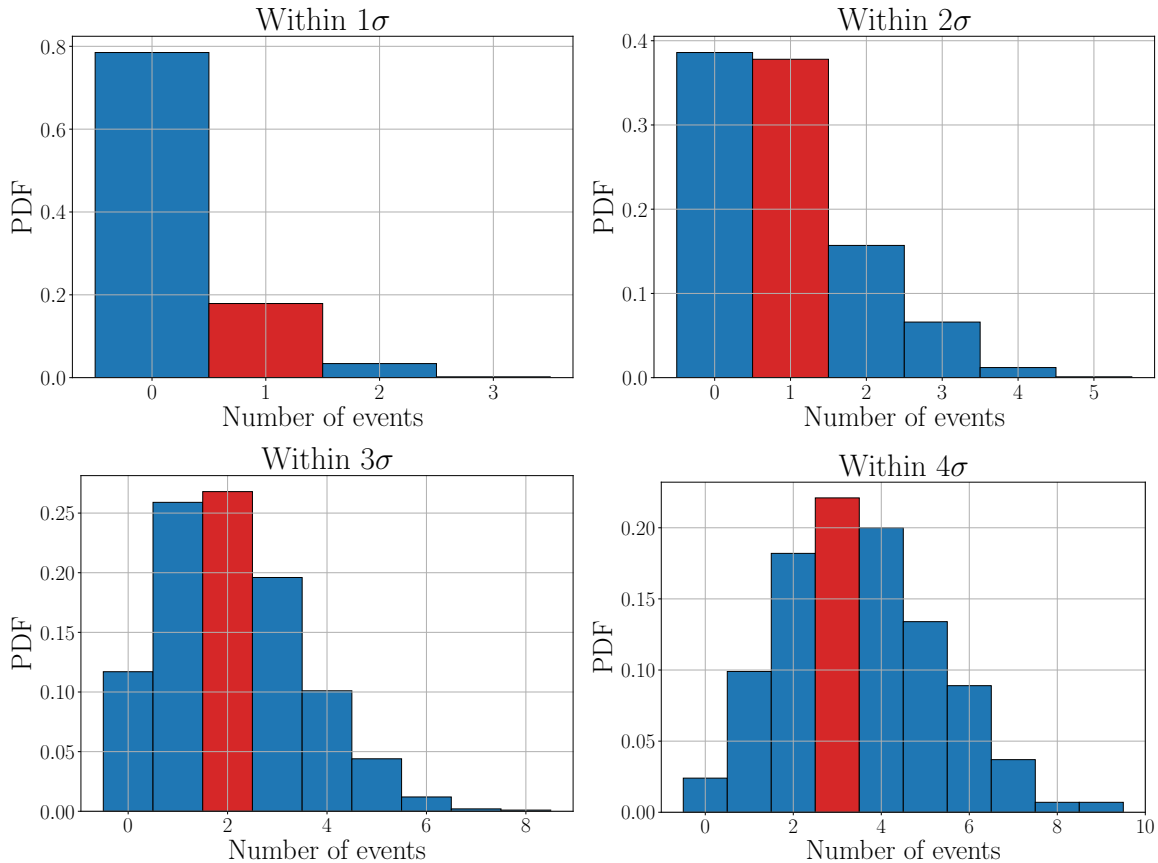


FIGURE D.6: Probability to obtain N temporally coincident events that spatially overlap within 1, 2, 3, and 4 standard deviations. Red bins indicate the result of the unblinded analysis. The equivalent image for a deviation of 5σ is shown in Fig. 5.20.

Bibliography

- [1] P. Coppin, K. D. de Vries, and N. van Eijndhoven. “Identification of gamma-ray burst precursors in Fermi-GBM bursts”. In: *Phys. Rev. D* 102.10, 103014 (Nov. 2020). DOI: 10.1103/PhysRevD.102.103014.
- [2] P. Coppin, K. D. de Vries, and N. van Eijndhoven. “A Catalogue of GRBs and their Precursors”. In: *Cosmic Rays and Neutrinos in the Multi-Messenger Era*. Dec. 2020. URL: <https://indico.in2p3.fr/event/20789/contributions/89398>.
- [3] P. Coppin, K. D. de Vries, and N. van Eijndhoven. “Gamma-ray burst precursors as observed by Fermi-GBM”. In: *PoS ICRC2021*, 40 (2021). DOI: 10.22323/1.395.0593.
- [4] P. Coppin and N. van Eijndhoven. “IceCube Search for High-Energy Neutrinos Produced in the Precursor Stages of Gamma-ray Bursts”. In: *PoS ICRC2019*, 859 (2019). DOI: 10.22323/1.358.0859.
- [5] K. Deoskar, L. Friedman, and P. Coppin. “Searches for Neutrinos from Precursors and Afterglows of Gamma-Ray Bursts using the IceCube Neutrino Observatory”. In: *PoS ICRC2021*, 1118 (2021). DOI: 10.22323/1.395.1118.
- [6] K. D. de Vries et al. “On the radar detection of high-energy neutrino-induced cascades in ice; From Radar scattering cross-section to sensitivity”. In: *arXiv e-prints* (2018). arXiv: 1802.05543 [astro-ph.HE].
- [7] S. Toscano et al. “Hybrid detection of high-energy cosmic neutrinos with the next generation neutrino detectors at the South Pole”. In: *PoS ICRC2019*, 1020 (2019). DOI: 10.22323/1.358.1020.
- [8] K. D. de Vries and S. Prohira. “The Radar Echo Telescope: Theory and Experiment”. In: *Neutrino*. June 2020. URL: <https://indico.fnal.gov/event/19348/contributions/186180>.
- [9] B. P. Abbott et al. “GW170817: Observation of Gravitational Waves from a Binary Neutron Star Inspiral”. In: *Phys. Rev. Lett.* 119.16, 161101 (Oct. 2017). DOI: 10.1103/PhysRevLett.119.161101.
- [10] B. P. Abbott et al. “Gravitational Waves and Gamma-Rays from a Binary Neutron Star Merger: GW170817 and GRB 170817A”. In: *ApJ* 848.2 (Oct. 2017), p. L13. DOI: 10.3847/2041-8213/aa920c.
- [11] M. Ajello et al. “Fermi and Swift Observations of GRB 190114C: Tracing the Evolution of High-Energy Emission from Prompt to Afterglow”. In: *ApJ* 890.1, 9 (Feb. 2020), p. 9. DOI: 10.3847/1538-4357/ab5b05.
- [12] United Nations. *Treaty banning nuclear weapon tests in the atmosphere, in outer space and under water*. 1963. URL: <https://treaties.un.org/pages/showDetails.aspx?objid=08000002801313d9> (visited on Jan. 5, 2021).
- [13] S. Singer. “The Vela satellite program for detection of high-altitude nuclear detonations”. In: *Proceedings of the IEEE* 53.12 (Dec. 1965), pp. 1935–1948. DOI: 10.1109/PROC.1965.4470.
- [14] T. L. Cline et al. “Energy Spectra of Cosmic Gamma-Ray Bursts”. In: *ApJ* 185 (Oct. 1973), p. L1. DOI: 10.1086/181309.
- [15] R. W. Klebesadel, I. B. Strong, and R. A. Olson. “Observations of Gamma-Ray Bursts of Cosmic Origin”. In: *ApJ* 182 (June 1973), p. L85. DOI: 10.1086/181225.

- [16] W. A. Wheaton et al. "The Direction and Spectral Variability of a Cosmic Gamma-Ray Burst". In: *ApJ* 185 (Oct. 1973), p. L57. DOI: 10.1086/181320.
- [17] I. B. Strong and R. W. Klebesadel. "Cosmic gamma-ray bursts." In: *Sci. Am.* 235 (Oct. 1976), pp. 66–70. DOI: 10.1038/scientificamerican1076-66.
- [18] B. Zhang. *The Physics of Gamma-Ray Bursts*. Cambridge University Press, 2018. DOI: 10.1017/9781139226530.
- [19] R. J. Nemiroff. "A Century of Gamma Ray Burst Models". In: *AIP Conf. Proc.* 307.1 (May 1994), pp. 730–734. DOI: 10.1063/1.45838.
- [20] J. van Paradijs et al. "Transient optical emission from the error box of the γ -ray burst of 28 February 1997". In: *Nature* 386.6626 (Apr. 1997), pp. 686–689. DOI: 10.1038/386686a0.
- [21] T. J. Galama et al. "GRB 970508". In: *IAU Circ.* 6655 (May 1997), p. 1.
- [22] G. J. Fishman et al. "Burst and Transient Source Experiment (BATSE) for the Gamma Ray Observatory (GRO)". In: *ICRC1985*. Vol. 3. Aug. 1985, 343-346.
- [23] G. J. Fishman and C. A. Meegan. "Gamma-Ray Bursts". In: *ARA&A* 33 (Jan. 1995), pp. 415–458. DOI: 10.1146/annurev.aa.33.090195.002215.
- [24] J. C. Higdon and R. E. Lingenfelter. "Gamma-Ray Bursts". In: *Annu. Rev. Astron. Astrophys.* 28.1 (1990), pp. 401–436. DOI: 10.1146/annurev.aa.28.090190.002153.
- [25] T. Murakami et al. "Ginga observations of gamma-ray bursts". In: *AIP Conf. Proc.* 265 (Sept. 1991), pp. 28–31. DOI: 10.1063/1.42796.
- [26] J. C. Higdon and M. Schmidt. "Apparent Spatial Uniformity of the Gamma-Ray Bursts Detected by the KONUS Experiment on Venera 11 and Venera 12". In: *ApJ* 355 (May 1990), p. 13. DOI: 10.1086/168735.
- [27] A. Dauvillier. "Nature of gamma-ray bursts". In: *C. R. Acad. Sci.* 285.15 (Nov. 1977), pp. 341–344.
- [28] E. P. Mazets et al. "Catalog of cosmic gamma-ray bursts from the KONUS experiment data - A". In: *Ap&SS* 80.1 (Nov. 1981), pp. 3–83. DOI: 10.1007/BF00649140.
- [29] E. P. Mazets et al. "Catalog of cosmic gamma-ray bursts from the KONUS experiment data - B". In: *Ap&SS* 80.1 (Nov. 1981), pp. 85–117. DOI: 10.1007/BF00649141.
- [30] W. S. Paciesas et al. "The Fourth BATSE Gamma-Ray Burst Catalog (Revised)". In: *ApJS* 122.2 (June 1999), pp. 465–495. DOI: 10.1086/313224.
- [31] A. Lien et al. "Probing the Cosmic Gamma-Ray Burst Rate with Trigger Simulations of the Swift Burst Alert Telescope". In: *ApJ* 783.1 (Mar. 2014), p. 24. DOI: 10.1088/0004-637X/783/1/24.
- [32] C. Kouveliotou et al. "Identification of Two Classes of Gamma-Ray Bursts". In: *ApJ* 413 (Aug. 1993), p. L101. DOI: 10.1086/186969.
- [33] G. Boella et al. "BeppoSAX, the wide band mission for X-ray astronomy". In: *A&AS* 122 (Apr. 1997), pp. 299–307. DOI: 10.1051/aas:1997136.
- [34] E. Waxman, S. R. Kulkarni, and D. A. Frail. "Implications of the Radio Afterglow from the Gamma-Ray Burst of 1997 May 8". In: *ApJ* 497.1 (Apr. 1998), pp. 288–293. DOI: 10.1086/305467.
- [35] T. J. Galama et al. "On the possible association of SN 1998bw and GRB 980425". In: *A&AS* 138 (Sept. 1999), pp. 465–466. DOI: 10.1051/aas:1999311.
- [36] Z. Cano et al. "The Observer's Guide to the Gamma-Ray Burst Supernova Connection". In: *Adv. Astron.* 2017, 8929054 (Jan. 2017). DOI: 10.1155/2017/8929054.
- [37] K. Z. Stanek et al. "Spectroscopic Discovery of the Supernova 2003dh Associated with GRB 030329". In: *ApJ* 591.1 (July 2003), pp. L17–L20. DOI: 10.1086/376976.
- [38] P. Murdin. "High Energy Transient Experiment (HETE) 2". In: *Encyclopedia of Astronomy and Astrophysics*. 2002, E4644. DOI: 10.1888/0333750888/4644.
- [39] B. Paczyński. "Are Gamma-Ray Bursts in Star-Forming Regions?" In: *ApJ* 494.1 (Feb. 1998), pp. L45–L48. DOI: 10.1086/311148.

- [40] A. S. Fruchter et al. "Long γ -ray bursts and core-collapse supernovae have different environments". In: *Nature* 441.7092 (May 2006), pp. 463–468. DOI: 10.1038/nature04787.
- [41] M. Modjaz et al. "Host Galaxies of Type Ic and Broad-lined Type Ic Supernovae from the Palomar Transient Factory: Implications for Jet Production". In: *ApJ* 892.2 (Apr. 2020), p. 153. DOI: 10.3847/1538-4357/ab4185.
- [42] S. D. Barthelmy et al. "The Burst Alert Telescope (BAT) on the SWIFT Midex Mission". In: *Space Sci. Rev.* 120.3-4 (Oct. 2005), pp. 143–164. DOI: 10.1007/s11214-005-5096-3.
- [43] N. Gehrels et al. "The Swift Gamma-Ray Burst Mission". In: *ApJ* 611.2 (Aug. 2004), pp. 1005–1020. DOI: 10.1086/422091.
- [44] F. Y. Wang and Z. G. Dai. "Self-organized criticality in X-ray flares of gamma-ray-burst afterglows". In: *Nat. Phys.* 9.8 (Aug. 2013), pp. 465–467. DOI: 10.1038/nphys2670.
- [45] E. Berger et al. "The afterglow and elliptical host galaxy of the short γ -ray burst GRB 050724". In: *Nature* 438.7070 (Dec. 2005), pp. 988–990. DOI: 10.1038/nature04238.
- [46] A. Cucchiara et al. "A Photometric Redshift of $z \sim 9.4$ for GRB 090429B". In: *ApJ* 736.1 (July 2011), p. 7. DOI: 10.1088/0004-637X/736/1/7.
- [47] N. Gehrels and S. Razzaque. "Gamma-ray bursts in the Swift-Fermi era". In: *Front. Phys.* 8.6 (Dec. 2013), pp. 661–678. DOI: 10.1007/s11467-013-0282-3.
- [48] M. Ajello et al. "A Decade of Gamma-Ray Bursts Observed by Fermi-LAT: The Second GRB Catalog". In: *ApJ* 878.1 (June 2019), p. 52. DOI: 10.3847/1538-4357/ab1d4e.
- [49] A. von Kienlin et al. "The Fourth Fermi-GBM Gamma-Ray Burst Catalog: A Decade of Data". In: *ApJ* 893.1, 46 (Apr. 2020). DOI: 10.3847/1538-4357/ab7a18.
- [50] HEASARC. *Public Fermi data*. <https://fermi.gsfc.nasa.gov/ssc/data/access/>.
- [51] R. L. Aptekar et al. "Konus-W Gamma-Ray Burst Experiment for the GGS Wind Spacecraft". In: *Space Sci. Rev.* 71.1-4 (Feb. 1995), pp. 265–272. DOI: 10.1007/BF00751332.
- [52] J. Řípa et al. "Search for gamma-ray burst classes with the RHESSI satellite". In: *A&A* 498.2 (May 2009), pp. 399–406. DOI: 10.1051/0004-6361/200810913.
- [53] A. Rau et al. "The 1st INTEGRAL SPI-ACS gamma-ray burst catalogue". In: *A&A* 438.3 (Aug. 2005), pp. 1175–1183. DOI: 10.1051/0004-6361:20053159.
- [54] K. Yamaoka et al. "Suzaku Wide-band All-sky Monitor (WAM) observations of GRBs and SGRs". In: *PASJ* 69.3, R2 (June 2017). DOI: 10.1093/pasj/psx026.
- [55] M. Galli et al. "AGILE mini-calorimeter gamma-ray burst catalog". In: *A&A* 553, A33 (May 2013). DOI: 10.1051/0004-6361/201220833.
- [56] M. Tavani et al. "The AGILE Mission". In: *A&A* 502.3 (Aug. 2009), pp. 995–1013. DOI: 10.1051/0004-6361/200810527.
- [57] M. Serino et al. "MAXI observations of gamma-ray bursts". In: *PASJ* 66.5, 87 (Oct. 2014), p. 87. DOI: 10.1093/pasj/psu063.
- [58] T. Chattopadhyay et al. "Prompt Emission Polarimetry of Gamma-Ray Bursts with the AstroSat CZT Imager". In: *ApJ* 884.2, 123 (Oct. 2019). DOI: 10.3847/1538-4357/ab40b7.
- [59] K. Hurley et al. "The Interplanetary Network Supplement to the Fermi GBM Catalog of Cosmic Gamma-Ray Bursts". In: *ApJS* 207.2 (Aug. 2013), p. 39. DOI: 10.1088/0067-0049/207/2/39.
- [60] J. van Casteren and M. Novara. "BepiColombo mission". In: *Mem. Soc. Astron. Italiana* 82 (Jan. 2011), p. 394.
- [61] P. Spence. "Mars Odyssey". In: *Encyclopedia of Astronomy and Astrophysics*. Ed. by P. Murdin. 2002, E5461. DOI: 10.1888/0333750888/5461.

- [62] C. Motch. "The SVOM mission". In: *Astron. Nachrichten* 338 (Dec. 2017), pp. 978–983. DOI: 10.1002/asna.201713415.
- [63] J. McEnery and Amego Team. "All Sky Medium Energy Gamma-ray Observatory (AMEGO): Exploring the Extreme Multimessenger Universe". In: *American Astronomical Society Meeting Abstracts*. Vol. 235. Jan. 2020, 372.15.
- [64] I. Martinez et al. "BurstCube: status and public alerts". In: *PoS ICRC2021*, 656 (2021). DOI: 10.22323/1.395.0656.
- [65] A. De Angelis et al. "The e-ASTROGAM mission. Exploring the extreme Universe with gamma rays in the MeV - GeV range". In: *Exp. Astron.* 44.1 (Oct. 2017), pp. 25–82. DOI: 10.1007/s10686-017-9533-6.
- [66] J. Knödseder. "The future of gamma-ray astronomy". In: *Comptes Rendus Physique* 17.6 (June 2016), pp. 663–678. DOI: 10.1016/j.crhy.2016.04.008.
- [67] D. A. Coulter et al. "Swope Supernova Survey 2017a (SSS17a), the optical counterpart to a gravitational wave source". In: *Science* 358.6370 (Dec. 2017), pp. 1556–1558. DOI: 10.1126/science.aap9811.
- [68] B. P. Abbott et al. "Multi-messenger Observations of a Binary Neutron Star Merger". In: *ApJ* 848.2, L12 (Oct. 2017). DOI: 10.3847/2041-8213/aa91c9.
- [69] P. Beniamini et al. "Ready, Set, Launch: Time Interval between a Binary Neutron Star Merger and Short Gamma-Ray Burst Jet Formation". In: *ApJ* 895.2, L33 (June 2020), p. L33. DOI: 10.3847/2041-8213/ab9223.
- [70] Y.-Z. Meng et al. "The Origin of the Prompt Emission for Short GRB 170817A: Photosphere Emission or Synchrotron Emission?" In: *ApJ* 860.1 (June 2018), p. 72. DOI: 10.3847/1538-4357/aac2d9.
- [71] T. Matsumoto and S. S. Kimura. "Delayed Jet Breakouts from Binary Neutron Star Mergers". In: *ApJ* 866.2, L16 (Oct. 2018), p. L16. DOI: 10.3847/2041-8213/aae51b.
- [72] N. R. Tanvir et al. "A 'kilonova' associated with the short-duration γ -ray burst GRB 130603B". In: *Nature* 500.7464 (Aug. 2013), pp. 547–549. DOI: 10.1038/nature12505.
- [73] E. Berger, W. Fong, and R. Chornock. "An r-process Kilonova Associated with the Short-hard GRB 130603B". In: *ApJ* 774.2, L23 (Sept. 2013). DOI: 10.1088/2041-8205/774/2/L23.
- [74] Z.-P. Jin et al. "The Macronova in GRB 050709 and the GRB-macronova connection". In: *Nat. Commun.* 7, 12898 (Sept. 2016). DOI: 10.1038/ncomms12898.
- [75] B. Yang et al. "A possible macronova in the late afterglow of the long-short burst GRB 060614". In: *Nat. Commun.* 6, 7323 (June 2015), p. 7323. DOI: 10.1038/ncomms8323.
- [76] V. Paschalidis, Z. B. Etienne, and S. L. Shapiro. "General-relativistic simulations of binary black hole-neutron stars: Precursor electromagnetic signals". In: *Phys. Rev. D* 88.2, 021504 (July 2013). DOI: 10.1103/PhysRevD.88.021504.
- [77] B. Paczynski. "Gamma-ray bursters at cosmological distances". In: *ApJ* 308 (Sept. 1986), pp. L43–L46. DOI: 10.1086/184740.
- [78] R. A. Hulse and J. H. Taylor. "Discovery of a pulsar in a binary system." In: *ApJ* 195 (Jan. 1975), pp. L51–L53. DOI: 10.1086/181708.
- [79] J. H. Taylor and J. M. Weisberg. "A new test of general relativity - Gravitational radiation and the binary pulsar PSR 1913+16". In: *ApJ* 253 (Feb. 1982), pp. 908–920. DOI: 10.1086/159690.
- [80] Nobel Media. 1993. URL: <https://www.nobelprize.org/prizes/physics/1993/press-release/> (visited on Jan. 18, 2021).
- [81] P. C. Peters. "Gravitational Radiation and the Motion of Two Point Masses". In: *Phys. Rev.* 136.4B (Nov. 1964), pp. 1224–1232. DOI: 10.1103/PhysRev.136.B1224.
- [82] P. C. Peters and J. Mathews. "Gravitational Radiation from Point Masses in a Keplerian Orbit". In: *Phys. Rev.* 131.1 (July 1963), pp. 435–440. DOI: 10.1103/PhysRev.131.435.

- [83] M. Shibata and K. Uryū. “Gravitational Waves from Merger of Binary Neutron Stars in Fully General Relativistic Simulation”. In: *Prog. Theor. Phys.* 107.2 (Feb. 2002), pp. 265–303. DOI: 10.1143/PTP.107.265.
- [84] M. Vereecken. “Aspects of astrophysical particle production and beyond the Standard Model phenomenology”. In: *arXiv e-prints* (Nov. 2019). arXiv: 1911.12244 [hep-ph].
- [85] B. P. Abbott et al. “Observation of Gravitational Waves from a Binary Black Hole Merger”. In: *Phys. Rev. Lett.* 116.6, 061102 (Feb. 2016). DOI: 10.1103/PhysRevLett.116.061102.
- [86] V. Connaughton et al. “Fermi GBM Observations of LIGO Gravitational-wave Event GW150914”. In: *ApJ* 826.1, L6 (July 2016). DOI: 10.3847/2041-8205/826/1/L6.
- [87] K. D. de Vries et al. “Constraints and prospects on GW and neutrino emissions using GW150914”. In: *arXiv e-prints* (Dec. 2016). arXiv: 1612.02648 [astro-ph.HE].
- [88] B. P. Abbott et al. “GW190425: Observation of a Compact Binary Coalescence with Total Mass $\sim 3.4 M_{\odot}$ ”. In: *ApJ* 892.1, L3 (Mar. 2020). DOI: 10.3847/2041-8213/ab75f5.
- [89] M. J. Graham et al. “Candidate Electromagnetic Counterpart to the Binary Black Hole Merger Gravitational-Wave Event S190521g*”. In: *Phys. Rev. Lett.* 124.25, 251102 (June 2020). DOI: 10.1103/PhysRevLett.124.251102.
- [90] J. A. González et al. “Supermassive Recoil Velocities for Binary Black-Hole Mergers with Antialigned Spins”. In: *Phys. Rev. Lett.* 98.23, 231101 (June 2007). DOI: 10.1103/PhysRevLett.98.231101.
- [91] V. A. Acciari et al. “Teraelectronvolt emission from the γ -ray burst GRB 190114C”. In: *Nature* 575.7783 (2019), pp. 455–458. DOI: 10.1038/s41586-019-1750-x.
- [92] J. Cortina, F. Goebel, and T. Schweizer. “Technical Performance of the MAGIC Telescopes”. In: *arXiv e-prints* (July 2009). arXiv: 0907.1211 [astro-ph.IM].
- [93] W. B. Atwood et al. “The Large Area Telescope on the Fermi Gamma-Ray Space Telescope Mission”. In: *ApJ* 697.2 (June 2009), pp. 1071–1102. DOI: 10.1088/0004-637X/697/2/1071.
- [94] E. Dwek and F. Krennrich. “The extragalactic background light and the gamma-ray opacity of the universe”. In: *Astropart. Phys.* 43 (2013), pp. 112–133. ISSN: 0927-6505. DOI: 10.1016/j.astropartphys.2012.09.003.
- [95] J. D. Finke, S. Razzaque, and C. D. Dermer. “Modeling the Extragalactic Background Light from Stars and Dust”. In: *ApJ* 712.1 (Mar. 2010), pp. 238–249. DOI: 10.1088/0004-637X/712/1/238.
- [96] V. A. Acciari et al. “MAGIC Observations of the Nearby Short Gamma-Ray Burst GRB 160821B”. In: *ApJ* 908.1, 90 (Feb. 2021). DOI: 10.3847/1538-4357/abd249.
- [97] O. Blanch et al. “MAGIC observations of GRB 201015A: hint of very high energy gamma-ray signal”. In: *GCN 28659* (Oct. 2020), p. 1. URL: <https://gcn.gsfc.nasa.gov/gcn3/28659.gcn3>.
- [98] O. Blanch et al. “GRB 201216C: MAGIC detection in very high energy gamma rays”. In: *GCN 29075* (Dec. 2020), p. 1. URL: <https://gcn.gsfc.nasa.gov/gcn3/29075.gcn3>.
- [99] W. Hofmann et al. “The high energy stereoscopic system (HESS) project”. In: vol. 515. AIP Conf. Proc. June 2000, pp. 500–509. DOI: 10.1063/1.1291416.
- [100] T. C. Weekes et al. “VERITAS: the Very Energetic Radiation Imaging Telescope Array System”. In: *Astropart. Phys.* 17.2 (May 2002), pp. 221–243. DOI: 10.1016/S0927-6505(01)00152-9.
- [101] H. Abdalla et al. “A very-high-energy component deep in the γ -ray burst afterglow”. In: *Nature* 575.7783 (Nov. 2019), pp. 464–467. DOI: 10.1038/s41586-019-1743-9.

- [102] H. Abdalla et al. "Revealing x-ray and gamma ray temporal and spectral similarities in the GRB 190829A afterglow". In: *Science* 372.6546 (2021), pp. 1081–1085. DOI: 10.1126/science.abe8560.
- [103] M. de Naurois. "GRB190829A: Detection of VHE gamma-ray emission with H.E.S.S.". In: *The Astronomer's Telegram* 13052 (Aug. 2019), p. 1.
- [104] R. Atkins et al. "Evidence for TeV Emission from GRB 970417a". In: *Astrophys. J. Lett.* 533.2 (Apr. 2000), pp. L119–L122. DOI: 10.1086/312629.
- [105] R. Atkins et al. "The High-Energy Gamma-Ray Fluence and Energy Spectrum of GRB 970417a from Observations with Milagrito". In: *ApJ* 583.2 (Feb. 2003), pp. 824–832. DOI: 10.1086/345499.
- [106] T. Aune. "A Search for GeV-TeV Emission from GRBs Using the Milagro Detector". In: *AIP Conf. Proc.* 1133 (May 2009), pp. 385–387. DOI: 10.1063/1.3155925.
- [107] I. Taboada and R. C. Gilmore. "Prospects for the detection of GRBs with HAWC". In: *Nucl. Instrum. Methods Phys. Res.* 742 (Apr. 2014), pp. 276–277. DOI: 10.1016/j.nima.2013.09.013.
- [108] N. M. Budnev et al. "The primary cosmic-ray energy spectrum measured with the Tunka-133 array". In: *Astropart. Phys.* 117, 102406 (Jan. 2020). DOI: 10.1016/j.astropartphys.2019.102406.
- [109] T. K. Gaisser, R. Engel, and E. Resconi. *Cosmic Rays and Particle Physics*. 2nd ed. Cambridge University Press, 2016. ISBN: 9781316598436. DOI: 10.1017/CB09781139192194.
- [110] Particle Data Group. "Review of Particle Physics". In: *Prog. Theor. Exp. Phys.* 2020.8 (Aug. 2020). 083C01. ISSN: 2050-3911. DOI: 10.1093/ptep/ptaa104.
- [111] K. Greisen. "End to the Cosmic-Ray Spectrum?" In: *Phys. Rev. Lett.* 16.17 (Apr. 1966), pp. 748–750. DOI: 10.1103/PhysRevLett.16.748.
- [112] G. T. Zatsepin and V. A. Kuz'min. "Upper Limit of the Spectrum of Cosmic Rays". In: *J. Exp. Theor. Phys.* 4 (Aug. 1966), p. 78.
- [113] J. A. Aguilar et al. "Design and sensitivity of the Radio Neutrino Observatory in Greenland (RNO-G)". In: *J. Instrum.* 16.3, P03025 (Mar. 2021). DOI: 10.1088/1748-0221/16/03/P03025.
- [114] K. D. de Vries and S. Prohira. "The Radar Echo Telescope for Neutrinos". In: *PoS ICRC2021*, 1195 (2021). DOI: 10.22323/1.395.1195.
- [115] D. J. Bird et al. "Evidence for correlated changes in the spectrum and composition of cosmic rays at extremely high energies". In: *Phys. Rev. Lett.* 71.21 (Nov. 1993), pp. 3401–3404. DOI: 10.1103/PhysRevLett.71.3401.
- [116] S. Yoshida et al. "The cosmic ray energy spectrum above 3×10^{18} eV measured by the Akeno Giant Air Shower Array". In: *Astropart. Phys.* 3.2 (Mar. 1995), pp. 105–123. DOI: 10.1016/0927-6505(94)00036-3.
- [117] E. Waxman. "Cosmological Gamma-Ray Bursts and the Highest Energy Cosmic Rays". In: *Phys. Rev. Lett.* 75.3 (July 1995), pp. 386–389. DOI: 10.1103/PhysRevLett.75.386.
- [118] M. Milgrom and V. Usov. "Possible Association of Ultra-High-Energy Cosmic-Ray Events with Strong Gamma-Ray Bursts". In: *ApJ* 449 (Aug. 1995), p. L37. DOI: 10.1086/309633.
- [119] M. Vietri. "The Acceleration of Ultra-High-Energy Cosmic Rays in Gamma-Ray Bursts". In: *ApJ* 453 (Nov. 1995), p. 883. DOI: 10.1086/176448.
- [120] A. M. Hillas. "The Origin of Ultra-High-Energy Cosmic Rays". In: *ARA&A* 22.1 (1984), pp. 425–444. DOI: 10.1146/annurev.aa.22.090184.002233.
- [121] K. V. Ptitsyna and S. V. Troitsky. "Physical conditions in potential accelerators of ultra-high-energy cosmic rays: updated Hillas plot and radiation-loss constraints".

- In: *Phys.-Uspekhi*. 53.7 (Oct. 2010), pp. 691–701. DOI: 10.3367/UFNe.0180.201007c.0723.
- [122] P. Baerwald, M. Bustamante, and W. Winter. “Are gamma-ray bursts the sources of ultra-high energy cosmic rays?” In: *Astropart. Phys.* 62 (Mar. 2015), pp. 66–91. DOI: 10.1016/j.astropartphys.2014.07.007.
- [123] E. Waxman and J. Bahcall. “High Energy Neutrinos from Cosmological Gamma-Ray Burst Fireballs”. In: *Phys. Rev. Lett.* 78.12 (Mar. 1997), pp. 2292–2295. DOI: 10.1103/PhysRevLett.78.2292.
- [124] E. Waxman and J. Bahcall. “High energy neutrinos from astrophysical sources: An upper bound”. In: *Phys. Rev. D* 59.2, 023002 (Jan. 1999), p. 023002. DOI: 10.1103/PhysRevD.59.023002.
- [125] S. D. Barthelmy et al. “BACODINE, the Real-Time BATSE Gamma-Ray Burst Coordinates Distribution Network”. In: *Ap&SS* 231.1-2 (Sept. 1995), pp. 235–238. DOI: 10.1007/BF00658623.
- [126] S. D. Barthelmy. “Observing strategies using GCN”. In: *AIP Conf. Proc.* 428 (May 1998), pp. 129–133. DOI: 10.1063/1.55308.
- [127] P. Gries, J. Campbell, and J. Montojo. *Practical Programming: An Introduction to Computer Science Using Python 3*. Pragmatic Programmers. CreateSpace Independent Publishing Platform, 2016. ISBN: 9781530427451.
- [128] T. Converse, J. Park, and C. Morgan. *PHP5 and MySQL Bible*. Bible. Wiley, 2004. ISBN: 9780764571824.
- [129] A. Lien et al. “The Third Swift Burst Alert Telescope Gamma-Ray Burst Catalog”. In: *ApJ* 829.1 (Sept. 2016), p. 7. DOI: 10.3847/0004-637X/829/1/7.
- [130] F. Frontera et al. “The Gamma-Ray Burst Catalog Obtained with the Gamma-Ray Burst Monitor Aboard BeppoSAX”. In: *ApJS* 180.1 (Jan. 2009), pp. 192–223. DOI: 10.1088/0067-0049/180/1/192.
- [131] M. S. Briggs et al. “The Accuracy of GBM GRB Locations”. In: *AIP Conf. Proc.* 1133 (May 2009), pp. 40–42. DOI: 10.1063/1.3155935.
- [132] V. Connaughton et al. “Localization of Gamma-Ray Bursts Using the Fermi Gamma-Ray Burst Monitor”. In: *ApJS* 216.2, 32 (Feb. 2015). DOI: 10.1088/0067-0049/216/2/32.
- [133] A. Goldstein et al. “Evaluation of Automated Fermi GBM Localizations of Gamma-Ray Bursts”. In: *ApJ* 895.1, 40 (May 2020). DOI: 10.3847/1538-4357/ab8bdb.
- [134] K. M. Górski et al. “HEALPix: A Framework for High-Resolution Discretization and Fast Analysis of Data Distributed on the Sphere”. In: *ApJ* 622.2 (Apr. 2005), pp. 759–771. DOI: 10.1086/427976.
- [135] M. Oguri. “Strong gravitational lensing of explosive transients”. In: *Rep. Prog. Phys.* 82.12, 126901 (Dec. 2019). DOI: 10.1088/1361-6633/ab4fc5.
- [136] C.-Y. Li and L.-X. Li. “Search for strong gravitational lensing effect in the current GRB data of BATSE”. In: *Sci. China: Phys. Mech. Astron.* 57.8 (Aug. 2014), pp. 1592–1599. DOI: 10.1007/s11433-014-5513-2.
- [137] P. Veres et al. “Fermi-GBM Observations of GRB 210812A: Signatures of a Million Solar Mass Gravitational Lens”. In: *ApJ* 921.2 (Nov. 2021), p. L30. DOI: 10.3847/2041-8213/ac2ee6.
- [138] J. Reid. *HTML5 Programmer’s Reference*. Apress, 2015. ISBN: 9781430263685.
- [139] M. Driscoll. *Jupyter Notebook 101*. R. R. Bowker LLC, 2018. ISBN: 9780996062886.
- [140] J.-A. Aguilar. “Online Gamma-Ray Burst catalog for neutrino telescopes”. In: *PoS ICRC2011*, 235 (2011). DOI: 10.7529/ICRC2011/V08/1063.
- [141] T. M. Koshut et al. “Systematic Effects on Duration Measurements of Gamma-Ray Bursts”. In: *ApJ* 463 (June 1996), p. 570. DOI: 10.1086/177272.

- [142] Y. Qin et al. "A Comprehensive Analysis of Fermi Gamma-Ray Burst Data. III. Energy-dependent T_{90} Distributions of GBM GRBs and Instrumental Selection Effect on Duration Classification". In: *ApJ* 763.1, 15 (Jan. 2013), p. 15. DOI: 10.1088/0004-637X/763/1/15.
- [143] I. Horváth. "A Third Class of Gamma-Ray Bursts?" In: *ApJ* 508.2 (Dec. 1998), pp. 757–759. DOI: 10.1086/306416.
- [144] S. Kulkarni and S. Desai. "Classification of gamma-ray burst durations using robust model-comparison techniques". In: *Ap&SS* 362.4, 70 (Apr. 2017), p. 70. DOI: 10.1007/s10509-017-3047-6.
- [145] M. Boër, B. Gendre, and G. Stratta. "Are Ultra-long Gamma-Ray Bursts Different?" In: *ApJ* 800.1 (Feb. 2015), p. 16. DOI: 10.1088/0004-637X/800/1/16.
- [146] A. Cucchiara et al. "Happy Birthday Swift: Ultra-long GRB 141121A and Its Broadband Afterglow". In: *ApJ* 812.2, 122 (Oct. 2015). DOI: 10.1088/0004-637X/812/2/122.
- [147] D. Band et al. "BATSE Observations of Gamma-Ray Burst Spectra. I. Spectral Diversity". In: *ApJ* 413 (Aug. 1993), p. 281. DOI: 10.1086/172995.
- [148] R. D. Preece et al. "The BATSE Gamma-Ray Burst Spectral Catalog. I. High Time Resolution Spectroscopy of Bright Bursts Using High Energy Resolution Data". In: *ApJS* 126.1 (Jan. 2000), pp. 19–36. DOI: 10.1086/313289.
- [149] L. Nava. "High-energy emission from gamma-ray bursts". In: *Int. J. Mod. Phys. D* 27.13, 1842003 (Jan. 2018). DOI: 10.1142/S0218271818420038.
- [150] G. A. MacLachlan et al. "Minimum variability time-scales of long and short GRBs". In: *MNRAS* 432.2 (June 2013), pp. 857–865. DOI: 10.1093/mnras/stt241.
- [151] S. B. Cenko et al. "Dark Bursts in the Swift Era: The Palomar 60 Inch-Swift Early Optical Afterglow Catalog". In: *ApJ* 693.2 (Mar. 2009), pp. 1484–1493. DOI: 10.1088/0004-637X/693/2/1484.
- [152] J. Greiner et al. "The nature of "dark" gamma-ray bursts". In: *A&A* 526 (Feb. 2011), A30. DOI: 10.1051/0004-6361/201015458.
- [153] A. B. Higgins et al. "Detailed multiwavelength modelling of the dark GRB 140713A and its host galaxy". In: *MNRAS* 484.4 (Apr. 2019), pp. 5245–5255. DOI: 10.1093/mnras/stz384.
- [154] A. D. Falcone et al. "Late-Time X-ray Flares during GRB Afterglows: Extended Internal Engine Activity". In: *AIP Conf. Proc.* 836 (May 2006), pp. 386–391. DOI: 10.1063/1.2207925.
- [155] B.-B. Zhang et al. "How Long does a Burst Burst?" In: *ApJ* 787.1 (May 2014), p. 66. DOI: 10.1088/0004-637X/787/1/66.
- [156] Y. Wang et al. "Revisiting the statistics of x-ray flares in gamma-ray bursts". In: *Mem. Soc. Astron. Italiana* 89 (Jan. 2018), p. 293. arXiv: 1802.01693 [astro-ph.HE].
- [157] E. W. Liang et al. "Testing the Curvature Effect and Internal Origin of Gamma-Ray Burst Prompt Emissions and X-Ray Flares with Swift Data". In: *ApJ* 646.1 (July 2006), pp. 351–357. DOI: 10.1086/504684.
- [158] C. A. Swenson et al. "Gamma-Ray Burst Flares: Ultraviolet/Optical Flaring. I." In: *ApJ* 774.1 (Sept. 2013), p. 2. DOI: 10.1088/0004-637X/774/1/2.
- [159] J. A. Osborne, F. Bagheri, and A. Shahmoradi. "Are there radio-loud and radio-quiet Gamma-Ray Bursts?" In: *MNRAS* 502.4 (Feb. 2021), pp. 5622–5630. DOI: 10.1093/mnras/stab425.
- [160] C. G. Mundell et al. "Highly polarized light from stable ordered magnetic fields in GRB 120308A". In: *Nature* 504.7478 (Dec. 2013), pp. 119–121. DOI: 10.1038/nature12814.
- [161] Y. Urata et al. "First Detection of Radio Linear Polarization in a Gamma-Ray Burst Afterglow". In: *ApJ* 884.2 (Oct. 2019), p. L58. DOI: 10.3847/2041-8213/ab48f3.

- [162] S. Bonometto and A. Saggion. "Polarization in Inverse Compton Scattering of Synchrotron Radiation". In: *A&A* 23 (Feb. 1973), p. 9.
- [163] H. Krawczynski. "The Polarization Properties of Inverse Compton Emission and Implications for Blazar Observations with the GEMS X-Ray Polarimeter". In: *ApJ* 744.1 (Jan. 2012), p. 30. DOI: 10.1088/0004-637X/744/1/30.
- [164] S. Covino and D. Gotz. "Polarization of prompt and afterglow emission of Gamma-Ray Bursts". In: *Astron. Astrophys. Trans.* 29.2 (Jan. 2016), pp. 205–244.
- [165] F. Govoni and L. Feretti. "Magnetic Fields in Clusters of Galaxies". In: *Int. J. Mod. Phys. D* 13.8 (Jan. 2004), pp. 1549–1594. DOI: 10.1142/S0218271804005080.
- [166] E. Troja et al. "Significant and variable linear polarization during the prompt optical flash of GRB 160625B." In: *Nature* 547 (July 2017), pp. 425–427. DOI: 10.1038/nature23289.
- [167] V. Chand et al. "Violation of Synchrotron Line of Death by the Highly Polarized GRB 160802A". In: *ApJ* 862.2, 154 (Aug. 2018). DOI: 10.3847/1538-4357/aacd12.
- [168] S.-N. Zhang et al. "Detailed polarization measurements of the prompt emission of five gamma-ray bursts". In: *Nat. Astron.* 3 (Jan. 2019), pp. 258–264. DOI: 10.1038/s41550-018-0664-0.
- [169] J. M. Burgess et al. "Time-resolved GRB polarization with POLAR and GBM. Simultaneous spectral and polarization analysis with synchrotron emission". In: *A&A* 627 (July 2019), A105. DOI: 10.1051/0004-6361/201935056.
- [170] P. A. Mazzali et al. "A neutron-star-driven X-ray flash associated with supernova SN 2006aj". In: *Nature* 442.7106 (Aug. 2006), pp. 1018–1020. DOI: 10.1038/nature05081.
- [171] J. Wang et al. "Spectroscopy of the Type Ic Supernova SN 2017iuk Associated with Low-redshift GRB 171205A". In: *ApJ* 867.2 (Nov. 2018), p. 147. DOI: 10.3847/1538-4357/aae6c3.
- [172] L. Caito et al. "GRB060614: a "fake" short GRB from a merging binary system". In: *A&A* 498.2 (May 2009), pp. 501–507. DOI: 10.1051/0004-6361/200810676.
- [173] N. Gehrels et al. "A new γ -ray burst classification scheme from GRB060614". In: *Nature* 444.7122 (Dec. 2006), pp. 1044–1046. DOI: 10.1038/nature05376.
- [174] S. Dado and A. Dar. "Universal afterglow of supernovaless gamma-ray bursts". In: *Phys. Rev. D* 99.12, 123031 (June 2019). DOI: 10.1103/PhysRevD.99.123031.
- [175] S. M. Adams et al. "The search for failed supernovae with the Large Binocular Telescope: constraints from 7 yr of data". In: *MNRAS* 469.2 (Aug. 2017), pp. 1445–1455. DOI: 10.1093/mnras/stx898.
- [176] T. Krühler. "The host galaxies of long gamma-ray bursts through cosmic time". In: *Int. J. Mod. Phys. D* 27.13, 1842001 (Jan. 2018). DOI: 10.1142/S0218271818420014.
- [177] A. Gomboc. "Unveiling the secrets of gamma ray bursts". In: *Contemp. Phys.* 53.4 (July 2012), pp. 339–355. DOI: 10.1080/00107514.2012.701453.
- [178] E. Berger. "Short-Duration Gamma-Ray Bursts". In: *ARA&A* 52 (Aug. 2014), pp. 43–105. DOI: 10.1146/annurev-astro-081913-035926.
- [179] R. L. Tunnicliffe et al. "On the nature of the 'hostless' short GRBs". In: *MNRAS* 437.2 (Jan. 2014), pp. 1495–1510. DOI: 10.1093/mnras/stt1975.
- [180] D. Lai. "Core-collapse Supernovae and Neutron Star Kicks". In: *Radio Pulsars*. Vol. 302. ASPCS. Jan. 2003, p. 307. arXiv: astro-ph/0212140 [astro-ph].
- [181] V. I. Dokuchaev and Y. N. Eroshenko. "Supernovae-optical precursors of short gamma-ray bursts". In: *Astron. Lett.* 37.2 (Feb. 2011), pp. 83–90. DOI: 10.1134/S1063773710120035.
- [182] E. Michaely and H. B. Perets. "Supernova and Prompt Gravitational-wave Precursors to LIGO Gravitational-wave Sources and Short GRBs". In: *ApJ* 855.1 (Mar. 2018), p. L12. DOI: 10.3847/2041-8213/aaacfc.

- [183] D. Guetta and T. Piran. "The BATSE-Swift luminosity and redshift distributions of short-duration GRBs". In: *A&A* 453.3 (July 2006), pp. 823–828. DOI: 10.1051/0004-6361:20054498.
- [184] E. Nakar, A. Gal-Yam, and D. B. Fox. "The Local Rate and the Progenitor Lifetimes of Short-Hard Gamma-Ray Bursts: Synthesis and Predictions for the Laser Interferometer Gravitational-Wave Observatory". In: *ApJ* 650.1 (Oct. 2006), pp. 281–290. DOI: 10.1086/505855.
- [185] F. J. Virgili et al. "Are All Short-hard Gamma-ray Bursts Produced from Mergers of Compact Stellar Objects?" In: *ApJ* 727.2, 109 (Feb. 2011). DOI: 10.1088/0004-637X/727/2/109.
- [186] M. Ruderman. "Theories of gamma -ray bursts." In: *Ann. N. Y. Acad. Sci.* 262.1 (Oct. 1975), pp. 164–180. DOI: 10.1111/j.1749-6632.1975.tb31430.x.
- [187] T. Piran. "The physics of gamma-ray bursts". In: *Rev. Mod. Phys.* 76.4 (Oct. 2004), pp. 1143–1210. DOI: 10.1103/RevModPhys.76.1143.
- [188] S. B. Cenko et al. "The Collimation and Energetics of the Brightest Swift Gamma-ray Bursts". In: *ApJ* 711.2 (Mar. 2010), pp. 641–654. DOI: 10.1088/0004-637X/711/2/641.
- [189] J. Granot. "The Structure and Dynamics of GRB Jets". In: *Rev. Mex. A&A*. Vol. 27. Mar. 2007, pp. 140–165. arXiv: astro-ph/0610379 [astro-ph].
- [190] F. A. Harrison et al. "Optical and Radio Observations of the Afterglow from GRB 990510: Evidence for a Jet". In: *ApJ* 523.2 (Oct. 1999), pp. L121–L124. DOI: 10.1086/312282.
- [191] A. Goldstein et al. "Estimating Long GRB Jet Opening Angles and Rest-frame Energetics". In: *ApJ* 818.1, 18 (Feb. 2016). DOI: 10.3847/0004-637X/818/1/18.
- [192] T. Totani and A. Panaitescu. "Orphan Afterglows of Collimated Gamma-Ray Bursts: Rate Predictions and Prospects for Detection". In: *ApJ* 576.1 (Sept. 2002), pp. 120–134. DOI: 10.1086/341738.
- [193] Y. F. Huang, Z. G. Dai, and T. Lu. "Failed gamma-ray bursts and orphan afterglows". In: *MNRAS* 332.3 (May 2002), pp. 735–740. DOI: 10.1046/j.1365-8711.2002.05334.x.
- [194] S. B. Cenko et al. "iPTF14yb: The First Discovery of a Gamma-Ray Burst Afterglow Independent of a High-energy Trigger". In: *ApJ* 803.2, L24 (Apr. 2015). DOI: 10.1088/2041-8205/803/2/L24.
- [195] F. E. Bauer et al. "A new, faint population of X-ray transients". In: *MNRAS* 467.4 (June 2017), pp. 4841–4857. DOI: 10.1093/mnras/stx417.
- [196] G. F. Krymskii. "A regular mechanism for the acceleration of charged particles on the front of a shock wave". In: *Dokl. Akad. Nauk SSSR* 234 (June 1977), pp. 1306–1308.
- [197] A. R. Bell. "The acceleration of cosmic rays in shock fronts - I." In: *MNRAS* 182 (Jan. 1978), pp. 147–156. DOI: 10.1093/mnras/182.2.147.
- [198] R. Blandford and D. Eichler. "Particle acceleration at astrophysical shocks: A theory of cosmic ray origin". In: *Phys. Rep.* 154.1 (Oct. 1987), pp. 1–75. DOI: 10.1016/0370-1573(87)90134-7.
- [199] A. Spitkovsky. "Particle Acceleration in Relativistic Collisionless Shocks: Fermi Process at Last?" In: *ApJ* 682.1 (July 2008), p. L5. DOI: 10.1086/590248.
- [200] A. Achterberg et al. "Particle acceleration by ultrarelativistic shocks: theory and simulations". In: *MNRAS* 328.2 (Dec. 2001), pp. 393–408. DOI: 10.1046/j.1365-8711.2001.04851.x.
- [201] U. Keshet and E. Waxman. "Energy Spectrum of Particles Accelerated in Relativistic Collisionless Shocks". In: *Phys. Rev. Lett.* 94.11, 111102 (Mar. 2005). DOI: 10.1103/PhysRevLett.94.111102.
- [202] P. Kumar and B. Zhang. "The physics of gamma-ray bursts & relativistic jets". In: *Phys. Rep.* 561 (Feb. 2015), pp. 1–109. DOI: 10.1016/j.physrep.2014.09.008.

- [203] I. Vurm and J. Poutanen. “Time-Dependent Modeling of Radiative Processes in Hot Magnetized Plasmas”. In: *ApJ* 698.1 (June 2009), pp. 293–316. DOI: 10.1088/0004-637X/698/1/293.
- [204] R. D. Preece et al. “On the Consistency of Gamma-Ray Burst Spectral Indices with the Synchrotron Shock Model”. In: *ApJ* 581.2 (Dec. 2002), pp. 1248–1255. DOI: 10.1086/344252.
- [205] R. D. Preece et al. “The Synchrotron Shock Model Confronts a “Line of Death” in the BATSE Gamma-Ray Burst Data”. In: *ApJ* 506.1 (Oct. 1998), pp. L23–L26. DOI: 10.1086/311644.
- [206] J. K. Becker. “High-energy neutrinos in the context of multimessenger astrophysics”. In: *Phys. Rep.* 458.4-5 (Mar. 2008), pp. 173–246. DOI: 10.1016/j.physrep.2007.10.006.
- [207] D. Guetta et al. “Neutrinos from individual gamma-ray bursts in the BATSE catalog”. In: *Astropart. Phys.* 20.4 (Jan. 2004), pp. 429–455. DOI: 10.1016/S0927-6505(03)00211-1.
- [208] S. Hümmer, P. Baerwald, and W. Winter. “Neutrino Emission from Gamma-Ray Burst Fireballs, Revised”. In: *Phys. Rev. Lett.* 108.23, 231101 (June 2012). DOI: 10.1103/PhysRevLett.108.231101.
- [209] Z. Li. “Note on the normalization of predicted gamma-ray burst neutrino flux”. In: *Phys. Rev. D* 85.2, 027301 (Jan. 2012). DOI: 10.1103/PhysRevD.85.027301.
- [210] A. Mücke et al. “Photomeson production in astrophysical sources”. In: *Nucl. Phys. B Proc. Suppl.* 80 (Jan. 2000), pp. 08–10.
- [211] R. Moharana and N. Gupta. “Neutrinos from decaying muons, pions, neutrons and kaons in gamma ray bursts”. In: *Astropart. Phys.* 36.1 (2012), pp. 195–203. ISSN: 0927-6505. DOI: 10.1016/j.astropartphys.2012.05.019.
- [212] P. Baerwald, M. Bustamante, and W. Winter. “UHECR Escape Mechanisms for Protons and Neutrons from Gamma-Ray Bursts, and the Cosmic-Ray-Neutrino Connection”. In: *ApJ* 768.2 (May 2013), p. 186. DOI: 10.1088/0004-637X/768/2/186.
- [213] H. L. Lai et al. “Global QCD analysis of parton structure of the nucleon: CTEQ5 parton distributions”. In: *Eur. Phys. J. C* 12.3 (Feb. 2000), pp. 375–392. DOI: 10.1007/s100529900196.
- [214] T. Liu, W.-M. Gu, and B. Zhang. “Neutrino-dominated accretion flows as the central engine of gamma-ray bursts”. In: *New A Rev.* 79 (Nov. 2017), pp. 1–25. DOI: 10.1016/j.newar.2017.07.001.
- [215] T. Liu et al. “Vertical Convection in Neutrino-dominated Accretion Flows”. In: *ApJ* 805.1 (May 2015), p. 37. DOI: 10.1088/0004-637X/805/1/37.
- [216] R. D. Blandford and R. L. Znajek. “Electromagnetic extraction of energy from Kerr black holes.” In: *MNRAS* 179 (May 1977), pp. 433–456. DOI: 10.1093/mnras/179.3.433.
- [217] R. Penrose and R. M. Floyd. “Extraction of Rotational Energy from a Black Hole”. In: *Nature Physical Science* 229.6 (Feb. 1971), pp. 177–179. DOI: 10.1038/physci229177a0.
- [218] W. H. Lei et al. “Magnetically Torqued Neutrino-dominated Accretion Flows for Gamma-ray Bursts”. In: *ApJ* 700.2 (Aug. 2009), pp. 1970–1976. DOI: 10.1088/0004-637X/700/2/1970.
- [219] W. Xie, W.-H. Lei, and D.-X. Wang. “Numerical and Analytical Solutions of Neutrino-dominated Accretion Flows with a Non-zero Torque Boundary Condition and its Applications in Gamma-Ray Bursts”. In: *ApJ* 833.2 (Dec. 2016), p. 129. DOI: 10.3847/1538-4357/833/2/129.
- [220] N. Kawanaka and Y. Masada. “Neutrino-dominated Accretion Flows with Magnetic Prandtl Number-dependent MRI-driven Turbulence”. In: *ApJ* 881.2, 138 (Aug. 2019), p. 138. DOI: 10.3847/1538-4357/ab2e71.

- [221] W. Xie, W.-H. Lei, and D.-X. Wang. "What Can We Learn about GRB from the Variability Timescale Related Correlations?" In: *ApJ* 838.2 (Apr. 2017), p. 143. DOI: 10.3847/1538-4357/aa6718.
- [222] H. C. Spruit. "The source of magnetic fields in (neutron-) stars". In: *Cosmic Magnetic Fields: From Planets, to Stars and Galaxies*. Vol. 259. Apr. 2009, pp. 61–74. DOI: 10.1017/S1743921309030075.
- [223] S. Konar. "Magnetic Fields of Neutron Stars". In: *J. Astrophys. Astron.* 38.3 (Sept. 2017), p. 47. DOI: 10.1007/s12036-017-9467-4.
- [224] C. Thompson and R. C. Duncan. "The Soft Gamma Repeaters as Very Strongly Magnetized Neutron Stars. II. Quiescent Neutrino, X-Ray, and Alfvén Wave Emission". In: *ApJ* 473 (Dec. 1996), p. 322. DOI: 10.1086/178147.
- [225] R. Turolla, S. Zane, and A. L. Watts. "Magnetars: the physics behind observations. A review". In: *Rep. Prog. Phys.* 78.11, 116901 (Nov. 2015). DOI: 10.1088/0034-4885/78/11/116901.
- [226] S. Rosswog, E. Ramirez-Ruiz, and M. B. Davies. "High-resolution calculations of merging neutron stars - III. Gamma-ray bursts". In: *MNRAS* 345.4 (Nov. 2003), pp. 1077–1090. DOI: 10.1046/j.1365-2966.2003.07032.x.
- [227] S. L. Shapiro. "Differential Rotation in Neutron Stars: Magnetic Braking and Viscous Damping". In: *ApJ* 544.1 (Nov. 2000), pp. 397–408. DOI: 10.1086/317209.
- [228] D. Zhang and Z. G. Dai. "Hyperaccreting Neutron Star Disks and Neutrino Annihilation". In: *ApJ* 703.1 (Sept. 2009), pp. 461–478. DOI: 10.1088/0004-637X/703/1/461.
- [229] A. R. Bodmer. "Collapsed Nuclei". In: *Phys. Rev. D* 4.6 (Sept. 1971), pp. 1601–1606. DOI: 10.1103/PhysRevD.4.1601.
- [230] E. Witten. "Cosmic separation of phases". In: *Phys. Rev. D* 30.2 (July 1984), pp. 272–285. DOI: 10.1103/PhysRevD.30.272.
- [231] Z. Dai, Q. Peng, and T. Lu. "The Conversion of Two-Flavor to Three-Flavor Quark Matter in a Supernova Core". In: *ApJ* 440 (Feb. 1995), p. 815. DOI: 10.1086/175316.
- [232] I. Bombaci and B. Datta. "Conversion of Neutron Stars to Strange Stars as the Central Engine of Gamma-Ray Bursts". In: *ApJ* 530.2 (Feb. 2000), pp. L69–L72. DOI: 10.1086/312497.
- [233] G. Arroyo-Chávez et al. "Neutron and quark stars: constraining the parameters for simple EoS using the GW170817". In: *Ap&SS* 365.2, 43 (Feb. 2020). DOI: 10.1007/s10509-020-03756-y.
- [234] A. M. Beloborodov and P. Mészáros. "Photospheric Emission of Gamma-Ray Bursts". In: *Space Sci. Rev.* 207.1-4 (July 2017), pp. 87–110. DOI: 10.1007/s11214-017-0348-6.
- [235] M. Bhattacharya and P. Kumar. "Explaining GRB prompt emission with sub-photospheric dissipation and Comptonization". In: *MNRAS* 491.4 (Feb. 2020), pp. 4656–4671. DOI: 10.1093/mnras/stz3182.
- [236] P. Mészáros et al. "X-Ray-rich Gamma-Ray Bursts, Photospheres, and Variability". In: *ApJ* 578.2 (Oct. 2002), pp. 812–817. DOI: 10.1086/342611.
- [237] V. Valan and J. Larsson. "A comprehensive view of blackbody components in the X-ray spectra of GRBs". In: *MNRAS* 501.4 (Mar. 2021), pp. 4974–4997. DOI: 10.1093/mnras/staa3978.
- [238] T. Piran, A. Shemi, and R. Narayan. "Hydrodynamics of Relativistic Fireballs". In: *MNRAS* 263 (Aug. 1993), p. 861. DOI: 10.1093/mnras/263.4.861.
- [239] B. Zhang, S. Kobayashi, and P. Mészáros. "Gamma-Ray Burst Early Optical Afterglows: Implications for the Initial Lorentz Factor and the Central Engine". In: *ApJ* 595.2 (Oct. 2003), pp. 950–954. DOI: 10.1086/377363.
- [240] E.-W. Liang et al. "Constraining Gamma-ray Burst Initial Lorentz Factor with the Afterglow Onset Feature and Discovery of a Tight Γ_0 - $E_{\gamma,iso}$ Correlation". In: *ApJ* 725.2 (Dec. 2010), pp. 2209–2224. DOI: 10.1088/0004-637X/725/2/2209.

- [241] C. D. Dermer, M. Böttcher, and J. Chiang. “The External Shock Model of Gamma-Ray Bursts: Three Predictions and a Paradox Resolved”. In: *ApJ* 515.2 (Apr. 1999), pp. L49–L52. DOI: 10.1086/311972.
- [242] Y.-D. Hu et al. “Internal Energy Dissipation of Gamma-Ray Bursts Observed with Swift: Precursors, Prompt Gamma-Rays, Extended Emission, and Late X-Ray Flares”. In: *ApJ* 789.2 (July 2014), p. 145. DOI: 10.1088/0004-637X/789/2/145.
- [243] H. C. Spruit, F. Daigne, and G. Drenkhahn. “Large scale magnetic fields and their dissipation in GRB fireballs”. In: *A&A* 369 (Apr. 2001), pp. 694–705. DOI: 10.1051/0004-6361:20010131.
- [244] M. Lyutikov and R. Blandford. “Gamma Ray Bursts as Electromagnetic Outflows”. In: *arXiv e-prints* (Dec. 2003). arXiv: astro-ph/0312347 [astro-ph].
- [245] M. Lyutikov and R. Blandford. “Electromagnetic Outflows and GRBs”. In: *Beaming and Jets in Gamma Ray Bursts*. Ed. by Rachid Ouyed. Jan. 2002, p. 146. arXiv: astro-ph/0210671 [astro-ph].
- [246] C. Thompson. “A model of gamma-ray bursts.” In: *MNRAS* 270 (Oct. 1994), pp. 480–498. DOI: 10.1093/mnras/270.3.480.
- [247] B. Zhang and H. Yan. “The Internal-collision-induced Magnetic Reconnection and Turbulence (ICMART) Model of Gamma-ray Bursts”. In: *ApJ* 726.2, 90 (Jan. 2011). DOI: 10.1088/0004-637X/726/2/90.
- [248] T. Inoue, K. Asano, and K. Ioka. “Three-dimensional Simulations of Magnetohydrodynamic Turbulence Behind Relativistic Shock Waves and Their Implications for Gamma-Ray Bursts”. In: *ApJ* 734.2, 77 (June 2011). DOI: 10.1088/0004-637X/734/2/77.
- [249] L. Sironi and A. Spitkovsky. “Particle Acceleration in Relativistic Magnetized Collisionless Electron-Ion Shocks”. In: *ApJ* 726.2, 75 (Jan. 2011). DOI: 10.1088/0004-637X/726/2/75.
- [250] A. Dar and A. De Rújula. “The Cannonball Model of Gamma Ray Bursts: high-energy neutrinos and γ -rays”. In: *arXiv e-prints* (May 2001). arXiv: astro-ph/0105094 [astro-ph].
- [251] A. Dar and A. de Rújula. “Towards a complete theory of gamma-ray bursts”. In: *Phys. Rep.* 405.4 (Dec. 2004), pp. 203–278. DOI: 10.1016/j.physrep.2004.09.008.
- [252] S. Heinz and M. C. Begelman. “A Shotgun Model for Gamma-Ray Bursts”. In: *ApJ* 527.1 (Dec. 1999), pp. L35–L38. DOI: 10.1086/312391.
- [253] R. Ruffini et al. “On the pair electromagnetic pulse of a black hole with electromagnetic structure”. In: *A&A* 350 (Oct. 1999), pp. 334–343. arXiv: astro-ph/9907030 [astro-ph].
- [254] R. Ruffini et al. “The canonical Gamma-Ray Bursts and their “precursors””. In: *AIP Conf. Proc.* 1065 (Oct. 2008), pp. 219–222. DOI: 10.1063/1.3027915.
- [255] R. Ruffini et al. “On the Interpretation of the Burst Structure of Gamma-Ray Bursts”. In: *ApJ* 555.2 (July 2001), pp. L113–L116. DOI: 10.1086/323176.
- [256] M. Lyutikov. “Electromagnetic (versus Fireball) Model of GRBs”. In: *AIP Conf. Proc.* 727 (Sept. 2004), pp. 552–556. DOI: 10.1063/1.1810906.
- [257] M. G. Aartsen et al. “Extending the Search for Muon Neutrinos Coincident with Gamma-Ray Bursts in IceCube Data”. In: *ApJ* 843.2 (July 2017), p. 112. DOI: 10.3847/1538-4357/aa7569.
- [258] B. Zhang and P. Kumar. “Model-Dependent High-Energy Neutrino Flux from Gamma-Ray Bursts”. In: *Phys. Rev. Lett.* 110.12, 121101 (Mar. 2013). DOI: 10.1103/PhysRevLett.110.121101.
- [259] M. Bustamante et al. “Multi-messenger Light Curves from Gamma-Ray Bursts in the Internal Shock Model”. In: *ApJ* 837.1 (Mar. 2017), p. 33. DOI: 10.3847/1538-4357/837/1/33.

- [260] T. Liu et al. “Detectable MeV neutrinos from black hole neutrino-dominated accretion flows”. In: *Phys. Rev. D* 93.12, 123004 (June 2016). DOI: 10.1103/PhysRevD.93.123004.
- [261] J. N. Bahcall and P. Mészáros. “5-10 GeV Neutrinos from Gamma-Ray Burst Fireballs”. In: *Phys. Rev. Lett.* 85.7 (Aug. 2000), pp. 1362–1365. DOI: 10.1103/PhysRevLett.85.1362.
- [262] K. Asano and K. Murase. “Gamma-Ray Bursts as Multienergy Neutrino Sources”. In: *Adv. Astron.* 2015, 568516 (Jan. 2015), p. 568516. DOI: 10.1155/2015/568516.
- [263] J. P. Rachen and P. Mészáros. “Photohadronic neutrinos from transients in astrophysical sources”. In: *Phys. Rev. D* 58.12, 123005 (Dec. 1998). DOI: 10.1103/PhysRevD.58.123005.
- [264] A. I. MacFadyen and S. E. Woosley. “Collapsars: Gamma-Ray Bursts and Explosions in “Failed Supernovae””. In: *ApJ* 524.1 (Oct. 1999), pp. 262–289. DOI: 10.1086/307790.
- [265] H. Sana et al. “Binary Interaction Dominates the Evolution of Massive Stars”. In: *Science* 337.6093 (July 2012), p. 444. DOI: 10.1126/science.1223344.
- [266] T. Ahumada et al. “Discovery and confirmation of the shortest gamma-ray burst from a collapsar”. In: *Nat. Astron.* 5 (July 2021), pp. 917–927. DOI: 10.1038/s41550-021-01428-7.
- [267] O. Bromberg et al. “An Observational Imprint of the Collapsar Model of Long Gamma-Ray Bursts”. In: *ApJ* 749.2, 110 (Apr. 2012). DOI: 10.1088/0004-637X/749/2/110.
- [268] N. Senno, K. Murase, and P. Mészáros. “Choked jets and low-luminosity gamma-ray bursts as hidden neutrino sources”. In: *Phys. Rev. D* 93.8, 083003 (Apr. 2016). DOI: 10.1103/PhysRevD.93.083003.
- [269] P. Mészáros and E. Waxman. “TeV Neutrinos from Successful and Choked Gamma-Ray Bursts”. In: *Phys. Rev. Lett.* 87.17, 171102 (Oct. 2001). DOI: 10.1103/PhysRevLett.87.171102.
- [270] M. Fasano et al. “Estimating the neutrino flux from choked gamma-ray bursts”. In: *J. Cosmology Astropart. Phys.* 2021.9 (Sept. 2021), p. 044. DOI: 10.1088/1475-7516/2021/09/044.
- [271] C. C. Thöne et al. “The unusual γ -ray burst GRB 101225A from a helium star/neutron star merger at redshift 0.33”. In: *Nature* 480.7375 (Dec. 2011), pp. 72–74. DOI: 10.1038/nature10611.
- [272] A. V. Penacchioni et al. “GRB 110709B in the induced gravitational collapse paradigm”. In: *A&A* 551 (Mar. 2013), A133. DOI: 10.1051/0004-6361/201220679.
- [273] B.-B. Zhang et al. “Unusual Central Engine Activity in the Double Burst GRB 110709B”. In: *ApJ* 748.2 (Apr. 2012), p. 132. DOI: 10.1088/0004-637X/748/2/132.
- [274] J. A. Rueda et al. “Simulating the induced gravitational collapse scenario of long gamma-ray bursts”. In: *Int. J. Mod. Phys. A*. 33.31 (2018), p. 1844031. DOI: 10.1142/S0217751X18440311.
- [275] L. Becerra et al. “SPH Simulations of the Induced Gravitational Collapse Scenario of Long Gamma-Ray Bursts Associated with Supernovae”. In: *ApJ* 871.1, 14 (Jan. 2019). DOI: 10.3847/1538-4357/aaf6b3.
- [276] C. S. Kochanek. “Coalescing Binary Neutron Stars”. In: *ApJ* 398 (Oct. 1992), p. 234. DOI: 10.1086/171851.
- [277] D. A. Kann et al. “The Afterglows of Swift-era Gamma-Ray Bursts. II. Type I GRB versus Type II GRB Optical Afterglows”. In: *ApJ* 734.2 (June 2011), p. 96. DOI: 10.1088/0004-637X/734/2/96.

- [278] J. A. Faber et al. “Black Hole-Neutron Star Binary Merger Calculations: GRB Progenitors and the Stability of Mass Transfer”. In: *AIP Conf. Proc.* 861 (Nov. 2006), pp. 622–629. DOI: 10.1063/1.2399634.
- [279] J. M. Lattimer and D. N. Schramm. “The tidal disruption of neutron stars by black holes in close binaries.” In: *ApJ* 210 (Dec. 1976), pp. 549–567. DOI: 10.1086/154860.
- [280] R. Abbott et al. “Observation of Gravitational Waves from Two Neutron Star-Black Hole Coalescences”. In: *ApJ* 915.1 (July 2021), p. L5. DOI: 10.3847/2041-8213/ac082e.
- [281] R. Narayan, T. Piran, and P. Kumar. “Accretion Models of Gamma-Ray Bursts”. In: *ApJ* 557.2 (Aug. 2001), pp. 949–957. DOI: 10.1086/322267.
- [282] N. R. Tanvir et al. “An origin in the local Universe for some short γ -ray bursts”. In: *Nature* 438.7070 (Dec. 2005), pp. 991–993. DOI: 10.1038/nature04310.
- [283] S. Mandhai et al. “The Rate of Short-Duration Gamma-Ray Bursts in the Local Universe”. In: *Galaxies* 6.4 (Nov. 2018), p. 130. DOI: 10.3390/galaxies6040130.
- [284] D. S. Svinkin et al. “A search for giant flares from soft gamma-ray repeaters in nearby galaxies in the Konus-WIND short burst sample”. In: *MNRAS* 447.1 (Feb. 2015), pp. 1028–1032. DOI: 10.1093/mnras/stu2436.
- [285] E. Burns et al. “Identification of a Local Sample of Gamma-Ray Bursts Consistent with a Magnetar Giant Flare Origin”. In: *ApJ* 907.2 (Feb. 2021), p. L28. DOI: 10.3847/2041-8213/abd8c8.
- [286] R. Chapman et al. “How common are long gamma-ray bursts in the local Universe?” In: *MNRAS* 382.1 (Nov. 2007), pp. L21–L25. DOI: 10.1111/j.1745-3933.2007.00381.x.
- [287] A. M. Soderberg et al. “An extremely luminous X-ray outburst at the birth of a supernova”. In: *Nature* 453.7194 (May 2008), pp. 469–474. DOI: 10.1038/nature06997.
- [288] J. S. Bloom et al. “A Possible Relativistic Jetted Outburst from a Massive Black Hole Fed by a Tidally Disrupted Star”. In: *Science* 333.6039 (July 2011), p. 203. DOI: 10.1126/science.1207150.
- [289] T. Murakami et al. “A γ -ray burst preceded by X-ray activity”. In: *Nature* 350.6319 (Apr. 1991), pp. 592–594. DOI: 10.1038/350592a0.
- [290] T. M. Koshut et al. “Gamma-Ray Burst Precursor Activity as Observed with BATSE”. In: *ApJ* 452 (Oct. 1995), p. 145. DOI: 10.1086/176286.
- [291] E. Troja, S. Rosswog, and N. Gehrels. “Precursors of Short Gamma-Ray Bursts”. In: *ApJ* 723.2 (Oct. 2010), pp. 1711–1717. DOI: 10.1088/0004-637x/723/2/1711.
- [292] S. Zhu. “Precursors in Gamma-ray Bursts Observed by Fermi”. PhD thesis. 2015. DOI: 10.13016/M2CH9N.
- [293] D. Lazzati. “Precursor activity in bright, long BATSE gamma-ray bursts”. In: *MNRAS* 357.2 (Feb. 2005), pp. 722–731. DOI: 10.1111/j.1365-2966.2005.08687.x.
- [294] D. Burlon et al. “Precursors in Swift Gamma Ray Bursts with Redshift”. In: *ApJ* 685.1 (Sept. 2008), p. L19. DOI: 10.1086/592350.
- [295] M. Charisi, S. Márka, and I. Bartos. “Catalogue of isolated emission episodes in gamma-ray bursts from Fermi, Swift and BATSE”. In: *MNRAS* 448.3 (Apr. 2015), pp. 2624–2633. DOI: 10.1093/mnras/stu2667.
- [296] F. Nappo et al. “Afterglows from precursors in gamma-ray bursts. Application to the optical afterglow of GRB 091024”. In: *MNRAS* 445.2 (Dec. 2014), pp. 1625–1635. DOI: 10.1093/mnras/stu1832.
- [297] D. Burlon et al. “Time resolved spectral behavior of bright BATSE precursors”. In: *A&A* 505.2 (Oct. 2009), pp. 569–575. DOI: 10.1051/0004-6361/200912662.
- [298] G. Calderone et al. “Search for precursor activity in Swift/BAT gamma-ray bursts”. In: *The 7th INTEGRAL Workshop*. Jan. 2008, 18, p. 18.

- [299] E. Ramirez-Ruiz and A. Merloni. “Quiescent times in gamma-ray bursts - I. An observed correlation between the durations of subsequent emission episodes”. In: *MNRAS* 320.3 (Jan. 2001), pp. L25–L29. DOI: 10.1046/j.1365-8711.2001.04130.x.
- [300] S.-Q. Zhong et al. “Precursors in Short Gamma-Ray Bursts as a Possible Probe of Progenitors”. In: *ApJ* 884.1 (Oct. 2019), p. 25. DOI: 10.3847/1538-4357/ab3e48.
- [301] L. Lan et al. “Characteristics of Two-episode Emission Patterns in Fermi Long Gamma-Ray Bursts”. In: *ApJ* 862.2 (Aug. 2018), p. 155. DOI: 10.3847/1538-4357/aacda6.
- [302] K. L. Page et al. “GRB 061121: Broadband Spectral Evolution through the Prompt and Afterglow Phases of a Bright Burst”. In: *ApJ* 663.2 (July 2007), pp. 1125–1138. DOI: 10.1086/518821.
- [303] L. Piro et al. “Probing the Environment in Gamma-Ray Bursts: The Case of an X-Ray Precursor, Afterglow Late Onset, and Wind Versus Constant Density Profile in GRB 011121 and GRB 011211”. In: *ApJ* 623.1 (Apr. 2005), pp. 314–324. DOI: 10.1086/428377.
- [304] R. Vanderspek et al. “HETE Observations of the Gamma-Ray Burst GRB 030329: Evidence for an Underlying Soft X-Ray Component”. In: *ApJ* 617.2 (Dec. 2004), pp. 1251–1257. DOI: 10.1086/423923.
- [305] X. J. Li et al. “Temporal Properties of Precursors, Main Peaks, and Extended Emissions of Short GRBs in the Third Swift/BAT GRB Catalog”. In: *ApJS* 252.2 (Feb. 2021), p. 16. DOI: 10.3847/1538-4365/abd3fd.
- [306] D. Lazzati et al. “GRB Jets Inside and Outside the Star: Precursors and Cosmological Implications”. In: *22nd Texas Symposium on Relativistic Astrophysics*. Jan. 2005, pp. 48–56. arXiv: astro-ph/0503630 [astro-ph].
- [307] J. D. Scargle et al. “Studies in Astronomical Time Series Analysis. VI. Bayesian Block Representations”. In: *ApJ* 764.2 (Feb. 2013), p. 167. DOI: 10.1088/0004-637X/764/2/167.
- [308] P. Y. Minaev and A. S. Pozanenko. “Precursors of short gamma-ray bursts in the SPI-ACS/INTEGRAL experiment.” In: *Astron. Lett.* 43.1 (Jan. 2017), pp. 1–20. DOI: 10.1134/S1063773717010017.
- [309] B. Baret et al. “Bounding the time delay between high-energy neutrinos and gravitational-wave transients from gamma-ray bursts”. In: *Astropart. Phys.* 35.1 (Aug. 2011), pp. 1–7. DOI: 10.1016/j.astropartphys.2011.04.001.
- [310] M. Lyutikov and V. V. Usov. “Precursors of Gamma-Ray Bursts: A Clue to the Burster’s Nature”. In: *ApJ* 543.2 (Nov. 2000), pp. L129–L132. DOI: 10.1086/317278.
- [311] L.-X. Li. “Gamma-ray burst precursors as the remnant of the thermal radiation initially trapped in the fireball”. In: *MNRAS* 380.2 (Sept. 2007), pp. 621–636. DOI: 10.1111/j.1365-2966.2007.12083.x.
- [312] D. M. Worrall. “The gaseous environments of radio galaxies”. In: *New A Rev.* 46.2-7 (May 2002), pp. 121–134. DOI: 10.1016/S1387-6473(01)00167-1.
- [313] L. Izzo et al. “Signatures of a jet cocoon in early spectra of a supernova associated with a γ -ray burst”. In: *Nature* 565.7739 (Jan. 2019), pp. 324–327. DOI: 10.1038/s41586-018-0826-3.
- [314] D. Lazzati and M. C. Begelman. “Universal GRB Jets from Jet-Cocoon Interaction in Massive Stars”. In: *ApJ* 629.2 (Aug. 2005), pp. 903–907. DOI: 10.1086/430877.
- [315] A. Murguia-Berthier et al. “Necessary Conditions for Short Gamma-Ray Burst Production in Binary Neutron Star Mergers”. In: *ApJ* 788.1 (June 2014), p. L8. DOI: 10.1088/2041-8205/788/1/L8.
- [316] X.-Y. Wang and P. Mészáros. “GRB Precursors in the Fallback Collapsar Scenario”. In: *ApJ* 670.2 (Dec. 2007), pp. 1247–1253. DOI: 10.1086/522820.

- [317] M. Vietri and L. Stella. “Supranova Events from Spun-up Neutron Stars: An Explosion in Search of an Observation”. In: *ApJ* 527.1 (Dec. 1999), pp. L43–L46. DOI: 10.1086/312386.
- [318] B. Margalit, B. D. Metzger, and A. M. Beloborodov. “Does the Collapse of a Supramassive Neutron Star Leave a Debris Disk?” In: *Phys. Rev. Lett.* 115.17, 171101 (Oct. 2015). DOI: 10.1103/PhysRevLett.115.171101.
- [319] G. V. Lipunova. “A burst of electromagnetic radiation from a collapsing magnetized star”. In: *Astron. Lett.* 23.1 (Jan. 1997), pp. 84–92. arXiv: astro-ph/9703006 [astro-ph].
- [320] V. M. Lipunov and E. S. Gorbovskoy. “Spinar paradigm and the central engine of gamma-ray bursts”. In: *MNRAS* 383.4 (Jan. 2008), pp. 1397–1412. ISSN: 0035-8711. DOI: 10.1111/j.1365-2966.2007.12489.x.
- [321] G. V. Lipunova et al. “Population synthesis of gamma-ray bursts with precursor activity and the spinar paradigm”. In: *MNRAS* 397.3 (Aug. 2009), pp. 1695–1704. DOI: 10.1111/j.1365-2966.2009.15079.x.
- [322] B. M. S. Hansen and M. Lyutikov. “Radio and X-ray signatures of merging neutron stars”. In: *MNRAS* 322.4 (Apr. 2001), pp. 695–701. DOI: 10.1046/j.1365-8711.2001.04103.x.
- [323] B. D. Metzger and C. Zivancev. “Pair fireball precursors of neutron star mergers”. In: *MNRAS* 461.4 (Oct. 2016), pp. 4435–4440. DOI: 10.1093/mnras/stw1800.
- [324] H. Tong, C. Yu, and L. Huang. “A magnetically driven origin for the low luminosity GRB 170817A associated with GW170817”. In: *Res. Astron. Astrophys.* 18.6 (June 2018), p. 67. DOI: 10.1088/1674-4527/18/6/67.
- [325] D. Tsang et al. “Resonant Shattering of Neutron Star Crusts”. In: *Phys. Rev. Lett.* 108.1, 011102 (Jan. 2012). DOI: 10.1103/PhysRevLett.108.011102.
- [326] H. Alfvén. “Existence of Electromagnetic-Hydrodynamic Waves”. In: *Nature* 150.3805 (Oct. 1942), pp. 405–406. DOI: 10.1038/150405d0.
- [327] A. G. Suvorov and K. D. Kokkotas. “Precursor flares of short gamma-ray bursts from crust yielding due to tidal resonances in coalescing binaries of rotating, magnetized neutron stars”. In: *Phys. Rev. D* 101 (8 Apr. 2020), p. 083002. DOI: 10.1103/PhysRevD.101.083002.
- [328] A. J. Penner et al. “Crustal Failure During Binary Inspiral”. In: *ApJ* 749.2 (Apr. 2012), p. L36. DOI: 10.1088/2041-8205/749/2/L36.
- [329] A. J. Penner et al. “Tidal deformations of neutron stars: The role of stratification and elasticity”. In: *Phys. Rev. D* 84.10, 103006 (Nov. 2011). DOI: 10.1103/PhysRevD.84.103006.
- [330] M. G. Bernardini et al. “How to Switch a Gamma-Ray Burst On and Off through a Magnetar”. In: *ApJ* 775.1 (Sept. 2013), p. 67. DOI: 10.1088/0004-637X/775/1/67.
- [331] H. Umeda et al. “Precursors and Main Bursts of Gamma-Ray Bursts in a Hypernova Scenario”. In: *ApJ* 633.1 (Nov. 2005), pp. L17–L20. DOI: 10.1086/498136.
- [332] P. C. Duffell and A. Y. Q. Ho. “How Dense a CSM is Sufficient to Choke a Jet?” In: *arXiv e-prints* (July 2019). arXiv: 1907.03768 [astro-ph.HE].
- [333] S. Razzaque, P. Mészáros, and E. Waxman. “Neutrino tomography of gamma ray bursts and massive stellar collapses”. In: *Phys. Rev. D* 68.8, 083001 (Oct. 2003). DOI: 10.1103/PhysRevD.68.083001.
- [334] K. Ioka. “Very High Lorentz Factor Fireballs and Gamma-Ray Burst Spectra”. In: *Prog. Theor. Exp. Phys.* 124.4 (Oct. 2010), pp. 667–710. DOI: 10.1143/PTP.124.667.
- [335] K. Murase. “Prompt high-energy neutrinos from gamma-ray bursts in photospheric and synchrotron self-Compton scenarios”. In: *Phys. Rev. D* 78.10, 101302 (Nov. 2008). DOI: 10.1103/PhysRevD.78.101302.

- [336] K. Murase and K. Ioka. “TeV-PeV Neutrinos from Low-Power Gamma-Ray Burst Jets inside Stars”. In: *Phys. Rev. Lett.* 111.12, 121102 (Sept. 2013). DOI: 10.1103/PhysRevLett.111.121102.
- [337] S. Razzaque, P. Mészáros, and E. Waxman. “High Energy Neutrinos from Gamma-Ray Bursts with Precursor Supernovae”. In: *Phys. Rev. Lett.* 90.24, 241103 (June 2003). DOI: 10.1103/PhysRevLett.90.241103.
- [338] S. Razzaque, P. Mészáros, and E. Waxman. “Neutrino signatures of the supernova: Gamma ray burst relationship”. In: *Phys. Rev. D* 69.2, 023001 (Jan. 2004). DOI: 10.1103/PhysRevD.69.023001.
- [339] J. Granot and D. Guetta. “Neutrinos from Pulsar Wind Bubbles as Precursors to Gamma-Ray Bursts”. In: *Phys. Rev. Lett.* 90.19, 191102 (May 2003). DOI: 10.1103/PhysRevLett.90.191102.
- [340] J. D. Scargle. “Studies in Astronomical Time Series Analysis. V. Bayesian Blocks, a New Method to Analyze Structure in Photon Counting Data”. In: *ApJ* 504.1 (Sept. 1998), pp. 405–418. DOI: 10.1086/306064.
- [341] C. Meegan et al. “The Fermi Gamma-ray Burst Monitor”. In: *ApJ* 702.1 (Sept. 2009), pp. 791–804. DOI: 10.1088/0004-637X/702/1/791.
- [342] M. Ajello et al. “Fermi Large Area Telescope Performance after 10 Years of Operation”. In: *ApJS* 256.1 (Sept. 2021), p. 12. DOI: 10.3847/1538-4365/ac0ceb.
- [343] P. Cumani et al. “Background for a gamma-ray satellite on a low-Earth orbit”. In: *Exp. Astron.* 47.3 (June 2019), pp. 273–302. DOI: 10.1007/s10686-019-09624-0.
- [344] J. A. Van Allen, C. E. McIlwain, and G. H. Ludwig. “Radiation observations with satellite 1958 ϵ ”. In: *J. Geophys. Res.* 64.3 (1959), pp. 271–286. DOI: 10.1029/JZ064i003p00271.
- [345] E. Bissaldi et al. “Ground-based calibration and characterization of the Fermi gamma-ray burst monitor detectors”. In: *Exp. Astron.* 24.1-3 (May 2009), pp. 47–88. DOI: 10.1007/s10686-008-9135-4.
- [346] National Institute of Standards and Technology. *XCOM: Photon Cross Sections Database*. 2022. URL: <https://www.nist.gov/pml/xcom-photon-cross-sections-database> (visited on Jan. 31, 2022).
- [347] S. Abdollahi et al. “Fermi Large Area Telescope Fourth Source Catalog”. In: *ApJS* 247.1 (Mar. 2020), p. 33. DOI: 10.3847/1538-4365/ab6bcb.
- [348] A. Shepetov et al. “The prolonged gamma ray enhancement and the short radiation burst events observed in thunderstorms at Tien Shan”. In: *Atmos. Res.* 248, 105266 (Jan. 2021). DOI: 10.1016/j.atmosres.2020.105266.
- [349] O. J. Roberts et al. “The First Fermi-GBM Terrestrial Gamma Ray Flash Catalog”. In: *J. Geophys. Res. Space Phys.* 123.5 (May 2018), pp. 4381–4401. DOI: 10.1029/2017JA024837.
- [350] M. S. Briggs et al. “Electron-positron beams from terrestrial lightning observed with Fermi GBM”. In: *Geophys. Res. Lett.* 38.2, L02808 (Jan. 2011). DOI: 10.1029/2010GL046259.
- [351] M. Ackermann et al. “Measurement of the high-energy gamma-ray emission from the Moon with the Fermi Large Area Telescope”. In: *Phys. Rev. D* 93.8, 082001 (Apr. 2016). DOI: 10.1103/PhysRevD.93.082001.
- [352] N. Hasebe et al. “Gamma-ray spectrometer (GRS) for lunar polar orbiter SELENE”. In: *Earth Planets Space* 60 (Apr. 2008), pp. 299–312. DOI: 10.1186/BF03352795.
- [353] P. F. Michelson, W. B. Atwood, and S. Ritz. “Fermi Gamma-ray Space Telescope: high-energy results from the first year”. In: *Rep. Prog. Phys.* 73.7, 074901 (July 2010). DOI: 10.1088/0034-4885/73/7/074901.
- [354] M. Ajello et al. “First Fermi-LAT Solar Flare Catalog”. In: *ApJS* 252.2 (Feb. 2021), p. 13. DOI: 10.3847/1538-4365/abd32e.

- [355] L. R. Nittler et al. "The Chemical Composition of Mercury". In: *Mercury. The View after MESSENGER*. 2018, pp. 30–51. DOI: 10.1017/9781316650684.003.
- [356] F. Aharonian et al. "An Exceptional Very High Energy Gamma-Ray Flare of PKS 2155-304". In: *ApJ* 664.2 (Aug. 2007), pp. L71–L74. DOI: 10.1086/520635.
- [357] D. Szécsi et al. "Direction dependent background fitting for the Fermi GBM data". In: *A&A* 557 (Sept. 2013), A8. DOI: 10.1051/0004-6361/201321068.
- [358] B. Biltzinger et al. "A physical background model for the Fermi Gamma-ray Burst Monitor". In: *A&A* 640 (Aug. 2020), A8. DOI: 10.1051/0004-6361/201937347.
- [359] D. Freedman and P. Diaconis. "On the histogram as a density estimator: L 2 theory". In: *Zeitschrift für Wahrscheinlichkeitstheorie und Verwandte Gebiete* 57 (Dec. 1981), pp. 453–476. DOI: 10.1007/BF01025868.
- [360] M. A. Markov. "On high energy neutrino physics". In: *10th International Conference on High Energy Physics*. 1960, pp. 578–581.
- [361] M. G. Aartsen et al. "Evidence for High-Energy Extraterrestrial Neutrinos at the IceCube Detector". In: *Science* 342.6161, 1242856 (Nov. 2013). DOI: 10.1126/science.1242856.
- [362] M. G. Aartsen et al. "Time-Integrated Neutrino Source Searches with 10 Years of IceCube Data". In: *Phys. Rev. Lett.* 124.5, 051103 (Feb. 2020). DOI: 10.1103/PhysRevLett.124.051103.
- [363] M. G. Aartsen et al. "All-sky Search for Time-integrated Neutrino Emission from Astrophysical Sources with 7 yr of IceCube Data". In: *ApJ* 835.2 (Feb. 2017), p. 151. DOI: 10.3847/1538-4357/835/2/151.
- [364] R. Abbasi et al. "IceCube high-energy starting event sample: Description and flux characterization with 7.5 years of data". In: *Phys. Rev. D* 104.2, 022002 (July 2021). DOI: 10.1103/PhysRevD.104.022002.
- [365] H. M. Niederhausen and Y. Xu. "High Energy Astrophysical Neutrino Flux Measurement Using Neutrino-induced Cascades Observed in 4 Years of IceCube Data". In: *PoS ICRC2017* (2018), p. 968. DOI: 10.22323/1.301.0968.
- [366] J. Stettner. "Measurement of the diffuse astrophysical muon-neutrino spectrum with ten years of IceCube data". In: *PoS ICRC2019*, 1017 (2019). DOI: 10.22323/1.358.1017.
- [367] M. G. Aartsen et al. "Multimessenger observations of a flaring blazar coincident with high-energy neutrino IceCube-170922A". In: *Science* 361.6398, eaat1378 (July 2018). DOI: 10.1126/science.aat1378.
- [368] Y.-F. Liang et al. "Search for GeV flare coincident with the IceCube neutrino flare". In: *arXiv e-prints* (July 2018). arXiv: 1807.05057 [astro-ph.HE].
- [369] M. G. Aartsen et al. "Neutrino emission from the direction of the blazar TXS 0506+056 prior to the IceCube-170922A alert". In: *Science* 361.6398 (July 2018), pp. 147–151. DOI: 10.1126/science.aat2890.
- [370] A. Lamastra et al. "Galactic outflow driven by the active nucleus and the origin of the gamma-ray emission in NGC 1068". In: *A&A* 596 (Dec. 2016), A68. DOI: 10.1051/0004-6361/201628667.
- [371] R. Stein et al. "A tidal disruption event coincident with a high-energy neutrino". In: *Nat. Astron.* 5 (Feb. 2021), pp. 510–518. DOI: 10.1038/s41550-020-01295-8.
- [372] A. V. Plavin et al. "Radio astronomy locates the neutrino origin in bright blazars". In: *PoS ICRC2021*, 967 (2021). DOI: 10.22323/1.395.0967.
- [373] H. Harari. "Neutrino masses, mixing and decays beyond the standard model". In: *13th International Conference on Neutrino Physics and Astrophysics*. Nov. 1988.
- [374] M. Kowalski. "Status of High-Energy Neutrino Astronomy". In: *Journal of Physics Conference Series*. Vol. 632. Aug. 2015, 012039. DOI: 10.1088/1742-6596/632/1/012039.

- [375] M. G. Aartsen et al. "Search for steady point-like sources in the astrophysical muon neutrino flux with 8 years of IceCube data". In: *Eur. Phys. J. C* 79.3 (Mar. 2019), p. 234. DOI: 10.1140/epjc/s10052-019-6680-0.
- [376] M. G. Aartsen et al. "Constraints on Minute-Scale Transient Astrophysical Neutrino Sources". In: *Phys. Rev. Lett.* 122.5, 051102 (Feb. 2019). DOI: 10.1103/PhysRevLett.122.051102.
- [377] M. G. Aartsen et al. "First search for dark matter annihilations in the Earth with the IceCube detector". In: *Eur. Phys. J. C* 77.2 (Feb. 2017), p. 82. DOI: 10.1140/epjc/s10052-016-4582-y.
- [378] M. G. Aartsen et al. "Search for annihilating dark matter in the Sun with 3 years of IceCube data". In: *Eur. Phys. J. C* 77.3 (Mar. 2017), p. 146. DOI: 10.1140/epjc/s10052-017-4689-9.
- [379] A. Albert et al. "Combined search for neutrinos from dark matter self-annihilation in the Galactic Center with ANTARES and IceCube". In: *Phys. Rev. D* 102.8, 082002 (Oct. 2020). DOI: 10.1103/PhysRevD.102.082002.
- [380] F. H. Lauber. "New Flux Limits in the Low Relativistic Regime for Magnetic Monopoles at IceCube". In: *PoS ICRC2019*, 534 (2019). DOI: 10.22323/1.395.0534.
- [381] M. G. Aartsen et al. "Measurement of Atmospheric Neutrino Oscillations at 6-56 GeV with IceCube DeepCore". In: *Phys. Rev. Lett.* 120.7, 071801 (Feb. 2018). DOI: 10.1103/PhysRevLett.120.071801.
- [382] M. G. Aartsen et al. "Cosmic ray spectrum and composition from PeV to EeV using 3 years of data from IceTop and IceCube". In: *Phys. Rev. D* 100.8, 082002 (Oct. 2019). DOI: 10.1103/PhysRevD.100.082002.
- [383] A. U. Abeysekara et al. "All-sky Measurement of the Anisotropy of Cosmic Rays at 10 TeV and Mapping of the Local Interstellar Magnetic Field". In: *ApJ* 871.1 (Jan. 2019), p. 96. DOI: 10.3847/1538-4357/aaf5cc.
- [384] D. Chirkin and M. Rongen. "Light diffusion in birefringent polycrystals and the IceCube ice anisotropy". In: *PoS ICRC2019*, 854 (2019). DOI: 10.22323/1.358.0854.
- [385] A. Albert et al. "All-flavor Search for a Diffuse Flux of Cosmic Neutrinos with Nine Years of ANTARES Data". In: *ApJ* 853.1 (Jan. 2018), p. L7. DOI: 10.3847/2041-8213/aaa4f6.
- [386] M. Ageron et al. "ANTARES: The first undersea neutrino telescope". In: *Nucl. Instrum. Methods Phys. Res. A* 656.1 (Nov. 2011), pp. 11–38. DOI: 10.1016/j.nima.2011.06.103.
- [387] R. Wischniewski et al. "The Baikal neutrino telescope - results and plans". In: *Int. J. Mod. Phys. A* 20.29 (Nov. 2005), 6932–6936. ISSN: 1793-656X. DOI: 10.1142/S0217751x0503051x.
- [388] S. Adrián-Martínez et al. "Letter of intent for KM3NeT 2.0". In: *J. Phys. G. Nucl. Phys.* 43.8, 084001 (Aug. 2016). DOI: 10.1088/0954-3899/43/8/084001.
- [389] G. Safronov. "Baikal-GVD: status and first results". In: *PoS ICRC2021*, 606 (July 2021). DOI: 10.22323/1.390.0606.
- [390] D. Dornic et al. "Real-time follow-up of multi-messenger alerts with the ANTARES neutrino telescope". In: *PoS ICRC2019*, 872 (2019). DOI: 10.22323/1.358.0872.
- [391] H. A. Ayala Solares et al. "A Search for Cosmic Neutrino and Gamma-Ray Emitting Transients in 7.3 yr of ANTARES and Fermi LAT Data". In: *ApJ* 886.2 (Dec. 2019), p. 98. DOI: 10.3847/1538-4357/ab4a74.
- [392] A. Albert et al. "Search for high-energy neutrinos from bright GRBs with ANTARES". In: *MNRAS* 469.1 (July 2017), pp. 906–915. DOI: 10.1093/mnras/stx902.
- [393] S. Adrián-Martínez et al. "Search for muon neutrinos from gamma-ray bursts with the ANTARES neutrino telescope using 2008 to 2011 data". In: *A&A* 559, A9 (Nov. 2013). DOI: 10.1051/0004-6361/201322169.

- [394] A. Albert et al. “Constraining the contribution of Gamma-Ray Bursts to the high-energy diffuse neutrino flux with 10 yr of ANTARES data”. In: *MNRAS* 500.4 (Jan. 2021), pp. 5614–5628. DOI: 10.1093/mnras/staa3503.
- [395] A. Albert et al. “ANTARES upper limits on the multi-TeV neutrino emission from the GRBs detected by IACTs”. In: *J. Cosmology Astropart. Phys.* 2021.3 (Mar. 2021), p. 92. DOI: 10.1088/1475-7516/2021/03/092.
- [396] A. Orii et al. “Search for tens of MeV neutrinos associated with gamma-ray bursts in Super-Kamiokande”. In: *Prog. Theor. Exp. Phys.* 2021.10 (Oct. 2021). DOI: 10.1093/ptep/ptab081.
- [397] M. G. Aartsen et al. “An All-sky Search for Three Flavors of Neutrinos from Gamma-ray Bursts with the IceCube Neutrino Observatory”. In: *ApJ* 824.2 (June 2016), p. 115. DOI: 10.3847/0004-637X/824/2/115.
- [398] A. Aab et al. “Limits on point-like sources of ultra-high-energy neutrinos with the Pierre Auger Observatory”. In: *J. Cosmology Astropart. Phys.* 2019.11 (Nov. 2019), p. 004. DOI: 10.1088/1475-7516/2019/11/004.
- [399] R. U. Abbasi et al. “Search for Ultra-High-Energy Neutrinos with the Telescope Array Surface Detector”. In: *J. Exp. Theor. Phys.* 131.2 (Sept. 2020), pp. 255–264. DOI: 10.1134/S106377612005012X.
- [400] C. Deaconu et al. “A search for ultrahigh-energy neutrinos associated with astrophysical sources using the third flight of ANITA”. In: *J. Cosmology Astropart. Phys.* 2021.4 (Apr. 2021), p. 17. DOI: 10.1088/1475-7516/2021/04/017.
- [401] P. Allison et al. “Constraints on the diffuse flux of ultrahigh energy neutrinos from four years of Askaryan Radio Array data in two stations”. In: *Phys. Rev. D* 102, 043021 (4 2020). DOI: 10.1103/PhysRevD.102.043021.
- [402] A. Anker et al. “A search for cosmogenic neutrinos with the ARIANNA test bed using 4.5 years of data”. In: *J. Cosmology Astropart. Phys.* 2020.3 (Mar. 2020), p. 53. DOI: 10.1088/1475-7516/2020/03/053.
- [403] M. Ahlers and F. Halzen. “Minimal cosmogenic neutrinos”. In: *Phys. Rev. D* 86.8, 083010 (Oct. 2012). DOI: 10.1103/PhysRevD.86.083010.
- [404] N. Aghanim et al. “Planck 2018 results. VI. Cosmological parameters”. In: *A&A* 641 (Sept. 2020), A6. DOI: 10.1051/0004-6361/201833910.
- [405] M. Aker et al. “Improved Upper Limit on the Neutrino Mass from a Direct Kinematic Method by KATRIN”. In: *Phys. Rev. Lett.* 123.22, 221802 (Nov. 2019). DOI: 10.1103/PhysRevLett.123.221802.
- [406] J. P. Kneller and G. C. McLaughlin. “Three flavor neutrino oscillations in matter: Flavor diagonal potentials, the adiabatic basis, and the CP phase”. In: *Phys. Rev. D* 80.5, 053002 (Sept. 2009). DOI: 10.1103/PhysRevD.80.053002.
- [407] I. Esteban et al. “The fate of hints: updated global analysis of three-flavor neutrino oscillations”. In: *J. High Energy Phys.* 2020.9 (Sept. 2020), p. 178. DOI: 10.1007/JHEP09(2020)178.
- [408] C. A. Argüelles, T. Katori, and J. Salvado. “Effect of New Physics in Astrophysical Neutrino Flavor”. In: *Phys. Rev. Lett.* 115.16, 161303 (Oct. 2015). DOI: 10.1103/PhysRevLett.115.161303.
- [409] P. Coppin. *Inice veto studies for the future IceCube-Gen2 neutrino observatory*. 2017. URL: <https://iihe.ac.be/sites/default/files/thesis-paul-coppin-icecube-master-2017pdf/thesis-paul-coppin-icecube-master-2017.pdf>.
- [410] M. Thomson. *Modern Particle Physics*. Modern Particle Physics. Cambridge University Press, 2013. ISBN: 9781107034266.
- [411] R. Gandhi et al. “Ultrahigh-energy neutrino interactions”. In: *Astropart. Phys.* 5.2 (Aug. 1996), pp. 81–110. DOI: 10.1016/0927-6505(96)00008-4.

- [412] A. Connolly, R. S. Thorne, and D. Waters. "Calculation of high energy neutrino-nucleon cross sections and uncertainties using the Martin-Stirling-Thorne-Watt parton distribution functions and implications for future experiments". In: *Phys. Rev. D* 83.11, 113009 (June 2011). DOI: 10.1103/PhysRevD.83.113009.
- [413] F. Vannucci. "Interactions of neutrinos with matter". In: *Prog. Part. Nucl. Phys.* 95 (July 2017), pp. 1–47. DOI: 10.1016/j.pnpnp.2017.03.003.
- [414] S. L. Glashow. "Resonant Scattering of Antineutrinos". In: *Phys. Rev.* 118.1 (Apr. 1960), pp. 316–317. DOI: 10.1103/PhysRev.118.316.
- [415] M. G. Aartsen et al. "Detection of a particle shower at the Glashow resonance with IceCube". In: *Nature* 591.7849 (Jan. 2021), pp. 220–224. DOI: 10.1038/s41586-021-03256-1.
- [416] P. A. Čerenkov. "Visible Radiation Produced by Electrons Moving in a Medium with Velocities Exceeding that of Light". In: *Phys. Rev.* 52.4 (Aug. 1937), pp. 378–379. DOI: 10.1103/PhysRev.52.378.
- [417] P. A. Čerenkov. "Visible luminescence of pure liquids under the influence of γ -radiation". In: *Dokl. Akad. Nauk SSSR* 2.8 (1934), pp. 451–454. DOI: 10.3367/UFNr.0093.196710n.0385.
- [418] C. Grupen et al. *Astroparticle Physics*. Springer Berlin Heidelberg, 2005. ISBN: 9783540276708.
- [419] I. M. Frank and I. E. Tamm. "Coherent visible radiation of fast electrons passing through matter". In: *Compt. Rend. Acad. Sci. URSS* 14.3 (1937), pp. 109–114. DOI: 10.3367/UFNr.0093.196710o.0388.
- [420] M. G. Aartsen et al. "Energy reconstruction methods in the IceCube neutrino telescope". In: *JINST* 9.3, P03009 (Mar. 2014). DOI: 10.1088/1748-0221/9/03/P03009.
- [421] M. Ahlers, K. Helbing, and C. Pérez de los Heros. "Probing particle physics with IceCube". In: *Eur. Phys. J. C* 78.11 (Nov. 2018), p. 924. DOI: 10.1140/epjc/s10052-018-6369-9.
- [422] L. Rädcl and C. Wiebusch. "Calculation of the Cherenkov light yield from low energetic secondary particles accompanying high-energy muons in ice and water with Geant4 simulations". In: *Astropart. Phys.* 38 (Oct. 2012), pp. 53–67. DOI: 10.1016/j.astropartphys.2012.09.008.
- [423] J. Álvarez-Muñiz et al. "The Giant Radio Array for Neutrino Detection (GRAND): Science and design". In: *Sci. China Phys. Mech.* 63.1, 219501 (Jan. 2020). DOI: 10.1007/s11433-018-9385-7.
- [424] G. A. Askaryan. "Excess Negative Charge of the Electron-Photon Shower and Coherent Radiation Originating from It. Radio Recording of Showers under the Ground and on the Moon". In: *J. Phys. Soc. Japan Supplement* 17 (Jan. 1962), p. 257.
- [425] S. Prohira et al. "The Radar Echo Telescope for Cosmic Rays: Pathfinder experiment for a next-generation neutrino observatory". In: *Phys. Rev. D* 104.10, 102006 (Nov. 2021). DOI: 10.1103/PhysRevD.104.102006.
- [426] R. S. Stanley and S. De Kockere. "Simulation and Optimisation for the Radar Echo Telescope for Cosmic Rays". In: *PoS ICRC2021*, 416 (2021). DOI: 10.22323/1.395.0416.
- [427] S. Prohira and K. D. de Vries. "Toward High Energy Neutrino Detection with the Radar Echo Telescope for Cosmic Rays (RET-CR)". In: *PoS ICRC2021*, 1082 (2021). DOI: 10.22323/1.395.1082.
- [428] G. A. Askaryan. "Self-focusing and Focusing of Ultrasound and Hypersound". In: *Sov. J. Exp. Theor. Phys. Lett.* 4 (Aug. 1966), p. 99.
- [429] R. Abbasi et al. "Background studies for acoustic neutrino detection at the South Pole". In: *Astropart. Phys.* 35.6 (Jan. 2012), pp. 312–324. DOI: 10.1016/j.astropartphys.2011.09.004.

- [430] R. Lahmann. “Acoustic Detection of Neutrinos: Review and Future Potential”. In: *Nucl. Part. Phys. Proc.* 273-275 (Apr. 2016), pp. 406–413. DOI: 10.1016/j.nuclphysbps.2015.09.059.
- [431] S. Bevan et al. “Study of the acoustic signature of UHE neutrino interactions in water and ice”. In: *Nucl. Instrum. Methods Phys. Res. A* 607.2 (Aug. 2009), pp. 398–411. DOI: 10.1016/j.nima.2009.05.009.
- [432] R. Lahmann. “Acoustic detection of high energy neutrinos in sea water: status and prospects”. In: *EPJ Web Conf.* Vol. 135. Mar. 2017, 06001. DOI: 10.1051/epjconf/201713506001.
- [433] M. G. Aartsen et al. “The IceCube Neutrino Observatory: instrumentation and online systems”. In: *JINST* 12.3 (Mar. 2017), P03012. DOI: 10.1088/1748-0221/12/03/P03012.
- [434] S. R. Klein. “IceCube: A Cubic Kilometer Radiation Detector”. In: *IEEE Trans. Nucl. Sci.* 56.3 (June 2009), pp. 1141–1147. DOI: 10.1109/TNS.2009.2015300.
- [435] M. H. Minh. “Reconstruction of Neutrino Events in IceCube using Graph Neural Networks”. In: *PoS ICRC2021*, 1044 (July 2021). DOI: 10.22323/1.395.1044.
- [436] R. Abbasi et al. “The IceCube data acquisition system: Signal capture, digitization, and timestamping”. In: *Nucl. Instrum. Methods Phys. Res. A* 601.3 (Apr. 2009), pp. 294–316. DOI: 10.1016/j.nima.2009.01.001.
- [437] R. Abbasi et al. “Calibration and characterization of the IceCube photomultiplier tube”. In: *Nucl. Instrum. Methods Phys. Res. A* 618.1-3 (June 2010), pp. 139–152. DOI: 10.1016/j.nima.2010.03.102.
- [438] J. L. Kelley and IceCube Collaboration. “Event triggering in the IceCube data acquisition system”. In: *AIP Conf. Proc.* 1630.1 (2014), pp. 154–157. DOI: 10.1063/1.4902795.
- [439] N. Whitehorn. “A Search for High-Energy Neutrino Emission from Gamma-Ray Bursts”. PhD thesis. The University of Wisconsin - Madison, May 2012. URL: <https://docushare.icecube.wisc.edu/dsweb/Get/Document-60879/thesis.pdf>.
- [440] C. L. Lawson and R. J. Hanson. *Solving Least Squares Problems*. Classics in Applied Mathematics. Society for Industrial and Applied Mathematics, 1995. ISBN: 9780898713565.
- [441] T. Kintscher. “Rapid Response to Extraordinary Events: Transient Neutrino Sources with the IceCube Experiment”. PhD thesis. Humboldt University, Berlin, Sept. 2020. DOI: 10.18452/21948.
- [442] M. D. Richman. “A Search For Muon Neutrinos Coincident With Gamma-Ray Bursts Using IceCube”. PhD thesis. University of Maryland, 2015. DOI: 10.13016/M2CS5W.
- [443] P. J. Huber. “Robust Estimation of a Location Parameter”. In: *The Annals of Mathematical Statistics* 35.1 (1964), pp. 73–101. DOI: 10.1214/aoms/1177703732.
- [444] M. G. Aartsen et al. “Improvement in fast particle track reconstruction with robust statistics”. In: *Nucl. Instrum. Methods Phys. Res. A* 736 (Feb. 2014), pp. 143–149. DOI: 10.1016/j.nima.2013.10.074.
- [445] D. Pandel. “Bestimmung von Wasser- und Detektorparametern und Rekonstruktion von Myonen bis 100 TeV mit dem Baikal- Neutrino teleskop NT-72”. PhD thesis. Humboldt University, 1996.
- [446] N. van Eijndhoven, O. Fadiran, and G. Japaridze. “Implementation of a Gauss convoluted Pandel PDF for track reconstruction in neutrino telescopes”. In: *Astropart. Phys.* 28.4-5 (Dec. 2007), pp. 456–462. DOI: 10.1016/j.astropartphys.2007.09.001.
- [447] J. Ahrens et al. “Muon track reconstruction and data selection techniques in AMANDA”. In: *Nucl. Instrum. Methods Phys. Res. A* 524.1-3 (May 2004), pp. 169–194. DOI: 10.1016/j.nima.2004.01.065.
- [448] M. Ackermann et al. “Optical properties of deep glacial ice at the South Pole”. In: *J. Geophys. Res. Atmos.* 111.D13 (2006). DOI: 10.1029/2005JD006687.

- [449] M. G. Aartsen et al. "Observation of the cosmic-ray shadow of the Moon with IceCube". In: *Phys. Rev. D* 89 (10 May 2014). DOI: 10.1103/PhysRevD.89.102004.
- [450] S. Philippen, T. Glüsenskamp, and S. Schindler. "Testing the Pointing of IceCube using the Moon Shadow in Cosmic-Ray Induced Muons". In: *PoS ICRC2021*, 1087 (2021). DOI: 10.22323/1.395.1087.
- [451] M. G. Aartsen et al. "Detection of the Temporal Variation of the Sun's Cosmic Ray Shadow with the IceCube Detector". In: *ApJ* 872.2 (Feb. 2019), p. 133. DOI: 10.3847/1538-4357/aaffd1.
- [452] H. Cramér. *Mathematical Methods of Statistics*. Goldstine Printed Materials. Princeton University Press, 1946. ISBN: 9780691080048.
- [453] C. R. Rao. "Information and the Accuracy Attainable in the Estimation of Statistical Parameters". In: *Bull. Calcutta Math. Soc.* 37 (1945), 81–91.
- [454] J. Lünemann. "Suche nach Dunkler Materie in Galaxien und Galaxienhaufen mit dem Neutrino teleskop IceCube". PhD thesis. Johannes Gutenberg University - Mainz, 2013. DOI: 10.25358/openscience-4219.
- [455] R. Abbasi et al. "Time-integrated Searches for Point-like Sources of Neutrinos with the 40-string IceCube Detector". In: *ApJ* 732.1 (May 2011), p. 18. DOI: 10.1088/0004-637X/732/1/18.
- [456] E. Pinat. "The IceCube Neutrino Observatory: search for extended sources of neutrinos and preliminary study of a communication protocol for its future upgrade". PhD thesis. Université Libre de Bruxelles, June 2017. URL: <https://iihe.ac.be/sites/default/files/thesis-elisa-pinat-icecube-phd-2017pdf/thesis-elisa-pinat-icecube-phd-2017.pdf>.
- [457] A. Gazizov and M. Kowalski. "ANIS: High energy neutrino generator for neutrino telescopes". In: *Comput. Phys. Commun.* 172.3 (Nov. 2005), pp. 203–213. DOI: 10.1016/j.cpc.2005.03.113.
- [458] A. M. Dziewonski and D. L. Anderson. "Preliminary reference Earth model". In: *Phys. Earth Planet. Inter.* 25.4 (1981), pp. 297–356. ISSN: 0031-9201. DOI: 10.1016/0031-9201(81)90046-7.
- [459] D. Chirkin and W. Rhode. "Muon Monte Carlo: A new high precision tool for muon propagation through matter". In: *2nd Workshop on Methodical Aspects of Underwater/Ice Neutrino Telescopes*. Aug. 2002, pp. 15–22.
- [460] J. H. Koehne et al. "PROPOSAL: A tool for propagation of charged leptons". In: *Comput. Phys. Commun.* 184.9 (Sept. 2013), pp. 2070–2090. DOI: 10.1016/j.cpc.2013.04.001.
- [461] C. Dmitry. "Photon tracking with GPUs in IceCube". In: *Nucl. Instrum. Methods Phys. Res. A* 725 (2013), pp. 141–143. ISSN: 0168-9002. DOI: 10.1016/j.nima.2012.11.170.
- [462] IceCube Collaboration. *DOMLauncher Project*. 2020. URL: <https://docs.icecube.aq/icetray/main/projects/DOMLauncher/index.html> (visited on Nov. 22, 2021).
- [463] M. Voge. "Searches for Neutrinos from Supernovae Using Cherenkov In-Ice Detectors". PhD thesis. Bonn University, Sept. 2016. URL: <https://hdl.handle.net/20.500.11811/7138>.
- [464] M. G. Aartsen et al. "The IceCube realtime alert system". In: *Astropart. Phys.* 92 (June 2017), pp. 30–41. DOI: 10.1016/j.astropartphys.2017.05.002.
- [465] P. Correa, K. D. de Vries, and N. van Eijndhoven. "IceCube Search for High-Energy Neutrinos from Ultra-Luminous Infrared Galaxies". In: *PoS ICRC2021*, 1115 (2021). DOI: 10.22323/1.395.1115.
- [466] E. A. Friedman. "All-Sky Search for Neutrinos Correlated with Gamma-Ray Bursts in Extended Time Windows Using Eight Years of IceCube Data". PhD thesis. University of Maryland, 2021. DOI: 10.13016/yqa1-0vmh.

- [467] R. Abbasi et al. "Search for Muon Neutrinos from Gamma-ray Bursts with the IceCube Neutrino Telescope". In: *ApJ* 710.1 (Feb. 2010), pp. 346–359. DOI: 10.1088/0004-637X/710/1/346.
- [468] R. Abbasi et al. "Limits on Neutrino Emission from Gamma-Ray Bursts with the 40 String IceCube Detector". In: *Phys. Rev. Lett.* 106.14, 141101 (Apr. 2011). DOI: 10.1103/PhysRevLett.106.141101.
- [469] K. J. Meagher. "Limits on Neutrino Emission from Gamma-Ray Bursts with the 40 String IceCube Detector". PhD thesis. University of Maryland, 2012. URL: <http://hdl.handle.net/1903/12644>.
- [470] D. Diederix. *Model Independent Search for Neutrinos from Gamma Ray Bursts with the IceCube Detector*. Dec. 2010. URL: <https://iihe.ac.be/sites/default/files/thesis-dennis-diederix-icecube-master-2010pdf/thesis-dennis-diederix-icecube-master-2010.pdf>.
- [471] R. Abbasi et al. "An absence of neutrinos associated with cosmic-ray acceleration in γ -ray bursts". In: *Nature* 484.7394 (Apr. 2012), pp. 351–354. DOI: 10.1038/nature11068.
- [472] M. G. Aartsen et al. "Search for Prompt Neutrino Emission from Gamma-Ray Bursts with IceCube". In: *ApJ* 805.1 (May 2015), p. L5. DOI: 10.1088/2041-8205/805/1/L5.
- [473] R. E. Hellauer. "An all-sky, three-flavor search for neutrinos from gamma-ray bursts with the icecube neutrino observatory". PhD thesis. University of Maryland, Jan. 2015. DOI: 10.13016/M27D9C.
- [474] J. Casey. "Search for high energy GRB neutrinos in IceCube". PhD thesis. Georgia Institute of Technology, Aug. 2015. URL: <http://hdl.handle.net/1853/53839>.
- [475] B. Volker. "Search for low energetic neutrino signals from Galactic Supernovae and collisionally heated Gamma-Ray Bursts with the IceCube Neutrino Observatory". PhD thesis. Johannes Gutenberg-Universität Mainz, 2017. DOI: 10.25358/openscience-1372.
- [476] L. Brayeur. "Search for High-Energy Neutrinos Associated with Long Gamma Ray Bursts using the IceCube Detector". PhD thesis. Vrije Universiteit Brussel, Nov. 2015. URL: <https://iihe.ac.be/sites/default/files/thesis-lionel-brayeur-icecube-phd-2015pdf/thesis-lionel-brayeur-icecube-phd-2015.pdf>.
- [477] J. Neyman, E. S. Pearson, and K. Pearson. "IX. On the problem of the most efficient tests of statistical hypotheses". In: *Philos. Trans. Royal Soc. A* 231.694-706 (1933), pp. 289–337. DOI: 10.1098/rsta.1933.0009.
- [478] T. P. Li and Y. Q. Ma. "Analysis methods for results in gamma-ray astronomy." In: *ApJ* 272 (Sept. 1983), pp. 317–324. DOI: 10.1086/161295.
- [479] J. Braun et al. "Methods for point source analysis in high energy neutrino telescopes". In: *Astropart. Phys.* 29.4 (May 2008), pp. 299–305. DOI: 10.1016/j.astropartphys.2008.02.007.
- [480] R. S. Pilla, C. Loader, and C. C. Taylor. "New Technique for Finding Needles in Haystacks: Geometric Approach to Distinguishing between a New Source and Random Fluctuations". In: *Phys. Rev. Lett.* 95.23 (Dec. 2005), p. 230202. DOI: 10.1103/PhysRevLett.95.230202.
- [481] D. Bose et al. "Bayesian approach for counting experiment statistics applied to a neutrino point source analysis". In: *Astropart. Phys.* 50 (Dec. 2013), pp. 57–64. DOI: 10.1016/j.astropartphys.2013.09.009.
- [482] P. C. Correa. *Comparison of statistical methods to evaluate the IceCube discovery potential for steady point sources*. June 2017. URL: <https://iihe.ac.be/sites/default/files/thesis-pablo-correa-icecube-master-2017pdf/thesis-pablo-correa-icecube-master-2017.pdf>.

- [483] M. Casier. “Search for High-Energy Neutrino Production in Short Gamma Ray Bursts with the IceCube Neutrino Observatory”. PhD thesis. Vrije Universiteit Brussel, Sept. 2015. URL: <https://iihe.ac.be/sites/default/files/thesis-martin-casier-icecube-phd-2015pdf/thesis-martin-casier-icecube-phd-2015.pdf>.
- [484] A. Goldstein. personal communication. Dec. 27, 2019.
- [485] S. S. Wilks. “The Large-Sample Distribution of the Likelihood Ratio for Testing Composite Hypotheses”. In: *Ann. Math. Stat.* 9.1 (1938), pp. 60–62. DOI: 10.1214/aoms/1177732360.
- [486] F. Bradascio. *ns bias for large catalogues*. 2020. URL: https://drive.google.com/file/d/1MY5A-nI3fZrEy_H62m9-sKK40I_Ype2W/view (visited on Feb. 24, 2020).
- [487] R. E. Maunu. “A Search for Muon Neutrinos in Coincidence with Gamma-Ray Bursts in the Southern Hemisphere Sky Using the IceCube Neutrino Observatory”. PhD thesis. University of Maryland, 2016. DOI: 10.13016/M2449P.
- [488] K. Hurley et al. “IPN triangulation of GRB 141029B”. In: *GCN 16988* (Oct. 2014), p. 1. URL: <https://gcn.gsfc.nasa.gov/gcn3/16988.gcn3>.
- [489] P. D’Avanzo et al. “A complete sample of bright Swift short gamma-ray bursts”. In: *MNRAS* 442.3 (Aug. 2014), pp. 2342–2356. DOI: 10.1093/mnras/stu994.
- [490] P. D’Avanzo. “Short gamma-ray bursts: A review”. In: *J. High Energy Phys.* 7 (Sept. 2015), pp. 73–80. DOI: 10.1016/j.jhep.2015.07.002.
- [491] M. Ahlers and F. Halzen. “Pinpointing extragalactic neutrino sources in light of recent IceCube observations”. In: *Phys. Rev. D* 90.4, 043005 (Aug. 2014). DOI: 10.1103/PhysRevD.90.043005.
- [492] D. N. Spergel et al. “Three-Year Wilkinson Microwave Anisotropy Probe (WMAP) Observations: Implications for Cosmology”. In: *ApJS* 170.2 (June 2007), pp. 377–408. DOI: 10.1086/513700.
- [493] R. Zanin et al. “CTA – the World’s largest ground-based gamma-ray observatory”. In: *PoS ICRC2021*, 5 (2021). DOI: 10.22323/1.395.0005.
- [494] A. Carosin, A. López-Oramas, and F. Longo. “The Cherenkov Telescope Array transient and multi-messenger program”. In: *PoS ICRC2021*, 736 (2021). DOI: 10.22323/1.395.0736.